

Science

Science
Advances

Science
Immunology

Science
Robotics

Science
Signaling

Science
Translational
Medicine

[SPECIAL
EDITION]

NEUROSCIENCE



aaas.org/science-journals

RISING STAR AWARD IN BRAIN SCIENCE TECHNOLOGY



INTERNATIONAL CALL FOR SUBMISSIONS

The Mahoney Institute for Neurosciences (MINS) at the University of Pennsylvania is proud to announce its annual call for submissions for the **Rising Star Award** in neuroscience research.

The **Rising Star Award** celebrates the convergence on Penn's campus of multiple disciplines – from advanced imaging and computation to bioengineering – in support of the **“Year of Brain Science Technology,”** and it honors a young researcher for outstanding contributions to Brain Science Technology with a USD 10,000 honorarium at the **36th Annual MINS Retreat and Symposium on April 28th, 2020.**

“Technological advances often precipitate paradigm shifts in knowledge. Novel methods for measuring the living brain with ever higher spatial and temporal resolution are providing new insights into brain organization and function. The 2020 MINS Rising Star Award will honor a researcher whose focus on the latest acquisition and analysis methods is expanding the frontiers of basic and clinical neuroscience research.”

– John A. Detre, M.D., Professor and Vice Chair for Research,
Department of Neurology, and Director of the new Brain Science Center at Penn

-
- Eligibility**
- Researchers who received their first advanced degree, such as the Ph.D., in 2006 or more recently are invited to submit an entry.
 - Winner must be able to travel to the University of Pennsylvania to present a research seminar.

- Award**
- In addition to the USD 10,000 personal honorarium, the award recipient will present a research seminar at the symposium.
 - Also at the symposium, Polina Anikeeva, Ph.D., of MIT will give the Sprague Lecture, and Anthony Zador, M.D., Ph.D., of the Cold Spring Harbor Laboratory, will give the Adler Lecture.

- Submission**
- Applicants should submit a single PDF file with a one-page description of their contribution to Brain Science Research, full curricula vitae, and the names of three references.
 - The deadline for submissions is **December 10, 2019** to **MINSRisingStarAward@lists.upenn.edu**.
More information can be found at www.med.upenn.edu/ins.

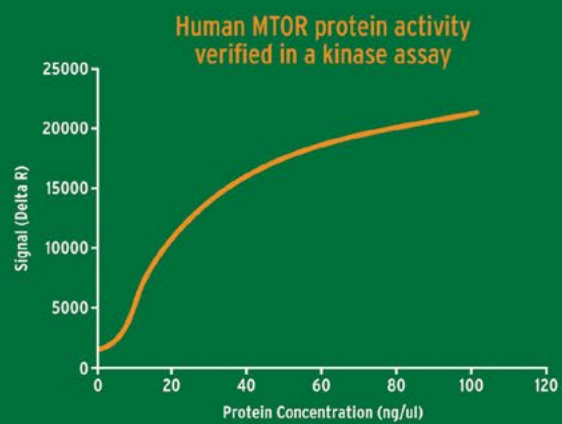
10,000 Human Proteins Made from Human Cells

Better Preservation
of PTMs and
Functions



The Largest Collection of Mammalian Cell-Derived Proteins

- Protein functional studies
- Compound screening
- Protein microarrays
- Immunogens for antibody production
- Assay standards: ELISA, Mass Spec, and more



origene.com/protein

© 2019 OriGene Technologies, Inc. All Rights Reserved.

Gain unique insights for your scientific discoveries.



ZEISS Microscopes for Life Sciences

Choose the ideal imaging technologies for your scientific question. The unique ZEISS portfolio of light, electron, ion and X-ray microscopes lets you combine complementary views to gain new insights into your sample's biology.

zeiss.com/life-sciences



Seeing beyond

SPECIAL EDITION: Neuroscience

Select research published in *Science*, *Science Advances*, *Science Immunology*, *Science Signaling*, *Science Robotics*, and *Science Translational Medicine*

All *Science* family of journals are Green Open Access with the exception of *Science Advances* which is Gold.



This booklet features research articles from all six journals of the *Science* family. These articles cover a range of topics, including perception, behavior, neuroinflammation, neuroimaging, neurodevelopment, neuroprosthetics, and neurodegenerative diseases.

Image: Hybrid Medical/Science Source

Science | AAAS

Science is a leading outlet for scientific news, commentary, and cutting-edge research. The journal publishes original peer-reviewed research across the sciences, with articles that consistently rank among the most cited in the world.

Editors

Lisa D. Chong, Ph.D.
Valda J. Vinson, Ph.D.
Jake S. Yeston, Ph.D.

Neuroscience Editors

Pamela J. Hines, Ph.D.
Stella Hurtley, Ph.D.
Peter Stern, Ph.D.

Science Advances | AAAS OPEN ACCESS

Science Advances is the digital, open access expansion of *Science* magazine. The journal publishes significant, innovative original research that advances the frontiers of science across a broad range of disciplines, from bioscience and medicine to neuroscience, physics, ecology, and material sciences.

Managing Editor

Philippa J. Benson, Ph.D.

Editor

Ali Shalatifard, Ph.D.

Deputy Editors

Lynden Archer, Ph.D.
Julia Chan, Ph.D.
Aaron Clauset, Ph.D.
Juan de Pablo, Ph.D.
Dale Dorset, Ph.D.
Sarah Fortune, M.D.
Karen Gleason, Ph.D.
Kip Hodges, Ph.D.
Jeremy Jackson, Ph.D.

Jonathan Katz, Ph.D.
Kevin LaBar, Ph.D.
Shahid Naeem, Ph.D.
Nicholas Peppas, Ph.D.
John Rogers, Ph.D.
Leslie Vosshall, Ph.D.
Philip Yeagle, Ph.D.
Warren Warren, Ph.D.

Science Immunology | AAAS

Science Immunology publishes original, peer-reviewed, science-based research articles that report critical advances in all areas of immunological research, including important new tools and techniques.

Chief Scientific Advisors

Abul K. Abbas, M.D.
University of California, San Francisco
Federica Sallusto, Ph.D.
Università della Svizzera Italiana

Editor

Ifor Williams, M.D., Ph.D.

Editorial Team

Anand Balasubramani, Ph.D.



Editor-in-Chief

Jeremy Berg, Ph.D.

Science family of journals, AAAS

Science Robotics | AAAS

Science Robotics publishes original, peer-reviewed, science and engineering-based research articles that advance the field of robotics bearing the quality hallmark of the *Science* family of journals.

Managing Editor

Trista Wagoner, M.A.

Editorial Team

Howie Choset, Ph.D.
Steve Collins, Ph.D.
Peer Fischer, Ph.D.
Ken Goldberg, Ph.D.
Neil Jacobstein

Editor

Guang-Zhong Yang, Ph.D.

Danica Kragic, Ph.D.
Cecilia Laschi, Ph.D.
Robin Murphy, Ph.D.
Bradley Nelson, Ph.D.
Robert Wood, Ph.D.

Science Signaling | AAAS

Science Signaling publishes peer-reviewed, original research investigating cell signaling that underlies physiology and disease, on the molecular, cellular, intercellular and organismal levels.

Chief Scientific Editor

Michael B. Yaffe, M.D., Ph.D.
Massachusetts Institute of Technology

Editor

John F. Foley, Ph.D.

Deputy Editor

Wei Wong, Ph.D.

Editorial Team

Leslie K. Ferrarelli, Ph.D.
Annalisa M. VanHook, Ph.D.
Erin R. Williams, Ph.D.

Science Translational Medicine | AAAS

Science Translational Medicine is an interdisciplinary journal that publishes translational research with impact for human health that fills the knowledge gaps between preclinical studies and clinical applications.

Chief Scientific Advisors

Elazer R. Edelman, M.D., Ph.D.
Massachusetts Institute of Technology

Garret FitzGerald, M.D.

University of Pennsylvania

Editor

Orla M. Smith, Ph.D.

Editorial Team

Catherine A. Charneski, Ph.D.
Caitlin A. Czajka, Ph.D.
Mattia Maroso, Ph.D.
Yevgeniya Nusinovich, M.D., Ph.D.
Lindsey Pujanandez, Ph.D.

Learn more and submit your research today: aaas.org/science-journals

NO MORE NEEDLESS INJECTIONS



(Actual size, 100 µl)



One and done

ALZET® Osmotic Pumps are small infusion pumps inserted at the beginning of your study and then, that's it. There's no dosing schedule. No repeated injections. Just a continuous, predictable release of your test agent for the entire study. Days. Nights. Even weekends. Anywhere from one day to six weeks. With no external connections to monitor and less need for handling, it's less stress for you and your lab animals. Learn more about ALZET Osmotic Pumps and just how needless injections can be at alzet.com.

alzet[®]
OSMOTIC PUMPS

Find out more at
alzet.com

VISIT US AT
EXHIBIT
#904

A product of
DURECT

©2019 DURECT Corporation
All Rights Reserved

IN THIS BOOKLET

Science

8 REPORT

Schema cells in the macaque hippocampus
P. Baraduc *et al.* (S. Wirth)

13 REPORT

Prenatal activity from thalamic neurons governs the emergence of functional cortical maps in mice
Noelia Antón-Bolaños *et al.* (Guillermina López-Bendito)

Science Advances

17 RESEARCH ARTICLE

Sleepmore in Seattle: Later school start times are associated with more sleep and better performance in high school students
Gideon P. Dunster *et al.* (Horacio O. de la Iglesia)

24 RESEARCH ARTICLE

Human consciousness is supported by dynamic complex patterns of brain signal coordination
A. Demertzi *et al.* (J. D. Sitt)

Science Immunology

36 RESEARCH ARTICLE

Conventional DCs sample and present myelin antigens in the healthy CNS and allow parenchymal T cell entry to initiate neuroinflammation

Sarah Mundt *et al.* (Burkhard Becher)

46 REVIEW

The anatomy and immunology of vasculature in the central nervous system

Panagiotis Mastorakos and Dorian McGavern



Science Robotics

60 RESEARCH ARTICLE

Noninvasive neuroimaging enhances continuous neural tracking for robotic device control

B. J. Edelman *et al.* (B. He)

73 RESEARCH ARTICLE

Long-term implant of intramuscular sensors and nerve transfers for wireless control of robotic arms in above-elbow amputees

S. Salminger *et al.* (O. C. Aszmann)

Science Signaling

82 RESEARCH ARTICLE

Pharmacologic inhibition of LIMK1 provides dendritic spine resilience against β-amyloid

Benjamin W. Henderson *et al.* (Jeremy H. Herskowitz)

94 RESEARCH ARTICLE

L-Serine dietary supplementation is associated with clinical improvement of loss-of-function *GRIN2B*-related pediatric encephalopathy

David Soto *et al.* (Xavier Altafaj)

Science Translational Medicine

109 RESEARCH ARTICLE

Reduced non-rapid eye movement sleep is associated with tau pathology in early Alzheimer's disease

Brendan P. Lucey *et al.* (David M. Holtzman)

122 RESEARCH ARTICLE

A farnesyltransferase inhibitor activates lysosomes and reduces tau pathology in mice with tauopathy

Israel Hernandez *et al.* (Kenneth S. Kosik)

Publisher/Science family of journals: Bill Moran

AD/Business Development: Justin Sawyers

Marketing Manager: Shawana Arnold

Layout/Design: Kim Huynh

Sponsorship Opportunities:

Tracy Holmes, *Science*

tholmes@science-int.co.uk | (44) 1223 326525 ext 5525

1200 New York Ave NW, Washington DC 20005

Learn more and submit your research today: aaas.org/science-journals

© 2019 by The American Association for the Advancement of Science. All Rights Reserved.

NEUROSCIENCE

Schema cells in the macaque hippocampus

P. Baraduc^{1,2*}, J.-R. Duhamel¹, S. Wirth^{1*}

Concept cells in the human hippocampus encode the meaning conveyed by stimuli over their perceptual aspects. Here we investigate whether analogous cells in the macaque can form conceptual schemas of spatial environments. Each day, monkeys were presented with a familiar and a novel virtual maze, sharing a common schema but differing by surface features (landmarks). In both environments, animals searched for a hidden reward goal only defined in relation to landmarks. With learning, many neurons developed a firing map integrating goal-centered and task-related information of the novel maze that matched that for the familiar maze. Thus, these hippocampal cells abstract the spatial concepts from the superficial details of the environment and encode space into a schema-like representation.

The human hippocampus is home to concept cells that represent the meaning of a stimulus—a person or an object—rather than its immediate sensory properties (1). This invariance involves an abstraction from the percept to extract only relevant features and attribute an explicit meaning to them (2, 3). Whereas concept cells are emblematic of the human hippocampus, place cells, which fire when the animal is in a particular place, are typical of rodent hippocampus (4). Place and concept cells share properties, such as stimulus selectivity. Concept cells are specific to one person or object, and place cells are selective to one position within an environment. Furthermore, place cells identified in one environment are silent in a different environment (5). Exceptions to this likely stem from resemblance or common elements across spaces (6–10). However, in humans and rodents, it is unknown whether hippocampal cells can represent a spatial abstraction. We tested this possibility in monkeys, in which hippocampal neurons develop high-level spatial representations (11). We hypothesized that spatial abstraction involves elementary schemas (12, 13), extracting commonalities across experiences beyond superficial details to signify interrelations among elements (14, 15). We accordingly trained macaques to explore a virtual maze with a joystick in search of an invisible reward whose location had to be triangulated with respect to visible landmarks (Fig. 1, A and B, and fig. S1). After monkeys were proficient in this familiar maze (more than 90% correct, fig. S2), they were tested in an isomorphic novel maze bearing never-before-seen landmarks (Fig. 1B), presented for each session after or before the familiar maze. Thereupon, animals rapidly displayed flexible spatial inference and rapidly reached good performance [figs. S2 and S3 and (11)], indicating that they had constructed a

schema of the task (fig. S3) (16) rather than a series of stimulus response associations (learning set). We tested whether this process results in environment-specific memories or in a single schema for both spaces.

We compared the activity of 101 cells active in both environments out of 189 hippocampal cells (Fig. 1C). We first examined neural activity (17) mapped in two ways: as a function of animal position and as a function of task-related state (Fig. 1D). The latter parses navigation behavior into all the possible action trajectories (rotation, translation) as a function of the virtual head orientation. This conjunctive variable better captures the coding of hippocampal cells than any single parameter such as position, direction, or point of gaze (11).

Overall, 70 cells (69.3%) exhibited a significant information content (IC) in at least one environment (familiar or novel) and map type (position or state space). Approximately half of the cells ($N = 30$) coded only one environment, whereas a proportion significantly higher than chance ($N = 40$) coded both familiar and novel environments in at least one map type ($P < 10^{-4}$, chi-square test; Fig. 1E). Thus, although many cells discriminated between the different environments, consistent with observed remapping in the rodent (5, 18), others participated in the representation of both environments. This afforded us a systematic comparison of their activity profiles across mazes.

A subpopulation of cells active in both environments showed similar firing when their maps were realigned with respect to reward position. Figure 1F illustrates the individual maps of four cells in position and state spaces. Unlike cells exhibiting a discrete place field, these cells displayed a complex pattern of activity in position and state space that was similar in both environments. We term these neurons “schema cells,” because reward-centered map similarity reflects a conceptual knowledge of space structure: Reward was not signaled by specific cues but had to be triangulated from landmarks. Similarly, cell activity was not anchored to specific stimuli or events but organized by knowledge of the maze layout. Thus, in both environments, cells fired in corre-

Copyright © 2019
The Authors, some
rights reserved;
exclusive licensee
American Association
for the Advancement
of Science. No claim
to original U.S.
Government Works.

sponding parts of the animal’s trajectory in the task. We quantified these task-situated similarities by computing spatial correlations between the maps. Because processes linked to reward expectation and consumption could affect our analysis, we excluded spikes recorded in the period from -500 to $+1500$ ms around reward delivery. For neurons with significant IC in at least one of their neural maps, familiar and novel maps were significantly correlated in 32.3% ($N = 20$) of cells when computed in state space and in 30.7% ($N = 19$) of cells when computed in position space (all $P < 10^{-4}$, Fig. 1G). To further investigate the stability of the created schema, we recorded a subset of cells while one animal learned two successive novel environments. Position and state-space neural maps were also significantly closely correlated between two different novel environments (fig. S4).

We next examined alternative explanations. First, if cells were responsive to visual elements (paths, grass, or sky) shared between environments, then those responses, even though not informative for reward position, could cause the observed homologies. Because these elements obeyed a fivefold symmetry, correlations should be high for maps rotated by any multiple of 72° . Although Fig. 1F illustrates such an example (cell K-40226/11), observing significant correlations for all rotated versions of a neural map (even without Bonferroni correction) was actually rare (see hatching in Fig. 1G). Therefore, the familiar-novel correlations went beyond simple superficial geometrical similarity and were more deeply informed by the reward location with respect to other cues.

Next, to further ascertain whether the correlations derived from a common spatial concept rather than from apparent visual cues, we analyzed cell activity as a function of the animal’s instantaneous point of regard (point-of-gaze maps; Fig. 2, A and B). The neurons with significant IC in their point-of-gaze neural maps did not encode both environments more often than expected by chance ($P = 0.27$, chi-square test, Fig. 2E). Moreover, their maps were less similar across environments: Only 15.4% of the cells displayed a significant correlation between familiar and novel ($P = 0.0016$, Fig. 2F). Furthermore, the greater specificity of the firing patterns for each environment was not caused by a systematic difference in visual exploration behavior in novel compared to familiar: The behavioral gaze-point density maps were comparable in the two environments, both overall (Fig. 2C) and when articulated by behavioral epochs (Fig. 2D). This lower correlation of neural point-of-gaze maps is an additional indication that visual elements shared across the two environments did not drive the map correlations. More fundamentally, it is consistent with our interpretation of schema cells, because spatial concepts do not depend on view.

We also pursued the possibility that correlations were artifacts of overlooked elements of the virtual world or of the experimental setup. If so, correlations should be strong from the start of the session and should not evolve with learning.

¹Institut des Sciences Cognitives Marc Jeannerod, CNRS UMR 5229, Université Claude Bernard Lyon 1, 67 Boulevard Pinel, 69675 Bron, France. ²GIPSA-lab, CNRS UMR 5216, Grenoble-INP, Université Grenoble-Alpes, 38000 Grenoble, France.

*Corresponding author. Email: pierre.baraduc@gipsa-lab.fr (P.B.); sylvia.wirth@isc.cnrs.fr (S.W.)

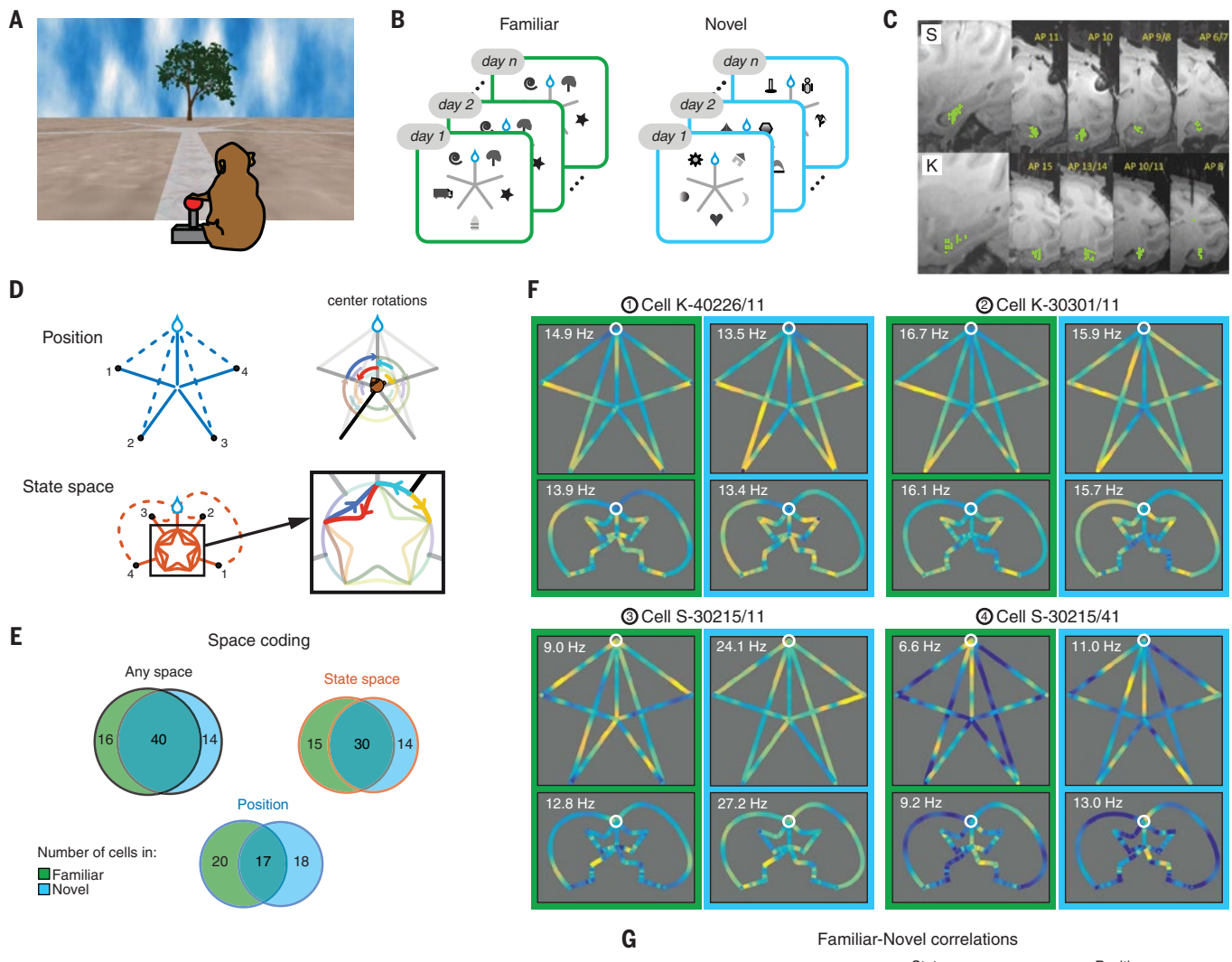


Fig. 1. Hippocampal neurons show correlated activity for two functionally equivalent environments. (A) Task setup. The animal viewed the screen in stereopsis through projector-synchronized shutter goggles and virtually moved in the three-dimensional maze via a joystick. **(B)** Familiar and novel mazes. Each day, the monkey searched for the hidden reward (depicted as a blue drop of liquid) in a familiar maze (left, green outline) and a novel maze (right, cyan outline). Landmarks of a novel environment were only present in one session. **(C)** Anatomical MRI images showing the location of the recording sites (green dots) in monkeys S and K. Left panels: Sagittal section at 13 mm lateral from midline showing the recording sites throughout the hippocampus. Right panels: Coronal sections at four antero-posterior locations with respect to interaural line, in mm. **(D)** Correspondence between position and state space. The state-space graph is laid out so that a state position relative to the center aligns with the direction of the current field of view of the animal. Dashed lines indicate passive return paths. Colored arrows on the right indicate the possible rotations of the animal in the center of the maze, viewed in the physical space (top) or in the state space (bottom). **(E)** Number of cells with significant IC in familiar, novel, or both environments, as a function of decoding space. **(F)** Four schema cells showing similar activity maps in the familiar (left, green outline) and novel environments (right, cyan outline) in position (top) and state-space (bottom) coordinates. Color scale ranges from blue (minimum activity) to yellow (peak activity). For each cell, the peak firing rate is indicated. White circles represent reward location. In both environments, cell 1 fires more on the extremity of the arms, cell 2 fires more on the northwest arm, cell 3 fires more on the second turn toward the reward goal, and cell 4 has a high activity for left turns in the center. **(G)** Correlations between neural maps in the familiar and novel environments. (Left) About a third of neural maps were correlated between familiar and novel mazes (hachures show cells with map correlations insensitive to rotation). (Middle and Right) Distribution of map correlation coefficients in position and state space (dark orange and dark blue). The histogram highlights significant positive correlations (light orange and light blue) and negative correlations (black). The gray outline indicates the distribution of correlations for the random surrogate datasets (scale on right).

Alternatively, if neural map similitude reveals a common space concept, learning should be accompanied by an increase in map correlation. We binned trials longitudinally across the novel session, from the moment performance rose above chance (fig. S2). The structure of these neural maps

tended to converge across trials toward the familiar map (Fig. 3A, four example cells in position or state spaces). Over the population of neurons encoding both environments in either position or state space, the correlation between familiar and novel maps significantly increased across trials

(Fig. 3, left panel of B and C). A similar increase was not observed in cells that coded both environments in point of gaze, as expected if these cells represented either some elements common to the two mazes (which, by design, bore no spatial information) or some maze-specific feature. Cells that significantly encoded only one environment also displayed no such trend (right panel of Fig. 3B), ruling out a nonspecific change. This convergence of representations was not due to an increase of spatial information (Fig. 3D), nor was it mirrored in a significant increase of the success rate (Fig. 3D).

Finally, we explored whether the map correlations reflected (i) only a reward-centric self-positioning or (ii) an isomorphism between more elaborated task-informed representations. In contrast to the position maps, the state-space maps differentiate activity in the central choice point of the maze according to view orientation, rotation direction, and task context (an initial center rotation versus a later one). The higher correlation of state-space maps (fig. S5; Wilcoxon test, $P = 0.024$) suggests that a task-situated representation of space tended to be shared across environments. Thus, this schematic representation probably encompassed dimensions other than physical space and assimilated task-related internal variables, such as present and future action.

In sum, our data show that whereas the majority of primate hippocampal neurons displayed environment-specific activity [“remapping,” (19)], about a third of hippocampal neurons displayed components that generalized across environments. This pattern is apparent when activity is analyzed in position or state space, but less so according to point of gaze. Thus, activity was not dominated by what the animal fixated but rather by an awareness of situation with respect to the goal, that is, a schema.

The role of the hippocampus in schema formation and updating has been shown in the rat by lesion and inactivation studies (14, 20, 21) during learning of spatially arranged odor-location pairs. Now, our results indicate that generic spatial or task schemas extracted across repeated experiences are encoded by primate hippocampal cells. The convergence of schema cell activity through learning is consistent with the role of schemas in organizing past experiences (12, 13) and in promoting knowledge acquisition (14, 15). That animals needed months of training to master the familiar environment but thereafter needed only a dozen trials to reach a similar proficiency in novel mazes attests to the advantage offered by such conceptual generalization. This generalization goes beyond the contextual modulation of rat place cells depending on trajectories and/or goal (22–24). When present in rodents, spatial invariance across spaces stemmed from sensory similarity (8, 9, 18). Although rat hippocampal cells may encode schemas in the sense of relational representations (10, 25), their coding for a schema of spatial structure across environments (that is, spatial abstraction) remains to be demonstrated.

In humans, conceptual coding in the hippocampus has been shown for social or object

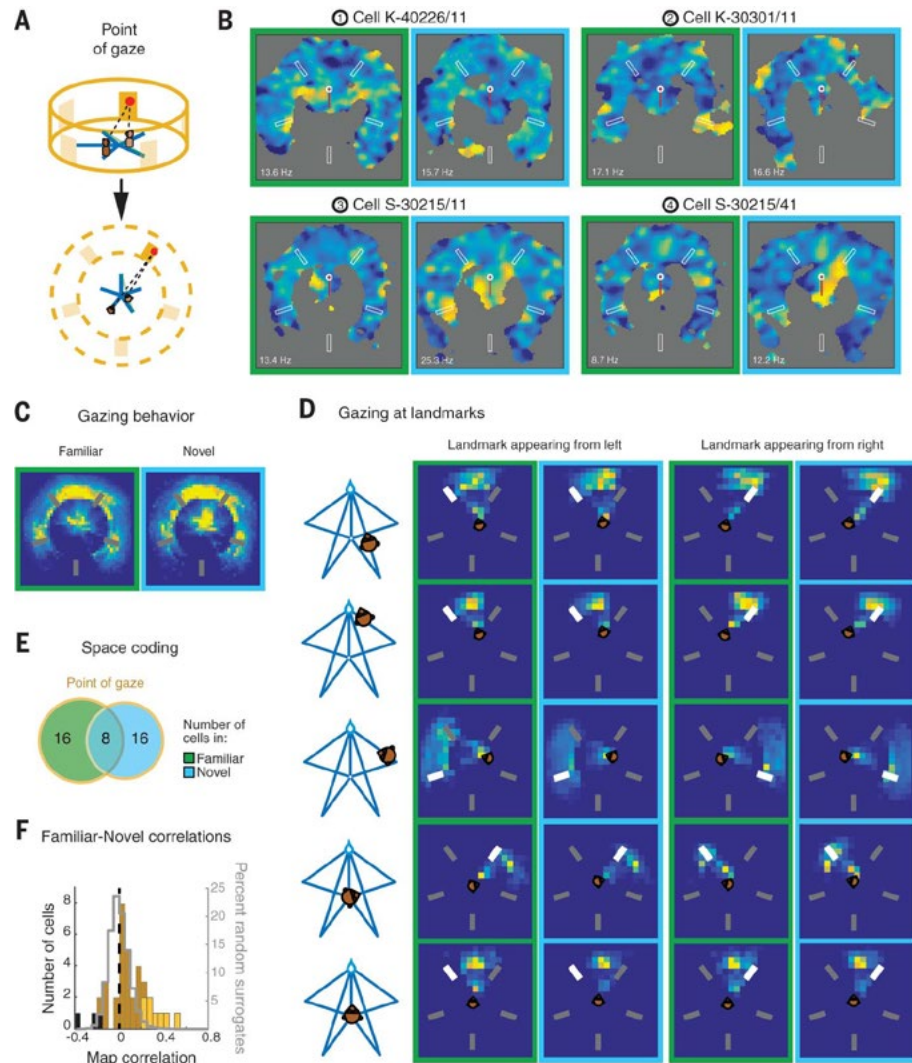


Fig. 2. Neural activity maps with respect to point of gaze showed little correlation, though gazing behavior did. (A) Geometrical projection used for the point-of-gaze maps. (Top) Definition of the animal's point of gaze (red dot) in three-dimensional space. Brown rectangles indicate landmark positions. When directed above the ground and not on a landmark, the point of gaze was ascribed to an invisible wall at landmark distance from the maze center. Two different positions of the monkey are illustrated. (Bottom) Projected view from above used for plotting the gaze-referred neural maps (B). (B) Neural activity maps of the same four cells as in Fig. 1F, as a function of point of gaze in each environment (familiar, green outline; novel, cyan outline). Open white rectangles, landmark locations; red bar, path leading to the reward from the maze center. Other graphical conventions as in Fig. 1F. (C) Density of gaze position in familiar or novel environments. Color coding is the same as in (B) but applied to point-of-gaze density instead of firing rate. Gray rectangles, landmarks. (D) Density of gaze position at the time of landmark appearance in the field of view, separated by behavioral epoch (or edge on state-space graph) and side of landmark appearance for familiar and novel environments. The left column illustrates the situation when landmarks appear on the left. Color coding is the same as in (C). White rectangle, appearing landmark. (E) Number of cells with significant IC in familiar or novel environment. (F) Distribution of the correlation coefficients. The significant positive correlations are shown in light brown. Other graphical conventions are the same as in Fig. 1G.

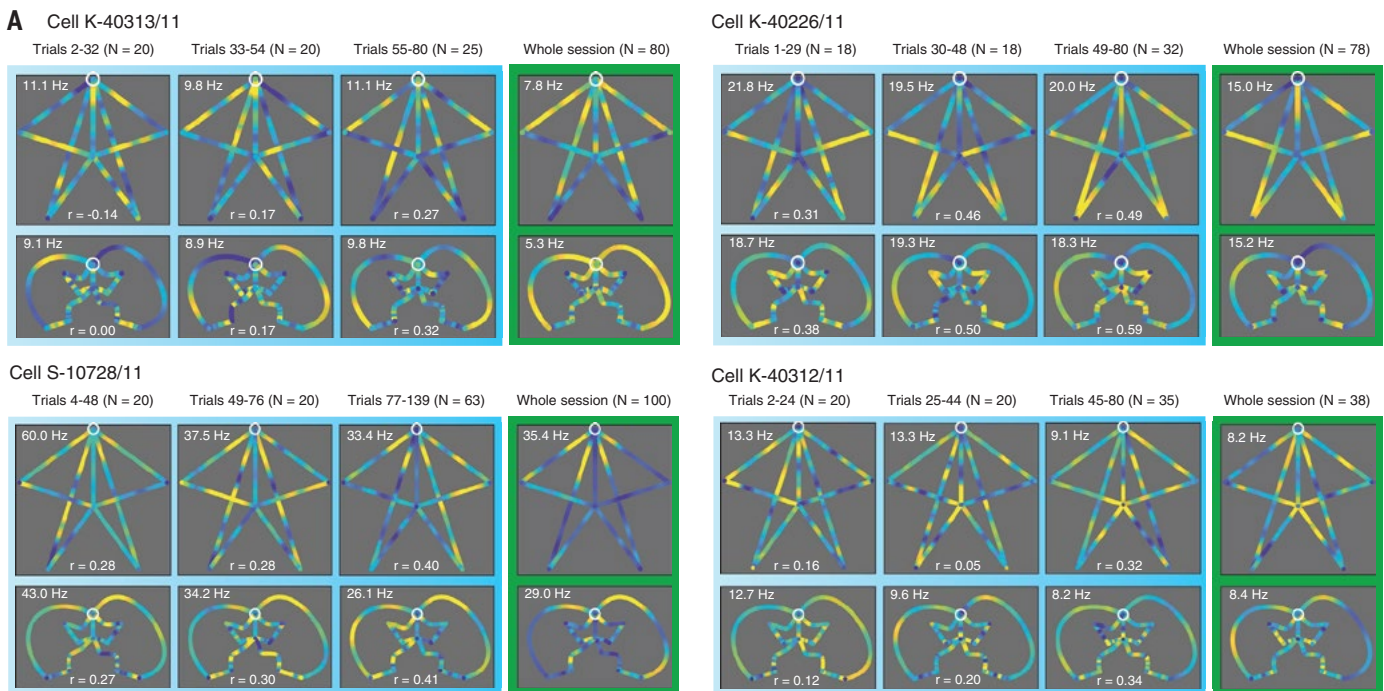


Fig. 3. Correlation between familiar and novel mazes increased as a function of learning.

(A) Activity maps of four example cells, computed at three different stages of learning (cyan outline) and for the whole familiar session (green outline). N , number of successful trials used for each map; r , familiar-novel correlation coefficient for each learning stage.

(B) Average cross-correlation for cells with a significant IC in familiar and novel environments (left) and for cells with a significant IC in only one environment (right), as a function of trial after reaching performance (perf.) criterion. Error bars indicate confidence intervals. $*P < 0.05$; $**P < 0.01$; $***P < 0.001$.

(C) Distribution of correlation coefficients for cells with significant IC in both environments, early and late in learning. The difference is shaded. Colors identify decoding space, as in (B).

(D) IC as a function of relative trial number in the novel environment, for cells with significant IC in both familiar and novel environments. Colors identify decoding space, as in (B). Error bars indicate confidence intervals. Gray dashed line indicates success rate (scale on the right). bit/sp., bit per spike.

categories in single cells (3) and for categorical or relational domains via functional magnetic resonance imaging (26–28). Capture of higher-order structure across experiences may involve a recurrence of information through an entorhinal–hippocampal loop (29) or a hippocampal–prefrontal interaction (30). In the spatial domain, the human hippocampus codes morphological homologies between layouts (31) but also differentiates environments containing common elements through pattern separation (32). Our results shed light on the neural mechanisms underlying these observations: The monkey hippocampus simultaneously represents both environment-specific items (episodic memory) via cells that express remapping, and schemas that apply to these different episodes via schema cells. Such complementarity has important representational properties (data compression), while facilitating adaptive behavior. Indeed, schema cells do not signal sim-

ple geometry per se but encode an abstract, behaviorally relevant structure of space. In this respect, they are the closest documented example of a nonhuman primate analog to human concept cells (3). Spatial abstraction seems thus to exist in a species lacking both symbolic language and any proven ability for symbolic representation of space. The activity of these schema cells likely participates in translating the recognition of a space context into a possible array of actions, thereby encoding the functional importance of the present environment. This link in the memory chain connecting a spatiotemporal sensorimotor context to behavioral decisions would not necessitate symbolic associations.

REFERENCES AND NOTES

- R. Q. Quiroga, L. Reddy, G. Kreiman, C. Koch, I. Fried, *Nature* **435**, 1102–1107 (2005).
- M. Cerf et al., *Nature* **467**, 1104–1108 (2010).
- R. Q. Quiroga, *Nat. Rev. Neurosci.* **13**, 587–597 (2012).
- J. O’Keefe, L. Nadel, *The Hippocampus as a Cognitive Map* (Clarendon Press, 1978).
- S. Leutgeb et al., *Science* **309**, 619–623 (2005).
- A. C. Singer, M. P. Karlsson, A. R. Nathe, M. F. Carr, L. M. Frank, *J. Neurosci.* **30**, 11586–11604 (2010).
- A. S. Bahar, P. R. Shirvalkar, M. L. Shapiro, *J. Neurosci.* **31**, 12270–12281 (2011).
- H. J. Spiers, R. M. A. Hayman, A. Jovalekic, E. Marozzi, K. J. Jeffery, *Cereb. Cortex* **25**, 10–25 (2015).
- R. M. Grieves, B. W. Jenkins, B. C. Harland, E. R. Wood, P. A. Dudchenko, *Hippocampus* **26**, 118–134 (2016).
- S. McKenzie et al., *Neuron* **83**, 202–215 (2014).
- S. Wirth, P. Baraduc, A. Planté, S. Piñéde, J.-R. Duhamel, *PLOS Biol.* **15**, e2001045 (2017).
- S. F. C. Bartlett, *Remembering* (Cambridge Univ. Press, 1932).
- J. Piaget, *Le Langage et la pensée chez l’enfant* (Delachaux et Niestlé, Paris, 1923).
- D. Tse et al., *Science* **316**, 76–82 (2007).
- V. E. Ghosh, A. Gilboa, *Neuropsychologia* **53**, 104–114 (2014).
- S. A. Marchette, J. Ryan, R. A. Epstein, *Cognition* **158**, 68–80 (2017).
- For each neuron, 999 surrogate datasets were created by randomly shifting spiking chunks of 5 s; these datasets allowed us to normalize variables and derive nonparametric statistics.

18. C. B. Alme *et al.*, *Proc. Natl. Acad. Sci. U.S.A.* **111**, 18428–18435 (2014).
19. Results obtained in virtual reality; direct comparison with remapping in the rodent must be taken with care.
20. D. Tse *et al.*, *Science* **333**, 891–895 (2011).
21. I. Bethus, D. Tse, R. G. M. Morris, *J. Neurosci.* **30**, 1610–1618 (2010).
22. L. M. Frank, E. N. Brown, M. Wilson, *Neuron* **27**, 169–178 (2000).
23. J. A. Ainge, M. Tamisunaite, F. Woergoetter, P. A. Dudchenko, *J. Neurosci.* **27**, 9769–9779 (2007).
24. J. Ferbinteanu, P. Shirvalkar, M. L. Shapiro, *J. Neurosci.* **31**, 9135–9146 (2011).
25. S. McKenzie, N. T. M. Robinson, L. Herrera, J. C. Churchill, H. Eichenbaum, *J. Neurosci.* **33**, 10243–10256 (2013).
26. R. M. Tavares *et al.*, *Neuron* **87**, 231–243 (2015).
27. M. L. Mack, B. C. Love, A. R. Preston, *Proc. Natl. Acad. Sci. U.S.A.* **113**, 13203–13208 (2016).
28. M. M. Garvert, R. J. Dolan, T. E. Behrens, *eLife* **6**, e17086 (2017).
29. R. Koster *et al.*, *Neuron* **99**, 1342–1354.e6 (2018).
30. M. T. R. van Kesteren *et al.*, *Neuropsychologia* **51**, 2352–2359 (2013).
31. S. A. Marchette, L. K. Vass, J. Ryan, R. A. Epstein, *Nat. Neurosci.* **17**, 1598–1606 (2014).
32. C. T. Kyle, J. D. Stokes, J. S. Lieberman, A. S. Hassan, A. D. Ekstrom, *eLife* **4**, e10499 (2015).

ACKNOWLEDGMENTS

The authors thank A. Planté for help with data collection and animal training; O. Zitvogel and S. Pinède for task and set-up programming; and L. Parsons for editing the English. **Funding:** LABEX-CORTEX of the University of Lyon, www.labex-cortex.com (grant number ANR-11-LABEX-0042); Marie Curie Reintegration Grant, <https://erc.europa.eu/> (grant number MIRG-CT-21939); Centre National de la Recherche Scientifique, www.cnrs.fr (grants PEPII and PEPS to P.B.); and Agence Nationale pour la Recherche, www.agence-nationale-recherche.fr (ANR-08-BLAN-0088- Brain-GPS to J.-R.D. and S.W. and ANR-17-0015-Navi-GPS to S.W.).

Author contributions: Conceptualization: S.W. and J.-R.D. Data curation: S.W. Formal analysis: P.B. Funding acquisition: S.W. Investigation: S.W. and P.B. Methodology: P.B. and S.W. Project administration: S.W. Resources: S.W. and J.-R.D. Software: P.B. Supervision: P.B. and S.W. Validation: P.B. and S.W. Visualization: P.B. and S.W. Writing, original draft: P.B. and S.W. Writing, review and editing: P.B., J.-R.D., and S.W. **Competing interests:** The authors declare no competing interests. **Data and materials availability:** Data are available at <http://crcns.org/data-sets/hc/hc-21>.

SUPPLEMENTARY MATERIALS

www.sciencemag.org/content/363/6427/635/suppl/DC1
Materials and Methods
Figs. S1 to S5
References (33–35)

5 October 2018; accepted 9 January 2019
10.1126/science.aav5404

NEURODEVELOPMENT

Copyright © 2019 The Authors, some rights reserved*

Prenatal activity from thalamic neurons governs the emergence of functional cortical maps in mice

Noelia Antón-Bolaños*, Alejandro Sempere-Ferrández*, Teresa Guillamón-Vivancos, Francisco J. Martini, Leticia Pérez-Saiz, Henrik Gezelius†, Anton Filipchuk‡, Miguel Valdeolmillos, Guillermínna López-Bendito§

The mammalian brain's somatosensory cortex is a topographic map of the body's sensory experience. In mice, cortical barrels reflect whisker input. We asked whether these cortical structures require sensory input to develop or are driven by intrinsic activity. Thalamocortical columns, connecting the thalamus to the cortex, emerge before sensory input and concur with calcium waves in the embryonic thalamus. We show that the columnar organization of the thalamocortical somatotopic map exists in the mouse embryo before sensory input, thus linking spontaneous embryonic thalamic activity to somatosensory map formation. Without thalamic calcium waves, cortical circuits become hyperexcitable, columnar and barrel organization does not emerge, and the somatosensory map lacks anatomical and functional structure. Thus, a self-organized protomap in the embryonic thalamus drives the functional assembly of murine thalamocortical sensory circuits.

The mammalian cerebral cortex is arranged into radial columns that coalesce during development. These columns become functionally organized before adulthood (1–3). Some evidence suggests that genetic factors regulate initial columnar patterning (4); other evidence suggests that functional maps arise postnatally as a result of sensory experience (5–9). However, spatially organized patterns of spontaneous activity are evident in the embryonic thalamus, before cortical neurons have completed their radial migration (10). One well-studied functional map is the somatotopic correspondence between whiskers and their associated clusters of layer 4 neurons (called barrels) in the rodent primary somatosensory cortex (S1) (11). Although barrels are apparent anatomically at postnatal day 4 (P4) (12), domains of spontaneously co-activated neurons can be identified at birth in S1 *in vivo* (13–15). We asked whether the emergence of anatomically discernable structures is preceded by organized activity in the mouse embryo. We discovered that structured patterns of neuronal activity in the embryonic thalamus define functional cortical columns and the concomitant functional somatotopic map in the immature cortex.

The functional properties of embryonic thalamocortical connections were assessed by recording the somatosensory cortical calcium responses elicited by the activation of the ventral posteromedial nucleus (VPM) of the thalamus in slices.

By embryonic day 17.5 (E17.5), electrical stimulation of the VPM triggered calcium waves that propagated over a large area of the nucleus, resembling previously reported spontaneous activity (10). This thalamic stimulation elicited a cortical calcium response in the S1 (Fig. 1, A and B; fig. S1A; and movie S1). Whereas the activation of thalamocortical axons is confined to the subplate at this stage (fig. S1B), the cortical response spanned the entire thickness of the cortical plate, suggesting that thalamocortical axons activate a radially organized cortical network. From E18.5 onward, VPM stimulation activated a progressively restricted territory within the nucleus (fig. S1C), allowing us to define the functional topography of the nascent thalamocortical projection. Perithreshold stimulation of adjacent regions in the VPM activated distinct columnar territories in the cortex (Fig. 1, C and D), indicating the existence of a functional protomap present in these embryonic thalamocortical circuits. This was evaluated *in vivo* by transcranial calcium imaging of glutamatergic cortical neurons at E18.5. Mechanical stimulation of juxtaposed areas of the whisker pad activated discrete, segregated, and spatially consistent cortical territories in the contralateral S1 (Fig. 1, E and F, and movie S2), confirming the existence of a cortical somatosensory protomap in the intact embryo.

We then tested whether embryonic thalamic calcium waves influence the emergence of the functional cortical columns that presage the formation of the somatotopic barrel map. To change the normal pattern of spontaneous thalamic activity, we crossed a tamoxifen-dependent *Gbx2CreERT2* mouse with a floxed line expressing the inward rectifier potassium channel 2.1 (Kir) fused to the mCherry reporter (fig. S2) (10). In this model (referred to hereafter as *Th^{Kir}*), 78% of the VPM neurons express Kir-mCherry protein

upon tamoxifen administration at E10.5 (fig. S2). In control slices, more than half of the spontaneous synchronous events in the VPM corresponded to large-amplitude, highly synchronized calcium waves, whereas the remaining activity reflected low-amplitude, poorly synchronized events. The highly synchronized waves were not detected in the *Th^{Kir}* mice, in which only small-amplitude and mostly asynchronous activity persisted, although at a higher frequency than in controls (Fig. 2, A to C, and movies S3 and S4). Collectively, Kir overexpression shifted the pattern of spontaneous activity in the thalamus from synchronized waves to asynchronous activity.

At the cellular level, whereas control neurons were relatively depolarized at E16.5, *Th^{Kir}* cells displayed a bistable pattern of activity with spontaneously alternating periods of hyperpolarized and depolarized membrane potential (Fig. 2D and fig. S3). Action potentials were generated in the depolarized phase in both control and *Th^{Kir}* cells. This change in the electrical properties of the *Th^{Kir}* neurons was sufficient to impede the generation of calcium waves. Barium, an ion that blocks Kir channels (16), reversed the electrophysiological profile of *Th^{Kir}* neurons, recovering the wavelike activity in *Th^{Kir}* VPM networks (fig. S4 and movie S5). Thus, although there were no propagating calcium waves in the thalamus of *Th^{Kir}* mice, the preservation of thalamic asynchronous activity meant that the thalamus was not silent.

We analyzed how altering the pattern of spontaneous thalamic activity in our *Th^{Kir}* model affected the functional columnar organization in S1. Perithreshold VPM stimulation in E17.5 to E18.5 slices from control mice triggered a columnar-like cortical response (fig. S5A and movie S6). Conversely, this stimulation in *Th^{Kir}* slices consistently elicited a broader (laterally) cortical calcium wave (fig. S5A and movies S7 and S8). Despite these differences, the subplate was the earliest cortical compartment activated in both control and *Th^{Kir}* mice, followed by the upper cortex (fig. S5, B to D). Next, we tested whether the emergence of the functional topographic map was affected in the *Th^{Kir}* mice. Stimulation of adjacent regions in the VPM in the *Th^{Kir}* slices, unlike that in the controls, activated highly overlapping territories in the cortex (Fig. 3A), indicating that the topographical representation of the thalamocortical circuit does not emerge in the absence of embryonic thalamic waves. Postnatally, the cortical response to VPM stimulation narrowed progressively with time in control slices, coinciding at P4 with the dimensions of the cortical barrel, yet this spatial restriction occurred to a lesser extent in the *Th^{Kir}* mice (Fig. 3, B and C, and movies S9 and S10). These differences were observed irrespective of the stimulation strength (fig. S6).

The extended cortical activation in the *Th^{Kir}* mice was not due to more extensive activation of the VPM (fig. S7), yet it was associated with increased levels of intrinsic cortical excitability. This was reflected by the high frequency of spontaneous cortical waves in *Th^{Kir}* slices (fig. S8,

Instituto de Neurociencias de Alicante, Universidad Miguel Hernández-Consejo Superior de Investigaciones Científicas (UMH-CSIC), Sant Joan d'Alacant, Spain.

*These authors contributed equally to this work. †Present address: Science for Life Laboratory, Tomtebodavägen 23A, 17165 Solna, Sweden. ‡Present address: Department of Integrative and Computational Neuroscience (ICN), Paris-Saclay Institute of Neuroscience (NeuroPSI), CNRS/University Paris-Sud, 91198 Gif-sur-Yvette, France. §Corresponding author. Email: g.lbendito@umh.es

A and B) and the widespread cortical response to intracortical stimulation (fig. S8, C to E). Next, we tested whether this change in cortical network excitability occurred in the *Th^{Kir}* mice in vivo. Because cortical traveling waves were associated with action potential bursts (fig. S8F), we recorded extracellular cortical activity with multichannel electrodes. We found extensive spontaneous events of synchronous activity spreading horizontally in the *Th^{Kir}* mice at P2 to P3 (Fig. 3, D to F), consistent with the hyperexcitability observed ex vivo. We then ana-

lyzed the possible origin for this excitability and found that the amplitude of the calcium response was the same in the subplate but larger in the upper cortex in the *Th^{Kir}* mice (fig. S9), suggesting a local alteration in the upper cortical network. As metabotropic glutamate receptors (mGluRs) participate in the propagation of cortical spontaneous activity in newborn rodents (17, 18), we tested whether mGluRs could be involved in the hyperexcitability of cortical networks in *Th^{Kir}* mice. Bath application of 2-methyl-6-(phenylethynyl)pyridine (MPEP) (100 μ M),

an mGlu5-specific antagonist, rescued the activation of the thalamocortically induced cortical network into a column-like domain in *Th^{Kir}* mice. Although MPEP decreased the overall signal intensity in both conditions, it had no effect on the width of the cortical response in controls (fig. S10, A to C). These results are consistent with increased expression of cortical mGlu5 in the *Th^{Kir}* mice at P0 (fig. S10D). Together, these data reveal that the emergence of functional columns and a somatotopic map in the S1 relies on thalamic control of cortical excitability, implicating mGluRs.

Fig. 1. Embryonic thalamocortical stimulation reveals an organized prenatal cortical map.

(A) Experimental design. The maximal projection of the calcium responses [measured as the ratio of the change in fluorescence to the baseline fluorescence ($\Delta F/F_0$)] (color coded) in the VPM and cortex after VPM stimulation at E17.5 is shown.

(B) Calcium transients from boxes in (A).

(C) Experimental design.

The maximal projection of cortical responses after the stimulation of three adjacent VPM regions (St1 to St3) at E18.5 is shown.

(D) Plot of the stimulated VPM

area versus the cortical response width (the black dot represents the mean value). (Right) Plot of the stimulus position in the VPM versus the cortical response location ($n = 16$ stimulation sites from 4 slices). Colored circles represent the data in (C). (E) Experimental design. Cortical calcium responses were elicited by mechanical stimulation of three contralateral whisker pad (Wp) sites (St1 to St3) at E18.5. (Right) High-magnification images and transients recorded in each region of interest (ROI) (boxes labeled 1 to 3). (F) Plot of the position of each cortical response relative to the centroid of the activated area ($n = 8$ mice). dLGN, dorsolateral geniculate nucleus; RT, reticular thalamus; SuP, subplate; TCAs, thalamocortical axons; Cal520, calcium indicator 520; Ctx, cortex; GCaMP6f-EGFP, calmodulin-based genetically encoded fluorescent calcium indicator 6-fast. Scale bars, 200 μ m in (A), 1 mm in (left and middle), and 500 μ m in (E) (right).

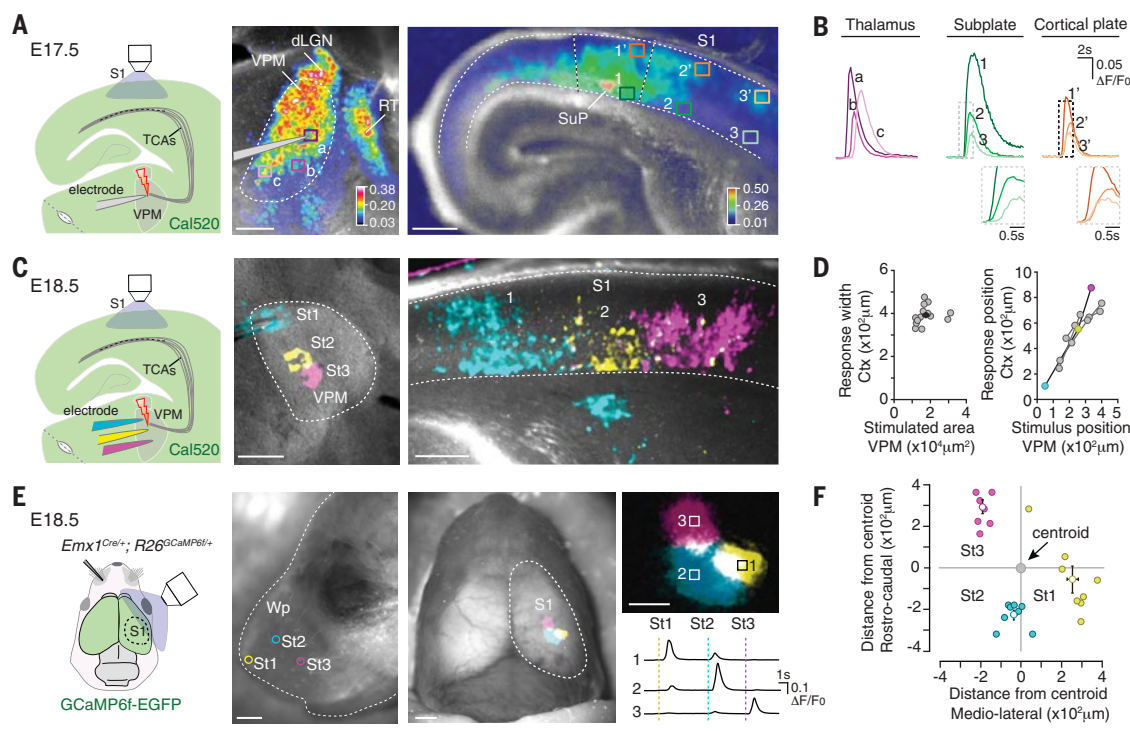
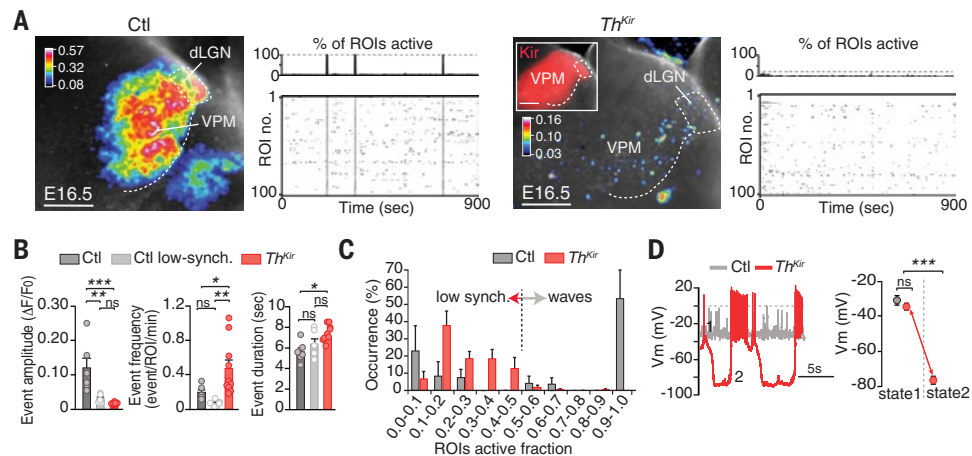


Fig. 2. Desynchronizing the embryonic thalamic pattern of activity.

(A) Maximal projection of ex vivo spontaneous calcium activity in the VPM and accompanying raster plots for control (Ctl) and *Th^{Kir}* slices at E16.5.

(B) Properties of the VPM calcium events ($n = 6$ control slices, $n = 10$ *Th^{Kir}* slices; ns, not significant; * $P < 0.05$, ** $P < 0.01$, *** $P < 0.001$). (C) Percent distribution of active ROIs. (D) Representative traces and quantification of membrane potential (V_m) in control and *Th^{Kir}* neurons recorded at E16.5 to E18.5 (control, $n = 7$ slices; *Th^{Kir}*, $n = 7$ slices). *** $P < 0.001$. Scale bars, 200 μ m. Data are means \pm SEM.



To ascertain whether embryonic thalamic activity and functional columns are prerequisites to establish the postnatal anatomy of the barrel map, we examined thalamocortical axons clustering in the *Th^{Kir}* mice in which this projection

was labeled by green fluorescent protein (GFP) (TCA-GFP mice) (19). The barrel map was evident at P4 in control mice (12, 20), but no barrels were detected in tangential or coronal sections of *Th^{Kir}* mice, where thalamocortical axons targeted layer

4 but did not segregate into discrete clusters (Fig. 4A and fig. S11). Furthermore, there was no arrangement of layer 4 cells into barrel walls in the *Th^{Kir}* mice. The absence of barrels did not seem to originate from the loss of neurotransmitter

Fig. 3. Loss of functional cortical prebarrel columns in the *Th^{Kir}* mice.

(A) Maximal projection of cortical responses after the stimulation (stim) of two adjacent VPM regions in *Th^{Kir}* slices. (Right) Quantifications of the activated area ($n = 6$ control slices, $n = 6$ *Th^{Kir}* slices; ns, not significant; * $P < 0.05$, ** $P < 0.01$). Arrowheads indicate the cortical territory with overlapping activation. (B) Cortical activation elicited by VPM stimulation at P2 (inset, P4) in control (Ctl) and *Th^{Kir}* slices. (C) Quantification of the horizontal spread of the cortical response [E17 to E18 (emb.), $n = 8$ control slices, $n = 9$ *Th^{Kir}* slices; P0 to P1, $n = 5$ control, $n = 4$ *Th^{Kir}*; P2 to P3, $n = 5$ control, $n = 5$ *Th^{Kir}*; P4 to P7, $n = 5$ control, $n = 6$ *Th^{Kir}*; ns, not significant; * $P < 0.05$, ** $P < 0.01$. (Right) Same in layer 4 at P4 to P7 ($n = 6$ control slices, $n = 6$ *Th^{Kir}* slices; ** $P < 0.01$). (D) Experimental design and coronal image showing the four-shank (s1 to s4) electrode insertion in S1 (red). (E) Representative in vivo recordings of spontaneous cortical network activity. (F) Quantification of the cross-correlation coefficient among shanks in control mice ($n = 3$) and *Th^{Kir}* mice ($n = 6$). ** $P < 0.01$. L4, layer 4; norm., normalized; Dil, 1,1'-dioctadecyl 3,3,3',3'-tetramethylindocarbocyanine perchlorate; DAPI, 4',6-diamidino-2-phenylindole. Scale bars, 200 μ m. Data are means \pm SEM.

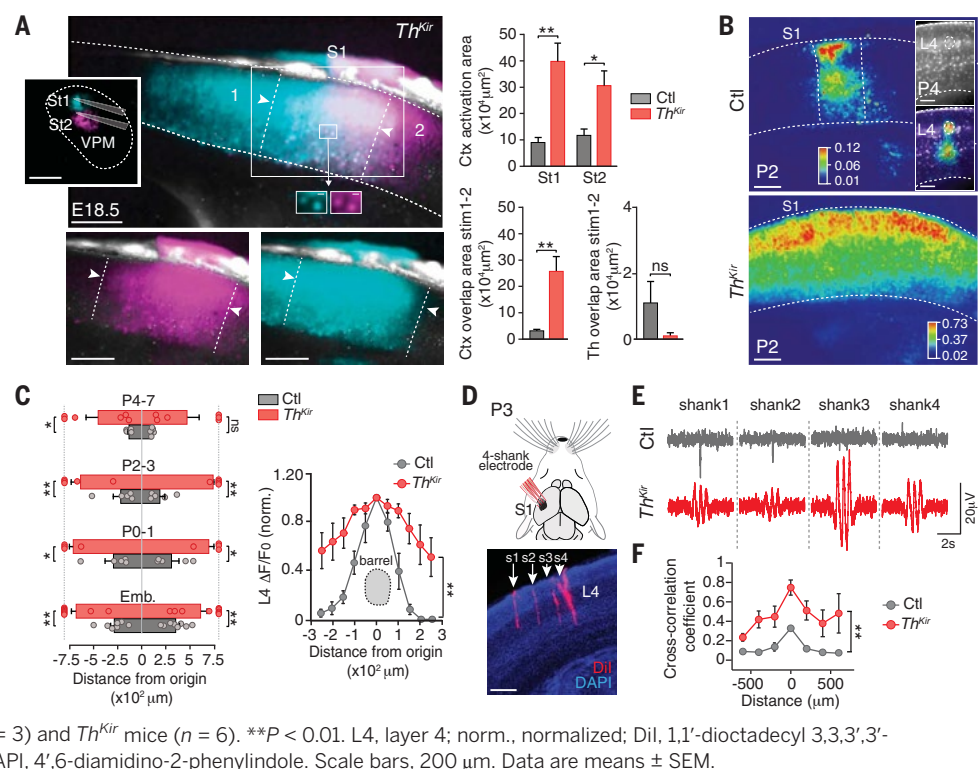
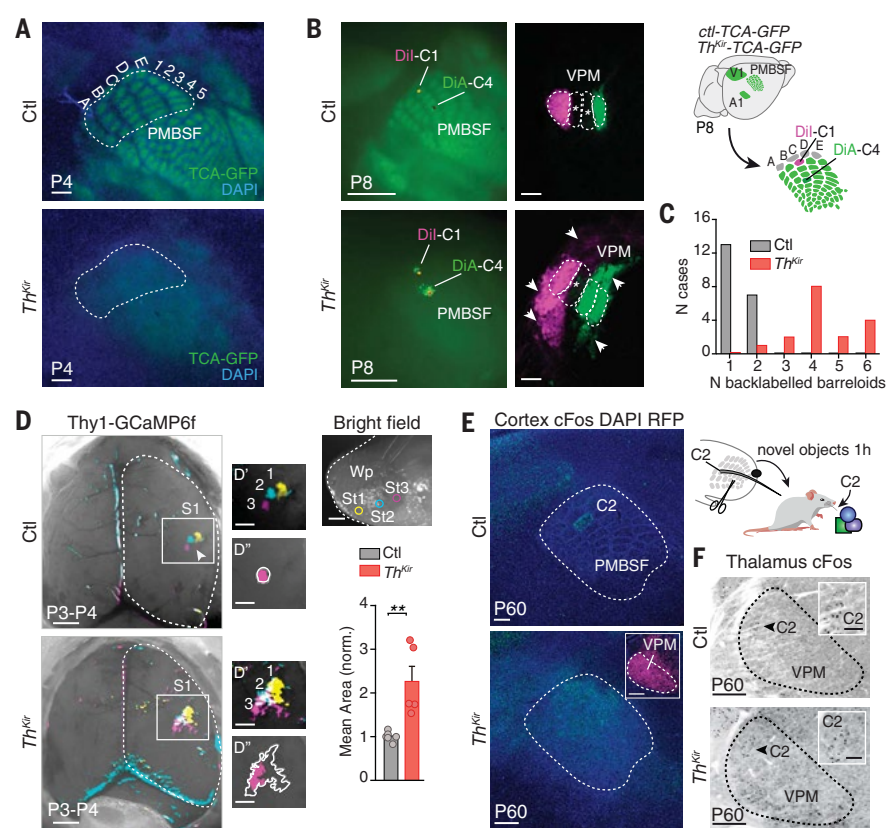


Fig. 4. Long-term anatomical and functional changes in S1 of the *Th^{Kir}* mice.

(A) Tangential sections showing the posteromedial barrel subfield (PMBSF) in control (Ctl) and *Th^{Kir}* TCA-GFP mice at P4. Letters and numbers correspond to the diagram in (B). (B) Experimental design and images showing PMBSF injection sites and back-labeled barreloids in the VPM. Arrowheads show back-labeling outside the expected barreloids and asterisks indicate the non-back-labeled barreloids. (C) Quantification of data shown in (B) ($n = 10$ control slices, $n = 10$ *Th^{Kir}* slices). (D) Maximal projection of the in vivo contralateral cortical responses elicited by mechanical stimulation of three whisker pad (Wp) sites (St1 to St3) at P3 to P4 (top right). (D') High-power views. (D'') Drawing of initial (pink) and maximal (outline) extension of representative responses. (Bottom right) Quantification of the data ($n = 6$ control mice, $n = 5$ *Th^{Kir}* mice; ** $P < 0.01$). (E) Experimental design and cortical cFos immunostaining. (F) VPM cFos immunostaining. Scale bars, 300 μ m in (A), (B) (right), (E), and (F) (insets, 100 μ m); 1 mm in (B) (left) and (D) (insets, 500 μ m). DiA, 4-Di-16-ASP (4-(4-(dihexadecylamino)styryl)-N-methylpyridinium iodide); A1, primary auditory cortex; V1, primary visual cortex; RFP, red fluorescent protein. Data are means \pm SEM.



release (21, 22), as thalamic neurons in the *Th*^{Kir} mice fire action potentials and activate synaptic currents in cortical cells (figs. S4A, S9D, and S12, A to C) and respond normally to whisker stimulation *in vivo* (fig. S12, D and E).

The disrupted barrel map in *Th*^{Kir} mice may reflect altered point-to-point connectivity at several subcortical levels (8, 23, 24). However, the organization of brainstem barrelettes and thalamic barreloids in the *Th*^{Kir} mice was normal (fig. S13). As the barrel map ultimately relies on the specific topographic organization of thalamocortical axons (25), we explored whether some spatial segregation was conserved in the *Th*^{Kir} mice. Although dye deposition in barrels C1 and C4 back-labeled cells in the corresponding barreloids of control mice, the back-labeled territories in *Th*^{Kir} mice were more extensive, including cells located in neighboring barreloids (Fig. 4, B and C). Anterograde tracing from single barreloids also revealed a broader horizontal disposition of thalamocortical axons in layer 4 of the *Th*^{Kir} mice (fig. S14). Lastly, we determined how this aberrant topographic map generated by the lack of thalamic calcium waves affected the relay of sensory stimuli in early postnatal mice *in vivo*. Whereas the stimulation of distinct points on the whisker pad at P3 to P4 activated discrete barrel-like patches in the control S1, similar stimulations of *Th*^{Kir} mice led to enlarged responses in the barrel field (Fig. 4D and movies S11 and S12). Together, these data demonstrate that the postnatal anatomic clustering of thalamocortical axons and the somatotopic functional map are disrupted in the absence of embryonic thalamic waves.

As the critical period of thalamocortical plasticity in the S1 closes between P3 and P7 in rodents (6, 20, 26), we assessed whether the loss of columnar organization in the *Th*^{Kir} mice could be overcome by sensory experience. The loss of barrel organization and the lack of a precise functional map persisted in adult *Th*^{Kir} mice, as indicated by vGlut2 (vesicular glutamate trans-

porter 2) staining and the unrestrained cortical activation of cFos (Fig. 4E and fig. S15). The thalamus of *Th*^{Kir} mice retained a normal functional topography when whiskers were stimulated (Fig. 4F). Hence, the natural period of somatosensory-driven plasticity cannot overcome the altered organization that occurs in the embryo.

Our data reveal that embryonic patterns of thalamic activity organize the architecture of the somatosensory map. We have shown that the development of this map involves the emergence of functional cortical columns in embryos, driven by spontaneous thalamic wavelike activity. These embryonic columns display spatial segregation and somatotopic organization, despite the immature state of the cortical sheet in which they materialize. We propose that patterned activity in precortical relay stations during embryonic stages prepares cortical areas and circuits for upcoming sensory input. As thalamic waves are not exclusive to the somatosensory nucleus but propagate to other sensory nuclei [e.g., visual or auditory (10)], the principles of cortical map organization described here may be common to other developing sensory systems.

REFERENCES AND NOTES

1. V. B. Mountcastle, *J. Neurophysiol.* **20**, 408–434 (1957).
2. P. Rakic, *Science* **241**, 170–176 (1988).
3. D. H. Hubel, T. N. Wiesel, *J. Physiol.* **160**, 106–154 (1962).
4. P. Rakic, A. E. Ayoub, J. J. Breunig, M. H. Dominguez, *Trends Neurosci.* **32**, 291–301 (2009).
5. A. Tiriac, B. E. Smith, M. B. Feller, *Neuron* **100**, 1059–1065.e4 (2018).
6. T. K. Hensch, *Annu. Rev. Neurosci.* **27**, 549–579 (2004).
7. P. Gaspar, N. Renier, *Curr. Opin. Neurobiol.* **53**, 43–49 (2018).
8. H. P. Killackey, G. Belford, R. Ryugo, D. K. Ryugo, *Brain Res.* **104**, 309–315 (1976).
9. T. A. Woolsey, J. R. Wann, *J. Comp. Neurol.* **170**, 53–66 (1976).
10. V. Moreno-Juan *et al.*, *Nat. Commun.* **8**, 14172 (2017).
11. T. A. Woolsey, H. Van der Loos, *Brain Res.* **17**, 205–242 (1970).
12. A. Agmon, L. T. Yang, E. G. Jones, D. K. O'Dowd, *J. Neurosci.* **15**, 549–561 (1995).
13. J. W. Yang *et al.*, *Cereb. Cortex* **23**, 1299–1316 (2013).
14. H. Mizuno *et al.*, *Cell Rep.* **22**, 123–135 (2018).
15. O. Mitrukhina, D. Suchkov, R. Khazipov, M. Minlebaev, *Cereb. Cortex* **25**, 3458–3467 (2015).
16. N. Alagem, M. Dvir, E. Reuveny, *J. Physiol.* **534**, 381–393 (2001).
17. J. Wagner, H. J. Luhmann, *Neuropharmacology* **51**, 848–857 (2006).
18. D. P. Calderon, N. Leverkova, A. Peinado, *J. Neurosci.* **25**, 1737–1749 (2005).
19. H. Mizuno *et al.*, *Neuron* **82**, 365–379 (2014).
20. R. S. Erzurumlu, P. Gaspar, *Eur. J. Neurosci.* **35**, 1540–1553 (2012).
21. H. Li *et al.*, *Neuron* **79**, 970–986 (2013).
22. N. Narboux-Nême *et al.*, *J. Neurosci.* **32**, 6183–6196 (2012).
23. H. Van der Loos, T. A. Woolsey, *Science* **179**, 395–398 (1973).
24. W. L. Weller, J. I. Johnson, *Brain Res.* **83**, 504–508 (1975).
25. L. Lokmane, S. Garel, *Semin. Cell Dev. Biol.* **35**, 147–155 (2014).
26. M. C. Crair, R. C. Malenka, *Nature* **375**, 325–328 (1995).

ACKNOWLEDGMENTS

We thank L.M. Rodríguez, R. Susin, and B. Andrés for technical support; T. Iwasato for providing the TCA-GFP mouse; A. Barco for advice on the behavioral experiments; R. Morris, S. Tole, M. Maravall, and D. Jabaudon for critical reading of the manuscript; and the López-Bendito laboratory for stimulating discussions.

Funding: This work was supported by grants from the European Research Council (ERC-2014-CoG-647012) and the Spanish Ministry of Science, Innovation and Universities (BFU2015-64432-R and Severo Ochoa grant SEV-2017-0723). N.A.-B. held an FPI fellowship from the MINECO. H.G. held postdoctoral fellowships from the Swedish Research Council and the Swedish Brain Foundation. **Author contributions:** N.A.-B., A.S.-F., M.V., and G.L.-B. designed the experiments. N.A.-B., A.S.-F., T.G.-V., F.J.M., and L.P.-S. performed the analysis. N.A.-B. conducted calcium imaging, tracing experiments, and the cFos assays. A.S.-F. conducted calcium imaging and the electrophysiology. T.G.-V. conducted the *in vivo* calcium imaging. F.J.M. performed the Matlab analysis. L.P.-S. and F.J.M. performed the *in vivo* multi-electrode recordings. H.G. generated the Kir-mCherry mouse and pioneered *Th*^{Kir} analysis. A.F. designed, performed, and analyzed initial spontaneous thalamic calcium imaging. G.L.-B. acquired funding. M.V. and G.L.-B. wrote the paper. **Competing interests:** None declared. **Data and materials availability:** All the data in the paper are presented in the main text or supplementary materials.

SUPPLEMENTARY MATERIALS

science.scienmag.org/content/364/6444/987/suppl/DC1 Materials and Methods

Figs. S1 to S15

References (27–31)

Movies S1 to S12

12 November 2018; resubmitted 22 March 2019

Accepted 23 April 2019

Published online 2 May 2019

10.1126/science.aav7617

DEVELOPMENTAL NEUROSCIENCE

Sleepmore in Seattle: Later school start times are associated with more sleep and better performance in high school students

Gideon P. Dunster¹, Luciano de la Iglesia¹, Miriam Ben-Hamo¹, Claire Nave¹, Jason G. Fleischer², Satchidananda Panda², Horacio O. de la Iglesia^{1,3*}

Most teenagers are chronically sleep deprived. One strategy proposed to lengthen adolescent sleep is to delay secondary school start times. This would allow students to wake up later without shifting their bedtime, which is biologically determined by the circadian clock, resulting in a net increase in sleep. So far, there is no objective quantitative data showing that a single intervention such as delaying the school start time significantly increases daily sleep. The Seattle School District delayed the secondary school start time by nearly an hour. We carried out a pre-/post-research study and show that there was an increase in the daily median sleep duration of 34 min, associated with a 4.5% increase in the median grades of the students and an improvement in attendance.

INTRODUCTION

Adolescents typically have a preference to stay active until late in the evening and to wake up late in the morning. This timing of daily activity or “chronotype” is not only a consequence of a change in social life and the use of electronic devices that keep teenagers awake during the evening, but is also a result of changes in both the circadian and homeostatic regulation of sleep (1). During puberty, the adolescent circadian system naturally delays the onset of sleep to a later time. One reason for this is an apparent lengthening of the circadian period during the teenage years (1), which typically leads to a later onset of the biological night relative to the light-dark cycle (2). Furthermore, there is evidence that the adolescent circadian clock is less sensitive to light during the morning when light advances the circadian clock and its timing of sleep (1). On the other hand, the homeostatic regulation of sleep, which increases sleep pressure with waking hours, is also modified in older adolescents. This allows them to stay awake longer, relative to younger adolescents, due to a decreased sleep pressure during wake periods (3, 4).

On the basis of these measurable changes in sleep regulation, adolescents find themselves caught between two competing yet equally important forces: their circadian and homeostatic regulation of sleep, which delays sleep onsets, and their social obligations, which impose early sleep offsets resulting in a net decrease in daily sleep. Most adolescents sleep less than the recommended daily sleep at this age (8 to 10 hours) (5, 6), and an intervention that has been proposed to increase sleep is delaying school start times (American Academy of Pediatrics, 2014). Although some studies have used survey data to show that when teens are allowed to go to school later, they report longer sleep times, so far, there is no objectively recorded data indicating that delaying the school start time lengthens daily sleep in adolescent students.

Increasing daily sleep duration in adolescents is not only critical because of the clear adverse physical and mental health outcomes associated with chronic sleep deprivation but also because of the role that normal sleep plays in learning and memory consolidation

(7). Any action that results in longer daily sleep duration should also result in better academic performance. The link between longer sleep and better school performance has been hard to establish in field studies; whether delayed secondary school start times result in better performance also remains to be determined.

RESULTS

The ideal field experiment to study the potential benefits of later school start time on both sleep and academic performance should include schools that switched from an early start to a late start (or vice versa), in which students of the same grade, taking the same classes, could be studied objectively. The Seattle (WA) School District decided to delay the start time for secondary schools from 07:50 to 08:45 a.m. This change was implemented for the 2016–2017 academic year and allowed us to conduct a pre-/post-study in which we measured sleep-wake cycles using wrist activity devices (Actiwatch Spectrum Plus, Philips Respironics) during the spring of 2016 (pre) and the spring of 2017 (post). The study populations included sophomores of two public high schools in Seattle. In each year, at the same time of the year, an independent sample of students taking the same science class was studied in each school. The study was implemented as a science laboratory practice in which the students could test predictions about their own sleep patterns. Both the Human Subject Division at the University of Washington and the Seattle Public School District Board approved our study. As part of the 2-week recording phase, each student wore an Actiwatch and completed a sleep diary (used to validate the Actiwatch data), the Beck Depression Index II (BDI-II) Questionnaire (8), the Epworth Sleepiness Scale Questionnaire, and the Munich (9) and Horne-Östberg (10) Chronotype Questionnaires.

Figure 1A presents the wrist activity mean waveforms for students pooled from both schools during each year. During school days, a two-way analysis of variance (ANOVA) yielded an effect of time [$F_{(143, 25,311)} = 224.8, P < 0.0001$], no effect of year, and an effect of the interaction [$F_{(143, 25,311)} = 18.43, P < 0.0001$]. Similar effects were found for the nonschool days [$F_{(143, 25,025)} = 161.5, P < 0.0001$ for time; and $F_{(143, 25,025)} = 2.19, P < 0.0001$ for the interaction]. However, multiple comparisons revealed that most of the differences in activity between the 2 years emerged from a different wakeup time during

Copyright © 2018
The Authors, some
rights reserved;
exclusive licensee
American Association
for the Advancement
of Science. No claim to
original U.S. Government
Works. Distributed
under a Creative
Commons Attribution
NonCommercial
License 4.0 (CC BY-NC).

¹Department of Biology, University of Washington, Seattle, WA 98195, USA. ²Regulatory Biology Laboratory, Salk Institute, La Jolla, CA 92037, USA. ³Program in Neuroscience, University of Washington, Seattle, WA 98195, USA.

*Corresponding author. Email: horacioid@uw.edu

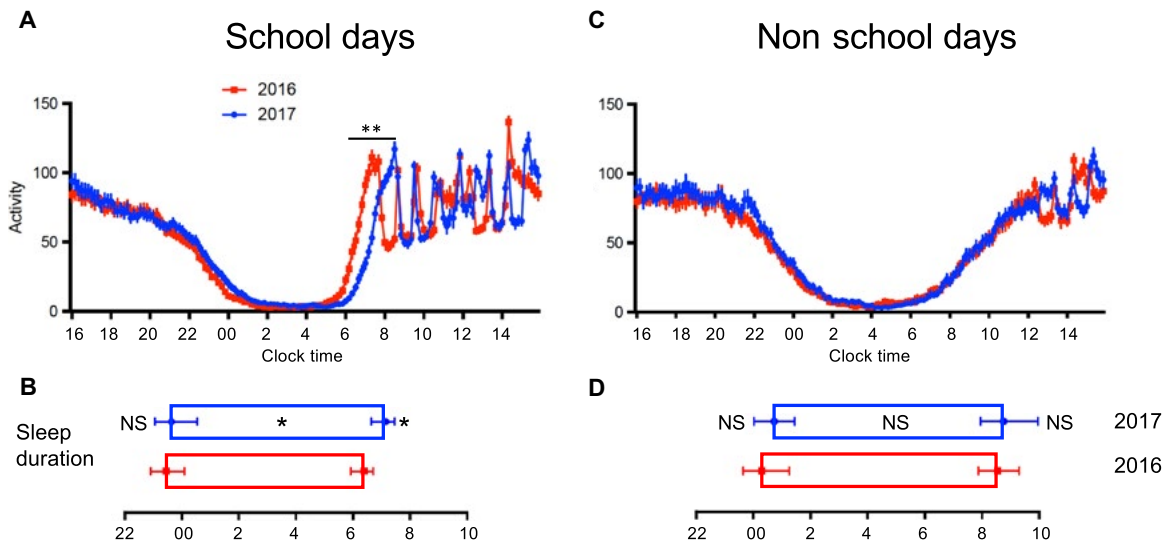


Fig. 1. Delayed school start times result in later sleep offset and longer sleep. Mean student activity waveforms and sleep summaries between years for school (A and B) and nonschool days (C and D). For both (A) and (C), there was a significant effect of time, year, and the interaction (see text). ** $P < 0.01$, difference between years (Sidak's comparisons). For (B), there is a significant delay in sleep offset ($P = 0.0007$), but not sleep onset ($P = 0.0459$), on weekdays in 2017 as compared to 2016, resulting in a significant increase of sleep duration on school days in 2017 ($P = 0.0007$); $P < 0.017$ threshold for significance for Wilcoxon signed-rank test corrected for multiple comparisons. The same analysis of sleep parameters on nonschool days shows no difference between years (D) [$n = 84$ (2017, school day) and $n = 94$ (2016, school day); $n = 76$ (2017, nonschool day) and $n = 81$ (2016, nonschool day)]. For (B) and (D), values represent median, and bars represent interquartile range. Sleep offset was also tested through generalized linear models (see text). Each student contributed at least five nights for the school-day data and three nights for the nonschool data. NS, not significant.

school days but not during nonschool days. That is, there was a clear difference in the timing of activity between years during school days but not during nonschool days. Notably, the regular peaks observed during the waking hours of school days reveal the break times between classes when students walk from one classroom to another. Analysis of the estimated sleep onset, offset, and sleep duration (see Materials and Methods) confirmed this interpretation. Wilcoxon signed-rank tests corrected for multiple comparisons revealed that students in 2017 had a 44 min later median sleep offset ($P < 0.0001$, effect size = 0.194), and a trend toward a later sleep onset that was not statistically significant. This asymmetric effect led to an overall 34-min increase in the sleep duration median during school days in 2017 ($P = 0.0007$, effect size = 0.353). In contrast to school days, nonschool days did not show any significant differences between years in any of these sleep parameters. The number of naps (counted after inspecting every actogram) students took was very similar between 2016 (152 total naps, 0.6 naps per student) and 2017 (150 total naps, 0.56 naps per student).

We also examined the change in social jet lag, a measure of the difference in sleep timing on school versus nonschool days. We predicted that given the delayed sleep pattern of students on school days in 2017, their sleep during school days would more closely align with their sleep on nonschool days. After controlling for oversleep during nonschool days, because of the accumulated sleep debt during the school days (see Materials and Methods), we observed a significant decrease in social jet lag in students from 2017 (median = 1.25, $n = 76$) as compared to 2016 (median = 1.60, $n = 81$; Wilcoxon signed-rank test, $P = 0.0118$, effect size = 0.616). Social jet lag was also evident when the sleep onset of students was compared between the night from Sunday to Monday and the night from Monday to Tuesday. On both years, Wilcoxon matched-pairs, signed-rank

tests revealed that, compared to Monday nights, sleep onset was later ($P = 0.0021$ for 2016 and $P = 0.0003$ for 2017) and sleep duration was shorter ($P = 0.0234$ for 2016 and $P = 0.0142$ for 2017) on Sunday nights; no differences were found for sleep offset. The reduction in social jet lag after the school start time delay further emphasizes the conclusion that later school start times allow students to better align sleep on school days with the circadian timing of their sleep.

A potential outcome of delaying school start times is that a trend for students to go to bed later could lead to exposure to artificial light later in the evening, which could in turn delay the master circadian clock. Figure 2 (A and B) shows the waveforms for exposure to light during different years. Visual inspection of the profiles during school days suggests that, compared to 2016, students in 2017 started their exposure to brighter light intensities later in the morning but did not necessarily end their exposure to bright light later in the evening. Furthermore, in both years, students appear to have a delayed exposure to light on nonschool days compared to school days. Because light intensities students are exposed to vary greatly—indoor light is several orders of magnitude lower intensity than outdoor light—light exposure never showed a normal distribution even after data transformation, precluding us from running a two-way ANOVA. Furthermore, Actiwatch light measurements are typically inaccurate at lower light intensities [see the Supplementary Materials and (11, 12)]. A more meaningful measure of the time course of light exposure is to assess when a student was exposed to a specific light threshold for the first time and the last time each day. We chose a 50-lux threshold as it is just above the threshold for inhibition of melatonin release (13). A two-way ANOVA with factors year and day of week (school versus nonschool) of time of first or time of last exposure to 50 lux yielded an effect of year and of day of week but not of interaction (Table 1 and Fig. 2C). Sidak's comparisons

Table 1. Two-way ANOVA results for first and last time of daily exposure to 50-lux light intensity.

| | Year | Day of the week | Interaction |
|-----------------------------------|-----------------------|-----------------|------------------------|
| First daily 50-lux light exposure | $F_{(1, 331)} = 18.2$ | $P < 0.0001$ | $F_{(1, 331)} = 258.1$ |
| Last daily 50-lux light exposure | $F_{(1, 331)} = 6.2$ | $P = 0.0136$ | $F_{(1, 331)} = 111.0$ |

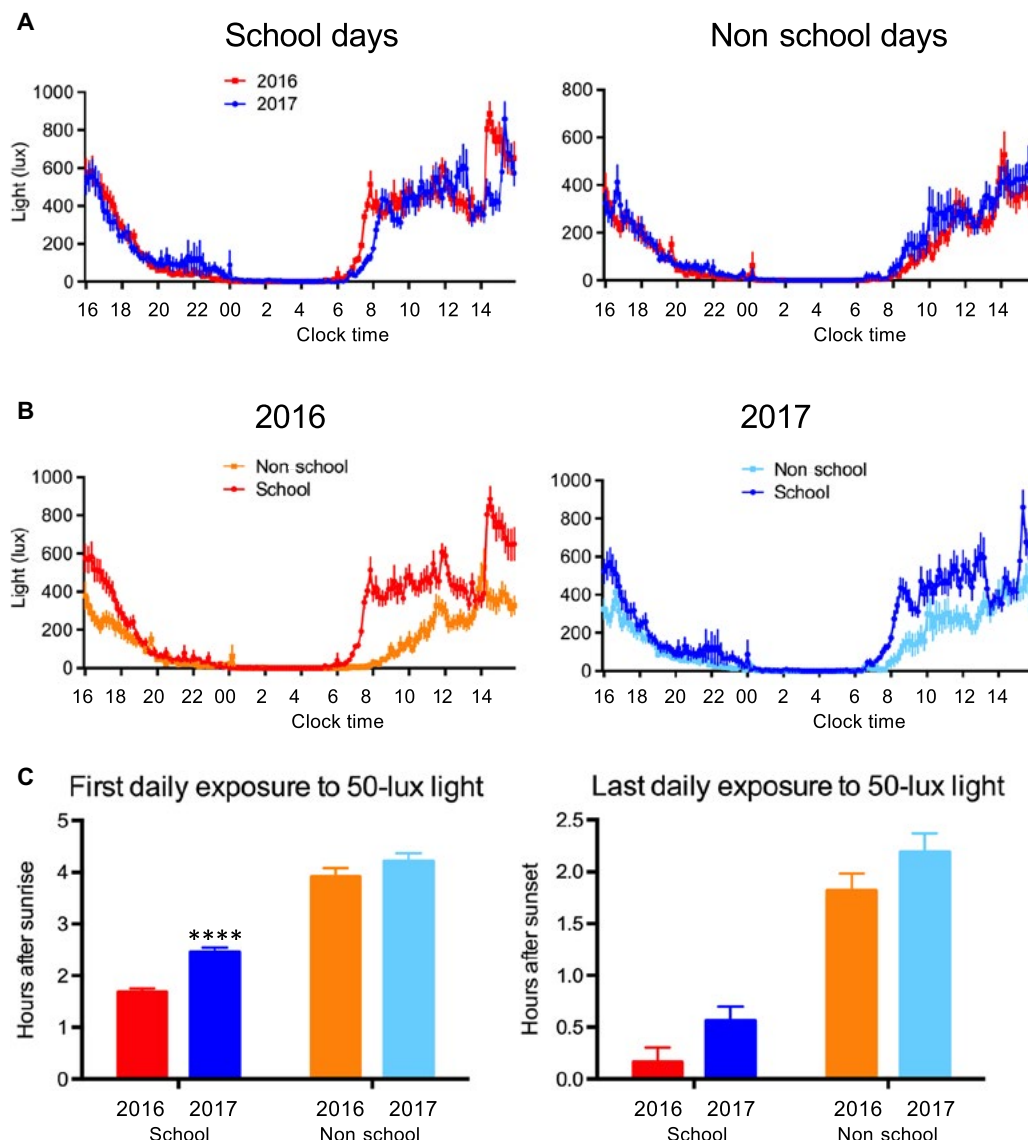


Fig. 2. Delayed school start times result in later exposure to light in the morning but not in the evening. (A) Mean student light exposure waveforms between years for school and nonschool days. During school days, students appear to have a delay in morning light exposure but not in evening light exposure. This delay is not evident in the data from nonschool days. (B) For both years, exposure to light is delayed in weekends relative to weekdays. (C) Because of the non-normal nature of the light data, the times for first and last exposure to 50-lux light on school, and nonschool days were tested for each year using a two-way ANOVA. There was a significant effect of day of week (school or nonschool) and year but not of the interaction (see Table 1); *** $P < 0.0001$, significant difference between years (Sidak's multiple comparisons). No difference was observed on nonschool days nor in the timing of the last daily exposure for school or nonschool days.

for school days demonstrated that while the first daily exposure to 50-lux light intensity occurred later in 2017 than in 2016, there was no difference between years in the last daily exposure to the same

light intensity. In both years, comparisons revealed that students' first and last daily exposure to 50-lux light intensity occurred later during nonschool days than during school days (Fig. 2C).

We used generalized linear models with years as the independent predictive variables to determine which dependent variables were significantly different between years. Because of the interdependence among sleep parameters (onset, offset, and duration), we tested one of these sleep variables separately in each model with the remaining parameters (school, sleepiness, depression index, chronotype, and grades). The final, best-fitting model included school, school day sleep offset, academic performance, mood, chronotype, and sleepiness, with sleep offset ($P = 2.8 \times 10^{-5}$; median₂₀₁₆ = 06:24 a.m., median₂₀₁₇ = 07:08 a.m.), performance ($P = 0.0261$; median₂₀₁₆ = 77.5%, median₂₀₁₇ = 82%), and sleepiness ($P = 0.0370$; median₂₀₁₆ = 7.0, median₂₀₁₇ = 6.0), emerging as significant factors between years (Fig. 3). None of the other variables, including school, sex, depression index, and chronotype, emerged as significantly different between years in the final models or any of the other models tested.

Attendance has been shown to improve and tardiness to decrease with later school start times in other school districts (14). We tested whether the later school start in 2017 improved attendance and punctuality by comparing the percent of absents and tardies among all students in the school in first period for each year in each school separately. Whereas Roosevelt High School (RHS) showed no difference

between years, students in Franklin High School (FHS) had significantly fewer tardies and absentees in 2017 than in 2016 (Fig. 3, C and D). Notably, FHS has many more economically disadvantaged students (88%) and ethnic minorities (68%) than RHS (31 and 7%, respectively).

DISCUSSION

We show that a delay in the high school start times from 7:50 to 8:45 a.m. had several measurable benefits for students. The change led to a significant lengthening of daily sleep of over half an hour. There is evidence that adolescents in most industrialized societies do not achieve the recommended approximately 9 hours of daily sleep during school days (5, 15), which is consistent with estimates that in the past 100 years, sleep has shortened by about 1 hour in children (16). Our study demonstrates a lengthening in the median daily sleep duration from 6 hours and 50 min to 7 hours and 24 min, restoring the historical sleep values present several decades before evenings within brightly lit environments and with access to light-emitting screens were common among teenagers. These results demonstrate that delaying high school start times brings students closer to reaching the recommended sleep amount and reverses the century-long trend in gradual sleep loss.

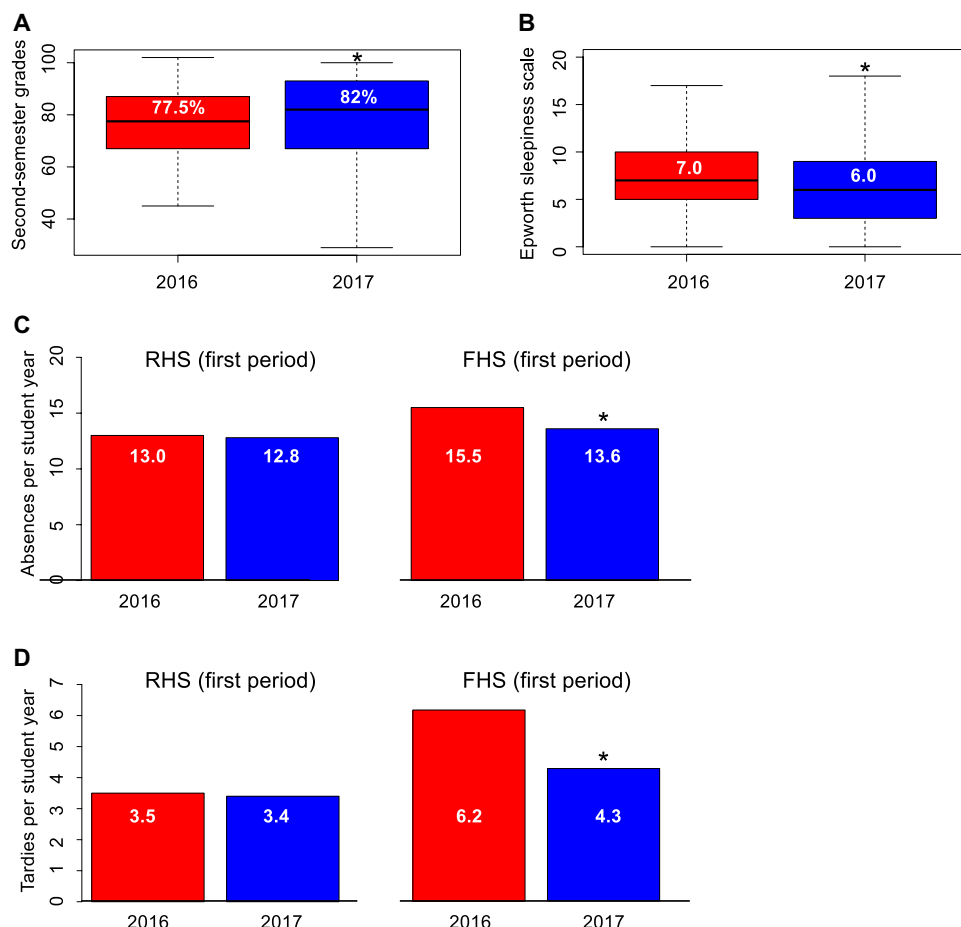


Fig. 3. Delayed school start times are associated with higher grades, reduced sleepiness, and improved attendance and punctuality. (A and B) Box plots of student performance and daytime sleepiness. Generalized linear models indicated that student performance, as measured by second-semester grades, was significantly higher (* $P = 0.0261$), whereas daytime sleepiness was significantly lower (* $P = 0.0370$) in 2017 than 2016. First-period absence (C) and tardy (D) data were compared between years using a χ^2 test. Students from FHS but not from RHS had a significant reduction in absences and tardies (* $P < 0.0001$) in 2017 as compared to 2016. Numbers within boxes in (A) and (B) represent medians, and numbers in bars in (C) and (D) represent absolute value.

We also show that the later school start time is associated with a better alignment of sleep timing with the circadian system (reduced social jet lag), reduced sleepiness, and increased academic performance. Although it is highly likely that increased sleep was the cause for reduced sleepiness, it is much harder to attribute causality for 4.5% higher grades on increased sleep; nevertheless, it is certainly reasonable that students who are better rested and more alert should display better academic performance. Last, the later school starts led to an increase in punctuality and attendance that, remarkably, was only evident in the economically disadvantaged school. Obviously, attending school and arriving on time to school is beneficial for learning, and this result suggests that delaying high school start times could decrease the learning gap between low and high socioeconomic groups. Other studies have shown impacts of later school start times that are consistent with our findings [see reviews in (14, 17)]. However, to our knowledge, ours is the first report to show that an across-the-district change in school start times results in a significant increase in daily sleep measured objectively with actimetry. Carskadon and colleagues (18) measured sleep in a group of high school students in one Rhode Island School District that transitioned from a 08:25 a.m. start time in ninth grade to a 7:20 a.m. start time in 10th grade and confirmed a shortening of daily sleep of approximately 20 min, which was also associated with a delay in the circadian phase and increased sleepiness. A recent study showed that a delay of 45 min in start times in one all-girls high school in Singapore resulted in a modest, almost 10 min, lengthening of daily sleep (19). This small change in sleep duration, in comparison to our study, could be related to several differences in the study design: (i) the authors performed the study on female students and within a larger range of ages and school grades; (ii) the study was performed longitudinally on the same students before and after the school start change, which not only introduces an age difference but can also be associated with changes in schedule; and (iii) sleep parameters were based on a single week of recordings and on less recorded days per student. The nature of our pre-/post-study prevents us from having a control group. However, in an intervention study with middle school students, in which the starting time was delayed by 1 hour for a week, students gained nearly 1 hour of daily sleep compared to themselves under the normal schedule or to nondelayed controls (20). The Seattle school start time delay of 55 min did not result in a gain of 55 min of sleep, suggesting that after a year—as opposed to an acute change lasting for 1 week—students may delay their bedtimes, indicating that there may be other factors that are keeping teens awake in the evenings of school days. Delayed school start times should be paired with advice on sleep hygiene, including preventing the increasingly pervasive use of screens late in the evening that is known to delay sleep onset (21). Given the widespread negative effects sleep deprivation has on adolescent physical and mental health, our study points to the value of a measure such as delaying the school start time toward improving teenage sleep and, in turn, health and academic outcomes.

MATERIALS AND METHODS

Data collection

Activity, light, and sleep data were collected using Actiwatch Spectrum Plus wrist activity monitors. Watches were programmed to collect data in 15-s epochs for 2 weeks (14 days), and students were instructed to press a marker button on the watch each time they went to sleep

and woke up. Philips Actiware (version 6) software was used to construct actograms and determine sleep intervals. Activity and light data were exported and analyzed separately for mean waveforms using R Studio and Prism. Students also completed a daily retrospective online diary, which included questions about sleep onset, offset, how they were awakened, if they took any naps, if they removed the watch, and a place for text comments. Diary information was used in the data cleanup procedure (described below) to validate the sleep bouts automatically determined by Philips Actiware.

Chronotype, daytime sleepiness, and mood were measured by a one-time completion of the respective surveys located in the same portal as the daily diary. Chronotype was assessed using the Horne-Östberg Chronotype Questionnaire (10) and the Munich Chronotype Questionnaire (9). Daytime sleepiness was measured using the Epworth Sleepiness Scale. Mood was measured using the BDI-II. Students who scored higher than 20 on the BDI-II were contacted by their teacher and reminded about access to mental health resources.

Student demographics, including sex, race, birthdate, commute time to school, and mode of transportation, were collected via a paper demographic survey handed out in class. Students were also given the opportunity to disclose any sleep disorders and/or scheduled responsibilities (work, child care, etc.) that might affect the data. In addition, students from the 2017 cohort were asked to disclose any school activities that were scheduled for before school as a result of the delayed start times; the number of cases was small and was not considered separately in the statistics. Second semester grades for the students included in the sleep study were provided by the teachers whom we partnered with for this study. These represent absolute (not normalized) grades and could carry an implicit bias from teachers who could have been for or against the school time change. Last, global attendance data for each school were provided by Seattle Public Schools.

Data were collected over the course of 6 weeks during the Spring of 2016–2017 in 2-week rounds. Students from the first period participated in data collection for the first 2 weeks, second period for the following 2 weeks, and third or fourth period for the final 2 weeks. Students in each round were given the same instructions. The data were stripped of all identifying information upon collection. At the end of the semester, the data were returned to the students for an in-class learning exercise on research methods, data interpretation, and the relationship between sleep and their lifestyles.

Participants

The first cohort of students was selected to participate from the first three periods of two sections of 10th grade Biology at RHS and one section from FHS in 2016. The second cohort of students was selected from the same grade, classes, and schools and during the same time of the year but in 2017, when the new school start time had been in effect for 7 months. Each section was taught by a separate instructor but instructors remained the same between years, and course credit was given for participating in the data collection as an in-class learning exercise. While all students were assigned to complete the online diary and surveys, watches were assigned to a subset of each section with the help of the instructors due to resource constraints. This assignment was designed to represent gender and underrepresented minorities in each class (table S1). Informed assent and consent were obtained from the students and their parents, respectively.

Inclusion criteria

Activity, light, and sleep data were segregated by school day nights (Sunday night to Thursday night) and nonschool day nights (Friday night, Saturday night, or the night before one holiday, Memorial Day) for analysis. School and nonschool days were treated separately. If a student was missing one or more nonschool nights (out of four), then the nonschool nights for that student were not included in the analysis. If a student was missing 5 or more school nights (out of 10), then the school nights for that student were not included in the analysis. Students missing both one or more nonschool night and five or more weekday nights were removed entirely from the analysis.

Activity data

Raw activity data for each subject were binned in 10-min intervals and then averaged across either school or nonschool days, giving each subject two averaged 24-hour activity profiles. Individual profiles were then used to construct activity waveforms for school and nonschool days in 2016–2017 (Fig. 1). Waveforms were analyzed using a two-way ANOVA with year and time of day as factors, followed by Sidak's multiple comparisons.

Light data

Light exposure data were analyzed using the “white light” reading supplied by the Actiwatch. Light readings are subject to occlusion by sleeves, and they are also attenuated when the light source is off-axis [50% attenuation at 50° to 60° and near-complete attenuation at 70° to 80° (11, 12)]. It is therefore conceivable that illuminances above 100 lux at normal arm position could result in momentary readings of 0 to 10 lux. Figure S1 shows that this does happen; even during the middle of the day, when an exposure to illuminances lower than 1 lux is extremely unlikely, a large proportion of individual readings are very low. In addition, levels of illuminance $<\sim 1$ lux resulted in a greatly increased measurement error with these devices (11, 12). Therefore, we excluded readings during which the subject was asleep, the watch was off wrist, or illumination was below 1 lux. Raw data for the same students that met inclusion criteria for activity were binned in 10-min intervals and processed for waveforms (Fig. 2).

The >1 lux criterion does not completely preclude momentary incorrect measurements. However, while Actiwatches can underestimate illuminance levels by more than an order of magnitude, they are not known to do the opposite, i.e., provide artificially high illuminance values. Therefore, the times of first and last exposure to a given light threshold represent a more meaningful measurement than the mean of the illuminance reading. While this measure does not fully describe the illuminance over the 24-hour period, it provides a direct measurement of how long a subject experienced light levels above a physiologically interesting value. Figure S2 portrays the difference between the probability of the mean of all readings within a 10-min interval being above 50 lux and the probability of a single reading being above the 50 lux. Inside a given 10-min bin of a student day, three possibilities exist: (i) no measurements are >50 lux; (ii) one or more measurements are >50 lux, but the mean is <50 lux; and (iii) the mean measurement is >50 lux. Figure S2 shows that during the early morning and late evening, when a person's watch produces a single reading above 50 lux, it is more likely that the mean of the readings in these 10-min intervals will be below 50 lux than it is for the mean to be above 50 lux. Given that most sub-

jects experience indoor light levels at this time range and the potential for inaccurately low, but not high, measurements discussed above, times of the first and last light measurements above a given threshold are a more accurate depiction than the mean illuminance reading at a given time. The former variable represents a better proxy for the overall window of time during which the subject experiences physiologically relevant levels of artificial light. This analysis could potentially use any threshold; the choice of 50 lux was based on the estimated threshold for the inhibition of melatonin release.

The time of first and last exposure to a given light intensity threshold was calculated separately for each student day. We report the mean value of first and last exposure to a 50-lux threshold intensity separately for school days and nonschool days for each school year (Fig. 2C). Data were analyzed by two-way ANOVA with day of week (school or nonschool) and year as factors, followed by Sidak's multiple comparisons. Light data were processed using Python v2.7.9, using the following libraries: pandas v0.22, numpy v1.14.0, and matplotlib 2.1.0.

Sleep data cleanup

For this study, we gathered three potential sources for sleep onset and offset data. The first was the watch, which extrapolated sleep intervals from the raw data using Philips Actiware software. The second were the self-report online diaries that the students were assigned to fill out every day. The third were the time stamps students could add to their recordings by pressing a button on their watch. To validate the sleep intervals, as determined by the watch software, we followed the following protocol:

- 1) We inspected every single actogram day by day to detect false software calls for sleep onsets or offsets. These represent obvious mistakes that can be easily detected upon inspection (fig. S3).

- 2) We then looked for discrepancies between the diary, or event recorder, and software calls for sleep onsets or offsets that were larger than 1 hour.

- 3) For all the nights in which the discrepancy was larger than 1 hour, we inspected once again the actograms on those nights to determine whether the 1 hour error was due to a software error or a student error, entering the wrong time in the diary or with the event marker.

After inspection of the actograms in step 3, we determined that 19% of the discrepancies had already been detected in step 1. Of the remaining discrepancies, 77% were caused by student error in the diary or event marker and 19% by a watch error, and on 4%, we were unable to determine the cause. This means that the error of taking the actimeter calls for sleep onset and offset after step 1 is $\leq 5\%$ and four times lower than the student-generated error, which was 19.5%.

Cleaned sleep data were broken up by onset, offset, duration, and efficiency for school and nonschool days. Sleep data were then exported and analyzed using Python and R Studio. Normality was tested by (i) visual inspection of distribution histograms, (ii) quantile/quantile plots, and (iii) through the Shapiro-Wilk test. None of the variables had normal distribution, and data on Fig. 1 were presented as medians \pm quartiles. Differences in sleep onset, offset, and duration for both school and nonschool days were tested using Wilcoxon signed-rank tests with a Bonferroni correction for multiple comparisons. For each student, social jet lag was calculated as the difference between mean mid-sleep on the nonschool days (after subtracting oversleep) minus mean mid-sleep on the school days (22). For the

Wilcoxon signed-rank tests, effect sizes were calculated by dividing the U statistic by the product of the N s (23).

Academic performance and attendance

Academic performance was assessed using second-semester grades from the science class that provided our pool of participants. School, academic performance, mood, chronotype, and sleepiness values were scaled and tested via generalized linear models using a binomial family with year as the dependent variable, testing the hypothesis that years differed on the basis of the other variables. Models included a single sleep variable (onset, offset, duration, and efficiency) at a time to avoid multicollinearity. Multiple models were tested, and the model with the lowest Akaike information criterion value was selected as the model of best fit. The final model included school, academic performance, mood, chronotype, sleepiness, and weekday offset. Ethnicity was not tested as a variable per se, but the two schools differ widely in their ethnic backgrounds (table S1). There were no sex differences between years or schools. There is no consensus on how to calculate the effect size for each variable that emerges as significant with generalized linear models; instead, we present the medians for each year, as the data were not normally distributed.

Attendance data were provided by the school district and contained the average number of tardies and absences per student by period for both schools in the study for 2016–2017. Predicted absentee and tardy data for 2017 were calculated on the basis of the rates from 2016, adjusted for changes in enrollment, and assessed using a χ^2 test. This analysis was only performed for the “first period,” namely, the first scheduled hour of class in the morning.

SUPPLEMENTARY MATERIALS

Supplementary material for this article is available at <http://advances.sciencemag.org/cgi/content/full/4/12/eaau6200/DC1>

Table S1. Demographics of students in each of the high schools included in the study.

Fig. S1. Probability of a light measurement (among all individuals recorded) being below threshold (X in legend) throughout the day.

Fig. S2. Probability distribution of light measurements across all watch data from Seattle high school students in 2016 and 2017.

Fig. S3. Representative actogram of a student in which the Actiwatch algorithm for sleep offset detection missed a sleep offset (white arrow).

REFERENCES AND NOTES

- M. A. Carskadon, in *Sleep in Children: Developmental Changes in Sleep Patterns*, C. L. Marcus, Ed. (Informa Healthcare, 2008).
- K. P. Wright Jr., C. Gronfier, J. F. Duffy, C. A. Czeisler, Intrinsic period and light intensity determine the phase relationship between melatonin and sleep in humans. *J. Biol. Rhythms* **20**, 168–177 (2005).
- D. J. Taylor, O. G. Jenni, C. Acebo, M. A. Carskadon, Sleep tendency during extended wakefulness: Insights into adolescent sleep regulation and behavior. *J. Sleep Res.* **14**, 239–244 (2005).
- O. G. Jenni, P. Achermann, M. A. Carskadon, Homeostatic sleep regulation in adolescents. *Sleep* **28**, 1446–1454 (2005).
- M. A. Carskadon, Sleep in adolescents: The perfect storm. *Pediatr. Clin. North Am.* **58**, 637–647 (2011).
- S. Paruthi, L. J. Brooks, C. D'Ambrosio, W. A. Hall, S. Kotagal, R. M. Lloyd, B. A. Malow, K. Maski, C. Nichols, S. F. Quan, C. L. Rosen, M. M. Troester, M. S. Wise, Recommended amount of sleep for pediatric populations: A consensus statement of the American Academy of Sleep Medicine. *J. Clin. Sleep Med.* **12**, 785–786 (2016).
- B. Rasch, J. Born, About sleep's role in memory. *Physiol. Rev.* **93**, 681–766 (2013).
- A. T. Beck, R. A. Steer, G. K. Brown, *Beck Depression Inventory-II (BDI-II)* (Pearson, 1996).
- T. Roenneberg, A. Wirz-Justice, M. Merrow, Life between clocks: Daily temporal patterns of human chronotypes. *J. Biol. Rhythms* **18**, 80–90 (2003).
- J. A. Horne, O. Ostberg, A self-assessment questionnaire to determine morningness-eveningness in human circadian rhythms. *Int. J. Chronobiol.* **4**, 97–110 (1976).
- M. G. Figueiro, R. Hamner, A. Bierman, M. S. Rea, Comparisons of three practical field devices used to measure personal light exposures and activity levels. *Light. Res. Technol.* **45**, 421–434 (2013).
- L. L. A. Price, M. Khazova, J. B. O'Hagan, Performance assessment of commercial circadian personal exposure devices. *Light. Res. Technol.* **44**, 17–26 (2012).
- S. Benloucif, H. J. Burgess, E. B. Klerman, A. J. Lewy, B. Middleton, P. J. Murphy, B. L. Parry, V. L. Revell, Measuring melatonin in humans. *J. Clin. Sleep Med.* **4**, 66–69 (2008).
- K. Wahlstrom, B. Dretzke, M. Gordon, K. Peterson, K. Edwards, J. Gdula, *Examining the Impact of Later High School Start Times on the Health and Academic Performance of High School Students: A Multi-Site Study* (University of Minnesota, 2014).
- M. A. Carskadon, K. Harvey, P. Duke, T. F. Anders, I. F. Litt, W. C. Dement, Pubertal changes in daytime sleepiness. *Sleep* **2**, 453–460 (1980).
- L. Matricciani, T. Olds, J. Petkov, In search of lost sleep: Secular trends in the sleep time of school-aged children and adolescents. *Sleep Med. Rev.* **16**, 203–211 (2012).
- K. E. Minges, N. S. Redeker, Delayed school start times and adolescent sleep: A systematic review of the experimental evidence. *Sleep Med. Rev.* **28**, 86–95 (2016).
- M. A. Carskadon, A. R. Wolfson, C. Acebo, O. Tzischinsky, R. Seifer, Adolescent sleep patterns, circadian timing, and sleepiness at a transition to early school days. *Sleep* **21**, 871–881 (1998).
- J. C. Lo, S. M. Lee, X. K. Lee, K. Sasmita, N. I. Y. N. Chee, J. Tandi, W. S. Cher, J. J. Gooley, M. W. L. Chee, Sustained benefits of delaying school start time on adolescent sleep and well-being. *Sleep* **41**, zsy052 (2018).
- D. Lufi, O. Tzischinsky, S. Hadar, Delaying school starting time by one hour: Some effects on attention levels in adolescents. *J. Clin. Sleep Med.* **7**, 137–143 (2011).
- E. D. Chinoy, J. F. Duffy, C. A. Czeisler, Unrestricted evening use of light-emitting tablet computers delays self-selected bedtime and disrupts circadian timing and alertness. *Physiol. Rep.* **6**, e13692 (2018).
- K. S. Jankowski, Social jet lag: Sleep-corrected formula. *Chronobiol. Int.* **34**, 531–535 (2017).
- R. J. Grissom, J. J. Kim, *Effect Sizes for Research* (Routledge, ed. 2, 2012).

Acknowledgments: We thank C. Jatul, A. J. Katzaroff, and T. Landboe for opening their classrooms doors for our sleep study, all the students at FHS and RHS for their participation, B. Brunton for help with data analysis, and D. Hurley whose IT support was and continues to be truly invaluable. **Funding:** This study was supported by NSF (award no. 1743364) to H.O.d.I.I. and by the Department of Biology, University of Washington. G.P.D. was supported by the Riddiford-Truman Award. S.P. was supported by NIH (grant no. EY016807) and Louis and Louise Nippert Charitable Foundation. **Author contributions:** All authors contributed to data analysis. G.P.D. and H.O.d.I.I. designed the research and collected the data. G.P.D., L.d.I.I., J.G.F., and H.O.d.I.I. wrote the manuscript. **Competing interests:** H.O.d.I.I. gave talks to school boards, superintendents, and other interest groups on the physiology of adolescent sleep. These talks may have influenced the Seattle School Board decision to delay the school start time. S.P. is the author of the book “The Circadian Code”. All other authors declare that they have no competing interests. Both the Human Subject Division at the University of Washington and the Seattle Public School District Board approved our study. **Data and materials availability:** All data needed to evaluate the conclusions in the paper are present in the paper and/or the Supplementary Materials. Additional data related to this paper may be requested from the authors. All data, code, and materials used in the analysis are available at <https://github.com/delaiglesialab/Dunster-et-al.-2018->.

Submitted 28 June 2018

Accepted 9 November 2018

Published 12 December 2018

10.1126/sciadv.aau6200

Citation: G. P. Dunster, L. de la Iglesia, M. Ben-Hamo, C. Nave, J. G. Fleischer, S. Panda, H. O. de la Iglesia, Sleepmore in Seattle: Later school start times are associated with more sleep and better performance in high school students. *Sci. Adv.* **4**, eaau6200 (2018).

COGNITIVE NEUROSCIENCE

Human consciousness is supported by dynamic complex patterns of brain signal coordination

A. Demertzi^{1,2,3*}, E. Tagliazucchi^{3,4*†}, S. Dehaene^{5,6}, G. Deco^{7,8}, P. Barttfeld^{9‡}, F. Raimondo^{1,2,3,10,11,12}, C. Martial¹, D. Fernández-Espejo^{13,14,15}, B. Rohaut^{2,3,16}, H. U. Voss¹⁷, N. D. Schiff¹⁸, A. M. Owen¹⁵, S. Laureys¹, L. Naccache^{2,3}, J. D. Sitt^{2,3*}

Adopting the framework of brain dynamics as a cornerstone of human consciousness, we determined whether dynamic signal coordination provides specific and generalizable patterns pertaining to conscious and unconscious states after brain damage. A dynamic pattern of coordinated and anticoordinated functional magnetic resonance imaging signals characterized healthy individuals and minimally conscious patients. The brains of unresponsive patients showed primarily a pattern of low interareal phase coherence mainly mediated by structural connectivity, and had smaller chances to transition between patterns. The complex pattern was further corroborated in patients with covert cognition, who could perform neuroimaging mental imagery tasks, validating this pattern's implication in consciousness. Anesthesia increased the probability of the less complex pattern to equal levels, validating its implication in unconsciousness. Our results establish that consciousness rests on the brain's ability to sustain rich brain dynamics and pave the way for determining specific and generalizable fingerprints of conscious and unconscious states.

INTRODUCTION

Consciousness is seemingly lost and recovered every day, from the moment we fall asleep until we wake up. Consciousness can also be transiently abolished by pharmacological agents or, more permanently, by brain injury. Each of these departures from conscious wakefulness brings about different changes in brain function, behavior, and neurochemistry. Yet, they all share a common feature: lack of reported subjective experience (1).

Finding reliable markers indicating the presence or absence of consciousness represents an outstanding open problem for science (2). We postulate that consciousness has specific characteristics that are based on the temporal dynamics of ongoing brain activity and its coordination over distant cortical regions. Our hypothesis stems from the common stance of various contemporary theories which propose that consciousness relates to a dynamic process of self-sustained, coordinated brain-scale activity assisting the tuning to a constantly evolving environment, rather than in static descriptions of brain function (3–5). In that respect, neural signals combine, dissolve, reconfigure, and recombine over time, allowing perception, emotion, and cognition to happen (6).

The first biological evidence for a constantly active brain came from electroencephalographic recordings showing electrical oscilla-

tions even when the participant was not performing any particular task. More recently, brain dynamics have been characterized by the presence of complex activity patterns, which cannot be completely attributed to background noise (7). Experiments with functional magnetic resonance imaging (fMRI) during normal wakefulness have shown that the brain spontaneously generates a dynamic series of constantly changing activity and connectivity between brain regions (8–10). This activity presents long-range temporal correlations in the sense that signal changes exert long-term influence on future dynamics (11). This translates to a complex temporal organization of the long-range coupling between brain regions, with temporally correlated series of transitions between discrete functional connectivity patterns (6). The spatiotemporal complexity of brain dynamics contributes toward efficient exchanges between neuronal populations (8), suggesting that the neural correlates of consciousness could be found in temporally evolving dynamic processes, as postulated by influential theoretical accounts (3–5).

In terms of states of consciousness, spontaneous fMRI dynamic connectivity has been investigated in different sleep stages (11, 12) and pharmacologically induced anesthesia in humans (13, 14) and animals (15, 16). These studies indicate that, during physiologically reversible unconscious states, cortical long-range correlations are

¹GIGA-Consciousness, GIGA Institute B34, University of Liège, Avenue de l'Hôpital, 11, 4000 Sart Tilman, Belgium. ²INSERM, U 1127, F-75013 Paris, France. ³Institut du Cerveau et de la Moelle Epinière, Hôpital Pitié-Salpêtrière, 47 bd de l'Hôpital, 75013 Paris, France. ⁴Instituto de Física de Buenos Aires and Physics Department (University of Buenos Aires), Buenos Aires, Argentina. ⁵Cognitive Neuroimaging Unit, CEA, INSERM, Université Paris-Sud, Université Paris-Saclay, F-91191 Gif/Yvette, France. ⁶Collège de France, 11, Place Marcelin Berthelot, 75005 Paris, France. ⁷Center for Brain and Cognition, Computational Neuroscience Group, Department of Information and Communication Technologies, Universitat Pompeu Fabra, Calle Ramon Trias Fargas 25-27, Barcelona 08005, Spain. ⁸Institut Catalana de la Recerca i Estudis Avançats (ICREA), Universitat Pompeu Fabra, Passeig Lluís Companys 23, Barcelona 08010, Spain. ⁹Laboratory of Integrative Neuroscience, Physics Department, FCEN UBA and IFIBA, CONICET, Pabellón 1, Ciudad Universitaria, 1428 Buenos Aires, Argentina. ¹⁰Department of Computer Science, Faculty of Exact and Natural Sciences, Intendente Güiraldes 2160–Ciudad Universitaria–C1428EGA, University of Buenos Aires, Argentina. ¹¹Sorbonne Universités, UPMC Université Paris 06, Faculté de Médecine Pitié-Salpêtrière, 91-105 bd de l'Hôpital, 75013 Paris, France. ¹²CONICET–Universidad de Buenos Aires, Instituto de Investigación en Ciencias de la Computación, Godoy Cruz 2290, C1425FOB Ciudad Autónoma de Buenos Aires, Argentina. ¹³Centre for Human Brain Health, University of Birmingham, B15 2TT Birmingham, UK. ¹⁴School of Psychology, University of Birmingham, B15 2TT, Birmingham, UK. ¹⁵The Brain and Mind Institute, Western Interdisciplinary Research Building, N6A 5B7 University of Western Ontario, London, Ontario, Canada. ¹⁶Department of Neurology, Columbia University, 710 West 168th Street, New York, NY 10032-3784, USA. ¹⁷Radiology Department, Citigroup Biomedical Imaging Center, Weill Cornell Medical College, 516 E. 72nd Street, New York, NY 10021, USA. ¹⁸Feil Family Brain and Mind Research Institute, Weill Cornell Medical College, 1300 York Avenue, New York, NY 10065, USA.

*Corresponding author. Email: a.demertzi@uliege.be (A.D.); tagliazucchi.enzo@googlemail.com (E.T.); jacobo.sitt@inserm.fr (J.D.S.)

†These authors contributed equally to this work.

‡Present address: Instituto de Investigaciones Psicológicas (IIPSI) CONICET, Enfermera Gordillo s/n, Córdoba, Argentina.

Copyright © 2019
The Authors, some
rights reserved;
exclusive licensee
American Association
for the Advancement
of Science. No claim to
original U.S. Government
Works. Distributed
under a Creative
Commons Attribution
NonCommercial
License 4.0 (CC BY-NC).

disrupted in both space and time, anticorrelated cortical states disappear, and the dynamic explorations are limited to specific patterns that are dominated by rigid functional configurations tied to the anatomical connectivity. Conversely, conscious wakefulness is characterized not only by global integration, evidenced by strong long-distance interactions between brain regions, but also by a dynamic exploration of a rich and flexible repertoire of functional brain configurations departing from the anatomical constraints (15). Another important characteristic observed predominantly during conscious wakefulness is the appearance of anticorrelations between the activity of different brain regions. This observation is in line with the prediction of the Global Neuronal Workspace theory stating that different streams of information in the brain compete for the global percolation (“ignition”) of a widespread network of regions, a phenomenon associated with conscious access. In terms of the fMRI blood oxygen level-dependent (BOLD) signal, this could manifest in the mutual inhibition of activity at different cortical regions, leading to anticorrelated dynamics (5).

Although dynamic connectivity has been investigated in physiological and pharmacological unresponsiveness, currently, the alterations in brain connectivity dynamics associated with pathological unconsciousness after severe brain injury remain unknown. The study of unresponsive brain-lesioned patients with preserved levels of vigilance offers unique insights into the necessary and potentially sufficient conditions for the capacity of sustaining conscious content. So far, the inference of consciousness in patients has rested on the use of active mental imagery neuroimaging paradigms (17) and by assessing the complexity of evoked (18) and spontaneous brain activity (19). Patients who successfully perform these active paradigms can no longer be considered unconscious and are thought to suffer from cognitive-motor dissociation (20). Given that nonresponsiveness can be associated with a variety of brain lesions, varying levels of vigilance, and covert cognition, we highlight the need to determine a common set of features capable of accounting for the capacity to sustain conscious experience. Given the above theoretical considerations, which agree in the characterization of consciousness as a global, temporally evolving process, we aimed at determining whether the dynamics of brain-wide coordination could provide such a set of common features in the form of transient patterns of connectivity that successfully generalize between different forms of nonresponsiveness in patients with brain injury.

RESULTS

We recorded fMRI data in a cohort of 159 participants scanned at four independent research sites (Liège: 21 healthy individuals and 63 patients; Paris: 15 healthy individuals and 22 patients; New York: 11 healthy individuals and 16 patients; London, Ontario: 11 patients). Patients were diagnosed in a vegetative state/unresponsive wakefulness syndrome (UWS) or in a minimally conscious state (MCS) with repetitive standardized behavioral assessments and were scanned under a resting condition, sedation free, or under anesthesia with propofol. The cohort was divided into three datasets: dataset 1 (Liège, Paris, and New York; $n = 125$) was used for the main analysis, dataset 2 (London, Ontario; $n = 11$) included patients with cognitive-motor dissociation, and dataset 3 (Liège, $n = 23$) included patients scanned under propofol anesthesia (clinical details are summarized in table S1).

Dynamic fMRI BOLD signal coordination was estimated between 42 nonoverlapping regions of interest (ROIs) representing six brain

networks implicated in functional/cognitive processes (table S2) (21). The coordination between the continuous fMRI time series was estimated on dataset 1 by means of phase synchronization, which determines the relative timing of the phases of two signals during each waveform cycle. We partitioned the phase-based coherence observations in a data-driven way (*k*-means clustering), leading to a discrete set of brain-wide coordination patterns and their corresponding rates of occurrence in each group. The analysis consistently revealed four distinguishable patterns (Fig. 1A), recurrently emerging even when varying the number of clusters in the algorithm (fig. S1). A pattern of high complexity (pattern 1), including positive and negative values of long-distance coordination, was more prevalent in healthy participants and in patients in MCS as compared to patients in UWS (Fig. 1B). The rate of this pattern also increased when moving from patients in UWS, to patients in MCS, and to healthy control individuals (UWS < MCS < HC, Spearman rank correlation between rate and group, rho = 0.7, $P < 10^{-16}$). In sharp contrast, a pattern of low interareal coordination (pattern 4) was more likely to occur in unresponsive patients compared to patients in MCS (Fig. 1B). This pattern also presented a decreasing probability rate from patients in UWS, to patients in MCS, and to healthy control individuals (UWS > MCS > HC, Spearman rank correlation between rate and group, rho = -0.6, $P < 10^{-11}$).

In comparison to pattern 4, pattern 1 was characterized by higher spatial complexity, long-distance edges, community structure, and high efficiency (fig. S2), suggestive of a more complex organization of brain-wide coordination. In addition, participant-level modularity, efficiency, integration, and distance showed systematic increases with respect to the participants’ state of consciousness (fig. S3). The robustness of the extracted patterns was tested by repeating the analysis separately for each scanning site and by demonstrating the emergence of similar patterns and dynamic configurations in each individual site (fig. S4). None of the patterns’ occurrence probabilities were mediated by scanning site (Supplementary Methods 1). Similarly, none of the patterns’ occurrence probabilities were mediated by etiology, chronicity, age, or gender (fig. S5). Patterns 2 and 3 were equally probable across all groups and conditions (Spearman rank correlation between rate and group, pattern 2: rho = 0.2, $P < 0.01$; pattern 3: rho = 0.02, $P = 0.8$). In addition, conscious participants showed a more uniform probabilistic distribution of the coordination patterns (Fig. 1D); in other words, the entropy of the temporal sequence of patterns increased with the level of consciousness.

To investigate the relationship between brain coordination dynamics and a representative network of the anatomical connections, we measured the observed dynamic patterns of brain coordination and an estimate of human anatomical connectivity independently acquired using diffusion spectrum imaging (DSI) data (fig. S6). The complex pattern 1 presented a low similarity to the anatomical connectivity, whereas pattern 4 was the most similar to the anatomy (Fig. 1C). We then quantified the relationship between the probability of each pattern’s occurrence (*y* axis) and the similarity to the anatomical connectivity (*x* axis) by means of the slope of the best least-squares linear fit. We found a weak relationship for healthy participants, suggesting the presence of diverse transient coordination patterns during conscious wakefulness (slope HC = 0.34 ± 0.31 , median \pm median absolute deviation). The increased slope seen in patients suggests that, despite persistent spontaneous neuronal activity, such activity is most likely to trace the fixed connectivity network (slope MCS = 0.94 ± 0.44 , UWS = 1.5 ± 0.31 , median \pm median absolute deviation).

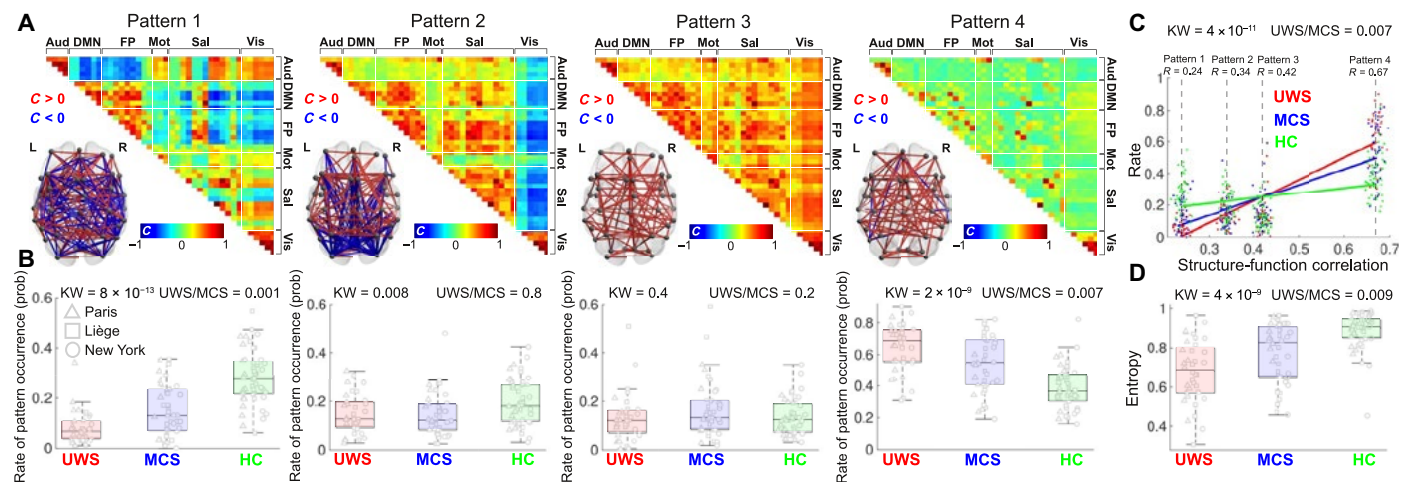


Fig. 1. The interareal coordination of ongoing brain dynamics is differentially orchestrated as a function of the state of consciousness. (A) Four patterns recurrently emerged from the data-driven analysis of phase-based coherence matrices. The patterns revealed diverse interareal coordination, from positive/negative long-range coherence (pattern 1), to predominantly occipital coherence (pattern 2), to overall high coherence (pattern 3), and overall low coherence (pattern 4). (B) Patient groups differed with respect to the likelihood of each coordination pattern occurrence. The complex interareal coordination pattern 1 presented a higher probability rate in healthy control participants (HC) and patients in MCS compared to patients in UWS, who predominantly resided in the overall low coordination pattern 4. Patterns 2 and 3 were equally probable across groups, potentially serving a transitional role. For the sake of visualization clarity, the scale in the last panel is different than in the other three. (C) Probability of each pattern's occurrence as a function of their similarity to the anatomical connectivity matrix. Complex pattern 1 showed low similarity to the anatomical connectivity, while pattern 4 was the most similar to the anatomical connectivity, suggesting that spontaneous neuronal activity during pattern 4 traces fixed structural connections. The slope of occurrence probability versus similarity relationship decreases with the state of consciousness. (D) Patients in UWS presented lower entropy values associated with the patterns' occurrence probability distribution, suggestive of a less uniform distribution compared to patients in MCS and healthy controls. Notes: (A) The patterns are ordered on the basis of their similarity to the anatomical connectivity, from the least (left) to the most (right) similar. The networks are rendered on the anatomical space (transverse view) and show the top 10% links between ROIs, within the absolute value of phase coherence > 0.2; red/blue edges indicate positive/negative coherence. Aud, auditory; DMN, default mode network; FP, frontoparietal; Mot, motor; Sal, salience; Vis, visual; KW, Kruskal-Wallis test *P* value; UWS/MCS, Wilcoxon test *P* value for the comparisons between patients in UWS and patients in MCS. (B) Boxplots represent the medians of the occurrence probabilities with interquartile range and maximum-minimum values (whiskers). (C) Lines are based on the best linear fit for each group; *R*, Spearman correlation.

Further characterization of coordination dynamics was obtained by computing the probabilities of transitioning between different brain coordination patterns (transition probabilities) and the duration of contiguous segments of pattern prevalence. Individuals with higher levels of consciousness were more likely to not only reside in pattern 1 but also to depart to and from this pattern toward patterns 2 and 3. The brains of patients in UWS were more likely to avoid this exploration of the complex coordination pattern and to preferentially reside in the less complex pattern 4. Last, patients in MCS were more likely not only to remain in pattern 1 but also to switch toward patterns 2 and 3 (Fig. 2) than patients in UWS. Controlling the transition probability for the patterns' absolute (static) frequency of occurrence also revealed an increase of autotransitioning in pattern 1 as a function of the level of consciousness (fig. S7). In addition, we also observed that the overall sequence predictability decreased alongside the state of consciousness, as shown by the systematic increases in entropy rates (estimated from the transitional probability matrices) from patients in UWS to patients in MCS and healthy controls (fig. S8).

To validate the implication of the identified brain patterns in consciousness, we quantified the generalization of the clustering model trained in dataset 1 into two independent datasets (fig. S9). First, we tested the rates of occurrence of the dataset 1 patterns in an independent group of patients, all of whom were behaviorally in UWS but some of whom presented a cognitive-motor dissociation (dataset 2), to determine their relevance in the capacity for conscious experience, regardless of behavioral output. The latter

clinical group presented higher rates of residence in the complex coordination pattern 1, with slopes similar to those observed in healthy controls (fig. S10). On the other hand, patients in UWS lacking evidence of command-following during neuroimaging tasks were more likely to reside in the low-complexity configuration (Fig. 3, left), with slopes comparable to those measured in anesthetized patients (fig. S10). Second, we tested again the rates of occurrence of the dataset 1 patterns in a third dataset of fMRI acquired in anesthetized patients with disorders of consciousness (dataset 3). Our hypothesis was that complex configurations would uniformly disappear across all patients, regardless of clinical diagnosis, as a result of the pharmacologically depressed arousal, cognitive function, and autonomic control typically induced by propofol (22). The pattern identification in anaesthetized patients with disorders of consciousness confirmed this hypothesis, revealing an equalization of occurrence probabilities regardless of clinical diagnosis, congruent with a uniform loss of awareness in this condition (Fig. 3, right).

DISCUSSION

We studied the brain's dynamic organization during conscious wakefulness and after severe brain injury leading to disorders of consciousness, with the aim of determining patterns of signal coordination specifically associated with conscious and unconscious states. We identified a pattern of positive and negative long-distance coordination, high modularity, with low similarity to the anatomical connectivity,

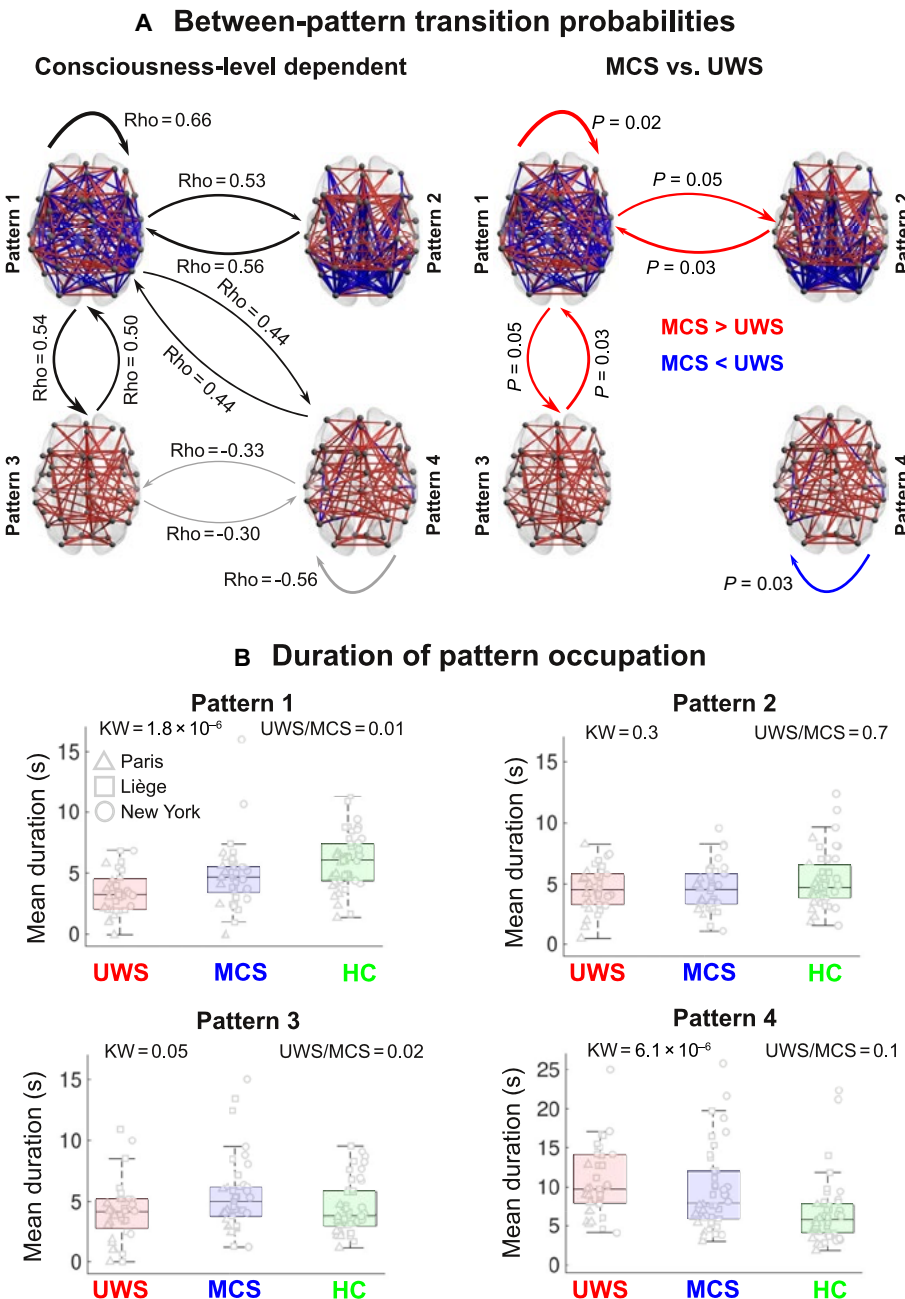
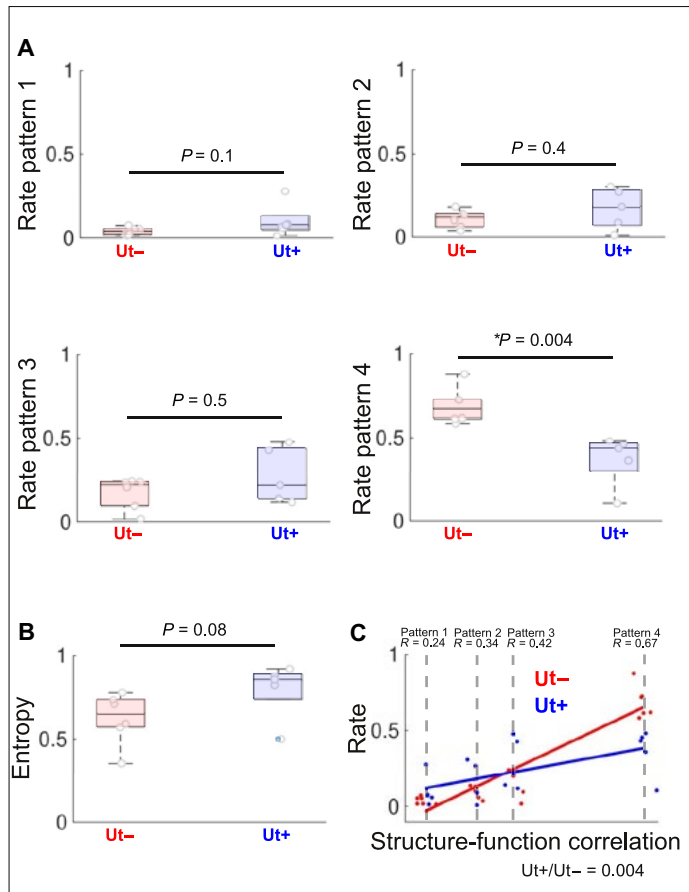


Fig. 2. The exploration of the identified coordination patterns differs with respect to the state of consciousness. (A) Left: The transition probabilities show an ordinal relationship with the level of consciousness. Black arrows indicate a higher probability to transit between the coordination patterns in healthy controls (HC) as opposed to patients in MCS and patients in UWS (HC > MCS > UWS). Gray arrows indicate the opposite trend (HC < MCS < UWS). Right: Patients in MCS were more likely to stay in the complex pattern 1 and to transition from this pattern to patterns 2 and 3. On the other hand, unresponsive patients were more likely to stay in the pattern most similar to anatomical constraints (pattern 4). Red arrows indicate higher transitional probabilities for patients in MCS, and blue arrows indicate higher transitional probabilities for unresponsive patients. (B) The clinical groups differ with respect to the contiguous amount of time spent in each pattern (after normalizing using randomly shuffled surrogate time series). The complex pattern 1 was explored during longer consecutive periods by healthy controls and patients in MCS, while patients in UWS spent higher periods of time in the overall low positive coordination pattern 4. Patterns 2 and 3 were explored similarly by all groups, further suggesting a transitional role. Notes: (A) Left: Groups are ranked ordinally from UWS, MCS, and HC (Rho: Spearman rank correlation). Right: P , Wilcoxon rank-sum test, false discovery rate corrected. (B) Boxplots represent the medians of mean pattern duration (in seconds) with interquartile range and maximum-minimum values (whiskers); Rho, Spearman rank correlation; UWS/MCS, Wilcoxon test P value for the comparisons between patients in UWS and patients in MCS.

potentially relevant for the support of conscious cognition (pattern 1). We also identified a pattern of low interregional dynamic coordination, low efficiency, with high similarity to anatomical connectivity, potentially specific to reduced or absent conscious processing (pattern

4). With respect to pattern 1, momentary neural coalitions have been previously shown to constitute a basis for complex cognitive function, with signals fluctuating between states of high and low connectivity and with more integrated states enabling faster and more accurate

Pattern prediction in cognitive-motor dissociation



Pattern prediction in anesthesia

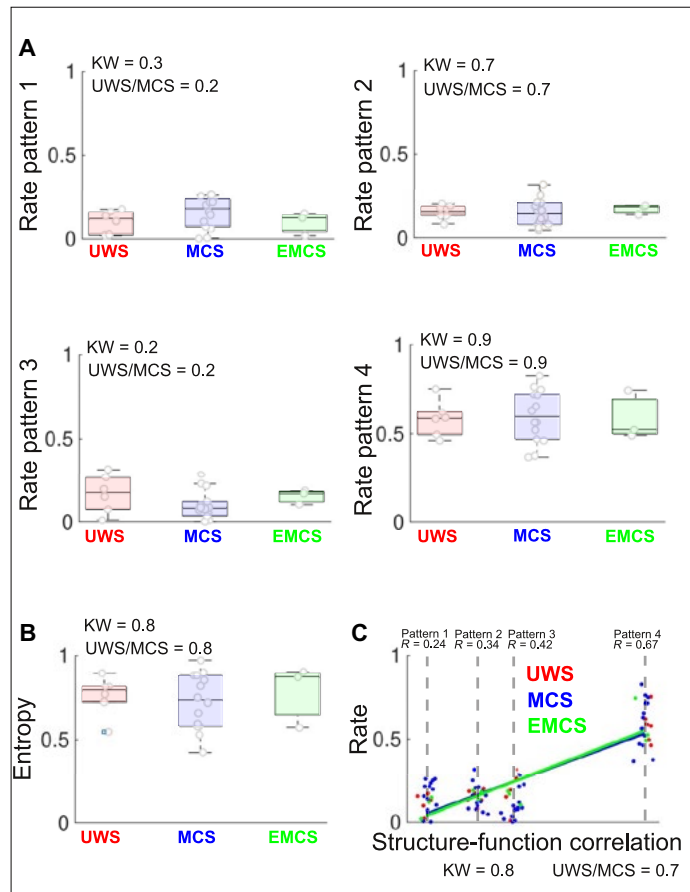


Fig. 3. The coordination patterns generalize to other states of preserved and diminished consciousness. (A) Left: Typical unresponsive patients who did not show command following in mental imagery tasks (Ut-) presented a higher probability of residing in the overall low coordination pattern 4. Conversely, behaviorally unresponsive patients who nevertheless successfully followed commands in mental imagery tasks (Ut+) showed significantly lower probabilities for the same pattern. (B) The sequence of pattern occurrences was more uniformly distributed in the Ut+ group as determined by higher entropy values. (C) The probability of each pattern's occurrence in Ut+ patients was less dependent on the similarity with the anatomical connectivity, supporting the idea that the dynamic coordination could not be entirely accounted for in terms of structural connections, but rather represented emergent functional processes. (A) Right: Under anesthesia, the complex coordination pattern 1 uniformly became less prevalent across unresponsive patients (UWS), patients in MCS, and conscious patients who have emerged from the MCS (EMCS); in other words, it was reduced independently of the clinical diagnosis. Conversely, the overall low-coordination pattern 4 became uniformly the most prevalent in all anesthetized patients, irrespective of clinical diagnosis, supporting the specificity of this dynamic configuration to unconsciousness. (B) Similar entropy values across all patients validated the hypothesis that propofol homogeneously abolished conscious awareness. (C) Under anesthesia, all clinical groups presented a stronger relationship (i.e., higher slope) between the patterns' probabilities and the structure-function correlation in comparison to conscious individuals (fig. S10), indicating that brain dynamics largely reflected activity constrained by fixed anatomical pathways. Notes: (C) The patterns are ordered on the basis of their similarity to anatomical connectivity, from the least (left) to the most (right) similar. Boxplots represent medians with interquartile range and maximum-minimum values (whiskers); Rho: Spearman rank correlation between rate and group; UWS/MCS, Wilcoxon test *P* value for the comparisons between patients in UWS and patients in MCS. Ut+, non-behavioral MCS/cognitive-motor dissociation; Ut-, unresponsive patients who do not show command following in mental imagery tasks.

performance during cognitive tasks (23). With respect to pattern 4, studies in physiological and pharmacological unconsciousness showed a breakdown of long-range interareal positive and negative connections. For example, during sleep, the presence of negative dynamic connections disappear (11). Our results are in line with previous findings in animals. As in the present study, the brain activity of anesthetized nonhuman primates resided most frequently in a pattern of low connectivity resembling the anatomy, which was sustained for longer periods of time in comparison to more complex patterns (15). In addition, we demonstrated that network properties, such as mod-

ularity, integration, distance relationship, and efficiency, increased with the participants' conscious state. The latter result is in line with the hypothesis that high-efficiency patterns carry higher metabolic costs (24), which are restricted under pathological unconscious conditions (25).

Our findings also align with theoretical considerations on dynamic connectivity, suggesting that alternating patterns of correlations and anticorrelations may constitute a fundamental property of information processing in the brain (26). Different models of consciousness propose that intermittent epochs of global synchronization grant segregated

and parallel network elements access to a global workspace, integrating them serially and allowing effortful conscious cognition (27). Therefore, the transient exploration of this global workspace could permit the brain to efficiently balance both segregated and integrated neural dynamics and to encode globally broadcasted and therefore reportable conscious contents (3). In the absence of transient epochs of global synchronization, the transmission of information is expected to be relatively ineffective (6).

With respect to patterns 2 and 3, these were not predominantly preferred by any group in terms of occurrence probabilities and duration and hence could represent transitional states (28). Pattern 3 showed the overall positive interareal coherence. For pattern 2, the significance of the overall negative coherence with regions of the visual network can only be speculated. For the moment, we suggest that it indicates the presence of a local coordination pattern reflecting the anatomical organization of the visual cortex (29).

Whether the identified dynamic coordination patterns entail the presence/absence of mental contents or cognitive function is difficult to assume without probing moment-to-moment changes in the contents of conscious experience. Although a link has been shown between intrinsic connectivity networks and various behavioral tasks (30), it has been suggested that BOLD correlations need not necessarily reflect moment-to-moment changes in cognitive content. Instead, they may predominantly reflect processes necessary for maintaining the stability of the brain's functional organization (31). Also, the BOLD signal is nonstationary (32), and some of its spontaneous fluctuations may not be a faithful reflection of functionally relevant brain dynamics or the underlying nonstationarities of neural activity and coordination (10). We also acknowledge that the identification of these dynamic configurations required time-resolved analyses of fMRI time series in the scale of few seconds. It can be argued that conscious cognition and the relevant features of our environment develop on a faster time scale of hundreds of milliseconds (3). However, the BOLD signal has been shown to correlate with infraslow neurophysiological oscillations, i.e., the slow cortical potential (33). The slow cortical potential is important for large-scale information integration, hence suggesting that the flow of the conscious experience could be supported by processes at slower time scales (34). Future experiments should address a potential relationship between conscious experience, the slow cortical potential, and functional network reconfigurations measured as with fMRI.

Regardless of the implicated time scales, our analyses did not aim at tracking the moment-to-moment contents of conscious experience, but at identifying brain-wide dynamic networks supporting different global states of consciousness. We consider that the four-pattern model can account for modes of conscious and unconscious information processing. Our interpretation is sustained by the additional tests for the validity and replicability of the main results. We found that the complex dynamic pattern 1 presented low probabilities of appearing in patients under propofol anesthesia (whether they were communicating or not at baseline) and that it was most likely to appear in patients with covert cognition (i.e., patients in UWS who successfully performed mental imagery neuroimaging tasks). Both findings suggest its implication in conscious states. We also found that the pattern of low interareal coordination (pattern 4) uniformly presented higher probabilities of appearing in all anesthetized patients, regardless of clinical diagnosis, and it was most likely to manifest in unresponsive patients who did not perform the mental imagery neuroimaging task, supporting its relationship to absent or reduced conscious cognition.

Pattern 4 remained visited by healthy controls even under typical wakeful conditions. In the absence of experience sampling during data acquisition, the interpretation of this finding can only be speculative. On the one hand, it could be that healthy controls entered transient microsleep states as a result of fluctuating levels of vigilance, a frequently observed phenomenon during resting-state experiments (35). Our experimental setup did not include simultaneous polysomnography recordings to directly test this hypothesis. However, we derived different fMRI-based proxies to assess the presence of microsleeps. First, we examined head movements time locked to the occurrence of all coordination patterns and found no substantial associations between the two variables, as could be expected if pattern 4 was related to lapses in vigilance. Second, we performed a whole-brain general linear model (GLM) analysis, with the coordination pattern time series as regressors. We did not observe significant positive/negative BOLD signal changes associated with the onset of the different coordination patterns; in particular, the presence of coordination pattern 4 did not result in BOLD signal changes typical of microsleeps. Last, the likelihood of pattern 4 occurring over time did not positively correlate with the elapsed scan time, as has been shown to occur for patterns associated with lapses in vigilance (35, 36). Once we rule out transient loss of vigilance as the cause of the intrusion of pattern 4 in conscious wakefulness, we can speculate that the flow of conscious cognition may be separated by periods of absent or reduced effortful information processing, as recently it was hypothesized that between two successive self-reports, a subject may present states of reduced awareness (37). Behaviorally, this could take the form of "mind blanks" during which participants are not engaged in cognitive demanding processes, although they remain vigilant (38). This interpretation is parsimonious with the observation that participants were instructed to rest inside the scanner, without engaging in any effortful cognitive task. The potential role of transient lapses of awareness in the stream of conscious contents during healthy wakefulness should be addressed by future experiments.

Together, our results suggest that, following loss of consciousness, coordinated brain activity is largely restricted to a positive pattern of interareal coherence dominated by the anatomical connections between brain regions. In contrast, conscious states are characterized by a higher prevalence of a complex configuration of interareal coordination that, while still constrained by brain anatomy, also deviates from it and presents both positive and negative long-distance interactions. It did not escape us that such a complex interareal coordination pattern sporadically appeared in the group of unresponsive patients. The real-time detection of this pattern and its reinforcement through externally induced manipulations could represent a promising avenue for the noninvasive restoration of consciousness. We conclude that these patterns of transient brain signal coordination are characteristic of conscious and unconscious brain states, warranting future research concerning their relationship to ongoing conscious content, and the possibility of modifying their prevalence by external perturbations, both in healthy and pathological individuals, as well as across species.

MATERIALS AND METHODS

Experimental design

Cross-sectional observational study. Measurement technique: fMRI, standardized behavioral assessments. Type of observations: BOLD time series, behavioral observations.

Participants

Data were collected from a cohort of 169 individuals scanned in four clinical expert centers in Belgium [Department of Radiology, Centre Hospitalier Universitaire (CHU), Liège; $n = 87$], France (Department of Neuroradiology, Pitié-Salpêtrière Hospital, Paris; $n = 43$), United States (Citigroup Biomedical Imaging Center, Weill Cornell Medical College, New York; $n = 28$), and Canada (Centre for Functional and Metabolic Mapping, Western's Robarts Research Institute, London, Ontario; $n = 11$). The cohort included 47 healthy controls and 122 patients suffering from disorders of consciousness leading to a vegetative state/UWS or in a MCS. Patients in UWS open their eyes but never exhibit nonreflex voluntary movements, indicating preserved awareness (39). Patients in MCS show more complex behaviors potentially declarative of awareness, such as visual pursuit, orientation to pain, or nonsystematic command following but who, nevertheless, remain unable to communicate their thoughts and feelings (40).

Inclusion criteria for patients were brain damage at least 7 days after the acute brain insult and behavioral diagnosis of the MCS or UWS performed with the Coma Recovery Scale-Revised (CRS-R) (41). The CRS-R evaluates 23 arranged items organized on subscales for auditory, visual, motor, oromotor, communication, and arousal function. Each item assesses the presence or absence of specific physical signs, which represent the integrity of brain function as generalized, localized, or cognitively mediated responsiveness. Patients were excluded when there was contraindication for MRI (e.g., the presence of ferromagnetic aneurysm clips and pacemakers). In addition, 10 patients (6 from Paris, 3 from Liège, and 1 from New York; 8 in MCS and 2 in UWS) were discarded because the signal extracted from the selected ROIs was partially missing during the recordings, resulting in the final cohort of 112 patients (table S1). Inclusion criteria for healthy controls were >18 years old and free of psychiatric and neurological history. The study was approved by the Ethics Committee of the Medical School of the University of Liège, the Ethics Committee of the Pitié-Salpêtrière Hospital, the Institutional Review Board at Weill Cornell Medical College, and the Western University Research Ethics Board. Informed consent to participate in the study was obtained directly from healthy control participants and the legal surrogates of the patients.

The cohort was divided into three datasets. Dataset 1 ($n = 125$) was used for the main analysis, with the aim of identifying the dynamic coordination patterns. It included 47 healthy controls and 78 patients, all scanned under an anesthesia-free resting-state condition [Liège: 21 healthy controls (8 females; mean age, 45 ± 17 years), 40 patients (23 in MCS, 17 in UWS, 11 females; mean age, 47 ± 18 years; 12 traumatic, 28 nontraumatic of which 17 anoxic, 10 patients assessed under acute condition, i.e., <30 days after insult); Paris: 15 healthy controls (9 females; mean age, 41 ± 13 years), 22 patients (9 in MCS, 13 in UWS, 9 females; mean age, 45 ± 17 years; 5 traumatic, 19 nontraumatic of which 12 anoxic, 3 patients assessed in acute setting, i.e., <30 days after insult); New York: 11 healthy controls (3 females; mean age, 32 ± 11 years), 16 patients (10 in MCS, 6 in UWS, 8 females; mean age, 44 ± 14 years; 8 traumatic, 8 nontraumatic of which 4 anoxic, all patients assessed chronic setting, i.e., >30 days after insult)]. Dataset 2 ($n = 11$) included patients with cognitive-motor dissociation (20), i.e., lacking overt conscious behavior yet evidenced using functional neuroimaging (Ut+), and patients who did not perform the imagery task and hence were considered in UWS (Ut-). This dataset was used to test the hypothesis that the complex coordination pattern would be more frequent in the Ut+ patients, whereas the low coordination pattern would be more frequent in patients in UWS who could not perform the task

(Ut-) [London, Ontario: 5 Ut+, 6 Ut-; seven females; mean age, 36 ± 15 years; two traumatic, nine nontraumatic of which eight anoxic, all patients assessed in chronic setting, i.e., >30 days after insult]. Dataset 3 ($n = 23$) included patients scanned under propofol anesthesia and was used to test the hypothesis that complex coordination would disappear as an effect of overall cerebral depression due to the administered anesthetic [Liège: 3 emergence from MCS, 14 in MCS, 6 in UWS; 6 females; mean age, 37 ± 14 years; 16 traumatic, 7 nontraumatic of which 3 anoxic, 21 patients assessed in chronic setting, i.e., >30 days after insult]. Details on patients' demographics and clinical characteristics are summarized in table S1.

Anesthesia protocol

Patients were scanned in anesthesia after medical decision, with the aim of minimizing motion in the scanner, and it was performed by a certified anesthesiologist. Before scanning, all patients fasted for at least 6 hours for solids and 2 hours for liquids. Propofol was administered through intravenous infusion using a target-controlled infusion system, and the concentration was kept to the minimum (1 to 2 $\mu\text{g}/\text{ml}$). To ensure adequate airing, some patients received assisted mechanical ventilation through a tracheostomy, a laryngeal mask, or an endotracheal tube when already in place. Additional oxygen was delivered in some cases, either through a face mask or through the airway instrumentation device. Patients' physiologic parameters (arterial blood pressure, electrocardiogram, breathing frequency, and pulse oximetry) were closely and continuously monitored. Propofol was titrated to achieve immobility in the scanner. Once obtained, the necessary plasma concentration of propofol was kept constant throughout the procedure. A complete resuscitation equipment was present during the procedure.

Imaging acquisition parameters

In Liège, data were acquired on a 3T Siemens TIM Trio MRI scanner (Siemens Medical Solutions, Erlangen, Germany): 300 T2*-weighted images were acquired with a gradient-echo echo-planar imaging (EPI) sequence using axial slice orientation and covering the whole brain (32 slices; slice thickness, 3 mm; repetition time, 2000 ms; echo time, 30 ms; voxel size, $3 \times 3 \times 3$ mm; flip angle, 78°; field of view, 192 mm by 192 mm). A structural T1 magnetization-prepared rapid gradient-echo (MPRAGE) sequence (120 slices; repetition time, 2300 ms; echo time, 2.47 ms; voxel size, $1.0 \times 1.0 \times 1.2$ mm; flip angle, 9°).

In Paris, data were acquired on a 3T General Electric Signa System (Milwaukee, WI): 200 T2*-weighted images were acquired with a gradient-echo EPI sequence using axial slice orientation and covering the whole brain (48 slices; slice thickness, 3 mm; repetition time, 2400 ms; echo time, 30 ms; voxel size, $3.4375 \times 3.4375 \times 3.4375$ mm; flip angle, 90°; field of view, 192 mm by 192 mm). A T1 MPRAGE sequence was further acquired in the same session (236 slices; repetition time, 7156 ms; echo time, 3.672 ms; voxel size, $0.4883 \times 0.4883 \times 0.4883$ mm; flip angle, 15°).

In New York, data were acquired on a 3T General Electric Signa System (Milwaukee, WI): 180 T2*-weighted images were acquired with a gradient-echo EPI sequence using axial slice orientation and covering the whole brain (28 slices; repetition time, 2000 ms; echo time, 40 ms; voxel size, $3.75 \times 3.75 \times 5$ mm; flip angle, 70°). A T1-weighted three-dimensional (3D) inversion recovery-prepared spoiled gradient echo sequence was further acquired in the same session (120 slices; repetition time, 8.864 ms; echo time, 3.524 ms; inversion time, 400 ms; voxel size, $0.9375 \times 0.9375 \times 1.2$ mm; flip angle, 13°).

In London, Ontario, data were acquired on 3T Siemens TIM Trio and 3T Siemens Prisma MRI scanners: 256 T2*-weighted images were acquired with a gradient-echo EPI sequence using axial slice orientation and covering the whole brain (33 slices; slice thickness, 3 mm; repetition time, 2000 ms; echo time, 30 ms; voxel size, $3 \times 3 \times 3$ mm; flip angle, 75°); a T1-weighted 3D inversion recovery-prepared spoiled gradient echo sequence was further acquired in the same session (176 slices; slice thickness, 1 mm; repetition time, 2530 ms; echo time, 3.34 ms; voxel size, $1 \times 1 \times 1$ mm; flip angle, 7°).

Data preprocessing and time series extraction

Preprocessing was performed as previously reported (21) using Statistical Parametric Mapping 12 (SPM12; www.fil.ion.ucl.ac.uk/spm). Preprocessing steps included slice-time correction, realignment, segmentation of structural data, normalization of functional and structural data into the standard stereotactic Montreal Neurological Institute space, and spatial smoothing using a Gaussian kernel of 6-mm full width at half-maximum. For functional data, the three initial volumes were discarded to avoid T1 saturation effects. Motion artifact detection and rejection were performed with the artifact detection toolbox (ART toolbox): An image was defined as an outlier or artifact image if the head displacement in the x , y , or z direction was greater than 2 mm from the previous frame, if the rotational displacement was greater than 0.02 rad from the previous frame, or if the global mean intensity in the image was greater than 3 SDs from the mean image intensity for the entire resting scan. Outliers in the global mean signal intensity and motion were subsequently included as nuisance regressors within the first-level GLM so that the temporal structure of the data would not be disrupted. As a data quality measure, we calculated the number of motion outliers that were detected during preprocessing. The number of motion outlier images was similar across the groups of healthy controls (mean rank, 61), patients in MCS (mean rank, 72), and patients in UWS [mean rank, 74; Kruskal-Wallis test, $H(2) = 2.5$, $P = 0.3$], suggesting comparable datasets.

For noise reduction, we modeled the influence of noise as a voxel-specific linear combination of multiple empirically estimated noise sources by deriving principal components from noise ROIs and by including them as nuisance parameters within the GLMs (as implemented in the CONN functional connectivity toolbox, v.16.b). Specifically, the anatomical image for each participant was segmented into white matter (WM), gray matter (GM), and cerebrospinal fluid (CSF) masks (old normalize function, SPM12). To minimize partial voluming with GM, the WM and CSF masks were eroded by one voxel, which resulted in smaller masks than the original segmentations. The eroded WM and CSF masks were then used as noise ROIs. Used time series were from the unsmoothed functional volumes to avoid additional risk of contaminating WM and CSF signals with GM signals. Five principal components of the signals from WM and CSF noise ROIs were removed with regression. A temporal band-pass filter of 0.008 to 0.09 Hz was applied on the time series to restrict the analysis to low-frequency fluctuations. Residual head motion parameters (three rotation and three translation parameters and six parameters representing their first-order temporal derivatives) were further regressed out. For each sphere ROI, time series were extracted by averaging all voxels' signal within the ROI at a given brain volume. A total of 42 network-based ROIs were selected (table S2). Concerning the positive coupling between ROIs belonging to the default mode network (DMN) and the frontoparietal (FP) network observed in some of our dynamic coordination patterns, we noted that previous articles (42, 43) using the same set of ROIs (as well as similar data

preprocessing) also reported positive connectivity between them. Therefore, it is possible that the precise choice of FP ROIs introduced in these articles does not robustly represent the FP/DMN anticorrelations present in the data. Most likely, this is due to the fact that some FP ROIs are located in the proximity of the FP/DMN boundary, and the spatial extent of RSN is known to present important interperson variability, especially in higher-order heteromodal association cortices (44). However, we noted that the DMN ROIs were anticorrelated to other task-positive ROIs, as expected.

Statistical analysis: Dynamic functional coordination analysis

Phase-based dynamic functional coordination was preferred to a sliding-window approach because it avoids the inclusion of overlapping signals in the estimation of temporal oscillations (6). To obtain a phase signal corresponding to the BOLD time series of each ROI, the analytic representation of the signals was used. The analytic signal was expressed in the imaginary space and was composed by the original signal (real part) and the corresponding Hilbert transform of this signal (imaginary part). This representation allows for the computation of the instantaneous phase. Using Euler's formula, the analytic signal can be represented as the combination of two instantaneous real signals: amplitude and phase. The phase was calculated as the inverse tangent of the ratio of the imaginary and real components. Afterward, the phase was "wrapped" to values between $-\pi$ and π , and the instantaneous phase $\theta(t)$ was related to zero crossings and BOLD peaks. Inter-ROI phase difference was computed using the difference of each pair of ROI instantaneous phase signals.

To assess the presence of recurrent coordination patterns across individuals and patients of dataset 1 ($n = 125$), we adopted the following steps. First, we restructured each scanning session as a matrix with phase-difference values in one dimension ($[42 \times (42 - 1)]/2 = 861$ features) and time in the other dimension (279 images). Second, we concatenated all the matrices by the time dimension, yielding a matrix of 861×34875 elements. Last, the k -means clustering algorithm was applied to the concatenated matrix using the L_1 distance (a.k.a. "Manhattan distance") as implemented in MATLAB (MathWorks Inc.). The clustering algorithm was applied 500 times to avoid local minima using a random initialization of centroid positions in each iteration. As a result of this procedure, we obtained (i) k cluster centroids (42×42 matrices), which are representative of the recurrent coordination patterns, and (ii) a label indicating the pattern corresponding to each image of the scanning session. The number of clusters k was determined as previously reported ($k = 4$) (36), although additional exploratory analyses varying k from 3 to 7 demonstrated consistent and robust results (fig. S1A). In addition, our results showed stable first and last coordination patterns (ordered in terms of their similarity to the anatomical connectivity) for all the choices of the clustering k (fig. S1B) and a maximal interpattern variance when setting this to obtain four clusters (fig. S1C).

For dataset 2 and dataset 3, we characterized the sequence of phase coherence matrices based on the coordination patterns obtained from dataset 1. More precisely, we computed the L_1 distance between each phase coherence matrix and the cluster centroids determined in dataset 1. Each scanning volume was then assigned the label of the centroid that minimized its distance with the phase coherence matrix associated with that volume.

In all cases, we computed the occurrence rate of each pattern for each individual as the total number of volumes for which that given

pattern was present divided by the total number of volumes of the acquisition. To rule out potential effects related to the scanning site on the identified brain patterns, we computed four independent analyses of variance (ANOVAs) (one for each pattern) with the pattern rate of occurrences as the dependent variable and the patient's clinical condition and scanning site as independent factors (see Supplementary Methods 1). Last, entropy was computed using the classical definition, which considers the sum of the probabilities of the patterns weighted by their corresponding logarithms ($H = -\sum_i^N p_i \log_2 p_i$, where N is the total number of patterns and p_i is the probability of observing the i th pattern). In this definition, we used a base-2 logarithm, which results in the equivalent definition of the amount of information contained in the symbolic sequence of patterns (measured in bits).

To further describe the dynamic nature of the pattern exploration, we obtained, for each participant, a matrix containing information about the probabilities that any given pattern to transition into another. This matrix contains, in its i th row, the normalized (i.e., sum equal to one) frequency distribution of observing a volume labeled as the i th pattern transitioning into the pattern corresponding to the j th column. The average contiguous amount of time spent in each pattern for each clinical group was corrected for random durations by subtracting the average duration of surrogate shuffled pattern series.

The sequence predictability for each individual was quantified using the entropy rate (Markov entropy) for the corresponding pattern probabilities and the transition probability matrices. The entropy rate for the sequence of brain patterns of each participant was computed as follows

$$H = -\sum_{ij} \mu_i P_{ij} \log_2 P_{ij}$$

where μ_i corresponds to the probability of observing pattern i and P_{ij} corresponds to the transition probability from pattern i to pattern j .

To investigate the dependence of brain dynamics on the state of consciousness, we defined a measure of similarity between functional and structural connectivity. We resorted to a widely used group estimate of human anatomical connectivity, measured with the non-invasive technique of DSI (fig. S6). The procedure followed to acquire DSI data and construct the anatomical connectivity network was extensively explained elsewhere (45). Briefly, high-resolution T1 and diffusion spectrum images were acquired for five healthy participants (mean age, 29.4 years; all male) and 998 ROIs (1.5-cm² area) placed throughout the cortex (excluding subcortical regions) of individual participants, being later mapped into a common space. WM tractography was applied to compute fiber trajectories and construct a network by linking every two nodes for which a fiber existed that started in one and ended in the other. A group consensus network was created by linking nodes connected in at least one of the participants, resulting in a binary network of density 0.0359. Since the choice of regions of the 998 ROIs used in (45) did not match our 42 ROIs (selected from literature performing independent component analysis), we resampled the network by considering 30-mm spheres centered at each of the 42 ROIs and computed the mean structural connectivity between all the original 998 regions within each pair of spheres. This resulted in a symmetric 42×42 matrix containing in each entry the mean anatomical connectivity value observed between the corresponding pair of ROIs. We obtained similar results when reducing the original DSI matrix using different sphere diameters (10 and 20 mm; fig. S11). Last, to compare the phase-based coherence and an-

atomical connectivity matrices, we computed the linear correlation coefficient between the entries of both matrices (coherence/anatomical correlation). This was performed for each phase-based coordination pattern obtained using the k -means algorithm. Last, for each participant, we computed the linear slope coefficient of the relationship between the occurrence rate of each brain pattern and the corresponding coherence/anatomical correlation. To better understand the identified patterns, a quantitative description by means of graph theory metrics was performed to reveal the level of underlying complexity that may not be evident upon direct observation (Supplementary Methods 2).

SUPPLEMENTARY MATERIALS

Supplementary material for this article is available at <http://advances.sciencemag.org/cgi/content/full/5/2/eaat7603/DC1>

Supplementary Methods 1

Supplementary Methods 2

Fig. S1. The four recurrent dynamic coordination patterns emerge at different dimensionalities.

Fig. S2. Network analysis of the identified patterns shows that consciousness-related patterns are characterized by higher spatial complexity, long-distance negative edges, community structure, and high efficiency.

Fig. S3. Network properties reflect the state of consciousness.

Fig. S4. Robustness of the extracted coordination patterns.

Fig. S5. Etiology, chronicity age, and gender do not mediate patients' temporal dynamics.

Fig. S6. The structural connectivity network is defined from DSI and contains systems-based ROIs.

Fig. S7. Transition probabilities normalized by the patterns' probabilities of occurrence.

Fig. S8. Entropy rate increases with respect to the state of consciousness.

Fig. S9. Pattern validation in dataset 2 ("Canada") and dataset 3 ("Anesthesia").

Fig. S10. Dataset slope comparisons.

Fig. S11. Replication of the structural-functional analysis with different granularity of the structural matrix reduction.

Table S1. Patients' demographic and clinical characteristics per scanning site ($n = 112$).

Table S2. Network-level ROIs used as seed areas.

References (46–48)

REFERENCES AND NOTES

- J. F. Storm, M. Boly, A. G. Casali, M. Massimini, U. Olcese, C. M. A. Pennartz, M. Wilke, Consciousness regained: Disentangling mechanisms, brain systems, and behavioral responses. *J. Neurosci.* **37**, 10882–10893 (2017).
- P. Stern, Neuroscience: In search of new concepts. *Science* **358**, 464–465 (2017).
- G. Tononi, Consciousness as integrated information: A provisional manifesto. *Biol. Bull.* **215**, 216–242 (2008).
- G. Northoff, Z. Huang, How do the brain's time and space mediate consciousness and its different dimensions? Temporo-spatial theory of consciousness (TTC). *Neurosci. Biobehav. Rev.* **80**, 630–645 (2017).
- S. Dehaene, J.-P. Changeux, Experimental and theoretical approaches to conscious processing. *Neuron* **70**, 200–227 (2011).
- G. Deco, M. L. Kringelbach, Metastability and coherence: Extending the communication through coherence hypothesis using a whole-brain computational perspective. *Trends Neurosci.* **39**, 125–135 (2016).
- M. Breakspear, Dynamic models of large-scale brain activity. *Nat. Neurosci.* **20**, 340–352 (2017).
- A. Zalesky, A. Fornito, L. Cocchi, L. L. Gollo, M. Breakspear, Time-resolved resting-state brain networks. *Proc. Natl. Acad. Sci. U.S.A.* **111**, 10341–10346 (2014).
- R. F. Betzel, M. Fukushima, Y. He, X.-N. Zuo, O. Sporns, Dynamic fluctuations coincide with periods of high and low modularity in resting-state functional brain networks. *Neuroimage* **127**, 287–297 (2016).
- R. M. Hutchison, T. Womelsdorf, E. A. Allen, P. A. Bandettini, V. D. Calhoun, M. Corbetta, S. Della Penna, J. H. Duyn, G. H. Glover, J. Gonzalez-Castillo, D. A. Handwerker, S. Keilholz, V. Kiviniemi, D. A. Leopold, F. de Pasquale, O. Sporns, M. Walter, C. Chang, Dynamical functional connectivity: Promise, issues, and interpretations. *Neuroimage* **80**, 360–378 (2013).
- E. Tagliazucchi, F. von Wegner, A. Morzelewski, V. Brodbeck, K. Jahnke, H. Laufs, Breakdown of long-range temporal dependence in default mode and attention networks during deep sleep. *Proc. Natl. Acad. Sci. U.S.A.* **110**, 15419–15424 (2013).

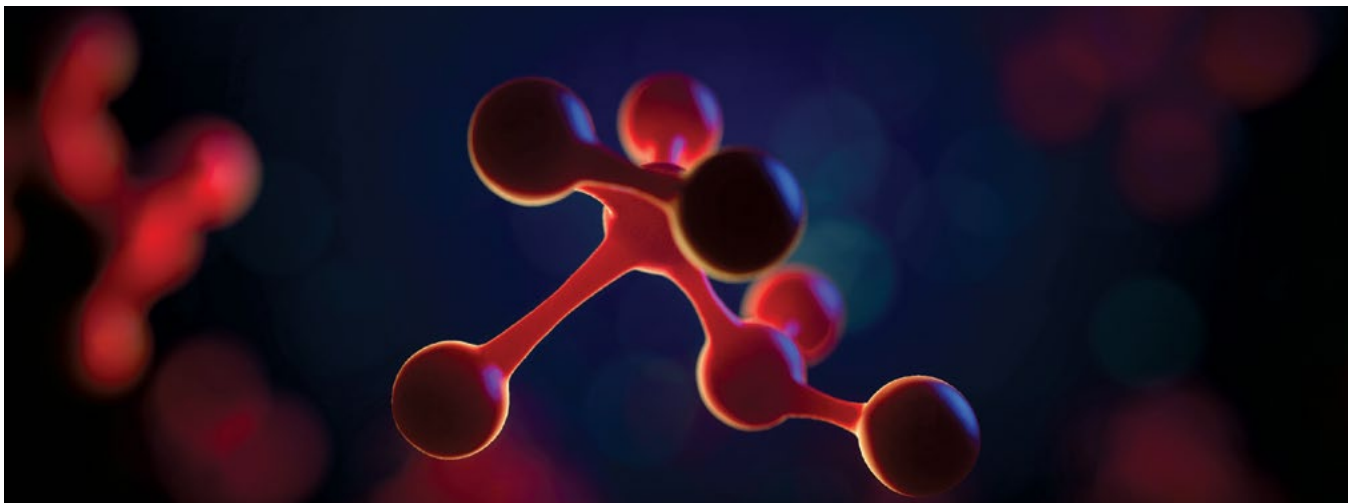
12. H. M. Chow, S. G. Horovitz, W. S. Carr, D. Picchioni, N. Coddington, M. Fukunaga, Y. Xu, T. J. Balkin, J. H. Duyn, A. R. Braun, Rhythmic alternating patterns of brain activity distinguish rapid eye movement sleep from other states of consciousness. *Proc. Natl. Acad. Sci. U.S.A.* **110**, 10300–10305 (2013).
13. E. Tagliazucchi, D. R. Chialvo, M. Siniatchkin, E. Amico, J.-F. Brichant, V. Bonhomme, Q. Noirhomme, H. Laufs, S. Laureys, Large-scale signatures of unconsciousness are consistent with a departure from critical dynamics. *J. R. Soc. Interface* **13**, 2015027 (2016).
14. E. Amico, F. Gomez, C. Di Perri, A. Vanhaudenhuyse, D. Lesenfants, P. Boveroux, V. Bonhomme, J.-F. Brichant, D. Marinazzo, S. Laureys, Posterior cingulate cortex-related co-activation patterns: A resting state fMRI study in propofol-induced loss of consciousness. *PLOS ONE* **9**, e100012 (2014).
15. P. Barttfeld, L. Uhrig, J. D. Sitt, M. Sigman, B. Jarraya, S. Dehaene, Signature of consciousness in the dynamics of resting-state brain activity. *Proc. Natl. Acad. Sci. U.S.A.* **112**, 887–892 (2015).
16. A. G. Hudetz, X. Liu, S. Pillay, Dynamic repertoire of intrinsic brain states is reduced in propofol-induced unconsciousness. *Brain Connect.* **5**, 10–22 (2015).
17. M. M. Monti, A. Vanhaudenhuyse, M. R. Coleman, M. Boly, J. D. Pickard, L. Tshibanda, A. M. Owen, S. Laureys, Willful modulation of brain activity in disorders of consciousness. *N. Engl. J. Med.* **362**, 579–589 (2010).
18. S. Casarotto, A. Comanducci, M. Rosanova, S. Sarasso, M. Fecchio, M. Napolitani, A. Pigorini, A. G. Casali, P. D. Trimarchi, M. Boly, O. Gosseries, O. Bodart, F. Curto, C. Landi, M. Mariotti, G. Devale, S. Laureys, G. Tononi, M. Massimini, Stratification of unresponsive patients by an independently validated index of brain complexity. *Ann. Neurol.* **80**, 718–729 (2016).
19. D. A. Engemann, F. Raimondo, J.-R. King, B. Rohaut, G. Louppe, F. Faugeras, J. Annen, H. Cassol, O. Gosseries, D. Fernandez-Slezak, S. Laureys, L. Naccache, S. Dehaene, J. D. Sitt, Robust EEG-based cross-site and cross-protocol classification of states of consciousness. *Brain* **141**, 3179–3192 (2018).
20. N. D. Schiff, Cognitive motor dissociation following severe brain injuries. *JAMA Neurol.* **72**, 1413–1415 (2015).
21. A. Demertzi, G. Antonopoulos, L. Heine, H. U. Voss, J. S. Crone, C. de Los Angeles, M. A. Bahri, C. Di Perri, A. Vanhaudenhuyse, V. Charland-Verville, M. Kronbichler, E. Trinka, C. Phillips, F. Gomez, L. Tshibanda, A. Soddu, N. D. Schiff, S. Whitfield-Gabrieli, S. Laureys, Intrinsic functional connectivity differentiates minimally conscious from unresponsive patients. *Brain* **138**, 2619–2631 (2015).
22. P. Fiset, T. Paus, T. Daleo, G. Plourde, P. Meuret, V. Bonhomme, N. Hajji-Ali, S. B. Backman, A. C. Evans, Brain mechanisms of propofol-induced loss of consciousness in humans: A positron emission tomographic study. *J. Neurosci.* **19**, 5506–5513 (1999).
23. J. M. Shine, P. G. Bissett, P. T. Bell, O. Koyejo, J. H. Balsters, K. J. Gorgolewski, C. A. Moodie, R. A. Poldrack, The dynamics of functional brain networks: Integrated network states during cognitive task performance. *Neuron* **92**, 544–554 (2016).
24. E. Bullmore, O. Sporns, The economy of brain network organization. *Nat. Rev. Neurosci.* **13**, 336–349 (2012).
25. J. Stender, K. N. Mortensen, A. Thibaut, S. Darkner, S. Laureys, A. Gjedde, R. Kupers, The minimal energetic requirement of sustained awareness after brain injury. *Curr. Biol.* **26**, 1494–1499 (2016).
26. A. Demertzi, A. Soddu, S. Laureys, Consciousness supporting networks. *Curr. Opin. Neurobiol.* **23**, 239–244 (2013).
27. S. Dehaene, M. Kerszberg, J.-P. Changeux, A neuronal model of a global workspace in effortful cognitive tasks. *Proc. Natl. Acad. Sci. U.S.A.* **95**, 14529–14534 (1998).
28. A. Fornito, B. J. Harrison, A. Zalesky, J. S. Simons, Competitive and cooperative dynamics of large-scale brain functional networks supporting recollection. *Proc. Natl. Acad. Sci. U.S.A.* **109**, 12788–12793 (2012).
29. E. Genç, M. L. Schölvinck, J. Bergmann, W. Singer, A. Kohler, Functional connectivity patterns of visual cortex reflect its anatomical organization. *Cereb. Cortex* **26**, 3719–3731 (2016).
30. A. R. Laird, P. M. Fox, S. B. Eickhoff, J. A. Turner, K. L. Ray, D. R. McKay, D. C. Glahn, C. F. Beckmann, S. M. Smith, P. T. Fox, Behavioral interpretations of intrinsic connectivity networks. *J. Cogn. Neurosci.* **23**, 4022–4037 (2011).
31. T. O. Laumann, A. Z. Snyder, A. Mitra, E. M. Gordon, C. Gratton, B. Adeyemo, A. W. Gilmore, S. M. Nelson, J. J. Berg, D. J. Greene, J. E. McCarthy, E. Tagliazucchi, H. Laufs, B. L. Schlaggar, N. U. F. Dosenbach, S. E. Petersen, On the stability of BOLD fMRI correlations. *Cereb. Cortex* **27**, 4719–4732 (2017).
32. M. Fukunaga, S. G. Horovitz, P. van Gelderen, J. A. de Zwart, J. M. Jansma, V. N. Ikonomidou, R. Chu, R. H. R. Deckers, D. A. Leopold, J. H. Duyn, Large-amplitude, spatially correlated fluctuations in BOLD fMRI signals during extended rest and early sleep stages. *Magn. Reson. Imaging* **24**, 979–992 (2006).
33. B. J. He, A. Z. Snyder, J. M. Zempel, M. D. Smyth, M. E. Raichle, Electrophysiological correlates of the brain's intrinsic large-scale functional architecture. *Proc. Natl. Acad. Sci. U.S.A.* **105**, 16039–16044 (2008).
34. B. J. He, M. E. Raichle, The fMRI signal, slow cortical potential and consciousness. *Trends Cogn. Sci.* **13**, 302–309 (2009).
35. E. Tagliazucchi, H. Laufs, Decoding wakefulness levels from typical fMRI resting-state data reveals reliable drifts between wakefulness and sleep. *Neuron* **82**, 695–708 (2014).
36. E. A. Allen, E. Damaraju, S. M. Plis, E. B. Erhardt, T. Eichele, V. D. Calhoun, Tracking whole-brain connectivity dynamics in the resting state. *Cereb. Cortex* **24**, 663–676 (2014).
37. L. Naccache, Why and how access consciousness can account for phenomenal consciousness. *Philos. Trans. R. Soc. B Biol. Sci.* **373**, 20170357 (2018).
38. A. F. Ward, D. M. Wegner, Mind-blanking: When the mind goes away. *Front. Psychol.* **4**, 650 (2013).
39. S. Laureys, G. G. Celestis, F. Cohadon, J. Lavrijsen, J. León-Carrión, W. G. Sannita, L. Sazbon, E. Schmutzhard, K. R. von Wild, A. Zeman, G. Dolce; European Task Force on Disorders of Consciousness, Unresponsive wakefulness syndrome: A new name for the vegetative state or apallic syndrome. *BMC Med.* **8**, 68 (2010).
40. J. T. Giacino, The minimally conscious state: Defining the borders of consciousness. *Prog. Brain Res.* **150**, 381–395 (2005).
41. J. T. Giacino, K. Kalmar, J. Whyte, The JFK Coma Recovery Scale-Revised: Measurement characteristics and diagnostic utility. *Arch. Phys. Med. Rehabil.* **85**, 2020–2029 (2004).
42. D. A. Fair, N. U. F. Dosenbach, J. A. Church, A. L. Cohen, S. Brahmabhatt, F. M. Miezin, D. M. Barch, M. E. Raichle, S. E. Petersen, B. L. Schlaggar, Development of distinct control networks through segregation and integration. *Proc. Natl. Acad. Sci. U.S.A.* **104**, 13507–13512 (2007).
43. N. U. F. Dosenbach, D. A. Fair, F. M. Miezin, A. L. Cohen, K. K. Wenger, R. A. T. Dosenbach, M. D. Fox, A. Z. Snyder, J. L. Vincent, M. E. Raichle, B. L. Schlaggar, S. E. Petersen, Distinct brain networks for adaptive and stable task control in humans. *Proc. Natl. Acad. Sci. U.S.A.* **104**, 11073–11078 (2007).
44. S. Mueller, D. Wang, M. D. Fox, B. T. Yeo, J. Sepulcre, M. R. Sabuncu, R. Shafee, J. Lu, H. Liu, Individual variability in functional connectivity architecture of the human brain. *Neuron* **77**, 586–595 (2013).
45. P. Hagmann, L. Cammoun, X. Gigandet, R. Meuli, C. J. Honey, V. J. Wedeen, O. Sporns, Mapping the structural core of human cerebral cortex. *PLOS Biol.* **6**, e159 (2008).
46. M. Rubinov, O. Sporns, Complex network measures of brain connectivity: Uses and interpretations. *Neuroimage* **52**, 1059–1069 (2010).
47. G. Deco, G. Tononi, M. Boly, M. L. Kringselbach, Rethinking segregation and integration: Contributions of whole-brain modelling. *Nat. Rev. Neurosci.* **16**, 430–439 (2015).
48. J. Annen, G. Frasso, J. S. Crone, L. Heine, C. Di Perri, C. Martial, H. Cassol, A. Demertzi, L. Naccache, S. Laureys; Coma Science Group Collaborators, Regional brain volumetry and brain function in severely brain-injured patients. *Ann. Neurol.* **83**, 842–853 (2018).

Acknowledgments: We would like to express our gratitude to V. Bonhomme and M. Kirsch (GIGA-Consciousness, Anesthesia and Intensive Care laboratories, CHU Liège) for assistance in performing anesthesia in patients. We thank L. Tshibanda (Liège CHU Neuroradiology Department) and D. Gallanaud (Hôpital Pitié-Salpêtrière Neuroradiology Department) for assistance in participant scanning. We thank L. E. Gonzalez-Lara (Brain and Mind Institute, University of Western Ontario) for assistance in data acquisition. We acknowledge the assistance of M. M. Conte (Brain and Mind Research Institute, Weill Cornell Medical College) for sharing neuroimaging data. We thank C. Aubinet and M. Carriere, PhD candidates (Coma Science Group, GIGA Consciousness, University of Liège), for assistance in neuroimaging data acquisition. We are grateful to V. Perlberg (Bioinformatics and Biostatistics Platform, IHU-A-ICM, Institut du Cerveau et de la Moelle épinière, Paris) for assistance during data preprocessing. We are highly grateful to the members of the Liège Coma Science Group and the Paris PICNIC Lab DOC Team for assistance in clinical evaluations. Last, we would like to express our gratitude to A. Schurger (Neurospin, Unicog, CEA-Saclay) for manuscript proofreading. **Funding:** The reported data have been collected and shared among partners participating in the James S. McDonnell Foundation Collaborative Activity Award “Recovery of Consciousness After Severe Brain Injury” (phases I and II; 2008–2017). This work has been further financially supported by the INSERM, the Belgian National Funds for Scientific Research (FNRS), the Institut du Cerveau et de la Moelle épinière (ICM), the Canada Excellence Research Chairs (CERC) program, the CIFAR Canadian Institute for Advanced Research, the Canadian Institutes of Health Research (CIHR), the European Commission, the Human Brain Project (EU-H2020-FETFLAGSHIP-HBP-SGA1-GA720270), the Luminous project (EU-H2020-fetopen-ga686764), the Center-TBI project (FP7-HEALTH- 602150), the Belgian American Education Foundation, the Wallonie-Bruxelles International, the Fonds Léon Frederiq, “Fondazione Europea di Ricerca Biomedica,” European Space Agency, Belspo, BIAL Foundation, the Mind Science Foundation, the French Speaking Community Concerted Research Action (ARC-06/11-340), and the University and University Hospital of Liège. **Author contributions:** A.D., E.T., and J.D.S. designed the research.

A.D., E.T., G.D., P.B., F.R., D.F.-E., and J.D.S. analyzed the data. A.D., E.T., S.D., N.D.S., A.M.O., S.L., L.N., and J.D.S. interpreted the data. N.D.S., A.M.O., S.L., L.N., B.R., C.M., and H.U.V. curated and provided the data. A.D., E.T., and J.D.S. wrote the manuscript. All authors contributed to the editing of the manuscript. **Competing interests:** The authors declare that they have no competing interests. **Data and materials availability:** Data have been stored locally, following national and EU laws on the protection of individuals with regard to the processing of personal data. The clinical data used in this paper may be available upon reasonable request. All data needed to evaluate the conclusions in the paper are present in the paper and/or the Supplementary Materials.

Submitted 5 April 2018
Accepted 19 December 2018
Published 6 February 2019
10.1126/sciadv.aat7603

Citation: A. Demertzi, E. Tagliazucchi, S. Dehaene, G. Deco, P. Barttfeld, F. Raimondo, C. Martial, D. Fernández-Espejo, B. Rohaut, H. U. Voss, N. D. Schiff, A. M. Owen, S. Laureys, L. Naccache, J. D. Sitt, Human consciousness is supported by dynamic complex patterns of brain signal coordination. *Sci. Adv.* **5**, eaat7603 (2019).



Publish your research in the *Science* family of journals

The *Science* family of journals (*Science*, *Science Advances*, *Science Immunology*, *Science Robotics*, *Science Signaling*, and *Science Translational Medicine*) are among the most highly-regarded journals in the world for quality and selectivity. Our peer-reviewed journals are committed to publishing cutting-edge research, incisive scientific commentary, and insights on what's important to the scientific world at the highest standards.

Submit your research today!
Learn more at ScienceMag.org/journals

Science
JOURNALS AAAS

Peak Your Curiosity.



FLIPR Penta High-Throughput Cellular Screening System

Real-time screening of iPSC-derived neurons
and cardiomyocytes, as well as GPCR and
ion channel targets.

KEY BENEFITS

- Assay adaptability with configurable optics
- Throughput flexibility with user-exchangeable 96-, 384-, and 1536-well pipettors
- Multi-user flexibility with intuitive software
- Future ready with FLIPR® Cycler automation upgradeability

Learn more: moleculardevices.com/Penta



For Research Use Only. Not for use in diagnostic procedures.
©2019 Molecular Devices, LLC. All Rights Reserved. The trademarks mentioned
herein are the property of Molecular Devices, LLC or their respective owners.

 MOLECULAR
DEVICES

NEUROIMMUNOLOGY

Conventional DCs sample and present myelin antigens in the healthy CNS and allow parenchymal T cell entry to initiate neuroinflammation

Sarah Mundt¹, Dunja Mrdjen^{1*}, Sebastian G. Utz^{1†}, Melanie Greter¹, Bettina Schreiner^{1,2}, Burkhard Becher^{1‡}

The central nervous system (CNS) is under close surveillance by immune cells, which mediate tissue homeostasis, protection, and repair. Conversely, in neuroinflammation, dysregulated leukocyte invasion into the CNS leads to immunopathology and neurological disability. To invade the brain parenchyma, autoimmune encephalitogenic T helper (T_H) cells must encounter their cognate antigens (Ags) presented via local Ag-presenting cells (APCs). The precise identity of the APC that samples, processes, and presents CNS-derived Ags to autoaggressive T cells is unknown. Here, we used a combination of high-dimensional single-cell mapping and conditional MHC class II ablation across all CNS APCs to systematically interrogate each population for its ability to reactivate encephalitogenic T_H cells *in vivo*. We found a population of conventional dendritic cells, but not border-associated macrophages or microglia, to be essential for licensing T cells to initiate neuroinflammation.

INTRODUCTION

Multidirectional interactions between the central nervous system (CNS) and the immune system have a profound impact on brain protection and pathology. There is evidence that not only brain development and homeostasis but also social behavior, psychiatric disorders, and neurodegenerative diseases such as Alzheimer's disease and Parkinson's disease are influenced by innate and adaptive immunity (1). Multiple sclerosis (MS) is a prototypical paradigm for pathological CNS-immune interactions, because CNS-invading autoaggressive T helper (T_H) cells induce immunopathology, leading to demyelination, axonal loss, and brain atrophy (2). Even fully primed and activated encephalitogenic T_H cells must encounter their cognate antigen (Ag) in the CNS to cross the basal lamina of the blood-brain barrier (BBB) and to infiltrate the parenchyma (3). This local reconfirmation of the correct Ag then also triggers an inflammatory cascade and the recruitment of monocytes, which, in turn, mediate CNS tissue damage (3). The reactivation of myelin-reactive T_H cells outside but proximal to the parenchyma requires a CNS-resident population of major histocompatibility complex (MHC) class II (MHCII)-expressing Ag-presenting cells (APCs), which have sampled myelin protein from oligodendrocytes and present its peptides within the homeostatic CNS.

Within the CNS parenchyma, microglia are the only resident leukocytes and therefore the most likely candidate to directly interact with invading T cells (4). Recently, high-dimensional cytometry and algorithm-guided analyses revealed an abundant and complex immune cell landscape of CNS-blood and CNS-cerebrospinal fluid interfaces, which includes border-associated macrophages (BAMs), monocyte-derived cells (MdCs), dendritic cells (DCs), lymphocytes, and even granulocytes (5–8).

The prototypical tool to study T cell-mediated neuroinflammation *in vivo* is experimental autoimmune encephalomyelitis (EAE),

which not only serves as the preclinical model for MS but also permits the investigation of T cell-APC interactions in general. Most EAE-based studies that identify CNS APCs have used bone marrow chimeric rodents, which—largely due to the irradiation-induced cytokine storm—suffer from the infiltration of the CNS by various immune cells and, therefore, do not allow the study of T cell-Ag encounters within the steady-state CNS (9). Likewise, active immunization with complete Freund's adjuvant (CFA) also changes the CNS leukocyte landscape independent from the presence of auto-Ag (10). Complicating matters is the difficulty of distinguishing between CNS-resident and CNS-invading leukocytes because of overlapping phenotypes. We had previously presented data suggesting that CNS-associated DCs are the most potent APCs of the CNS (7). However, CD11c, which we had used to restrict MHCII expression to DCs, has been shown to not be specific to DCs, because microglia, BAMs, Ly6C^{hi}, and Ly6C^{low} monocytes—which are all present in the steady-state CNS—can also express this marker (5, 11–13). Moreover, there is some evidence for APC function in BAMs, microglia, and other CNS-resident cells (14–16).

To systematically interrogate each potential CNS APC population for its capacity to effectively present myelin Ag to encephalitogenic T_H cells, we took advantage of new *in vivo* genetic targeting and single-cell cytometry tools. We first performed mass cytometric [cytometry by time of flight (CyTOF)] analysis with subsequent high-dimensional data mining to identify and characterize all APCs of the steady-state brain. Conditional deletion of MHCII across CNS APCs in combination with adoptive transfer (AT) EAE allowed us to specifically investigate T cell reactivation in the CNS, independent of peripheral priming.

RESULTS

Multiple potential APCs are found in the steady-state CNS

To determine which cells of the CNS have the potential to present Ag, we scanned all CNS-associated leukocytes for MHCII expression in the steady-state brain. To be able to fully capture the complexity of CNS immune cells, we used our recently described workflow for the high-dimensional single-cell analysis by mass cytometry and

¹Institute of Experimental Immunology, University of Zurich, Zurich, Switzerland.

²Department of Neurology, University Hospital Zurich, Zurich, Switzerland.

*Present address: Department of Pathology, Stanford University, San Francisco, CA, USA.

†These authors contributed equally to this work.

‡Corresponding author. Email: becher@immunology.uzh.ch

Copyright © 2019
The Authors, some
rights reserved;
exclusive licensee
American Association
for the Advancement
of Science. No claim
to original U.S.
Government Works

computational data mining (5). Live, single cells were isolated from murine brains (C57BL/6), stained with metal-tagged antibodies, and acquired with a CyTOF analyzer. After preprocessing and manual gating of CD45⁺ MHCII⁺ cells (Fig. 1A), the data were visualized on a t-distributed stochastic neighbor embedding (t-SNE) map (17), and the cells were grouped into populations by Flow-Self Organizing Map (SOM)-guided clustering for an unbiased identification and overview of the major MHCII-expressing leukocyte populations in the CNS (5, 18, 19). We identified eight distinct APC populations by their specific expression profile (Fig. 1, B and C, and fig. S1A): BAMs (42%), CD172a⁺ conventional type 2 DCs (cDC2s) (25%), Ly6C^{int} MDCs (7%), mature B cells (10%), a microglia subpopulation (6%), CD24^{hi} immature B cells (6%), CD11b^{lo} cDC1s (2%), and plasmacytoid DCs (pDCs) (1.5%) (Fig. 1D). MHCII expression on microglia, pDCs, and immature B cells was low compared with moderate MHCII levels on MDCs and B cells and high expression on BAMs and cDCs (Fig. 1E). CD86 expression was low on immature B cells, B cells, and microglia, was moderately expressed in BAMs, and was highest in pDCs and cDCs, whereas MDCs displayed an exceptionally activated phenotype with high co-inhibitory programmed death-ligand 1 (PD-L1) expression (Fig. 1E).

Regarding the localization of MHCII-expressing cells across the CNS, we found immature B cells, pDCs, and MDCs to be abundant in the dura mater of the naïve CNS, whereas other brain compartments were almost devoid of these cell types (fig. S1B). In contrast to the inner layer of leptomeninges, the dura mater is not involved in lymphocyte trafficking into the CNS (20, 21). We therefore excluded the dura mater from further experiments and focused our analysis on cell types, which do not exclusively reside in this compartment.

Because of their strategic location at the interface of systemic circulation and the CNS parenchyma, brain endothelial cells were also considered as potential APCs (14). However, we failed to detect MHCII expression on CD31⁺ cells in the steady-state brain (fig. S1, C and D) or in active neuroinflammation (fig. S1E). We thus also excluded endothelial cells from further detailed interrogation.

Microglia are dispensable for T cell reactivation within the CNS

Microglia globally up-regulate MHCII during neuroinflammation, revealing their potential as APCs (fig. S2A) (5). In the steady state, however, the bulk of microglia (97 to 100%) did not express MHCII (fig. S2, A and B). The small subset of MHCII⁺ microglia occasionally detected in the brain of naïve mice expressed only low MHCII (Fig. 1, B, C, and E, and fig. S2B) (5). We recently described *Sall1* as a microglial signature gene allowing microglia-specific manipulation (22). Using *Sall1*^{GFP} reporter mice, we confirmed the identity of MHCII⁺ microglia, which we had identified by FlowSOM clustering (Fig. 1B and fig. S2B). Next, we crossed *Sall1*^{CreERT2} mice to *Iab*^{f/f} mice carrying a conditional loxP-flanked *Iab* allele (23) (Fig. 2A) to specifically delete MHCII in microglia (Fig. 2B) and to investigate the role of the small steady-state MHCII⁺ microglial subset on myelin Ag presentation to CNS-infiltrating T cells. Because of the small and varying numbers of MHCII-expressing microglia, the targeting efficiency of this system could not be determined in the naïve brain. MHCII expression of non-microglial APCs remained unchanged in *Sall1*^{CreERT2/+} *Iab*^{f/f} mice (Fig. 2C).

We adoptively transferred lymphocytes from actively immunized T cell receptor (TCR) transgenic 2D2 mice (24) into tamoxifen-treated *Sall1*^{CreERT2/+} *Iab*^{f/f} and littermate controls (Fig. 2B). The TCR in 2D2 mice recognizes the myelin oligodendrocyte glycoprotein

(MOG)_{35–55} peptide in the context of MHCII. We developed an AT EAE protocol omitting the irradiation of recipient mice (25), thereby preserving steady-state conditions of the CNS and the integrity of the BBB. Both *Sall1*^{CreERT2/+} *Iab*^{f/f} mice and *Sall1*^{+/+} *Iab*^{f/f} littermates developed EAE with similar kinetics, clinical scores (Fig. 2D), and inflammatory CNS infiltration (Fig. 2E). This is in line with a recent report by Wolf and colleagues (26), which, using a different targeting approach, also showed MHCII in microglia to have no function in T cell entry during EAE or demyelination. Activation-induced microglial MHCII expression was completely aborted in *Sall1*^{CreERT2/+} *Iab*^{f/f} mice (Fig. 2F), whereas other cell types retained MHCII (Fig. 2G), confirming the specificity of *Sall1*^{CreERT2} for parenchymal microglia.

The *Iab* locus is hypersensitive to Cre-mediated targeting

Having excluded microglia as vital APCs in neuroinflammation, we next aimed to target non-microglial CNS-associated APCs (DCs, BAMs, and B cells). First, to delete MHCII expression in BAMs, we crossed the myeloid cell-specific *Lyz2*^{Cre} mice to the *Iab*^f strain (fig. S2E) (27). In the steady-state brain of *Lyz2*^{Cre/+} *Iab*^{f/f} mice, MHCII expression not only on Lyve1[−] BAMs (containing the MHCII⁺ BAM subset) (5) but also on other APCs, including cDC1s, cDC2s, and even B cells, was strongly diminished when compared with littermate controls (fig. S2G; gating strategy: fig. S2, C and D), indicative of promiscuous gene targeting outside the target populations. AT of encephalitogenic T cells into these *Lyz2*^{Cre/+} *Iab*^{f/f} mice expectedly revealed protection from EAE (fig. S2G). We next used *Itgax*^{Cre/+} *Iab*^{f/f} mice to specifically delete MHCII expression in CD11c-expressing APCs (28), namely, DCs in the steady-state CNS. However, similar to what we observed with the *Lyz2*^{Cre} system, MHCII was deleted across the entire APC compartment of the steady-state brain (fig. S3H). In addition, the *Itgax*^{CreEGFP/+} *Iab*^{f/f} strain (29), which has been generated by a knock-in strategy to deliver a more faithful targeting pattern, resulted in an overreaching of the targeting frequency (fig. S3I). The same problem arose in *Zbtb46*^{Cre/+} *Iab*^{f/f} mice, where Cre expression is directed by the *Zbtb46* gene, a transcription factor reported to be exclusively expressed in cDCs and endothelial cells (fig. S3J) (30). These findings demonstrate that constitutive Cre-mediated targeting of *Iab* is unreliable in that it leads to almost complete ablation of MHCII expression across numerous cell types.

Deleting MHCII in CNS cDCs, but not macrophages, confers protection to AT EAE

To overcome the limitations of the hypersensitive *Iab* locus, we opted to test an inducible targeting system. Taking advantage of the differences in cell longevity, the *Cx3cr1*^{CreERT2} strain permits the specific targeting of CX3CR1⁺ macrophages (including BAMs and microglia), Ly6C^{low} monocytes, and DCs (8, 31) by inducing recombination at different time points (Fig. 3, A and B). We used two tamoxifen treatment protocols to differentially target CX3CR1⁺ MHCII⁺ cells: an “early” and a “continuous” regimen.

In the early treatment regimen, mice were exposed to tamoxifen 4 weeks before AT of encephalitogenic T cells [referred to as *Cx3cr1*^{CreERT2/+} *Iab*^{f/f} (early)] (Fig. 3B) to target long-lived, self-maintaining CX3CR1⁺ cells, namely, microglia, and perivascular and meningeal BAMs in the CNS; short-lived DCs and monocytes are replaced over time and will not be targeted at the time point of AT (8, 31). Accordingly, MHCII expression was specifically reduced in BAMs (~89%) of the steady-state brain, whereas DCs, B cells, and

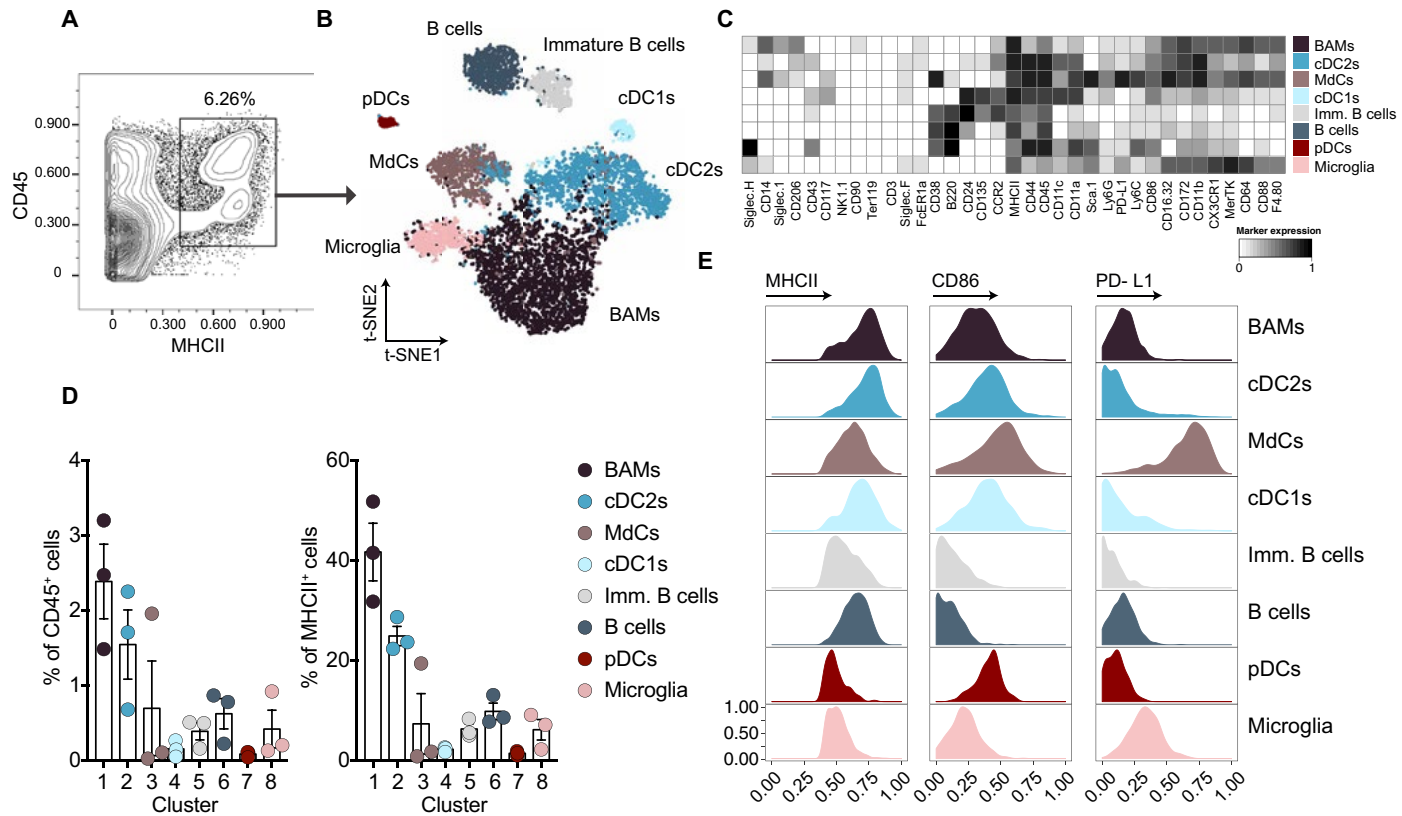


Fig. 1. Identification of MHCII⁺ cells in the steady-state CNS. (A) Immune cell populations from the whole steady-state brain (i.e., parenchyma, parenchymal vessels, intact choroid plexus, and the adhering leptomeninges) including the dura mater were analyzed by CyTOF. After gating on live singlets, MHCII⁺ CD45⁺ cells were exported as an FCS file using the FlowJo software. (B) The MHCII⁺ fraction of CNS immune cells was visualized using t-SNE and clustered using the FlowSOM algorithm in R (6907 total cells; max iterations = 5000, perplexity = 50, θ = 0.5). (C) Median relative expression of all panel markers. (D) Frequency of CD45⁺ (left graph) and MHCII⁺ cells (right graph) of FlowSOM cell clusters. (E) FlowSOM cell clusters were analyzed for MHCII, CD86, and PD-L1 expression intensity (after percentile normalization) and plotted as histograms for each cluster using R. Shown are pooled data from $n = 3$ mice.

other APCs retained MHCII expression (Fig. 3C; gating strategy: fig. S2, C and D). After AT of encephalitogenic T cells, *Cx3cr1*^{CreERT2/+} *Iab*^{f/f} (early) mice and tamoxifen-treated littermates developed similar signs of EAE with comparable incidence, mean maximum score (Fig. 3D), and inflammatory CNS infiltration (Fig. 3E).

In the continuous treatment regimen, mice were exposed to tamoxifen 1 week before steady-state CNS analysis and treatment was continued during AT EAE [referred to as *Cx3cr1*^{CreERT2/+} *Iab*^{f/f} (cont.)], to deplete MHCII expression across all CX3CR1⁺ cells, regardless of their ontogeny or lifespan. Accordingly, we observed that MHCII expression was abrogated not only in BAMs (~94%) but also in cDC1 cells (~65%) and cDC2 cells (~72%) (Fig. 3C; gating strategy: fig. S2, C and D). cDC1s and cDC2s display low-to-moderate CX3CR1 expression in the steady-state brain and are thus targeted with continuous tamoxifen treatment (fig. S3A). Continuous tamoxifen treatment resulted in markedly reduced clinical EAE symptoms in *Cx3cr1*^{CreERT2/+} *Iab*^{f/f} (cont.) mice compared with tamoxifen-treated littermates (Fig. 3D), accompanied by reduced CNS infiltrates at the peak of EAE (Fig. 3E). Continuous tamoxifen treatment itself had no impact on the clinical outcome of AT EAE (fig. S3B). Microglia of *Cx3cr1*^{CreERT2/+} *Iab*^{f/f} mice did not up-regulate MHCII expression during EAE, regardless of the treatment regimen, thus confirming the expected targeting of microglia with both strategies (fig. S3C). Together, differential targeting of CX3CR1-expressing cells in the CNS revealed

that, in contrast to microglia and BAMs, cDCs are required for the reactivation of encephalitogenic T cells and the initiation of CNS infiltration and neuroinflammatory events in EAE.

Distinct subsets of DCs reside at CNS interfaces

Because of a lack of specific markers, traditional methods have thus far not allowed a thorough characterization of DCs in the steady-state CNS. We further characterized the CNS DCs by enriching for this rare cell population by fluorescence-activated cell sorting (FACS) from the steady-state brain and then categorized the cells using our mass cytometry workflow with a DC subset-focused antibody panel. Here, we confirmed the existence of three major populations: cDC1s, cDC2s, and pDCs. The vast majority of DCs were CD11b⁺ CD172a⁺ cDC2s (76%), as observed in other peripheral tissues (Fig. 4, A and B) (32). We also identified two distinct CD11b^{lo} cDC1 subpopulations, which differ with respect to XCR1, CD103, and CD205 expression. Last, Ly6C⁺, B220⁺, Siglec-H⁺ pDCs could be clustered into MHCII^{int} and MHCII^{low} cells.

Despite their critical role in T cell reactivation, cDCs are sparsely distributed in the steady-state CNS. Using immunohistochemistry, we localized CD11c⁺ MHCII⁺ cells [which almost exclusively consist of DCs in the steady-state brain (fig. S4B)] primarily in the leptomeninges and dura mater with fewer cells in the choroid plexus (Fig. 4C), whereas DCs were largely absent from the perivascular spaces, confirming

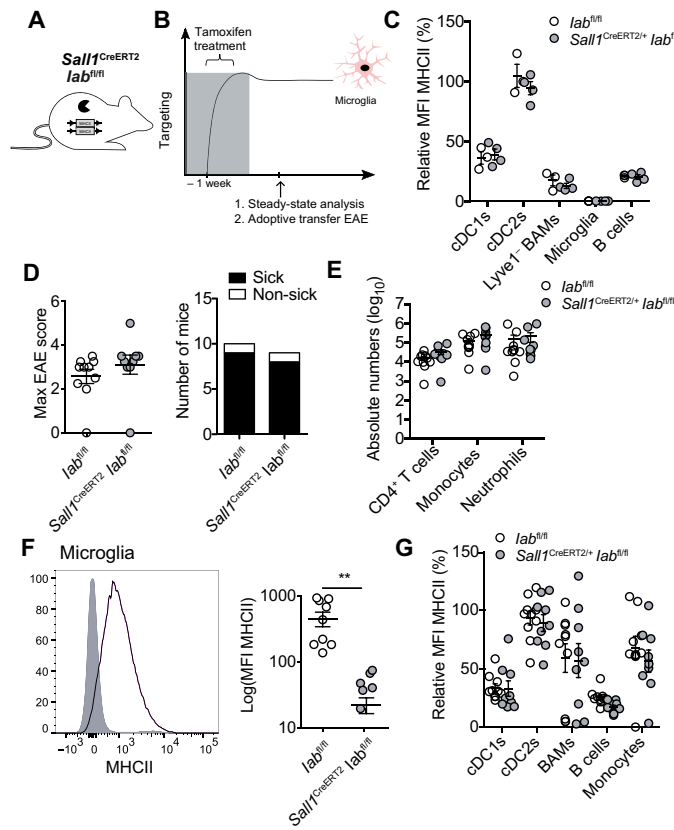


Fig. 2. Microglial MHCII is dispensable for AT EAE. (A) *Sall1*^{CreERT2} mice were crossed to *lab*^{fl/fl} mice carrying floxed MHCII alleles. (B) Graphical abstract to illustrate the tamoxifen treatment strategy of *Sall1*^{Cre/+} *lab*^{fl/fl} mice. Cre⁺ animals and Cre⁻ littermates were administered tamoxifen via oral gavage (three times on alternate days) to induce Cre recombinase expression in microglia. (C) MHCII targeting profile of whole steady-state brain APCs in *Sall1*^{CreERT2/+} *lab*^{fl/fl} and *Sall1*^{+/+} *lab*^{fl/fl} mice 1 week after tamoxifen treatment (for gating strategy, see fig. S2, C and D). The relative median fluorescence intensity (MFI) has been calculated by normalizing absolute MFIs of each cell population to the MFI of cDC2s (which do express the highest MHCII levels). The MFI of cDC2s of one mouse was set to 100%. Data are representative of one of two independent experiments ($n > 7$ mice per group). (D) EAE was induced by AT of encephalitogenic 2D2 cells into recipient mice. Data show individual maximal EAE score and number of mice with clinical EAE symptoms. (E to G) At the peak of disease, the CNS (whole brain and spinal cord pooled) was analyzed for inflammatory infiltrates (E) and MHCII targeting of APCs (F and G) by flow cytometry. (E) Infiltrating monocytes (Ly6C⁺, Ly6G⁻, CD11b⁺), neutrophils (Ly6C^{int}, Ly6G⁺, CD11b⁺), and CD4⁺ T cells (CD4⁺, CD11b⁻, CD11c⁺) were manually gated in FlowJo; absolute numbers (log₁₀) per brain \pm SEM are shown. (F) MHCII targeting profile (log₁₀ MFI MHCII) in microglia and (G) other CNS-infiltrating and CNS-resident APCs at peak EAE (relative MFI) (manually gated in FlowJo without using MHCII for the gating). (D to G) Data are pooled from three independent experiments ($n > 9$ mice per group).

previous observations (5–7). Early T cell encounters with brain-derived Ags specifically occur in the parenchyma surrounding leptomeningeal spaces (consisting of the pia and arachnoid mater), highlighting the strategic localization of DCs to reactivate CNS-infiltrating T cells (15, 20). We confirmed that DCs in the leptomeninges and dura mater consisted mainly of CD11b⁺ cDC2s, whereas CD11b⁻ cDC1s were the dominant DC subset in the choroid plexus (Fig. 4C). To quantify the relative distribution of cDCs across different CNS compartments, we physically separated the dura mater, leptomeninges, choroid plexus, and parenchyma/perivascular spaces and analyzed

the subset composition of each compartment using flow cytometry. This approach is only an approximation because of potential cross-contamination of different brain compartments (mainly of the leptomeninges with parenchymal tissue) and because it is not possible to isolate the complete leptomeninges of adult mice. However, using algorithm-guided clustering (FlowSOM), we found that cDC2s make up to 80% of brain DCs in the dura mater, the pia mater, and the parenchyma/perivascular spaces (here, we only found very low numbers of CD11c MHCII⁺ DCs). In contrast, the choroid plexus revealed a dominant presence of the cDC1 subset (Fig. 4D and fig. S4C). This was also confirmed using a manual gating strategy to quantify cDC1 and cDC2 cells (fig. S4D). Together with the rarity of cDC1 cells, that *Batf3*^{-/-} mice, which lack cDC1s in the CNS (fig. S4, E and F), were fully susceptible to transfer EAE, provides an additional argument against a role of cDC1s in the reactivation process of encephalitogenic CD4⁺ T cells.

cDCs process and present myelin Ag to infiltrating T cells

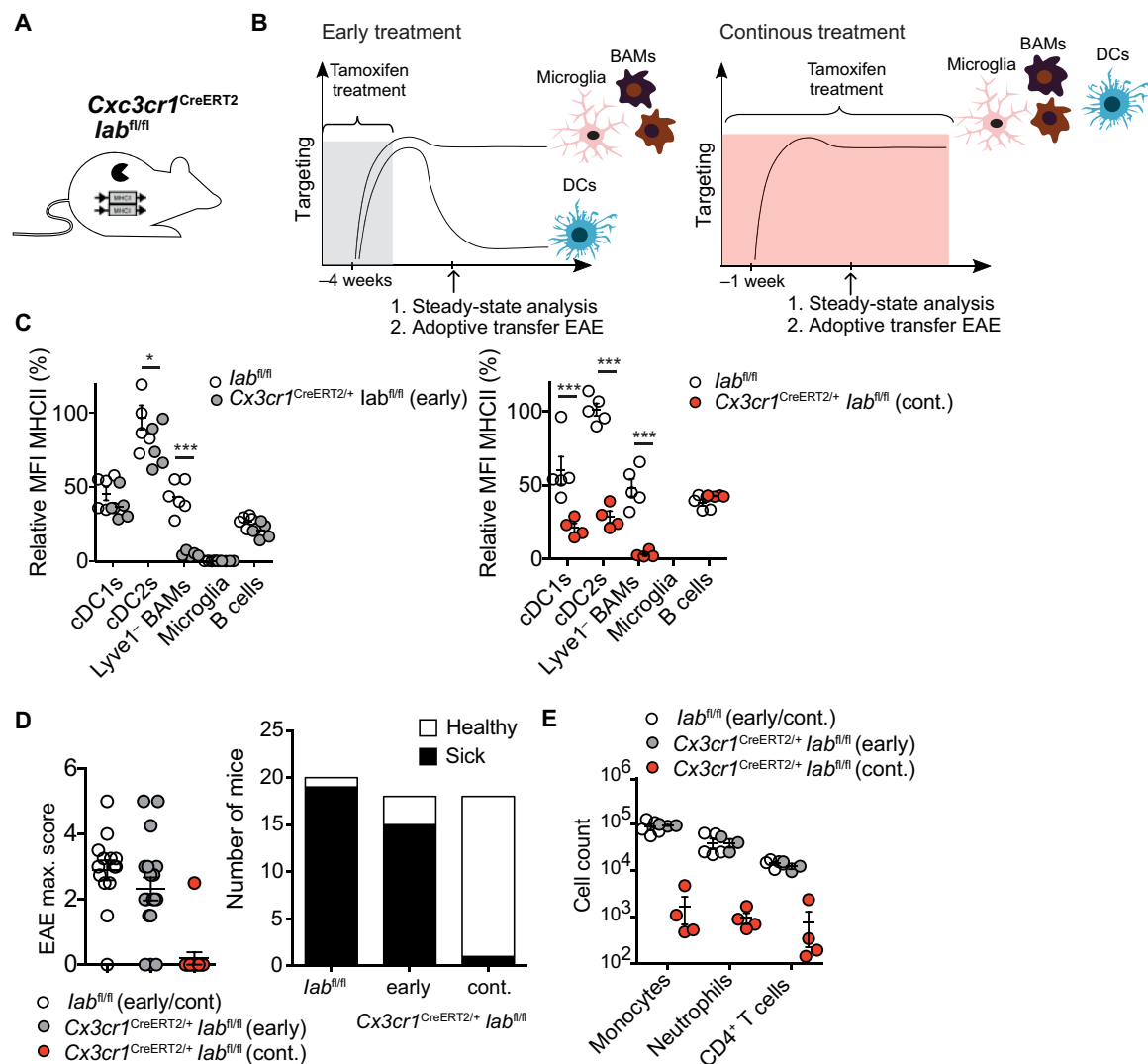
Last, to independently compare the ability of CNS APCs to reactivate infiltrating MOG_{35–55}-specific T cells in vitro, we sorted cDCs, BAMs, B cells, and microglia from the steady-state brain of adult C57BL/6 mice (fig. S4G) and incubated them with in vivo-primed 2D2 CD4⁺ T cells in the presence or absence of MOG_{35–55} peptide. In the presence of exogenous peptide, cDCs induced the strongest activation of T cells in terms of interferon-γ (IFN-γ) expression as measured by enzyme-linked immunospot (ELISPOT) assay (Fig. 4F). The second most potent APCs were BAMs, whereas B cells and microglia failed to induce IFN-γ production in primed 2D2 cells. We observed that DCs could reactivate myelin-specific 2D2 T cells even in the absence of exogenous peptide (Fig. 4F). No other APC was able to reactivate primed CD4⁺ T cells without the addition of MOG_{35–55} peptide in vitro. These findings demonstrate that CNS cDCs actively process and present endogenous MOG protein in the steady-state CNS and confirm their superior Ag presentation capacity compared with other APCs (6).

DISCUSSION

Active communication between the CNS and the immune system has a profound impact on tissue maintenance and pathology. Yet, even already primed T_H cells are relatively innocuous when they do not reencounter their cognate Ag in the respective target tissues. The nature and origin of the APCs required to reactivate CNS-specific, encephalitogenic T_H cells has been heavily disputed because the strong overlap in CNS-associated myeloid cell phenotypes has hindered deciphering their individual contributions in this critical process (7, 15, 33–35). We here present a precise categorization of MHCII-expressing cells in the steady-state CNS and a systematic study of their individual ability to elicit inflammatory immune responses in the CNS.

EAE has served for decades as a model for autoimmunity, cellular immune activation, T cell–APC interactions, and cytokine networks in inflammation (36). The AT EAE model resembles several aspects of MS, as it mimics immune infiltration into the healthy CNS in the absence of systemic inflammation. Because the transient contact between adoptively transferred encephalitogenic T cells with stromal cells in the periphery is MHCII independent (7, 37), our investigation of the MHCII-dependent T cell reactivation could be restricted to the CNS, rather than other peripheral organs. Crossing the endothelial

Fig. 3. cDCs, but not BAMs or microglia, are required for the reactivation of 2D2 CD4⁺ T cells in the CNS. (A) *Cx3cr1*^{CreERT2} mice were crossed to *lab*^{f/f} mice. (B) *Cx3cr1*^{CreERT2/+} *lab*^{f/f} (early) mice and *Cx3cr1*^{+/+} *lab*^{f/f} littermates received a short, early tamoxifen treatment via oral gavage (three times on alternate days) 4 weeks before AT EAE or steady-state CNS analysis. Tamoxifen treatment of *Cx3cr1*^{CreERT2/+} *lab*^{f/f} (cont.) and *Cx3cr1*^{+/+} *lab*^{f/f} littermates was initiated 1 week before induction of AT EAE or steady-state brain analysis and continued until the end of the experiment. (C) MHCII targeting profile in APCs of naïve *Cx3cr1*^{+/+} *lab*^{f/f} (white circles) and *Cx3cr1*^{CreERT2/+} *lab*^{f/f} mice (early: gray circles; cont.: red circles) from the whole steady-state brain. Data represent the MFI (\pm SEM) of MHCII of each manually gated (for gating strategy, see fig. S2, C and D) population and are representative of one of more than three independent experiments (total of $n > 12$ mice per group). (D) Encephalitogenic 2D2 cells were adoptively transferred, and the clinical outcome was compared between *Cx3cr1*^{CreERT2/+} *lab*^{f/f} mice (early, gray circles; cont., red circles) and *Cx3cr1*^{+/+} *lab*^{f/f} littermates (white circles) over time. Data represent the individual maximal EAE score and the number of mice with clinical EAE (pooled from three independent experiments with $n > 14$ mice per group); $P < 0.0001$, χ^2 analysis. (E) At the peak of disease (days 12 to 14), the CNS (whole brain and spinal cord pooled) was analyzed for inflammatory infiltrates by flow cytometry. Infiltrating monocytes (Ly6C⁺, Ly6G⁻, CD11b⁺), neutrophils (Ly6C^{int}, Ly6G⁺, CD11b⁺), and CD4⁺ T cells (CD4⁺, CD11b⁻, CD11c⁺) were manually gated in FlowJo, and absolute numbers (\log_{10}) per brain \pm SEM are shown. Data are representative of one of three independent experiments (total of $n > 10$ mice per group).



cell barrier from the vessel lumen to the meninges by encephalitogenic T cells occurs in an Ag-independent manner (20, 37), whereas the presentation of myelin epitopes by CNS APCs in the leptomeningeal space is required for their entry into the CNS parenchyma and for the initiation of disease (20).

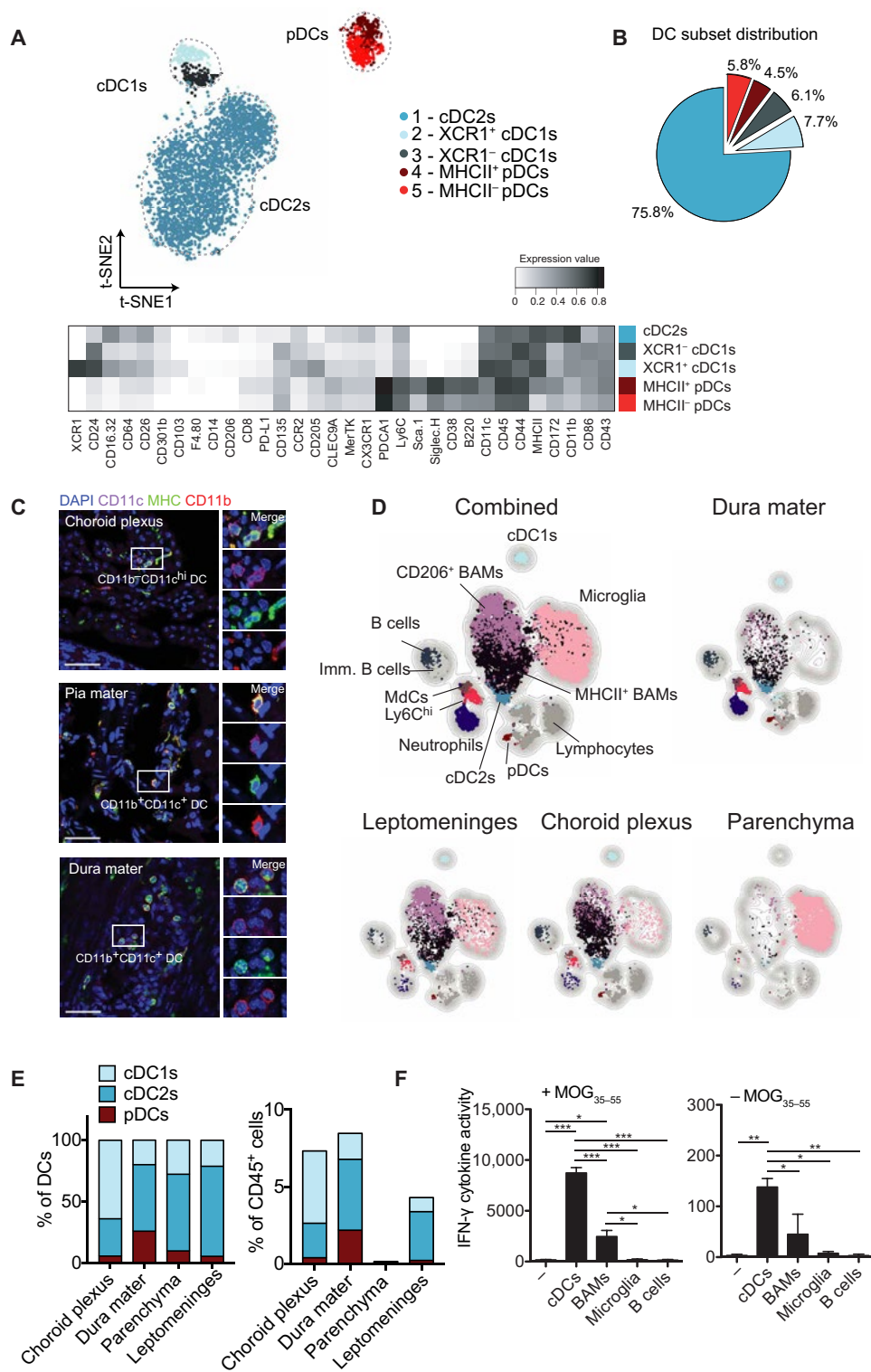
Astrocytes, pericytes, and endothelial cells have been suggested as possible APCs in the CNS (14). In the non-inflamed brain, however, most cell types (particularly non-immune cells) do not express MHCII or costimulatory molecules and are therefore unlikely to be responsible for the initial reactivation of encephalitogenic T cells. In addition, microglia, the only leukocytes of the steady-state brain parenchyma, have been implicated to promote the pathogenesis of EAE (38). We identified a minor MHCII⁺ microglial cell population (up to 3% of total microglia) in the steady-state CNS. However, although microglia have the capacity to process and present exogenous Ag onto MHCII molecules in principle, their anatomical loca-

tion is distant from the CNS interfaces, where T cells make initial contact with the brain. Using *Sall1*^{CreERT2/+} and *Cx3cr1*^{CreERT2/+} *lab*^{f/f} mice, we confirmed that microglia do not have an essential role in initial T cell reactivation in AT EAE (7, 26).

Considering the relative abundance of bona fide MHCII-expressing cells in the steady-state CNS interfaces (pia mater, choroid plexus, and perivascular spaces) implicated in T cell reactivation (15, 20, 21), we considered BAMs, cDCs, and B cells as the main candidate APCs to reactivate T cells in EAE. In MS, B cells recently have been shown to induce autoprolyliferation in brain-homing T cells in an human leukocyte antigen (HLA)-DR-dependent manner (39); however, for the reactivation of CNS-infiltrating encephalitogenic T cells in the MOG_{35–55}-dependent EAE model, they appear to be entirely dispensable (40). We here confirmed that even with external MOG_{35–55} loading, CNS-associated B cells are relatively poor APCs to myelin-specific T cells. The most hotly debated CNS APCs are BAMs

Fig. 4. CNS-associated cDC2s reside in the steady-state brain leptomeninges and reactivate 2D2 T cells in vitro.

(A) In-depth CyTOF analysis of DC subsets from pre-enriched whole-brain leukocytes ($n = 20$ naive brains): DCs were identified and subset from the initial data, subjected to t-SNE dimensionality reduction (3509 total cells; max iterations = 750, perplexity = 200, $\theta = 0.5$), and clustered into three main subsets using FlowSOM-guided clustering according to their marker expression. **(B)** Relative abundance of the DC subsets within total CNS DCs. **(C)** Representative immunofluorescence images of CD11c⁺ MHCII⁺ CD11b⁻ cDC1s and CD11b⁺ cDC2s in the dura mater, leptomeninges, and choroid plexus of the steady-state brain ($n \geq 2$ mice, ≥ 4 sections per mouse). Scale bar, 50 μ m. A zoomed-in view is shown. **(D)** Brain compartments [leptomeninges, dura mater, choroid plexus, and parenchyma (hippocampus)] were dissected from $n = 10$ brains. Individual compartments were pooled and single cells were analyzed by flow cytometry followed by computational high-dimensional data analysis. After gating on live singlets, CD45⁺ cells were exported as an FCS file using the FlowJo software. Shown are pooled data from $n = 10$ mice, visualized using t-SNE and clustered using the FlowSOM algorithm in R (142,655 total cells; max iterations = 10000, perplexity = 50, $\theta = 0.5$). Plots show FlowSOM clusters of leukocytes overlaid onto a t-SNE map of the combined dataset (left) or shown separately for each compartment as indicated. **(E)** Data show frequencies of cDC1s, cDC2s, and pDCs of total DCs (left graph) or CD45⁺ cells (right graph) as determined by FlowSOM clustering. **(F)** DCs (CD11c^{hi}, MHCII⁺, B220⁻, MerTK⁻), BAMs (MerTK⁺, CD11b⁺, CD45^{hi}, MHCII⁺), microglia (MerTK⁺, CD45^{lo}, CD11b⁺), and B cells (CD11b⁻, B220⁺, CD11c⁻, MHCII⁺) were isolated from pooled whole steady-state brains of 20 to 25 C57BL/6 mice and incubated with in vivo activated encephalitogenic 2D2 cells in the presence [2000:55,000 (APC:T cell); upper graph] or absence [11,000:55,000 (APC:T cell); lower graph] of MOG_{35–55} peptide for 72 hours. IFN- γ production was measured by ELISPOT assay. Data represent the mean \pm SD cytokine activity of IFN- γ from technical duplicates and are representative of one of two independent experiments.



and DCs (7, 15, 41–43). Similar to microglia, most CNS BAMs are embryonically derived cells (4, 8), and we found that most of those cells do not express MHCII in the steady-state brain (5). However, others have observed that macrophage depletion in EAE can reduce clin-

ical progression by blocking parenchymal T cell invasion (41). BAMs are strategically located at CNS-immune interfaces (5, 8, 15) as ideal candidates to present Ag to incoming T cells. However, “meningeal macrophages,” as described by Schläger *et al.* (15), were so named on

the basis of their morphology and ability to take up dextran molecules. We found morphology alone not to allow the unambiguous discrimination of BAMs from other members of the mononuclear phagocyte system, most notably cDCs (5). Compared with CNS BAMs, DCs are a very rare population and, as such, have often evaded detection in the steady-state CNS. It is likely that the steady state function of these rare CNS DCs is tolerance maintenance. Global CD11c⁺ cell depletion was shown to exacerbate the clinical outcome of actively induced EAE (34, 44).

In contrast, tolerance is bypassed in AT EAE by the infusion of primed, encephalitogenic T cells, which, in turn, must encounter their cognate neuro-Ag in the tissue. The threshold for reactivation of already primed T cells is much lower, and the cognate TCR/MHCII peptide encounter is dominant (45). AT of encephalitogenic T cells into DC-depleted recipients failed to trigger disease (33, 46). Moreover, DCs have been proposed previously to be sufficient to reactivate CNS-infiltrating T cells when MHCII expression was confined to CD11c⁺ cells (7). However, *in vivo* cell depletion often results in collateral inflammation and alteration of tissue homeostasis because other cells often invade the empty cellular niche (47). In addition, CD11c can no longer be considered a DC-specific marker (11–13, 38). Hence, a more systematic interrogation of APC capacity across the CNS-leukocyte landscape was necessary.

New insights into the differences between brain-associated myeloid cells in terms of ontogeny and longevity made it possible for us to exploit the *Cx3cr1*^{CreERT2/+} *Iab*^{f/f} system to differentially target MHCII⁺ expression in macrophages and DCs by using different tamoxifen treatment regimens. Using this strategy, we revealed that cDCs, but not embryonically derived BAMs and microglia, are required for initial T cell reactivation and parenchymal infiltration. Furthermore, we showed that cDCs isolated from the CNS of naïve C57BL/6 mice are superior in presenting MOG_{35–55} Ag to TCR transgenic primed 2D2 cells when compared with microglia, B cells, or MHCII⁺ BAMs. We also found clear evidence for myelin sampling, processing, and presentation by CNS cDCs, when freshly isolated CNS cDCs were capable of triggering specific T cell reactivation even in the absence of pulsed peptides. In line with *in vivo* imaging data in rodent EAE models, there is mounting evidence to support that meningeal inflammation precedes the clinical manifestation of MS (48, 49). Whereas the choroid plexus is mainly home to CD11b⁻ cDC1s, the cDC2 subset is enriched in the CNS meninges (5–7, 33). Most of the initial CNS-invading T cells accumulate in the leptomeninges rather than the choroid plexus (15, 20). This is in line with the view that cDC2 cells, which are found in the leptomeninges and not in the choroid plexus, are the main facilitators of early T cell entry into the CNS.

In summary, our data demonstrate that parenchymal microglia do not serve as early APCs to myelin Ag-restricted T cells. Further, despite their relative abundance and ideal location at the CNS-immune interface, BAMs are unable to process and present myelin Ag to arriving T cells. By contrast, and despite their scarcity, CNS-associated cDCs, in particular the leptomeningeal-associated cDC2 subset, are exquisite and powerful APCs and the only bridging cellular element that can permit effective T cell–CNS interactions.

MATERIALS AND METHODS

Study design

This study aimed at identifying and characterizing CNS-resident APCs in the steady state and their ability to sample myelin Ag for

presentation to T cells. For this, we used a combination of multi-parametric single-cell mass cytometry and algorithm-guided computational analysis. To then interrogate the ability of different CNS APC populations to engage with the first-arriving encephalitogenic T cells, we used Cre-loxP-mediated MHCII ablation during AT EAE *in vivo*.

Mice

2D2 TCR transgenic mice [C57BL/6-Tg(Tcra2D2,Tcrb2D2)1Kuch/J; #006912] (24), *Lyz2*^{Cre} mice [B6.129P2-*Lyz2*^{tm1(Cre)Ifa}/J; #004781] (27), *Itgax*^{Cre} mice [B6.Cg-Tg(Itgax-Cre)1-1Reiz/J; #008068] (28), *Itgax*^{CreEGFP} mice [C57BL/6 J-Tg(Itgax-Cre,-EGFP)4097Ach/J; #007567] (29), *Zbtb46*^{Cre} mice [B6.Cg-*Zbtb46*^{tm3.1(Cre)Mnz}/J; #028538] (30), *Iab*^{f/f} mice (B6.129X1-*H2-Ab1*^{tm1Koni}/J; #013181) (23), and *Batf3*^{-/-} mice [B6.129S(C)-*Batf3tm1Kmm*/J; #013755] (50) were purchased from the Jackson Laboratory. *Cx3cr1*^{CreERT2} mice [B6.129P2(C)-*Cx3cr1tm2.1*(Cre/ERT2)Jung/J; #020940] (31) were provided by S. Jung (Weizmann Institute of Science, Israel), and *Sall1*^{CreERT2} and *Sall1*^{GFP} mice (51) were provided by R. Nishinakamura (Kumamoto University, Japan). Transgenic mice were bred in house, and C57BL/6 mice were purchased from Janvier. Age- and sex-matched (male and female) 6- to 12-week-old mice were used for all experiments. All experiments performed in this study were approved by the Swiss Veterinary Office and performed according to federal and institutional guidelines.

Tamoxifen treatment

Tamoxifen (Sigma) was dissolved in ethanol and corn oil (1:9) to 25 mg/ml and administered in 200-μl doses via oral gavage (5 mg per dose).

Adoptive transfer EAE

Donor mice (2D2) were immunized with 200 μg of MOG_{35–55} emulsified in CFA and treated with 200 ng of pertussis toxin (intraperitoneally) on the day of immunization and again 2 days later. After 9 days, splenocytes and lymph node (inguinal, axillary, and brachial) cells were cultured in complete RPMI (10% fetal calf serum, penicillin/streptomycin, and β-mercaptoethanol) containing MOG_{35–55} (20 μg/ml; GenScript), recombinant IL-23:Fc fusion protein (10 ng/ml; ACRO-Biosystems), and anti-IFN-γ (5 μg/ml; R4-6A2; BioExpress) at a density of 6 × 10⁶ to 8 × 10⁶ cells/ml for 72 hours. To induce EAE, we injected (intraperitoneally) up to 20 × 10⁶ cells into recipient mice.

Tissue preparation and single-cell suspension

In brief, tissues (whole brain and spinal cord) were cut into small pieces and incubated with collagenase type IV (0.4 mg/ml) and deoxyribonuclease I (DNase I) (0.2 mg/ml) (Sigma-Aldrich) for 30 to 40 min and passed through a 19-gauge needle to obtain a homogeneous single-cell suspension. CNS cell suspensions were further enriched by Percoll gradient (30%) centrifugation (1590g, 4°C, 30 min, no brake).

Individual brain compartments—including leptomeninges, dura mater, choroid plexus, and parenchyma (hippocampus without leptomeninges or choroid plexus)—were microdissected. The dura mater was removed from the skull after cortex removal. The leptomeninges was partially removed from the cortex by starting at the olfactory bulb and gently peeling off the soft meningeal layer. The choroid plexus was dissected from the fourth ventricle by separating the cerebellum from the cerebral cortex. Next, the two cerebral hemispheres were gently separated, and the choroid plexus from the lateral ventricles and the third ventricle was harvested. To exclude contamination of residual leptomeninges on the surface of the cortex, we dissected the hippocampus from both hemispheres after the choroid plexus was removed.

The hippocampus was used as a control for the parenchyma and perivascular spaces because it only harbors blood vessels without contamination by leptomeninges or choroid plexus. All brain compartments were separately subjected to collagenase type IV/DNase I digestion (see above). CNS leukocytes from the parenchymal hippocampus samples were further enriched by Percoll gradient centrifugation (see above).

Flow cytometry

Flow cytometry was performed on an LSRII Fortessa (Becton Dickinson) and analyzed with FlowJo software (Tree Star). Fluorochrome-conjugated monoclonal antibodies specific for mouse MHCII I-A/I-E (clone M5/114.15.2), CD11b (clone M1/70), CD11c (clone N418), CD45 (clone 30-F11), CD24 (clone M1/69), Ly6G (clone 1A8), Ly6C (clone HK1.4), F4/80 (clone Cl:A3-1), CX3CR1 (clone SA011F11), MerTK (DS5MMER), CD4 (clone GK1.5), Flt3 (clone A2F10), CD31 (clone 390), Lyve1 (clone ALY7), XCR1 (clone ZET), B220 (clone RA3-6B2), GR-1 (clone RB6-8C5), and CD206 (C068C2) were purchased from either BD Biosciences, eBioscience, or BioLegend. Dead cells were excluded using a LIVE/DEAD stain kit (Invitrogen), and doublets were excluded by FCS-H versus FSC-A in FlowJo.

Ex vivo Ag presentation assay

DCs ($\text{CD11c}^{\text{high}}$, MerTK $^+$, MHCII $^{\text{hi}}$), MHCII $^+$ BAMs (MerTK $^+$, CD11b $^+$, MHCII $^+$), microglia (MerTK $^+$, CD45 $^{\text{low}}$, CD11b $^+$), and B cells (B220 $^+$, MHCII $^+$) were sorted by FACS and incubated with activated (day 9 active EAE) magnetically sorted (negative selection, CD4 $^+$ T Cell Isolation Kit from Miltenyi Biotec) 2D2 CD4 $^+$ T cells in the presence or absence of MOG_{35–55} peptide (20 µg/ml) at 37°C for 72 hours. Cells were analyzed for IFN-γ expression by ELISPOT (Abcam).

Mass cytometry

Mass cytometry experiments were performed exactly as recently described (5). Mass cytometry antibodies were either labeled in-house using antibody-labeling kits and protocols or purchased from Fluidigm. Antibodies were individually titrated and optimized for the final panel before use to ensure that each parameter was informative. For MHCII $^+$ population identification, data were taken from Mrdjen *et al.* (5). Here, five palladium metal isotopes were used for live cell barcoding of samples with CD45 while keeping CD45-¹⁴⁷Sm as a common channel to identify cells expressing varying degrees of CD45, such as microglia (5). Briefly, cells from individual naïve adult C57BL/6 brains were incubated with respective CD45-Pd + CD45-¹⁴⁷Sm antibodies in phosphate-buffered saline (PBS) for 30 min at 37°C, after which they were washed twice with FACS buffer (PBS supplemented with 0.5% bovine serum albumin) and then combined into composite samples. For DC subset analysis, we used a DC-focused antibody panel with additional DC markers. Here, brain samples were prepared as described and pooled without barcoding. After pooling, cells were enriched by FACS to remove the majority of non-DC populations. Cells were stained with the cocktail of primary CyTOF antibodies for 30 min at 37°C, washed with FACS buffer, and then incubated with secondary antibodies for 20 min at 4°C. After washing, samples were incubated with intercalating solution (iridium from Sigma) in Maxpar Fix/Perm buffer (Fluidigm) overnight at 4°C. Before acquisition, the samples were washed twice with FACS buffer and once with Milli-Q water. Barcoded composite samples were acquired on a Helios mass cytometer (Fluidigm). Quality control and tuning processes on the Helios were performed by routine before acquisition.

Preprocessing of mass and flow cytometry data

Cytometry data were processed as previously described (5, 18). Mass cytometry data were normalized to EQ Four Element Beads (Fluidigm), and live cells were exported by gating on event_length, DNA (¹⁹¹Ir and ¹⁹³Ir positive), and live cells (¹⁹⁵Pt negative) using FlowJo software (Tree Star). For the barcoded samples, debarcoding was achieved by Boolean gating in FlowJo. After quality control for each channel, the debarcoded gates or complete pooled sample FCS files were imported into the R environment and transformed using an inverse hyperbolic sine (arcsinh) function with a cofactor of 5.

For flow cytometry data, after compensation correction in FlowJo, live, single, quality-controlled, and compensated cells were exported by manual gating. The appropriate transformation cofactors were determined by uploading the files into Cytobank (www.cytobank.org) and using the Scales feature; thereafter, transformation was carried out in MATLAB, and transformed files were imported into the R environment for further preprocessing and analysis. To equalize the contribution of each marker in subsequent automated data analysis steps of both mass and flow cytometry data, we performed percentile normalization, normalizing all data to the 99.9th percentile of the merged sample in each experiment, depending on the number of outliers present. This process preserves biologically relevant differences in expression values (staining indices) but normalizes inter-marker maximum and minimum expression values from 0 to 1.

Automated population identification in high-dimensional data analysis

Preprocessing of the raw data was followed by dimensionality reduction and visualization by t-SNE (17). Initial clustering and meta-clustering with FlowSOM (19) was followed by expert-guided manual merging of some of the metaclusters using the information from the t-SNE with overlaid marker expression values and a heatmap of median expression values (18).

Statistical analysis

For clinical scores over time, influence on MHCII expression in different cell populations, or analysis of CNS infiltration of different cell types between different groups, differences were evaluated by two-way analysis of variance (ANOVA) with Bonferroni's post hoc test, Tukey's or Sidak's multiple comparisons. Differences for one parameter were evaluated by one-way ANOVA with Bonferroni's post hoc test when comparing more than two groups and by the two-tailed Student's *t* test when comparing two groups (unpaired *t* test with Welch's correction when the two samples have unequal variances and unequal sample sizes). χ^2 test was applied to compare incidence of EAE. *P* values of less than 0.05 were considered statistically significant, with **P* ≤ 0.05, ***P* ≤ 0.01, and ****P* ≤ 0.001.

Immunohistochemistry

After transcardiac perfusion of mice with PBS and 4% (w/v) paraformaldehyde (PFA) in 0.1 M phosphate buffer (pH 7.4), CNS tissue was postfixed overnight at 4°C, followed by cryoprotection with 30% (w/v) sucrose in PBS. Sections were cut at 14 µm and mounted on slides, or free-floating sections were cut at a thickness of 30 µm using a Hyrax C60 cryostat (Zeiss). CNS tissue sections were permeabilized by incubation in blocking solution (PBS supplemented with 0.1% Triton X-100 and 4% normal goat serum) for 30 min to 1 hour at room temperature. Subsequently, sections were incubated with the following primary antibodies (diluted in blocking solution)

for 24 to 72 hours at 4°C: anti-GLUT-1 (1:500; Millipore), anti-Iba1 (1:500; Wako), anti-MHCII (1:200; BioLegend), anti-CD206 (1:100; BioLegend), anti-CD11c (1:40; BioLegend), and anti-CD11b (1:50; BioLegend). After washing, samples were incubated either at 4°C overnight or at room temperature for 1 to 2 hours with the respective Alexa Fluor-conjugated secondary antibodies (1:500; Life Technologies). Counterstaining was performed using SlowFade Gold antifade reagent with 4',6-diamidino-2-phenylindole (DAPI) (Invitrogen). Fluorescence photomicrographs were captured with a confocal laser scanning microscope (SP5; Leica, Heerbrugg, Switzerland) equipped with argon and helium lasers using a 40× objective (oil immersion; numerical aperture, 1.25). Images were processed and merged using Imaris imaging software (Bitplane, Zurich, Switzerland).

Histopathological analysis of EAE tissue

LFB (Luxol fast blue)-PAS (periodic acid-Schiff) stainings were done according to standard protocols on 4% PFA-fixed, decalcified paraffin-embedded 6-μm-thick tissue sections. We analyzed EAE histopathology on cross sections (four to six per mouse) of lumbar spinal cords and recorded digital images of tissue sections with a light microscope (Olympus BX41). Total demyelinated area of LFB- and PAS-stained sections was measured by Fiji/ImageJ version 1.46j software (National Institutes of Health), and the area of demyelination was calculated as the percentage of the whole area of white matter within a given section.

SUPPLEMENTARY MATERIALS

immunology.scienmag.org/cgi/content/full/4/31/eaau8380/DC1

Fig. S1. Identification of MHCII⁺ cells in the steady-state CNS.

Fig. S2. Microglial MHCII is dispensable for AT EAE.

Fig. S3. cDCs, but not BAMs or microglia, are required for the reactivation of 2D2 CD4⁺ T cells in the CNS.

Fig. S4. Different DC subsets reside at the steady-state brain interfaces and present myelin Ag to CD4⁺ 2D2 T cells.

Table S1. Raw data.

REFERENCES AND NOTES

- M. Schwartz, J. Kipnis, S. Rivest, A. Prat, How do immune cells support and shape the brain in health, disease, and aging? *J. Neurosci.* **33**, 17587–17596 (2013).
- L. Steinman, Multiple sclerosis: A coordinated immunological attack against myelin in the central nervous system. *Cell* **85**, 299–302 (1996).
- A. L. Croxford, M. Lanzinger, F. J. Hartmann, B. Schreiner, F. Mair, P. Pelczar, B. E. Clausen, S. Jung, M. Greter, B. Becher, The cytokine GM-CSF drives the inflammatory signature of CCR2+ monocytes and licenses autoimmunity. *Immunity* **43**, 502–514 (2015).
- F. Ginhoux, M. Greter, M. Leboeuf, S. Nandi, P. See, S. Gokhan, M. F. Mehler, S. J. Conway, L. G. Ng, E. R. Stanley, I. M. Samokhvalov, M. Merad, Fate mapping analysis reveals that adult microglia derive from primitive macrophages. *Science* **330**, 841–845 (2010).
- D. Mrdjen, A. Pavlovic, F. J. Hartmann, B. Schreiner, S. G. Utz, B. P. Leung, I. Lelios, F. L. Heppner, J. Kipnis, D. Merkler, M. Greter, B. Becher, High-dimensional single-cell mapping of central nervous system immune cells reveals distinct myeloid subsets in health, aging, and disease. *Immunity* **48**, 380–395.e6 (2018).
- N. Anandasabapathy, G. D. Victoria, M. Meredith, R. Feder, B. Dong, C. Kluger, K. Yao, M. L. Dustin, M. C. Nussenzeig, R. M. Steinman, K. Liu, Flt3L controls the development of radiosensitive dendritic cells in the meninges and choroid plexus of the steady-state mouse brain. *J. Exp. Med.* **208**, 1695–1705 (2011).
- M. Greter, F. L. Heppner, M. P. Lemos, B. M. Odermann, N. Goebels, T. Laufer, R. J. Noelle, B. Becher, Dendritic cells permit immune invasion of the CNS in an animal model of multiple sclerosis. *Nat. Med.* **11**, 328–334 (2005).
- T. Goldmann, P. Wieghofer, M. J. C. Jordão, F. Prutek, N. Hagemeyer, K. Frenzel, L. Amann, O. Staszewski, K. Kierdorf, M. Krueger, G. Locatelli, H. Hochgerner, R. Zeiser, S. Epelman, F. Geissmann, J. Priller, F. M. V. Rossi, I. Bechmann, M. Kerschensteiner, S. Linnarsson, S. Jung, M. Prinz, Origin, fate and dynamics of macrophages at central nervous system interfaces. *Nat. Immunol.* **17**, 797–805 (2016).
- A. Mildner, H. Schmidt, M. Nitsche, D. Merkler, U.-K. Hanisch, M. Mack, M. Heikenwalder, W. Brück, J. Priller, M. Prinz, Microglia in the adult brain arise from Ly-6C^{hi}CCR2⁺ monocytes only under defined host conditions. *Nat. Neurosci.* **10**, 1544–1553 (2007).
- V. Raghavendra, F. Y. Tang, J. A. DeLeo, Complete Freunds adjuvant-induced peripheral inflammation evokes glial activation and proinflammatory cytokine expression in the CNS. *Eur. J. Neurosci.* **20**, 467–473 (2004).
- C. Prodinger, J. Bunse, M. Krüger, F. Schiehenhovel, C. Brandt, J. D. Laman, M. Greter, K. Immig, F. Heppner, B. Becher, I. Bechmann, CD11c-expressing cells reside in the juxtaglomerular parenchyma and extend processes into the glia limitans of the mouse nervous system. *Acta Neuropathol.* **121**, 445–458 (2011).
- F. Geissmann, S. Jung, D. R. Littman, Blood monocytes consist of two principal subsets with distinct migratory properties. *Immunity* **19**, 71–82 (2003).
- E. L. Gautier, T. Shay, J. Miller, M. Greter, C. Jakubzik, S. Ivanov, J. Helft, A. Chow, K. G. Elpek, S. Gordonov, A. R. Mazloom, A. Ma'ayan, W.-J. Chua, T. H. H. Hansen, S. J. Turley, M. Merad, G. J. Randolph; Immunological Genome Consortium, Gene-expression profiles and transcriptional regulatory pathways that underlie the identity and diversity of mouse tissue macrophages. *Nat. Immunol.* **13**, 1118–1128 (2012).
- B. Becher, I. Bechmann, M. Greter, Antigen presentation in autoimmunity and CNS inflammation: How T lymphocytes recognize the brain. *J. Mol. Med.* **84**, 532–543 (2006).
- C. Schläger, H. Körner, M. Krueger, S. Vidoli, M. Haberl, D. Mielke, E. Brylla, T. Issekutz, C. Cabañas, P. J. Nelson, T. Ziemssen, V. Rohde, I. Bechmann, D. Lodygin, F. Odoardi, A. Flügel, Effector T-cell trafficking between the leptomeninges and the cerebrospinal fluid. *Nature* **530**, 349–353 (2016).
- A. Waisman, L. Johann, Antigen-presenting cell diversity for T cell reactivation in central nervous system autoimmunity. *J. Mol. Med.* **96**, 1279–1292 (2018).
- E.-a. D. Amir el, K. L. Davis, M. D. Tadmor, E. F. Simonds, J. H. Levine, S. C. Bendall, D. K. Shenfeld, S. Krishnaswamy, G. P. Nolan, D. Pe'er, tSNE enables visualization of high dimensional single-cell data and reveals phenotypic heterogeneity of leukemia. *Nat. Biotechnol.* **31**, 545–552 (2013).
- F. J. Hartmann, R. Bernard-Valnet, C. Quérault, D. Mrdjen, L. M. Weber, E. Galli, C. Krieg, M. D. Robinson, X.-H. Nguyen, Y. Dauvilliers, R. S. Liblau, B. Becher, High-dimensional single-cell analysis reveals the immune signature of narcolepsy. *J. Exp. Med.* **213**, 2621–2633 (2016).
- S. Van Gassen, B. Callebaut, M. J. Van Helden, B. N. Lambrecht, P. Demeester, T. Dhaene, Y. Saeyns, FlowSOM: Using self-organizing maps for visualization and interpretation of cytometry data. *Cytometry A* **87**, 636–645 (2015).
- I. Bartholomäus, N. Kawakami, F. Odoardi, C. Schläger, D. Miljkovic, J. W. Ellwart, W. E. F. Klinkert, C. Flügel-Koch, T. B. Issekutz, H. Wekerle, A. Flügel, Effector T cell interactions with meningeal vascular structures in nascent autoimmune CNS lesions. *Nature* **462**, 94–98 (2009).
- B. Engelhardt, P. Vajkoczy, R. O. Weller, The movers and shapers in immune privilege of the CNS. *Nat. Immunol.* **18**, 123–131 (2017).
- A. Buttigereit, I. Lelios, X. Yu, M. Vrohlings, N. R. Krakoski, E. L. Gautier, R. Nishinakamura, B. Becher, M. Greter, Sall1 is a transcriptional regulator defining microglia identity and function. *Nat. Immunol.* **17**, 1397–1406 (2016).
- K. Hashimoto, S. K. Joshi, P. A. Koni, A conditional null allele of the major histocompatibility IA-beta chain gene. *Genesis* **32**, 152–153 (2002).
- E. Bettelli, M. Pagany, H. L. Weiner, C. Linington, R. A. Sobel, V. K. Kuchroo, Myelin oligodendrocyte glycoprotein-specific T cell receptor transgenic mice develop spontaneous autoimmune optic neuritis. *J. Exp. Med.* **197**, 1073–1081 (2003).
- I. M. Stromnes, J. M. Goverman, Passive induction of experimental allergic encephalomyelitis. *Nat. Protoc.* **1**, 1952–1960 (2006).
- Y. Wolf, A. Shemer, L. Levy-Efrati, M. Gross, J.-S. Kim, A. Engel, E. David, L. Chappell-Maor, J. Grozovski, R. Rotkopf, I. Biton, R. Eilam-Altmaster, S. Jung, Microglial MHC class II is dispensable for experimental autoimmune encephalomyelitis and cuprizone-induced demyelination. *Eur. J. Immunol.* **48**, 1308–1318 (2018).
- B. E. Clausen, C. Burkhardt, W. Reith, R. Renkawitz, I. Förster, Conditional gene targeting in macrophages and granulocytes using LysMcre mice. *Transgenic Res.* **8**, 265–277 (1999).
- M. L. Caton, M. R. Smith-Raska, B. Reizis, Notch-RBP-J signaling controls the homeostasis of CD8- dendritic cells in the spleen. *J. Exp. Med.* **204**, 1653–1664 (2007).
- P. B. Stranges, J. Watson, C. J. Cooper, C.-M. Choisy-Rossi, A. C. Stonebraker, R. A. Beighton, H. Hartig, J. P. Sundberg, S. Servick, G. Kaufmann, P. J. Fink, A. V. Chevovsky, Elimination of antigen-presenting cells and autoreactive T cells by Fas contributes to prevention of autoimmunity. *Immunity* **26**, 629–641 (2007).
- J. Loschko, G. J. Rieke, H. A. Schreiber, M. M. Meredith, K.-H. Yao, P. Guermonprez, M. C. Nussenzeig, Inducible targeting of cDCs and their subsets in vivo. *J. Immunol. Methods* **434**, 32–38 (2016).
- S. Yona, K.-W. Kim, Y. Wolf, A. Mildner, D. Varol, M. Breker, D. Strauss-Ayal, S. Viukov, M. Guilliams, A. Misharin, D. A. Hume, H. Perlman, B. Malissen, E. Zelzer, S. Jung, Fate mapping reveals origins and dynamics of monocytes and tissue macrophages under homeostasis. *Immunity* **38**, 79–91 (2013).
- M. Guilliams, C. A. Dutertre, C. L. Scott, N. McGovern, D. Sichien, S. Chakarov, S. Van Gassen, J. Chen, M. Poidinger, S. De Prijck, S. J. Tavernier, I. Low, S. E. Iraç, C. N. Mattar, H. R. Sumatoh, G. H. L. Low, T. J. K. Chung, D. K. H. Chan, K. K. Tan, T. L. K. Hon, E. Fossum, B. Bogen, M. Choolani, J. K. Y. Chan, A. Larbi, H. Luche, S. Henri,

- Y. Saeys, E. W. Newell, B. N. Lambrecht, B. Malissen, F. Ginhoux, Unsupervised high-dimensional analysis aligns dendritic cells across tissues and species. *Immunity* **45**, 669–684 (2016).
33. M. Paterka, V. Siffrin, J. O. Voss, J. Werr, N. Hoppmann, R. Gollan, P. Belikan, J. Bruttger, J. Birkenstock, S. Jung, E. Esplugues, N. Yogeve, R. A. Flavell, T. Bopp, F. Zipp, Gatekeeper role of brain antigen-presenting CD11c⁺ cells in neuroinflammation. *EMBO J.* **35**, 89–101 (2016).
34. N. Yogeve, F. Frommer, D. Lukas, K. Kautz-Neu, K. Karram, D. Ielo, E. von Stebut, H. C. Probst, M. van den Broek, D. Riethmacher, T. Birnberg, T. Blank, B. Reizis, T. Korn, H. Wiendl, S. Jung, M. Prinz, F. C. Kurschus, A. Waisman, Dendritic cells ameliorate autoimmunity in the CNS by controlling the homeostasis of PD-1 receptor(+) regulatory T cells. *Immunity* **37**, 264–275 (2012).
35. E. R. Pierson, I. M. Strommes, J. M. Goverman, B cells promote induction of experimental autoimmune encephalomyelitis by facilitating reactivation of T cells in the central nervous system. *J. Immunol.* **192**, 929–939 (2014).
36. B. Schreiner, F. L. Heppner, B. Becher, Modeling multiple sclerosis in laboratory animals. *Semin. Immunopathol.* **31**, 479–495 (2009).
37. N. I. Kyrtatos, I. J. Bauer, G. Zhang, M. Pesic, I. Bartholomaus, M. Mues, P. Fang, M. Wörner, S. Everts, J. W. Ellwart, J. M. Watt, B. V. L. Potter, R. Hohlfeld, H. Wekerle, N. Kawakami, Visualizing context-dependent calcium signaling in encephalitogenic T cells in vivo by two-photon microscopy. *Proc. Natl. Acad. Sci. U.S.A.* **114**, E6381–E6389 (2017).
38. E. D. Ponomarev, L. P. Shriner, K. Maresz, B. N. Dittel, Microglial cell activation and proliferation precedes the onset of CNS autoimmunity. *J. Neurosci. Res.* **81**, 374–389 (2005).
39. I. Jelicic, F. Al Nimer, J. Wang, V. Lentsch, R. Planas, I. Jelicic, A. Madjovski, S. Ruhrmann, W. Faigle, K. Frauenknecht, C. Pinilla, R. Santos, C. Hammer, Y. Ortiz, L. Opitz, H. Grönlund, G. Rogler, O. Boyman, R. Reynolds, A. Lutterotti, M. Khademi, T. Olsson, F. Piehl, M. Sospedra, R. Martin, Memory B cells activate brain-homing, autoreactive CD4⁺ T cells in multiple sclerosis. *Cell* **175**, 85–100.e23 (2018).
40. A. S. Archambault, J. A. Carrero, L. G. Barnett, N. G. McGee, J. Sim, J. O. Wright, T. Raabe, P. Chen, H. Ding, E. J. Allenspach, I. Dragatsis, T. M. Laufer, G. F. Wu, Cutting edge: Conditional MHC class II expression reveals a limited role for B cell antigen presentation in primary and secondary CD4 T cell responses. *J. Immunol.* **191**, 545–550 (2013).
41. E. H. Tran, K. Hoekstra, N. van Rooijen, C. D. Dijkstra, T. Owens, Immune invasion of the central nervous system parenchyma and experimental allergic encephalomyelitis, but not leukocyte extravasation from blood, are prevented in macrophage-depleted mice. *J. Immunol.* **161**, 3767–3775 (1998).
42. J. Karman, C. Ling, M. Sandor, Z. Fabry, Initiation of immune responses in brain is promoted by local dendritic cells. *J. Immunol.* **173**, 2353–2361 (2004).
43. C. W. Keller, C. Sina, M. B. Kotur, G. Ramelli, S. Mundt, I. Quast, L.-A. Ligeon, P. Weber, B. Becher, C. Münz, J. D. Lünemann, ATG-dependent phagocytosis in dendritic cells drives myelin-specific CD4⁺ T cell pathogenicity during CNS inflammation. *Proc. Natl. Acad. Sci. U.S.A.* **114**, E11228–E11237 (2017).
44. M. Paterka, J. O. Voss, J. Werr, E. Reuter, S. Franck, T. Leuenberger, J. Herz, H. Radbruch, T. Bopp, V. Siffrin, F. Zipp, Dendritic cells tip the balance towards induction of regulatory T cells upon priming in experimental autoimmune encephalomyelitis. *J. Autoimmun.* **76**, 108–114 (2017).
45. N. Kawakami, S. Lassmann, Z. Li, F. Odoardi, T. Ritter, T. Ziemssen, W. E. F. Klinkert, J. W. Ellwart, M. Bradl, K. Krivacic, H. Lassmann, R. M. Ransohoff, H.-D. Volk, H. Wekerle, C. Linington, A. Flügel, The activation status of neuroantigen-specific T cells in the target organ determines the clinical outcome of autoimmune encephalomyelitis. *J. Exp. Med.* **199**, 185–197 (2004).
46. D. A. Giles, P. C. Duncker, N. M. Wilkinson, J. M. Washnock-Schmid, B. M. Segal, CNS-resident classical DCs play a critical role in CNS autoimmune disease. *J. Clin. Invest.* **128**, 5322–5334 (2018).
47. C. Ruedl, S. Jung, DTR-mediated conditional cell ablation—Progress and challenges. *Eur. J. Immunol.* **48**, 1114–1119 (2018).
48. C. F. Lucchinetti, B. F. G. Popescu, R. F. Bunyan, N. M. Moll, S. F. Roemer, H. Lassmann, W. Brück, J. E. Parisi, B. W. Scheithauer, C. Giannini, S. D. Weigand, J. Mandrekar, R. M. Ransohoff, Inflammatory cortical demyelination in early multiple sclerosis. *N. Engl. J. Med.* **365**, 2188–2197 (2011).
49. A. E. Russi, M. A. Brown, The meninges: New therapeutic targets for multiple sclerosis. *Transl. Res.* **165**, 255–269 (2015).
50. K. Hildner, B. T. Edelson, W. E. Purtha, M. Diamond, H. Matsushita, M. Kohyama, B. Calderon, B. U. Schraml, E. R. Unanue, M. S. Diamond, R. D. Schreiber, T. L. Murphy, K. M. Murphy, *Batf3* deficiency reveals a critical role for CD8α⁺ dendritic cells in cytotoxic T cell immunity. *Science* **322**, 1097–1100 (2008).
51. S. Inoue, M. Inoue, S. Fujimura, R. Nishinakamura, A mouse line expressing *Sall1*-driven inducible Cre recombinase in the kidney mesenchyme. *Genesis* **48**, 207–212 (2010).

Acknowledgments: We thank the Cytometry Facility (University of Zurich) and the Center for Microscopy and Image Analysis (University of Zurich) for technical assistance, Insight Editing London for critical review and editing of the manuscript, and N. Puertas for excellent technical assistance. **Funding:** This work was supported by grants from the Swiss National Science Foundation (PP00P3_144781 to M.G. and 310030_146130, 310030_150768, and 310030_170320 to B.B.), the European Union FP7 ITN_NeuroKine (to B.B.), the European Union FP7 Project ATECT (to B.B.), and the University Research Priority Project Translational Cancer Research (to B.B.). **Author contributions:** S.M. and B.B. conceived the study. B.B. supervised the study, and S.M. performed all experiments and statistical analysis with support from D.M. for mass cytometry experiments, D.M. and S.G.U. for FACS, and B.S. and S.G.U. for immunohistochemistry experiments. S.M. and B.B. wrote the manuscript with critical review from D.M., S.G.U., B.S., and M.G. **Competing interests:** The authors declare that they have no competing interests. **Data and materials availability:** The CyTOF data have already been made public under <https://community.cytobank.org/cytobank/experiments/69323> (5). The CyTOF data shown in Fig. 4 are available at <https://community.cytobank.org/cytobank/experiments/71307>.

Submitted 19 July 2018

Accepted 3 January 2019

Published 25 January 2019

10.1126/sciimmunol.aau8380

Citation: S. Mundt, D. Mrdjen, S. G. Utz, M. Greter, B. Schreiner, B. Becher, Conventional DCs sample and present myelin antigens in the healthy CNS and allow parenchymal T cell entry to initiate neuroinflammation. *Sci. Immunol.* **4**, eaau8380 (2019).

NEUROIMMUNOLOGY

The anatomy and immunology of vasculature in the central nervous system

Panagiotis Mastorakos and Dorian McGavern*

Barriers between circulation and the central nervous system (CNS) play a key role in the development and modulation of CNS immune responses. Structural variations in the vasculature traversing different anatomical regions within the CNS strongly influence where and how CNS immune responses first develop. Here, we provide an overview of cerebrovascular anatomy, focusing on the blood-CNS interface and how anatomical variations influence steady-state immunology in the compartment. We then discuss how CNS vasculature is affected by and influences the development of different pathophysiological states, such as CNS autoimmune disease, cerebrovascular injury, cerebral ischemia, and infection.

INTRODUCTION

The central nervous system (CNS) has a complex barrier system and has evolved specialized mechanisms to mount and regulate immune reactions. CNS immune responses differ based on anatomical location, and a clear distinction exists between responses that develop in the fluid spaces and membranous lining (or meninges) relative to the parenchyma (1). For example, early studies demonstrated that mouse sarcoma cells grow rapidly when injected into the brain parenchyma of rats but were immunologically rejected when placed close to a ventricle [a space filled with cerebrospinal fluid (CSF)] (2). These findings show that the development of robust immune reactions against parenchymal antigens depends on their entry into fluid spaces, which promotes egress into draining lymph nodes. Although the CNS parenchyma does not have a conventional lymphatic drainage system (3), lymphatics have been discovered in the dura mater and just outside holes in the skull bone (4–9). Once an immune response is mobilized in peripheral lymphoid tissues, leukocyte traffic into the CNS is heavily regulated by barriers that include the blood-brain barrier (BBB), blood-CSF barrier, and blood-meningeal barrier (10). Structural variations in these barriers influence the location and development of CNS immune responses that enter through vasculature. These barriers essentially control immune cell entry into different CNS compartments. Here, we review the anatomy and physiology of CNS vasculature and associated barriers and how these structures influence immune surveillance under steady-state and inflammatory conditions.

NEUROANATOMICAL OVERVIEW

Arterial blood enters the cranial cavity, primarily through two sets of blood vessels: the internal carotid arteries, which give rise to anterior brain circulation, and the vertebral arteries, which give rise to posterior circulation. These are interconnected through the circle of Willis located in subarachnoid cisterns at the base of the brain (11). The circle of Willis allows any one of these four vessels to take over brain perfusion and provides a protective mechanism against ischemia. The internal carotid arteries supply the cerebrum, whereas the vertebral arteries join to form the basilar artery that supplies the brainstem

and cerebellum. Second-order branches form vessels that traverse the subarachnoid space and pia mater, giving rise to smaller arterioles (Fig. 1) that enter the brain parenchyma (Fig. 1A) (12). These penetrating vessels are surrounded by perivascular spaces that can vary in size. For example, in the cortex, a packed barrier of endothelial cells, basement membrane, and glia limitans surrounds penetrating arteries, leaving little to no fluid-filled space, whereas the lenticulostriate branches in the basal ganglia are surrounded by a larger perivascular space (13). Pia mater covers all arteries in the subarachnoid space, whereas coverage of veins is incomplete. In addition, the fluid in perivascular spaces can move directly into the subarachnoid space through fenestrations in the pia mater (Fig. 1A) (14). This allows direct communication between perivascular, subpial, and subarachnoid spaces. The communication of the perivascular compartment with the subarachnoid space plays an important role in antigen presentation, which will be described in more detail below. Venous drainage in the CNS occurs through an interconnected system of valveless veins and dural sinuses. Postcapillary venules in the CNS parenchyma drain capillaries and are surrounded by fluid-filled perivascular spaces (Figs. 1, A and B, and 2) (15). They connect into a deep and superficial venous system. Deep venous drainage occurs through the subependymal veins, internal cerebral veins, basal vein, and the great vein of Galen, which connect into the straight sinus beneath the brain. Superficial drainage occurs through cortical veins in the pia mater that drain into the dural sinuses. The venous system ultimately drains into the jugular veins or pterygoid plexus (11).

The meningeal vasculature is a major point of entry into the CNS and should be considered separately from those that traverse the CNS parenchyma. The meninges are three membranes that envelop the CNS and consist of dura, arachnoid, and pia mater (Fig. 1A). In humans, the dura is a ~1-mm-thick fibrous structure with an inner and outer layer that separate to form large venous sinuses. The outer layer is attached to the inner surface of the skull and extends vascular connections into the bone. Blood vessels within the dura mater are fenestrated and do not have tight junctions, leaving this structure open to peripheral circulation (Fig. 1A). The arachnoid mater is a ~200-μm translucent avascular membrane that is structurally contiguous to the dura mater and is composed of two layers of squamous epithelial cells that express varying amounts of laminin α5+ basement membrane. The inner cell layer consists of ramified epithelial cells with long cytoplasmic processes, and these cells are connected by tight junctions (16–18). Beneath the sealed arachnoid mater is the

Viral Immunology and Intravital Imaging Section, National Institute of Neurological Disorders and Stroke, National Institutes of Health, Bethesda, MD, USA.

*Corresponding author. Email: mcgavernd@mail.nih.gov

Copyright © 2019
The Authors, some
rights reserved;
exclusive licensee
American Association
for the Advancement
of Science. No claim
to original U.S.
Government Works

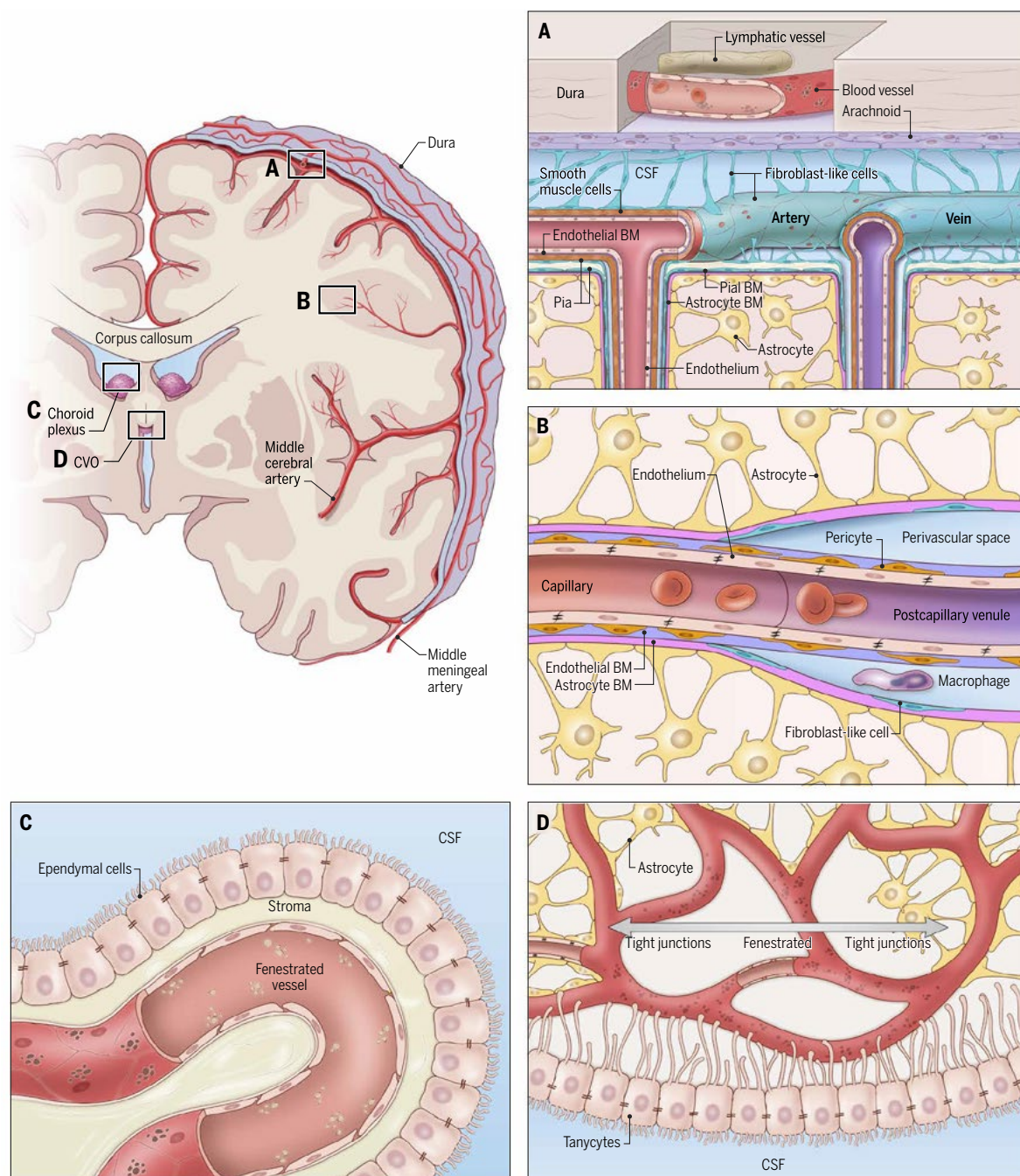


Fig. 1. Structural variations in the anatomy of cerebrovascular barriers. Coronal depiction of cerebrum and dura mater in relation to the middle cerebral and middle meningeal arteries. (A) Meningeal and cortical vascular anatomy. The dura mater contains lymphatics and fenestrated blood vessels that lack tight junctions. The arachnoid mater is an epithelial layer that provides a barrier between the peripheral vasculature of the dura mater and the CSF through tight junctions and efflux pumps. Leptomeningeal blood vessels in the pia mater lack astrocytic ensheathment, but their endothelial cells are connected by tight junctions. There are small stomata in the connective tissue (fibroblastic reticular cells) covering pial vessels that allow an exchange of fluid between the CSF and perivascular space. Pial arteries penetrate the brain and are covered by a densely packed perivascular layer of astrocytic foot processes; astrocytic (pink), pial (gray), and endothelial (purple) basement membranes; and smooth muscle cells. Veins exiting the parenchyma have a perivascular space flanked by astrocytic foot processes as well as endothelial basement membranes (BMs). The pial BM is only present in the superficial portion of the veins. (B) Capillary and postcapillary venule within the brain parenchyma. The capillary endothelial BM (purple) is juxtaposed to the astrocytic BM (pink), whereas the postcapillary venule is surrounded by a perivascular CSF-filled space that separates the endothelial BM from the astrocytic BM. Fibroblast-like cells (green) form an interrupted extension of the pia mater in the postcapillary venules. (C) Vessels in the choroid plexus are fenestrated and lack tight junctions. The ependymal cells overlying the choroid plexus have tight junctions that are tasked with forming a blood-CSF barrier. (D) Vasculatures at the center of CVOs (such as the subfornical organ) are fenestrated and lack tight junctions, allowing exposure to solutes from the circulation. Vasculatures around the perimeter of CVOs have a traditional BBB surrounded by astrocytic foot processes and more closely resemble vessels found in the CNS parenchyma. Overlying ependymal tanycytes are highly specialized cells with tight junctions that separate CVOs from the CSF.

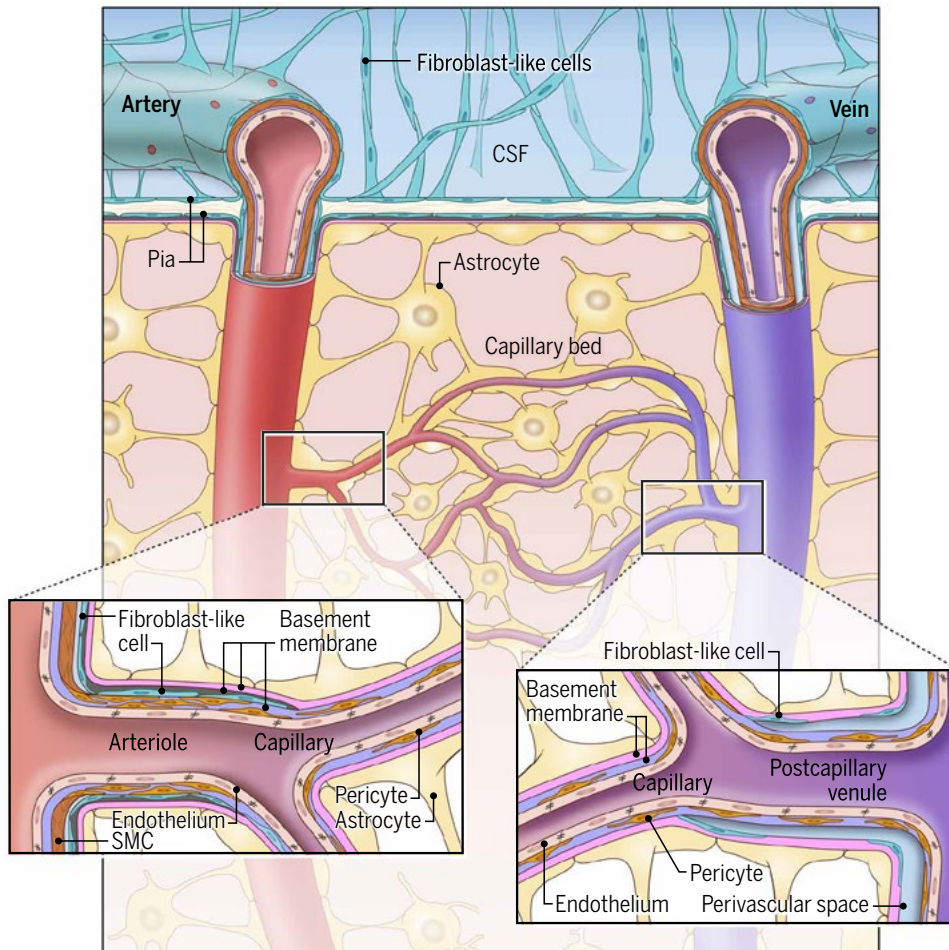


Fig. 2. Schematic representation of a cortical cerebrovascular bed. Leptomeningeal arteries penetrate the cortex, giving rise to arterioles, capillaries, and postcapillary venules that lastly drain into cortical veins that exit the parenchyma. Leptomeningeal arteries and veins are surrounded by fibroblast-like cells and a collagen layer. Penetrating arteries are ensheathed by smooth muscle cells (SMCs) that transition to a pericyte layer at arteriole branch points. The pial layer of fibroblast-like cells ends abruptly at the transition from arteriole to capillary. In capillaries, the astrocytic BM (pink) is adjacent to the endothelial cell BM (purple). These membranes separate at the level of the postcapillary venule to form a perivascular space. Interrupted fibroblast-like cells are also present along postcapillary venules and veins as they exit the CNS parenchyma.

subarachnoid space, which is filled with CSF. Fibroblast-like cells and sheet-like collagenous trabeculae connect the inner arachnoid membrane to the pia mater, dividing the subarachnoid space into relatively distinct CSF compartments (Fig. 1A) (19). The pia mater is composed of epithelial cells that produce a laminin $\alpha 1+$ basement membrane and fibroblast-like cells and separates the subarachnoid space from brain parenchyma and perivascular spaces (18, 20). This structure does not have tight junctions like the arachnoid mater. Together, the arachnoid and pia mater comprise the leptomeninges.

Most of the blood supply to the cranial dura mater comes from meningeal arteries originating from the internal carotid artery, vertebral artery, and external carotid artery (Fig. 1). The dura mater is supplied anteriorly by the anterior meningeal arteries that arise from the ophthalmic artery. The middle meningeal arteries, on the other hand, arise from the maxillary artery, and the posterior meningeal arteries arise from the occipital and vertebral arteries (11). There is also blood supply to the dura mater from the aforementioned pial

vessels, which include olfactory branches and pericallosal branches, the anterior falcine artery, the medial dural tentorial branch, the subarcuate artery, and the posterior meningeal artery (21). The arachnoid and pia mater are relatively avascular when compared with the dura mater (16).

An abundant anastomotic arterial network covers the dura mater and is in the outer layer of this structure. Venous drainage occurs through satellite veins that accompany the arteries and through an irregular network of veins and venous lakes that drain into the venous sinuses (22). There are also venous connections between the dura mater and skull bone. Diploic veins are large veins with irregular dilatations that connect skull bone marrow pockets to meningeal veins, dural sinuses, and pericranial veins. Emissary veins, on the other hand, traverse the entire skull bone and make connections between venous sinuses in the dura mater and extracranial veins in the scalp (23, 24). Two additional CNS structures that require special consideration from a vascular perspective are the choroid plexus within the ventricles (Fig. 1C) and the circumventricular organs (CVOs) (Fig. 1D). Blood vessels within these two structures have endothelia that lack tight junctions and are open to peripheral circulation (25, 26). The ventricles are a communicating system of five cavities within the brain parenchyma, lined with ependymal cells and filled with cerebrospinal fluid (Fig. 1C). The choroid plexus is a spongy, vascularized structure that produces CSF and is attached to the walls of ventricles. It contains capillaries of choroidal arteries that are covered by an ependymal epithelial layer. The ependymal cells express

tight junctions, providing a barrier between the fenestrated blood vessels and the CSF (Fig. 1C). The choroid plexus extends from the inferior horn of the lateral ventricle to the interventricular foramen where it connects to the choroid plexus of the roof of the third ventricle. There is also choroid plexus located at the roof of the fourth ventricle. The choroid plexus of the lateral and third ventricles is supplied by branches of the internal carotid artery and the posterior cerebral artery. The choroid plexus of the fourth ventricle is supplied by the posterior circulation (23).

The CVOs of the brain are a distinct group of structures bordering the third and fourth ventricles that perform homeostatic and neurosecretory functions and lack a BBB (Fig. 1D). The CVOs provide a connection between the CNS and peripheral blood and are usually divided into two categories: sensory and secretory. Sensory CVOs include the subfornical organ, area postrema, and vascular organ of the lamina terminalis. These sample the contents of the systemic circulation and relay information to the CNS. By contrast,

secretory CVOs—such as the subcommissural organ, median eminence, posterior pituitary, and pineal gland—secrete substances such as peptides directly into the circulation (25).

Apart from these classical neuroanatomical descriptions, it is important to understand the structural changes in CNS blood vessels as they progress from leptomeningeal arteries to parenchymal arterioles, capillaries, postcapillary venules, venules, and, lastly, veins (Fig. 2). The surface of the CNS parenchyma consists of glia limitans basement membrane and pia mater that follow penetrating arteries to points of arteriole branching (18). More specifically, laminin $\alpha 1+$ basement membrane and fibroblast-like cells are observed before these branch points in the parenchyma. Fibroblast-like cells are also found along postcapillary venules, where they are sparse and not accompanied by a fully formed basement membrane. Postcapillary venules and veins have a more pronounced CSF-filled perivascular space than the other types of parenchyma blood vessels (15), and these spaces support a lot of immune activity. Mural cells in the form of pericytes and smooth muscle cells are present throughout the arteriovenous continuum. Arterial smooth muscle cells gradually transition to pericytes at the level of the arteriole. Recent single-cell transcriptomic (27) and immunohistochemical studies (18) have provided molecular definitions for the principal cell types along the CNS arteriovenous continuum and have also mapped the distinct forms of basement membrane.

BLOOD-CNS INTERFACE

P. Ehrlich was the first to recognize that there is a barrier between the circulation and brain that differs from most peripheral organs. He injected coerulean-S sulfate intravenously into rodents and observed lack of extravasation into the brain (28). Since then, it has been observed that although intravascular tracers do not enter the brain parenchyma, they are found in the leptomeninges, choroid plexus, and perivascular spaces (29). Therefore, it is of importance to consider the differential permeability of these different anatomical compartments. The BBB should be considered a summation of mechanisms that control the exchange of substances and cells between the circulation and CNS. Collectively, the BBB is composed of endothelial cells, basement membrane, pericytes, glia limitans, and microglia. Interactions among these different cells and structures along with neurons refine the functions of the BBB and together act as a neurovascular unit (30). BBB endothelial cells selectively restrict movement of substances into the CNS by means of tight junctions and enzymatic reactions. However, these cells can also selectively transport small and large molecules into the CNS through passive diffusion, facilitated diffusion, and active transport. The endothelial cells comprising most CNS blood vessels, including subpial and parenchymal vessels, lack fenestrations and have diminished pinocytosis. They are also connected by tight junctions, which consist of occludin and claudins, that link to the cytoskeleton through scaffolding proteins [such as zonula occluden-1 (ZO-1), ZO-2, ZO-3, and cingulin] (Fig. 3). Adherens junctions, including cadherin, also link endothelial cells and connect to actin filaments through α -, β -, and γ -catenins; vinculin; and actinin (31). Activation of Rho guanosine triphosphatases (GTPases) regulates the length of these actin fibers, thus controlling the integrity of both adherens junctions and tight junctions (32).

The matrix components of the basal lamina—which include laminins, proteoglycans, fibronectin, and type IV collagen—also play

an important role in the regulation of the BBB and contribute to the interactions between endothelial cells and astrocytic endfeet (Fig. 3). This is mediated by integrin $\alpha\beta$ receptors bound to laminin and fibronectin as well as dystroglycan, which binds to laminins, agrin, and perlecan (33). The endothelial and astrocytic basement membranes have a similar structure but differ in their composition of laminin isoforms. The endothelial basement membrane is composed primarily of laminins $\alpha 4$ and $\alpha 5$, whereas the astrocytic basement membrane is composed of laminin $\alpha 2$ and, to a lesser extent, laminin $\alpha 1$ (Fig. 3) (18). Pericytes are undifferentiated contractile connective tissue cells embedded within the endothelial basement membrane (Fig. 2) (34). For capillary endothelial cells, basement membrane is either directly attached to or closely juxtaposed to the basement membrane of astrocytic endfeet (18). This negatively charged tight structure permits free migration of macromolecules with low charge, such as ferritin with a 13-nm-diameter (35) and intrathecally injected immunoglobulin G (36). In postcapillary venules, there is a better defined fluid-filled perivascular space surrounding the basement membrane (Fig. 2) (37).

Astrocytic endfeet form the glia limitans, which covers the entire surface of the brain and spinal cord (glia limitans superficialis) and separates the perivascular space from the brain parenchyma (glia limitans perivascularis) (Figs. 1, A and B, and 2). They cover >99% of the vascular surface and densely surround tight junctions, creating an additional barrier that limits entry into the CNS parenchyma (38). Molecules from 0.8 to 70 kDa have been shown to penetrate the glia limitans to varying degrees, whereas molecules from 150 to 2000 kDa are confined within the perivascular space (18, 39, 40). The 20-nm gaps between astrocytic endfeet likely generate a crucial cutoff for diffusion of molecules into the interstitial fluid (ISF) (40); however, it is unclear whether astrocytic coverage is complete (41), and the tightly compacted basement membrane may also play an important role in preventing solute diffusion into the brain parenchyma (18). The glia limitans and basement membranes form the rate-limiting barrier between CSF and ISF. Molecule exchange between these two fluids depends on size, lipophilicity, concentration gradients, and astrocytic transport mechanisms, among others. The glia limitans and basement membranes also create a barrier between circulating components of the immune system and the CNS parenchyma, a division that is integral to the neuroimmune axis (42). The close proximity of astrocytic endfeet and endothelial cells has led to the notion that the glia limitans can directly affect BBB permeability (43). Although all the astrocytic factors that promote permeability are not known, those often implicated in the process are glutamate, aspartate (43), interleukin-1 β (IL-1 β) (44, 45), endothelin-1, nitric oxide (46), interferon- γ (45), and tumor necrosis factor- α (TNF α) (45, 47).

Within the meninges, blood vessels differ based on their anatomical location. For example, endothelial cells comprising blood vessels in the dura mater lack tight junctions and allow extravasation of solutes as large as 43 kDa (Fig. 1A) (48). The dura mater has lymphatic drainage (4–8) and in many ways resembles a peripheral tissue. However, the arachnoid mater, which has tight junctions and efflux pumps, serves as an important barrier between the fenestrated peripheral vasculature of the dura and the CSF (49). The arachnoid and pia mater are sometimes referred to together as the leptomeninges, and blood vessels within this structure have endothelial cells connected by tight junctions but lack astrocytic foot processes (Fig. 1A). The paracellular junctions between these endothelial cells vary in tightness.

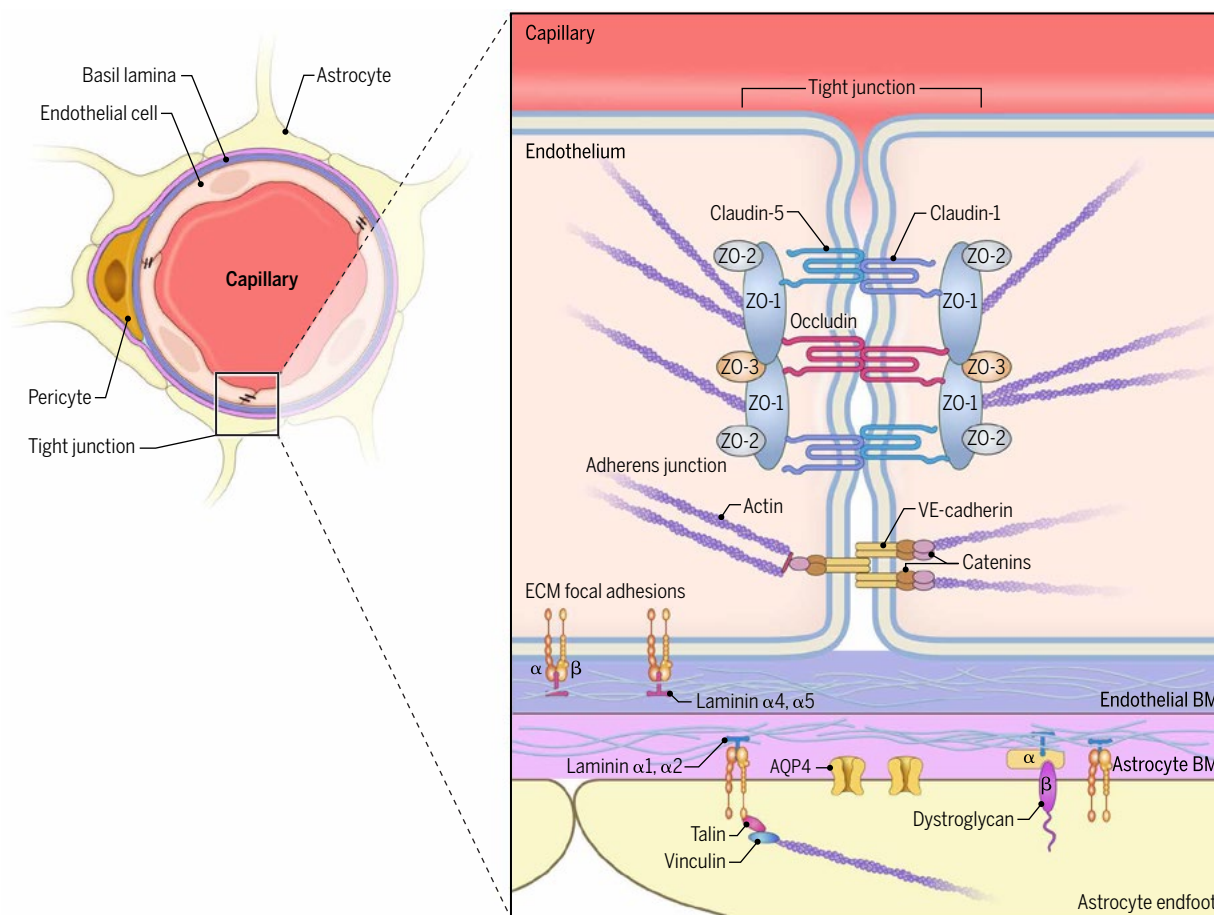


Fig. 3. Anatomy of parenchymal capillary barriers. Tight junction proteins—such as occludin; claudin-3, claudin-5, and claudin-12; and ZO-1 and ZO-2—and JAMs form tight junctions between cerebrovascular endothelial cells that limit the passage of materials from the blood into the CNS. These are linked to the actin cytoskeleton within endothelial cells. Vascular endothelial cadherins and intracellular catenins form adherens junctions that provide tensile force between endothelial cells through linkage to the actin cytoskeleton. The endothelial BM is primarily composed of laminins $\alpha 4$ and $\alpha 5$ and is juxtaposed to the astrocytic BM, which is composed of laminins $\alpha 1$ and $\alpha 2$. The endothelial cells interact with the basal lamina through α and β integrins that bind to laminins and fibronectin. Similarly, astrocytic endfeet interact with BM through integrins and dystroglycan.

Some are similar to those found on parenchymal vessels, whereas others have 2.8-nm gaps (50). Nevertheless, pial vessels are not permeable to the majority of molecules, including 44-kDa horseradish peroxidase and 0.4-kDa fluorescein (51). Pial vessels do have 1- to 3- μ m stomata in the adventitia (a layer of connective tissue covering the vessels) (Fig. 1A), potentially allowing an exchange of macromolecules between the CSF and perivascular space (36).

The blood-CSF barrier within the choroid plexus has fundamentally different properties than those of the BBB. The endothelium on choroid plexus vessels is fenestrated and lacks tight junctions and a glia limitans (Fig. 1C). However, ependymal cells overlying these vessels do have tight junctions and are tasked with forming a blood-CSF barrier composed of transmembrane proteins such as occludin, claudin-1, claudin-2, and claudin-11 (52, 53). Large proteins in plasma can diffuse out of choroidal capillaries but are restricted by the tight junction-expressing ependyma. The choroid plexus, which is located within the ventricles, has a very narrow connection to surrounding parenchyma at the choroid vessel entry point (11). Therefore, solutes extravasating from choroid plexus capillaries cannot travel directly into the brain parenchyma.

Like vessels in the choroid plexus, CVO vasculature is also fenestrated, with circular pores 40 to 60 nm in diameter that allow exposure to solutes from circulation (54). More specifically, blood vessels at the center of CVOs lack tight junction molecules, whereas vasculature in the periphery of these organs more closely resembles vessels with a traditional BBB in the brain parenchyma (Fig. 1D). In addition, the capillaries at the center of the CVO lack a glia limitans (25). Therefore, capillaries in central CVO subdivisions have higher vascular permeability compared with those around the perimeter. Within the CVO, the endothelial cell basement membrane on all capillaries is covered by an outer basement membrane. After intravenous administration, 10-kDa dextran was observed in the perivascular spaces of CVO capillaries but did not enter the organ. By contrast, tracers with a smaller molecular weight (such as fluorescein and 3-kDa dextran) were able to enter the CVO but not the surrounding brain tissue because of a densely packed perimeter of astrocytes-tanyocytes that express tight junction proteins (25). Similar to the choroid plexus, the CVO has highly specialized ependymal cells (referred to as tanyocytes) that extend processes into the CVO parenchyma and form a barrier between the CVO parenchyma and the CSF. Tanyocytes are connected with tight junctions

that include ZO-1, occludin, claudin-5, and claudin-1 that limit diffusion of macromolecules from the CSF into the CVO (55).

CNS IMMUNE SURVEILLANCE

The elaborate barrier system between the brain parenchyma and circulation combined with restricted afferent and efferent communication with lymphatic tissue limits immune surveillance of the CNS relative to other peripheral tissues. CNS immune privilege differs substantially between the brain parenchyma and CSF-filled spaces such as the meninges (56). The glia limitans separates the brain parenchyma from the CSF/perivascular spaces and plays a major role in compartmentalizing CNS immune reactions.

The perivascular space plays a role in antigen drainage from the CNS parenchyma. Only a small fraction of ISF (15%) is secreted into the CSF (57), and the role of an intraparenchymal convective flow (the glymphatic system) (40) in this process remains controversial (58, 59). Movement of ISF from the brain parenchyma occurs primarily between basement membranes in the perivascular spaces of capillaries and arteries. This continues along basement membranes in the tunica media of cerebral and leptomeningeal arteries (13). Antigen, antibody, and complement complexes can become entrapped in this arterial basement membrane drainage pathway and impair perivascular lymphatic drainage (60).

As noted previously, the inner and outer basement membranes of parenchymal capillaries are directly apposed and have minimal space for perivascular fluid. This limits the ability of immune cells to traffic from the brain parenchyma to draining lymph nodes. In fact, fluorescent tracers (3-kDa dextran and 40-kDa ovalbumin) were shown to move from the brain parenchyma along basement membranes, whereas particulates (0.2 to 1.0 μm in diameter) remained trapped in the parenchyma. By contrast, injection of these same particulates into the CSF resulted in egress to the cervical lymph nodes (61). This result explains why intracerebral injection of BCG (62) or influenza virus (56) directly into the brain parenchyma does not elicit an adaptive immune response. Antigens are known to move from the CSF compartment to mandibular and deep cervical lymph nodes by exiting through perineural pathways—including the olfactory, optic, and trigeminal nerves (9, 63)—into an extensive network of lymphatic vessels that reside outside the CNS. Antigen drainage from the dura mater occurs in a similar fashion by way of lymphatic vessels traversing the dura mater and draining to the deep cervical lymph nodes (4, 5, 64).

Immune surveillance and the initiation of CNS immune responses is dependent on antigen-presenting cells (APCs) that reside alongside important barriers such as perivascular spaces, leptomeningeal vessels, the choroid plexus, and the subarachnoid space (65–68). These spaces contain bone marrow-derived dendritic cells (DCs) and relatively long-lived macrophages, although the DCs are generally more efficient at presenting antigen (67, 69, 70). Like microglia, most macrophages residing in the leptomeninges and perivascular spaces are derived from early yolk sac-derived erythromyeloid progenitors, and during steady state, these cells have minimal turnover. This contrasts with macrophages in the choroid plexus and dura mater, which do turn over and receive some input from peripheral blood monocytes during adulthood (71–73). This is likely because both compartments contain fenestrated blood vessels and are open to peripheral circulation. In fact, the choroid plexus is proposed to serve as an immune gateway (74, 75), and the dura mater similarly hosts a high amount of immune traffic.

To survey peptides displayed on the surface of CNS APCs, T cells must access the spaces in which these APCs reside. Whereas diffusion of solutes in the CNS parenchyma is regulated mostly at the level of capillaries, immune cell extravasation often occurs along postcapillary venules (Fig. 4) (76). Leukocytes can traverse vascular endothelium through trans- or paracellular routes (77). To access the brain parenchyma, these cells need to migrate across endothelial cells and inner basement membrane as well as the glia limitans and outer basement membrane, which is a two-step process (78). Under steady state, brain endothelial cells do not support myeloid cell adhesion because of a lack of surface P-selectin expression (79). In fact, leukocyte migration across the BBB is limited to very few activated CD8 $^{+}$ and CD4 $^{+}$ T cells but not innate immune cells (80). $\alpha 4$ -Integrins mediate capture of activated CD4 $^{+}$ T cells on BBB endothelium by binding to adhesion molecules such as vascular cell adhesion molecule-1 (VCAM-1). This is followed by G protein-dependent strengthening of the interaction and eventual extravasation (Fig. 4) (81). Activated T cells can enter the perivascular space independent of antigen specificity (82), but are unable to traverse the astrocytic basement membrane and glia limitans. CXCL12 expression by endothelial cells contributes, in part, to retaining activated CD4 $^{+}$ T cells within the perivascular space through CXCR4 binding (Fig. 4) (83). In addition, activated T cells need to recognize cognate antigen presented by perivascular APCs to enter the CNS parenchyma (65, 84); otherwise, they undergo apoptosis or reenter the circulation. The importance of this T cell-dependent surveillance process is exemplified by the development of progressive multifocal leukoencephalopathy, a CNS disease induced by John Cunningham virus infection, in some patients that receive therapeutic antibodies directed against $\alpha 4$ -integrins (85).

Subarachnoid and pial vessels also restrict extravasation of leukocytes; however, migration across these vessels is more efficient relative to parenchymal vessels (86). This is because meningeal, unlike parenchymal, vascular endothelial cells constitutively express P-selectin during steady state, which is stored in Weibel-Palade bodies, allowing rapid release to the endothelial surface (79, 86). Also, CCR7-dependent extravasation of leukemic T cells in the leptomeninges suggests that local expression of CCL19 can promote memory CCR7 $^{+}$ T cell extravasation across leptomeningeal blood vessels (87). In general, CNS compartments such as the meninges, choroid plexus, and CVOs are more permissive to steady-state immune cell surveillance. Steady-state immune cell traffic through the choroid plexus is influenced by type I and type II interferon signaling. With age, a type I interferon-induced gene expression is observed in the choroid plexus that negatively affects brain function (88, 89). Blockade of type I interferon improves brain function and restores the choroid plexus to a homeostatic type II interferon-dependent signature. Immune traffic through the choroid plexus appears to rely partly on expression of intercellular adhesion molecule-1 (ICAM-1) and VCAM-1, which are expressed on the apical surface of choroid plexus epithelial cells (90). CVOs such as the area postrema have also been shown to support T cell traffic in the healthy brain (91). Because the choroid plexus, CVOs, and dura mater are open to peripheral circulation, elevated T cell surveillance is likely required to keep these compartments free of infections.

The outermost layer of the meninges (or dura mater) is quite different than most other parts of the CNS enveloped by the underlying arachnoid mater. The dura mater resembles the periphery with its permeable vasculature, lymphatic drainage, and diverse assortment

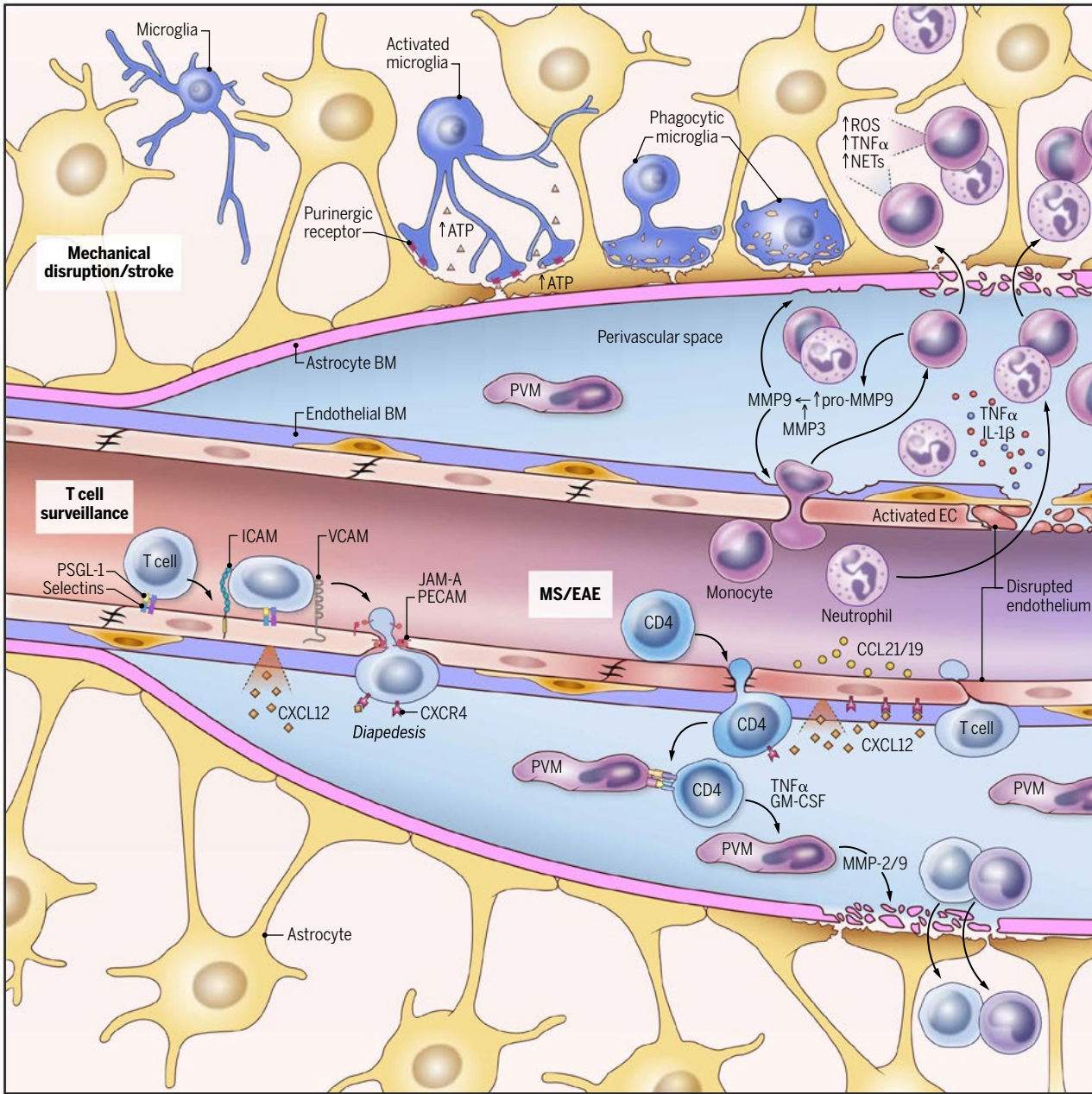


Fig. 4. Blood-CNS interface during inflammation. This schematic of a CNS blood vessel summarizes three different immunological scenarios: steady-state T cell surveillance, CNS autoimmune disease, and cerebrovascular injury and stroke. T cell surveillance: During steady state, leukocyte extravasation across the BBB is limited to few activated T lymphocytes that interact with ICAM-1 and VCAM-1 expressed on the lumen of vascular endothelial cells. CXCL12 expression by endothelial cells on the abluminal side contributes to sequestering these activated CD4⁺ T cells in the perivascular space through binding to CXCR4 on the T cell. EAE: During CNS autoimmune diseases such as EAE, the efficiency of leukocyte diapedesis is increased. CCL19, CCL21, and CXCL12 are up-regulated by cerebrovascular endothelial cells that promote the recruitment and adhesion of encephalitogenic CD4⁺ T cells. Vascular adherence and extravasation are also facilitated by selectins (P-selectin-PSGL-1 interactions) and integrins (LFA-1-ICAM-1 and VLA-4-VCAM-1 interactions). CXCR7, expressed on the abluminal surface of endothelial cells, binds to CXCL12 and reduces T cell sequestration in the perivascular space. After extravasation, T cells interact with APCs, including perivascular macrophages (PVMs), in the perivascular space. Recognition of cognate-peptide MHC complexes results in production of chemokines and cytokines (such as TNF α and granulocyte-macrophage colony-stimulating factor) that promote recruitment of myelomonocytic cells from the blood. This is followed by production of metalloproteinases (such as MMP-2 and MMP-9) that selectively cleave dystroglycan in the astrocytic foot processes, allowing penetration of effector T cells into the CNS parenchyma. Vascular injury and stroke: Mechanical disruption of the glia limitans leads to a rapid release of ATP that is detected by purinergic receptors expressed on microglia. The microglia provide immediate barrier support and debris clearance. Cerebrovascular injury can also cause resident and infiltrating monocyte-derived macrophages to release cytokines (TNF α and IL-1 β), chemokines, ROS, and metalloproteinases (pro-MMP-9). TNF α and IL-1 β trigger endothelial cell activation, promoting further myelomonocytic cell invasion. Pro-MMP-9 becomes activated by MMP-3, causing additional destruction of the glia limitans. Once in the parenchyma, neutrophils can release ROS and NETs in an attempt to control pathogens that are not present. These effector mechanisms contribute to tissue damage.

of resident immune cells (such as macrophages, DCs, mast cells, innate lymphoid cells, B cells, and T cells) (92). CD4⁺ T cells can traffic into the meninges from circulation and scan the tissue for antigens before departing to the deep cervical lymph nodes (93). In addition, the dura mater contains a high concentration of perivascular macrophages that continuously sample the tissue. On the basis of high-parameter mass cytometry and single-cell RNA-sequencing studies, the dural macrophages appear to be distinct from those residing in the pia and underlying parenchyma (73, 94).

There is also vasculature (diploic veins) that connects bone marrow pockets residing in the cancellous layer of the skull bone to dural vessels. These vessels provide an additional point of entry for immune cells, which can travel directly from the skull bone marrow to the dura mater through 100-μm bone channels (95). Similarly, cancer cells were also shown to use this route of entry. During acute lymphoblastic leukemia, lymphocytes use α6-integrins to enter the leptomeninges by migrating in the perivascular space along diploic and emissary veins that run through the skull bone. These cancer cells never traverse the BBB but do enter the subarachnoid space (96). During steady state, the arachnoid mater typically serves as a barrier between the dura mater and underlying CNS; however, the study of acute lymphoblastic leukemia cells has uncovered a means to breach this barrier.

BLOOD-CNS INTERFACE DURING INFLAMMATION

Cytokines

The CNS is affected by cytokines (97), and this can occur through a variety of different mechanisms, including direct transfer across the BBB, stimulation of CVOs, nerve stimulation, or release from infiltrating or resident immune cells, among others (98). Cytokines are transported into the CNS by using saturable transport mechanisms. This can occur in a cytokine receptor-dependent [for example, TNFα (99)] or cytokine receptor-independent (for example, IL-1) manner. Moreover, circulating cytokines can promote abluminal expression of soluble mediators such as prostaglandin E2 by binding to the luminal surface of cerebrovascular endothelial cells (100). In this way, the BBB can actively serve as a relay station for immune signaling between the blood and CNS. The dura mater, choroid plexus, and CVOs are particularly exposed to the effects of circulating cytokines given their fenestrated blood vessels and relative openness to factors in the blood (25). For example, ablation of the vascular organ of the lamina terminalis (a CVO) reduces cytokine-induced fever after injection of lipopolysaccharide (LPS) (101). LPS administration is also known to promote rapid expression of pro-inflammatory cytokines such as TNFα in all sensory CVOs as well as the meninges and choroid plexus (102). CVOs and other CNS barrier tissues can, in turn, respond to various inflammatory stimuli through expression of cytokine receptors (103), Toll-like receptors (TLRs) (104), and CD14 (105). As mentioned, CVOs are separated from adjacent neural tissue in the brain parenchyma by tanyctic astrocytes that limit diffusion of solutes from the CVO to the surrounding tissue (25). However, bidirectional neuronal projections to the hypothalamus, hippocampus, and amygdala may relay inflammatory signals from CVOs to other areas of the CNS. In addition, lipophilic molecules such as prostaglandins, produced within the CVO in response to cytokines, can traverse the CVO barrier and affect surrounding neural tissue (106).

Experimental autoimmune encephalomyelitis

Experimental autoimmune encephalomyelitis (EAE) is often used as a model for human multiple sclerosis (MS) and to study autoreactive immune cell traffic into the CNS (107). Because a detailed summary of MS literature is beyond the scope of this review, the reader should refer to other excellent reviews on this topic (108, 109). EAE is usually induced by triggering an autoreactive T cell response against myelin, either through myelin peptide immunization or through adoptive transfer of myelin-reactive T cells. Similar to steady state, the process of diapedesis during CNS autoimmune disease involves T cell interactions with endothelial selectins through P-selectin glycoprotein ligand-1 (PSGL-1), although the requirement for selectins is not absolute. This results in T cell rolling and eventual arrest mediated by LFA-1-ICAM-1 and VLA-4-VCAM-1 interactions (Fig. 4), as observed by using the proteolipid protein (PLP139-151) immunization model of EAE (110). Activated leukocyte cell adhesion molecule (CD166) can also foster diapedesis of monocytes and, to a lesser extent, CD4 T cells during EAE (111, 112). In addition to adhesion molecules, T cell arrest is often linked to G protein signaling in vessels (110), which is facilitated by chemokines such as CCL19 and CCL21 that are produced by vascular endothelial cells (113). CXCL12 expression is elevated during EAE as well and is not confined to the abluminal surface of blood vessels (114). Using the myelin oligodendrocyte glycoprotein (MOG35-55) immunization model of EAE, it was shown that CXCR7 expression on the abluminal side of endothelial cells binds CXCL12, limiting the ability of this chemokine to trap leukocytes in the perivascular space, as it does during steady state (Fig. 4) (115).

The process of T cell diapedesis across CNS blood vessels involves firm attachment to endothelial cells (dependent on ICAM-1, ICAM-2, and VCAM-1) to resist the shear forces of vascular flow. This then allows LFA-1-dependent T cell crawling against blood flow until a location permissive to diapedesis is found (116). Prolonged T cell crawling before diapedesis is thought to depend on the properties of CNS vascular endothelial cells because the process is more rapid with peripheral endothelial cells (117). Early CD4⁺ T cell extravasation was observed primarily through leptomeningeal vasculature in the Lewis rat model of EAE (66) as well as the choroid plexus in the MOG35-55 model (118) and, to a less extent, postcapillary venules in the CNS parenchyma. Upon extravasation, the autoreactive T cells interact with peptide-major histocompatibility complex (MHC) II-bearing APCs (such as DCs) in the perivascular spaces, triggering up-regulation of chemokines that recruit myeloid cells and release of TNFα that increases production of metalloproteinases MMP-2 and MMP-9 by resident and recruited myeloid cells (Fig. 4) (65, 67, 84, 119, 120). The metalloproteinases selectively cleave dystroglycan, which tethers astrocytic foot processes to the basement membrane (Fig. 3), allowing penetration of effector T cells and myeloid cells into the CNS parenchyma in the MOG35-55 EAE model (121). This is a rate-limiting step for the initiation of EAE and the eventual destruction of parenchyma white matter. In the choroid plexus, encephalitogenic CD4⁺ T cells enter the CSF in a CCR6-dependent manner, which is likely linked to expression of the chemoattractant CCL20 produced by choroid plexus epithelial cells (118). After entering the CSF through the choroid plexus, CD4⁺ T cells accumulate in leptomeningeal spaces, suggesting that the choroid plexus might be one of the earliest CNS entry points for autoreactive T cells during the development of EAE (118). Another adhesion molecule that can facilitate the accumulation of autoreactive T cells in the CNS during

MOG35-55 EAE is melanoma cell adhesion molecule (MCAM) (122, 123). MCAM⁺ effector T cells migrate more efficiently across the BBB than their MCAM-negative counterparts and appear to do so through homotypic binding with MCAM expressed on vascular endothelial cells (123) and through interactions with laminin-411 (124). Injection of anti-MCAM antibodies into mice also reduces the severity of EAE, demonstrating the importance of this adhesion molecule in disease pathogenesis (122, 123).

Traumatic cerebrovascular injury

Traumatic cerebrovascular injury is an important aspect of traumatic brain injury (TBI) and contributes to a subsequent inflammatory response. TBI can disrupt vascular integrity in the meninges and brain parenchyma, resulting in leakage of materials from the blood supply into CNS (Fig. 4) (125–127). In fact, ultrastructural studies in primates have revealed substantial cerebrovascular disruption, with widening of intercellular junctions between endothelial cells and swelling of perivascular astrocytes (128). The duration of the leakage varies from patient to patient and can extend for months or even years after the initial injury. In animal models of TBI, reduced microvascular densities were observed in the brain within a day of injury, although the density returned to normal within 2 weeks, suggesting engagement of vascular repair mechanisms (129). Vascular repair was also observed in the meninges after TBI and was dependent on the recruitment of nonclassical monocytes from the blood (127). Thus, it is possible to repair CNS vasculature after TBI; however, it is unclear whether the anatomy is ever completely restored to its original configuration.

TBI and the associated CNS vascular damage is a type of sterile injury [recently reviewed in (130)]. A great deal is known about sterile injuries; they involve release of alarmins detected by damage-associated molecular pattern (DAMP) sensors such as Toll-like and purinergic receptors (131). This, in turn, triggers a rapid inflammatory response characterized by inflammasome assembly, nuclear factor- κ B signaling, resident immune cell activation, cytokine and chemokine production (such as IL-6, TNF α , CXCL1, CXCL2, and CCL2), and recruitment of peripheral myelomonocytic cells, among others (Fig. 4) (130). TLR4 is up-regulated after TBI and recognizes LPSs and endogenous proteins, such as high-mobility group box 1 protein, heat shock proteins, and low-density lipoprotein (132). Purinergic receptors also play an important role in TBI by detecting adenosine 5'-triphosphate (ATP) and uridine 5'-diphosphate, which are released after tissue damage (133).

The speed of this reaction is crucial for the maintenance of CNS barriers, including the glia limitans and cerebrovasculature. For example, damage to the glia limitans superficialis after TBI results in a profound morphological transformation of the underlying microglia that depends on ATP release by surface-associated astrocytes and subsequent detection by microglial purinergic receptors (126). Real-time imaging studies revealed that microglia transform into honeycomb- and jellyfish-like morphologies that provide barrier support and debris clearance (126). In the absence of this transformation, the glia limitans leaked profoundly. Similar findings were made in a laser-induced model of focal BBB breakdown. In this model, focal cerebrovascular damage resulted in a rapid, purinergic receptor-dependent projection of microglia processes that walled off the damaged vessel, limiting the extent of BBB leakage (134). These findings demonstrate that the immune system has quick-response elements in place to deal with acute brain trauma and restore CNS barriers.

Cerebral ischemia

Ischemic stroke results from permanent or transient reduction in regional cerebral blood flow. A commonly used animal model involves occlusion of the middle cerebral artery (MCAO) (135). Neurons are especially susceptible to ischemia and the reperfusion injury that often follows an ischemic stroke. The acute phase after ischemia is characterized by the rapid-release DAMPs, which are sensed by endothelial cells as well as resident and circulating immune cells. Resident macrophages and invading myelomonocytic cells release cytokines (such as TNF α and IL-1 β), chemokines, reactive oxygen species (ROS), neutrophil extracellular traps (NETs), and MMP-9, which lead to further disruption of the BBB, brain edema, neuronal death, and hemorrhagic transformation (Fig. 4) (136).

Neutrophils are among the first peripheral immunes recruited to the brain after an ischemic-reperfusion event and are thought to contribute to the injury in at least some brain regions (137). The process of neutrophil recruitment in most peripheral tissues involves engagement of E- and P-selectins through PSGL-1. Inflammatory cytokines such as TNF α and IL-1 β promote cell-surface translocation of P-selectin from intracellular storage in the Weibel-Palade bodies as well as expression of E-selectin, ICAM-1, and VCAM-1 on the surface of endothelial cells (138). Engagement of selectins by neutrophils allow them to slow down and detect chemoattractants (such as CXCL1 and CXCL2) bound to endothelial cells by CXCR2, which subsequently triggers activation of LFA-1 and macrophage-1 antigen (Mac-1) (139). LFA-1 interaction with ICAM-1 results in neutrophil arrest and Mac-1-facilitated neutrophil diapedesis. Paracellular diapedesis is mediated by platelet endothelial cell adhesion molecule-1, CD99, and junctional adhesion molecule-A (JAM-A) (140). After extravasation, neutrophils are programmed to eradicate pathogens by means of release of free radicals and NETs (141).

In contrast to most peripheral vasculature, blood vessels in the CNS parenchyma lack P-selectin in Weibel-Palade bodies and only express low levels of this protein under steady state (79). In fact, constitutive expression of P-selectin is only present in meningeal vessels. Although expression of P-selectin can be up-regulated in meningeal and parenchymal vessels during inflammation, the delayed availability of this protein in the CNS leads to slower leukocyte recruitment kinetics when compared with the periphery. After cerebral ischemia or subarachnoid hemorrhage, neutrophils rapidly accumulate in the leptomeningeal space (142). However, these cells become confined by the astrocytic basement membrane and glia limitans to the perivascular space (143, 144).

Neutrophil extravasation into the brain parenchyma after ischemia is dependent on MMP activity (145). Astrocytes secrete MMP-2 from their endfeet, and pro-MMP-9 and pro-MMP-3 are produced by endothelial cells, microglia, and pericytes. Up-regulation of hypoxia-inducible factor-1 α after hypoxia leads to furin production, which activates MMP-14 that, in turn, activates MMP-2. In addition, TNF α and IL-1 β induce expression of pro-MMP-9 and pro-MMP-3, and the latter is responsible for activating MMP-9. This combination of inflammatory events leads to tight junction and glia limitans degradation as well as leukocyte infiltration of the brain parenchyma and vasogenic edema (Fig. 4) (145). Pro-inflammatory monocytes eventually follow neutrophils into the brain parenchyma and enter in a CCR2-dependent manner, eventually differentiating into Ly6C^{low} phagocytes. However, depletion of these cells has a negative impact on stroke outcome and increases the incidence of hemorrhagic transformation (146). To date, a number of preclinical and clinical trials

have failed to improve ischemic stroke outcomes or lesion size by preventing leukocyte diapedesis (142, 147), indicating that our knowledge of the inflammatory response to this condition is incomplete.

Infection

Differences in the anatomy of CNS vasculature affect the tropism and pathophysiology of infectious diseases. Pathogens can more easily enter the CNS through fenestrated blood vessels that lack tight junctions, such as those residing in the dura mater, choroid plexus, and CVOs (Fig. 1) (148). Subpial and parenchymal vascular endothelial cells have tight junctions and low pinocytotic activity that greatly restrict the access of pathogens to CNS tissue. Even if pathogens do enter the dura mater, choroid plexus, or CVOs, they must still traverse tight junction–expressing barriers such as the arachnoid mater, choroid plexus ependyma, and tanycytes, respectively. Moreover, once within the CSF, drainage of antigenic material to peripheral lymph nodes is a crucial component of the CNS defense against invading microbes.

Although one way to traverse CNS barriers is to infect the cells that comprise them, another strategy is to alter barrier integrity. For example, group B streptococcus, a microbe that causes bacterial meningitis, promotes expression of a transcriptional repressor (Snail1) in CNS vascular endothelial cells, causing down-regulation of tight junction proteins (occluding, ZO-1, and claudin-5) and a loss of barrier integrity (149). This type of mechanism enables microbes to more easily invade the CNS. Inflammatory cytokines released in the defense against microbes can also modulate CNS barrier integrity. During West Nile virus (WNV) infection, type I and type III interferon signaling promotes tightening of the BBB in CNS vascular endothelial cells, restricting virus from accessing the CNS (150, 151). At least for type I interferon, BBB tightening is mediated by activation of small GTPases, Rac1 and RhoA, which counterbalance endothelial cells against the barrier-opening effects of cytokines such as TNF α and IL-1 β (150). Endothelial TAM receptors also have barrier-sealing properties in the context of viral infection. TAM receptors (Tyro3, Axl, and Mertk) are immune-dampening tyrosine kinases that recognize ligands (Gas6 and protein S) that bind to phosphatidylserine on apoptotic cells. Enveloped viruses sometimes incorporate phosphatidylserine into their outer membrane. Detection of this ligand by the TAM receptor Mertk in CNS vascular endothelial cells results in barrier tightening because of synergy with type I interferon signaling (152). Deficiency in this receptor renders the CNS more susceptible to infection by neuroinvasive viruses such as La Crosse encephalitis virus and WNV.

Unless a pathogen is injected directly into the CNS parenchyma (56), infection typically results in a rapid recruitment of peripheral blood leukocytes, especially to the dura mater, leptomeninges, and choroid plexus. After coronavirus infection, endothelial and fibroblastic reticular cells in the meninges release CCL19 and CCL21 to recruit and reactivate antiviral CCR7 $^+$ CD8 $^+$ T cells (153). Timely recruitment of these T cells is required to prevent fatal CNS disease after infection with this virus. Although infiltrating leukocytes are usually necessary in the fight against microbes, these cells can sometimes cause great harm to CNS barriers. For example, infection of the meninges with a noncytopathic pathogen such as lymphocytic choriomeningitis (LCMV) causes fatal meningitis (154). During this disease, recruited CD8 $^+$ T cells and myelomonocytic cells damage meningeal vasculature and the walls of the ventricular system, causing severe edema and brainstem herniation (154, 155). Similar damage to

meningeal and parenchymal vasculature is observed during cerebral malaria. This potentially fatal disease is initiated by infection with *Plasmodium falciparum* in humans and *Plasmodium berghei* ANKA in rodents. Similar to LCMV meningitis, death from cerebral malaria results from the accumulation of water in the cranium and brain-stem herniation (156, 157). In rodents, it was revealed that BBB breakdown and fatal edema are caused by parasite-specific CD8 $^+$ T cell engagement of cerebrovascular endothelial cells that cross-present parasite antigen (157, 158). Displacement of these T cells from CNS vasculature by means of therapeutic administration of antibodies to LFA-1 and VLA-4 prevented the disease (157). Collectively, these findings demonstrate that the inflammatory response to pathogens has the potential to tighten and harm CNS barriers depending on the context.

CONCLUSIONS

CNS vasculature serves as the entry point for peripheral immune cells, and their entry is influenced by structural variations in the barriers surrounding blood vessels. The CNS parenchyma contains a highly fortified barrier system (the BBB) and is consequently very selective when it comes to peripheral immune cell entry. In general, peripheral immune cells do not enter the CNS parenchyma during steady state. However, they can traverse the BBB during pathophysiological conditions (such as autoimmune disease, injury, stroke, or infection) but only after acquiring the ability to move from the perivascular space across the glia limitans. The glia limitans serves as a barrier to peripheral immune cells and can be disrupted mechanically (such as injury) or enzymatically (such as metalloproteinases). Both allow peripheral immune cells to enter the parenchyma. The meninges are generally more supportive of peripheral immune traffic than the CNS parenchyma and serve as the initiation site for many CNS immune responses that involve peripheral immune cells. Blood vessels beneath the arachnoid mater have tight junctions and are more secure than those in the meningeal layer above (the dura mater). In fact, the dura mater, with its fenestrated blood vessels and lymphatic drainage, in many ways resembles a peripheral tissue. The choroid plexus and CVOs also contain fenestrated blood vessels that lack tight junctions and are supportive of peripheral immune cell traffic. These vascular beds are walled off from the CNS by specialized epithelial cells and/or astrocytes. Similarly, the arachnoid mater keeps the dura mater separate from the underlying subarachnoid space, which contains CSF. All these barriers are composed of biological materials and are by no means absolute, but they do compartmentalize peripheral immune cells until the barriers are breached. It is essential that we acquire a more detailed understanding of the mechanisms that underlie the degradation and reassembly of blood-CNS barriers if we want to restore homeostasis in the CNS after injury, ischemia, autoimmune disease, and infection. Much emphasis over the years has been placed on the BBB; however, as discussed in this review, several other CNS barriers exist that require detailed studies as well. The blood-CNS interface is incredibly sophisticated and should be considered from the perspective of each anatomical subdivision for all CNS inflammatory diseases.

REFERENCES AND NOTES

1. B. Engelhardt, P. Vajkoczy, R. O. Weller, The movers and shapers in immune privilege of the CNS. *Nat. Immunol.* **18**, 123–131 (2017).
2. J. B. Murphy, E. Sturm, Conditions determining the transplantability of tissues in the brain. *J. Exp. Med.* **38**, 183–197 (1923).
3. I. Galea, I. Bechmann, V. H. Perry, What is immune privilege (not)? *Trends Immunol.* **28**, 12–18 (2007).

4. A. Louveau, I. Smirnov, T. J. Keyes, J. D. Eccles, S. J. Rouhani, J. D. Peske, N. C. Derecki, D. Castle, J. W. Mandell, K. S. Lee, T. H. Harris, J. Kipnis, Structural and functional features of central nervous system lymphatic vessels. *Nature* **523**, 337–341 (2015).
5. A. Apellund, S. Antila, S. T. Proulx, T. V. Karlson, S. Karaman, M. Detmar, H. Wiig, K. Alitalo, A dural lymphatic vascular system that drains brain interstitial fluid and macromolecules. *J. Exp. Med.* **212**, 991–999 (2015).
6. P. Mascagni, *Vasorum Lymphaticorum Corporis Humani Historia et Ichnographia* (P. Carli, 1787).
7. J. D. Waggener, J. Beggs, The membranous coverings of neural tissues: An electron microscopy study. *J. Neuropathol. Exp. Neurol.* **26**, 412–426 (1967).
8. K. H. Andres, M. von Düring, K. Muszynski, R. F. Schmidt, Nerve fibres and their terminals of the dura mater encephali of the rat. *Anat. Embryol.* **175**, 289–301 (1987).
9. Q. Ma, B. V. Ineichen, M. Detmar, S. T. Proulx, Outflow of cerebrospinal fluid is predominantly through lymphatic vessels and is reduced in aged mice. *Nat. Commun.* **8**, 1434 (2017).
10. M. A. Lopes Pinheiro, G. Kooij, M. R. Mizee, A. Kamermans, G. Enzmann, R. Lyck, M. Schwaninger, B. Engelhardt, H. E. de Vries, Immune cell trafficking across the barriers of the central nervous system in multiple sclerosis and stroke. *Biochim. Biophys. Acta* **1862**, 461–471 (2016).
11. J. R. Youmans, *Neurological Surgery: A Comprehensive Reference Guide to the Diagnosis and Management of Neurosurgical Problems* (Saunders, ed. 3, 1990).
12. E. G. Jones, On the mode of entry of blood vessels into the cerebral cortex. *J. Anat.* **106**, 507–520 (1970).
13. A. W. J. Morris, M. MacGregor Sharp, N. J. Albargothy, R. Fernandes, C. A. Hawkes, A. Verma, R. O. Weller, R. O. Carare, Vascular basement membranes as pathways for the passage of fluid into and out of the brain. *Acta Neuropathol.* **131**, 725–736 (2016).
14. T. Ichimura, P. A. Fraser, H. F. Cserr, Distribution of extracellular tracers in perivascular spaces of the rat brain. *Brain Res.* **545**, 103–113 (1991).
15. E. T. Zhang, C. B. Inman, R. O. Weller, Interrelationships of the pia mater and the perivascular (Virchow-Robin) spaces in the human cerebrum. *J. Anat.* **170**, 111–123 (1990).
16. R. Alcolado, R. O. Weller, E. P. Parrish, D. Garrod, The cranial arachnoid and pia mater in man: Anatomical and ultrastructural observations. *Neuropathol. Appl. Neurobiol.* **14**, 1–17 (1988).
17. Y. Oda, I. Nakanishi, Ultrastructure of the mouse leptomeninx. *J. Comp. Neurol.* **225**, 448–457 (1984).
18. M.-J. Hitchens, M. E. Pizzo, J. Huppert, T. Deshpande, N. J. Abbott, R. G. Thorne, L. Sorokin, Molecular characterization of perivascular drainage pathways in the murine brain. *J. Cereb. Blood Flow Metab.* **38**, 669–686 (2018).
19. R. O. Weller, Microscopic morphology and histology of the human meninges. *Morphologie* **89**, 22–34 (2005).
20. M. Hutchings, R. O. Weller, Anatomical relationships of the pia mater to cerebral blood vessels in man. *J. Neurosurg.* **65**, 316–325 (1986).
21. P. Bhogal, H. L. D. Makalanda, P. A. Brouwer, V. Gontu, G. Rodesch, P. Mercier, M. Söderman, Normal pio-dural arterial connections. *Interv. Neuroradiol.* **21**, 750–758 (2015).
22. J. Roland, C. Bernard, S. Bracard, A. Czorny, J. Floquet, J. M. Race, P. Forlодou, L. Picard, Microvascularization of the intracranial dura mater. *Surg. Radiol. Anat.* **9**, 43–49 (1987).
23. R. F. Spetzler, M. Y. S. Kalani, P. Nakaji, *Neurovascular Surgery* (Thieme, 2015).
24. M. M. Mortazavi, R. S. Tubbs, S. Riech, K. Verma, M. M. Shojai, A. Zurada, B. Benninger, M. Loukas, A. A. Cohen Gadol, Anatomy and pathology of the cranial emissary veins: A review with surgical implications. *Neurosurgery* **70**, 1312–1318; discussion 1318–1319 (2012).
25. S. Morita, E. Furube, T. Mannari, H. Okuda, K. Tatsumi, A. Wanaka, S. Miyata, Heterogeneous vascular permeability and alternative diffusion barrier in sensory circumventricular organs of adult mouse brain. *Cell Tissue Res.* **363**, 497–511 (2016).
26. C. Kaur, G. Rathnasamy, E.-A. Ling, The choroid plexus in healthy and diseased brain. *J. Neuropathol. Exp. Neurol.* **75**, 198–213 (2016).
27. M. Vanlandewijck, L. He, M. A. Mäe, J. Andrae, K. Ando, F. Del Gaudio, K. Nahar, T. Lebouvier, B. Laviña, L. Gouveia, Y. Sun, E. Raschperger, M. Räsänen, Y. Zarb, N. Mochizuki, A. Keller, U. Lendahl, C. Betsholtz, A molecular atlas of cell types and zonation in the brain vasculature. *Nature* **554**, 475–480 (2018).
28. M. Ehrlich, *Königthum und staatswesen der alten Hebräer: Nach biblischen und talmudischen quellen bearbeitet* (Gedruckt bei J. v. Bertalanffy, Steinamanger, 1885).
29. H. Obersteiner, Ueber einige Lymphräume im Gehirn. *wien.acad. Sitzungsber. LXI. 1. Abthl.* (1870).
30. N. J. Abbott, L. Rönnbäck, E. Hansson, Astrocyte-endothelial interactions at the blood-brain barrier. *Nat. Rev. Neurosci.* **7**, 41–53 (2006).
31. S. Tietz, B. Engelhardt, Brain barriers: Crosstalk between complex tight junctions and adherens junctions. *J. Cell Biol.* **209**, 493–506 (2015).
32. S. M. Stamatovic, R. F. Keep, S. L. Kunkel, A. V. Andjelkovic, Potential role of MCP-1 in endothelial cell tight junction ‘opening’: Signaling via Rho and Rho kinase. *J. Cell Sci.* **116**, 4615–4628 (2003).
33. G. J. del Zoppo, R. Milner, Integrin-matrix interactions in the cerebral microvasculature. *Arterioscler. Thromb. Vasc. Biol.* **26**, 1966–1975 (2006).
34. G. Allt, J. G. Lawrenson, Pericytes: Cell biology and pathology. *Cells Tissues Organs* **169**, 1–11 (2001).
35. M. W. Brightman, The brain’s interstitial clefts and their glial walls. *J. Neurocytol.* **31**, 595–603 (2002).
36. M. E. Pizzo, D. J. Wolak, N. N. Kumar, E. Brunette, C. L. Bruniquell, M.-J. Hitchens, N. J. Abbott, M. E. Meyerand, L. Sorokin, D. B. Stanimirovic, R. G. Thorne, Intrathecal antibody distribution in the rat brain: Surface diffusion, perivascular transport and osmotic enhancement of delivery. *J. Physiol.* **596**, 445–475 (2018).
37. R. V. Krstić, *Die Gewebe des Menschen und der Säugetiere: ein Atlas zum Studium für Mediziner und Biologen* (Springer-Verlag, ed. 2, korrigierter Nachdruck der 1. Aufl., 1984).
38. K. Kacem, P. Lacombe, J. Seylaz, G. Bonvento, Structural organization of the perivascular astrocyte endfeet and their relationship with the endothelial glucose transporter: A confocal microscopy study. *Glia* **23**, 1–10 (1998).
39. B. Bedussi, M. G. J. T. B. van Lier, J. W. Bartstra, J. de Vos, M. Siebes, E. VanBavel, E. N. T. Bakker, Clearance from the mouse brain by convection of interstitial fluid towards the ventricular system. *Fluids Barriers CNS* **12**, 23 (2015).
40. J. J. Iliff, M. Wang, Y. Liao, B. A. Plogg, W. Peng, G. A. Gundersen, H. Benveniste, G. E. Vates, R. Deane, S. A. Goldman, E. A. Nagelhus, M. Nedergaard, A paravascular pathway facilitates CSF flow through the brain parenchyma and the clearance of interstitial solutes, including amyloid β. *Sci. Transl. Med.* **4**, 147ra111 (2012).
41. N. Korogod, C. C. H. Petersen, G. W. Knott, Ultrastructural analysis of adult mouse neocortex comparing aldehyde perfusion with cryo fixation. *eLife* **4**, e05793 (2015).
42. S. Horng, A. Therattil, S. Moyon, A. Gordon, K. Kim, A. T. Argaw, Y. Hara, J. N. Mariani, S. Sawai, P. Flodby, E. D. Crandall, Z. Borok, M. V. Sofroniew, C. Chapouly, G. R. John, Astrocytic tight junctions control inflammatory CNS lesion pathogenesis. *J. Clin. Invest.* **127**, 3136–3151 (2017).
43. N. J. Abbott, Astrocyte-endothelial interactions and blood-brain barrier permeability. *J. Anat.* **200**, 629–638 (2002).
44. W. Zhang, C. Smith, C. Howlett, D. Stanimirovic, Inflammatory activation of human brain endothelial cells by hypoxic astrocytes in vitro is mediated by IL-1β. *J. Cereb. Blood Flow Metab.* **20**, 967–978 (2000).
45. L. T. Lau, A. C.-H. Yu, Astrocytes produce and release interleukin-1, interleukin-6, tumor necrosis factor alpha and interferon-gamma following traumatic and metabolic injury. *J. Neurotrauma* **18**, 351–359 (2001).
46. Y. Chen, R. M. McCarron, N. Azzam, J. Bembry, C. Reutzel, F. A. Lenz, M. Spatz, Endothelin-1 and nitric oxide affect human cerebromicrovascular endothelial responses and signal transduction. *Acta Neurochir. Suppl.* **76**, 131–135 (2000).
47. I. Y. Chung, E. N. Benveniste, Tumor necrosis factor-alpha production by astrocytes. Induction by lipopolysaccharide, IFN-gamma, and IL-1 beta. *J. Immunol.* **144**, 2999–3007 (1990).
48. B. J. Balin, R. D. Broadwell, M. Salzman, M. El-Kalliny, Avenues for entry of peripherally administered protein to the central nervous system in mouse, rat, and squirrel monkey. *J. Comp. Neurol.* **251**, 260–280 (1986).
49. K. Yasuda, C. Cline, P. Vogel, M. Onciu, S. Fatima, B. P. Sorrentino, R. K. Thirumaran, S. Ekins, Y. Urade, K. Fujimori, E. G. Schuetz, Drug transporters on arachnoid barrier cells contribute to the blood-cerebrospinal fluid barrier. *Drug Metab. Dispos.* **41**, 923–931 (2013).
50. J. P. Cassella, J. G. Lawrenson, J. A. Firth, Development of endothelial paracellular clefts and their tight junctions in the pial microvessels of the rat. *J. Neurocytol.* **26**, 567–575 (1997).
51. S. Nag, Pathophysiology of blood-brain barrier breakdown. *Methods Mol. Med.* **89**, 97–119 (2003).
52. H. F. Cserr, M. Bundgaard, Blood-brain interfaces in vertebrates: A comparative approach. *Am. J. Physiol.* **246**, R277–R288 (1984).
53. H. Wolburg, K. Wolburg-Buchholz, S. Liebner, B. Engelhardt, Claudin-1, claudin-2 and claudin-11 are present in tight junctions of choroid plexus epithelium of the mouse. *Neurosci. Lett.* **307**, 77–80 (2001).
54. P. Ciolfi, M. Garret, O. Lapirot, P. Lafon, A. Loyens, V. Prévot, J. E. Levine, Brain-endocrine interactions: A microvascular route in the mediobasal hypothalamus. *Endocrinology* **150**, 5509–5519 (2009).
55. F. Langlet, A. Mullier, S. G. Bouret, V. Prevot, B. Dehouck, Tanyocyte-like cells form a blood-cerebrospinal fluid barrier in the circumventricular organs of the mouse brain. *J. Comp. Neurol.* **521**, 3389–3405 (2013).
56. P. G. Stevenson, S. Hawke, D. J. Sloan, C. R. Bangham, The immunogenicity of intracerebral virus infection depends on anatomical site. *J. Virol.* **71**, 145–151 (1997).
57. I. Szentivanyi, C. S. Patlak, R. A. Ellis, H. F. Cserr, Drainage of interstitial fluid from different regions of rat brain. *Am. J. Physiol.* **246**, F835–F844 (1984).
58. N. J. Abbott, M. E. Pizzo, J. E. Preston, D. Janigro, R. G. Thorne, The role of brain barriers in fluid movement in the CNS: Is there a ‘glymphatic’ system? *Acta Neuropathol.* **135**, 387–407 (2018).

59. A. J. Smith, X. Yao, J. A. Dix, B.-J. Jin, A. S. Verkman, Test of the 'glymphatic' hypothesis demonstrates diffusive and aquaporin-4-independent solute transport in rodent brain parenchyma. *eLife* **6**, e27679 (2017).
60. R. O. Carare, J. L. Teeling, C. A. Hawkes, U. Püntener, R. O. Weller, J. A. R. Nicoll, V. H. Perry, Immune complex formation impairs the elimination of solutes from the brain: Implications for immunotherapy in Alzheimer's disease. *Acta Neuropathol. Commun.* **1**, 48 (2013).
61. R. O. Carare, M. Bernardes-Silva, T. A. Newman, A. M. Page, J. A. R. Nicoll, V. H. Perry, R. O. Weller, Solutes, but not cells, drain from the brain parenchyma along basement membranes of capillaries and arteries: Significance for cerebral amyloid angiopathy and neuroimmunology. *Neuropathol. Appl. Neurobiol.* **34**, 131–144 (2008).
62. M. K. Matyszak, V. H. Perry, *Bacillus Calmette-Guérin* sequestered in the brain parenchyma escapes immune recognition. *J. Neuroimmunol.* **82**, 73–80 (1998).
63. S. Kida, A. Pantazis, R. O. Weller, CSF drains directly from the subarachnoid space into nasal lymphatics in the rat: Anatomy, histology and immunological significance. *Neuropathol. Appl. Neurobiol.* **19**, 480–488 (1993).
64. A. Louveau, J. Herz, M. N. Alme, A. F. Salvador, M. Q. Dong, K. E. Viar, S. G. Herod, J. Knopp, J. C. Setliff, A. L. Lupi, S. Da Mesquita, E. L. Frost, A. Gaultier, T. H. Harris, R. Cao, S. Hu, J. R. Lukens, I. Smirnov, C. C. Overall, G. Oliver, J. Kipnis, CNS lymphatic drainage and neuroinflammation are regulated by meningeal lymphatic vasculature. *Nat. Neurosci.* **21**, 1380–1391 (2018).
65. M. Greter, F. L. Heppner, M. P. Lemos, B. M. Odermatt, N. Goebels, T. Laufer, R. J. Noelle, B. Becher, Dendritic cells permit immune invasion of the CNS in an animal model of multiple sclerosis. *Nat. Med.* **11**, 328–334 (2005).
66. I. Bartholomäus, N. Kawakami, F. Odoardi, C. Schläger, D. Miljkovic, J. W. Ellwart, W. E. F. Klinkert, C. Flügel-Koch, T. B. Issekutz, H. Wekerle, A. Flügel, Effector T cell interactions with meningeal vascular structures in nascent autoimmune CNS lesions. *Nature* **462**, 94–98 (2009).
67. S. Mundt, D. Mrdjen, S. G. Utz, M. Greter, B. Schreiner, B. Becher, Conventional DCs sample and present myelin antigens in the healthy CNS and allow parenchymal T cell entry to initiate neuroinflammation. *Sci. Immunol.* **4**, eaau8380 (2019).
68. D. Nayak, B. H. Zinselmeyer, K. N. Corps, D. B. McGavern, In vivo dynamics of innate immune sentinels in the CNS. *Intravital* **1**, 95–106 (2012).
69. N. Anandasabapathy, G. D. Victora, M. Meredith, R. Feder, B. Dong, C. Kluger, K. Yao, M. L. Dustin, M. C. Nussenzweig, R. M. Steinman, K. Liu, Flt3L controls the development of radiosensitive dendritic cells in the meninges and choroid plexus of the steady-state mouse brain. *J. Exp. Med.* **208**, 1695–1705 (2011).
70. H. Lauterbach, E. I. Zuniga, P. Truong, M. B. A. Oldstone, D. B. McGavern, Adoptive immunotherapy induces CNS dendritic cell recruitment and antigen presentation during clearance of a persistent viral infection. *J. Exp. Med.* **203**, 1963–1975 (2006).
71. T. Goldmann, P. Wieghofer, M. J. Costa Jordão, F. Prutek, N. Hagemeyer, K. Frenzel, L. Amann, O. Staszewski, K. Kierdorf, M. Krueger, G. Locatelli, H. Hochgerner, R. Zeiser, S. Epelman, F. Geissmann, J. Priller, F. M. V. Rossi, I. Bechmann, M. Kerschensteiner, S. Linnarsson, S. Jung, M. Prinz, Origin, fate and dynamics of macrophages at central nervous system interfaces. *Nat. Immunol.* **17**, 797–805 (2016).
72. R. Rua, J. Y. Lee, A. B. Silva, I. S. Swafford, D. Maric, K. R. Johnson, D. B. McGavern, Infection drives meningeal engraftment by inflammatory monocytes that impairs CNS immunity. *Nat. Immunol.* **20**, 407–419 (2019).
73. H. Van Hove, L. Martens, I. Scheijtjens, K. De Vlaminck, A. R. Pombo Antunes, S. De Prijck, N. Vandamme, S. De Schepper, G. Van Isterdael, C. L. Scott, J. Aerts, G. Berx, G. E. Boeckxstaens, R. E. Vandenbroucke, L. Vereecke, D. Moechars, M. Guillemins, J. A. Van Ginderachter, Y. Saeyns, K. Movahedi, A single-cell atlas of mouse brain macrophages reveals unique transcriptional identities shaped by ontogeny and tissue environment. *Nat. Neurosci.* **22**, 1021–1035 (2019).
74. G. Kunis, K. Baruch, N. Rosenzweig, A. Kertser, O. Miller, T. Berkutzki, M. Schwartz, IFN- γ -dependent activation of the brain's choroid plexus for CNS immune surveillance and repair. *Brain* **136**, 3427–3440 (2013).
75. K. Baruch, M. Schwartz, CNS-specific T cells shape brain function via the choroid plexus. *Brain Behav. Immun.* **34**, 11–16 (2013).
76. C. S. Raine, B. Cannella, A. M. Duijvestijn, A. H. Cross, Horning to central nervous system vasculature by antigen-specific lymphocytes. II. Lymphocyte/endothelial cell adhesion during the initial stages of autoimmune demyelination. *Lab. Invest.* **63**, 476–489 (1990).
77. H. Wolburg, K. Wolburg-Buchholz, B. Engelhardt, Diapedesis of mononuclear cells across cerebral venules during experimental autoimmune encephalomyelitis leaves tight junctions intact. *Acta Neuropathol.* **109**, 181–190 (2005).
78. T. Owens, I. Bechmann, B. Engelhardt, Perivascular spaces and the two steps to neuroinflammation. *J. Neuropathol. Exp. Neurol.* **67**, 1113–1121 (2008).
79. F. J. Barkalow, M. J. Goodman, M. E. Gerritsen, T. N. Mayadas, Brain endothelium lack one of two pathways of P-selectin-mediated neutrophil adhesion. *Blood* **88**, 4585–4593 (1996).
80. B. Engelhardt, R. M. Ransohoff, Capture, crawl, cross: The T cell code to breach the blood-brain barriers. *Trends Immunol.* **33**, 579–589 (2012).
81. P. Vajkoczy, M. Laschinger, B. Engelhardt, Alpha4-integrin-VCAM-1 binding mediates G protein-independent capture of encephalitogenic T cell blasts to CNS white matter microvessels. *J. Clin. Invest.* **108**, 557–565 (2001).
82. N. Kawakami, U. V. Nägerl, F. Odoardi, T. Bonhoeffer, H. Wekerle, A. Flügel, Live imaging of effector cell trafficking and autoantigen recognition within the unfolding autoimmune encephalomyelitis lesion. *J. Exp. Med.* **201**, 1805–1814 (2005).
83. E. E. McCandless, Q. Wang, B. M. Woerner, J. M. Harper, R. S. Klein, CXCL12 limits inflammation by localizing mononuclear infiltrates to the perivascular space during experimental autoimmune encephalomyelitis. *J. Immunol.* **177**, 8053–8064 (2006).
84. D. Lodygin, F. Odoardi, C. Schläger, H. Körner, A. Kitz, M. Nosov, J. van den Brandt, H. M. Reichardt, M. Haberl, A. Flügel, A combination of fluorescent NFAT and H2B sensors uncovers dynamics of T cell activation in real time during CNS autoimmunity. *Nat. Med.* **19**, 784–790 (2013).
85. T. A. Youss, E. O. Major, C. Ryschkewitsch, G. Fahle, S. Fischer, J. Hou, B. Curfman, K. Miszkiel, N. Mueller-Lenke, E. Sanchez, F. Barkhof, E.-W. Radue, H. R. Jäger, D. B. Clifford, Evaluation of patients treated with natalizumab for progressive multifocal leukoencephalopathy. *N. Engl. J. Med.* **354**, 924–933 (2006).
86. M. D. Carrithers, I. Visintin, S. J. Kang, C. A. Janeway Jr., Differential adhesion molecule requirements for immune surveillance and inflammatory recruitment. *Brain* **123** (Pt. 6), 1092–1101 (2000).
87. S. Buonamici, T. Trimarchi, M. G. Ruocco, L. Reavie, S. Cathelin, B. G. Mar, A. Klinakis, Y. Lukyanov, J.-C. Tseng, F. Sen, E. Gehrie, M. Li, E. Newcomb, J. Zavadil, D. Meruelo, M. Lipp, S. Ibrahim, A. Efstratiadis, D. Zagzag, J. S. Bromberg, M. L. Dustin, I. Aifantis, CCR7 signalling as an essential regulator of CNS infiltration in T-cell leukaemia. *Nature* **459**, 1000–1004 (2009).
88. K. Baruch, A. Deczkowska, E. David, J. M. Castellano, O. Miller, A. Kertser, T. Berkutzki, Z. Barnett-Itzhaki, D. Bezalel, T. Wyss-Coray, I. Amit, M. Schwartz, Aging-induced type I interferon response at the choroid plexus negatively affects brain function. *Science* **346**, 89–93 (2014).
89. A. Deczkowska, K. Baruch, M. Schwartz, Type I/II interferon balance in the regulation of brain physiology and pathology. *Trends Immunol.* **37**, 181–192 (2016).
90. K. Wolburg, H. Gerhardt, M. Schulz, H. Wolburg, B. Engelhardt, Ultrastructural localization of adhesion molecules in the healthy and inflamed choroid plexus of the mouse. *Cell Tissue Res.* **296**, 259–269 (1999).
91. C. Loeffler, K. Dietz, A. Schleich, H. Schlaszus, M. Stoll, R. Meyermann, M. Mittelbronn, Immune surveillance of the normal human CNS takes place in dependence of the locoregional blood-brain barrier configuration and is mainly performed by CD3⁺/CD8⁺ lymphocytes. *Neuropathology* **31**, 230–238 (2011).
92. R. Rua, D. B. McGavern, Advances in meningeal immunity. *Trends Mol. Med.* **24**, 542–559 (2018).
93. A. Radjavi, I. Smirnov, N. Derecki, J. Kipnis, Dynamics of the meningeal CD4⁺ T-cell repertoire are defined by the cervical lymph nodes and facilitate cognitive task performance in mice. *Mol. Psych.* **19**, 531–533 (2014).
94. D. Mrdjen, A. Pavlovic, F. J. Hartmann, B. Schreiner, S. G. Utz, B. P. Leung, I. Lelios, F. L. Heppner, J. Kipnis, D. Merkler, M. Greter, B. Becher, High-dimensional single-cell mapping of central nervous system immune cells reveals distinct myeloid subsets in health, aging, and disease. *Immunity* **48**, 599 (2018).
95. F. Herisson, V. Frodermann, G. Courties, D. Rohde, Y. Sun, K. Vandoorne, G. R. Wojtkiewicz, G. S. Masson, C. Vinegoni, J. Kim, D.-E. Kim, R. Weissleder, F. K. Swirski, M. A. Moskowitz, M. Nahrendorf, Direct vascular channels connect skull bone marrow and the brain surface enabling myeloid cell migration. *Nat. Neurosci.* **21**, 1209–1217 (2018).
96. H. Yao, T. T. Price, G. Cantelli, B. Ngo, M. J. Warner, L. Olivere, S. M. Ridge, E. M. Jablonski, J. Therrien, S. Tannheimer, C. M. McCall, A. Chenn, D. A. Sipkins, Leukaemia hijacks a neural mechanism to invade the central nervous system. *Nature* **560**, 55–60 (2018).
97. S. Ching, H. Zhang, N. Belevych, L. He, W. Lai, X.-a. Pu, L. B. Jaeger, Q. Chen, N. Quan, Endothelial-specific knockdown of interleukin-1 (IL-1) type 1 receptor differentially alters CNS responses to IL-1 depending on its route of administration. *J. Neurosci.* **27**, 10476–10486 (2007).
98. W. A. Banks, Blood-brain barrier transport of cytokines: A mechanism for neuropathology. *Curr. Pharm. Des.* **11**, 973–984 (2005).
99. W. Pan, A. J. Kastin, TNF α transport across the blood-brain barrier is abolished in receptor knockout mice. *Exp. Neurol.* **174**, 193–200 (2002).
100. M. Lazarus, K. Yoshida, R. Coppari, C. E. Bass, T. Mochizuki, B. B. Lowell, C. B. Saper, EP3 prostaglandin receptors in the median preoptic nucleus are critical for fever responses. *Nat. Neurosci.* **10**, 1131–1133 (2007).
101. C. M. Blatteis, S. L. Bealer, W. S. Hunter, J.-Q. Lianos, R. A. Ahokas, T. A. Mashburn Jr., Suppression of fever after lesions of the anteroventral third ventricle in guinea pigs. *Brain Res. Bull.* **11**, 519–526 (1983).
102. S. Nadeau, S. Rivest, Regulation of the gene encoding tumor necrosis factor alpha (TNF- α) in the rat brain and pituitary in response to different models of systemic immune challenge. *J. Neuropathol. Exp. Neurol.* **58**, 61–77 (1999).
103. A. Ericsson, C. Liu, R. P. Hart, P. E. Sawchenko, Type 1 interleukin-1 receptor in the rat brain: Distribution, regulation, and relationship to sites of IL-1-induced cellular activation. *J. Comp. Neurol.* **361**, 681–698 (1995).

104. N. Laflamme, S. Rivest, Toll-like receptor 4: The missing link of the cerebral innate immune response triggered by circulating gram-negative bacterial cell wall components. *FASEB J.* **15**, 155–163 (2001).
105. S. Lacroix, D. Feinstein, S. Rivest, The bacterial endotoxin lipopolysaccharide has the ability to target the brain in upregulating its membrane CD14 receptor within specific cellular populations. *Brain Pathol.* **8**, 625–640 (1998).
106. G. Komaki, A. Arimura, K. Koves, Effect of intravenous injection of IL-1 beta on PGE2 levels in several brain areas as determined by microdialysis. *Am. J. Physiol.* **262**, E246–E251 (1992).
107. H. Lassmann, Models of multiple sclerosis: New insights into pathophysiology and repair. *Curr. Opin. Neurol.* **21**, 242–247 (2008).
108. C. A. Dendrou, L. Fugger, M. A. Friese, Immunopathology of multiple sclerosis. *Nat. Rev. Immunol.* **15**, 545–558 (2015).
109. D. S. Reich, C. F. Lucchinetti, P. A. Calabresi, Multiple sclerosis. *N. Engl. J. Med.* **378**, 169–180 (2018).
110. L. Piccio, B. Rossi, E. Scarpini, C. Laudanna, C. Giagulli, A. C. Issekutz, D. Vestweber, E. C. Butcher, G. Constantin, Molecular mechanisms involved in lymphocyte recruitment in inflamed brain microvessels: Critical roles for P-selectin glycoprotein ligand-1 and heterotrimeric G_i-linked receptors. *J. Immunol.* **168**, 1940–1949 (2002).
111. R. Lyck, M.-A. Lécuyer, M. Abadier, C. B. Wyss, C. Matti, M. Rosito, G. Enzmann, T. Zeis, L. Michel, A. B. García Martín, F. Sallusto, F. Gosselé, U. Deutsch, J. A. Weiner, N. Schaeren-Wiemers, A. Prat, B. Engelhardt, ALCAM (CD166) is involved in extravasation of monocytes rather than T cells across the blood-brain barrier. *J. Cereb. Blood Flow Metab.* **37**, 2894–2909 (2017).
112. R. Cayrol, K. Wosik, J. L. Berard, A. Dodelet-Devillers, I. Ifergan, H. Kebir, A. S. Haqqani, K. Kreymborg, S. Krug, R. Moudjian, A. Bouthillier, B. Becher, N. Arbour, S. David, D. Stanimirovic, A. Prat, Activated leukocyte cell adhesion molecule promotes leukocyte trafficking into the central nervous system. *Nat. Immunol.* **9**, 137–145 (2008).
113. C. Alt, M. Laschinger, B. Engelhardt, Functional expression of the lymphoid chemokines CCL19 (ELC) and CCL 21 (SLC) at the blood-brain barrier suggests their involvement in G-protein-dependent lymphocyte recruitment into the central nervous system during experimental autoimmune encephalomyelitis. *Eur. J. Immunol.* **32**, 2133–2144 (2002).
114. E. E. McCandless, L. Piccio, B. M. Woerner, R. E. Schmidt, J. B. Rubin, A. H. Cross, R. S. Klein, Pathological expression of CXCL12 at the blood-brain barrier correlates with severity of multiple sclerosis. *Am. J. Pathol.* **172**, 799–808 (2008).
115. L. Cruz-Orengo, D. W. Holman, D. Dorsey, L. Zhou, P. Zhang, M. Wright, E. E. McCandless, J. R. Patel, G. D. Luker, D. R. Littman, J. H. Russell, R. S. Klein, CXCR7 influences leukocyte entry into the CNS parenchyma by controlling abluminal CXCL12 abundance during autoimmunity. *J. Exp. Med.* **208**, 327–339 (2011).
116. O. Steiner, C. Coisne, R. Cecchelli, R. Boscacci, U. Deutsch, B. Engelhardt, R. Lyck, Differential roles for endothelial ICAM-1, ICAM-2, and VCAM-1 in shear-resistant T cell arrest, polarization, and directed crawling on blood-brain barrier endothelium. *J. Immunol.* **185**, 4846–4855 (2010).
117. O. Steiner, C. Coisne, B. Engelhardt, R. Lyck, Comparison of immortalized bEnd5 and primary mouse brain microvascular endothelial cells as in vitro blood-brain barrier models for the study of T cell extravasation. *J. Cereb. Blood Flow Metab.* **31**, 315–327 (2010).
118. A. Reboldi, C. Coisne, D. Baumjohann, F. Benvenuto, D. Bottinelli, S. Lira, A. Uccelli, A. Lanzavecchia, B. Engelhardt, F. Sallusto, C-C chemokine receptor 6-regulated entry of TH-17 cells into the CNS through the choroid plexus is required for the initiation of EAE. *Nat. Immunol.* **10**, 514–523 (2009).
119. J. Song, C. Wu, E. Korpos, X. Zhang, S. M. Agrawal, Y. Wang, C. Faber, M. Schäfers, H. Körner, G. Opdenakker, R. Hallmann, L. Sorokin, Focal MMP-2 and MMP-9 activity at the blood-brain barrier promotes chemokine-induced leukocyte migration. *Cell Rep.* **10**, 1040–1054 (2015).
120. M. J. C. Jordao, R. Sankowski, S. M. Brendecke, Sagar, G. Locatelli, Y.-H. Tai, T. L. Tay, E. Schramm, S. Armbruster, N. Hagemeyer, O. Groß, D. Mai, Ö. Çiçek, T. Falk, M. Kerschensteiner, D. Grün, M. Prinz, Single-cell profiling identifies myeloid cell subsets with distinct fates during neuroinflammation. *Science* **363**, eaat7554 (2019).
121. S. Agrawal, P. Anderson, M. Durbeej, N. van Rooijen, F. Ivars, G. Opdenakker, L. M. Sorokin, Dystroglycan is selectively cleaved at the parenchymal basement membrane at sites of leukocyte extravasation in experimental autoimmune encephalomyelitis. *J. Exp. Med.* **203**, 1007–1019 (2006).
122. H. Duan, S. Xing, Y. Luo, L. Feng, I. Gramaglia, Y. Zhang, D. Lu, Q. Zeng, K. Fan, J. Feng, D. Yang, Z. Qin, P.-O. Couraud, I. A. Romero, B. Weksler, X. Yan, Targeting endothelial CD146 attenuates neuroinflammation by limiting lymphocyte extravasation to the CNS. *Sci. Rep.* **3**, 1687 (2013).
123. C. Larochelle, R. Cayrol, H. Kebir, J. I. Alvarez, M.-A. Lécuyer, I. Ifergan, É. Viel, L. Bourbonnière, D. Beauseigle, S. Terouz, L. Hachehouche, S. Gendron, J. Poirier, C. Jobin, P. Duquette, K. Flanagan, T. Yednock, N. Arbour, A. Prat, Melanoma cell adhesion molecule identifies encephalitogenic T lymphocytes and promotes their recruitment to the central nervous system. *Brain* **135**, 2906–2924 (2012).
124. K. Flanagan, K. Fitzgerald, J. Baker, K. Regnstrom, S. Gardai, F. Bard, S. Mocci, P. Seto, M. You, C. Larochelle, A. Prat, S. Chow, L. Li, C. Vandever, W. Zago, C. Lorenzana, C. Nishioka, J. Hoffman, R. Botelho, C. Willits, K. Tanaka, J. Johnston, T. Yednock, Laminin-411 is a vascular ligand for MCAM and facilitates TH17 cell entry into the CNS. *PLOS ONE* **7**, e40443 (2012).
125. D. Shlosberg, M. Benifla, D. Kaufer, A. Friedman, Blood-brain barrier breakdown as a therapeutic target in traumatic brain injury. *Nat. Rev. Neurol.* **6**, 393–403 (2010).
126. T. L. Roth, D. Nayak, T. Atanasichev, A. P. Koretsky, L. L. Latour, D. B. McGavern, Transcranial amelioration of inflammation and cell death after brain injury. *Nature* **505**, 223–228 (2014).
127. M. V. Russo, L. L. Latour, D. B. McGavern, Distinct myeloid cell subsets promote meningeal remodeling and vascular repair after mild traumatic brain injury. *Nat. Immunol.* **19**, 442–452 (2018).
128. W. L. Maxwell, A. Irvine, J. H. Adams, D. I. Graham, T. A. Gennarelli, Response of cerebral microvasculature to brain injury. *J. Pathol.* **155**, 327–335 (1988).
129. E. Park, J. D. Bell, I. P. Siddiqi, A. J. Baker, An analysis of regional microvascular loss and recovery following two grades of fluid percussion trauma: A role for hypoxia-inducible factors in traumatic brain injury. *J. Cereb. Blood Flow Metab.* **29**, 575–584 (2008).
130. Y. N. Jassam, S. Izzy, M. Whalen, D. B. McGavern, J. El Khoury, Neuroimmunology of traumatic brain injury: Time for a paradigm shift. *Neuron* **95**, 1246–1265 (2017).
131. M. V. Russo, D. B. McGavern, Immune surveillance of the CNS following infection and injury. *Trends Immunol.* **36**, 637–650 (2015).
132. H. Lee, S. Lee, I.-H. Cho, S. J. Lee, Toll-like receptors: Sensor molecules for detecting damage to the nervous system. *Curr. Protein Pept. Sci.* **14**, 33–42 (2013).
133. K. N. Corps, T. L. Roth, D. B. McGavern, Inflammation and neuroprotection in traumatic brain injury. *JAMA Neurol.* **72**, 355–362 (2015).
134. N. Lou, T. Takano, Y. Pei, A. L. Xavier, S. A. Goldman, M. Nedergaard, Purinergic receptor P2RY12-dependent microglial closure of the injured blood-brain barrier. *Proc. Natl. Acad. Sci. U.S.A.* **113**, 1074–1079 (2016).
135. E. H. Lo, Experimental models, neurovascular mechanisms and translational issues in stroke research. *Br. J. Pharmacol.* **153** (suppl. 1), S396–S405 (2008).
136. J. Kriz, Inflammation in ischemic brain injury: Timing is important. *Crit. Rev. Neurobiol.* **18**, 145–157 (2006).
137. V. Beray-Berthat, N. Croci, M. Plotkine, I. Margail, Polymorphonuclear neutrophils contribute to infarction and oxidative stress in the cortex but not in the striatum after ischemia-reperfusion in rats. *Brain Res.* **987**, 32–38 (2003).
138. J.-K. Min, Y.-M. Kim, S. W. Kim, M.-C. Kwon, Y.-Y. Kong, I. K. Hwang, M. H. Won, J. Rho, Y.-G. Kwon, TNF-related activation-induced cytokine enhances leukocyte adhesiveness: Induction of ICAM-1 and VCAM-1 via TNF receptor-associated factor and protein kinase C-dependent NF-κB activation in endothelial cells. *J. Immunol.* **175**, 531–540 (2005).
139. M.-J. Sanz, P. Kubis, Neutrophil-active chemokines in vivo imaging of neutrophil trafficking. *Eur. J. Immunol.* **42**, 278–283 (2012).
140. A. Woodfin, M.-B. Voisin, B. A. Imhof, E. Dejana, B. Engelhardt, S. Nourshargh, Endothelial cell activation leads to neutrophil transmigration as supported by the sequential roles of ICAM-2, JAM-A, and PECAM-1. *Blood* **113**, 6246–6257 (2009).
141. V. Brinkmann, U. Reichard, C. Goosmann, B. Fauler, Y. Uhlemann, D. S. Weiss, Y. Weinrauch, A. Zychlinsky, Neutrophil extracellular traps kill bacteria. *Science* **303**, 1532–1535 (2004).
142. G. Enzmann, S. Kargaran, B. Engelhardt, Ischemia-reperfusion injury in stroke: Impact of the brain barriers and brain immune privilege on neutrophil function. *Ther. Adv. Neurol. Disord.* **11**, 1756286418794184 (2018).
143. G. Enzmann, C. Mysiorek, R. Gorina, Y.-J. Cheng, S. Ghavamour, M.-J. Hannocks, V. Prinz, U. Dirnagl, M. Endres, M. Prinz, R. Beschorner, P. N. Harter, M. Mittelbronn, B. Engelhardt, L. Sorokin, The neurovascular unit as a selective barrier to polymorphonuclear granulocyte (PMN) infiltration into the brain after ischemic injury. *Acta Neuropathol.* **125**, 395–412 (2013).
144. I. Perez-de-Puig, F. Miró-Mur, M. Ferrer-Ferrer, E. Gelpi, J. Pedragosa, C. Justicia, X. Urria, A. Chamorro, A. M. Planas, Neutrophil recruitment to the brain in mouse and human ischemic stroke. *Acta Neuropathol.* **129**, 239–257 (2015).
145. Y. Yang, G. A. Rosenberg, Matrix metalloproteinases as therapeutic targets for stroke. *Brain Res.* **1623**, 30–38 (2015).
146. M. Gliem, A. K. Mausberg, J.-I. Lee, I. Simiantonakis, N. van Rooijen, H.-P. Hartung, S. Jander, Macrophages prevent hemorrhagic infarct transformation in murine stroke models. *Ann. Neurol.* **71**, 743–752 (2012).
147. J. Elkins, R. Veltkamp, J. Montaner, S. C. Johnston, A. B. Singhal, K. Becker, M. G. Lansberg, W. Tang, I. Chang, K. Muralidharan, S. Gheuens, L. Mehta, M. S. V. Elkkind, Safety and efficacy of natalizumab in patients with acute ischaemic stroke (ACTION): A randomised, placebo-controlled, double-blind phase 2 trial. *Lancet Neurol.* **16**, 217–226 (2017).
148. C. Schwerk, T. Tenenbaum, K. S. Kim, H. Schroten, The choroid plexus—A multi-role player during infectious diseases of the CNS. *Front. Cell. Neurosci.* **9**, 80 (2015).

149. B. J. Kim, B. M. Hancock, A. Bermudez, N. D. Cid, E. Reyes, N. M. van Sorge, X. Lauth, C. A. Smurthwaite, B. J. Hilton, A. Stotland, A. Banerjee, J. Buchanan, R. Wolkowicz, D. Traver, K. S. Doran, Bacterial induction of Snail1 contributes to blood-brain barrier disruption. *J. Clin. Invest.* **125**, 2473–2483 (2015).
150. B. P. Daniels, D. W. Holman, L. Cruz-Orengo, H. Jujiavarapu, D. M. Durrant, R. S. Klein, Viral pathogen-associated molecular patterns regulate blood-brain barrier integrity via competing innate cytokine signals. *mBio* **5**, e01476–14 (2014).
151. H. M. Lazear, B. P. Daniels, A. K. Pinto, A. C. Huang, S. C. Vick, S. E. Doyle, M. Gale Jr., R. S. Klein, M. S. Diamond, Interferon-lambda restricts West Nile virus neuroinvasion by tightening the blood-brain barrier. *Sci. Transl. Med.* **7**, 284ra59 (2015).
152. J. J. Miner, B. P. Daniels, B. Shrestha, J. L. Proenca-Modena, E. D. Lew, H. M. Lazear, M. J. Gorman, G. Lemke, R. S. Klein, M. S. Diamond, The TAM receptor Mertk protects against neuroinvasive viral infection by maintaining blood-brain barrier integrity. *Nat. Med.* **21**, 1464–1472 (2015).
153. J. Cupovic, L. Onder, C. Gil-Cruz, E. Weiler, S. Caviezel-Firner, C. Perez-Shibayama, T. Rülicke, I. Bechmann, B. Ludewig, Central nervous system stromal cells control local CD8⁺ T cell responses during virus-induced neuroinflammation. *Immunity* **44**, 622–633 (2016).
154. J. V. Kim, S. S. Kang, M. L. Dustin, D. B. McGavern, Myelomonocytic cell recruitment causes fatal CNS vascular injury during acute viral meningitis. *Nature* **457**, 191–195 (2009).
155. C. M. Matullo, K. J. O'Regan, H. Hensley, M. Curtis, G. F. Rall, Lymphocytic choriomeningitis virus-induced mortality in mice is triggered by edema and brain herniation. *J. Virol.* **84**, 312–320 (2009).
156. K. B. Seydel, S. D. Kampondeni, C. Valim, M. J. Potchen, D. A. Milner, F. W. Muwalo, G. L. Birbeck, W. G. Bradley, L. L. Fox, S. J. Glover, C. A. Hammond, R. S. Heyderman, C. A. Chilingulu, M. E. Molneux, T. E. Taylor, Brain swelling and death in children with cerebral malaria. *N. Engl. J. Med.* **372**, 1126–1137 (2015).
157. P. A. Swanson II, G. T. Hart, M. V. Russo, D. Nayak, T. Yazew, M. Peña, S. M. Khan, C. J. Janse, S. K. Pierce, D. B. McGavern, CD8⁺ T cells induce fatal brainstem pathology during cerebral malaria via luminal antigen-specific engagement of brain vasculature. *PLOS Pathog.* **12**, e1006022 (2016).
158. S. W. Howland, C. M. Poh, S. Y. Gun, C. Claser, B. Malleret, N. Shastri, F. Ginhoux, G. M. Grotenbreg, L. Réna, Brain microvessel cross-presentation is a hallmark of experimental cerebral malaria. *EMBO Mol. Med.* **5**, 984–999 (2013).

Acknowledgments: We thank A. Hoofring in the NIH Medical Arts Design Section for help with all the illustrations. **Funding:** This work was supported by the intramural program at the National Institute of Neurological Disorders and Stroke (NINDS), NIH.

Submitted 18 February 2019

Accepted 13 June 2019

Published 12 July 2019

10.1126/sciimmunol.aav0492

Citation: P. Mastorakos, D. McGavern, The anatomy and immunology of vasculature in the central nervous system. *Sci. Immunol.* **4**, eaav0492 (2019).

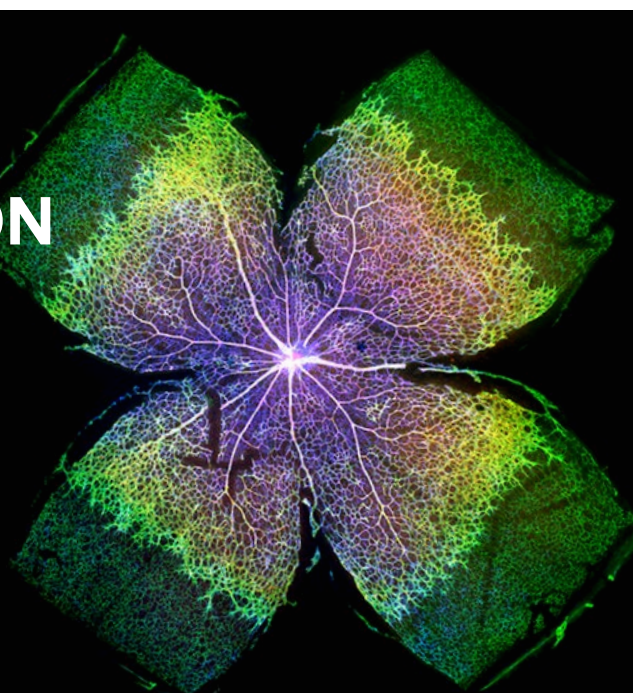
THIS IS NOT SCIENCE FICTION

This is captivating, impactful Science

Contact us today to discuss pricing options for adding any of these journals to your collection of *Science* resources.

Institutional Licensing

ScienceMag.org/request | scienceonline@aaas.org
1-866-265-4152 (USA) | +1-202-326-6730 (outside USA)



Science
AAAS

Science Advances

Science Immunology

Science Robotics

Science Signaling

Science Translational Medicine

HUMAN-ROBOT INTERACTION

Noninvasive neuroimaging enhances continuous neural tracking for robotic device control

B. J. Edelman^{1*}, J. Meng^{2†}, D. Suma^{2†}, C. Zurn¹, E. Nagarajan³, B. S. Baxter^{1‡}, C. C. Cline^{1§}, B. He^{2||}

Brain-computer interfaces (BCIs) using signals acquired with intracortical implants have achieved successful high-dimensional robotic device control useful for completing daily tasks. However, the substantial amount of medical and surgical expertise required to correctly implant and operate these systems greatly limits their use beyond a few clinical cases. A noninvasive counterpart requiring less intervention that can provide high-quality control would profoundly improve the integration of BCIs into the clinical and home setting. Here, we present and validate a noninvasive framework using electroencephalography (EEG) to achieve the neural control of a robotic device for continuous random target tracking. This framework addresses and improves upon both the “brain” and “computer” components by increasing, respectively, user engagement through a continuous pursuit task and associated training paradigm and the spatial resolution of noninvasive neural data through EEG source imaging. In all, our unique framework enhanced BCI learning by nearly 60% for traditional center-out tasks and by more than 500% in the more realistic continuous pursuit task. We further demonstrated an additional enhancement in BCI control of almost 10% by using online noninvasive neuroimaging. Last, this framework was deployed in a physical task, demonstrating a near-seamless transition from the control of an unconstrained virtual cursor to the real-time control of a robotic arm. Such combined advances in the quality of neural decoding and the practical utility of noninvasive robotic arm control will have major implications for the eventual development and implementation of neurorobotics by means of noninvasive BCI.

INTRODUCTION

Detecting mental intent and controlling external devices through brain-computer interface (BCI) technology has opened doors to improving the lives of patients suffering from various neurological disorders, including amyotrophic lateral sclerosis and spinal cord injury (1–5). These realizations have enabled patients to communicate with attending clinicians and researchers in the laboratory by simply imagining actions of different body parts (6, 7). Although achievable task complexity varies between invasive and noninvasive systems, BCIs in both domains have restored once-lost bodily functions that include independent ambulation (8), functional manipulations of the hands (3, 4), and linguistic communication (9, 10). Hence, clinical interest is rapidly building for systems that allow patients to interact with their environment through autonomous neural control (2, 8, 11). Nevertheless, although technology targeting the restoration or augmentation of arm and hand control is of the highest priority in the intended patient populations, electroencephalography (EEG)-based BCIs targeting such restorative interventions are some of the least effective (12, 13). With exemplary clinical applications focusing on robotic- or orthosis-assisted hand control (4), it is paramount to improve coordinated navigation of a robotic arm, because precise positioning will be vital for the success of downstream actions (14). To meet this need, we present here a unified noninvasive frame-

work for the continuous EEG-based two-dimensional (2D) control of a physical robotic arm.

BCI learning rates can vary among individuals, but it is generally thought that a user’s motivation and cognitive arousal play significant roles in the process of skill acquisition and eventual task performance (15, 16). Although levels of internal motivation vary across populations and time (17), engaging users and maintaining attention via stimulating task paradigms may diminish these differences. Current BCI task paradigms overwhelmingly involve simple cued center-out tasks defined by discrete trials (DTs) of neural control (18). These tasks provide robust test beds for new decoding algorithms but do not account for the random perturbations that invariably occur in daily life. Continuous analogs, in which users are not bound by time-limited objectives, enable control strategies that facilitate the extension of BCI toward the realistic control of physical devices in the home and clinic (8). Here, to produce robust robotic arm control that would be useful for daily life, we developed a continuous pursuit (CP) task, in which users performed motor imagination (MI) to chase a randomly moving target (movies S1 to S3) (18, 19). We found that CP task training produced stronger behavioral and physiological learning effects than traditional DT task training, an effect that can be credited to the Yerkes-Dodson law (20).

Poor signal quality can further complicate the ability to decode neural events, especially when using noninvasive signals such as EEG (21). Spatial filtering has long been used to denoise noninvasive BCI signals (22, 23) and has recently offered promise in detecting increasingly diverse realistic commands (10, 24, 25). Electrical source imaging (ESI) is one such approach that uses the electrical properties and geometry of the head to mitigate the effects of volume conduction and estimate cortical activity (26). Dramatic improvements in offline neural decoding have been observed when using ESI compared with traditional sensor techniques (24, 27); however, these approaches have yet to be validated online. By developing a real-time ESI platform, we were able to isolate and evaluate neural decoding in both the sensor

¹Department of Biomedical Engineering, University of Minnesota, Minneapolis, MN 55455, USA. ²Department of Biomedical Engineering, Carnegie Mellon University, Pittsburgh, PA 15213, USA. ³Department of Neuroscience, University of Minnesota, Minneapolis, MN 55455, USA.

*Present address: Stanford University, Stanford, CA 94304, USA.

†These authors contributed equally to this work.

||Present address: Massachusetts General Hospital, Charlestown, MA 02114, USA, and Harvard Medical School, Boston, MA 02115, USA.

§Present address: Stanford University, Stanford, CA 94304, USA, and Veterans Affairs Palo Alto Healthcare System, Palo Alto, CA 94394, USA.

||Corresponding author. Email: bhe1@andrew.cmu.edu

Copyright © 2019
The Authors, some
rights reserved;
exclusive licensee
American Association
for the Advancement
of Science. No claim
to original U.S.
Government Works

and the source domains without introducing the confounding online processing steps that often accompany other spatial filtering techniques (different classifiers, time windows, etc.).

In all, the framework presented here demonstrates a systematic approach to achieving continuous robotic arm control through the targeted improvement of both the user learning (“brain” component) and the machine learning (“computer” component) elements of a BCI. Specifically, using a CP task training paradigm increased BCI learning by nearly 60% for traditional DT tasks and by more than 500% in the more realistic CP task. The utility of real-time ESI further introduced a significant 10% improvement in CP BCI control for users experienced in classical sensor-based BCI. Through the integration of these improvements, we demonstrated the continuous control of a robotic arm (movies S4 to S7) at almost identical levels to that of virtual cursor control, highlighting the potential of noninvasive BCI to translate to real-world devices for practical tasks and eventual clinical applications.

RESULTS

Before addressing whether our online ESI-based decoding strategy could be used for the continuous control of a robotic arm, the CP task and source signal approaches needed to be thoroughly validated as useful training and control strategies, respectively (Fig. 1). Thirty-three individuals naïve to BCI participated in a virtual cursor BCI learning phase. The training length was set at 10 sessions to facilitate practical data acquisition and to establish a threshold for future training applications. These 33 users were split into three groups: sensor domain CP training (CP), sensor domain DT training (DT), and source domain CP training (using real-time ESI; sCP). This design allowed us to answer (i) which training task (CP versus DT) and (ii) which neurofeedback domain (source versus sensor control) led to more effective BCI skill acquisition (see Materials and Methods for details on participant demographics and baseline group metrics). The within-session effects of source versus sensor control (virtual cursor) on CP BCI performance were tested on 29 individuals, 16 with previous BCI experience (sensor control) and 13 naïve to BCI. Furthermore, six individuals with BCI experience (sensor DT cursor control) participated in experiments designed to compare performances between virtual cursor and robotic arm control in a physically constrained variation of the CP task.

Noninvasive continuous virtual target tracking via motor intent

Throughout all experimental sessions, users were instructed to control the trajectory of a virtual cursor using MI tasks; left- and right-hand MI for the corresponding left and right movement, and both hands MI and rest for up and down movement,

respectively. These tasks were chosen on the basis of previous cursor control (28) and neurophysiological (19) exploration. Horizontal and vertical cursor movements were controlled independently. CP trials lasted 60 s each and required users to track a randomly moving target within a square workspace (Fig. 2, A and B; fig. S1, A and B; and movies S1 to S3). Previous implementations of similar tasks used technician-controlled (manual) target trajectories, which can introduce inconsistencies and biases during tracking (29). To avoid such scenarios, we governed target trajectories in the current work by a Gaussian random process (see Materials and Methods). Nevertheless, it is possible for such a random process to drive the target toward stagnation at an edge/corner, which could synthetically distort performance. Therefore, to better estimate the difference between DT and CP task training, and contrary to previous work (18, 29), our initial CP task allowed the cursor and target to fluidly wrap from one side of the workspace to the other (top to bottom, left to right, and vice versa) upon crossing an edge (Fig. 2, A and B; fig. S1, A and B; and movies S1 to S3). Trajectories from experienced users were unwrapped (fig. S1C) to reveal squared tracking correlations of $\rho_{hor}^2 = 0.48 \pm 0.20$ and $\rho_{ver}^2 = 0.47 \pm 0.19$ (fig. S2).

BCI skill acquisition and user engagement

We investigated the utility of using the CP task for BCI skill acquisition in a pre-post study design by comparing BCI performance between populations trained by either CP or DT task. Twenty-two

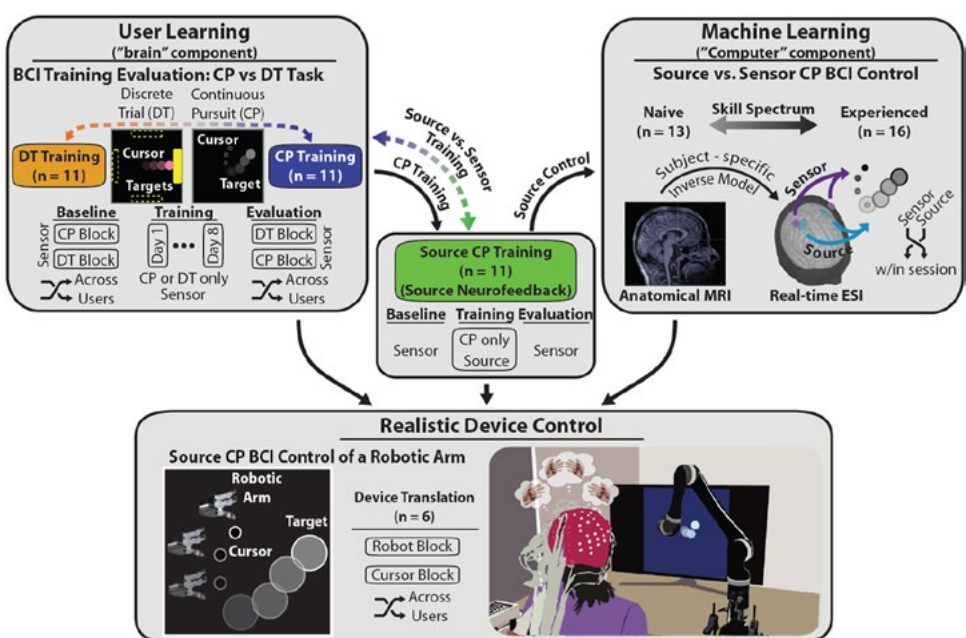


Fig. 1. Source-based CP BCI robotic arm framework. The proposed framework addressed both user and machine learning aspects of BCI technology before being implemented in the control of a realistic robotic device. User learning was addressed by investigating the behavioral and physiological effects of BCI training using sensor-level neurofeedback with a traditional DT center-out task ($n = 11$) and a more realistic CP task ($n = 11$) (top left). The effects of BCI training were further tested in the CP task using source-level neurofeedback ($n = 11$) obtained through online ESI with user-specific anatomical models (center). This design allowed us to determine both the optimal task and neurofeedback domain for BCI skill acquisition. The machine learning aspect was further examined across the skill spectrum by testing the effects of source-level neurofeedback, compared with sensor-level neurofeedback, in naïve ($n = 13$) and experienced ($n = 16$) users in a randomized single-blinded design (top right). The user and machine learning components of the proposed framework were then combined to achieve real-time continuous source-based control of a robotic arm ($n = 6$) (bottom). Comparing BCI performance of robotic arm and virtual cursor control demonstrated the ease of translating neural control of a virtual object to a realistic assistive device useful for clinical applications.

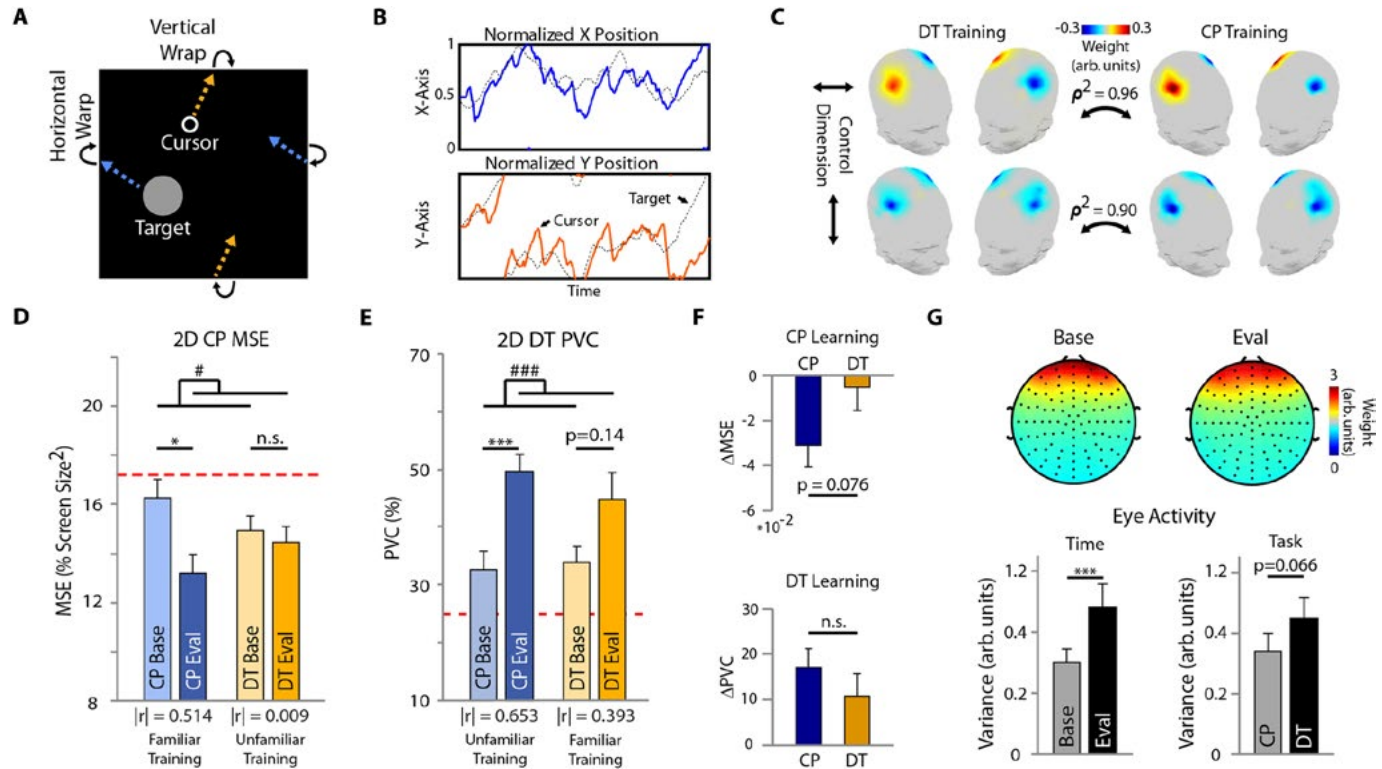


Fig. 2. BCI performance and user engagement. (A) Depiction of the CP edge wrapping feature. (B) Tracking trajectory during an example 2D CP trial. (C) Training feature maps for the DT and CP training groups for horizontal (top) and vertical (bottom) cursor control. p^2 , squared correlation coefficient. (D and E) 2D BCI performance for the CP (D) and DT (E) task at baseline and evaluation for the CP and DT training groups. The red dotted line indicates chance level. The effect size, $|r|$, is indicated under each pair of bars. (F) Task learning for the CP (top) and DT (bottom) tasks. (G) Eye blink EEG component scalp topography (top) and activity (bottom left) at baseline and evaluation, and activity during each task (CP versus DT) (bottom right). Bars indicate mean + SEM. Statistical analysis using a one- (F) or two-way repeated-measures (D, E, and G) ANOVA ($n = 11$ per group) with main effects of task, and time and task, respectively. Main effect of time: * $P < 0.05$, ** $P < 0.005$. Tukey's HSD post hoc test: * $P < 0.05$, *** $P < 0.005$.

individuals participated in a baseline session, eight training sessions, and an evaluation session. Baseline and evaluation sessions contained both DT and CP tasks (and MI without feedback), whereas training sessions contained only one task type, consistent throughout training according to each user's assigned group (DT or CP, $n = 11$ per group; see Materials and Methods). All sessions for both groups used scalp sensor information. 1D horizontal DT performance was used to baseline match the two groups (fig. S3A).

Electrodes used for online control were optimized on a session-by-session basis (see Materials and Methods), chosen from a set of 57 sensors covering the sensorimotor regions. Electrodes were identified for the horizontal and vertical control dimensions independently using the corresponding right-hand MI versus left-hand MI and both hands MI versus rest datasets. Throughout training, the two groups derived nearly identical feature (electrode) maps in the sensor domain containing focal bilateral scalp clusters overlying the cortical hand regions (Fig. 2C). These clusters were located and weighted in accordance with the underlying event-related (de)synchronization generated during the corresponding MI tasks (19) and are similar to those used in other noninvasive cursor control studies, identified through either data-driven (30) or manual (28) selection processes.

DT task performance was measured in terms of percent valid correct (PVC), computed as the number of hit trials divided by the total number of trials, in which a final decision was made (valid trials). The corresponding CP task performance metric was mean squared error

(MSE), i.e., the average normalized squared error between the target and cursor location over the course of a single run. Across these 22 participants, the results of a repeated-measures two-way analysis of variance (ANOVA) revealed a significant main effect of time for both the CP MSE ($F_{1,20} = 7.39$, $P < 0.05$; Fig. 2D) and DT PVC ($F_{1,20} = 19.80$, $P < 0.005$; Fig. 2E) metrics. To examine skill generalizability, we specifically considered the effects of training on the performance of familiar and unfamiliar tasks. Individuals trained with the CP task significantly improved in the same task after training [Tukey's honestly significant difference (HSD) post hoc test, $P < 0.05$; Fig. 2D, left bars], whereas those trained with the DT task did not (Tukey's HSD post hoc test, $P = 0.14$; Fig. 2E, right bars). Previous work has indicated that DT task training can lead to strong learning effects (31); however, some users have required nearly 70 training sessions to do so (18). When considering unfamiliar tasks, the DT training group only modestly improved in the CP task after training (Tukey's HSD post hoc test, $P = 0.96$; Fig. 2D, right bars), whereas the CP training group displayed a significant improvement in the DT task (Tukey's HSD post hoc test, $P < 0.005$; Fig. 2E, left bars).

Because the two tasks varied greatly in control dynamics, it was difficult to draw comparisons between these differences. Therefore, in addition to statistical testing, we also examined the effect size (point biserial correlation, see Materials and Methods), a measure, unconfounded by sample size, of the magnitude of the difference within each performance metric between baseline and evaluation sessions.

Compared with the DT group, the effect sizes were far larger for the CP group for both tasks (Fig. 2, D and E), displaying a 500% learning improvement in the CP task and a nearly 60% learning improvement in the DT task (Fig. 2F).

To delineate the underlying physiology of these training differences, we investigated user engagement during both tasks by quantifying eye blink activity. Decreased blink activity has been implicated in heightened attentional processes and cognitive arousal during various tasks (32). These mental states can dramatically influence task training and performance; whereas stimulating tasks can facilitate skill acquisition, boring or frustrating tasks can inhibit performance (20). The eye blink component of the EEG was extracted during the baseline and evaluation sessions using independent component analysis (ICA) (Fig. 2G and fig. S4). Across all participants, blink activity was strongly dampened at the baseline ($F_{1,63} = 9.84, P < 0.005$; Fig. 2G), suggesting heightened attention that was likely due to the novelty of BCI in general. Increased blink activity at the evaluation supports user skill acquisition, because less attention was required for improved performance. The large reduction in blink activity observed during the CP task, compared with the DT task ($F_{1,63} = 3.51, P = 0.066$; Fig. 2G), suggests that the CP task elicited heightened user engagement during active control, a feature that may explain the more dramatic positive training effects.

Learning to modulate sensorimotor rhythms

Whereas BCI feedback plays a significant role in facilitating sensorimotor rhythm modulation (33), MI without feedback can provide a measure of a user's natural ability to produce the associated discriminative EEG patterns. Left-hand MI versus right-hand MI (left versus right) and both hands MI versus rest (up versus down) runs were analyzed individually. An index of modulation between any two mental states is represented as the regression output (R^2) between the EEG alpha power and the task labels (see Materials and Methods). Only the 57 sensorimotor electrodes used for online control were included in this analysis. Although sensorimotor modulation significantly increased for both task pairs from baseline to evaluation (horizontal: $F_{1,20} = 4.70, P < 0.05$; vertical: $F_{1,20} = 21.01, P < 0.005$; Fig. 3, A and C), the spatial distribution of these improvements is more meaningful in evaluating the effectiveness of BCI training. Except for mild baseline modulation in the DT group, no strong patterns were apparent for either task pair before training. For the horizontal dimension at the evaluation session, the CP group produced highly focal bilateral modulation patterns, whereas more global modulation was observed for the DT group (Fig. 3B). Evaluation topographies were more consistent between the two training groups for the vertical dimension (Fig. 3D). Electrodes displaying a significant improvement in modulation were far more numerous for the CP group than for the DT group for both horizontal (CP, 12; DT, 3; Fig. 3E) and vertical (CP, 37; DT, 13; Fig. 3F) tasks. Furthermore, these significant electrodes clustered far closer to scalp regions covering the approximate hand cortical regions (e.g., C3-4 and CP3-4) in the CP group. These localized changes provide compelling evidence that the enhanced behavioral improvement seen in the CP training group was accompanied by consistent physiological changes in sensorimotor modulation (R^2 values) (34).

Source neurofeedback does not further facilitate CP BCI learning

Whereas the CP task allowed us to target user learning and progress toward the robust online control of a robotic arm, we additionally wanted to address the machine learning element. To evaluate whether

real-time ESI-based decoding improved performance throughout training, we recruited an additional group of BCI naïve individuals ($n = 11$) for CP training using source neurofeedback (source control, sCP). This sCP group was baseline-matched to the previous CP (and DT) group (sensor control) (fig. S5A). For source control, we implemented user- and session-specific inverse models into the online decoding pipeline for the CP task. Similar to the CP group, the sCP group significantly improved in both the 2D CP (Tukey's HSD post hoc test, $P < 0.05$; Fig. 4A, right bars) and the 2D DT tasks (Tukey's HSD post hoc test, $P < 0.05$; Fig. 4B, right bars) after training. Accordingly, very similar learning effects were observed for both tasks in the CP and sCP groups (Fig. 4C). The final performance and learning rates were consistent between the two training groups (CP and sCP), supporting the groups' shared familiar and unfamiliar task proficiency.

Feature selection in the source domain identified distinct cortical clusters, optimized through anatomical and functional constraints, for online control and was performed on a session-by-session basis (see Materials and Methods). As expected, sCP training feature maps highlighted hand cortical regions for both control dimensions throughout training (Fig. 4D). It should be noted that the baseline and evaluation sessions for the sCP group were completed in the sensor domain to maintain consistent conditions with the other training groups. Although training duration was fixed at eight sessions with no intermediary testing, further investigation at different stages of learning may help pinpoint when source-based decoding may benefit BCI skill acquisition.

EEG source imaging enhances neural control in defined skill states

To thoroughly investigate the effects of source control (real-time ESI) on CP task performance (and potential future benefits for robotic arm control), we performed within-session comparisons of source and sensor virtual cursor control on users in stable skill states. The CP task was chosen for further analysis because it is more applicable to robotic arm control than the DT task and displayed both increased difficulty and skill acquisition. Our investigation included both extremes of the BCI skill spectrum; experienced users (12.8 ± 8.9 hours of previous BCI training, $n = 16$) participated in up to three sessions, and naïve users (no previous BCI training, $n = 13$) participated in a single session (to avoid confounding effects of early learning in more than one session). User- and session-specific inverse models were also used for these participants.

For experienced users, source control improved performance over that of conventional sensor control, producing a significant reduction in the 2D MSE ($F_{1,69} = 9.83, P < 0.01$; Fig. 5A). Unsurprisingly, the sensor and source MSE values clustered near those of the CP training group after training (evaluation), reinforcing their skilled state. The spatial extent of the observed improvement in the CP task was characterized through squared error histograms (Fig. 5B), with source values shifting toward smaller errors and sensor values shifting toward larger errors. By fitting gamma functions to these histograms, we derived a quantitative threshold, independent of cursor/target size, for statistically testing the spatial extent of the performance difference (fig. S6). Experienced users dwelt within this defined region, a disc with a diameter of 16.67% of the workspace width centered on the target (Fig. 5E), for significantly more time during source control than sensor control ($F_{1,69} = 20.96, P < 0.005$; Fig. 5F).

Naïve users also demonstrated an overall improvement in online performance with source control, although this improvement did not

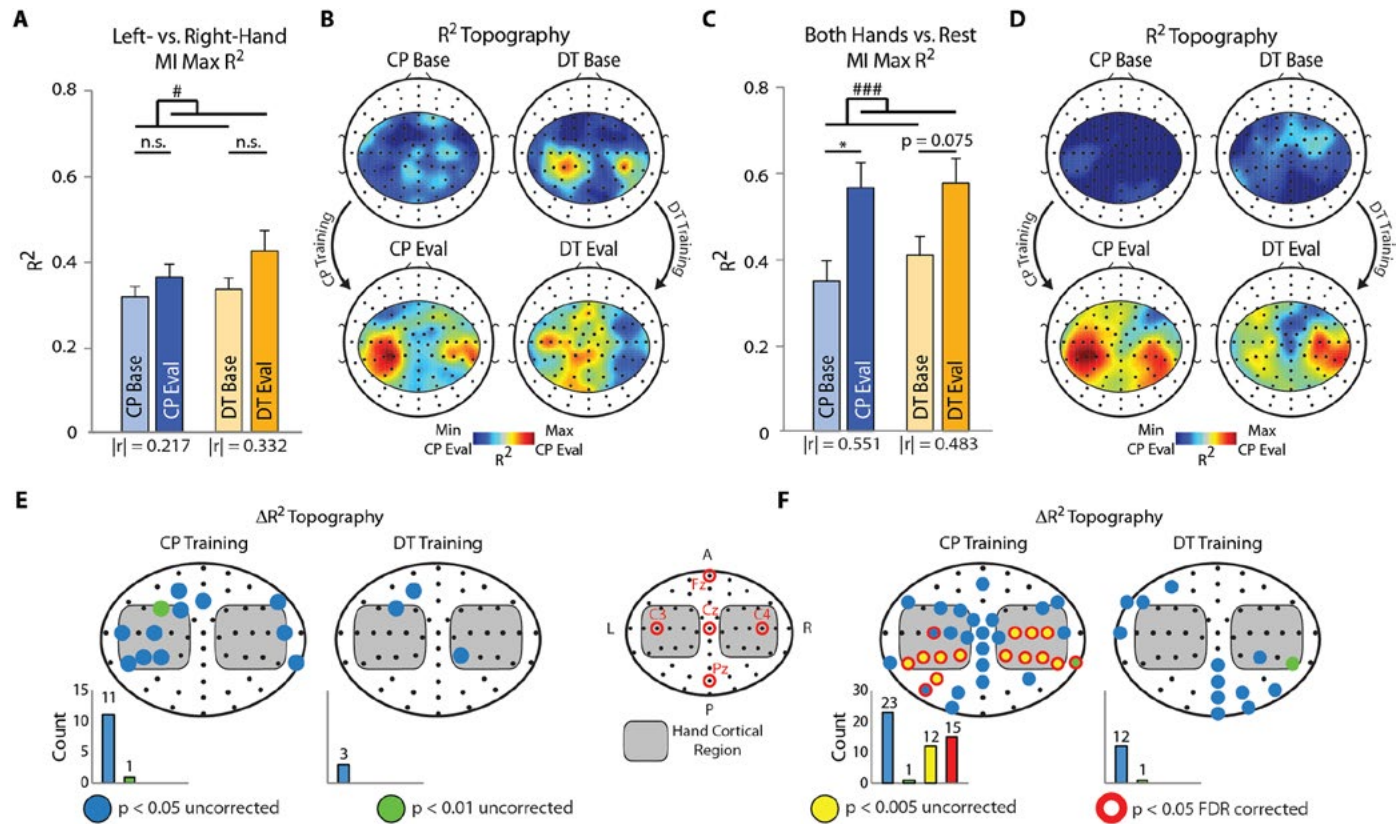


Fig. 3. Electrophysiological learning effects. (A and B) Left versus right MI task analysis. (A) Maximum sensorimotor R^2 value for the CP and DT training groups for horizontal control task. The effect size, $|r|$, is indicated under each pair of bars. (B) R^2 topographies at baseline (top row) and evaluation (bottom row) for the CP and DT training groups for horizontal control tasks. (C and D) Both hands versus rest MI task analysis. Same as (A) and (B) for vertical control tasks. (E and F) Statistical topographies indicating electrodes that displayed a significant increase in R^2 values for the horizontal (E) and vertical (F) control tasks. The electrode map in the middle provides a reference for the electrodes shown. Bar graphs below each topography provide a count for the number of electrodes meeting the various significance thresholds. Bars indicate mean + SEM. Statistical analysis using a one- (E and F) or two-way repeated-measures (A and C) ANOVA ($n = 11$ per group) with main effects of time [blue, $P < 0.05$; green, $P < 0.01$; yellow, $P < 0.005$; red outline, $P < 0.05$, false discovery rate (FDR) corrected] and time (${}^*P < 0.05$, ${}^{**}P < 0.005$) and training task, respectively. Tukey's HSD post hoc test: $*P < 0.05$.

reach significance for 2D control ($F_{1,12} = 3.02$, $P = 0.11$; Fig. 5C). Nevertheless, the effect size for the performance difference was notably similar to that of experienced users (Fig. 5, A and C, and table S1), indicating an improvement of similar magnitude. As expected, the sensor and source control MSE values for the naïve users were comparable with those of the CP training group before training (baseline, also naïve). This consistency, independent of skill level, highlights a robust positive influence of source control on online performance. Furthermore, the squared error histograms (Fig. 5D) and extent threshold measures for naïve users (Fig. 5E) displayed analogous trends to those of experienced users; however, these did not reach significance ($F_{1,12} = 2.02$, $P = 0.18$; Fig. 5F).

When looking at the feature maps (Fig. 5G), an important dichotomy can be observed between naïve (weak, sporadic clusters) and experienced (strong, focal clusters) users for both control dimensions that parallels the trends previously observed in the modulation index topographies before (low, sporadic modulation) and after (high, focal modulation) training (Fig. 3, B and D). To quantify the focality/diffuseness of these features, we computed the spread of the group-level feature maps (Fig. 5H), defined as the average weighted distance between the feature location and the hand knob (source space) or C3/C4 electrode (sensor space) (see Materials and Methods). We observed both signif-

icant or near-significant reductions in the feature spread for experienced users, compared with naïve users, in both the horizontal (Mann-Whitney U test with Bonferroni correction: source, $P < 0.005$; sensor, $P < 0.05$) and the vertical (Mann-Whitney U test with Bonferroni correction: source, $P < 0.005$; sensor, $P = 0.22$) control dimensions. This physiological difference between naïve and experienced users is in line with their performance difference (MSE) and further supports the contrast in BCI proficiency among the two groups and the overarching effect of source-based control depending on user skill level.

Source-based CP BCI control of a robotic arm

Having robustly validated our proposed BCI framework in a controlled environment, we completed our study by transitioning to the applied physical source control of a robotic arm (Fig. 6A). Although the cursor and target wrapping allowed for more complicated control strategies and scenarios, such a feature could not exist in a real-world setting. Therefore, we implemented a modified form of the CP task in a robotic arm control paradigm, where the edge-wrapping feature was replaced with an edge repulsing feature (Fig. 6B and movies S4 to S7). Six experienced users (8.3 ± 2.9 hours of previous BCI training) participated in five source CP BCI sessions containing both virtual cursor and robotic arm control, block-randomized across individuals and

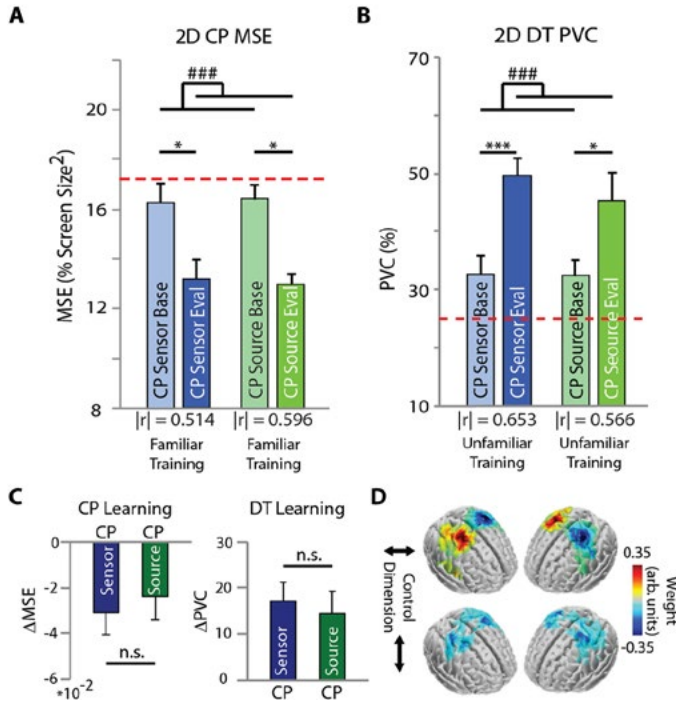


Fig. 4. Source-level neurofeedback. (A and B) 2D BCI performance for the CP (A) and DT (B) task at baseline and evaluation for the CP and source CP (sCP) training groups. The red dotted line indicates chance level. The effect size, $|r|$, is indicated under each pair of bars. (C) Task learning for the CP (left) and DT (right) tasks. Bars indicate mean \pm SEM. Statistical analysis using a one- (C) or two-way repeated-measures (A and B) ANOVA ($n = 11$ per group) with main effects of training decoding domain, and time and training decoding domain, respectively. Main effect of time: ${}^{\#}P < 0.05$, ${}^{\#\#\#}P < 0.005$. Tukey's HSD post hoc test: $*P < 0.05$, $***P < 0.005$. n.s., not significant. (D) Group-level training feature maps for the training groups for horizontal (top) and vertical (bottom) cursor control. User-specific features were projected onto a template brain for group averaging.

sessions. Because no paradigm was implemented to determine performance values before and after training in the modified task, participants were screened for experience and skill level beforehand (see Materials and Methods). Physiological support for user skill level was additionally observed in the group-level feature maps (Fig. 6C) that displayed comparable characteristics with those of other experienced users participating in this study (Fig. 5G).

When users were directly controlling the robotic arm, the behavior of a hidden virtual cursor was also recorded to ensure proper mapping of the arm position in physical space. Across all sessions and individuals, median squared tracking correlation values reached $\rho_{\text{hor}}^2 = 0.13$ (IQR = 0.04 – 0.32) and $\rho_{\text{ver}}^2 = 0.09$ (IQR = 0.03 – 0.28) in the horizontal and vertical dimensions, respectively, for 2D control. In transitioning between virtual cursor and robotic arm control, we observed similar MSE values among the three tracking conditions—virtual cursor, hidden cursor, and robotic arm ($F_{2,40} = 2.62$, $P = 0.086$; Fig. 6D)—indicating a smooth transition from the control of a virtual object to a real-world device. This likeness in control quality was further revealed through a lack of significant difference in the squared tracking correlation (ρ^2) for both the horizontal ($F_{2,40} = 0.13$, $P = 0.88$; Fig. 6E) and vertical ($F_{2,40} = 0.77$, $P = 0.47$; Fig. 6E) dimensions. Tracking performance was significantly greater than the chance levels determined for all control conditions and dimensions (Mann-

Whitney U test with Bonferroni correction, all $P < 0.05$). Overall, the notable similarity between virtual cursor control and robotic arm control highlights the possibility of integrating virtual cursor exposure into future clinical training paradigms, where patients have limited access to robotic arm training time.

DISCUSSION

The research presented here describes an encompassing approach aimed at driving noninvasive neural control toward the realistic daily use of a robotic device. We have demonstrated that the CP BCI paradigm not only can be used to successfully gauge a user's BCI proficiency but also can serve as a more effective training tool than traditional center-out DT tasks, accelerating the acquisition of neural cursor control and driving the associated physiological changes. Contrary to users trained with the DT task, those trained with the CP task displayed significant performance improvements in familiar and unfamiliar tasks (Fig. 2, D to F), demonstrating highly flexible skill acquisition. These results were further supported in a third group that also trained with the CP task (Fig. 4, A to C). Participants in this group (sCP) displayed nearly identical learning effects as the original sensor CP group while training with source control, providing confidence for the reproducibility of the effects of CP task training.

As training progressed, it became apparent that the strategies developed by users differed significantly, depending on the training task. For example, various individuals in the DT training group reported using strategies involving selectively attending to their hand(s) through peripheral vision without necessarily focusing on the cursor position. Although such strategies were effective for DT tasks, users using them often struggled with the CP tasks in the evaluation session, because the moving target and cursor required constant visual attention and adjustment of motor-related mental intent. In this sense, many of these users somewhat ignored the feedback when training with the DT task and treated it similarly to the MI without feedback, reducing its effectiveness (33). The lower success of such strategies manifested within the MI EEG of the DT group as sporadic patterns of modulation after training (Fig. 3D), which are also consistent with the lower levels of cognitive arousal observed during the traditional DT task compared with the CP task (Fig. 2G). We believe that the target dynamics and screen wrapping feature of the CP task (Fig. 2A) likely perturb fluid target tracking and require heightened attention during cursor control. These conclusions support the overarching concept of integrating human factors, such as virtual reality techniques (34, 35), into cognitive-based training tools for improving both user engagement and task performance (20, 36–38) and should be considered in future generations of BCIs.

Seminal works implementing similar continuous tracking tasks using invasively acquired signals reported comparable squared tracking correlation values over a decade ago (29). Although the field of invasive neural decoding has surpassed these benchmark results to include high degree-of-freedom and anthropomorphically functional tasks (3, 39, 40), qualitative similarities can be seen between these two modalities. In accordance with invasive reports, users in our study struggled to keep the cursor in a single location, often exhibiting oscillatory tracking behavior around the target (Fig. 2B and fig. S1, A and B). Although these actions demonstrate directed cursor trajectories toward the target and highlight the ability of our system to accurately capture the users' dynamic mental intent, the tracking correlation is effectively reduced and may benefit from more advanced decoding methods.

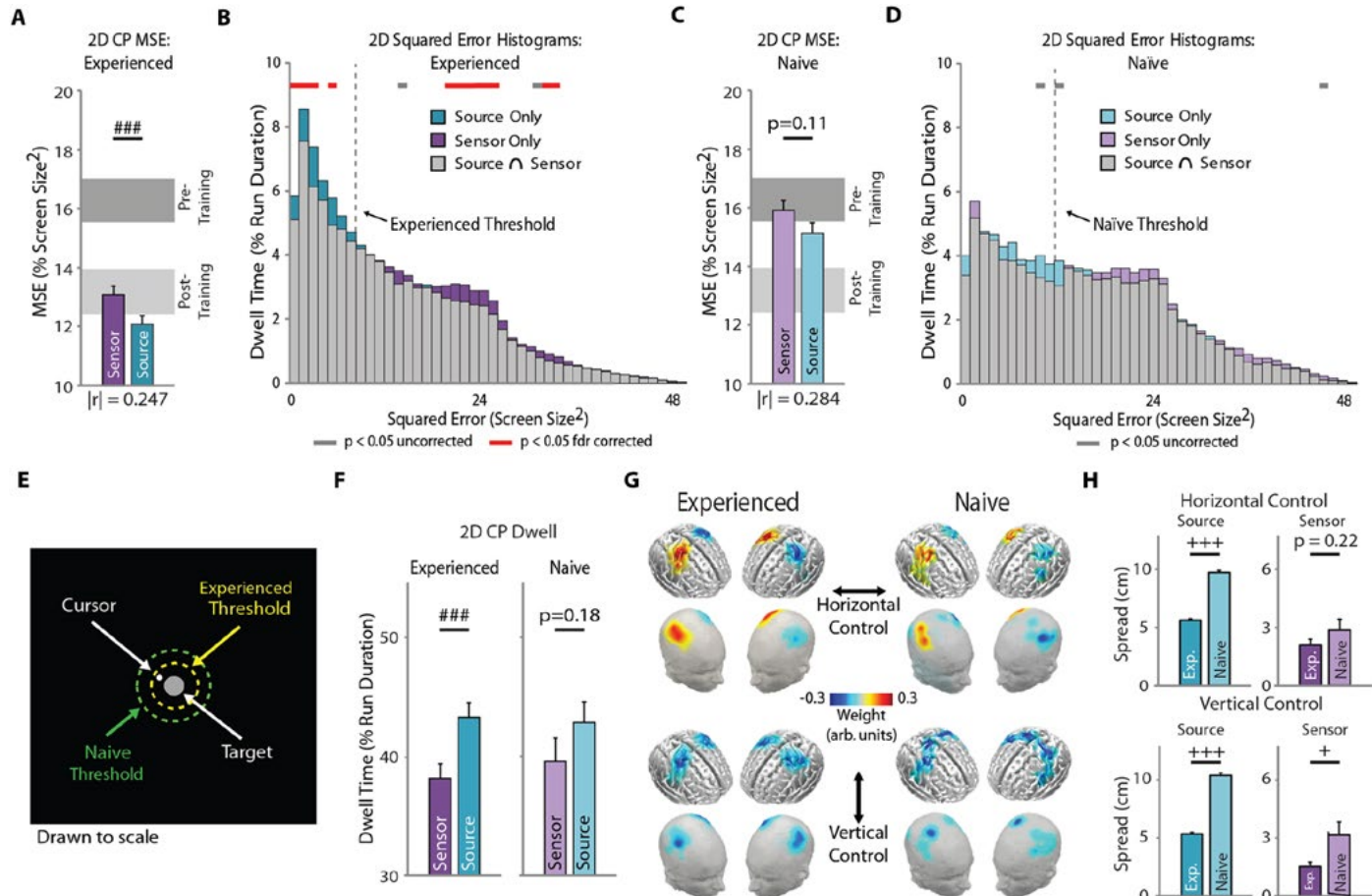


Fig. 5. Online 2D CP source versus sensor BCI performance. (A and B) Experienced user performance ($n = 16$). (A) Group-level MSE for source and sensor 2D CP cursor control. Light and dark gray blocks represent performance for the CP training group ($n = 11$; Fig. 2D) before (naïve) and after training (experienced). The effect size, $|r|$, is indicated under the pair of bars. (B) Group-level squared-error histograms for 2D CP sensor and source cursor control. (C and D) Naïve user performance ($n = 13$). Same as (A) and (B) for naïve user data. (E) Scale drawing of the CP paradigm workspace displaying the spatial threshold derived from experienced (yellow) and naïve (green) user data (fig. S6). (F) Cursor dwell time within the spatial threshold for experienced (left) and naïve (right) users. (G) Group-level feature maps for horizontal (top) and vertical (bottom) cursor control for naïve (right) and experienced (left) users. User-specific features were projected onto a template brain for group averaging. (H) Feature spread analysis between experienced and naïve users for source (left) and sensor (right) features for horizontal (top) and vertical (bottom) control. Bars indicate mean \pm SEM. Statistical analysis using a one- (C and D) or two-way repeated-measures (A and B) ANOVA with main effects of decoding domain, and time and decoding domain, respectively. Main effect of decoding domain: $^{###}P < 0.005$ (A, C, and F), gray bar; $P < 0.05$ uncorrected, red bar; $P < 0.05$, FDR corrected (B and D). Mann-Whitney U test with Bonferroni correction for multiple comparisons (H): $^+P < 0.05$, $^{++}P < 0.005$.

It has been argued that motor neurons encode cursor velocity during neural cursor control (41), with numerous decoding algorithms using such properties to drastically improve user performance over classical techniques (38). In particular, modeling neuronal behavior as a dynamical system has recently yielded significantly improved online decoding results (42) and may provide even more complex and efficient device control in upcoming invasive and noninvasive work. This decoding strategy would be particularly attractive to neural control in the CP task presented here, given the clear analog of our control output to under-damped control dynamics. Although this information would be valuable to reduce or eliminate the previously described cursor oscillations, it has yet to be observed whether these details can be detected via scalp recordings. Nevertheless, noninvasive neural signals have recently been shown to contain information encoded on the spatial scale of cortical columns (submillimeter), indicating the ability to decode neural activity with very fine spatial-temporal resolution from outside the skull (43).

Over the past few decades, the reconstruction of cortical activity through ESI has exemplified the push to increase the spatial specificity of noninvasive recordings and has been shown to provide superior neural decoding when compared with scalp sensor information (23, 24, 27). Similar to these previous works, we found that, in general, source features were more correlated with cued motor-related mental states than sensor features (fig. S9) (44, 45). Furthermore, in closed-loop CP BCI control, we found that the inclusion of online ESI improved performance in naïve and experienced users, consistent with offline enhancements (Fig. 5 and figs. S7 to S9). The increased task-specific source modulation indicates a higher sensitivity for detecting changes in a user's motor-related mental state and is likely a product of the principles of ESI and its use in modeling and counteracting volume conduction. CP cursor control requires highly dynamic cognitive processes to recognize and correct for the random and sudden changes in the target's trajectory during tracking. We therefore hypothesize that the fast, real-time control required during the CP paradigm takes advantage of the

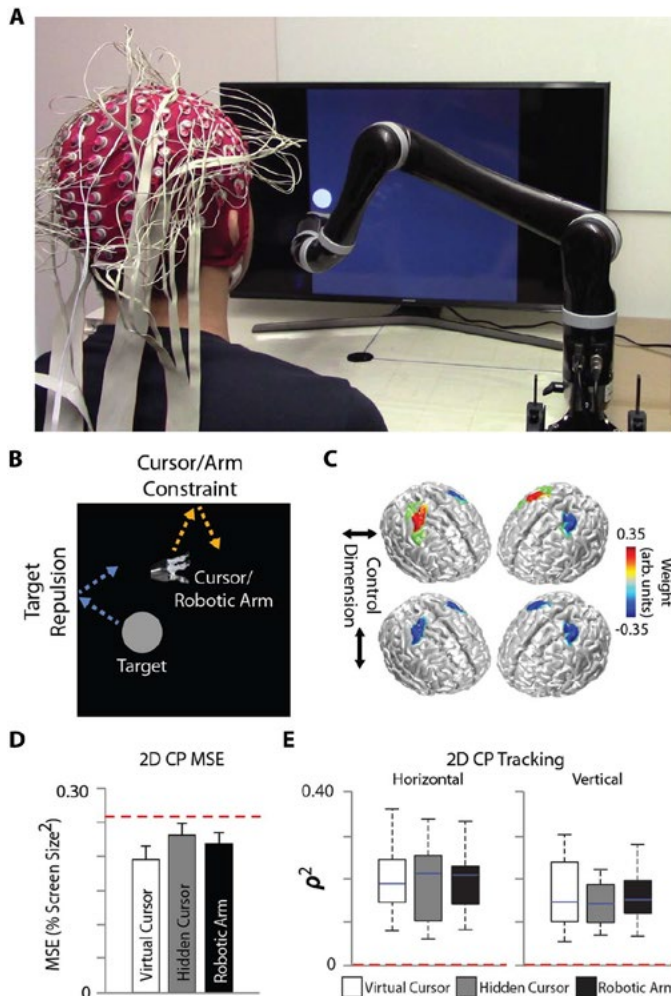


Fig. 6. Source-based CP BCI robotic arm control. (A) Robotic arm CP BCI setup. Users controlled the 2D continuous movement of a 7-degree of freedom robotic arm to track a randomly moving target on a computer screen. (B) Depiction of the CP edge repulsion feature (in contrast to the edge wrapping feature; Fig. 2A) used to accommodate the physical limitations of the robotic arm. (C) Group-level feature maps for the horizontal (top row) and vertical (bottom row) control dimensions projected onto a template brain. (D) Group-level 2D MSE for the various control conditions. Bars indicate mean + SEM. (E) Box-and-whisker plots for the group-level squared tracking correlation (ρ^2) values for the horizontal (left) and vertical (right) dimensions during 2D CP control for the various control conditions. Blue lines indicate the medians, tops and bottoms of the boxes indicate the 25th and 75th percentiles, and the top and bottom whiskers indicate the respective minimum and maximum values. Control conditions include virtual cursor (white), hidden cursor (gray), and robotic arm (black). The red dotted line indicates chance level. Statistical analysis using a repeated-measures two-way ANOVA ($n = 6$ per condition) with main effects of time and control condition.

heightened sensitivity of ESI modulation, allowing for quicker responses that more accurately resemble the dynamics involved in the CP task. This phenomenon was apparent during the within-session comparisons of source and sensor control (Fig. 5 and figs. S7 and S8); however, it is possible that, with sufficient training, the feedback domain becomes less important for skill acquisition (Fig. 4).

We feel that it is necessary to acknowledge the decline in performance that occurred between the original CP task and the modified CP task, which we believe to be strongly attributed to the task mod-

ifications made for the physical constraints of the robotic arm. The presence of the physical robotic device inherently creates a more distracting environment for neural control compared with that of a virtual cursor. We found that, with the robotic arm mounted on the right side of the user (Figs. 1, bottom, and 6A), visual obstruction of the target was common when the arm was directed to reach across the user to the left side of the screen, often perturbing target tracking. In addition, although participants here displayed previous BCI proficiency, they had less experience than those participating in the original CP task validation. We believe that this combination of reduced user experience and enhanced sensory loading caused by the more complex human-device interaction involving the robotic arm led to a reduction in performance compared with the highly controlled virtual cursor control environment.

The results presented here demonstrate that CP control provides a unique opportunity for the complex control of a virtual cursor and robotic device (14, 39), without requiring discretized, prolonged task sequences (46) that can make even simple task completion long and frustrating. Users were able to smoothly transition between virtual cursor and robotic arm control with minimal changes in performance (Fig. 6, D and E), indicating the potential ease of integrating such a noninvasive assistive tool into clinical applications for autonomous use in daily life. Invasive systems have already demonstrated a level of control similar to such a noninvasive hypothetical; however, although such invasive approaches may offer much-needed help to a restricted number of patients with severe physical dysfunctions, most impaired persons will likely not qualify for participation due to both medical and financial limitations. Additionally, previous work has suggested that accessing sufficiently large patient populations for concrete and statistically significant conclusions may be difficult to obtain (1–5, 8, 11, 29, 39). Therefore, there is a strong need to further develop noninvasive BCI technology so that it can benefit most patients and even the general population in the future. The effective training paradigm and additional ESI-based performance improvement demonstrated here, as well as the integration of such targeted enhancements toward robotic arm control, offer increasing confidence that noninvasive BCIs may be able to expand to widespread clinical investigation. We observed that, for robotic arm control, generic head models, rather than those derived from user-specific magnetic resonance imaging (MRI), were sufficient for high-quality performance (see Materials and Methods). Therefore, in all, the work presented in this paper is necessary for current EEG-based BCI paradigms to achieve useful and effective noninvasive robotic device control, and its results are pertinent in directing both ongoing and future studies.

MATERIALS AND METHODS

BCI tasks

Motor imagery without feedback

EEG data during motor imagination (MI) without feedback were collected at the beginning of each session, one run for left-hand MI versus right-hand MI and one for the both hands MI versus rest. Each run consisted of 10 randomly presented trials per task. Each trial consisted of 3 s of rest, followed by 4 s of a visually cued MI task.

DT task

The DT paradigm was composed of fixed target locations and center-out intended cursor trajectories. This paradigm consisted of 21 trials, with targets presented in a random order. Each trial began with a 3-s rest period, followed by a 2-s preparation period, in which the target

was presented to the user. Users were then given up to 6 s to move the cursor to hit the target. A 1-s intertrial interval bridged two adjacent trials. Feedback (cursor movement) was not provided during the first trial to calibrate the normalizer as described in the “Online signal processing” section.

During baseline and evaluation sessions, trials ended either upon a collision with a target or after 6 s with no collision. During training sessions, each trial lasted a full 6 s, requiring users to maintain their cursor over the target location for as long as possible within a boundary-constrained workspace. In this sense, during training, each DT run contained 120 s of online BCI control, consistent with the 120-s CP runs.

CP task

The CP stimulus paradigm was implemented using custom Python scripts in the BCPy2000 application module of BCI2000 (47). This paradigm involved the continuous tracking of a target; each run was composed of two 60-s trials separated by a 1-s intertrial interval. To produce smoothly varying random target movement, the position of the target was updated in each frame using a simple kinematic model. Random motion was obtained by applying a randomly generated 1D or 2D external force \vec{F}_{ext} , as in Eq. 1, drawn from a zero-mean fixed-variance normal distribution.

$$\vec{F}_{\text{ext}} \sim \mathcal{N}_2(0, \sigma^2) \quad (1)$$

To effectively limit maximum target velocity, we also applied a friction force \vec{F}_f and a drag force \vec{F}_d . The friction and drag forces are represented in Eqs. 2 and 3, respectively, where μ indicates the coefficient of friction, δ indicates the drag, and $\vec{v}^{(t)}$ indicates the velocity of the cursor at time step t . Here, $\|\cdot\|$ denotes the Euclidian norm

$$\vec{F}_f = -\mu \frac{\vec{v}^{(t)}}{\|\vec{v}^{(t)}\|_2} \quad (2)$$

$$\vec{F}_d = -\delta \vec{v}^{(t)} \|\vec{v}^{(t)}\|_2 \quad (3)$$

When divided by the arbitrary target mass m , the combination of these forces represents the total instantaneous acceleration of the target. Integrating with respect to time, as noted in Eq. 4, produces the updated target velocity $\vec{v}^{(t+1)}$ at the new time point

$$\vec{v}^{(t+1)} = \vec{v}^{(t)} + \frac{\vec{F}_{\text{ext}} + \vec{F}_f + \vec{F}_d}{m} dt \quad (4)$$

For the training and source versus sensor experiments described in subsequent sections, the cursor and target were allowed to wrap from one side of the workspace to the other (left to right, top to bottom, and vice versa). Contrary to this, for the robotic arm versus virtual cursor experiments, the target was repelled by the edges of the workspace to make the task more realistic and accommodate the physical limitations of the robotic arm. Repulsion was accomplished by inverting all applied forces that would push the target continuously into a wall while still randomly generating magnitudes and directions for irrelevant forces. Unlike the target dynamics, the cursor and robotic arm could press against the edge of the bounded region, given the appropriate force vector.

Noise/chance performance estimation

Chance performance in the CP paradigm was estimated by collecting 15 (standard) or 70 (physically constrained) datasets each for 1D horizontal (LR), 1D vertical (UD), and 2D control tasks with the electrode sets plugged in but not connected to a human scalp. Chance performance in the DT paradigm was determined by dividing 100% by the number of targets in each control dimension. This is valid because trials that time out are typically excluded when calculating performance for the DT task.

Experimental design

Sixty-eight healthy humans were informed and participated in different phases of this study after providing written consent to a protocol approved by the relevant Institutional Review Board at the University of Minnesota or Carnegie Mellon University.

Training

Thirty-three individuals (average age: 24.8 ± 10.6 years, 30 right handed, 18 male) naïve to BCI participated in longitudinal BCI training over the course of 10 experimental sessions that included one baseline session, eight training sessions, and one evaluation session. Participants were tested on all tasks at the baseline and evaluation time points to assess training effectiveness, completing one block of DT tasks and one block of CP tasks, block-wise randomized across individuals. The blocks for each paradigm were composed of two runs of 1D LR, 1D UD, and 2D control. Participants were divided into three training groups using the 1D LR DT performance as the balancing metric (figs. S3A and S5A). Naïve participants obtaining PVC values of >80% for both runs of any of the three DT dimensions were excluded from the training cohort because these users are often considered proficient ($n = 5/38$) (14, 28). Participants underwent eight training sessions at 12 runs per session, with only their specified task paradigm—DT sensor, CP sensor, or CP source. These eight training sessions were broken into 2×1 D LR, 2×1 D UD, and 4×2 D control to progress toward more difficult tasks near the end of training. The evaluation session was identical to the baseline session, again with the task block order randomized across individuals. Baseline and evaluation sessions were all completed using sensor control for consistency across groups. Participants underwent two to three sessions per week with an average intersession interval of 3.69 ± 2.99 days.

Source versus sensor

Twenty-nine individuals participated in experiments testing the within-session effects of source versus sensor control on the CP BCI task. Sixteen users (average age: 22.67 ± 8.1 years, 15 right handed, 6 male) with an average of 12.8 ± 8.9 hours of previous BCI experience and 13 users (average age: 21.8 ± 5.0 years, 12 right handed, 8 male) naïve to BCI participated in this portion of the study. Experienced users participated in up to three BCI sessions, and the naïve users participated in a single session to avoid the confounding effects of learning. There were no exclusion criteria in this phase of the study because participants were in well-defined naïve or experienced states. A user-specific anatomical MRI was collected for each individual according to the MRI acquisition section. In each BCI session, participants completed 12 runs of CP BCI (4×1 D LR, 4×1 D UD, and 4×2 D), with the decoding strategy (sensor or source) being randomized and balanced across the population.

Robotic arm versus virtual cursor

Six individuals (average age: 25.2 ± 6.5 years, five right handed, three male, 8.3 ± 2.9 hours of previous BCI training) participated in experiments comparing virtual cursor and robotic arm control. Participants for this phase were screened using sensor-based 1D and 2D DT tasks

using the BCI2000 AR alpha (8 to 13 Hz) power estimation of C3 and C4, spatially filtered with the local pseudo-Laplacian using a Neuroscan Synamps2 (Compumedics Ltd., Victoria, Australia) 64-channel system. Participants were excluded on the basis of a two-stage performance evaluation: (i) failure to achieve >70% 1D PVC (sessions 1 and 2) or >40% 2D PVC (session 2) in two sequential runs and (ii) failure to achieve >90% 1D PVC and >70% 2D PVC (sessions 3 to 5) in two sequential runs. Six of 19 recruited participants passed these criteria.

All robotic arm experiments were conducted on a Samsung 43-inch 4K television, allowing large, practical workspaces for both the robotic arm and the virtual cursor. Each user participated in five source CP BCI sessions containing 12 runs (60 s) (sessions 1 and 2, 6 × 1D LR and 6 × 1D UD; sessions 3 to 5, 3 × 1D LR, 3 × 1D UD, and 6 × 2D) of both virtual cursor and robotic arm control in block-randomized order across users. Some users were asked to return for a sixth session to record video of continuous robotic arm and virtual cursor control. Robotic arm endpoint locations were mapped 1:1 to cursor positions on the screen, with inverse kinematics used to solve for optimal joint angles and arm trajectories. The robotic arm workspace was square with a 0.48-m side length. All robotic arm control was conducted using the Kinova JACO Assistive Robotic Arm with a three-finger attached gripper.

For all BCI sessions, participants were seated in a padded chair about 90 cm from a computer screen. Unless otherwise stated, users were fitted with a 128-channel Biosemi (Biosemi, Amsterdam, The Netherlands) EEG headcap of appropriate size and positioned according to the international 10-20 system. EEG was recorded at 1024 Hz using an ActiveTwo amplifier with active electrodes (Biosemi, Amsterdam, The Netherlands).

MRI acquisition

User-specific anatomical MRI images were acquired on a 3T MRI machine (Siemens Prisma, Erlangen, Germany) using a 32-channel head coil. High-resolution (1-mm isotropic) anatomical images were acquired for each participant using a T1-weighted magnetization prepared rapid acquisition gradient echo sequence (repetition time/echo time, 2350 ms/3.65 ms; flip angle, 7°; acquisition time, 05:06 min; $R = 2$ acceleration; matrix size, 256 by 256; field of view, 256 mm by 256 mm).

Frequency-domain ESI

For the source versus sensor experiments, the anatomical MRI from each user was segmented in FreeSurfer and uploaded into the MATLAB-based Brainstorm toolbox. For the robotic arm versus virtual cursor experiments, the Colin27 template brain was used for all users. The cortex was downsampled to a tessellated mesh of ~15,000 surface vertices and broken into 12 bilateral regions based on the Destrieux atlas. A central region of interest (ROI), composed of various sensorimotor areas (table S2), was used for feature extraction and online source control.

At the beginning of each BCI session in the source versus sensor experiments, EEG electrode locations were recorded using a FASTRAK digitizer (Polhemus, Colchester, Vermont) using the Brainstorm toolbox. Electrode locations were co-registered with the user's MRI using the nasion and left and right preauricular landmarks. A three-shell realistic geometry head model with a conductivity ratio of 1:1/20:1 was generated using the boundary element method implemented in the OpenMEG toolbox.

The inverse operator for each session was generated according to the following theory. Equation 5 depicts the linear system relating scalp and cortical activity, where $\phi(t)$ represents the scalp-recorded EEG at

time t , L represents the user- and session-specific leadfield, and $J(t)$ represents the cortical current density at time t

$$\phi(t) = LJ(t) \quad (5)$$

Linear programming techniques can help stabilize the often ill-conditioned nature of the leadfield to find optimal estimates of the source distribution. In the current work, we used Tikhonov regularization (Eq. 6). This optimization suggests a solution $J(t)$ that depends on various known parameters that include the sensor covariance matrix C , source covariance matrix R , regularization parameter λ , leadfield, and scalp EEG

$$\min_J \|C^{-1/2}(\phi(t) - LJ(t))\|_2^2 + \lambda^2 \|R^{-1/2}J(t)\|_2^2, \\ \text{where } \lambda^2 = \frac{\text{tr}(LRL^T)}{\text{tr}(C)\text{SNR}^2} \quad (6)$$

The closed-form solution to Eq. 6, solving for an optimal source distribution $\hat{J}(t)$, is shown in Eq. 7 in the time domain and belongs to the family of minimum-norm estimates. Here, 20 s of resting-state EEG collected at the beginning of each session was used to compute a diagonal sensor covariance matrix C . The source covariance matrix was also a diagonal matrix, with nonzero elements containing a depth-weighted reciprocal of source location power. This modification to the source covariance matrix forms the weighted minimum-norm estimate.

$$\hat{J}(t) = RL^T (LRL^T + \lambda^2 C)^{-1} \phi(t) \quad (7)$$

This solution can be applied in the frequency domain by solving for both the real and imaginary frequency-specific cortical activity independently (45) and subsequently taking the magnitude at each cortical location (Eq. 8)

$$\hat{J}_{\text{Re}}(f) = RL^T (LRL^T + \lambda^2 C_{\text{Re}})^{-1} \phi_{\text{Re}}(f) \\ \hat{J}_{\text{Im}}(f) = RL^T (LRL^T + \lambda^2 C_{\text{Im}})^{-1} \phi_{\text{Im}}(f) \quad (8)$$

To use the spatial filtering properties of inverse imaging and extract task-related activity, we subjected the reconstructed cortical activity to both anatomical and functional constraints. The anatomical constraint is represented by limiting cortical activity to the central sensorimotor ROI previously described. The functional constraint is based on the data-driven parcellation of the ROI into discretized, functionally coherent cortical clusters. Parcellation is particularly attractive for real-time applications because it improves the condition of the EEG inverse problem and reduces computation time (48). Parcellation was performed using the multivariate source prelocalization algorithm using the MI without feedback data collected at the beginning of each session (48). Solving for the activity in each of these cortical clusters extends Eqs. 8 to 9, where the subscript k represents the number of cortical parcels

$$\hat{J}_{k, \text{Re}}(f) = R_k L_k^T \left(\left(\sum_k L_k R_k L_k^T \right) + \lambda_{\text{Re}}^2 C_{\text{Re}} \right)^{-1} \phi_{\text{Re}}(f) \\ \hat{J}_{k, \text{Im}}(f) = R_k L_k^T \left(\left(\sum_k L_k R_k L_k^T \right) + \lambda_{\text{Im}}^2 C_{\text{Im}} \right)^{-1} \phi_{\text{Im}}(f) \quad (9)$$

Channel-frequency optimization

Each of the MI without feedback runs was analyzed individually to identify features used to control cursor movement in the two dimensions.

For the sensor domain, the alpha power (8 to 13 Hz) at each electrode was extracted at a 1-Hz resolution using a Morlet wavelet technique previously described in (24). A stepwise linear regression approach similar to (30) was used with a forward inclusion step ($P < 0.01$) and backward removal step ($P < 0.01$) to find the electrodes and weights that best separated the two tasks used for each control dimension. This procedure was applied to frequency-specific R^2 montages in the order of descending maximum values until at least one electrode survived the statistic thresholding. The weight of each selected electrode was set to -1 or $+1$ based on the sign of the regression beta coefficient. A weight of 0 was applied to all other electrodes not selected. If no electrodes were selected for any frequency, then a default setup assigned -1 and $+1$ to the C3 and C4 electrodes, respectively, for horizontal control and -1 and -1 to both electrodes for vertical control (28).

For feature selection in the source domain, the MI EEG was first mapped to the cortical model according to Eq. 9. The stepwise linear regression procedure was applied to all ROI parcels, and weights were assigned accordingly. If no parcels were selected, then the default source setup was defined by assigning a weight of -1 to those parcels containing the left motor cortex hand knob, $+1$ to those containing the right motor cortex hand knob for horizontal control, and -1 to bilateral hand knob parcels for vertical control. These parcels were identified on the basis of seed points assigned to the hand knobs [similar to (44)] by the operators before the experimental session.

Feature spread was calculated as the average Euclidean distance between the feature location and the lateral hand knob (source space) or C3/C4 electrode (sensor space). The hand knob location was defined as the average location of the previously mentioned seed points. The distance was also weighted by the magnitude of the feature weight to account for its strength. Distances were calculated for the left and right sides of the head individually and pooled together for each dimension.

Online signal processing

All online processing was performed using custom MATLAB (MathWorks Inc., MA, USA) scripts that communicated with BCI2000 using the FieldTrip buffer signal processing module. Fifty-seven electrodes covering the motor-parietal region of the scalp were used for online processing. The EEG was downsampled to 256 Hz and bandpass-filtered between 8 and 13 Hz using a fourth-order Butterworth filter before common average referencing. The most recent 250 ms of data was analyzed and used to update the cursor velocity every 100 ms. The instantaneous control signal was computed as the weighted sum of the alpha power in the selected electrodes. If $\phi_t(f)$ represents the magnitude of the alpha power across the entire EEG montage at time window t and x_h and x_v are vectors containing the electrode weights ($1s$, $-1s$, and $0s$) assigned during the optimization process, then the instantaneous control signal for each dimension can be represented as

$$C_{h,t} = x_h^T \phi_t(f) \quad C_{v,t} = x_v^T \phi_t(f) \quad (10)$$

The velocity of the cursor in each dimension was then derived by normalizing these values to zero mean and unit variance based on the values stored from the previous 30 s of online control in the respective dimension

$$\vec{V}_{h,t} = \frac{C_{h,t} - \bar{C}_{h,t-n:t-1}}{\sigma_{C_{h,t-n:t-1}}} \quad \vec{V}_{v,t} = \frac{C_{v,t} - \bar{C}_{v,t-n:t-1}}{\sigma_{C_{v,t-n:t-1}}} \quad (11)$$

The same procedure was performed for source control using the reconstructed cortical frequency information $\hat{f}_t(f)$ and the corresponding cortical cluster weights. Robotic arm positions were controlled via a custom C++ script, which read and translated cursor positions into optimal joint angles.

Offline data analysis

CP data files contained cursor and target positions. These values were normalized to the screen size and used to obtain an error, defined as the Euclidean distance between the cursor and target, at each time point. The tracking correlation was computed as the Pearson correlation coefficient (ρ) between the target and cursor position time series. The MSE value was computed as the average of the error time series between these same two position vectors. The choice to use ρ^2 (squared tracking correlation) was based on the concept of user control; signed values of ρ much less than 0 are superior to small positive values (e.g., -1 versus $+0.01$) because they suggest high-quality control that is inverted and that the simple inversion of weights can lead to high tracking performance. Furthermore, very few tracking correlation values were negative for both the original and physically constrained CP tasks. DT data files contained target and result codes for each trial used to compute PVC values. Artifactual trials for both DT and CP runs were identified during online BCI control or by offline visual inspection of the EEG and removed from subsequent analysis.

MI without feedback data files contained the 128-channel EEG and MI task labels. Nonstationary high-variance signals were initially removed from the raw EEG using the artifact subspace reconstruction EEGLab plugin. Bad channels were spherically interpolated. The clean EEG was downsampled to 128 Hz, filtered between 5 and 30 Hz using a fourth-order Butterworth filter, and re-referenced to the common average. The alpha (8 to 13 Hz) power was extracted from each channel using a Morlet wavelet for the time periods of 0.5 to 4.0 s after each stimulus presentation; a 0.5-s delay was included to account for user reaction time (after the visual cue). The alpha power in each channel and each frequency was regressed against the task labels. For the source domain, cortical alpha power was computed according to the frequency-domain ESI section and regressed against the task labels.

Eye activity was extracted using ICA. Clean EEG data for all tasks in the baseline and evaluation sessions were concatenated into separate datasets and decomposed using the extended infomax algorithm. The dimensionality of the data was first reduced using principal components analysis. The vertical and horizontal eye activity components (for fig. S4 analysis) were identified as those containing high delta (1 to 4 Hz) activity and strong monopolar and bipolar frontal electrode projections, respectively (49). Not all sessions contained both distinct components meeting these criteria. Blink activity was computed as the variance of the (vertical/blink) independent component (IC) activation sequence during DT and CP control separately. To determine the influence of eye activity on BCI performance, we performed a regression analysis between the vertical or horizontal eye activity IC activation sequence and target location in the corresponding dimension.

Statistical analysis

Statistical analysis was performed using custom R and MATLAB scripts. Effect sizes are reported throughout the article as the point biserial correlation, $|r|$, to highlight within-group (e.g., training) and across-condition (e.g., source versus sensor and robotic arm versus virtual cursor) differences. The point biserial correlation was computed according to Eq. 12, where M_1 and M_2 are the means of the two

distributions being compared and is the pooled SD (d is also known as Cohen's d)

$$r = \frac{d}{\sqrt{d^2 + 4}}, d = \frac{M_1 - M_2}{SD_{\text{pooled}}} \quad (12)$$

Unless otherwise stated, two-way repeated-measures ANOVAs were used with main effects of time and training task (DT versus CP), decoding domain (source versus sensor), or control method (robotic arm versus virtual cursor). All behavioral and electrophysiological metrics were first evaluated with the Shapiro-Wilk test to test for the normality of the residuals of a standard ANOVA. If the P value of the majority of all multiple comparisons was less than 0.05, then a rank-transformed ANOVA was used. Otherwise, a standard ANOVA was used. If less than 10 multiple comparisons were made, then a Tukey's post hoc test was used to correct for multiple comparisons, and if greater than 10 comparisons were made, then FDR correction ($P < 0.05$) was used. A Mann-Whitney U test with Bonferroni correction for multiple comparisons was used for specific cases: comparing squared tracking correlation values (ρ^2) of neural control with noise in the constrained CP task and comparing the feature spread in the source and sensor domains in naïve and experienced users.

SUPPLEMENTARY MATERIALS

robotics.sciencemag.org/cgi/content/full/4/31/eaaw6844/DC1

Fig. S1. Example CP trajectories.

Fig. S2. Squared tracking correlation histograms.

Fig. S3. CP versus DT BCI learning.

Fig. S4. Influence of eye activity on BCI control.

Fig. S5. Source versus sensor BCI learning.

Fig. S6. 2D CP source versus sensor spatial threshold.

Fig. S7. Online 1D horizontal CP source versus sensor BCI performance.

Fig. S8. Online 1D vertical CP source versus sensor BCI performance.

Fig. S9. Offline source versus sensor sensorimotor modulation.

Table S1. Absolute effect sizes for source-based versus sensor-based CP control.

Table S2. Source-level sensorimotor ROI anatomical structures.

Movie S1. 1D horizontal CP (unconstrained) BCI virtual cursor control example trial.

Movie S2. 1D vertical CP (unconstrained) BCI virtual cursor control example trial.

Movie S3. 2D CP (unconstrained) BCI virtual cursor control example trial.

Movie S4. 1D horizontal CP (physically constrained) BCI robotic arm control example trial.

Movie S5. 1D vertical CP (physically constrained) BCI robotic arm control example trial.

Movie S6. 2D CP (physically constrained) BCI robotic arm control example trial.

Movie S7. 2D CP (physically constrained) BCI virtual cursor control example trial.

REFERENCES AND NOTES

- C. Pandarinath, P. Nuyujukian, C. H. Blabe, B. L. Sorice, J. Saab, F. R. Willett, L. R. Hochberg, K. V. Shenoy, J. M. Henderson, High performance communication by people with paralysis using an intracortical brain-computer interface. *eLife* **6**, e18554 (2017).
- M. J. Vansteensel, E. G. M. Pels, M. G. Bleichner, M. P. Branco, T. Denison, Z. V. Freudentburg, P. Gosselaar, S. Leinders, T. H. Ottens, M. A. van den Boom, P. C. Van Rijen, E. J. Aarnoutse, N. F. Ramsey, Fully implanted brain-computer interface in a locked-in patient with ALS. *N. Engl. J. Med.* **375**, 2060–2066 (2016).
- C. E. Bouton, A. Shaikhouni, N. V. Annetta, M. A. Bockbrader, D. A. Friedenberg, D. M. Nielson, G. Sharma, P. B. Sederberg, B. C. Glenn, W. J. Mysiw, A. G. Morgan, M. Deogaonkar, A. R. Rezai, Restoring cortical control of functional movement in a human with quadriplegia. *Nature* **533**, 247–250 (2016).
- S. R. Soekadar, M. Witkowski, C. Gómez, E. Opisso, J. Medina, M. Cortese, M. Cempini, M. C. Carrozza, L. G. Cohen, N. Birbaumer, N. Vitiello, Hybrid EEG/EOG-based brain-neural hand exoskeleton restores fully independent living activities after quadriplegia. *Sci. Robot.* **1**, eaeg3296 (2016).
- U. Chaudhary, B. Xia, S. Silvoni, L. G. Cohen, N. Birbaumer, Brain-computer interface-based communication in the completely locked-in state. *PLOS Biol.* **15**, e1002593 (2017).
- B. He, B. Baxter, B. J. Edelman, C. C. Cline, W. W. W. Ye, Noninvasive brain-computer interfaces based on sensorimotor rhythms. *Proc. IEEE* **103**, 907–925 (2015).
- J. d. R. Millán, R. Rupp, G. R. Müller-Putz, R. Murray-Smith, C. Giugliemma, M. Tangermann, C. Vidaurre, F. Cincotti, A. Kübler, R. Leeb, C. Neuper, K.-R. Müller, D. Mattia, Combining brain-computer interfaces and assistive technologies: State-of-the-art and challenges. *Front. Neurosci.* **4**, 161 (2010).
- B. R. Leeb, L. Tonin, M. Rohm, L. Desideri, T. Carlson, J. d. R. Millán, Towards independence: A BCI telepresence robot for people with severe motor disabilities. *Proc. IEEE* **103**, 969–982 (2015).
- V. Gilja, C. Pandarinath, C. H. Blabe, P. Nuyujukian, J. D. Simmeral, A. A. Sarma, B. L. Sorice, J. A. Perge, B. Jarosiewicz, L. R. Hochberg, K. V. Shenoy, J. M. Henderson, Clinical translation of a high-performance neural prosthesis. *Nat. Med.* **21**, 1142–1145 (2015).
- X. Chen, Y. Wang, M. Nakanishi, X. Gao, T.-P. Jung, S. Gao, High-speed spelling with a noninvasive brain-computer interface. *Proc. Natl. Acad. Sci.* **112**, E6058–E6067 (2015).
- E. M. Holz, L. Botrel, T. Kaufmann, A. Kübler, Long-term independent brain-computer interface home use improves quality of life of a patient in the locked-in state: A case study. *Arch. Phys. Med. Rehabil.* **96**, S16–S26 (2015).
- J. L. Collinger, M. A. Kryger, R. Barbara, T. Better, K. Bowsher, E. H. P. Brown, S. T. Clanton, A. D. Degenhart, S. T. Foldes, R. A. Gaunt, F. E. Gyulai, E. A. Harchick, D. Harrington, J. B. Helder, T. Hemmes, M. S. Johannes, K. D. Katyal, G. S. F. Ling, A. J. C. McMorland, K. Palko, M. P. Para, J. Scheuermann, A. B. Schwartz, E. R. Skidmore, F. Solzbacher, A. V. Srikanth, D. P. Swanson, S. Swetz, E. C. Tyler-Kabara, M. Velliste, W. Wang, D. J. Weber, B. Wodlinger, M. L. Boninger, Collaborative approach in the development of high-performance brain-computer interfaces for a neuroprosthetic arm: Translation from animal models to human control. *Clin. Transl. Sci.* **7**, 52–59 (2014).
- K. D. Anderson, Targeting recovery: Priorities of the spinal cord-injured population. *J. Neurotrauma* **21**, 1371–1383 (2004).
- U. Chaudhary, N. Birbaumer, A. Ramos-Murgui, Brain-computer interfaces for communication and rehabilitation. *Nat. Rev. Neurosci.* **12**, 513–525 (2016).
- M. Lotze, C. Braun, N. Birbaumer, S. Anders, L. G. Cohen, Motor learning elicited by voluntary drive. *Brain* **126**, 866–872 (2003).
- S. Musallam, B. D. Corneil, B. Greger, H. Scherberger, R. A. Andersen, Cognitive control signals for neural prosthetics. *Science* **305**, 258–262 (2004).
- J. J. Daly, J. R. Wolpaw, Brain-computer interfaces in neurological rehabilitation. *Lancet Neurol.* **7**, 1032–1043 (2008).
- J. R. Wolpaw, D. J. McFarland, Control of a two-dimensional movement signal by a noninvasive brain-computer interface in humans. *Proc. Natl. Acad. Sci. U.S.A.* **101**, 17849–17854 (2004).
- G. Pfurtscheller, F. H. Lopes da Silva, Event-related EEG/MEG synchronization and desynchronization: Basic principles. *Clin. Neurophysiol.* **110**, 1842–1857 (1999).
- R. M. Verkes, J. D. Dodson, The relation of strength of stimulus to rapidity of habit-formation. *J. Comp. Neurol. Psychol.* **18**, 459–482 (1908).
- T. Ball, M. Kern, I. Mutschler, A. Aertsen, A. Schulze-Bonhage, Signal quality of simultaneously recorded invasive and non-invasive EEG. *Neuroimage* **46**, 708–716 (2009).
- H. Ramoser, J. Müller-Gerking, G. Pfurtscheller, Optimal spatial filtering of single trial EEG during imagined hand movement. *IEEE Trans. Rehabil. Eng.* **8**, 441–446 (2000).
- L. Qin, L. Ding, B. He, Motor imagery classification by means of source analysis for brain-computer interface applications. *J. Neural Eng.* **1**, 135–141 (2004).
- B. J. Edelman, B. Baxter, B. He, EEG source imaging enhances the decoding of complex right-hand motor imagery tasks. *IEEE Trans. Biomed. Eng.* **63**, 4–14 (2016).
- K. K. Ang, Z. Y. Chin, C. Wang, C. Guan, H. Zhang, Filter bank common spatial pattern algorithm on BCI competition IV datasets 2a and 2b. *Front. Neurosci.* **6**, 39 (2012).
- B. He, A. Sohrabpour, E. Brown, Z. Liu, Electrophysiological source imaging: A noninvasive window to brain dynamics. *Annu. Rev. Biomed. Eng.* **20**, 171–196 (2018).
- V. Shenoy Handiru, A. P. Vinod, C. Guan, EEG source space analysis of the supervised factor analytic approach for the classification of multi-directional arm movement. *J. Neural Eng.* **14**, 46008 (2017).
- K. LaFleur, K. Cassady, A. Doud, K. Shades, E. Rogin, B. He, Quadcopter control in three-dimensional space using a noninvasive motor imagery-based brain-computer interface. *J. Neural Eng.* **10**, 46003 (2013).
- L. R. Hochberg, M. D. Serruya, G. M. Friehs, J. A. Mukand, M. Saleh, A. H. Caplan, A. Branner, D. Chen, R. D. Penn, J. P. Donoghue, Neuronal ensemble control of prosthetic devices by a human with tetraplegia. *Nature* **442**, 164–171 (2006).
- D. J. McFarland, W. A. Sarnacki, J. R. Wolpaw, Electroencephalographic (EEG) control of three-dimensional movement. *J. Neural Eng.* **7**, 36007 (2010).
- N. Birbaumer, L. G. Cohen, Brain-computer interfaces: Communication and restoration of movement in paralysis. *J. Physiol.* **579**, 621–636 (2007).
- M. K. Holland, G. Tarlow, Blinking and mental load. *Psychol. Rep.* **31**, 119–127 (1972).
- T. Ono, A. Kimura, J. Ushiba, Daily training with realistic visual feedback improves reproducibility of event-related desynchronization following hand motor imagery. *Clin. Neurophysiol.* **124**, 1779–1786 (2013).

34. S. Perdikis, L. Tonin, S. Saeedi, C. Schneider, J. d. R. Millán, The Cybathlon BCI race: Successful longitudinal mutual learning with two tetraplegic users. *PLOS Biol.* **16**, e2003787 (2018).
35. J. A. Anguera, J. Boccanfuso, J. L. Rintoul, O. Al-Hashimi, F. Faraji, J. Janowich, E. Kong, Y. Laraburo, C. Rolle, E. Johnston, A. Gazzaley, Video game training enhances cognitive control in older adults. *Nature* **501**, 97–101 (2013).
36. A. Myrden, T. Chau, Effects of user mental state on EEG-BCI performance. *Front. Hum. Neurosci.* **9**, 308 (2015).
37. J. Gottlieb, Attention, learning, and the value of information. *Neuron* **76**, 281–295 (2012).
38. V. Gilja, P. Nuyujukian, C. A. Chestek, J. P. Cunningham, B. M. Yu, J. M. Fan, M. M. Churchland, M. T. Kaufman, J. C. Kao, S. I. Ryu, K. V. Shenoy, A high-performance neural prosthesis enabled by control algorithm design. *Nat. Neurosci.* **15**, 1752–1757 (2012).
39. L. R. Hochberg, D. Bacher, B. Jarosiewicz, N. Y. Masse, J. D. Simeral, J. Vogel, S. Haddadin, J. Liu, S. S. Cash, P. van der Smagt, J. P. Donoghue, Reach and grasp by people with tetraplegia using a neurally controlled robotic arm. *Nature* **485**, 372–375 (2012).
40. B. Wodlinger, J. E. Downey, E. C. Tyler-Kabara, A. B. Schwartz, M. L. Boninger, J. L. Collinger, Ten-dimensional anthropomorphic arm control in a human brain-machine interface: Difficulties, solutions, and limitations. *J. Neural Eng.* **12**, 16011 (2015).
41. J. M. Carmen, M. A. Lebedev, R. E. Crist, J. E. O'Deherty, D. M. Santucci, D. F. Dimitrov, P. G. Patil, C. S. Henriquez, M. A. L. Nicolelis, Learning to control a brain-machine interface for reaching and grasping by primates. *PLOS Biol.* **1**, 193–208 (2003).
42. J. C. Kao, P. Nuyujukian, S. I. Ryu, M. M. Churchland, J. P. Cunningham, K. V. Shenoy, Single-trial dynamics of motor cortex and their applications to brain-machine interfaces. *Nat. Commun.* **6**, 7759 (2015).
43. R. M. Cichy, F. M. Ramirez, D. Pantazis, Can visual information encoded in cortical columns be decoded from magnetoencephalography data in humans? *Neuroimage* **121**, 193–204 (2015).
44. F. Cincotti, D. Mattia, F. Aloise, S. Bufalari, L. Astolfi, F. De Vico Fallani, A. Tocci, L. Bianchi, M. G. Marciani, S. Gao, J. Millan, F. Babiloni, High-resolution EEG techniques for brain-computer interface applications. *J. Neurosci. Methods* **167**, 31–42 (2008).
45. H. Yuan, A. Doud, A. Gururajan, B. He, Cortical imaging of event-related (de) synchronization during online control of brain-computer interface using minimum-norm estimates in frequency domain. *IEEE Trans. Neural Syst. Rehabil. Eng.* **16**, 425–431 (2008).
46. J. Meng, S. Zhang, A. Bekyo, J. Olsoe, B. Baxter, B. He, Noninvasive electroencephalogram based control of a robotic arm for reach and grasp tasks. *Sci. Rep.* **6**, 38565 (2016).
47. G. Schalk, D. J. McFarland, T. Hinterberger, N. Birbaumer, J. R. Wolpaw, BCI2000: A general-purpose brain-computer interface (BCI) system. *IEEE Trans. Biomed. Eng.* **51**, 1034–1043 (2004).
48. J. Mattout, M. Pélégriini-Issac, L. Garnero, H. Benali, Multivariate source prelocalization (MSP): Use of functionally informed basis functions for better conditioning the MEG inverse problem. *Neuroimage* **26**, 356–373 (2005).
49. T.-P. Jung, S. Makeig, M. Westerfield, J. Townsend, E. Courchesne, T. J. Sejnowski, Removal of eye activity artifacts from visual event-related potentials in normal and clinical subjects. *Clin. Neurophysiol.* **111**, 1745–1758 (2000).

Acknowledgments: We thank A. Sohrabpour for helpful discussions and S. Sherman for help in participant recruitment. **Funding:** This work was supported, in part, by NIH AT009263, MH114233, EB021027, NS096761, and NSF CBET-1264782. B.J.E. was supported, in part, by NIH/NINDS Fellowship F31NS096964. **Author contributions:** B.J.E., J.M., D.S., B.S.B., and B.H. designed experiments. B.J.E., J.M., D.S., C.Z., and E.N. collected the data. B.J.E., J.M., and D.S. analyzed the data. B.J.E., J.M., D.S., and B.H. wrote the manuscript. B.J.E. created the real-time processing software. C.C.C. designed the CP task. J.M. designed the robotic arm interface. B.H. supervised the project involving all aspects of the study design and data collection and analysis. **Competing interests:** The authors declare that they have no competing interests. **Data and materials availability:** All data needed to evaluate the conclusions in the paper are present in the paper or the Supplementary Materials. BCI and EEG data used to create Figs. 2, 3, and 5 will be available at doi:10.5061/dryad.v46p2jh. Additional materials can be requested from B.H. under a material transfer agreement with Carnegie Mellon University.

Submitted 15 January 2019

Accepted 17 May 2019

Published 19 June 2019

10.1126/scirobotics.aaw6844

Citation: B. J. Edelman, J. Meng, D. Suma, C. Zurn, E. Nagarajan, B. S. Baxter, C. C. Cline, B. He, Noninvasive neuroimaging enhances continuous neural tracking for robotic device control. *Sci. Robot.* **4**, eaaw6844 (2019).

MEDICAL ROBOTS

Long-term implant of intramuscular sensors and nerve transfers for wireless control of robotic arms in above-elbow amputees

S. Salminger^{1,2}, A. Sturma^{2,3}, C. Hofer^{2,4}, M. Evangelista⁵, M. Perrin⁵, K. D. Bergmeister^{1,2}, A. D. Roche^{2,6,7}, T. Hasenoehrl⁸, H. Dietl⁴, D. Farina³, O. C. Aszmann^{1,2,*}

Targeted muscle reinnervation (TMR) amplifies the electrical activity of nerves at the stump of amputees by redirecting them in remnant muscles above the amputation. The electrical activity of the reinnervated muscles can be used to extract natural control signals. Nonetheless, current control systems, mainly based on noninvasive muscle recordings, fail to provide accurate and reliable control over time. This is one of the major reasons for prosthetic abandonment. This prospective interventional study includes three unilateral above-elbow amputees and reports the long-term (2.5 years) implant of wireless myoelectric sensors in the reinnervation sites after TMR and their use for control of robotic arms in daily life. It therefore demonstrates the clinical viability of chronically implanted myoelectric interfaces that amplify nerve activity through TMR. The patients showed substantial functional improvements using the implanted system compared with control based on surface electrodes. The combination of TMR and chronically implanted sensors may drastically improve robotic limb replacement in above-elbow amputees.

Copyright © 2019
The Authors, some
rights reserved;
exclusive licensee
American Association
for the Advancement
of Science. No claim
to original U.S.
Government Works

INTRODUCTION

Robotic arm replacement in above-elbow amputees is challenging (1). Cumbersome control, poor and unreliable myosignal quality, as well as uncomfortable and mechanically unstable sockets determine the high rates of prosthesis abandonment reported in upper limb amputees (2, 3). The success of targeted muscle reinnervation (TMR) (4) and the development of multiple degree-of-freedom (DOF) prosthetic devices have highlighted the limitations of the current man-machine interface (5, 6). Prosthetic hardware, including multi-articulating hands, is more advanced than the available strategies to control these mechatronic devices (7).

Prosthetic arms are clinically controlled by surface electromyographic (EMG) signals recorded by electrodes placed on the skin overlying remnant muscles above the amputation (8, 9). With this approach, only superficial muscles in the residual limb can be used for prosthetic control. Moreover, the surface EMG signal quality depends on loading of the prosthesis, causing soft tissue displacement, changing contact pressure, and movement between the skin surface and the electrodes, and is influenced by environmental conditions, skin texture, and perspiration. In addition, in TMR patients with up to six myoelectric sites, surface EMG recordings are susceptible to myoelectric cross-talk that reduces the number of independent control sites (10).

Despite the limitations of surface EMG as source of control signals, the increased number of EMG sites achieved by TMR surgery using

selective nerve transfers enables prosthetic control in a more intuitive manner than with naturally innervated muscles alone (11). The functional benefit of TMR in above-elbow amputees compared with conventional myoelectric or body-powered prostheses has been previously shown (1, 4, 12). Yet, it is well known that prosthetic control is challenging in these patients, even after TMR (1). Therefore, the rate of abandonment of prostheses in above-elbow amputees is particularly high.

To improve the man-machine interface in above-elbow amputees, a direct skeletal attachment penetrating the skin has been proposed (10, 13). With this attachment, wires can pass through the percutaneous port of an osseointegrated system (10). Although some of these solutions are promising, percutaneous interfaces disturb the skin barrier, resulting in the risk of superficial and deep infections as well as wire breakage, unstable connectors, and possible subsequent need for surgical intervention (10, 14).

Here, we establish a man-machine interface for robotic arm control in above-elbow amputees based on a wireless implantable myoelectric sensor (IMES) system originally developed by Weir and colleagues (15) and then by the Alfred Mann Foundation (California, USA) (16). IMESs are implants with a ceramic housing of cylindrical shape, 16-mm long and 2.5 mm in diameter, and metal end caps acting as electrodes for recording intramuscular EMG (16). The IMESs wirelessly transmit EMG data to the prosthesis and are powered by inductive coupling using an external coil integrated into the prosthetic socket. Despite the potential high impact of IMES for man-machine interfacing in robotics, so far, there has been only one case report of their use in humans (16). This previous study reported on the use of IMES in a below-elbow amputee using naturally innervated EMG signals (16). In this study, we present the long-term implant of IMES in conjunction with TMR and in above-elbow amputees, for whom recovery of function is much more challenging than in below-elbow amputees. The aim was therefore to evaluate whether long-term implants of intramuscular sensors can pick up and transmit neural information after selective nerve transfers for establishing natural prosthetic control in the limited space available in above-elbow amputees.

¹Division of Plastic and Reconstructive Surgery, Department of Surgery, Medical University of Vienna, Waehringer Guertel 18-20, A-1090 Vienna, Austria. ²Christian Doppler Laboratory for Restoration of Extremity Function, Medical University of Vienna, Waehringer Guertel 18-20, A-1090 Vienna, Austria. ³Department of Bioengineering, Royal School of Mines, Imperial College London, South Kensington Campus, Kensington, London SW7 2AZ, UK. ⁴Otto Bock Healthcare Products GmbH, Brehmstraße 16, A-1110 Vienna, Austria. ⁵Alfred Mann Foundation, 25134 Rye Canyon Loop #200, Valencia, CA 91355, USA. ⁶Deanery of Clinical Sciences, The University of Edinburgh, Scotland, UK. ⁷Department of Plastic & Reconstructive Surgery, NHS Lothian, Scotland, UK. ⁸Department of Physical Medicine and Rehabilitation, Medical University of Vienna, Waehringer Guertel 18-20, A-1090 Vienna, Austria.

*Corresponding author. Email: oskar.aszmann@meduniwien.ac.at

We provide clinical outcome results over a period of >2.5 years for an implanted wireless system after selective nerve transfers in a case series of three above-elbow amputees.

RESULTS

IMES and TMR surgery

In the three patients, implantation of the IMES combined with TMR surgery was successfully performed 1.03 ± 0.50 years after the amputation. Depending on the number of available target muscles, five to six IMESs were used.

For TMR surgery, our standard nerve transfer matrix (Table 1) was used in all three patients (5). Because of the short length of the residual stump, the brachioradialis muscle was not present in one of the patients (patient II), and thus, only five instead of six individual myosignals could be established. The nerve coaptation was performed between 1.5 and 2.5 cm from the epimysium. An IMES was implanted in each targeted muscle as well as available natively innervated muscles. Therefore, six IMESs were implanted in patients I and III and five IMESs were implanted in patient II. In this way, patients I and III had a distinct muscle with an implanted sensor for each prosthetic function (Table 1). Patient II distinguished between pronation and supination using low or high contraction force of the brachialis muscle.

The IMESs were placed intramuscularly near the motor entry point of the targeted muscle. At the end of the surgery, a communication test verified proper function of each sensor. The position of each IMES was evaluated with x-rays in the anterior/posterior and lateral axis. Immediate and 1-year postoperative x-ray showed no migration or axial rotation of the sensors (Fig. 1, A and B).

Myosignals

During the time of reinnervation of the targeted muscles, the patients were able to use the natively innervated long head of the biceps and the long/medial head of the triceps as myosignals for prosthetic control. Once the postoperative soft tissue swelling had resolved and stump circumference measures were stable, patients were fitted with a telemetry test socket using the two natively innervated EMG signals. The circumference was measured at the midway between the axillary fold and the distal stump end. Preoperatively, the three patients showed a mean circumference of 31.5 cm. Eight weeks after surgery, the soft tissue swelling had resolved, and the stump circumference measures (in mean, 32.67 cm) had almost returned to pre-operative levels. These measures were stable afterward, except from patient I, where body weight changes led to stump volume changes. Over time, as the new signal sites emerged, they were progressively

integrated into the control algorithm. The final prosthetic fitting with small socket adjustments was completed at 20, 12, and 10 months postoperatively in the three patients, respectively. The longer time in patient I was due to weight changes of the patient and resulting stump volume changes. Because of this socket issue, patient I missed two of five scheduled outcome measurements.

The first TMR myosignals were detected via IMES 3 months postoperatively, whereas surface EMG electrodes provided useful signals only after 6 months. Between 3 and 4 months postoperatively, all newly established myosignals could be detected in all patients with the IMES. At 5 months, all implanted sensors could actively be integrated for prosthetic control. Prosthetic control was based on the direct association between myosignals and prosthetic DOF (direct control). The gains of the IMES were adjusted during the first 6 months only. All other adjustments (threshold values and speed of prosthetic movement) were performed during the prosthetic fitting and never retuned. The procedure used for optimizing control was the same regardless of technology used for EMG recording, IMES, or surface electrodes.

The rehabilitation started immediately after surgery with training of posture and mirror therapy. As soon as the first new myosignals were detected, a previously described rehabilitation program was initiated to improve control of the individual TMR signals (17).

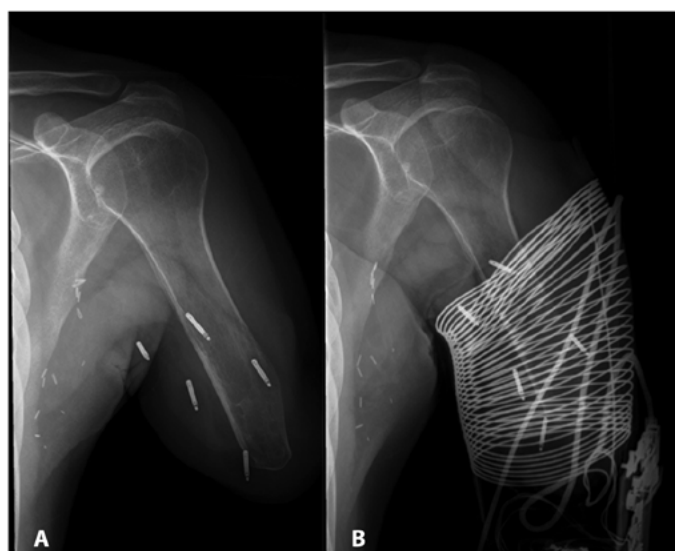


Fig. 1. Implants and magnetic coil. (A) X-ray of patient II with five IMES sensors implanted. (B) X-ray of patient II with telemetry socket (magnetic coil laminated within the socket) and the prosthetic device.

Table 1. TMR nerve transfer matrix for the above-elbow level of amputation.

| Targeted muscles | Nerves | Prosthetic function | Innervation |
|---------------------------------|-------------------------------|---------------------|-------------|
| M. biceps caput longum | N. musculocutaneous | Elbow flexion | Original |
| M. biceps caput breve | N. ulnaris | Hand close | Transferred |
| M. brachialis | N. medianus | Pronation | Transferred |
| M. triceps caput longum/mediale | N. radialis | Elbow extension | Original |
| M. triceps caput laterale | Split ramus prof. N. radialis | Hand open | Transferred |
| M. brachioradialis | Split ramus prof. N. radialis | Supination | Transferred |

Table 2. Functional outcome using SHAP, BBT, CPRT, and AC. NA, not available.

| Patient | SHAP | | | BBT | | | CPRT | | | AC | | |
|---------|-------|-------|---------|------|-------|---------|--------|-------|---------|------|---------|--|
| | Pre | IMES | Surface | Pre | IMES | Surface | Pre | IMES | Surface | IMES | Surface | |
| 1 | 39 | 45 | 27 | 12 | 12 | 11 | 86.98 | 26 | 43.33 | 2.83 | 2.33 | |
| 2 | 36 | 44 | 23 | 9 | 10 | 3.33 | 49.38 | 42.06 | NA | 2.95 | 2.22 | |
| 3 | 24 | 52 | 45 | 2 | 15 | 6.67 | 117.00 | 14.67 | 37.58 | 3 | 2.33 | |
| Mean | 33.00 | 47.00 | 31.67 | 7.67 | 12.33 | 7.00 | 84.45 | 27.58 | 40.46 | 2.93 | 2.29 | |
| SD | 7.94 | 4.32 | 11.72 | 5.13 | 2.52 | 3.85 | 33.88 | 13.76 | 4.07 | 0.09 | 0.06 | |

Table 3. Patient demographics.

| Patient | Age at amputation | Side of amputation | Dominant hand before amputation | Years from amputation to surgery | Follow-up from surgery (years) | Time from surgery to evaluation (years) | Nature of loss | Number of IMES implanted |
|---------|-------------------|--------------------|---------------------------------|----------------------------------|--------------------------------|---|---------------------|--------------------------|
| 1 | 15.92 | Right | Right | 1.08 | 3.00 | 3.00 | Traffic accident | 6 |
| 2 | 31.42 | Left | Right | 1.50 | 2.75 | 2.00 | Motorcycle accident | 5 |
| 3 | 47.17 | Right | Right | 0.50 | 2.50 | 1.92 | Machine accident | 6 |
| | 31.50 | | | 1.03 | 2.75 | 2.31 | | |
| | 15.63 | | | 0.50 | 0.25 | 0.60 | | |

This process is essential for any patient having received selective nerve transfers (17). The three patients received 15, 22, and 28 hours of specific TMR rehabilitation within the complete follow-up process after surgery. At the last follow-up visit at 3, 2.75, and 2.5 years post-operatively, all IMES showed reliable communication. In addition, no events of disconnection between the sensors and the prosthetic device were reported by the patients or were identified during functional assessments.

Functional outcomes

The most effective way of testing man-machine interfacing systems for robotic limb control is through clinical tests that provide direct functional measures of outcome (18). We therefore mainly focused on clinical functional tests for assessing the performance of the system and its clinical impact. The functional outcome scores are summarized in Table 2. Final functional outcome measurements took place 2.31 ± 0.60 years after TMR and IMES surgery (Table 3 and movie S1). These evaluations were performed on two consecutive days. In the first day, the telemetric IMES prosthesis was used, whereas in the second day the surface EMG control was tested, as a reference. In addition, all patients were tested preoperatively with their standard two-signal surface EMG prosthetic device, and these results were used as baseline measurements. The patients showed improvements in Southampton Hand Assessment Procedure (SHAP) of 15.4, 22.2, and 116.7% using TMR signals and implantable electrodes compared with the baseline measurements. However, patients I and II showed declines in performance of 30.8 and 36.1% using TMR signals and surface electrodes compared with the baselines (surface electrodes and no TMR), whereas patient III showed an improvement of 187.5% with TMR and surface electrodes. With respect to baselines, the times needed to complete the Clothespin-Relocation Test (CPRT)

decreased by 70.1, 8.3, and 87.4% with TMR and IMES, but only by 50.2 and 67.9% with TMR and surface electrodes, with respect to baselines. Patient II could not perform the test when using TMR and surface electrodes. The numbers of transferred blocks in the Box and Blocks Test (BBT) increased in patients II and III by 11.1 and 650% but decreased by 5.6% in patient I using TMR and IMES compared with baselines. Using TMR and surface electrodes, the transferred blocks decreased by 8.3 and 63.0% in patients I and II and increased by 233.5% in patient III compared with baselines. In addition, using surface electrodes, the accuracy test (AC) decreased by 17.3, 24.7, and 22.3% compared with the use of TMR signals with implanted electrodes (movie S2). During the rehabilitation process, longitudinal assessments were performed on the patients. Figure 2 documents the learning curve in SHAP, CPRT, BBT, and AC within this time.

DISCUSSION

The use of implantable intramuscular sensors enables the extraction and transmission of neural signals after selective nerve transfers in above-elbow amputees, resulting in intuitive and dexterous control of robotic arms. Because of the intramuscular placement, signals are independent of loading and position of the prostheses. For the same reason, these signals can be detected early after nerve transfer surgery with significant decrease in rehabilitation time. Here, we have reported on the long-term use of an implanted wireless system for dexterous and intuitive prosthetic control in three above-elbow amputees after TMR surgery. The results showed improvement in prosthetic function using the combination of implantable electrodes together with nerve transfers with respect to the current clinical state of the art. As a necessary first step in showing the potential of the muscle implanted technology, the study was limited by the number of participants

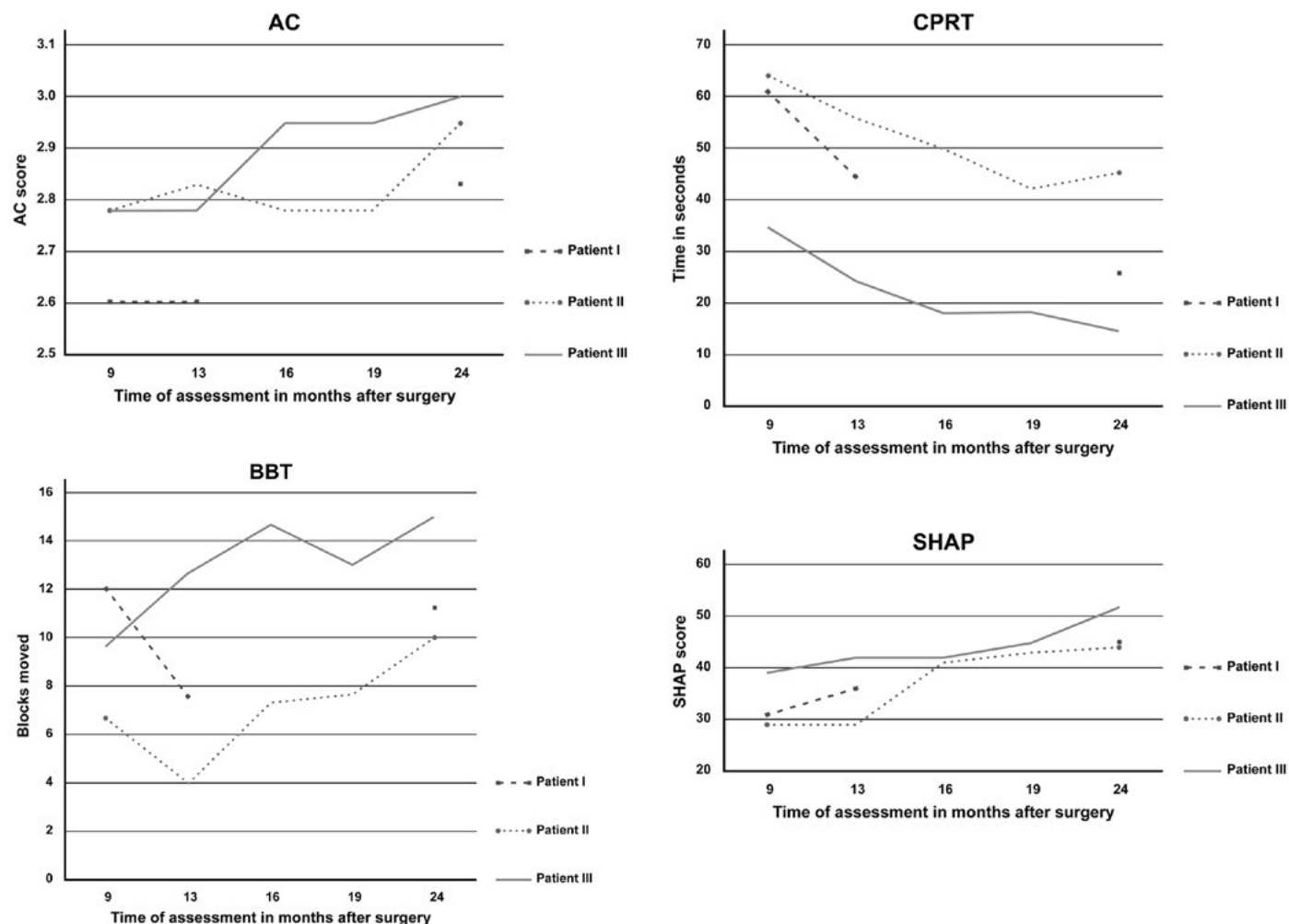


Fig. 2. Learning curves for SHAP, CPRT, BBT, and AC during the rehabilitation when using IMES for control.

and sessions, which hindered the possibility of statistical analyses and provided descriptive results. This limitation is common to previous studies testing implantable systems. Nonetheless, the clinical impact of these results is evident and paves the way to further research on larger clinical samples.

As opposed to below-elbow amputees, in above-elbow amputees, there are no naturally innervated muscles for the control of hand function. However, in these patients, the neural signals for hand and arm function are still available and thus can be manifested within the targeted muscles after nerve transfers. The challenge is the limited space for electrode location and signal cross-talk. Therefore, standard surface electrodes provide poor control signals for prosthetic control in this patient population (10). Moreover, in classic myo-control by surface electrodes, and especially in TMR patients with multiple signal sites, finding the best location for surface EMG sensors is difficult and time consuming. Incorrect placement of the surface electrodes substantially influences the control performance. In addition, contact loss due to limb movement or loading of the socket can result in malfunction of the robotic device. As a consequence, threshold values are used to discriminate between volitional EMG signals and background noise and artefacts. The use of a threshold determines the need for relatively strong muscular contractions,

which limits the accuracy in proportional myoelectric control and may result in fatigue (10, 19). The fact that two of three patients within this study showed higher SHAP scores using conventional two-signal control preoperatively compared with TMR and surface electrodes postoperatively indicates that a greater number of myosignals are only useful if signal recording and transmission are accurate and precise. In most of the tasks of the SHAP, patients only need to control one DOF; therefore, they do not need to change control between the different prosthetic joints. The advantage of TMR is more noticeable in the CPRT, where all patients improved after TMR surgery. In BBT, the patients did not use the prosthetic elbow most of the time at the baseline assessment. Thus, the improvement after TMR was limited. There was a positive learning curve in the different assessments showing the success of rehabilitation after TMR surgery using telemetric signals. Still, at the end of the rehabilitation process, functional outcomes showed remarkable improvements using IMES compared with surface electrodes tested on two consecutive days.

The housing of the IMES sensor was previously used in an implantable microstimulation device (the BION) for poststroke hemiplegic patients with shoulder subluxation (20). The BIONs showed no migration over long periods of time and were well tolerated (21). This was also confirmed in this study with a follow-up of 2.75 ± 0.25 years.

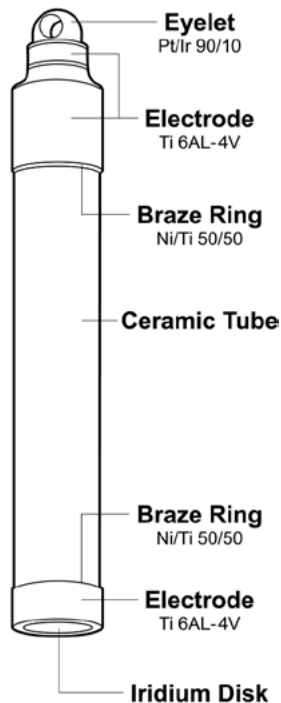


Fig. 3. Schematic drawing of the IMES sensor.

Continuous use of the prosthetic device requires constant signal transmission, resulting in increased power support (7). To optimize energy consumption, the IMES sensors were placed close to each other in the longitudinal axis to decrease the width of the coil. Because the IMESs were implanted directly at the reinnervation sites, they recorded EMG signals with high sensitivity immediately after reinnervation. The nerve coaptation was performed between 1.5 and 2.5 cm from the epimysium, and the first myosignals were detected already at 3 months after surgery. The early signal detection allowed starting the rehabilitation program earlier and therefore reducing the time from surgery to fully functional control of the prosthesis. Whereas the time from surgery to the final fitting using surface electrodes is about 1 year (5), prosthetic fitting and control of three DOFs was achieved after only 5 ± 1 months in the three patients of this study.

The implanted sensors have originally been designed to be placed using an ultrasound-guided minimal invasive technique. However, because the TMR surgery changes the muscle and nerve anatomy and all relevant structures are identified during this procedure, in this study, the implantation was performed during the TMR surgery. Thus, the IMES could be placed intramuscularly near the motor entry point of the targeted muscle. This would also be valid for regenerative peripheral nerve interfaces, where the information of single-nerve fascicles could potentially be used for prosthetic control (22).

Recent control systems for TMR patients based on pattern recognition algorithms showed significantly improved performance with respect to direct control and have the potential to be further improved (23). Pattern recognition is mostly needed because of unreliable control with surface EMG. In patients with IMES, however, the signal quality from the implanted sensors is superior to that from surface systems and allows for direct simultaneous and proportional control without retraining (23, 24). The use of implantable sensors will have future impact on the surgical procedure of TMR, because these sensors can record from deep and small muscles that can become new targets for nerve transfers.

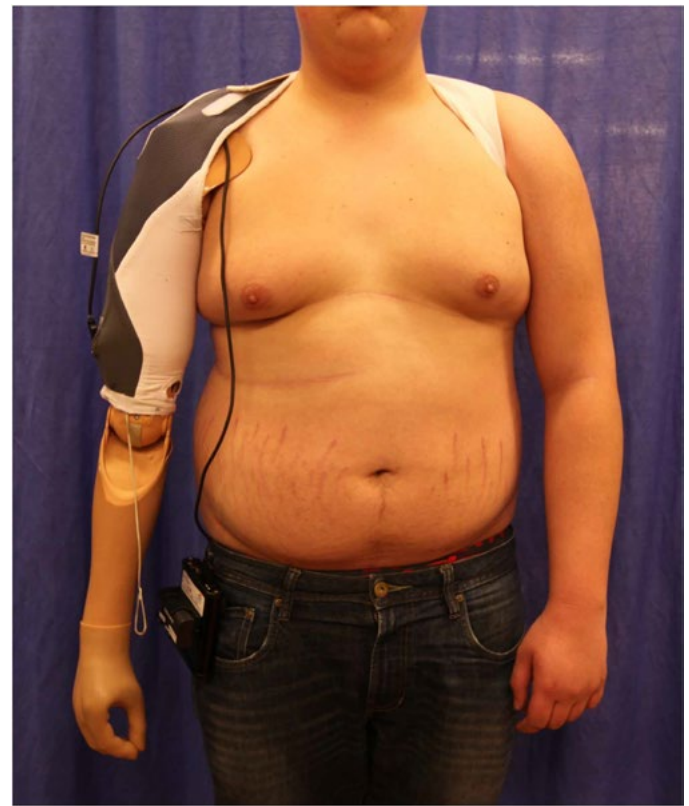


Fig. 4. Patient I wearing the IMES system.

Implanted sensors in muscles have been used for prosthetic control in chronic applications by wired transmission through the percutaneous metal implant of an osseointegrated prosthesis (10). The proposed combination of TMR and IMES does not include a percutaneous interface, making it a safe procedure without the constant risk of infection. Moreover, an alternative approach to extracting neural control signals is to establish a direct nerve interface (25). However, wireless and stable transmission of nerve signals for control has not been achieved yet. Moreover, reinnervation of severed nerves is necessary in most cases to remove neuromas (10), and once a target muscle is innervated, the muscle signals provide information on the nerve activity with greater signal-to-noise ratio and stability than a nerve interface. Last, high-density surface EMG systems have been proposed to decode nerve activity from reinnervated muscles (26). These systems have the potential to increase the information transfer for the man-machine interface (27) but have the same limitations as classic bipolar surface EMG electrodes in terms of robustness to change in shape of the soft tissue with respect to the underlying muscles. An implanted version of high-density EMG systems may provide in the future a further improvement in prosthesis control (28).

The current IMES system is not compatible with metal implants at the stump region. Thus, surgical procedures such as angulation osteotomy or osseointegration cannot be currently combined with the implantable system used in this study. In addition, because the coil has to be placed circumferentially around the stump, short above-elbow amputations or shoulder disarticulations cannot be treated with the current system. Furthermore, currently, no more than six IMESs, corresponding to direct control of three DOFs of the prosthetic device, can be used concurrently, with low transmission rate

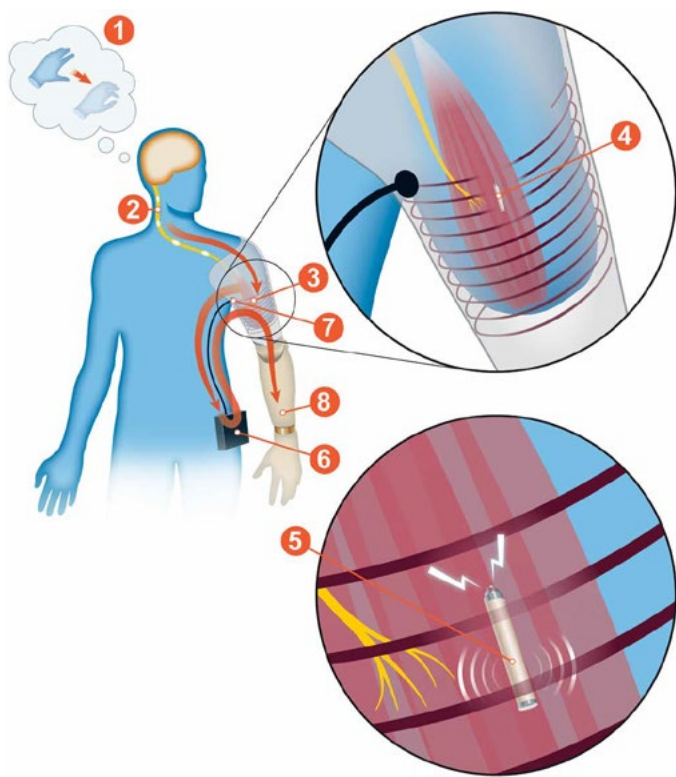


Fig. 5. Schematic signal pathway. To perform a specific motion of the prosthetic arm, the patient is thinking of this movement (1). This creates an impulse along the responsible nerve (2) and leads to a contraction of a specific muscle belly (3). The produced EMG signal is then recorded, rectified, and integrated within the IMES sensor (4). Via telemetry using a magnetic coil around the stump, these signals are transferred to the control unit, and forward telemetry is used to transmit power and configuration settings to the sensors (5). Within the belt-worn control unit, the preprocessed rectified EMG data (6) of the IMES are sent to the prosthesis (7), and the desired movement of the prosthetic device is performed (8).

that imposes the transmission of rectified and averaged EMG rather than the raw signals. This limits the use of the current system for future pattern recognition technologies that may require feature extraction from raw EMG signals. Thus, this study focused on the clinical prosthetic performance of the patients. In addition, because the sensors are passive devices, it is currently not possible to use them for stimulating to enable sensory feedback.

The combination of an implanted wireless system with TMR surgery, reported here for long-term clinical applications, represents a major milestone in prosthetic control. It eliminates some of the major reasons for prosthetic abandonment, such as cumbersome control and unreliable signal uptake. Moreover, IMES placement can be done at the time of the TMR surgery, with no need for an additional intervention and can provide excellent results after brief rehabilitation periods, as shown in this study. Yet, clinical challenges remain, such as the mechanical attachment of the prosthetic device or the establishment of a sensory feedback, for which current solutions are not yet optimal (10, 29–32).

MATERIALS AND METHODS

Study design

Three patients were implanted with IMES while undergoing routine TMR surgery to demonstrate functional benefits and stability over

time of intramuscular recorded EMG for prosthetic control. This prospective, self-controlled, nonrandomized interventional study was approved by the Austrian Agency for Health and Food Safety (approval no. TH-IMES 040714) and the local institutional review board (EK-number 1320/2014) as well as registered at clinicaltrials.gov (NCT03644394). All three patients gave written informed consent to take part in this study. Surgery in all three cases was performed by the senior author (O.C.A.).

The inclusion criteria were unilateral, above-elbow limb loss of half or greater residual upper arm length as determined by the contralateral side, age 16 or older, who were current users of a myoelectric prosthesis and qualified for TMR surgery. In addition, the patients had to be within the governmental insurance system and live within 3 hours from the study center. Potential patients were excluded because of an active implant (e.g., pacemaker, implanted cardiac defibrillator, neurostimulator, and drug infusion device), any metal implants located within the residual upper limb (e.g., screws, plates, and nails), or visual impairments or if they did not qualify for TMR surgery (1, 5).

Three consecutive patients who met all inclusion criteria were referred from a local prosthetic technician. They suffered a traumatic above-elbow amputation at the ages of 16, 31, and 47 years. All were male. Limb loss of the dominant right arm ($n = 2$) and nondominant left arm ($n = 1$) was due to high-velocity traffic accidents ($n = 2$) or a work-related injury with a hydraulic press ($n = 1$) (Table 3).

Materials

Each IMES (Alfred Mann Foundation, California, USA) is about 2.5 mm in diameter and 16-mm long, can be inserted into a muscle during the TMR surgery, and acts as an independent differential amplifier consisting of custom electronics housed within a biocompatible, hermetically sealed ceramic cylinder with titanium end caps (16, 33). The end caps serve as electrodes for picking up EMG activity during muscle contraction. Each sensor detects EMG signals in a frequency band between 4.4 and 2200 Hz (Fig. 3). The signals are then rectified and integrated (10-Hz cutoff frequency) within the IMES, and the resulting EMG envelope is digitized at a sampling rate of 72 samples per second. The latency from detection of the EMG signal to telemetry controller output is 100 ms. Reverse telemetry (via a coil around the arm) is used to transfer data from the implanted sensor, and forward telemetry is used to transmit power and configuration settings to the sensors. The coil and associated electronics are housed within the socket of the prosthesis. A control system, the prosthetic control interface that sends the preprocessed rectified data of the IMES associated with muscle contraction as inputs of the prosthesis, is housed in a belt-worn, battery-powered device. A cable attaches the control unit to the prosthetic socket. One IMES is implanted into each targeted muscle during the TMR surgery and used to control one function of the prosthetic arm. Therefore, two IMESs are needed for each DOF (Figs. 4 and 5).

All three patients of this study were fitted with DynamicArm Plus, Electric Wrist Rotator, and SensorHand Speed (Otto Bock HealthCare GmbH, Germany), resulting in three DOFs (elbow, wrist, and hand). This prosthetic arm was used on a daily basis by the three patients during the entire study period using the signals from the implanted electrodes for control.

TMR and implantation surgery

The implantation of the IMES was performed under general anesthesia during TMR surgery. Through a medial approach, the median,

ulnar, and musculocutaneous nerve were prepared and dissected. The motor branches to the medial and lateral head of the biceps and to the brachial muscle were identified. Dissection and separation of the different branches are important, and stimulation of the different branches should only provoke twitches in the targeted muscles selectively. Once the target muscles with their branches were identified, the short head of the biceps muscle was detached from its origin at the coracoid process to displace it to the medial distal aspect of the stump and separate it clearly from the long head of the biceps. The donor nerves have to be neurotomized at least to a level of palpable healthy fascicles. Through a second incision on the radial aspect of the above-elbow stump, blunt dissection between the triceps heads was performed to displace the lateral head and further dissect its muscle branch and the distal radial nerve until it ends in the distal neuroma. In patients I and III, with long stumps and the presence of the brachioradialis muscle, the distal radial nerve could be split along the fascicles in two parts, one to reinnervate the lateral head of the triceps and one to reinnervate the brachioradialis muscle to achieve separate signals for hand open and supination of the prosthetic device. The motor branches of the targeted muscles were transected close to the muscle to achieve a short regeneration time. The proximal part of the motor branches was transected a few centimeters back and buried deep to prevent it from reinnervating the targeted muscles. All nerve transfers were performed under loupe magnification in an end-to-end fashion using 8-0 or 9-0 ethilon sutures. The distal neuromas were not excised, because this would have implied additional dissection in regions of no interest. The nerve transfers and the corresponding prosthetic functions are reported in Table 1.

After the nerve transfers had been performed, a small incision (about 5 mm) was made into the epimysium and a probe was inserted. A cannulated dilator was advanced over the probe to reach the target implant position within the muscle. The implant depth was 46.25 ± 6.19 mm from the epimysium. The dilator and probe were then removed, leaving the sheath in place. A piece of absorbable suture was threaded through the eyelet end of the IMES to pull the sensor out in case of inappropriate placement. The IMES was then inserted into the muscle with a trocar. One resorbable suture was made to close the epimysium. The IMES should be aligned in parallel to the axis of the humerus for efficient signal and energy transmission between the coil and the IMES. However, a deviation of up to 45° to the humerus can be tolerated and does not limit signal transmission. Immediately after wound closure, a communication test with a test coil placed over the residual limb was performed to determine proper function of all implanted sensors.

Functional outcome measurements

Global upper extremity function was evaluated using SHAP (34), CPRT, (4), and BBT (35), which monitor hand and extremity function closely related to activities of daily living. The SHAP has been validated for assessment of pathological and prosthetic hand function, where normal hand function is regarded as equal to or above 100 points (34). For the CPRT, the time is recorded as the patient moves three clothespins from a horizontal to a vertical bar. The mean of three repetitions is calculated. The BBT measures unilateral gross manual dexterity. It is made up of a wooden box divided into two compartments, one filled with 100 blocks. The BBT score is equal to the number of cubes transferred from one compartment to another in 1 min (35). To evaluate the accuracy of the intended movement/myosignal, we asked the patient to execute a series of tasks with the activation of

the three DOFs separately. Each task was repeated three times (16). The patient scored three points when the intended movement was observed without any additional unintended movement, two points when additional movements were observed, and only one point when unintended movements were observed but not the intended one. Therefore, the maximum score was three.

The tests used for evaluating performance of the system have been selected because they provide a direct clinical information on functional gains. Other offline tests or tests in virtual reality environments were excluded because they have been shown to be poorly associated to the recovery of function (18). The results of the study provide a clinical evaluation of muscle implants for robotic arm control and indicate achievements superior to the current clinical state of the art.

Before IMES and TMR surgery, the patients were tested with their prosthetic device using a two-signal control with biceps and triceps and standard surface EMG electrodes. Nine months after the final fitting of the telemetry socket, a standard prosthesis with surface electrodes using the TMR signals was also created for comparison with the control system based on IMES. At this time, prosthetic functional outcome was evaluated in the three patients using both surface and implantable electrodes.

All outcome measures (SHAP, CPRT, BBT, and AC) were assessed by the same experienced physical therapist for all participants. The different outcomes measures were performed within one visit to the clinical laboratory. Assessment started with the SHAP, because this is the most time-consuming test, and was continued with the other measures after a break of 15 to 30 min. In case of fatigue, the patients had the opportunity to take a break at any time during the entire assessments. A randomization of the measurements was not performed.

SUPPLEMENTARY MATERIALS

robotics.sciencemag.org/cgi/content/full/4/32/eaaw6306/DC1

Movie S1. SHAP and CPRT of patient II.

Movie S2. Accuracy test of patient III with six myosignals and surface electrodes compared with implanted electrodes.

REFERENCES AND NOTES

1. G. A. Dumanian, J. H. Ko, K. D. O'Shaughnessy, P. S. Kim, C. J. Wilson, T. A. Kuiken, Targeted reinnervation for transhumeral amputees: Current surgical technique and update on results. *Plast. Reconstr. Surg.* **124**, 863–869 (2009).
2. T. W. Wright, A. D. Hagen, M. B. Wood, Prosthetic usage in major upper extremity amputations. *J. Hand Surg. Am.* **20**, 619–622 (1995).
3. D. Datta, J. Kingston, J. Ronald, Myoelectric prostheses for below-elbow amputees: The Trent experience. *Int. Disabil. Stud.* **11**, 167–170 (1989).
4. T. A. Kuiken, G. A. Dumanian, R. D. Lipschutz, L. A. Miller, K. A. Stubblefield, The use of targeted muscle reinnervation for improved myoelectric prosthesis control in a bilateral shoulder disarticulation amputee. *Prosthet. Orthot. Int.* **28**, 245–253 (2004).
5. S. Salninger, A. Sturma, M. Herceg, O. Riedl, K. Bergmeister, O. C. Aszmann, Prosthetic reconstruction in high amputations of the upper extremity. *Orthopade* **44**, 413–418 (2015).
6. S. M. Tintle, M. F. Baechler, G. P. Nanos, J. A. Forsberg, B. K. Potter, Traumatic and trauma-related amputations: Part II: Upper extremity and future directions. *J. Bone Joint Surg. Am.* **92**, 2934–2945 (2010).
7. M. Ortiz-Catalan, R. Bränemark, B. Häkansson, J. Delbeke, On the viability of implantable electrodes for the natural control of artificial limbs: Review and discussion. *Biomod. Eng. Online* **11**, 33 (2012).
8. A. D. Roche, H. Rehbaum, D. Farina, O. C. Aszmann, Prosthetic myoelectric control strategies: A clinical perspective. *Curr. Surg. Rep.* **2**, 44 (2014).
9. D. Farina, O. Aszmann, Bionic limbs: Clinical reality and academic promises. *Sci. Transl. Med.* **6**, 257ps12 (2014).
10. M. Ortiz-Catalan, B. Häkansson, R. Bränemark, An osseointegrated human-machine gateway for long-term sensory feedback and motor control of artificial limbs. *Sci. Transl. Med.* **6**, 257re6 (2014).
11. O. C. Aszmann, H. Dietl, M. Frey, Selective nerve transfers to improve the control of myoelectrical arm prostheses. *Handchir. Mikrochir. Plast. Chir.* **40**, 60–65 (2008).

12. K. D. O'Shaughnessy, G. Dumonian, R. Lipschutz, L. Miller, K. Stubblefield, T. Kuiken, Targeted reinnervation to improve prosthesis control in transhumeral amputees: A report of three cases. *J. Bone Joint Surg. Am.* **90**, 393–400 (2008).
13. J. A. Hoffer, G. E. Loeb, Implantable electrical and mechanical interfaces with nerve and muscle. *Ann. Biomed. Eng.* **8**, 351–360 (1980).
14. J. Tillander, K. Hagberg, Ö. Berlin, L. Hagberg, R. Bränemark, Osteomyelitis risk in patients with transfemoral amputations treated with osseointegration prostheses. *Clin. Orthop. Relat. Res.* **475**, 3100–3108 (2017).
15. R. F. Weir, P. R. Troyk, G. Demichele, D. Kerns, Technical details of the implantable myoelectric sensor (IMES) system for multifunction prosthesis control. *Conf. Proc. IEEE Eng. Med. Biol. Soc.* **7**, 7337–7340 (2005).
16. P. F. Pasquina, M. Evangelista, A. J. Carvalho, J. Lockhart, S. Griffin, G. Nanos, P. McKay, M. Hansen, D. Ipsen, J. Vandersea, J. Butkus, M. Miller, I. Murphy, D. Hankin, First-in-man demonstration of a fully implanted myoelectric sensors system to control an advanced electromechanical prosthetic hand. *J. Neurosci. Methods* **244**, 85–93 (2015).
17. A. Sturma, M. Herceg, B. Bischof, V. Fialka-Moser, O. C. Aszmann, Rehabilitation following targeted muscle reinnervation in amputees, in *Replace, Repair, Restore, Relieve—Bridging Clinical and Engineering Solutions in Neurorehabilitation*, W. Jensen, O. K. Andersen, M. Akay, Eds. (Springer, 2014), pp. 169–177.
18. I. Vujaklija, A. D. Roche, T. Hasenoehrl, A. Sturma, S. Amsuess, D. Farina, O. C. Aszmann, Translating research on myoelectric control into clinics—Are the performance assessment methods adequate? *Front. Neurorobot.* **11**, 7 (2017).
19. C. Almström, P. Herberts, L. Körner, Experience with Swedish multifunctional prosthetic hands controlled by pattern recognition of multiple myoelectric signals. *Int. Orthop.* **5**, 15–21 (1981).
20. A.-C. D. Salter, S. D. Bagg, J. L. Creasy, C. Romano, D. Romano, F. J. R. Richmond, G. E. Loeb, First clinical experience with BION implants for therapeutic electrical stimulation. *Neuromodulation* **7**, 38–47 (2004).
21. R. Davis, O. Sparrow, G. Cosendai, J. H. Burridge, C. Wulff, R. Turk, J. Schulman, Poststroke upper-limb rehabilitation using 5 to 7 inserted microstimulators: Implant procedure, safety, and efficacy for restoration of function. *Arch. Phys. Med. Rehabil.* **89**, 1907–1912 (2008).
22. M. G. Urbanchek, T. A. Kung, C. M. Frost, D. C. Martin, L. M. Larkin, A. Wollstein, P. S. Cederma, Development of a regenerative peripheral nerve interface for control of a neuroprosthetic limb. *Biomed. Res. Int.* **2016**, 5726730 (2016).
23. D. C. Tkach, A. J. Young, L. H. Smith, E. J. Rouse, L. J. Hargrove, Real-time and offline performance of pattern recognition myoelectric control using a generic electrode grid with targeted muscle reinnervation patients. *IEEE Trans. Neural Syst. Rehabil. Eng.* **22**, 727–734 (2014).
24. L. J. Hargrove, B. A. Lock, A. M. Simon, Pattern recognition control outperforms conventional myoelectric control in upper limb patients with targeted muscle reinnervation. *Conf. Proc. IEEE Eng. Med. Biol. Soc.* **2013**, 1599–1602 (2013).
25. S. Micera, J. Carpaneto, S. Raspovic, Control of hand prostheses using peripheral information. *IEEE Rev. Biomed. Eng.* **3**, 48–68 (2010).
26. D. Farina, H. Rehbaum, A. Holobar, I. Vujaklija, N. Jiang, C. Hofer, S. Salminger, H.-W. van Vliet, O. C. Aszmann, Noninvasive, accurate assessment of the behavior of representative populations of motor units in targeted reinnervated muscles. *IEEE Trans. Neural Syst. Rehabil. Eng.* **22**, 810–819 (2014).
27. T. Kapelner, N. Jiang, A. Holobar, I. Vujaklija, A. D. Roche, D. Farina, O. C. Aszmann, Motor unit characteristics after targeted muscle reinnervation. *PLOS ONE* **11**, e0149772 (2016).
28. K. D. Bergmeister, I. Vujaklija, S. Muceli, A. Sturma, L. A. Hruba, C. Prahm, O. Riedl, S. Salminger, K. Manzano-Szalai, M. Aman, M.-F. Russold, C. Hofer, J. Principe, D. Farina, O. C. Aszmann, Broadband prosthetic interfaces: Combining nerve transfers and implantable multichannel EMG technology to decode spinal motor neuron activity. *Front. Neurosci.* **11**, 421 (2017).
29. S. Salminger, A. Gradischar, R. Skiera, A. D. Roche, A. Sturma, C. Hofer, O. C. Aszmann, Attachment of upper arm prostheses with a subcutaneous osseointegrated implant in transhumeral amputees. *Prosthet. Orth. Int.* **42**, 93–100 (2016).
30. P. Svensson, U. Wijk, A. Björkman, C. Antfolk, A review of invasive and non-invasive sensory feedback in upper limb prostheses. *Expert Rev. Med. Devices* **14**, 439–447 (2017).
31. D. W. Tan, M. A. Schiefer, M. W. Keith, J. R. Anderson, J. Tyler, D. J. Tyler, A neural interface provides long-term stable natural touch perception. *Sci. Transl. Med.* **6**, 257ra138 (2014).
32. S. Raspovic, M. Capogrosso, F. M. Petrini, M. Bonizzato, J. Rigosa, G. di Pino, J. Carpaneto, M. Controzzi, T. Boretius, E. Fernandez, G. Granata, C. M. Oddo, L. Citi, A. L. Ciancio, C. Cipriani, M. C. Carrozza, W. Jensen, E. Guglielmelli, T. Stieglitz, P. M. Rossini, S. Micera, Restoring natural sensory feedback in real-time bidirectional hand prostheses. *Sci. Transl. Med.* **6**, 222ra19 (2014).
33. R. F. Weir, P. R. Troyk, G. A. DeMichele, D. A. Kerns, J. F. Schorsch, H. Maas, Implantable myoelectric sensors (IMESs) for intramuscular electromyogram recording. *IEEE Trans. Biomed. Eng.* **56**, 159–171 (2009).
34. P. J. Kyberd, A. Murgia, M. Gasson, T. Tjerkens, C. Metcalf, P. H. Chappell, K. Warwick, S. E. M. Lawson, T. Barnhill, Case studies to demonstrate the range of applications of the Southampton Hand Assessment Procedure. *Br. J. Occup. Ther.* **72**, 212–218 (2009).
35. V. Mathiowitz, G. Volland, N. Kashman, K. Weber, Adult norms for the Box and Block Test of manual dexterity. *Am. J. Occup. Ther.* **39**, 386–391 (1985).

Acknowledgments: We would like to acknowledge the time and effort provided by the patients in this study. In addition, we would like to thank A. Cserenyi for the preparation of the illustration included in the manuscript. **Funding:** This work was supported by the Christian Doppler Research Foundation, a subdivision of the Austrian Federal Ministry of Economy, Family and Youth; the Austrian Council for Research and Technology Development; and the European Research Council (ERC) under European Union's Horizon 2020 research and innovation program (grant agreement no. 810346). **Author contributions:** S.S. and O.C.A. made substantial contributions to the concept, and C.H., M.E., and M.P. made substantial contributions to the design. S.S., A.S., C.H., and T.H. participated in data acquisition. S.S., A.S., C.H., M.E., M.P., K.D.B., A.D.R., T.H., and H.D. contributed to analyses. S.S., A.S., C.H., D.F., and O.C.A. interpreted data. Most of the report writing was completed by S.S., D.F., and O.C.A. However, all authors participated in drafting or revising content for important intellectual content and gave approval of the final version to be published. **Competing interests:** The authors declare that they have no competing interests. **Data and materials availability:** All data needed to evaluate the conclusions in the paper are present in the paper or the Supplementary Materials.

Submitted 10 January 2019

Accepted 20 June 2019

Published 17 July 2019

10.1126/scirobotics.aaw6306

Citation: S. Salminger, A. Sturma, C. Hofer, M. Evangelista, M. Perrin, K. D. Bergmeister, A. D. Roche, T. Hasenoehrl, H. Dietl, D. Farina, O. C. Aszmann, Long-term implant of intramuscular sensors and nerve transfers for wireless control of robotic arms in above-elbow amputees. *Sci. Robot.* **4**, eaaw6306 (2019).

eppendorf
& Science

PRIZE FOR NEURO BIOLOGY

Congratulations
to Lauren Orefice, Ph.D.
Assistant Professor
Massachusetts General Hospital
& Harvard Medical School



Meet the Winner

Eppendorf & Science Prize for Neurobiology

Congratulations to Lauren Orefice on winning the 2019 Eppendorf & Science Prize for her work on the causes and potential therapies for autism spectrum disorders. Dr. Orefice found that peripheral sensory neurons – neurons outside the brain – are key areas where autism-associated gene mutations have a critical impact. She showed how abnormal function of peripheral sensory neurons causes touch over-reactivity. She demonstrated how this over-reactivity during development contributes to altered brain function and some autism-related behaviors in mice. Dr. Orefice's work changes how we think about the causes of autism spectrum disorders, and highlights peripheral sensory neurons as a possible novel therapeutic target.

The annual US\$25,000 Eppendorf & Science Prize for Neurobiology honors scientists, like Dr. Orefice, for their outstanding contributions to neurobiological research. Lauren Orefice is the 18th recipient of this international award. She will be presented with the Prize at a ceremony held during the week of the 2019 Annual Meeting of the Society for Neuroscience in Chicago.

You could be next to win this prize.

If you are 35 years of age or younger and currently performing neurobiological research, you could be next to win the 2020 Prize. Deadline for entries is June 15, 2020.

Learn more at: www.eppendorf.com/prize

eppendorf **Science**
AAAS

NEUROSCIENCE

Pharmacologic inhibition of LIMK1 provides dendritic spine resilience against β -amyloid

Benjamin W. Henderson^{1,2}, Kelsey M. Greathouse^{1,2}, Raksha Ramdas^{1,2}, Courtney K. Walker^{1,2}, Tejeshwar C. Rao³, Svitlana V. Bach⁴, Kendall A. Curtis^{1,2}, Jeremy J. Day⁴, Alexa L. Mattheyses³, Jeremy H. Herskowitz^{1,2*}

Alzheimer's disease (AD) therapies predominantly focus on β -amyloid ($A\beta$), but $A\beta$ effects may be maximal before clinical symptoms appear. Downstream of $A\beta$, dendritic spine loss correlates most strongly with cognitive decline in AD. Rho-associated kinases (ROCK1 and ROCK2) regulate the actin cytoskeleton, and ROCK1 and ROCK2 protein abundances are increased in early AD. Here, we found that the increased abundance of ROCK1 in cultured primary rat hippocampal neurons reduced dendritic spine length through a myosin-based pathway, whereas the increased abundance of ROCK2 induced spine loss through the serine and threonine kinase LIMK1. $A\beta_{42}$ oligomers can activate ROCKs. Here, using static imaging studies combined with multielectrode array analyses, we found that the ROCK2-LIMK1 pathway mediated $A\beta_{42}$ -induced spine degeneration and neuronal hyperexcitability. Live-cell microscopy revealed that pharmacologic inhibition of LIMK1 rendered dendritic spines resilient to $A\beta_{42}$ oligomers. Treatment of hAPP mice with a LIMK1 inhibitor rescued $A\beta$ -induced hippocampal spine loss and morphologic aberrations. Our data suggest that therapeutically targeting LIMK1 may provide dendritic spine resilience to $A\beta$ and therefore may benefit cognitively normal patients that are at high risk for developing dementia.

INTRODUCTION

Cognitive decline in Alzheimer's disease (AD) is the result of synapse loss in brain regions that are critical for memory processes. Synapse or dendritic spine loss correlates more strongly with cognitive impairment in AD than β -amyloid ($A\beta$) or neurofibrillary tangle pathology, yet few therapeutic strategies target spines or synapses (1–8). Synaptic strength and activity are inseparably linked to spine morphology (9). Several discoveries indicate that spine structure remodeling is a plausible mechanism to maintain synapses and provide cognitive resilience in patients with an apolipoprotein E $\epsilon 4$ allele and/or AD pathology (7, 8). These findings emphasize dendritic spines as therapeutic substrates with potential to protect cognitively normal patients at high risk for dementia.

$A\beta$ induces dendritic degeneration of neurons, and these detrimental effects cause neuronal hyperexcitability by rendering neurons more electrically compact (10). This leads to aberrant circuit synchronization and ultimately cognitive impairment in patients with AD and human amyloid precursor protein (hAPP) mice (11–16). $A\beta$ likely wreaks havoc on the dendritic cytoskeleton by activating the RhoA guanosine triphosphatase (GTPase) and its primary downstream effectors: the Rho-associated protein kinase (ROCK) isoforms, ROCK1 and ROCK2 (17–19). ROCKs regulate actin-myosin-mediated cytoskeleton contractility (20–24), and increased activity of ROCKs could have detrimental consequences on dendritic spine remodeling (25). Furthermore, ROCK1 and ROCK2 protein abundances are increased among patients with mild cognitive impairment (MCI) and AD, implying that ROCKs may contribute to synaptic

loss in early disease stages (17, 26). Pharmacologic studies with fasudil and Y-27632, the most widely characterized pan-ROCK inhibitors, suggest beneficial effects of ROCK inhibitors in AD models (27, 28). However, these and other ROCK inhibitors are not isoform specific and can inhibit other AGC family kinases, including protein kinase A and protein kinase C (29). Moreover, critical questions remain regarding the role of ROCKs in AD and the contribution of ROCK1 or ROCK2 to the observed beneficial effects of pan-ROCK inhibitors. Collectively, these barriers have stalled ROCK inhibitors from entering clinical trials for AD. Here, we elucidated distinct isoform-specific mechanisms by which ROCKs may drive dendritic spine degeneration in MCI and AD and identified the ROCK2-LIM domain kinase isoform 1 (LIMK1) pathway as a key therapeutic avenue to provide dendritic spine resilience against $A\beta$.

RESULTS

ROCK1 and ROCK2 regulate dendritic spine length and density through isoform-specific mechanisms

Past studies showed that ROCK1 and ROCK2 protein abundances were increased in MCI and AD brains compared to age-matched pathology-free controls and that increased ROCKs were not the result of microglia or astrocyte accumulation in disease cases (17, 26). These results suggest that activity of ROCKs is increased early and remains increased in neurons throughout AD progression, possibly contributing to synapse loss. When ROCKs are active, neurite structural plasticity is repressed (30–33). Therefore, we hypothesized that increased protein abundance of ROCK1 or ROCK2 in neurons would induce detrimental AD-like structural effects on dendritic spines. To test this, rat hippocampal neurons were isolated at embryonic day 18 (E18) and cultured at high density on glass coverslips, as previously described (25). At 14 days in vitro (DIV 14), neurons were transiently cotransfected with plasmids encoding Lifeact-GFP (green fluorescent protein), a fluorescently tagged small actin-binding peptide (34), and ROCK1, ROCK2, or empty vector constructs (fig. S1A).

¹Center for Neurodegeneration and Experimental Therapeutics, University of Alabama at Birmingham School of Medicine, Birmingham, AL 35294, USA. ²Department of Neurology, University of Alabama at Birmingham School of Medicine, Birmingham, AL 35294, USA. ³Department of Cell, Developmental and Integrative Biology, University of Alabama at Birmingham School of Medicine, Birmingham, AL 35294, USA.

⁴Department of Neurobiology, University of Alabama at Birmingham School of Medicine, Birmingham, AL 35294, USA.

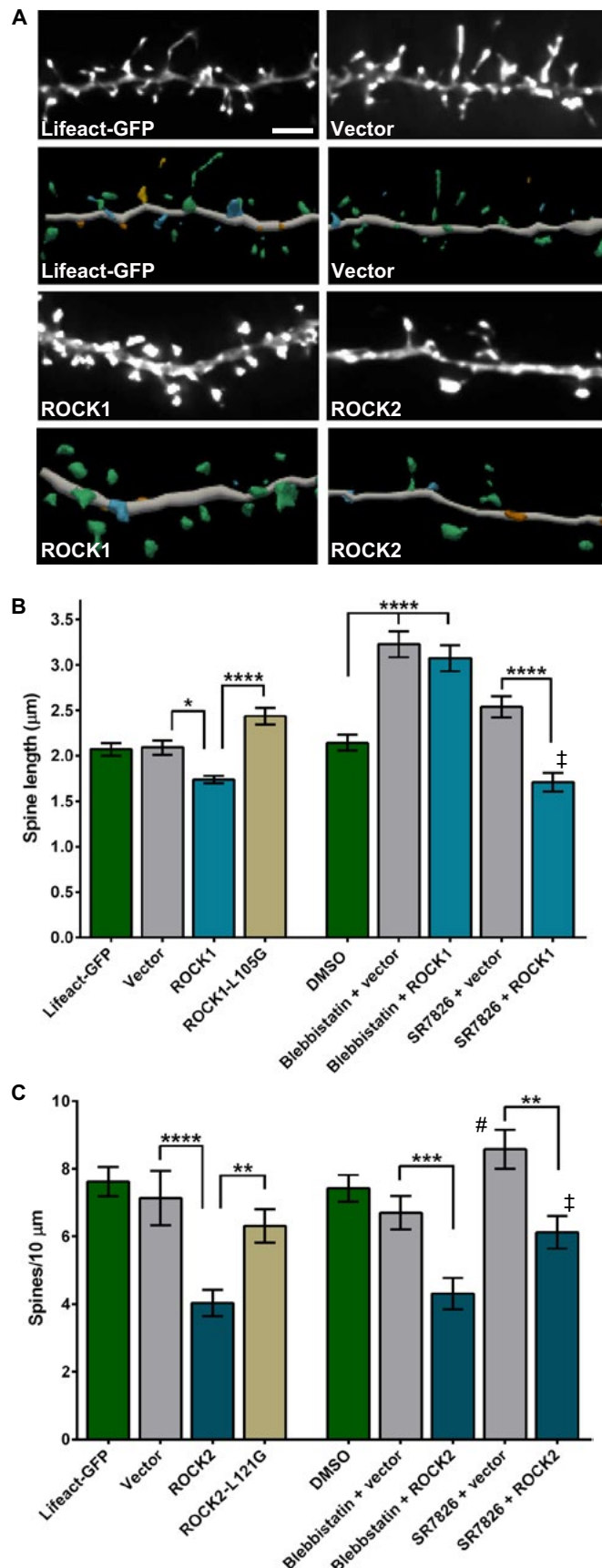
*Corresponding author. Email: jhersko@uab.edu

Copyright © 2019
The Authors, some
rights reserved;
exclusive licensee
American Association
for the Advancement
of Science. No claim
to original U.S.
Government Works

Fig. 1. ROCK1 and ROCK2 regulate dendritic spine length and density through isoform-specific mechanisms. (A) Representative maximum-intensity wide-field fluorescent images, after deconvolution, of hippocampal neurons expressing vector, ROCK1, or ROCK2 compared with the Lifeact-GFP control (top). Scale bar, 5 μ m. 3D digital reconstructions of dendrites (bottom). Reconstructions were generated in Neurolucida 360. $n = 10$ to 17 neurons (one dendrite per neuron) were analyzed per experimental condition in three independent cultures. (B) Dendritic spine length in hippocampal neurons expressing vector, wild-type human ROCK1, or ROCK1-L105G and treated with blebbistatin or SR7826. Controls were transfected with Lifeact-GFP and treated with DMSO. Data are means \pm SEM of three experiments. $****P < 0.0001$ and $*P < 0.05$ (versus vector, actual $P = 0.0230$; $^{\dagger}P = 0.0285$ versus DMSO) by one-way analysis of variance (ANOVA) with Šidák's test. (C) Dendritic spine density in hippocampal neurons expressing vector, wild-type human ROCK2, or ROCK2-L121G and treated with blebbistatin or SR7826. Data are means \pm SEM of three experiments. $****P < 0.0001$, $^{***}P < 0.001$, $^{**}P < 0.01$ (versus DMSO, actual $#P = 0.0083$), and $^{\ddagger}P = 0.0207$ versus SR7826 by one-way ANOVA with Šidák's test. Related data and analyses are shown in fig. S1.

Forty-eight hours after transfection, neurons were fixed and imaged using wide-field microscopy. Z series images were subjected to deconvolution followed by three-dimensional (3D) morphometry analysis (Fig. 1A). Dendritic spine length was reduced significantly in neurons expressing human ROCK1 compared to vector or Lifeact-GFP controls, whereas spine head diameter and density were similar among these conditions (Fig. 1B and fig. S1, B and C). Human ROCK2 expression reduced spine density significantly compared to vector or Lifeact-GFP; however, spine head diameter and length were not affected by ROCK2 (Fig. 1C and fig. S1, D and E). Lifeact-GFP alone or vector and Lifeact-GFP were comparable on all spine readouts (Fig. 1, B and C, and fig. S1, B to E). To test whether ROCK1 or ROCK2 kinase activity was required for their effects on spines, site-directed mutagenesis was used to substitute Leu¹⁰⁵ or Leu¹²¹ for glycine in the ROCK1 or ROCK2 kinase domain adenosine triphosphate-binding pocket, respectively, rendering the enzymes inactive (35). Spine density and morphology in neurons expressing ROCK1-L105G or ROCK2-L121G were comparable to vector controls, indicating that kinase activity of ROCKs is required for their effects on spines (Fig. 1, B and C, and fig. S1, B to E). Expression of ROCK1 and ROCK1-L105G or ROCK2 and ROCK2-L121G appeared similar in neuroblastoma cells, suggesting that mutation of Leu¹⁰⁵ or Leu¹²¹ to glycine does not perceptibly alter ROCK1 or ROCK2 protein stability, respectively (fig. S1A).

ROCKs share protein substrates related to actin regulation, including myosin light chain, myosin light chain phosphatase, and LIMK1 (36–38). We hypothesized that the distinct ROCK1 or ROCK2 effects on spine length or density, respectively, may be governed by different mechanisms. To test this, neurons expressing ROCK1 or ROCK2 were treated with blebbistatin, which inhibits myosin adenosine triphosphatase and thus relaxes actin-myosin contractility, or SR7826, a small-molecule inhibitor of LIMK1 that impedes its activity on cofilin (fig. S1F) (39, 40). Blebbistatin, but not SR7826, rescued ROCK1-mediated reduction of spine length, whereas SR7826, but not blebbistatin, prevented ROCK2-mediated reduction of spine density (Fig. 1, B and C). Blebbistatin and SR7826 significantly increased spine length and spine density, respectively, compared to dimethyl sulfoxide (DMSO) controls (Fig. 1, B and C). These results suggest that ROCK1 kinase activity regulates spine length through myosin-actin pathways, whereas ROCK2 kinase activity controls spine density through LIMK1-cofilin-actin signaling. Moreover, our findings hint that increased protein abundance of ROCK1 and



ROCK2 in MCI and AD may contribute to decreased spine structural plasticity and density that is observed in disease cases (8).

A β -induced dendritic spine degeneration is mediated by the ROCK2-LIMK1 pathway

$\text{A}\beta$ oligomers can wreak havoc on dendritic structure and degenerate spines in cellular and animal models of AD (10, 41, 42). Recent studies indicate that $\text{A}\beta$ oligomers have detrimental effects on actin cytoskeleton rearrangement in neurons and that Rho-GTPase pathways may be involved (27, 28). $\text{A}\beta_{42}$ oligomers can activate ROCKs, leading to increased phosphorylation of LIMK1 (17). To test whether ROCK1 or ROCK2 is necessary for $\text{A}\beta$ -induced dendritic spine degeneration, rat hippocampal neurons were transduced with lentivirus expressing ROCK1- or ROCK2-targeted or scramble short hairpin RNA (shRNA) (fig. S2, A and B). Ninety-six hours later, cultures were treated with $\text{A}\beta_{42}$ oligomers or DMSO for 6 hours and then fixed, imaged, and processed for 3D morphometry analyses. Neurons that were untransduced or those transduced with scramble shRNA or ROCK1 shRNA displayed similar and statistically significant reductions in spine density after exposure to $\text{A}\beta_{42}$ compared to DMSO-treated counterparts. However, shRNA-mediated depletion of ROCK2 significantly curbed $\text{A}\beta_{42}$ -induced spine loss compared to scramble shRNA-transduced neurons treated with $\text{A}\beta_{42}$ (Fig. 2, A and B). Reduction of ROCK1 or ROCK2 did not significantly alter spine density, length, or head diameter in comparison to scramble controls (Fig. 2B and fig. S2, C and D). These results suggest that $\text{A}\beta_{42}$ -induced spine degeneration is predominantly mediated by ROCK2, rather than ROCK1. On the basis of these data and those above demonstrating that LIMK1 inhibition blocked ROCK2-mediated spine loss (Fig. 1C), we hypothesized that suppressing LIMK1 activity would modulate $\text{A}\beta_{42}$ -induced spine degeneration. To test this, rat hippocampal neurons were treated simultaneously with SR7826 and $\text{A}\beta_{42}$ oligomers for 6 hours. $\text{A}\beta_{42}$ had no effect on spine density or morphology among neurons exposed to SR7826, indicating that LIMK1 inhibition prevented $\text{A}\beta_{42}$ -induced spine degeneration (Fig. 2C and fig. S2, E and F). Fasudil has been shown to block the negative effects of

$\text{A}\beta$ oligomers on dendritic spines (27, 28); similarly, our data here revealed that simultaneous exposure to fasudil and $\text{A}\beta_{42}$ oligomers for 6 hours had no effect on spine density or morphology (fig. S2G).

Maintenance and retention of dendritic spines are hypothesized to facilitate memory and information processing in patients who harbor

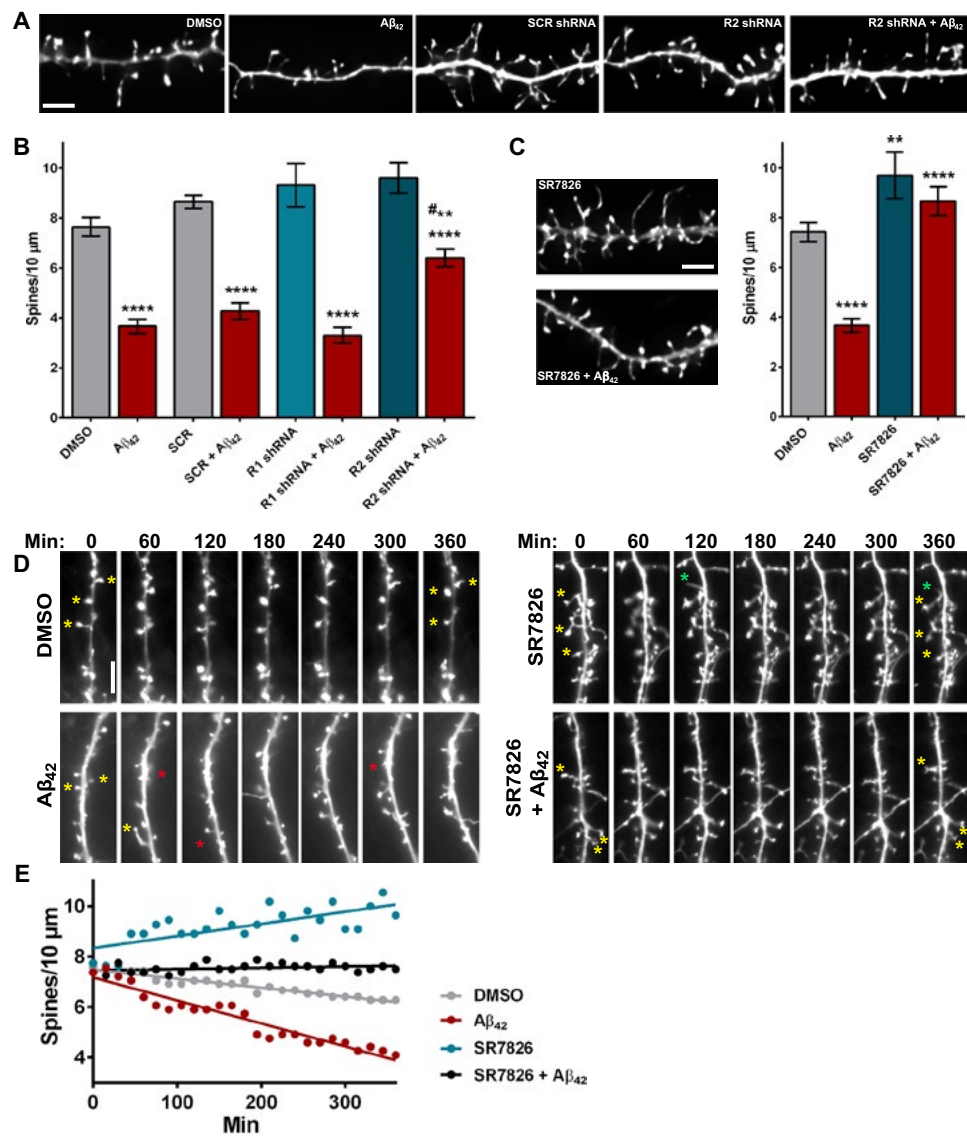


Fig. 2. $\text{A}\beta$ -induced dendritic spine degeneration is mediated by the ROCK2-LIMK1 pathway. (A) Representative maximum-intensity wide-field fluorescent images of hippocampal neurons after deconvolution. Scale bar, 5 μm . N = 9 to 17 neurons (one dendrite per neuron) were analyzed per experimental condition in three independent cultures. (B) Dendritic spine density in hippocampal neurons transduced with lentivirus expressing scramble (SCR) or ROCK1 (R1)-targeted, or ROCK2 (R2)-targeted shRNA and exposed to DMSO or oligomeric $\text{A}\beta_{42}$ (500 nM). Data are means \pm SEM of three experiments. ***P < 0.0001 ($\text{A}\beta_{42}$ versus DMSO controls) and **P < 0.001 (versus SCR and $\text{A}\beta_{42}$, actual P = 0.0069) by one-way ANOVA with Šidák's test. (C) Representative maximum-intensity wide-field fluorescent images (after deconvolution) of hippocampal neurons exposed to SR7826 (10 μM) with or without $\text{A}\beta_{42}$ (500 nM). Scale bar, 5 μm . Data (right) are means \pm SEM of three experiments. N = 6 to 17 neurons (one dendrite per neuron) were analyzed per experimental condition in three independent cultures. ****P < 0.0001 and **P < 0.01 (actual P = 0.0072) by one-way ANOVA with Šidák's test. (D) Representative wide-field live-cell fluorescent images of hippocampal neurons over time, exposed to DMSO, $\text{A}\beta_{42}$, SR7826, or SR7826 and $\text{A}\beta_{42}$. Asterisks highlight loss (red), maintenance (yellow), or formation (green) of dendritic spines. Scale bar, 5 μm . (E) Representative spine density counts in hippocampal neurons for 6 hours with the indicated treatments. Dots represent the spine density (spines per 10 μm) for a single dendrite at 15 min intervals for 6 hours. n = 3 to 5 neurons (one dendrite per neuron) were analyzed per experimental condition in three independent cultures. Related data are shown in fig. S2.

substantial A β pathology but are cognitively normal (7, 8). Therefore, therapeutics that protect spines from A β could be useful to prevent dementia onset. To this end, we tested whether SR7826 protected spines from A β_{42} oligomers or SR7826 generated spines to compensate for A β_{42} -induced spine loss. Treatment of hippocampal neurons with SR7826 and/or A β_{42} oligomers was performed for 6 hours on neurons transfected with plasmid expressing Lifeact-GFP. Live-cell imaging indicated that, for 6 hours, spine loss occurred more rapidly among neurons exposed to A β_{42} compared to DMSO controls (Fig. 2, D and E). Spine density increased over time in cultures treated with SR7826, whereas spine density remained static in neurons simultaneously exposed to A β_{42} and SR7826 (Fig. 2, D and E). These findings suggest that pharmacologic inhibition of LIMK1 can generate spines under normal conditions but protects spines in the presence of A β_{42} oligomers.

LIMK1 inhibition protects against A β -induced neuronal hyperexcitability

Dendritic degeneration in hAPP mice causes neuronal hyperexcitability by rendering neurons more electrically compact (10). These detrimental effects ultimately drive aberrant circuit synchronization and likely contribute to cognitive impairment in patients with AD. To evaluate the electrophysiological consequences of A β_{42} -induced spine loss in hippocampal neurons, we seeded cells directly on multielectrode arrays (MEAs) in individual cell culture plate wells and performed a baseline recording at DIV 14 (Fig. 3A). Immediately after the baseline recording, neurons were exposed to A β_{42} oligomers or DMSO for 6 hours, and at the end of 6 hours, a second recording was performed. Treatment with A β_{42} increased action potential frequency and the frequency of action potential bursts significantly compared to DMSO controls (Fig. 3, B to D). These results mirrored findings on hippocampal neuron hyperexcitability at the cellular and network level in hAPP mice (10). Neuronal hyperexcitability was not observed after simultaneous exposure to A β_{42} oligomers and SR7826 (Fig. 3, B to D). Fasudil blocked A β_{42} -induced hyperexcitability of neurons (fig. S3). This suggests that the dendritic spine resilience provided by LIMK1 inhibition is protective against the toxic hyperexcitability induced by A β_{42} oligomers.

LIMK1 inhibition rescues hippocampal thin spine loss in hAPP mice

Past studies indicated that A β can activate RhoA in brain but whether hAPP

leads to downstream activation of ROCKs remained to be determined (19). To address this, we evaluated hippocampal tissue homogenates from 6-month-old hAPPJ20 mice and age-matched nontransgenic (NTG) littermate controls by SDS-polyacrylamide gel electrophoresis (PAGE) and subsequent immunoblot (Fig. 4A). Densitometry analysis indicated that ROCK2, but not ROCK1, protein levels were elevated statistically significantly in hippocampal homogenates from hAPPJ20 brains compared to NTG controls. Moreover, phosphorylation of LIMK1 at Thr⁵⁰⁸ (pLIMK1) was increased significantly in hAPPJ20 mice compared to NTG littermates, indicating heightened activity of ROCKs in the hippocampus of hAPP mice (Fig. 4B). These results are consistent with increased amounts of ROCK2 protein and pLIMK1 in AD brains (18, 26).

Past studies demonstrated that hippocampal spine loss occurs in hAPPJ20 mice at 9 months of age when amyloid plaque load is still minimal (43). On the basis of our results above (Fig. 1C), increased

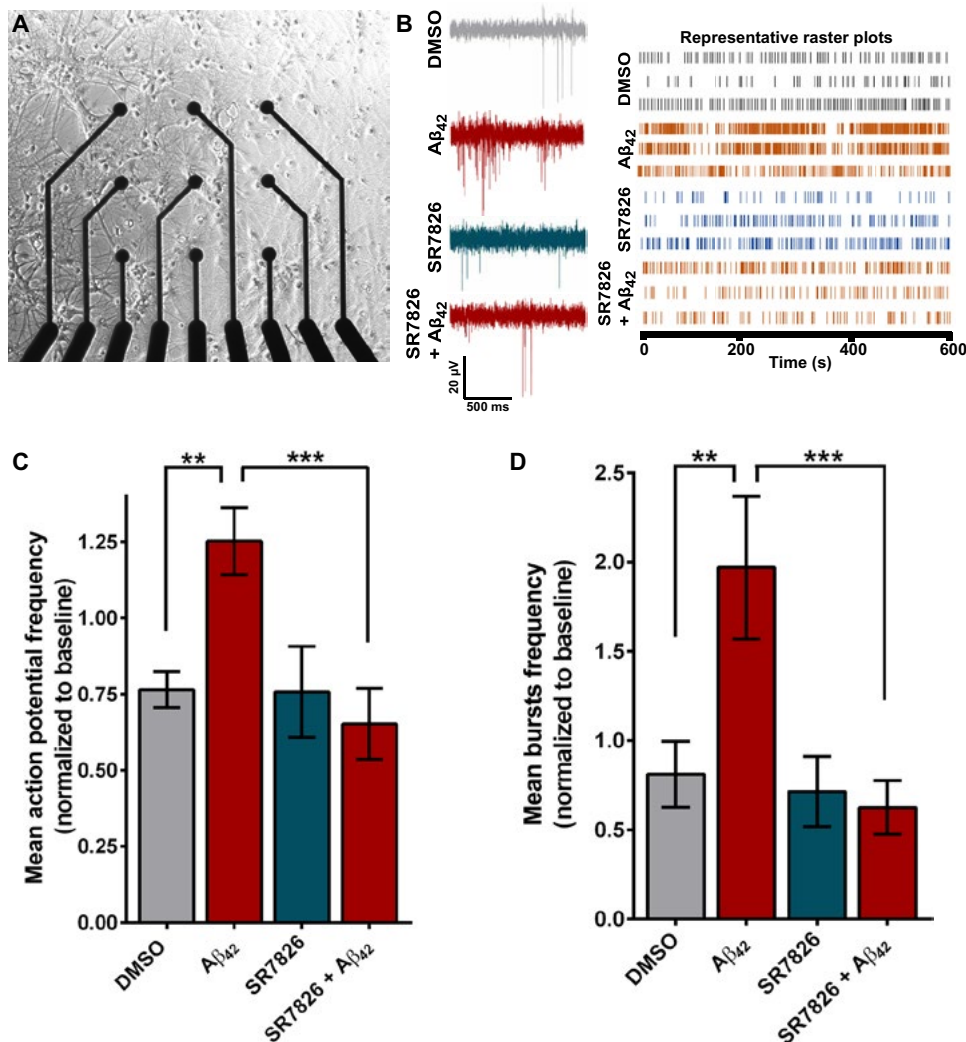
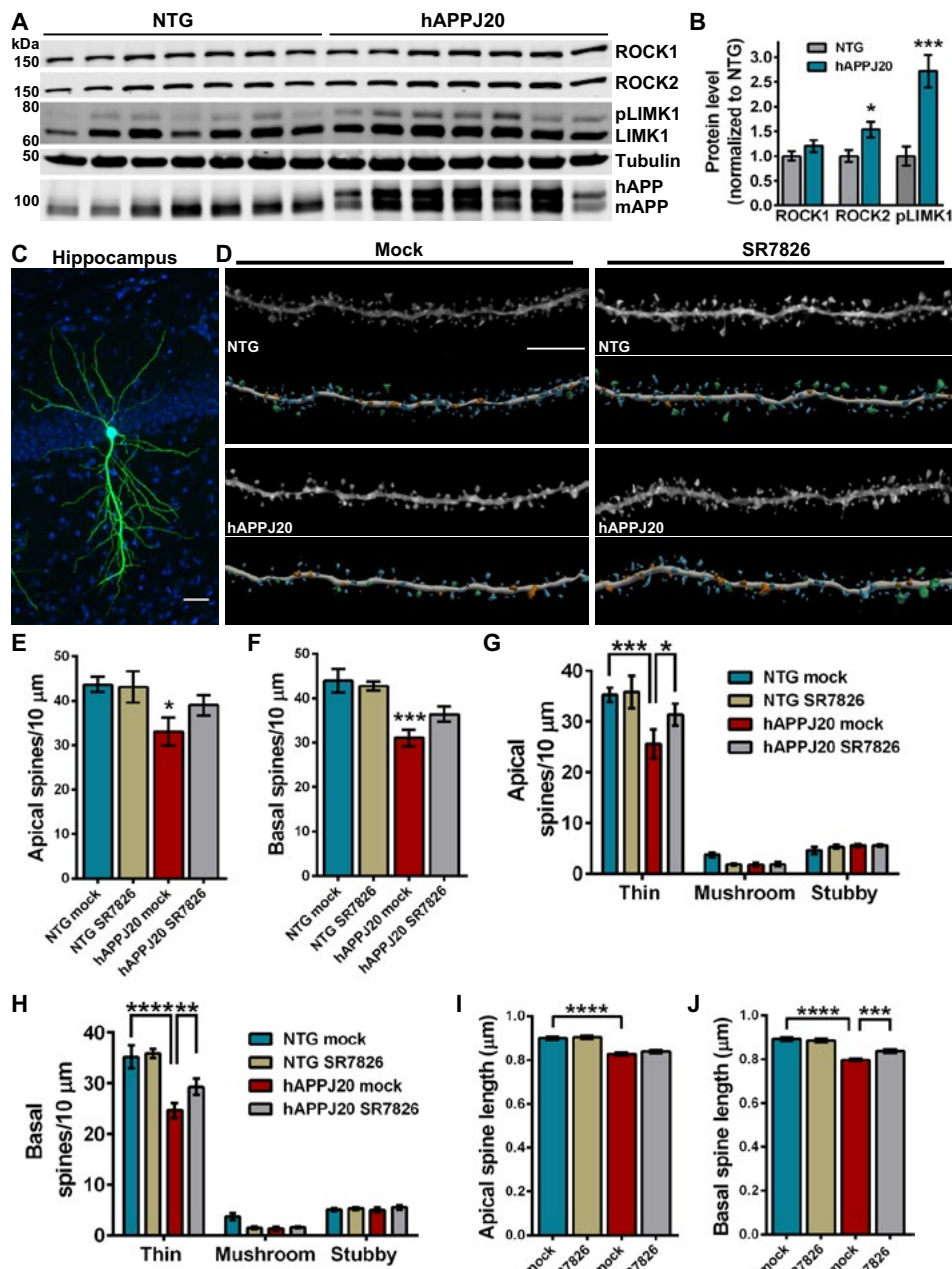


Fig. 3. LIMK1 inhibition protects against A β -induced neuronal hyperexcitability. (A) Representative bright-field image of primary hippocampal neuron cultures grown on a MEA plate. (B) Representative traces (left) and raster plots from three units (right) after exposure to DMSO, A β_{42} , SR7826, or SR7826 and A β_{42} . N = 17 to 24 wells per condition, which includes four to six neurons per well from three independent cultures. (C and D) Mean action potential frequency (C) and mean bursts frequency (D) over baseline in hippocampal neurons treated with DMSO, A β_{42} , or SR7826 with or without A β_{42} . Data are means \pm SEM of three experiments. ***P < 0.001 [actual P = 0.0009 (C) and 0.0003 (D)] and **P < 0.01 [actual P = 0.0062 (C) and 0.0016 (D)] by one-way ANOVA with Šidák's test.



in (E) and (F). * $P < 0.05$ (actual $P = 0.0398$), ** $P < 0.01$ (actual $P = 0.0098$), *** $P < 0.001$ (actual $P = 0.0002$), and **** $P < 0.0001$ by two-way ANOVA with Tukey's test. (I and J) Mean spine length of apical (I) and basal (J) spines among CA1 pyramidal neurons in the hippocampus from mock- or SR7826-treated hAPPJ20 and NTG mice. Data are means \pm SEM; N as given in (E) and (F). *** $P < 0.001$ (actual $P = 0.0003$) and **** $P < 0.0001$ by one-way ANOVA with Šidák's test.

amounts of ROCK2 and pLIMK1 at 6 months old would likely reduce spine density in the hippocampus of hAPPJ20 mice. Moreover, LIMK1 inhibition prevented A β_{42} -induced spine loss in hippocampal neurons when SR7826 and A β_{42} oligomers were applied simultaneously (Fig. 2, C to E). Therefore, we wondered whether treatment with SR7826 would benefit hippocampal spines undergoing degeneration in hAPPJ20 mice. Initially, we dosed 6-month-old hAPPJ20 mice and age-matched NTG controls with SR7826 (10 mg/kg)

or equivalent volume of DMSO (mock) by oral gavage and harvested brains 6 hours later to verify SR7826 target engagement. SDS-PAGE and immunoblot of synaptosome fractions from hippocampal tissue homogenates revealed that phosphorylation of cofilin at Ser³, a LIMK1 substrate (44, 45), was reduced significantly in mice treated with SR7826 (fig. S4, A and B). To test the therapeutic potential of LIMK1 inhibition, we dosed 6-month-old hAPPJ20 mice and age-matched NTG controls with SR7826 (10 mg/kg) or mock once a day

by oral gavage for 11 days. At the end of 11 days, all mice were weighed, transcardially perfused, and organs were collected for analysis. Treatment with SR7826 did not alter weight in hAPPJ20 or NTG mice, and histological examination of liver samples did not indicate SR7826-induced toxicity (fig. S4, C and D).

To evaluate spines, individual CA1 pyramidal neurons in the hippocampus were targeted for iontophoretic microinjection of the fluorescent dye Lucifer yellow followed by high-resolution confocal laser scanning microscopy and dendritic 3D reconstructions for morphometry analysis (Fig. 4, C and D). Comparison of apical and basal dendrites revealed statistically significant reductions in spine density among hAPPJ20 mock animals compared to NTG mock, supporting our hypothesis that A β -induced activity of the ROCK2-LIMK1 pathway causes robust spine loss. Global apical and basal spine densities in SR7826-treated hAPPJ20 mice were increased, but not significantly, compared to mock hAPPJ20 (Fig. 4, E and F). Spine morphology influences excitatory neurotransmission and synaptic plasticity, and spines can be classified on the basis of their 3D structure as stubby, mushroom, or thin (9, 46, 47). Examination of thin, mushroom, and stubby spine populations on apical and basal dendrites among each experimental condition revealed robust loss of thin spines in hAPPJ20 mock animals compared to NTG mock. This indicates that the reduction in thin spine density drove the global decrease in spine density among hAPPJ20 mock samples. Treatment with SR7826 increased both apical and basal thin spine density significantly in hAPPJ20 mice over mock-treated animals (Fig. 4, G and H). However, no statistically significant changes in density were observed in mushroom or stubby spine populations among the experimental conditions.

To further analyze spine structure, mean apical and basal spine length and head diameters were plotted for each experimental condition. Significant reductions in both apical and basal spine length were identified in hAPPJ20 mock animals compared to NTG mock; however, treatment with SR7826 increased basal spine length significantly in hAPPJ20 mice (Fig. 4, I and J). Mean apical and basal spine head diameters were similar among hAPPJ20 mock and NTG mock animals, whereas SR7826 reduced apical spine head diameter in NTG mice but increased basal spine head diameter in hAPPJ20 mice (fig. S5, A and B). We did not observe changes in soluble or insoluble A β_{42} or thioflavin S staining among hAPPJ20 mice treated with SR7826, suggesting that the beneficial effects of SR7826 on spines were not due to reductions in A β (fig. S6, A to C). Collectively, our findings link experimental models with human disease by demonstrating that A β -induced changes in ROCK2-LIMK1 signaling likely contribute to dendritic spine degeneration in AD. Moreover, pharmacologic inhibition of LIMK1 is identified as a rational therapeutic approach to protect spines from A β .

DISCUSSION

As the human population ages, the ability to maintain cognitive function with a brain that is accumulating AD pathology is likely linked to the preservation and maintenance of synapses and dendritic spines. Therefore, protecting dendritic spines from the degenerating forces of AD is critical for preventative therapeutics. In this report, we reveal that ROCKs govern dendritic spine density and morphology through isoform-specific cell biological mechanisms, and we discuss how this may affect spine structure in AD. Our findings support the hypothesis that A β_{42} oligomers induce hippocampal neuron spine degeneration and hyperexcitability through the ROCK2-LIMK1

pathway, and we assess the therapeutic potential of LIMK1 inhibition in cellular and animal models of AD.

The amount and activity of ROCK1 and ROCK2 proteins were increased in AD brains assessed in our study, and these changes are likely due to accumulation of A β (17, 18, 26). Here, we found that enhanced activity of ROCK1-myosin-actin or ROCK2-LIMK1-cofilin-actin signaling decreased spine length or density, respectively, in neurons. These findings implicate the ROCK2-LIMK1 pathway as a potential culprit of reduced spine density in AD; however, spine length was reported similar among age-matched pathology-free controls and AD cases (8). Increased spine length was observed exclusively in cognitively normal patients with AD pathology (CAD), suggesting (i) that enhancing spine length in patients with MCI may be beneficial or (ii) that increased spine length is a resilience mechanism before cognitive decline (7, 8). Whether ROCK1 amounts are decreased in CAD cases is unclear, and although these studies do not eliminate the rationale for pharmacologic inhibition of ROCK1, other caveats may be discussed below.

Epileptiform activity is an indicator of network hyperexcitability in hAPP mice, and high rates of subclinical epileptiform activity are detected in patients with AD (11, 14, 48). Network hyperexcitability in hAPP mice is driven by degeneration of hippocampal pyramidal neurons' dendrites and dendritic spines (10). Loss of dendrites and spines cause neuronal hyperexcitability by reducing the total surface area of the cell and thus rendering neurons more electrically compact. In a more compact neuron, synapse currents would be translated more efficiently into post-synaptic and axon-somatic depolarization, leading to increased action potential output (49). Consequences of this mechanism may include hyperexcitability of the neuron and aberrant circuit synchronization. Our culture work here directly supports these findings by linking A β -induced dendritic spine loss to increased neuronal firing rates. Including our data herein, we now know that these A β -induced structural and electrophysiological phenotypes are shared across humans, rodents, and cellular models of AD. Past studies provide evidence that A β oligomers can directly interact with the cellular prion protein (PrP^C) (50), which may induce PrP^C-mediated signaling of RhoA (51). These pathways would link extracellular A β to intracellular ROCK1 and/or ROCK2 signaling. Our data from this study showed that, while spine morphology was similar between A β_{42} -treated samples and controls in cultured hippocampal neurons, hAPPJ20 mice displayed substantial reductions in both spine density and length among hippocampal neurons, suggesting that activity of both ROCK1 and ROCK2 signaling pathways contributed to these effects. Moreover, thioflavin S staining was minimal in the 6-month-old hAPPJ20 mice, supporting the hypothesis that structural deficits and spine loss are most likely linked to A β oligomers rather than accumulation of plaques.

Two pan-ROCK inhibitors, fasudil and ripasudil, have been used to treat human disease (52). Previous studies have explored the potential to repurpose ROCK inhibitors for neurodegenerative disorders, including AD, frontotemporal dementia, Parkinson's disease, and amyotrophic lateral sclerosis (26, 28, 53–56). Despite the translational potential these compounds exhibit, target-selectivity caveats and ambiguity over ROCK1- or ROCK2-specific functions in neurons have stalled ROCK-based therapeutics for cognitive treatment (52, 57). Blood pressure reduction is an effect of pan-ROCK inhibitors and is predominantly due to ROCK1 inhibition; therefore, ROCK2-selective pathways and drugs may provide a better safety

profile (58). Fasudil was shown to block negative effects of A β oligomers on dendritic spines (27, 28). Our data here revealed that simultaneous exposure to fasudil and A β_{42} oligomers for 6 hours had no effect on spine density or morphology, supporting the published findings, and that fasudil blocked A β_{42} -induced hyperexcitability of neurons. Our shRNA results suggest that the beneficial effects of fasudil on A β -induced spine toxicity are predominantly modulated through inhibition of ROCK2 signaling. However, fasudil is not specific to ROCKs (29), therefore, moving down the ROCK2 pathway to LIMK1 inhibitors may be a safer, more efficient therapeutic strategy with fewer off-target effects. Although LIMK1 is predominantly expressed in the brain, both LIMK1 and LIMK2 can phosphorylate the actin-severing protein cofilin at Ser³ (45, 59). However, the identification of additional molecular substrates of LIMKs has been extremely limited (60). Six years before this study, several LIMK inhibitors have been found, some of which are highly selective, including SR7826, and are now undergoing further development and optimization (40, 60, 61). Future use of these compounds will increase our understanding of the LIMK isoforms' functions and fuel new therapeutic avenues.

Thin spine loss is a shared phenotype among hAPPJ20 mice (observed here) and patients with AD (8). Spine structure is inseparably linked to spine function, and spines can be classified on the basis of their 3D morphology as stubby, mushroom, or thin (46, 47, 62, 63). Stubby spines are hypothesized as transitional structures that may enlarge, possibly to mushroom spines, which are more stable entities with a wide head and thin neck. Thin spines are more dynamic and lack the wide head of mushroom spines. Spine morphology can robustly affect molecular diffusion. For instance, length and width of spine necks are predominant mediators of compartmentalization, facilitating efficient regulation of synaptic biochemical and electrical components (64). Our study revealed that thin spine loss and mean reduction of spine length were observed among both apical and basal dendrites in the CA1 region of the hippocampus of hAPPJ20s. Whereas LIMK1 inhibition increased apical and basal thin spine density, spine length was increased more robustly on basal dendrites. Moreover, SR7826 reduced mean spine head diameter on apical, but not on basal, dendrites in NTG mice, whereas SR7826 increased mean spine head diameter statistically significantly on basal dendrites in hAPPJ20 mice. These results are challenging to interpret but may suggest that LIMK1 regulates different aspects of spine morphology depending on the geographical location of the spine, and A β accumulation seemingly layers an additional level of complexity. Likely, consequences on dendritic spine structure after LIMK1 inhibition is steered by the electrophysiological activity of the brain region and neuronal network during the time of drug dosing (64–68). Therefore, strong influences on brain environment such as age and disease state will need to be considered for therapeutic strategies targeting dendritic structure in AD (7, 69).

MATERIALS AND METHODS

Primary rat hippocampal neuron and continuous cell culture

Rat hippocampal neurons were isolated from E18 Sprague-Dawley rat embryos and cultured at a density of 2×10^5 cells per coverslip on poly-L-lysine-coated 18-mm glass coverslips as previously described with minor modifications (25). Briefly, neurons were cultured in Neurobasal medium (Invitrogen) supplemented with B27 that was conditioned by separate cultures of primary rat astrocytes

and glia. Neurons were treated at DIV 4 with 5 μ M cytosine β -D-arabinofuranoside hydrochloride (Sigma-Aldrich) to eliminate the presence of native astrocytes and glia on the glass coverslips. Medium was changed every 3 to 4 days with new glia-conditioned Neurobasal medium for proper culture maintenance. At DIV 12, neurons were cotransfected with plasmids using Lipofectamine 2000 (Invitrogen) according to the manufacturer's instructions. Neuro-2A mouse neuroblastoma cells were maintained in Dulbecco's minimum essential medium with 10% fetal bovine serum and 1% penicillin/streptomycin.

DNA constructs, lentivirus, and shRNA

Lentivirus vectors for shRNA expression were constructed and generated as previously described (53, 70) (ROCK1 shRNA: 5'-GC-CAATGACTTACTTAGGA; ROCK2 shRNA: 5'-ATCAGACAG-CATCCTTTCT; and scramble: 5'-GGACTACTCTAGACGTATA). To generate ROCK1-L121G, complementary DNA (cDNA) encoding human ROCK1 was used as a template and QuikChange XL Site-Directed Mutagenesis Kit (Stratagene) was used (sense primer: 5'-CCACCAGGAAGGTATATGCTATGGGGCTCTCAGCAAATTGAAA; antisense primer: 5'-TTTCAAATTGCTGAGAAGCCCCATAGCATATACTTCCTGGTGG). To generate ROCK2-L121G, cDNA encoding human ROCK2 was used as a template (sense primer: 5'-GGCATCGCAGAAGGTTATGCTATGGG-GCTTCTTAGTAAGTTGA; antisense primer: 5'-TCAAACCTACT-AAGAACCCCCATAGCATAAACCTCTGCGATGCC). Constructs were verified by sequencing. Plasmid encoding Lifeact-GFP was a gift from G. Bassell (Emory University School of Medicine, Atlanta, GA, USA). Previous studies have demonstrated that Lifeact-expressing neurons display normal, physiological actin dynamics and dendritic spine morphology (34, 71).

Chemicals

A β_{42} (Bachem) oligomers were prepared as previously described (17). A β was resuspended in 1 \times Hanks' balanced salt solution and DMSO and then placed in 4°C overnight. At DIV 14, primary hippocampal neurons were treated with 500 nM A β_{42} for 6 hours. Fasudil (Selleckchem, catalog no. S1573) and SR7826 (Tocris, catalog no. 562610) were reconstituted to a 10 mM stock in either water or DMSO, respectively. At DIV 14, primary hippocampal neurons were dosed with 10 μ M SR7826, 30 μ M fasudil, or a combination of drug and A β_{42} for 6 hours. Six hours was chosen on the basis of past studies demonstrating that A β_{42} -induced spine loss in cultured neurons plateaus at about 6 hours after exposure (41), and pan-ROCK inhibitors induce robust changes in spine morphology on cultured hippocampal neurons after 6 hours of exposure (25). Blebbistatin (Tocris, catalog no. 1852) was reconstituted to a 10 mM stock in DMSO. At DIV 14, primary hippocampal neurons were treated with 5 μ M blebbistatin for 1 hour. One-hour incubation time was selected on the basis of previous studies (72, 73).

Cell lysate preparation, immunoblots, and antibodies

Cells were lysed in phosphate-buffered saline (PBS) and protease inhibitor cocktail (Roche Diagnostics, Risch-Rotkreuz, Switzerland), Halt phosphatase inhibitor cocktail (Pierce, Rockford, IL, USA), and lysis buffer containing 0.5% NP-40, 0.5% deoxycholate, 150 mM sodium chloride, and 50 mM tris-HCl (pH 7.4). All lysates were subjected to a 15,871g spin for 5 min to remove nuclei and debris. Protein

concentration was determined by bicinchoninic acid method (Pierce). Immunoblots were performed using standard procedures as described previously (74). A quantity of 50 µg of protein per sample was loaded per lane. Tubulin was used as a loading control. Images were captured using an Odyssey Image Station (Li-Cor), and band intensities were quantified using Odyssey Application Software Version 3.0 (Li-Cor). Primary antibodies include ROCK1 (Abcam, 45171), ROCK2 (Santa Cruz Biotechnology, catalog no. 5561), LIMK (Cell Signaling Technology, product no. 3842S), phospho-LIMK (Cell Signaling Technology, product no. 3841), phospho-cofilin (Cell Signaling Technology, product no. 3313), cofilin (Cell Signaling Technology, no. 3318), and tubulin (Iowa Hybridoma Bank). Secondary antibodies include Alexa Fluor 680 goat anti-rabbit (A21109, Life Technologies) and goat anti-mouse (Li-Cor, product no. 926-32210).

Oral gavage

All experimental procedures were performed under a protocol approved by the Institutional Animal Care and Use Committee at the University of Alabama at Birmingham. Six-month-old NTG and hAPPJ20 mice [B6.Cg-Zbtb20Tg(PDGFB-APPswInd)20Lms/2Mmjx] (MMRRC stock no: 34836-JAX J20, the Jackson Laboratory) were treated once daily with mock (90% H₂O and 10% DMSO) or SR7826 (dissolved in 90% H₂O and 10% DMSO) for 11 days via oral gavage using plastic gavage tips (Instech, catalog no. FTP-20-38). Treatment was given at 2:00 p.m. daily throughout the entirety of the treatment regimen. SR7826 was dissolved fresh each day at a concentration of 10 mg/kg (200 µl total volume per animal per day). Mice were euthanized at the end of the treatment period for postmortem analyses. For all experiments, age-matched and sex-matched animals were used. When necessary, additional details on mouse sex are provided in figure legends.

Perfusions and brain tissue processing

Animals were anesthetized with Fatal-Plus (Vortech Pharmaceuticals, catalog no. 0298-9373-68). Mice were transcardially perfused with cold 1% paraformaldehyde (PFA; Sigma-Aldrich, P6148) for 1 min followed by cold 4% PFA with 0.125% glutaraldehyde (Fisher Scientific, catalog no. BP2547) for 10 min. A peristaltic pump (Cole-Parmer) was used for consistent administration of PFA. Immediately after perfusion, mice were decapitated, and the whole brain was removed and drop-fixed in 4% PFA containing glutaraldehyde for 8 to 12 hours at 4°C. After fixation, the brains were sliced in 250-µm coronal sections using a Leica vibratome (VT1000 S) with a speed of 70 and frequency of 7. The platform was filled with cold 0.1 M phosphate buffer (PB), and the brain was glued (Loctite) perpendicular to the stage and the cerebellum side down. All slices were stored one slice per well in a 48-well plate containing 0.1% sodium azide (Fisher Scientific, catalog no. BP922I) in 0.1 M PB at 4°C. These procedures were performed according to (75). For PBS perfusions, animals were anesthetized with Fatal-Plus. Mice were transcardially perfused with cold 1× PBS for 2 min. Immediately after perfusion, the brain was extracted and dissected into two hemispheres. Each hemisphere was immediately flash-frozen in 2-methylbutane (Sigma-Aldrich, 320404), placed on dry ice, and stored at -80°C.

Synaptosome preparations

Hemibrains were bathed in a petri dish of ice-cold PBS with protease (Sigma-Aldrich, S8820) and phosphatase inhibitors (Thermo Scientific,

1861277). The hippocampus was isolated from each hemibrain, and synaptosomes were prepared using the following biochemical fractionation protocol, as previously described (76, 77). Subdissected tissue samples were bathed and homogenized for 30 s in TEVP buffer (10 mM tris base, 5 mM NaF, 1 mM Na₃VO₄, and 1 mM EDTA) with 320 mM sucrose and protease and phosphatase inhibitors. A small volume was saved as whole homogenate. Remaining sample was centrifuged at 800g for 10 min at 4°C. The supernatant (S1) was removed, and the pellet (P1) was stored in TEVP and inhibitors. S1 was centrifuged at 9200g for 10 min at 4°C. The supernatant (S2) was removed and stored. The pellet (P2) was resuspended in TEVP, 32 mM sucrose, and inhibitors and centrifuged at 25,000g for 20 min at 4°C. The supernatant (LS1) was removed and stored. The pellet (synaptosome fraction) was resuspended in TEVP and inhibitors and stored at -80°C.

Amyloid measurements

Soluble and insoluble Aβ₄₂ were extracted according to the human brain Aβ₄₂ enzyme-linked immunosorbent assay (Millipore) manufacturer's instructions. Plates were read at 450 nm on a Spectra Max Plus plate reader (Molecular Devices). For thioflavin S staining, perfused mouse brains were sectioned to 50-µm slices using a vibratome (Leica VT1000 S). Slices were then subjected to the following washes: 70% ethanol (EtOH) for 1 min, 80% EtOH for 1 min, thioflavin S in 80% EtOH for 15 min, 80% EtOH for 1 min, 70% EtOH for 1 min, and then two washes in DI H₂O. Coverslips were then mounted on glass slides with Vectashield aqueous mounting media (Vector Labs, catalog no. H1000). Images were captured on a Nikon (Tokyo, Japan) Eclipse Ni upright microscope, using a Nikon Intensilight and Photometrics Coolsnap HQ2 camera to image thioflavin S. Images were captured with Nikon Elements 4.20.02 image capture software using 4× objective [Nikon Plan Fluor 0.13-numerical aperture (NA) objective].

MEA recording and analysis

Single neuron electrophysiological activity was recorded using a MEA2100 Lite recording system (Multi Channel Systems). E18 rat primary hippocampal neurons were harvested as described above and plated in a six-well MEA at a density of 125,000 cells per well. Each MEA well contained nine extracellular recording electrodes and a ground electrode. At DIV 14, a 30-min MEA prerecording was performed followed by application of Aβ₄₂ or pharmacological inhibitors for 6 hours. After 6 hours, a follow-up 30-min MEA recording was performed to determine effects on neuronal firing properties. All recordings were performed while connected to a temperature-controlled headstage (37°C) with 5% CO₂ and containing a 60-bit amplifier. Electrical activity was measured by an interface board at 30 kHz, digitized, and transmitted to an external PC for data acquisition and analysis in MC_Rack software (Multi Channel Systems). All data were filtered using dual 10-Hz (high pass) and 10,000-Hz (low pass) Butterworth filters. Action potential thresholds were set manually for each electrode (typically >4 SDs from the mean signal). Neuronal waveforms collected in MC_Rack were exported to Offline Sorter (Plexon) for sorting of distinct waveforms corresponding to multiple units on one electrode channel and confirmation of waveform isolation using principal component analysis, interspike intervals, and auto- or cross-correlograms. Further analysis of burst activity and firing rate was performed in Neuro-Explorer. Mean firing frequency and bursting were calculated by

creating a ratio of firing or bursting at a 6-hour time point/baseline. Specifically, either the firing frequency or burst activity were averaged on a per-well basis after 6 hours of treatment and then divided by the average on a per-well basis at the baseline.

Static wide-field microscopy

On DIV 14, neurons were fixed with room temperature 2% PFA in 0.1 M PBS and washed two times with 1× PBS, and coverslips were mounted on microscope slides (Fisher Scientific, catalog no. 12-550-15) using Vectashield mounting media (Vector Labs, catalog no. H1000). A blinded experimenter performed all imaging. Images were captured on a Nikon (Tokyo, Japan) Eclipse Ni upright microscope, using a Nikon Intensilight and Photometrics Coolsnap HQ2 camera to image Lifeact-GFP. Images were captured with Nikon Elements 4.20.02 image capture software using 60× oil immersion objective (NA, 1.40; Nikon Plan Apo). Z series images were acquired at 0.15-μm increments through the entire visible dendrite. Dendrites were selected for imaging by using the following criteria: (i) minimum of 25 μm from the soma, (ii) no overlap with other branches, and (iii) must be a secondary dendritic branch. Before analysis, captured images were deconvolved using Huygens Deconvolution System (16.05, Scientific Volume Imaging, The Netherlands) with the following settings: CMLE; maximum iterations, 50; signal-to-noise ratio, 40; and quality, 0.01. Deconvolved images were saved in .tif format.

Live-cell wide-field microscopy

Primary rat hippocampal E18 neurons were plated on 25-mm round glass coverslips (Warner Instruments) at a density of 4×10^5 cells per coverslip. Cells were maintained as described above. Neurons were transfected at DIV 14 with Lifeact-GFP using Lipofectamine 2000 (Invitrogen) according to the manufacturer's instructions. Neurons were imaged with a 60× oil immersion objective (NA, 1.40; Nikon Plan Apo) on a Nikon (Tokyo, Japan) Ti2-E inverted microscope with a SOLA light source. Their environment was maintained with a Tokai Hit stage top incubation system with the following settings: top heater, 42.3°C; stage heater, 38.3°C; bath heater, 41°C; lens heater, 41°C; and CO₂ concentration, 5%. Neurons were imaged with the following parameters: SOLA light source, 10%; exposure, 200 ms; and image size, 1028 by 1028 pixels. Images were captured with an ORCA-Flash 4.0 V3 CMOS camera (Hamamatsu, Hamamatsu City, Japan). An image was captured every 15 min for a total of 6 hours. DMSO, 500 nM Aβ₄₂, and/or 10 μm of SR7826 were added after the first two images were acquired. For spine density analysis, spines from a representative secondary dendrite at least 25 μm from the soma were counted at each time point and plotted over time.

Iontophoretic microinjection of fluorescent dye

Microinjections were executed using previously described methods (75, 78). A Nikon Eclipse FN1 upright microscope with a 10× objective and a 40× water objective was placed on an air table. The tissue chamber used was assembled in the laboratory and consisted of a plastic base (50 mm × 75 mm) with a petri dish (60 mm × 10 mm) epoxied to the base. A platinum wire was attached so that the ground wire could be connected to the bath by an alligator clip. The negative terminal of the electric current source was connected to a glass micropipette filled with 2 μl of 8% Lucifer yellow dye (Thermo Fisher Scientific, catalog no. L453). Micropipettes (A-M Systems, catalog no. 603500) with highly tapered tips were pulled fresh the day of use. A manual micromanipulator was secured on the air table with

magnets that provided a 45° angle for injection. Brain slices were placed into a small petri dish containing 1× PBS and DAPI for 5 min at room temperature. After incubation in DAPI, slices were placed on dental wax, and then, a piece of filter paper was used to adhere the tissue. The filter paper was then transferred to the tissue chamber filled with 1× PBS and weighted down for stability. The 10× objective was used to visualize advancement of the tip of the micropipette in XY and Z until the tip was just a few micrometers above the tissue. The 40× objective was then used while advancing the tip into the CA1 region of the hippocampus. Once the microelectrode contacted a neuron, 2 nA of negative current was used for 5 min to fill the neuron with Lucifer yellow. After 5 min, the current was turned off, and the micropipette was removed from the neuron. Neuron impalement within the CA1 occurs randomly in a blind manner. If the entire neuron does not fill with dye after penetration, then the electrode is removed and the neuron is not used for analysis. Multiple neurons were injected in each hemisphere of the hippocampus of each animal. After injection, the filter paper containing the tissue was moved back into the chamber containing 1× PBS. The tissue was carefully lifted off the paper and placed on a glass slide with two 125-μm spacers (Electron Microscopy Sciences, catalog no. 70327-20S). Excess PBS was carefully removed with a Kimwipe, and the tissue was air-dried for 1 min. One drop of Vectashield (Vector Labs, catalog no. H1000) was added directly to the slice; the coverslip (Warner, catalog no. 64-0716) was added and sealed with nail polish. Injected tissue was stored at 4°C in the dark.

Confocal microscopy

Confocal microscopy was used to capture images of dendrites from the CA1 region of the hippocampus, based on previously described methods (75, 78). A blinded experimenter performed all imaging. Images were captured with a Nikon (Tokyo, Japan) Ti2 C2 confocal microscope. The experimenter identified secondary dendrites from dye-impregnated neurons and captured 3D z stacks of those meeting the following criteria: (i) within 80-μm working distance of microscope, (ii) relatively parallel with the surface of the coronal section, (iii) no overlap with other branches, (iv) minimum of 50 μm from the soma, and (v) maximum of 110 μm from the soma. For each dendrite, z stacks were captured with a 60× oil immersion objective (NA, 1.40; Nikon Plan Apo) using the following parameters: z step, 0.1 μm; image size; 1024 by 512 pixels (0.04 μm × 0.04 μm × 0.1 μm); zoom, 4.8×; line averaging, 4; and acquisition rate: 1 frame/s. Captured images were deconvolved using Huygens Deconvolution System (16.05, Scientific Volume Imaging, The Netherlands) and the following settings: GMLE; maximum iterations, 10; signal-to-noise ratio, 15; and quality, 0.003. Deconvolved images were saved in .tif format.

Dendritic spine morphometry analysis

Automated image analysis was performed with Neurolucida 360 (2.70.1, MBF Biosciences, Williston, Vermont) based on previously described methods (79). Deconvolved image stacks were imported into Neurolucida 360, and the full dendrite length was traced with semiautomatic directional kernel algorithm. The experimenter manually confirmed that all assigned points matched dendrite diameter and position in X, Y, and Z planes and adjusted each reconstruction if necessary. For wide-field microscopy, dendritic spine reconstruction was performed automatically using a voxel-clustering algorithm and the following parameters: outer range, 10.0 μm; minimum height, 0.5 μm; detector sensitivity, 100%; and minimum count, 8 voxels.

For confocal microscopy, dendritic spine reconstruction was performed automatically using a voxel-clustering algorithm and the following parameters: outer range, 5.0 μm ; minimum height, 0.3 μm ; detector sensitivity, 80%; and minimum count, 8 voxels. Next, the experimenter manually verified that the classifier correctly identified all protrusions. When necessary, the experimenter added any protrusions semiautomatically by increasing detector sensitivity. The morphology and backbone points of each spine were verified to ensure a representative spine shape, and merge and slice tools were used to correct inconsistencies. Each dendritic protrusion was automatically classified as a dendritic filopodium, thin spine, stubby spine, or mushroom spine based on previously described morphological measurements (78). Reconstructions were collected in Neurolucida Explorer (2.70.1, MBF Biosciences, Williston, VT, USA) for branched structure analysis and then exported to Microsoft Excel (Redmond, WA, USA). Spine density was calculated as the number of spines per 10 μm of dendrite length.

Statistical analysis

All analyses were conducted with Prism 6.0 (GraphPad Software, La Jolla, CA, USA). Data are presented as means \pm SEM, and all graph error bars represent SEM. All statistical tests were two tailed with threshold for statistical significance set at 0.05. Statistical comparisons are indicated in the figure legends and included unpaired *t* test, two-way ANOVA with Tukey's comparison's test, and one-way ANOVA with Šidák post hoc analysis. To compare aggregate spine densities or morphologies among experimental conditions, the mean spine density or morphologic measurement was calculated per experimental replicate (or *N*). These experiment means were then averaged per experimental condition and reported as a condition mean. See figure legends for details on *N* per experiment.

SUPPLEMENTARY MATERIALS

stke.sciencemag.org/cgi/content/full/12/587/eaaw9318/DC1

Fig. S1. Expression of human ROCKs in hippocampal neurons.

Fig. S2. A β_{42} -induced spine loss is prevented by fasudil.

Fig. S3. Fasudil protects against A β -induced neuronal hyperexcitability.

Fig. S4. SR7826 reduces the abundance of phosphorylated cofilin in the hippocampus.

Fig. S5. SR7826 alters mean spine head diameter.

Fig. S6. A β deposits are not substantially altered by SR7826.

REFERENCES AND NOTES

1. S. T. DeKosky, S. W. Scheff, Synapse loss in frontal cortex biopsies in Alzheimer's disease: Correlation with cognitive severity. *Ann. Neurol.* **27**, 457–464 (1990).
2. R. D. Terry, E. Masliah, D. P. Salmon, N. Butters, R. DeTeresa, R. Hill, L. A. Hansen, R. Katzman, Physical basis of cognitive alterations in Alzheimer's disease: Synapse loss is the major correlate of cognitive impairment. *Ann. Neurol.* **30**, 572–580 (1991).
3. S. W. Scheff, D. A. Price, F. A. Schmitt, E. J. Mufson, Hippocampal synaptic loss in early Alzheimer's disease and mild cognitive impairment. *Neurobiol. Aging* **27**, 1372–1384 (2006).
4. S. W. Scheff, D. A. Price, Synaptic pathology in Alzheimer's disease: A review of ultrastructural studies. *Neurobiol. Aging* **24**, 1029–1046 (2003).
5. C. I. Sze, J. C. Troncoso, C. Kawas, P. Mouton, D. L. Price, L. J. Martin, Loss of the presynaptic vesicle protein synaptophysin in hippocampus correlates with cognitive decline in Alzheimer disease. *J. Neuropathol. Exp. Neurol.* **56**, 933–944 (1997).
6. H. Braak, E. Braak, Neuropathological staging of Alzheimer-related changes. *Acta Neuropathol.* **82**, 239–259 (1991).
7. B. D. Boros, K. M. Gearing, J. H. Herskowitz, Dendritic spine remodeling accompanies Alzheimer's disease pathology and genetic susceptibility in cognitively normal aging. *Neurobiol. Aging* **73**, 92–103 (2019).
8. B. D. Boros, K. M. Gearinghouse, E. G. Gentry, K. A. Curtis, E. L. Birchall, M. Gearing, J. H. Herskowitz, Dendritic spines provide cognitive resilience against Alzheimer's disease. *Ann. Neurol.* **82**, 602–614 (2017).
9. Y. Hayashi, A. K. Majewska, Dendritic spine geometry: Functional implication and regulation. *Neuron* **46**, 529–532 (2005).
10. Z. Siskova, D. Justus, H. Kaneko, D. Friedrichs, N. Henneberg, T. Beutel, J. Pitsch, S. Schoch, A. Becker, H. von der Kammer, S. Remy, Dendritic structural degeneration is functionally linked to cellular hyperexcitability in a mouse model of Alzheimer's disease. *Neuron* **84**, 1023–1033 (2014).
11. J. J. Palop, J. Chin, E. D. Roberson, J. Wang, M. T. Thwin, N. Bien-Ly, J. Yoo, K. O. Ho, G.-Q. Yu, A. Kreitzer, S. Finkbeiner, J. L. Noebels, L. Mucke, Aberrant excitatory neuronal activity and compensatory remodeling of inhibitory hippocampal circuits in mouse models of Alzheimer's disease. *Neuron* **55**, 697–711 (2007).
12. R. Minkeviciene, S. Rheims, M. B. Dobcsay, M. Zilberter, J. Hartikainen, L. Fülöp, B. Penke, Y. Zilberter, T. Harkany, A. Pitkänen, H. Tanila, Amyloid beta-induced neuronal hyperexcitability triggers progressive epilepsy. *J. Neurosci.* **29**, 3453–3462 (2009).
13. K. A. Vossel, A. J. Beagle, G. D. Rabinovici, H. Shu, S. E. Lee, G. Naasan, M. Hegde, S. B. Cornes, M. L. Henry, A. B. Nelson, W. W. Seeley, M. D. Geschwind, M. L. Gorno-Tempini, T. Shih, H. E. Kirsch, P. A. Garcia, B. L. Miller, L. Mucke, Seizures and epileptiform activity in the early stages of Alzheimer disease. *JAMA Neurol.* **70**, 1158–1166 (2013).
14. P. E. Sanchez, L. Zhu, L. Verret, K. A. Vossel, A. G. Orr, J. R. Cirrito, N. Devidez, K. Ho, G.-Q. Yu, J. J. Palop, L. Mucke, Levetiracetam suppresses neuronal network dysfunction and reverses synaptic and cognitive deficits in an Alzheimer's disease model. *Proc. Natl. Acad. Sci. U.S.A.* **109**, E2895–E2903 (2012).
15. M. A. Busche, G. Eichhoff, H. Adelsberger, D. Abramowski, K.-H. Wiederhold, C. Haass, M. Staufenbiel, A. Konnerth, O. Garaschuk, Clusters of hyperactive neurons near amyloid plaques in a mouse model of Alzheimer's disease. *Science* **321**, 1686–1689 (2008).
16. M. A. Busche, X. Chen, H. A. Henning, J. Reichwald, M. Staufenbiel, B. Sakmann, A. Konnerth, Critical role of soluble amyloid- β for early hippocampal hyperactivity in a mouse model of Alzheimer's disease. *Proc. Natl. Acad. Sci. U.S.A.* **109**, 8740–8745 (2012).
17. B. W. Henderson, E. G. Gentry, T. Rush, J. C. Troncoso, M. Thambisetty, T. J. Montine, J. H. Herskowitz, Rho-associated protein kinase 1 (ROCK1) is increased in Alzheimer's disease and ROCK1 depletion reduces amyloid- β levels in brain. *J. Neurochem.* **138**, 525–531 (2016).
18. L. Heredia, P. Helguera, S. de Olmos, G. Kedikan, F. Solá Vigo, F. LaFerla, M. Staufenbiel, J. de Olmos, J. Busciglio, A. Caceres, A. Lorenzo, Phosphorylation of actin-depolymerizing factor/cofilin by LIM-kinase mediates amyloid- β -induced degeneration: A potential mechanism of neuronal dystrophy in Alzheimer's disease. *J. Neurosci.* **26**, 6533–6542 (2006).
19. S. Petratos, Q.-X. Li, A. J. George, X. Hou, M. L. Kerr, S. E. Unabia, I. Hatzinikisiou, D. Maksel, M.-I. Aguilar, D. H. Small, The β -amyloid protein of Alzheimer's disease increases neuronal CRMP-2 phosphorylation by a Rho-GTP mechanism. *Brain* **131**, 90–108 (2008).
20. T. Leung, X. Q. Chen, E. Manser, L. Lim, The p160 RhoA-binding kinase ROK alpha is a member of a kinase family and is involved in the reorganization of the cytoskeleton. *Mol. Cell. Biol.* **16**, 5313–5327 (1996).
21. T. Leung, E. Manser, L. Tan, L. Lim, A novel serine/threonine kinase binding the Ras-related RhoA GTPase which translocates the kinase to peripheral membranes. *J. Biol. Chem.* **270**, 29051–29054 (1995).
22. T. Matsui, M. Amano, T. Yamamoto, K. Chihara, M. Nakafuku, M. Ito, T. Nakano, K. Okawa, A. Iwamatsu, K. Kaibuchi, Rho-associated kinase, a novel serine/threonine kinase, as a putative target for small GTP binding protein Rho. *EMBO J.* **15**, 2208–2216 (1996).
23. T. Ishizaki, M. Maekawa, K. Fujisawa, K. Okawa, A. Iwamatsu, A. Fujita, N. Watanabe, Y. Saito, A. Kakizuka, N. Morii, S. Narumiya, The small GTP-binding protein Rho binds to and activates a 160 kDa Ser/Thr protein kinase homologous to myotonic dystrophy kinase. *EMBO J.* **15**, 1885–1893 (1996).
24. O. Nakagawa, K. Fujisawa, T. Ishizaki, Y. Saito, K. Nakao, S. Narumiya, ROCK-I and ROCK-II, two isoforms of Rho-associated coiled-coil forming protein serine/threonine kinase in mice. *FEBS Lett.* **392**, 189–193 (1996).
25. S. A. Swanger, A. L. Mattheyses, E. G. Gentry, J. H. Herskowitz, ROCK1 and ROCK2 inhibition alters dendritic spine morphology in hippocampal neurons. *Cell Logist.* **5**, e1133266 (2016).
26. J. H. Herskowitz, Y. Feng, A. L. Mattheyses, C. M. Hales, L. A. Higginbotham, D. M. Duong, T. J. Montine, J. C. Troncoso, M. Thambisetty, N. T. Seyfried, A. I. Levey, J. J. Lah, Pharmacologic inhibition of ROCK2 suppresses amyloid- β production in an Alzheimer's disease mouse model. *J. Neurosci.* **33**, 19086–19098 (2013).
27. T. Rush, J. Martinez-Hernandez, M. Dollmeyer, M. L. Frandemiche, E. Borel, S. Boisseau, M. Jacquier-Sarlin, A. Buisson, Synaptotoxicity in Alzheimer's disease involved a dysregulation of actin cytoskeleton dynamics through cofilin 1 phosphorylation. *J. Neurosci.* **38**, 10349–10361 (2018).
28. K. J. Sellers, C. Elliott, J. Jackson, A. Ghosh, E. Ribe, A. I. Rojo, H. H. Jarosz-Griffiths, I. A. Watson, W. Xia, M. Semenov, P. Morin, N. M. Hooper, R. Porter, J. Preston, R. Al-Shawi, G. Baillie, S. Lovestone, A. Cuadrado, M. Harte, P. Simons, D. P. Srivastava, R. Killick, Amyloid β synaptotoxicity is Wnt-PCP dependent and blocked by fasudil. *Alzheimers Dement.* **14**, 306–317 (2018).

29. S. P. Davies, H. Reddy, M. Caivano, P. Cohen, Specificity and mechanism of action of some commonly used protein kinase inhibitors. *Biochem. J.* **351**, 95–105 (2000).
30. H. Bito, T. Furuyashiki, H. Ishihara, Y. Shibusaki, K. Ohashi, K. Mizuno, M. Maekawa, T. Ishizaki, S. Narumiya, A critical role for a Rho-associated kinase, p160ROCK, in determining axon outgrowth in mammalian CNS neurons. *Neuron* **26**, 431–441 (2000).
31. S. Woo, T. M. Gomez, Rac1 and RhoA promote neurite outgrowth through formation and stabilization of growth cone point contacts. *J. Neurosci.* **26**, 1418–1428 (2006).
32. X.-b. Yuan, M. Jin, X. Xu, Y.-q. Song, C.-p. Wu, M.-m. Poo, S. Duan, Signalling and crosstalk of Rho GTPases in mediating axon guidance. *Nat. Cell Biol.* **5**, 38–45 (2003).
33. X.-F. Zhang, A. W. Schaefer, D. T. Burnett, V. T. Schoonderwoert, P. Forscher, Rho-dependent contractile responses in the neuronal growth cone are independent of classical peripheral retrograde actin flow. *Neuron* **40**, 931–944 (2003).
34. J. Riedl, A. H. Crevenna, K. Kessenbrock, J. H. Yu, D. Neukirchen, M. Bista, F. Bradke, D. Jenne, T. A. Holak, Z. Werb, M. Sixt, R. Wedlich-Söldner, Lifeact: A versatile marker to visualize F-actin. *Nat. Methods* **5**, 605–607 (2008).
35. M. Amano, K. Chihara, K. Kimura, Y. Fukata, N. Nakamura, Y. Matsuura, K. Kaibuchi, Formation of actin stress fibers and focal adhesions enhanced by Rho-kinase. *Science* **275**, 1308–1311 (1997).
36. M. Amano, M. Ito, K. Kimura, Y. Fukata, K. Chihara, T. Nakano, Y. Matsuura, K. Kaibuchi, Phosphorylation and activation of myosin by Rho-associated kinase (Rho-kinase). *J. Biol. Chem.* **271**, 20246–20249 (1996).
37. K. Kimura, M. Ito, M. Amano, K. Chihara, Y. Fukata, M. Nakafuku, B. Yamamori, J. Feng, T. Nakano, K. Okawa, A. Iwamatsu, K. Kaibuchi, Regulation of myosin phosphatase by Rho and Rho-associated kinase (Rho-kinase). *Science* **273**, 245–248 (1996).
38. T. Sumi, K. Matsumoto, T. Nakamura, Specific activation of LIM kinase 2 via phosphorylation of threonine 505 by ROCK, a Rho-dependent protein kinase. *J. Biol. Chem.* **276**, 670–676 (2001).
39. M. Kovács, J. Tóth, C. Hetényi, A. Málnási-Czizmadia, J. R. Sellers, Mechanism of blebbistatin inhibition of myosin II. *J. Biol. Chem.* **279**, 35557–35563 (2004).
40. Y. Yin, K. Zheng, N. Eid, S. Howard, J.-H. Jeong, F. Yi, J. Guo, C. M. Park, M. Bibian, W. Wu, P. Hernandez, H. Park, Y. Wu, J. L. Luo, P. V. LoGrasso, Y. Feng, Bis-aryl urea derivatives as potent and selective LIM kinase (Limk) inhibitors. *J. Med. Chem.* **58**, 1846–1861 (2015).
41. P. N. Lacor, M. C. Buniel, P. W. Furlow, A. S. Clemente, P. T. Velasco, M. Wood, K. L. Viola, W. L. Klein, A β oligomer-induced aberrations in synapse composition, shape, and density provide a molecular basis for loss of connectivity in Alzheimer's disease. *J. Neurosci.* **27**, 796–807 (2007).
42. T. L. Spires, M. Meyer-Luehmann, E. A. Stern, P. J. McLean, J. Skoch, P. T. Nguyen, B. J. Bacskai, B. T. Hyman, Dendritic spine abnormalities in amyloid precursor protein transgenic mice demonstrated by gene transfer and intravital multiphoton microscopy. *J. Neurosci.* **25**, 7278–7287 (2005).
43. J. Pozueta, R. Lefort, E. M. Ribe, C. M. Troy, O. Arancio, M. Shelanski, Caspase-2 is required for dendritic spine and behavioural alterations in J20 APP transgenic mice. *Nat. Commun.* **4**, 1939 (2013).
44. S. Arber, F. A. Barbayannis, H. Hanser, C. Schneider, C. A. Stanyon, O. Bernard, P. Caroni, Regulation of actin dynamics through phosphorylation of cofilin by LIM-kinase. *Nature* **393**, 805–809 (1998).
45. N. Yang, O. Higuchi, K. Ohashi, K. Nagata, A. Wada, K. Kangawa, E. Nishida, K. Mizuno, Cofilin phosphorylation by LIM-kinase 1 and its role in Rac-mediated actin reorganization. *Nature* **393**, 809–812 (1998).
46. K. M. Harris, F. E. Jensen, B. Tsao, Three-dimensional structure of dendritic spines and synapses in rat hippocampus (CA1) at postnatal day 15 and adult ages: Implications for the maturation of synaptic physiology and long-term potentiation. *J. Neurosci.* **12**, 2685–2705 (1992).
47. H. Hering, M. Sheng, Dendritic spines: Structure, dynamics and regulation. *Nat. Rev. Neurosci.* **2**, 880–888 (2001).
48. K. A. Vossel, K. G. Ranasinghe, A. J. Beagle, D. Mizuiri, S. M. Honma, A. F. Dowling, S. M. Darwishi, V. Van Berlo, D. E. Barnes, M. Mantle, A. M. Karydas, G. Coppola, E. D. Roberson, B. L. Miller, P. A. Garcia, H. E. Kirsch, L. Mucke, S. S. Nagarajan, Incidence and impact of subclinical epileptiform activity in Alzheimer's disease. *Ann. Neurol.* **80**, 858–870 (2016).
49. D. Johnston, J. C. Magee, C. M. Colbert, B. R. Christie, Active properties of neuronal dendrites. *Annu. Rev. Neurosci.* **19**, 165–186 (1996).
50. J. Lauren, D. A. Gimbel, H. B. Nygaard, J. W. Gilbert, S. M. Strittmatter, Cellular prion protein mediates impairment of synaptic plasticity by amyloid- β oligomers. *Nature* **457**, 1128–1132 (2009).
51. H.-J. Kim, H.-S. Choi, J.-H. Park, M.-J. Kim, H.-g. Lee, R. B. Petersen, Y.-S. Kim, J.-B. Park, E.-K. Choi, Regulation of RhoA activity by the cellular prion protein. *Cell Death Dis.* **8**, e2668 (2017).
52. Y. Feng, P. V. LoGrasso, O. Defert, R. Li, Rho kinase (ROCK) inhibitors and their therapeutic potential. *J. Med. Chem.* **59**, 2269–2300 (2016).
53. E. G. Gentry, B. W. Henderson, A. E. Arrant, M. Gearing, Y. Feng, N. C. Riddle, J. H. Herskowitz, Rho kinase inhibition as a therapeutic for progressive supranuclear palsy and corticobasal degeneration. *J. Neurosci.* **36**, 1316–1323 (2016).
54. R. Günther, A. Balck, J. C. Koch, T. Nientiedt, M. Sereda, M. Bähr, P. Lingor, L. Tönges, Rho kinase inhibition with fasudil in the SOD1^{G93A} mouse model of amyotrophic lateral sclerosis—Symptomatic treatment potential after disease onset. *Front. Pharmacol.* **8**, 17 (2017).
55. J. C. Koch, L. Tönges, E. Barski, U. Michel, M. Bähr, P. Lingor, ROCK2 is a major regulator of axonal degeneration, neuronal death and axonal regeneration in the CNS. *Cell Death Dis.* **5**, e1225 (2014).
56. L. Tatenhorst, K. Eckermann, V. Dambeck, L. Fonseca-Ornelas, H. Walle, T. Lopes da Fonseca, J. C. Koch, S. Becker, L. Tonges, M. Bahr, T. F. Outeiro, M. Zweckstetter, P. Lingor, Fasudil attenuates aggregation of α -synuclein in models of Parkinson's disease. *Acta Neuropathol. Commun.* **4**, 39 (2016).
57. L. Julian, M. F. Olson, Rho-associated coiled-coil containing kinases (ROCK). *Small GTPases* **5**, e29846 (2014).
58. Y. Feng, P. V. LoGrasso, Rho kinase inhibitors: A patent review (2012–2013). *Expert Opin. Ther. Pat.* **24**, 295–307 (2014).
59. V. C. Foletta, N. Moussi, P. D. Sarmiere, J. R. Bamburg, O. Bernard, LIM kinase 1, a key regulator of actin dynamics, is widely expressed in embryonic and adult tissues. *Exp. Cell Res.* **294**, 392–405 (2004).
60. C. Prunier, R. Prudent, R. Kapur, K. Sadoul, L. Lafanechère, LIM kinases: Cofilin and beyond. *Oncotarget* **8**, 41749–41763 (2017).
61. F. Manetti, LIM kinases are attractive targets with many macromolecular partners and only a few small molecule regulators. *Med. Res. Rev.* **32**, 968–998 (2012).
62. F.-L. Chang, W. T. Greenough, Transient and enduring morphological correlates of synaptic activity and efficacy change in the rat hippocampal slice. *Brain Res.* **309**, 35–46 (1984).
63. A. Peters, I. R. Kaiserman-Abramof, The small pyramidal neuron of the rat cerebral cortex. The perikaryon, dendrites and spines. *Am. J. Anat.* **127**, 321–355 (1970).
64. J. Tonnesen, G. Katona, B. Rozsa, U. V. Nägerl, Spine neck plasticity regulates compartmentalization of synapses. *Nat. Neurosci.* **17**, 678–685 (2014).
65. C. Lang, A. Barco, L. Zablow, E. R. Kandel, S. A. Siegelbaum, S. S. Zakharenko, Transient expansion of synaptically connected dendritic spines upon induction of hippocampal long-term potentiation. *Proc. Natl. Acad. Sci. U.S.A.* **101**, 16665–16670 (2004).
66. M. Matsuzaki, N. Honkura, G. C. R. Ellis-Davies, H. Kasai, Structural basis of long-term potentiation in single dendritic spines. *Nature* **429**, 761–766 (2004).
67. J.-i. Tanaka, Y. Horiike, M. Matsuzaki, T. Miyazaki, G. C. R. Ellis-Davies, H. Kasai, Protein synthesis and neurotrophin-dependent structural plasticity of single dendritic spines. *Science* **319**, 1683–1687 (2008).
68. C. D. Harvey, K. Svoboda, Locally dynamic synaptic learning rules in pyramidal neuron dendrites. *Nature* **450**, 1195–1200 (2007).
69. D. L. Dickstein, C. M. Weaver, J. I. Luebke, P. R. Hof, Dendritic spine changes associated with normal aging. *Neuroscience* **251**, 21–32 (2012).
70. J. H. Herskowitz, K. Offe, A. Deshpande, R. A. Kahn, A. I. Levey, J. J. Lah, GGA1-mediated endocytic traffic of LR11/SorLA alters APP intracellular distribution and amyloid- β production. *Mol. Biol. Cell* **23**, 2645–2657 (2012).
71. J. Riedl, K. C. Flynn, A. Raducanu, F. Gärtner, G. Beck, M. Bösl, F. Bradke, S. Massberg, A. Aszodi, M. Sixt, R. Wedlich-Söldner, Lifeact mice for studying F-actin dynamics. *Nat. Methods* **7**, 168–169 (2010).
72. R. Bzymek, M. Horsthemke, K. Isfort, S. Mohr, K. Tjaden, C. Müller-Tidow, M. Thomann, T. Schwerdtle, M. Bahler, A. Schwab, P. J. Hanley, Real-time two- and three-dimensional imaging of monocyte motility and navigation on planar surfaces and in collagen matrices: Roles of Rho. *Sci. Rep.* **6**, 25016 (2016).
73. J.-L. Maitre, H. Turlier, R. Illukumbura, B. Eismann, R. Niwayama, F. Nédélec, T. Hiiragi, Asymmetric division of contractile domains couples cell positioning and fate specification. *Nature* **536**, 344–348 (2016).
74. J. H. Herskowitz, N. T. Seyfried, M. Gearing, R. A. Kahn, J. Peng, A. I. Levey, J. J. Lah, Rho kinase II phosphorylation of the lipoprotein receptor LR11/SORLA alters amyloid-beta production. *J. Biol. Chem.* **286**, 6117–6127 (2011).
75. D. Dumitriu, A. Rodriguez, J. H. Morrison, High-throughput, detailed, cell-specific neuroanatomy of dendritic spines using microinjection and confocal microscopy. *Nat. Protoc.* **6**, 1391–1411 (2011).
76. P. J. Hallett, T. L. Collins, D. G. Standaert, A. W. Dunah, Biochemical fractionation of brain tissue for studies of receptor distribution and trafficking. *Curr. Protoc. Neurosci.* Chapter 1, Unit 1.16 (2008).
77. B. A. Warmus, D. R. Sekar, E. McCutchen, G. D. Schellenberg, R. C. Roberts, L. L. McMahon, E. D. Roberson, Tau-mediated NMDA receptor impairment underlies dysfunction of a selectively vulnerable network in a mouse model of frontotemporal dementia. *J. Neurosci.* **34**, 16482–16495 (2014).
78. K. M. Greathouse, B. D. Boros, J. F. Deslauriers, B. W. Henderson, K. A. Curtis, E. G. Gentry, J. H. Herskowitz, Distinct and complementary functions of rho kinase isoforms ROCK1

- and ROCK2 in prefrontal cortex structural plasticity. *Brain Struct. Funct.* **223**, 4227–4241 (2018).
79. D. L. Dickstein, D. R. Dickstein, W. G. M. Janssen, P. R. Hof, J. R. Glaser, A. Rodriguez, N. O'Connor, P. Angstman, S. J. Tappan, Automatic dendritic spine quantification from confocal data with neurulucida 360. *Curr. Protoc. Neurosci.* **77**, 1.27.1–1.27.21 (2016).

Acknowledgments: We thank Y. Feng at Reaction Biology and members of E. Roberson's laboratory at UAB for helpful discussions. Hematoxylin and eosin staining was provided by the UAB Pathology Core Research Lab. **Funding:** This work was supported by the National Institutes of Health through NIA AG061800, NIA AG054719, and NIA AG043552 (all to J.H.H.) and Emory Neuroscience NINDS Core Facilities grant P30NS055077, and B.W.H. was supported by T32 NS 061788. Additional support stemmed from a New Investigator Research grant 2015-NIRG-339422 (to J.H.H.) from the Alzheimer's Association. **Author contributions:** B.W.H., K.M.G., J.J.D., A.L.M., and J.H.H. conceived the project and designed the studies. B.W.H. performed and analyzed the in vitro experiments. J.J.D. and S.V.B. contributed to the

electrophysiological experiments. K.M.G., R.R., C.K.W., and K.A.C. performed and analyzed the in vivo experiments. K.M.G., T.C.R., and A.L.M. performed and analyzed the live-cell imaging experiments. B.W.H., K.M.G., C.K.W., and J.H.H. wrote the manuscript with comments from all authors. **Competing interests:** The authors declare that they have no competing interests. **Data and materials availability:** All data needed to evaluate the conclusions in the paper are present in the paper or the Supplementary Materials.

Submitted 6 February 2019
Accepted 30 May 2019
Published 25 June 2019
10.1126/scisignal.aaw9318

Citation: B. W. Henderson, K. M. Greathouse, R. Ramdas, C. K. Walker, T. C. Rao, S. V. Bach, K. A. Curtis, J. J. Day, A. L. Mattheyses, J. H. Herskowitz, Pharmacologic inhibition of LIMK1 provides dendritic spine resilience against β -amyloid. *Sci. Signal.* **12**, eaaw9318 (2019).

F O R C E F O R S C I E N C E . O R G

STAND TOGETHER

Be a Force for Science

GET THE FACTS

Understand the science behind the issues that matter.

FOLLOW AAAS ADVOCACY

Champion public discussion and evidence-based policy.

TAKE ACTION

Learn ways you can become an advocate and stand up for science.



AMERICAN ASSOCIATION FOR THE ADVANCEMENT OF SCIENCE

AAAS

NEURODEVELOPMENT

L-Serine dietary supplementation is associated with clinical improvement of loss-of-function *GRIN2B*-related pediatric encephalopathy

David Soto^{1,2,3*}, Mireia Olivella^{4*}, Cristina Grau^{5*}, Judith Armstrong⁶, Clara Alcon^{1,7}, Xavier Gasull^{1,2,3}, Ana Santos-Gómez⁵, Sílvia Locubiche⁵, Macarena Gómez de Salazar⁵, Roberto García-Díaz^{1,2,3,8}, Esther Gratacós-Batlle^{1,2,3}, David Ramos-Vicente^{9,10}, Emeline Chu-Van¹¹, Benoit Colsch¹¹, Víctor Fernández-Dueñas⁵, Francisco Ciruela⁵, Àlex Bayés^{9,10}, Carlos Sindreu^{1,7}, Anna López-Sala¹², Àngels García-Cazorla^{6,12†}, Xavier Altafaj^{5†}

Autosomal dominant mutations in *GRIN2B* are associated with severe encephalopathy, but little is known about the pathophysiological outcomes and any potential therapeutic interventions. Genetic studies have described the association between *de novo* mutations of genes encoding the subunits of the N-methyl-D-aspartate receptor (NMDAR) and severe neurological conditions. Here, we evaluated a missense mutation in *GRIN2B*, causing a proline-to-threonine switch (P553T) in the GluN2B subunit of NMDAR, which was found in a 5-year-old patient with Rett-like syndrome with severe encephalopathy. Structural molecular modeling predicted a reduced pore size of the mutant GluN2B-containing NMDARs. Electrophysiological recordings in a HEK-293T cell line expressing the mutated subunit confirmed this prediction and showed an associated reduced glutamate affinity. Moreover, GluN2B(P553T)-expressing primary murine hippocampal neurons showed decreased spine density, concomitant with reduced NMDA-evoked currents and impaired NMDAR-dependent insertion of the AMPA receptor subunit GluA1 at stimulated synapses. Furthermore, the naturally occurring coagonist D-serine restored function to GluN2B(P553T)-containing NMDARs. L-Serine dietary supplementation of the patient was hence initiated, resulting in the increased abundance of D-serine in the plasma and brain. The patient has shown notable improvements in motor and cognitive performance and communication after 11 and 17 months of L-serine dietary supplementation. Our data suggest that L-serine supplementation might ameliorate *GRIN2B*-related severe encephalopathy and other neurological conditions caused by glutamatergic signaling deficiency.

INTRODUCTION

Rett syndrome (RTT; Online Mendelian Inheritance in Man, OMIM: 312750) is a neurodevelopmental disorder affecting 1 in 10,000 live female births (1, 2). Clinical manifestations include microcephaly, loss of achieved psychomotor abilities, intellectual disability (ID), and autistic behaviors (3). Whereas most cases of typical RTT harbor loss-of-function mutations in the X-linked gene encoding methyl-CpG-binding protein 2 (*MECP2*) (4), mutations in genes encoding cyclin-dependent kinase-like 5 (*CDKL5*) and Forkhead box G1 (*FOXP1*) have also been identified (5). Rett-like syndrome mostly affects patients exhibiting symptoms that are similar to those seen in patients with RTT; however, the genetic

and molecular etiologies of this rare disease are different from those associated with RTT.

A growing number of genetic and functional studies are unraveling the complex scenario and molecular players involved in neurodevelopmental disorders and, in particular, in Rett-like syndrome. It has been shown that the dysregulation of synaptic proteins can lead to neurodevelopmental disorder (6–8). Genes encoding for the N-methyl-D-aspartate receptor (NMDAR) could play critical roles in the dysfunction of glutamatergic transmission associated with RTT. Functionally, NMDARs play critical roles in neurogenesis, synaptogenesis, and synaptic plasticity processes. Early in development, NMDAR subunit GluN2B expression is particularly high (9). Accordingly, it has been proposed that *GRIN2B* gene disturbance might markedly compromise critical steps of neuronal, synaptic, and brain circuitry development (10). Moreover, discrete *de novo* mutations of *GRIN2B* gene have been associated with neurodevelopmental disorders (11–13) such as early infantile epileptic encephalopathy-27 (EIEE27; OMIM: 616139) (14) and autosomal dominant mental retardation (MRD6; OMIM: 613970) (15–17).

In this study, we investigated the effects of a *de novo* missense mutation in the *GRIN2B* gene in a patient with Rett-like syndrome and severe encephalopathy. Functional studies showed that channel gating is altered in mutant NMDARs markedly reducing NMDAR-mediated currents. Dietary supplementation with L-serine—the precursor of D-serine, an endogenous NMDAR coagonist (18, 19)—during 17 months was associated with ameliorated intellectual, communication, and motor deficits in the patient. These results support the pathogenicity of *GRIN2B* mutation and suggest that enhancing NMDAR

¹Institute of Neurosciences, University of Barcelona, Barcelona 08036, Spain. ²Department of Biomedicine, University of Barcelona, Barcelona 08036, Spain. ³August Pi i Sunyer Biomedical Research Institute (IDIBAPS), Barcelona 08036, Spain. ⁴Bioinformatics and Medical Statistics Group, University of Vic-Central University of Catalonia, Vic 08500, Spain. ⁵Bellvitge Biomedical Research Institute (IDIBELL)-Unit of Neuropharmacology and Pain, University of Barcelona, Barcelona 08908, Spain. ⁶Genetics and Molecular Medicine Service, Hospital Sant Joan de Déu and CIBERER, Barcelona 08950, Spain. ⁷Department of Clinical Foundations, University of Barcelona, Barcelona 08036, Spain. ⁸Grupo de Investigación en Química y Biotecnología (QUIBIO), Universidad de Santiago de Cali, Santiago de Cali 760035, Colombia. ⁹Molecular Physiology of the Synapse Laboratory, Biomedical Research Institute Sant Pau (IIB Sant Pau), Barcelona 08026, Spain. ¹⁰Autonomous University of Barcelona, Bellaterra 08193, Spain. ¹¹Service de Pharmacologie et d'Immunoanalyse (SPI), Laboratoire d'Etude du Métabolisme des Médicaments, CEA, INRA, Université Paris Saclay, MetaboHUB, F-91191 Gif-sur-Yvette, France. ¹²Department of Neurology, Neurometabolic Unit, Hospital Sant Joan de Déu and CIBERER, Barcelona 08950, Spain. *These authors contributed equally to this work.

†Corresponding author. Email: xaltafaj@idibell.cat (X.A.); agarci@sjdhospitalbarcelona.org (À.G.-C.).

Copyright © 2019
The Authors, some
rights reserved;
exclusive licensee
American Association
for the Advancement
of Science. No claim
to original U.S.
Government Works

activity using L-serine dietary supplementation can have therapeutic benefits in certain neurodevelopmental disorders associated with NMDAR hypofunctionality.

RESULTS

Patient clinical symptomatology and genetic studies

The patient was a girl born after an uneventful pregnancy and with no family history of neurodevelopmental disorders. She was referred to our clinic at 1 year old, and the primary clinical examination showed a psychomotor delay with severe hypotonia (with the presence of osteotendinous reflexes and devoid of pyramidal signs) and an inability to hold up her head and to sit upright. Behaviorally, she had an overall “absence,” as manifested by a poor visual contact, an impairment in social interaction, and no interest in the environment. Along with these alterations, the patient showed high irritability with sleep disturbances. Considering these symptoms, together with the presence of “hand-washing” stereotypies, the girl was tentatively diagnosed with RTT rather than Rett-like phenotype. Cytogenetic analysis, brain magnetic resonance imaging, and neurometabolic analysis did not show abnormalities. At 2.5 years old, she was less irritable and had developed the capacity to hold up her head. Behaviorally, she had slightly improved social interaction, and 1 year later, her sleeping pattern was ameliorated. At that age (3.5 years old), an electroencephalogram (EEG) indicated the presence of epileptiform alterations of brain activity, she was treated with valproic acid, and later, the treatment was changed to levetiracetam to prevent changes in irritability. At 5 years and 10 months old, the patient’s adaptive behavior was assessed by the Vineland test, with scores indicative of a mental age below 1 year old (Fig. 5C).

As noted, the patient was tentatively diagnosed with RTT-like phenotype. Because no mutations of RTT candidate genes (*MECP2*, *CDKL5*, and *FOXP1*) were detected, whole-exome sequencing was performed (20). After genetic data filtering against parental variants and then against a pool of controls, we identified a de novo heterozygous missense mutation in *GRIN2B* gene coding for the GluN2B subunit of NMDARs, resulting in an amino acid substitution of a proline (Pro) residue by a threonine (Thr) at GluN2B subunit residue 553 (Fig. 1A).

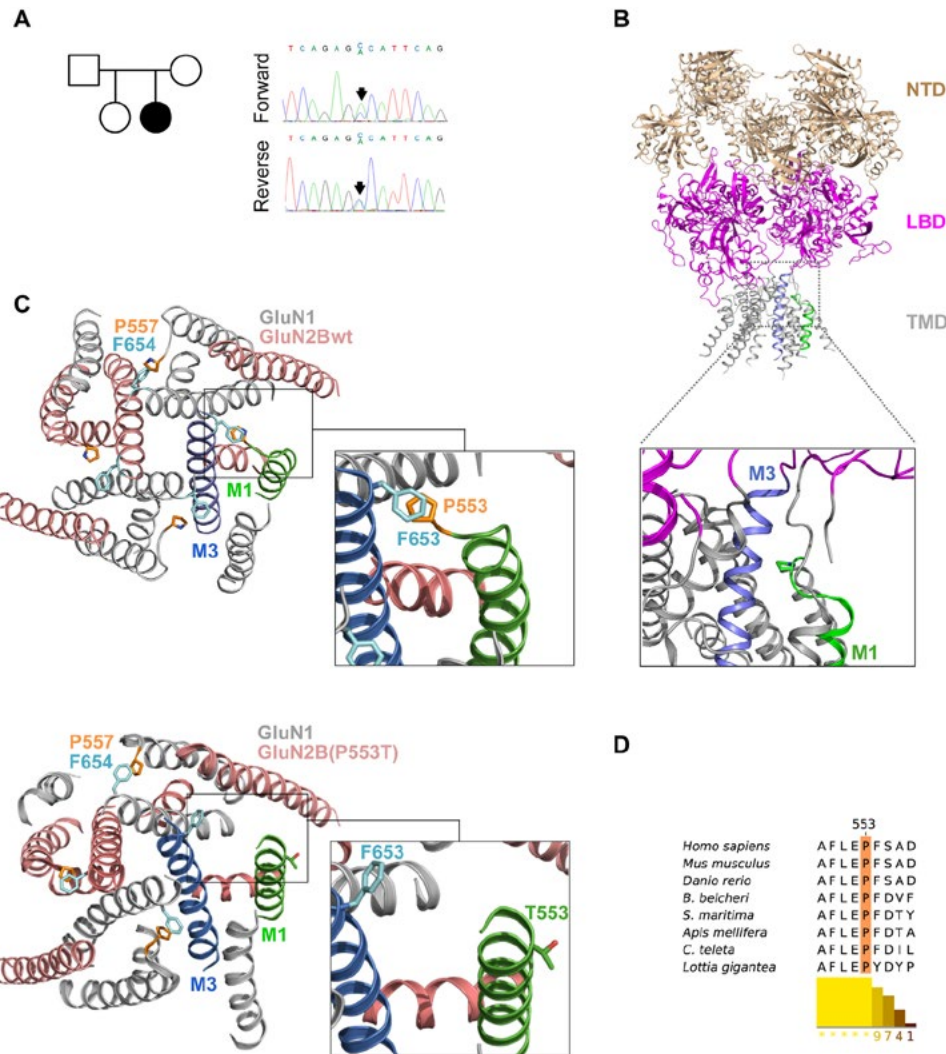


Fig. 1. Identification of GRIN2B(P553T) mutation associated with the case study and predicted structural consequences. (A) Left: Familial pedigree of the GRIN2B(P553T) case study. Right: Chromatograms of *GRIN2B* (c.1657C > A) mutated nucleotide (indicated by an arrow) using forward and reverse oligonucleotides. (B) Structure of heterotetrameric (GluN1)₂-(GluN2B)₂ NMDAR [Protein Data Bank (PDB) ID: 4PE5], according to Karakas and Furukawa (61), showing the N-terminal domain (NTD), the ligand-binding domain (LBD), and the transmembrane domain (TMD; containing the mutated amino acid P553T). Bottom: Magnification of the transmembrane domain, showing the topological position of Pro⁵⁵³ residue at the beginning of the M1 (P553; green) of the transmembrane domain, facing Phe⁶⁵³ residue (F653; light blue) at M3 (blue). (C) Top: Transmembrane domain structural molecular model of wild-type (GluN1)₂-(GluN2B)₂ receptor (from the extracellular domain). Inset: Magnification of residues Pro553(M1)-F653(M3) proximity. Bottom: Transmembrane domain structural molecular model of mutant (GluN1)₂-(GluN2B(P553T))₂ receptor (from the extracellular domain). Inset: Magnification of residues Pro553(M1)-F653(M3) distance. (D) GluN2B protein sequence alignment around residue Pro⁵⁵³. Representative sequences from a larger alignment containing 147 proteins from 12 metazoan species spanning seven phyla are shown. Displayed protein sequences are from the following species: *Homo sapiens* GluN2B (UniProt ref. Q13224), *Mus musculus* GluN2B (UniProt ref. Q01097), *Danio rerio* GluN2B (Ensembl ref. ENSDARG00000030376), *Branchiostoma belcheri* 254360R.t1 (from the database B.belcheri_v18h27.r3_ref_protein included in LanceletDB Genome browser; Sun Yat-sen University), *Saccoglossus kowalevskii* Sakowv30010297m (Metazome database), and *Strigamia maritima* SmarNMDAR2b, *Apis mellifera* GB48097, *Capitella teleta* CapteT179505, and *Lottia gigantea* LotgiT137890 (all from Ensembl Metazoa).

Molecular modeling of mutant (GluN1)₂-(GluN2B(P553T))₂ receptor

To identify the structural changes induced by GluN2B(P553T) mutation, molecular models of wild-type and mutant receptors were

generated by homology modeling (using crystal structures of NMDAR at closed state) and molecular dynamics simulation. The Pro⁵⁵³ residue in GluN2B is located at the beginning of the transmembrane helix 1 (M1; Fig. 1B). This model suggested a role for Pro⁵⁵³ in breaking M1 and bending it toward M3 (Fig. 1C, top), thereby enabling the interaction of Pro⁵⁵³ with Phe⁶⁵³ (M3) of the GluN2B subunits. In addition, according to this model, the residue Pro⁵⁵⁷ (M1) is also bending M1 to M3 through its Pro kink, allowing the interaction with Phe⁶⁵⁴ (M3) of the GluN1 subunit. This model predicted that the P553T mutation would prevent M1 bending, disrupting M1-M3 interaction (Fig. 1C, bottom), which in turn would bring M3 closer to the center of the pore and consequently induce a more closed channel conformation, altering the gating properties of the mutant receptor.

On the basis of this structural model, we investigated the evolutionary conservation of the GluN2B Pro⁵⁵³ residue and its predicted interacting residue Phe⁶⁵³. We found that the Pro⁵⁵³ motif was highly conserved across species (Fig. 1D). The GluN2B Phe⁶⁵³ and GluN1 Phe⁶⁵⁴ residues are within the SYTANLAAF motif (fig. S4), the most highly conserved motif among mammalian ionotropic glutamate receptors (iGluRs) (21, 22). Multiple sequence alignments of 147 metazoan iGluRs showed a high conservation of these residues (the Pro⁵⁵³ and Phe⁶⁵³ residues were detected in 144 and 131 iGluR protein-encoding gene sequences, respectively; fig. S4), supporting a potentially critical role of the Pro⁵⁵³ residue in GluN2B in NMDAR channel activity.

Heteromerization and trafficking of GluN1-GluN2B(P553T) receptors

To assess the effects of GluN2B(P553T) on the oligomerization and trafficking of NMDARs, we cotransfected human embryonic kidney (HEK) 293T cells with GluN1 and hemagglutinin (HA)-tagged GluN2A, together with either green fluorescent protein (GFP)-tagged wild-type GluN2B (GFP-GluN2Bwt) or the P553T mutant [GFP-GluN2B(P553T)]. Biochemical analysis showed that the protein abundance of GluN2B(P553T) was similar to that of GluN2Bwt in these cells (fig. S1A). Further, coimmunoprecipitation experiments showed the presence of GluN1 and HA-GluN2A subunits in anti-GFP pulldown complexes, indicating that the mutant GluN2B(P553T) subunit interacted—in similar abundance as GluN2Bwt—with GluN1 and/or GluN2A subunits (fig. S1B). Immunofluorescence analysis showed that the missense mutation on Pro⁵⁵³ does not abolish the trafficking of GluN1-GluN2B(P553T) to the surface of COS-7-transfected cells (fig. S1C), as previously reported for another GRIN2B missense variant affecting the same amino acid position, GluN2B(P553L) (23). In primary cortical murine neurons, the dendritic surface:intracellular abundance ratio of transfected GluN2B(P553T) was normal at days in vitro 7 (DIV7) and DIV11, with a slight decrease in DIV16 (fig. S1D).

Biophysical assessment of GluN2B(P553T) subunit-containing NMDARs

We performed patch-clamp experiments to evaluate the biophysical properties of GluN2B(P553T)-containing NMDARs in transfected HEK-293T cells. After a fast glutamate (1 mM) and glycine (50 μM) application, NMDAR-mediated current amplitudes were significantly reduced in HEK-293T cells expressing GluN1-GluN2B(P553T) receptors (Fig. 2, A to C), whereas voltage-dependent channel blockade by extracellular Mg²⁺ was spared (Fig. 2, D to F). Because the P553T mutation is located in the vicinity of the agonist binding site and the chan-

nel pore in GluN2B, we explored the possible effects of the mutation on channel kinetics. Electrophysiological recordings showed a significantly faster deactivation rate in mutant receptors (Fig. 2, G and H) and a faster desensitization thereof, quantified upon 5-s duration jumps (Fig. 2, I and J). Moreover, in agreement with aforementioned modeling predictions, nonstationary fluctuation analysis (NSFA) (24) showed a reduction of the single-channel conductance in mutant receptors (Fig. 2, K to M) and a reduced open probability (Fig. 2N). Together with the biochemical data indicating normal expression and oligomerization, we concluded that GluN1-GluN2B(P553T) receptors are intrinsically hypofunctional.

Because GluN2B subunits can assemble into both (GluN1)₂-GluN2B₂ heterodimers and (GluN1)₂-GluN2A-GluN2B heterotrimers (25), we explored whether the GluN2B(P553T) mutation may also impair heterotrimeric receptors in HEK-293T cells (26). NMDA current amplitudes were not significantly reduced in GluN2B(P553T)-containing heterotrimers, although their deactivation and desensitization rates were increased similar to those of GluN1-GluN2B(P553T) heterodimers (fig. S2, A and B). However, administration of 100 μM D-serine potentiated GluN1-GluN2A-GluN2B(P553T) heterotrimers more strongly than wild-type heterotrimers (fig. S2, A to C). Likewise, the desensitization and deactivation kinetics of triheteromeric mutants were increased compared with controls (fig. S2, D to H), recapitulating some of the effects observed in the mutant (GluN1)₂-[GluN2B(P553T)]₂ diheterodimers.

Evaluation of D-serine effect in GluN1-GluN2B(P553T) receptors

Next, we sought to enhance the activity of mutant NMDARs using D-serine, an endogenous NMDAR coagonist. In agreement with a previous report (19), D-serine administration dose-dependently increased NMDAR-mediated currents in HEK-293T cells (Fig. 3, A and B). The relative increase mediated by D-serine was stronger in HEK-293T cells expressing GluN1-GluN2B(P553T) than in cells expressing GluN1-GluN2Bwt (Fig. 3, A and B). Although not reaching GluN1-GluN2Bwt-mediated current density, hypofunctional GluN1-GluN2B(P553T) receptor-mediated currents were significantly increased in D-serine coapplication (Fig. 3C). Further, a similar increase was observed in the presence of a high dose of glycine (100 μM), as well as with a stronger potentiation in GluN1-GluN2B(P553T)-expressing cells compared with GluN1-GluN2Bwt-expressing HEK-293T cells (Fig. 3, D to E). The differential potency of D-serine and glycine might result from a reduced affinity for GluN1-GluN2B(P553T), leading to the enhanced potentiation and faster deactivation/desensitization rates at higher concentrations. Alternatively, because glutamate binding increases the dissociation rate of glycine/D-serine coagonist with NMDARs (27), these changes in D-serine potency might be explained by altered glutamate affinity. Concentration-response experiments showed no changes in D-serine median effective concentration (EC₅₀; Fig. 3F), whereas glutamate EC₅₀ increased by sevenfold in GluN1-GluN2B(P553T) receptors (Fig. 3G).

Evaluation of GluN2B(P553T) variant neuronal outcomes

To evaluate the neuronal impact of GluN2B(P553T), we overexpressed GluN2B(P553T) in primary hippocampal neurons and measured morphological parameters, synaptic plasticity processes, and NMDAR-mediated synaptic currents. Sholl analysis of dendrites labeled with GFP-GluN2B(P553T) or GFP-GluN2Bwt indicated similar distributions of the subunit across the dendritic arbor (Fig. 4A).

Fig. 2. Biophysical characterization of (GluN1)₂-(GluN2B(P553T))₂channel properties. (A) Representative whole-cell currents evoked by rapid application of 1 mM glutamate + 50 μ M glycine (0.5-s duration; -60 mV) in HEK-293T cells expressing GluN1-GluN2B (black trace) or GluN1-GluN2B(P553T) (red trace) receptors. $n = 19$ and 21 cells from six and five experiments, respectively. (B) Average of raw peak currents from HEK-293T cells expressing GluN2B and GluN2B(P553T). $n = 19$ and 21 cells from six and five experiments, respectively. *** $P < 0.001$ by Mann-Whitney U test. (C) Normalized peak currents (in pA/pF) in HEK-293T cells expressing GluN1-GluN2B and GluN1-GluN2B(P553T), with values from a representative experiment superimposed. Data are from six and five experiments, respectively. **** $P < 0.0001$ by Mann-Whitney U test. (D) Traces recorded at -60 mV in an HEK-293T cell expressing GluN1-GluN2B(P553T) with Mg²⁺ block of the NMDAR. Data are representative of five and seven cells from three independent cultures. (E) Percentage of current blocked at -60 mV by Mg²⁺ (1 mM) for GluN2Bwt- and GluN2B(P553T)-containing NMDARs. Single-value experiments are denoted as open circles for each condition. $n = 5$ and 7 cells, respectively, from three independent experiments per condition. n.s. (not significant) by Mann-Whitney U test. wt, wild-type. (F) Current-voltage relationship for GluN2B- and GluN2B(P553T)-containing NMDARs. $n = 3$ and 4, respectively, from two independent experiments. (G) Representative peak-scaled responses to 1 mM glutamate + 50 μ M glycine (0.5-s agonists application; -60 mV) for GluN1-GluN2B (black trace) and GluN1-GluN2B(P553T) (red trace). $n = 16$ and 17 cells from six and five experiments, respectively. (H) Average deactivation time constant (τ_w) fitted to a double exponential) fitted from tail currents for GluN1-GluN2B and GluN1-GluN2B(P553T). Values from a representative experiment are shown as open circles for each condition. $n = 16$ and 17 cells from six and five independent experiments per condition, respectively. **** $P < 0.0001$ and n.s. by Mann-Whitney U test. (I) Representative peak-scaled responses to 1 mM glutamate + 50 μ M glycine (long jumps of 5-s duration; -60 mV) in HEK-293T cells expressing GluN1-GluN2B or GluN1-GluN2B(P553T), for the comparison of desensitization rates. $n = 14$ cells from three independent experiments. (J) Desensitization weighted time constant (τ_w) for GluN2Bwt and GluN2B(P553T). Values from a representative experiment are shown as open circles for each condition. $n = 14$ from three independent experiments. ** $P < 0.01$ by Mann-Whitney U test. (K and L) Whole-cell currents activated by rapid application of 1 mM glutamate + 50 μ M glycine (0.5 s; -60 mV) from HEK-293T cells expressing GluN1-GluN2Bwt (K) or GluN1-GluN2B(P553T) (L). Gray traces represent single responses, and black lines are the average of 69 (wild-type) or 33 (P553T) responses. Insets: Current variance versus mean current plot calculated from the deactivating tail current. (M and N) Bar graph showing single-channel conductance values (M) and peak open probability (N) in GluN1-GluN2Bwt- and GluN1-GluN2B(P553T)-containing NMDARs expressed in HEK-293T cells. $n = 12$ and 9 cells, respectively, from four independent experiments. * $P < 0.05$ by Mann-Whitney U test. Single cells are shown as open circles superimposed to bar graph.

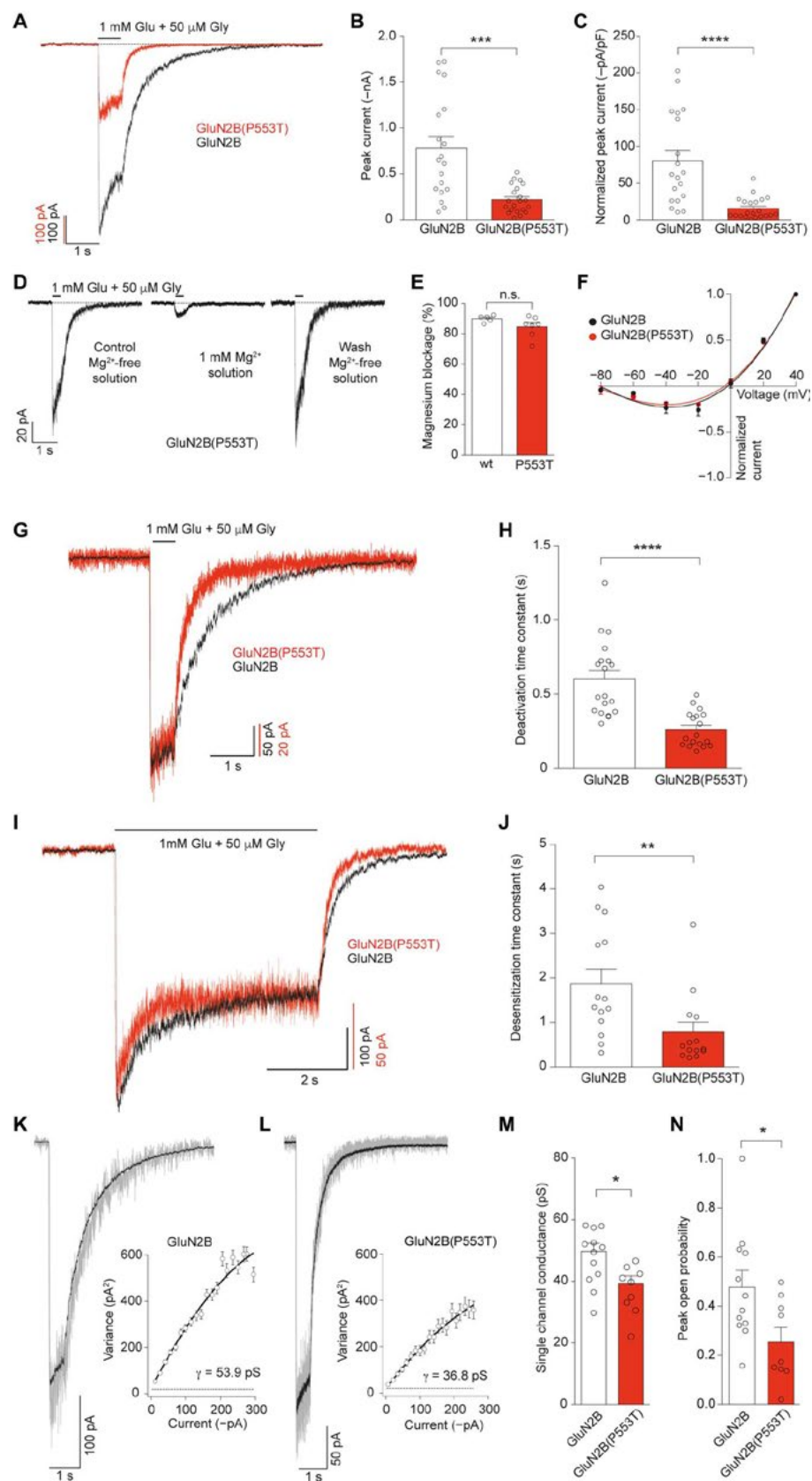


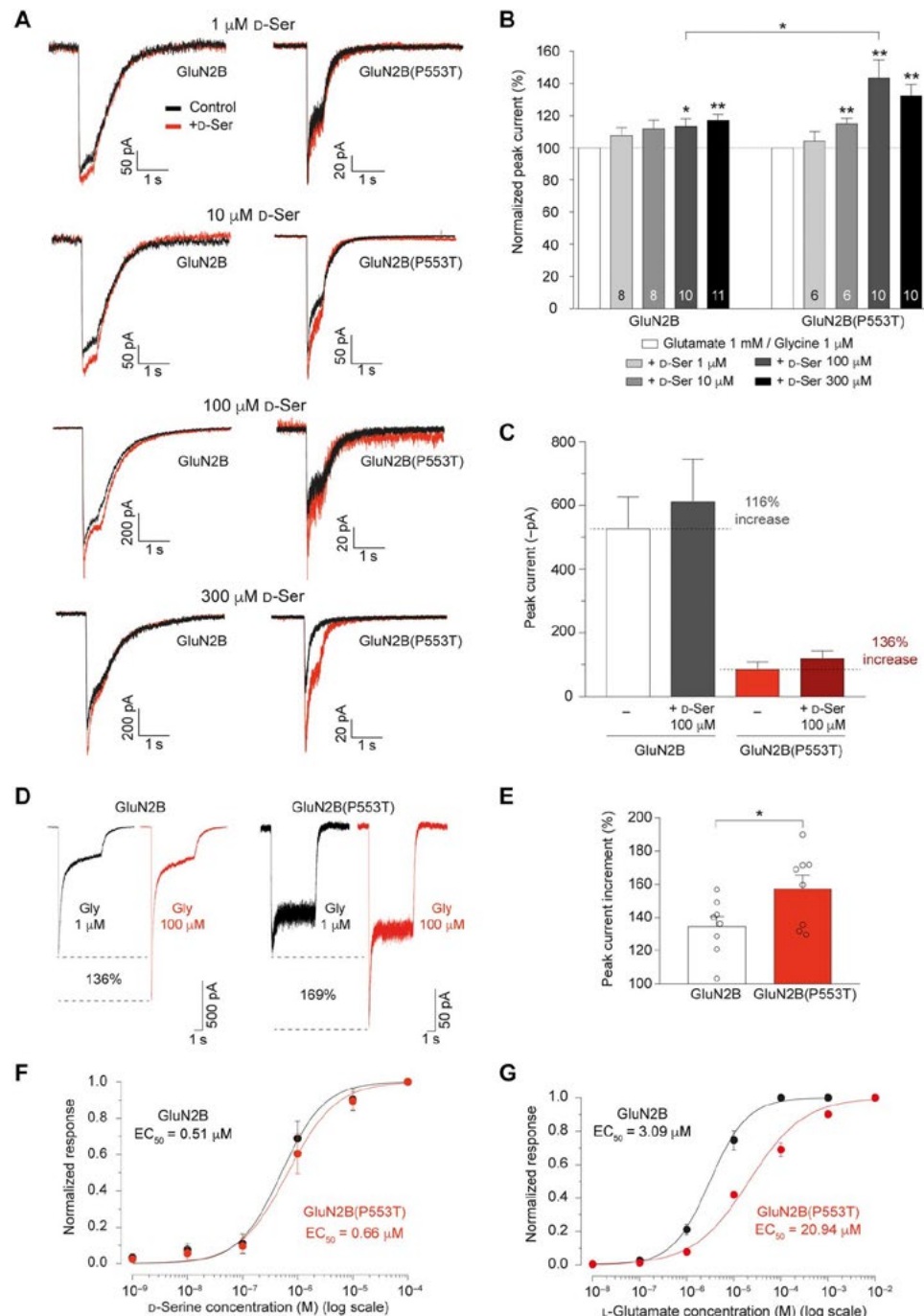
Fig. 3. D-Serine coapplication effect on wild-type and mutant (GluN1)₂-[GluN2B(P553T)]₂NMDARs.

(A) Representative traces evoked by physiological concentrations of 1 mM glutamate + 1 μ M glycine (0.5 s; -60 mV) from GluN1-GluN2Bwt- or GluN1-GluN2B(P553T)-expressing HEK-293T cells, either in the absence (black traces) or in the presence (red traces) of d-serine at different concentrations. $n \geq 6$ cells from at least two independent experiments. (B) Average peak current evoked in transfected HEK-293T cells by application of 1 mM glutamate + 1 μ M glycine in the presence of different d-Ser concentrations (gray bars) normalized to that of 1 mM glutamate + 1 μ M glycine without d-Ser (white bars). Numbers inside the bars denote the recordings for each condition, from at least two independent experiments. * $P < 0.05$ and ** $P < 0.01$ by Mann-Whitney U test. (C) Raw peak current responses from data shown in (B), indicating the percentage increase in current due to 100 μ M d-Ser. $n = 10$ cells from at least two experiments. (D) Representative recordings in HEK-293T cells expressing GluN1-GluN2Bwt or GluN1-GluN2B(P553T) receptors evoked by physiological applications (5 s; -60 mV) of 1 mM glutamate + 1 or 100 μ M glycine. $n = 8$ cells per condition from five independent experiments. (E) Bar graph representing peak current potentiation induced by high glycine concentration (100 μ M versus 1 μ M) with coapplication of 1 mM glutamate. $n = 8$ from five independent experiments for each condition. * $P < 0.05$ and n.s. by Student's t test. (F) d-Serine concentration-response curves recorded in GluN1-GluN2Bwt and GluN1-GluN2B(P553T) NMDARs expressed in HEK-293T cells, constructed from responses to 1 mM glutamate + the specified d-serine concentration in the absence of glycine. $n = 5$ cells per construct from two independent experiments. (G) Glutamate concentration-response curves recorded in GluN1-GluN2Bwt and GluN1-GluN2B(P553T) NMDARs expressed in HEK-293T cells. The dose-response curve was constructed from responses to 1 mM d-serine plus the specified glutamate concentration in the absence of glycine. $n = 5$ and 7 cells, respectively, from two independent experiments.

Nevertheless, spine density was significantly reduced in neurons expressing GluN2B(P553T), resulting from a decrease in the different spine subtypes (Fig. 4A).

Further, immunofluorescence analysis of the GluA1 AMPA receptor (AMPAR) subunit, which is overexpressed in RTT murine models (28), revealed a significant increase in GluA1 in DIV11 neurons overexpressing GluN2B(P553T) (fig. S3). Overall, these morphological and molecular changes indicated deficient spine development in hippocampal neurons expressing GluN2B(P553T).

Patch-clamp recordings revealed a decrease in the amplitude of spontaneous excitatory postsynaptic currents (EPSCs) mediated by NMDARs in neurons overexpressing mutant GluN2B(P553T) compared with GluN2Bwt (Fig. 4B, top traces and left bar graph), directly demonstrating an effect of this mutation in synaptic NMDARs. Because d-serine



administration enhanced the activity of GluN2B(P553T)-containing NMDARs in heterologous cells (see above), we assessed its effect in primary neurons. The addition of 100 μ M d-serine similarly increased EPSCs frequency in GluN2Bwt- and GluN2B(P553T)-overexpressing neurons (measured as a shortening of the interevent interval; Fig. 4B, bottom traces and right bar graph). In contrast to heterologous cell lines data, 100 μ M d-serine addition did not increase EPSC amplitudes (Fig. 4B, left bar graph), perhaps due to the recruitment of new synapses or increased desensitization at higher frequencies, thus masking a putative effect on EPSC amplitudes. The rate of recovery from desensitization for NMDARs is quite slow, spanning several seconds (29).

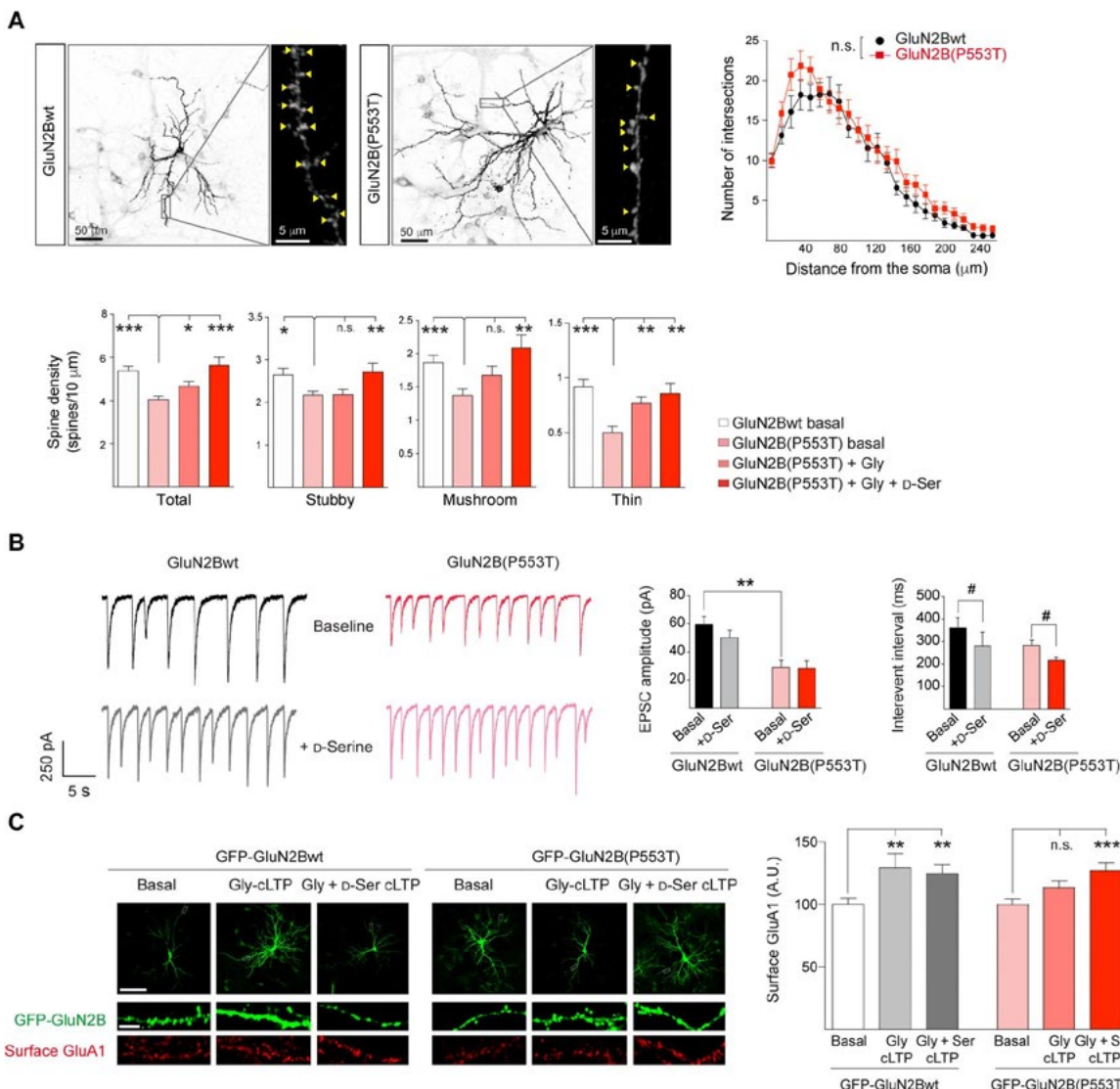


Fig. 4. Synaptic outcomes and d-serine effects on Gly-induced chemical long-term potentiation (Gly-cLTP) in GluN2B(P553T)-expressing primary hippocampal neurons. (A) Top left: Representative images of murine primary hippocampal neurons transfected with GFP-GluN2Bwt or GFP-GluN2B(P553T). Insets: Immunodecoration to visualize spines, indicated by yellow arrowheads. Top right: Immunofluorescence detection of GFP-GluN2B to analyze dendritic arborization by Sholl analysis. $n = 16$ to 18 neurons per condition from three independent experiments; $F = 0.71$, $P = 0.884$ by repeated measures two-way analysis of variance (ANOVA) and Bonferroni post hoc test. Bottom: Quantification of spine density and morphology in basal neurons and neurons treated with glycine alone or glycine and 100 μ M d-Ser. $n = 27$ to 48 dendrites per condition from three independent experiments. * $P < 0.05$, ** $P < 0.01$, *** $P < 0.001$, and n.s. by Student's *t* test or Mann-Whitney *U* test for parametric or nonparametric analyses, respectively. (B) Representative traces from spontaneous activity-dependent EPSCs recordings from GluN2Bwt- or GFP-GluN2B(P553T)-transfected murine hippocampal neuronal cultures, recorded at -70 mV in the presence of 50 μ M NBQX (2,3-dihydroxy-6-nitro-7-sulfamoylbenzo[f]quinoxaline 6-nitro-7-sulfamoylbenzo[f]quinoxaline-2,3-dione) and 10 μ M picrotoxin and in the absence of tetrodotoxin, both under basal conditions (top traces) or after 100 μ M d-serine application (bottom traces). Graphs show mean amplitudes (left) and mean time of interevent intervals (right) of the EPSCs recorded. $n = 8$ and 6 neurons, respectively, from three independent experiments. ** $P < 0.01$ and # $P < 0.05$ by Mann-Whitney *U* test. (C) Representative images and immunofluorescence analysis of surface abundance of the AMPAR subunit GluA1 (red) in murine primary hippocampal neurons (green) at DIV16 that had been transiently transfected at DIV11 with GFP-GluN2Bwt or with GFP-GluN2B(P553T) assessed under basal conditions, after Gly-cLTP, and after simultaneous Gly-cLTP induction and 100 μ M d-serine application (Gly + d-Ser cLTP). A.U., arbitrary units. Data are presented relative to the basal condition as means \pm SEM from $n = 30$ to 40 spines per dendrite from 14 to 40 dendrites and three to seven neurons per condition, obtained from three independent experiments. ** $P < 0.01$ and *** $P < 0.001$ by Student's *t* test.

Assessment of the effect of high-dose d-serine in GluN2B(P553T)-expressing neurons

Sustained activation of synaptic NMDARs modifies postsynaptic biochemical content (synaptic recruitment of AMPARs), induces morphological changes (synapse enlargement), and elicits LTP (30–32). Therefore, we assessed the ability of GluN2B(P553T)-expressing neu-

rons to support this form of synaptic plasticity. Transfected primary hippocampal cultures were treated either with 200 μ M glycine ("Gly-cLTP") or simultaneously with 200 μ M glycine and 100 μ M d-serine ("Gly + d-Ser cLTP"). The analysis of dendritic spines density showed a slight significant increase in Gly-cLTP condition (Fig. 4A). Coapplication of 100 μ M d-serine resulted in a more significant increase in spine

density in GluN2B(P553T)-expressing neurons, with a number of stubby, mushroom, and thin-shape spines similar to neurons expressing GluN2Bwt under basal conditions (Fig. 4A). Immunofluorescence analysis showed that Gly-cLTP significantly increased surface GluA1 abundance at spine-like structures in GluN2Bwt-transfected neurons (Fig. 4C, left images and bar graph). In contrast, GluA1 surface abundance was not significantly increased in GluN2B(P553T)-expressing neurons (Fig. 4C). These defects were rescued by simultaneous administration of glycine and D-serine (Fig. 4C), indicating that D-serine can also facilitate a major potentiation of NMDAR-dependent plasticity in the context of GluN2B(P553T) mutation.

Evaluation of biochemical and clinical effects of L-serine dietary supplementation in pediatric patient with GluN2B(P553T) variant

The partial restoration of mutant NMDAR function by D-serine prompted us to translate the therapeutic strategy to the clinical practice. Because D-serine use was still under investigation at the beginning of the study, the patient was supplemented with L-serine, an

approved nutraceutical amino acid acting as the endogenous D-serine precursor. We hypothesized that L-serine supplement might increase serine racemase substrate in the brain (33, 34), raising D-serine brain levels that might potentiate hypofunctional NMDARs. At 5 years and 10 months of age, the patient was administered L-serine (500 mg/kg per day) and continued to date (17 months at the time of writing this report). Ultraperformance liquid chromatography–tandem mass spectrometry (UPLC-MS/MS) analysis showed that L-serine treatment was associated with a 4.4-fold increase in the abundance of D-serine in the patient's plasma (Fig. 5A), whereas D-enantiomers of branched-chain amino acids (valine, isoleucine, and leucine) and plasma amino acids with a potential NMDAR modulatory role (such as glycine, taurine, and cysteine) showed no notable alterations (Fig. 5A). Furthermore, considering that L-serine is involved in sphingolipid biosynthesis, an untargeted UPLC-MS lipidomic analysis was conducted and revealed a strong alteration of the sphingolipidomic profile of the patient, which was not altered by L-serine dietary supplementation (table S1). Because D-serine racemase is strongly expressed in neurons (33), we reasoned that the increased D-serine plasma levels

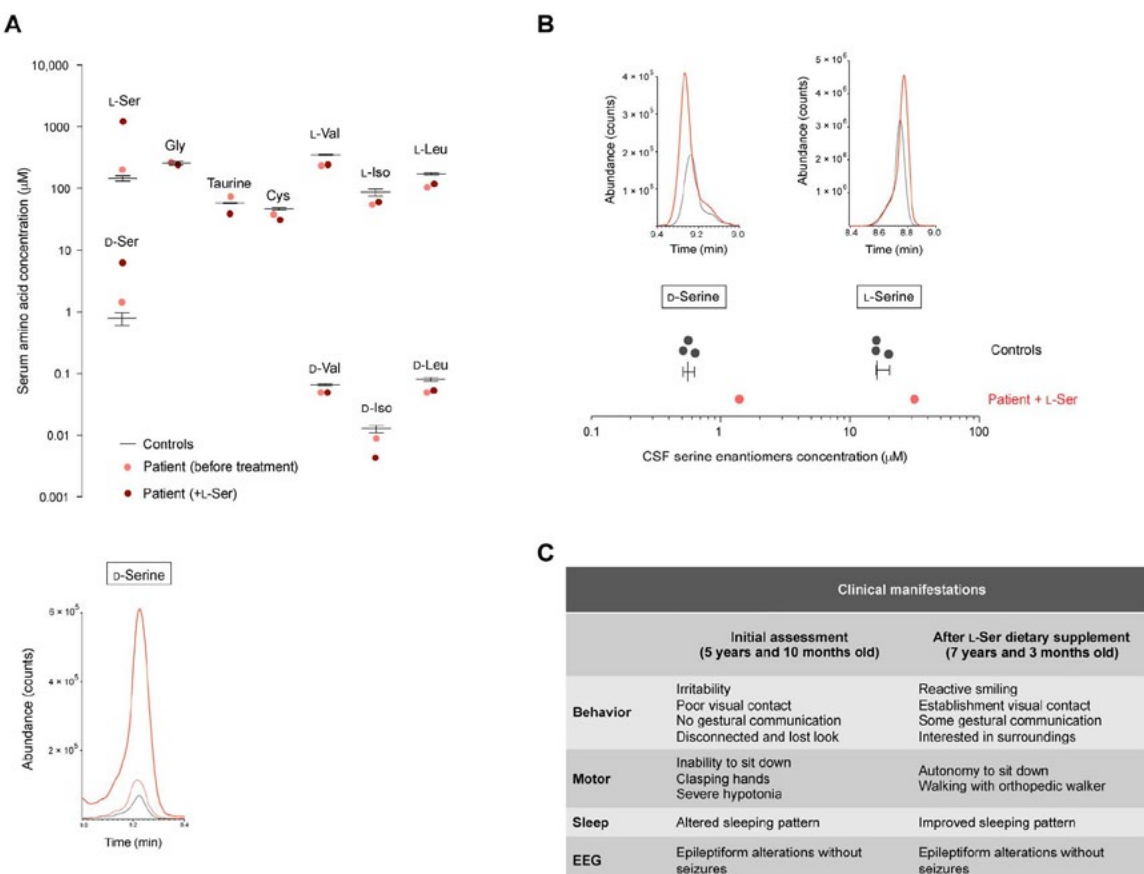


Fig. 5. Biochemical and behavioral assessment of GRIN2B(P553T) patient after L-serine dietary supplementation. (A) Top: Analysis of amino acid plasma concentration of D-L-serine, D-L-valine, D-L-isoleucine, D-L-leucine, glycine, taurine, and cysteine. Plasma samples analyzed correspond to the patient before and after L-serine treatment (light red and dark red dots, respectively) and the mean of controls (black lines; whiskers representation of mean-min-max values). Bottom: Chromatographic profiles of D-serine and L-serine enantiomers in plasma samples from the control individual (gray trace), the patient before treatment (light red trace), and the patient with L-serine dietary supplementation (dark red trace). (B) Top: Overlapping chromatographic profiles of D-serine and L-serine enantiomers (left and right, respectively) in CSF from a control (gray trace) and from the patient with GRIN2B(P553T) mutation, after L-serine dietary supplementation (red trace). Bottom: Serine enantiomers concentration analysis in CSF of controls (gray dots; whiskers representation of mean-min-max values; gray traces in the chromatogram) and the patient with L-serine dietary supplement (red dots and traces). (C) Clinical manifestations of the patient harboring a de novo GRIN2B(P553T) mutation, before and after 17 months of L-serine dietary supplementation.

most probably reflect increased D-serine abundance in the brain of the patient. UPLC-MS analysis showed highly increased D-serine levels in cerebrospinal fluid (CSF) of the treated patient (Fig. 5B).

Together with the biochemical profiling, a neuropsychological assessment was performed. Before treatment, the patient (5 years and 10 months old) had few communication skills, poor eye contact, did not pay attention to the activities of the parents, teachers, and schoolmates, did not have verbal language (any words or sounds), did not show the use of symbolic play, and could not move from the prone position to the sitting position, although she could then sit without support. The Vineland standard score (SS) test before treatment were 42 for communication, 36 for daily living skills, 49 for socialization, and 31 for motor skills (mean SS of 100 with an SD of 15), with an overall SS of 38.

After 11 months of L-serine dietary supplementation, although the EEG was still aberrant, the behavior of the patient was notably improved, as shown by the Vineland Adaptive Behavior Scale (VABS). The Vineland SSs were 42 for communication, 34 for daily living skills, 51 for socialization, and 38 for motor skills. This midterm assessment showed that her motor skills were strongly improved; she was able to stand from sitting and started to walk with external help. Behaviorally, the patient started to communicate with gestures (such as by extending her hands to be held), and her display of facial expressions increased. She started to react by turning her head when called by her name, had improved visual contact, and started to smile proactively. Overall, the clinical assessment indicated an attenuation of both motor and cognitive impairments.

After 17 months of treatment, the patient remarkably improved communication, social, and motor skills (Fig. 5C). The Vineland SSs (motor assessment cannot be performed beyond 7 years old) after L-serine treatment in the patient were 48 for communication, 48 for daily living skills, and 50 for socialization. Behaviorally, she was then interested in faces and had a persistent eye contact, followed the activities of surrounding humans with interest, was able to stretch her arms out to be held, turn her head when called, laugh at funny situations, and was generally (by outward assessments) happier. She could then also imitate toys and animal sounds, creep on the floor, and move from a prone to a sitting position, as well as from a sitting to standing position with support. She had also improved her sleeping pattern, was able to sit down without help, and notably could walk using an orthopedic walker. An EEG showed epileptiform alterations, but clinical seizures were not present. Despite pharmacological interventions to target them specifically (valproate first and levetiracetam later), the epileptiform alterations detected in the EEG were still present; thus, these treatments were stopped. Nonetheless, overall, the clinical assessments indicated an improvement in cognitive, communicative, and motor impairments associated with L-serine dietary supplementation.

DISCUSSION

NMDARs are critical players of glutamatergic neurotransmission and are fundamental actors in neuritogenesis, synaptogenesis, and synaptic plasticity processes. Currently, upon the development of next-generation sequencing, there is a growing body of data implicating de novo mutations of iGluRs (7, 8) in mental and behavioral disorders. Several mutations in subunits of the NMDAR have been related to neurodevelopmental diseases (11–13). However, these data require functional validation to unveil whether these mutations are really pathogenic. In the present study, we identified a GRIN2B(P553T) missense de novo mutation of the GluN2B subunit of the NMDAR in a patient with Rett-like syndrome with severe encephalopathy. This

mutation resulted in the exchange of a highly evolutionary conserved Pro into a Thr. A mutation affecting the same amino acid position GluN2B(P553L) was previously described in a patient from a cohort of individuals with ID (16). This patient exhibited phenotypic alterations similar to those of the case in the present study, including severe ID, hypotonia, and no speech. The phenotypic similarity between these two cases provides a strong evidence for a pathogenic role of GluN2B(Pro⁵⁵³) mutations under these neurodevelopmental conditions.

Electrophysiological studies confirmed the *in silico* structural studies predicting the hypofunctionality of mutant NMDARs. In addition to a reduction of the channel conductance and peak open probability, we found a significant increase in both the desensitization and the deactivation rates of GluN1-GluN2B(P553T) receptors. Whether the P553T mutation located far from the binding site is altering deactivation kinetics, an intrinsic property of the receptor, is an incognita, but electrophysiological concentration-response experiments indicate a decreased glutamate binding affinity of mutant NMDARs, triggering a decreased receptor efficacy that seems to be physiologically relevant. NMDAR function is largely determined by the high amount of Ca²⁺ influx, which is mostly dependent on channel kinetics, particularly the rates of desensitization and deactivation. Thus, we can speculate that kinetics changes detected on GluN2B(P553T) mutant receptors might be limiting Ca²⁺ influx, which in turn would alter Ca²⁺-mediated signaling pathways and synaptic plasticity.

Overall, these changes markedly reduce NMDAR-mediated currents and might be underlying the severe phenotype of the patient. GluN2B subunits are highly expressed at embryonic and initial postnatal stages, playing a critical role in neurodevelopmental processes (35). Consequently, the hypofunctionality of this major subtype of NMDARs might certainly affect neuritogenesis and synaptogenesis, leading to altered synaptic transmission. This hypothesis is supported by the morphological and biochemical findings, showing a significant decrease in spine density together with increased levels of GluA1 subunit of AMPARs. Pozzo-Miller's group (28, 36) has reported similar synaptic outcomes in patients with RTT and in primary murine neuronal cultures deficient or harboring mutations of *MeCP2*. Therefore, our data suggest that NMDAR-induced alterations of glutamatergic synapses might be involved in the pathophysiology of classical RTT condition.

In agreement with the proposed functional impact of de novo mutations of GluN2B subunit, previous studies have associated de novo mutations of *GRIN2B* with severe phenotypic alterations (6, 14, 15, 37). Lemke and collaborators (13, 38) described the functional consequences of *GRIN2B* mutations in patients with West syndrome and in individuals with ID with focal epilepsy. In the latter study, the patient with ID and focal epilepsy had a missense mutation in the extracellular glutamate-binding domain. De novo *GRIN2B* mutations lead to a gain of function, either significantly reducing Mg²⁺ block and increasing Ca²⁺ permeability (N615I and V618G mutations, affecting the M2 domain in the pore of the channel) or increasing the apparent glutamate binding affinity (R540H mutation, within the extracellular S1 domain). These gain-of-function mutations point out the important role of facilitated NMDAR signaling in epileptogenesis, with further therapeutic strategies consisting on the selective blockade of mutant leak/hyperactive channels. In contrast, loss-of-function mutations might be causing a hypoglutamatergic function that could be potentially rescued by increasing NMDAR activity with a therapeutic purpose.

The glutamatergic synapse is an extremely sophisticated system where a plethora of molecular actors reside and interact to finely tune neurotransmission. However, under pathological conditions,

the dysregulation of critical players might compromise glutamatergic neurotransmission, resulting on an enhancement or a reduction of glutamate signaling (8). In the present work, *in silico* and *in vitro* experiments concluded that GluN2B(P553T)-containing NMDARs are hypofunctional. Thus, we envisioned that enhancing NMDAR activity might recover normal glutamatergic neurotransmission and attenuate clinical manifestations. To this end, we evaluated the effect of D-serine, a coagonist of the GluN1 subunit, coapplied with physiological glycine concentrations (39). Our findings indicate an enhancement of mutant GluN1-GluN2B receptor activity, suggesting that the structural changes induced by the mutation are not transduced to GluN1 ligand-binding domain. The ability of D-serine to activate wild-type GluN1-GluN2B receptors (shown in this work) and all NMDAR subtypes (40, 41) should have a general effect on glutamatergic function. Because L-serine is a nutraceutical serine enantiomer already used in pediatric care, the patient was treated with L-serine dietary supplementation. This dietary supplement resulted in increased D-serine concentration in the patient's plasma, concomitant with strongly increased D-serine amounts in the CSF, in agreement with a previous report (42). Because L-serine is the substrate of serine racemase in the brain (34), our data support the hypothesis that L-serine supplement increases L-serine availability in the brain, which in turn promotes L-serine conversion to D-serine in the brain (43), likely potentiating hypofunctional NMDARs. The beneficial effect of D-serine in healthy individuals has been described in a clinical trial (44). In that work, Heresco-Levy and colleagues showed the procognitive effects of D-serine through NMDAR function and, as we propose in the present study, intended the development of NMDAR glycine site strategies for treating synaptopathies. In agreement with this, D-serine deficits have been associated with aging in rats, with functional rescue observed after exogenous D-serine administration (45, 46). In addition, serine deficiency disorders also provoke neurological phenotypes (psychomotor retardation, microcephaly, and seizures in newborns and children) that can be safely treated by serine oral replenishment (47). Together, these works and ours indicate that, independent of the molecular etiology (whether serine racemase deficit or NMDAR hypofunctionality), serine-potentiated NMDAR activity can partially rescue hypoglutamatergic function. In addition to the beneficial effect of L-serine-mediated increase in D-serine levels, the effect of some other L-serine metabolites and the neurodevelopmental factors might be considered. Regarding the former, our biochemical studies have shown that additional L-serine-derived amino acids and sphingolipids that potentially modulate the NMDAR were not modified by L-serine dietary supplementation. Regarding the neurodevelopmental aspects, the improved patient's condition might also be influenced by the developmental changes in GluN2 subunit expression, increasing the GluN2A:GluN2B ratio during development (9). Our findings indicate that mutant heterotrimeric NMDARs are less affected than heterodimeric mutant receptors. Therefore, in addition to the NMDAR-potentiating effect of L-serine treatment, GluN2 subunits, the developmental switch might also contribute to improve the clinical symptoms of the patient to some extent.

In summary, our data represent a proof-of-concept study to identify the pathogenicity of *de novo* mutations of NMDARs and the development of precision therapeutic strategies. The methodological pipeline developed along this study might be further implemented to functionally stratify *de novo* iGluR mutations associated with synaptic dysfunctions and to define therapeutic strategies. Moreover, they support the use of L-serine as a dietary supplement for the enhancement of glutamatergic neurotransmission and/or excitatory or inhib-

itory neurotransmitter imbalance that are associated with a large spectrum of neurological disorders.

MATERIALS AND METHODS

Patient neurodevelopmental and adaptive behavior assessments before and after dietary L-serine supplement

The study was approved by the appropriate informed consent of the patient's parents. The VABS-II (48) semistructured interview, allowing the assessment of four domains of adaptive behavior (communication, daily living skills, socialization, and motor skills), was conducted by a trained neuropsychologist before (at 5 years 10 months old) and after 11 and 17 months of L-serine supplementation (at 6 years and 9 months old and 7 years and 3 months old, respectively). Initially, L-serine dose started at 250 mg/kg per day (for 4 weeks), and upon the confirmation of a lack of side effects, the dose was increased to 500 mg/kg per day (divided into three dietary supplements of L-serine powder, mixed with food and/or drinks) and maintained along the extent of the trial.

Whole-exome sequencing

Coding regions were captured using the TruSeq DNA Sample Preparation and Exome Enrichment Kit (Illumina, San Diego, CA, USA), and paired-end 100 × 2 sequences were sequenced with the Illumina HiScanSQ system at National Center for Genomic Analysis in Barcelona (Catalonia, Spain). The overall coverage statistics for the trio are 381.451, 433.847, and 31.635 for the patient, the mother, and the father, respectively.

Bioinformatic pipeline

Sequence reads were aligned to the Genome Reference Consortium Human Genome Build 37 (GRCh37) hg19 using the Burrows-Wheeler Aligner (49). Properly mapped reads were filtered with SAMtools (1, 2), which was also used for sorting and indexing mapping files. Genome Analysis Toolkit (GATK) (3) was used to realign the reads around known indels and for base quality score recalibration. Once a satisfactory alignment was achieved, identification of single-nucleotide variants (SNVs) and indels was performed using GATK standard multisample variant calling protocol, including variant recalibration (4). For the final exome sequencing analysis report, the Annotate Variation (ANNOVAR) (5) tool was used to provide additional variant information to ease the final selection of candidates. In particular, minor allele frequency (MAF), obtained from dbSNP (Single-Nucleotide Polymorphism Database) (50, 51) and 1000 Genomes Project (6–8), was provided to help to select previously undescribed variants in healthy population.

De novo SNVs and small insertion or deletion events

To identify de novo SNVs and small insertion and/or deletion events, the patient's variants were filtered first against parental variants and then against a pool of controls made up by all healthy parents included in the study. SIFT (52) and PolyPhen-2 (Polymorphism Phenotyping v2) (53) damage scores were computed to predict putative impact over protein structures. The successive application of quality control filters and the prioritization by the parameters with potential functional impact was used to construct a list of candidate genes (and variants) ranked by its uniqueness in the cases (or very low frequency in the control population, as derived from the MAFs) and the putative potential impact.

Sanger sequencing

The variants were validated by Sanger sequencing using BigDye Terminator v3.1 Cycle Sequencing Kit (Life Technologies, Grand Island, NY, USA) in an Applied Biosystems 3730/DNA Analyzer (Applied Biosystems, Life Technologies, Grand Island, NY, USA) using the following set of primers: 5'-TACAATCTAACCTAGGCCCTGG-3' (forward) and 5'-TGGATATGCTAGGGAAAATGCAG-3' (reverse). The raw data were analyzed with CodonCode Aligner software (CodonCode Corporation, Centerville, MA, USA).

In silico prediction of mutation impact

The following four in silico prediction tools of functional mutation impact were used: SIFT, PolyPhen-2, Protein Variation Effect Analyzer (PROVEAN) (54), and MutationTaster2 (55). SIFT is a sequence homology-based tool that predicts variants as neutral or deleterious using normalized probability scores. Variants at position with a normalized probability score less than 0.05 are predicted to be deleterious, and a score greater than 0.05 is predicted to be neutral (56). PolyPhen-2 uses a combination of sequence and structure-based attributes and naive Bayesian classifier for the identification of an amino acid substitution and the effect of mutation. The output results of probably damaging and possibly damaging were classified as deleterious (≥ 0.5) and the benign level being classified as tolerated (≤ 0.5). PROVEAN uses a region-based delta alignment score, which measures the impact of an amino acid variation not only based on the amino acid residue at the position of interest but also on the quality of sequence alignment derived from the neighborhood flanking sequences. Variants with a PROVEAN score lower than -2.5 are predicted to be deleterious (57). MutationTaster2 also uses a Bayes classifier to generate predictions but includes all publicly available single-nucleotide polymorphisms and indels from the 1000 Genomes Project, as well as known disease variants from ClinVar (58) and the Human Gene Mutation Database (HGMD) (59). Alterations found more than four times in the homozygous state in 1000 Genomes or in HapMap (60) were automatically regarded as neutral. Variants marked as pathogenic in ClinVar were automatically predicted to be potentially disease causing.

Molecular modeling of wild-type and mutant (GluN1)₂-(GluN2B)₂ receptors

An initial homology model was constructed for the transmembrane domain of human (GluN1)₂-(GluN2B)₂ receptor using the coordinates of the crystal structure of rat receptor (PDB ID: 4PE5) (61). MODELLER v16 (62) was used to model the lacking residues of the loop connecting M1 and M3. The side-chain conformations for those residues were positioned according to SCWRL (63). The backbone conformation from residues 551 to 556 was modeled with MODELLER v16 software (62). Protein complexes were embedded in a model membrane containing 1-palmitoyl-2-oleoyl-sn-glycero-3-phosphocholine (POPC) lipids, water molecules, and 0.15 M NaCl in a rectangular box (64). The initial system was energy-minimized and then subjected to molecular dynamics equilibration (25 ns). Subsequently, the system was subjected to a production stage, extending 250 ns. All the simulations were performed with GROMACS 4.5 simulation package (65).

Phylogenetic analysis of GluN2B(P553)-containing domain

Genes coding for iGluRs subunits from different species belonging to the phylum metazoan were identified using the BLASTP tool and human iGluRs as queries. Subject sequences with an *E* value below 0.05 were selected as possible homologs. These were reblasted against

the National Center for Biotechnology Information “nonredundant protein sequences (nr)” database to establish their correspondence with glutamate receptors. These searches were performed against the Ensembl Metazoa database (<http://metazoa.ensembl.org/index.html>) for *L. gigantea*, *C. teleta*, *S. maritima*, *A. mellifera*, *Nematostella vectensis*, *Mnemiopsis leidyi*, and *Trichoplax adhaerens*; Metazome database (<https://metazome.jgi.doe.gov/pz/portal.html>) for *S. kowalevskii*; and alternative polyadenylation sites database (APAsdb) (<http://genome.bucm.edu.cn/utr/>) for *B. belcheri*. Sequences from poriferan species were taken from Riesgo’s group database (66). All vertebrate sequences were obtained from the Ensembl Metazoa database. A final set of 147 iGluR sequences from 12 metazoan species spanning seven phyla was used in the phylogenetic analysis. Sequence multiple alignment was made using MUSCLE tool (67) included in the MEGA6 software (68). The alignment was made with coding DNA sequences, using “codons” option, which allows maintaining nucleotide triplets coding for amino acids. Using MEGA6, we established that GTR + I + G (general time reversible with gamma rates and a proportion of invariant sites) was the best evolutionary model to use in the phylogenetic tree. The phylogenetic tree was constructed using the Bayesian inference method, with MrBayes 3.2 software (69). *Arabidopsis thaliana* iGluR sequences were obtained from the TAIR (The Arabidopsis Information Resource) database (www.arabidopsis.org/) and used as an external group of the tree. Two simultaneous trees were analyzed, and 3,630,000 iterations were run until both trees converged.

Plasmids

The expression plasmids for rat GluN1 and GFP-GluN2B were provided by S. Vicini (Georgetown University Medical Center, Washington, USA) (70). The plasmids used for the analysis of tri-heteromeric NMDARs were provided by P. Paoletti (École Normale Supérieure Paris, France, EU). Nucleotide change (the mutation of GluN2B serine at amino acid position 553 to a Thr residue) was achieved by oligonucleotide-directed mutagenesis, using the QuikChange site-directed mutagenesis kit according to the manufacturer’s instructions (Stratagene). The plasmid generated by site-directed mutagenesis was verified by DNA sequencing.

Coimmunoprecipitation experiments

For immunoprecipitation of heterologously expressed GluN1, HA-GluN2A, and GFP-GluN2B (wild-type or mutant), transfected HEK-293T cells were washed in cold phosphate-buffered saline (PBS) and subsequently solubilized in radioimmunoprecipitation assay buffer supplemented with protease and phosphatase inhibitor cocktail (PPIC), for further immunoprecipitation with anti-GFP. The homogenates were clarified by centrifugation at 4°C for 10 min at 16,000g. After preclearing the soluble lysates for 1 hour at 4°C with equilibrated protein G Sepharose, they were incubated overnight at 4°C with 10 µg of an anti-GFP mouse monoclonal antibody (Ab) (1:200; catalog no. 9777966, Clontech). Nonspecific mouse immunoglobulin G (catalog no. I5381, Sigma-Aldrich) was used as a control for specificity. The immunocomplexes were incubated with protein G Sepharose for 2 hours at 4°C, and the beads were then washed twice with lysis buffer and once with PBS. The bound proteins were eluted in Laemmli’s buffer and analyzed by Western blot.

Western blot analysis

For protein extraction, cells were washed once with PBS and scraped off the plate in 400 µl of lysis buffer [50 mM Hepes (pH 7.4), 150 mM NaCl,

2 mM EDTA, 1% NP-40, and PPIC]. After 10 min of incubation at 4°C, the cell debris was pelleted at 15,000g, the solubilized proteins were collected, and the protein concentration was determined using a bicinchoninic acid assay (BCA). Proteins were separated by 8% SDS-polyacrylamide gel electrophoresis and transferred to nitrocellulose membranes (Amersham), which were then blocked with 10% skimmed milk in 10 mM tris-HCl (pH 7.5)/100 mM NaCl [tris-buffered saline (TBS)] plus 0.1% Tween 20 (TBS-T). The membranes were probed overnight at 4°C with the primary Ab of interest (diluted in TBS-T + 5% skimmed milk) directed against GluN1 (1:500; catalog no. 05-432, Millipore), HA epitope (catalog no. MMS-101R-500, Covance Inc.), and GFP (Clontech). Ab binding was detected with an anti-mouse or anti-rabbit Ab coupled to horseradish peroxidase (Dako) for 1 hour at room temperature (RT), and the immunocomplexes were visualized by chemiluminescence (ECL detection system, Pierce), following the manufacturer's instructions. Immunosignals were analyzed densitometrically with ImageJ software [National Institutes of Health (NIH), USA].

Cell culture and transfection

HEK-293T and COS-7 cell lines were obtained from the American Type Culture Collection and maintained at 37°C in Dulbecco's modified Eagle's medium, supplemented with 10% fetal calf serum and antibiotics [penicillin (100 U/ml) and streptomycin (100 µg/ml)]. Furthermore, d-2-amino-5-phosphonopentanoic acid (Abcam) was added to the medium (final concentrations of 200 or 500 µM for HEK-293T and COS-7 cells, respectively) to avoid excitotoxicity. Transient transfection of HEK-293T cells was achieved by the calcium phosphate method (Clontech), and cell extracts were obtained 48 hours after transfection. COS-7 cells were transfected with Lipofectamine 2000 (Invitrogen), following the manufacturer's instructions, and cells were fixed 24 hours after, for further immunofluorescence analysis.

To prepare dissociated mouse hippocampal neuron cultures, mouse embryos (embryonic day 18) were obtained from pregnant CD1 females, the hippocampi were isolated and maintained in cold Hank's balanced salt solution (HBSS; Gibco) supplemented with 0.45% glucose (HBSS-glucose). After carefully removing the meninges, the hippocampi were digested mildly with trypsin for 17 min at 37°C and dissociated. The cells were washed three times in HBSS and resuspended in Neurobasal medium supplemented with 2 mM GlutaMAX (Gibco) before filtering in 70-µm mesh filters (BD Falcon). The cells were then plated onto glass coverslips (5×10^4 cells/cm²) coated with poly-L-lysine (0.1 mg/ml; Sigma-Aldrich), and 2 hours after seeding, the plating medium was substituted by complete growth medium, consisting on Neurobasal medium supplemented with 2% B27 (Invitrogen) and 2 mM GlutaMAX, and the coverslips were incubated at 37°C in a humidified 5% CO₂ atmosphere. Every 3 to 4 days, half of the conditioned medium was removed and replaced by fresh growth medium. Primary cultures were transfected with 0.8 µg of DNA (Lipofectamine 2000, Invitrogen) on DIV4, DIV7, or DIV11 for further surface expression analysis of GFP-GluN2B constructs and endogenous GluA1. All the experimental procedures were carried out according to European Union guidelines (Directive 2010/63/EU) and following protocols that were approved by the Ethics Committee of the Bellvitge Biomedical Research Institute (IDIBELL).

Immunofluorescence analysis of surface NMDARs

The surface-to-total expression of NMDARs in COS-7 cells was performed as previously described (71). Briefly, cells were washed twice with PBS before they were fixed with 4% paraformaldehyde (PFA).

Surface expression of GFP-GluN2B constructs was detected using an Ab against GFP (1:1000; catalog no. A11122, Life Technologies) that recognizes the extracellular epitope of heterologously expressed receptors and that was visualized with an Alexa Fluor 555-conjugated goat anti-rabbit Ab (1:500; catalog no. A-31851, Thermo Fisher Scientific). The total pool of receptors was detected by the fluorescent signal emitted by the GFP-GluN2B construct.

To analyze the surface expression of the transfected NMDARs in primary hippocampal neuronal cultures, cells were washed twice with PBS and fixed with 4% PFA in PBS containing 4% sucrose. The surface expression of GFP-GluN2B constructs was detected by incubating with anti-GFP (1:1000; catalog no. A11122, Life Technologies) during 1 hour at RT and visualized with an Alexa Fluor 488-conjugated goat anti-rabbit Ab (1:500; catalog no. A-11078, Thermo Fisher Scientific). The intracellular pool of receptors was identified by permeabilizing cells with 0.1% Triton X-100 and labeling them with a rabbit anti-GFP-Alexa Fluor 555-conjugated Ab (1:2000; catalog no. A-31851, Thermo Fisher Scientific).

Fluorescence was visualized with a Leica TCS SL spectral confocal microscope (Leica Microsystems, Wetzlar, Germany) using a Plan-Apochromat 63×/1.4-numerical aperture immersion oil objective (Leica Microsystems) and a pinhole aperture of 114.54 or 202 µm (for surface receptors). To excite the different fluorophores, the confocal system is equipped with excitation laser beams at 488 and 546 nm. In each experiment, the fluorescence intensity was measured in 10 to 15 dendrites from at least two to three pyramidal neurons (or in 10 to 15 COS-7 cells) per condition. Fluorescence was quantified using Adobe Photoshop CS5 software (Adobe Systems Inc.), and the results are represented as the means ± SEM of the ratio of surface:intracellular (primary cell culture) or surface:total (COS-7 cells) GluN2B immunofluorescence signal, analyzing at least three independent experiments.

Morphological analysis of dendritic arborization and spines

GFP-GluN2Bwt- and GFP-GluN2B(P553T)-transfected neurons were immunolabeled, and Z-stack images were acquired. The resulting maximum projections were analyzed using "Sholl analysis" ImageJ plugin (72). Dendrites were manually traced with Neuron Studio software (<http://research.mssm.edu/cnic/tools-ns.html>). Dendritic spines from tertiary neurites were counted and classified into morphological categories (thin, mushroom, and stubby), using Neuron Studio software automatic analysis, followed by manual revision to discard artifacts and/or spines counts redundancy.

Chemical LTP-induced recruitment of AMPARs in the cell surface and synaptic morphology changes

Gly-cLTP assay was performed at DIV14 on primary hippocampal neurons transiently transfected at DIV11 with either GFP-GluN2Bwt + GFP (4:1 ratio) or GFP-GluN2B(P553T) + GFP (4:1 ratio), adapting the protocols previously described (31, 32). Briefly, basal conditions (nonstimulated neurons) consisted in the incubation of primary cultures with Krebs-Ringer solution supplemented with 1 mM Mg²⁺ and 1 µM tetrodotoxin. For Gly-cLTP induction, cells were briefly washed in 20 µM bicuculline (BIC) + 20 µM strychnine and then incubated for 5 min in Krebs-Ringer solution supplemented with 20 µM BIC + 1 µM strychnine and 200 µM Gly (100 µM D-serine supplement, for Gly + D-Ser condition). The solutions were replaced by a medium supplemented with 20 µM BIC, 20 µM strychnine, and 1 mM Mg²⁺. After 20 min of incubation at 37°C (GluA1 surface recruitment studies) or 35 min of incubation at 37°C (dendritic spines analysis), cells were fixed

with ice-cold 4% PFA in PBS containing 4% sucrose. For immunofluorescence analysis of GluA1 surface recruitment, neurons were incubated at RT for 30 min with anti-GluA1 Ab (1:200; catalog no. MAB2263, Millipore) and incubated with Alexa Fluor 555-conjugated goat anti-mouse Ab (1:500; catalog no. A31570, Molecular Probes). After permeabilization/blocking, cells were incubated with rabbit anti-GFP (1:1000; catalog no. A11122, Life Technologies) and then with Alexa Fluor 488-conjugated goat anti-rabbit Ab (1:500; catalog no. A-11078, Thermo Fisher Scientific), and washed and mounted for confocal microscopy analysis. Secondary dendritic processes expressing the GFP-GluN2B constructs were analyzed by quantifying the fluorescence intensity of GluA1 puncta with ImageJ software (NIH), and tertiary dendritic processes were included for spines density and morphology analysis.

Electrophysiological recordings of diheteromeric and triheteromeric NMDAR-mediated whole-cell currents in HEK-293T cells

Electrophysiological recordings were obtained 18 to 24 hours after transfection, perfusing the cells continuously at RT with an extracellular physiological bath solution: 140 mM NaCl, 5 mM KCl, 1 mM CaCl₂, 10 mM glucose, and 10 mM Hepes, adjusted to pH 7.42 with NaOH. Glutamate (1 mM; Sigma-Aldrich), in the presence of glycine (1, 50, or 100 μM depending the experiment type; Tocris) and D-serine (0 to 300 μM) was applied for 0.5 s by piezoelectric translation (P-601.30; Physik Instrumente) of a theta-barrel application tool made from borosilicate glass (1.5 mm outside diameter; Sutter Instruments), and the activated currents were recorded in the whole-cell configuration at a holding potential of -60 mV, acquired at 5 kHz and filtered at 2 kHz by means of Axopatch 200B amplifier, Digidata 1440A interface, and pClamp10 software (Molecular Devices Corporation). Electrodes with open-tip resistances of 2 to 4 megohms were made from borosilicate glass (1.5 mm outside diameter, 0.86 mm outside diameter; Harvard Apparatus), pulled with a PC-10 vertical puller (Narishige), and filled with intracellular pipette solution containing 140 mM CsCl, 5 mM EGTA, 4 mM Na₂ATP, 0.1 mM Na₃GTP, and 10 mM Hepes, adjusted to pH 7.25 with CsOH. Glutamate and glycine-evoked currents were expressed as current density (in pA/pF; maximum current divided by input capacitance as measured from the amplifier settings) to avoid differences due to surface area in the recorded cells.

The kinetics of deactivation and desensitization of the NMDAR responses were determined by fitting the glutamate/glycine-evoked responses at $V_m - 60$ mV to a double-exponential function to determine the weighted time constant ($\tau_{w,des}$)

$$\tau_{w,des} = \tau_f \left(\frac{A_f}{A_f + A_s} \right) + \tau_s \left(\frac{A_s}{A_f + A_s} \right)$$

where A_f and τ_f are the amplitude and time constant of the fast component of desensitization, respectively, and A_s and τ_s are the amplitude and time constant of the slow component of desensitization, respectively.

To infer single-channel conductance values from macroscopic deactivating currents, we used NSFA as previously described (24). The single-channel current (i) was calculated by plotting the ensemble variance against mean current (I) and fitting with Sigworth parabolic function (73)

$$\sigma^2 = \sigma_B^2 + \left(i\bar{I} - \left(\frac{\bar{I}^2}{N} \right) \right)$$

where σ_B^2 is the background variance and N is the total number of channels contributing to the response. The weighted-mean single-channel conductance was determined from the single-channel current and the holding potential of -60 mV.

NMDAR agonists dose-response experiments

To determine the affinity for D-serine or glutamate in GluN2B- and GluN2B(P553T)-transfected cells, concentration-response curves were constructed from whole-cell currents elicited by rapid jumps of 0.5-s duration at different concentrations of the coagonist D-serine (10^{-9} to 10^{-4} M) in the presence of 1 mM glutamate or at different concentrations of the agonist glutamate (10^{-8} to 10^{-2} M) in the presence of 1 mM D-serine. Concentration-response curves were fitted individually for every cell using the Hill equation

$$I = \frac{I_{max}}{1 + \left(\frac{EC_{50}}{[A]} \right)^{n_H}}$$

where I_{max} is the maximum current, $[A]$ is the concentration of D-serine, n_H is the slope (Hill) coefficient, and EC_{50} is the concentration of D-serine or glutamate that produces a half-maximum response. Each data point was then normalized to the maximum response obtained in the fit. The average of the normalized values with their SEM were plotted together and fitted again with the Hill equation. The minimum and maximum values were constrained to asymptote 0 and 1, respectively.

Electrophysiological recordings of NMDA EPSCs in hippocampal neurons

Spontaneous activity-dependent NMDAR-mediated EPSCs were recorded in cultures of hippocampal neurons (DIV16). Whole-cell recordings were obtained from transfected neurons (at DIV12) with GluN2B-GFP or GluN2B(P553T). Extracellular solution contained 140 mM NaCl, 3.5 mM KCl, 2 mM CaCl₂, 20 mM glucose, and 10 mM Hepes, (Mg²⁺-free) adjusted to pH 7.42 with NaOH. To isolate NMDAR component, 50 μM NBQX and 100 μM picrotoxin were added to block AMPAR and γ-aminobutyric acid type A receptor-mediated PSCs, respectively. Intracellular pipette solution contained 116 mM K-gluconate, 6 mM KCl, 8 mM NaCl, 0.2 mM EGTA, 2 mM MgATP, 0.3 mM Na₃GTP, and 10 mM Hepes, adjusted to pH 7.25 with KOH. QX-314 (2.5 mM) was included into the pipette solution to block action potential firing. EPSCs were acquired at 5 kHz and filtered at 2 kHz as described for cell lines at a holding potential of -70 mV. EPSCs were measured in 5-min periods in the presence of NBQX (baseline) and NBQX + D-serine (100 μM), as indicated. After D-serine treatment, 2-amino-5-phosphonopentanoic acid (50 μM) was added to validate that EPSCs recorded were NMDAR-mediated. pClamp10/Clampfit10.6 (Molecular Devices) was used to record, detect, and analyze the amplitude, interevent interval, and charge transfer (as area under the curve, in pA*ms) from single EPSCs.

Quantitative analysis of total and stereoselective amino acids in human samples

Amino acid analysis was performed on an ACQUITY UPLC H-class instrument (Waters Co., Milford, MA, USA) with a reversed-phase C-18 column using water and acetonitrile, 0.1% formic acid as mobile phases (run time, 9 min). The detection was performed with a Xevo TQD triple-quadrupole mass spectrometer (Waters Co., Milford,

MA, USA) using positive electrospray ionization in the multiple reaction monitoring mode. For the quantification of L- and D-amino acids enantiomers of human biological fluids (plasma and CSF), a UPLC-MS/MS-based method was performed, using *N*-(4-nitrophenoxy carbonyl)-L-phenylalanine 2-methoxyethyl ester [(S)-NIFE method], as previously reported (74). Briefly, EDTA-anticoagulated plasma and CSF samples were collected from control age-matched individuals (normal diet) and from the patient (before and after L-serine dietary supplementation, for plasma analysis; after L-serine supplement, for CSF analysis), as previously described (75). All samples were stored at -80°C until use. Plasma and CSF samples were mixed with internal standard solution. After 10 min of incubation at 4°C, ice-cold acetonitrile was added, and the mixture was incubated for >15 min on ice. Precipitates were removed by centrifugation, and the supernatant was evaporated to dryness under a stream of nitrogen, using a heating block set to 40°C. The residue was dissolved in water, followed by the addition of sodium tetraborate and (S)-NIFE solution in acetonitrile. After 10 min of incubation at RT, the reaction was terminated by hydrogen chloride addition. The derivatized and filtrated samples were immediately separated on a 100 mm by 2.1 mm ACQUITY 1.7-μm BEH C18 column, using an ACQUITY UPLC system coupled to a Xevo tandem MS (Waters Co., Milford, MA, USA).

Untargeted sphingolipidomic studies in human samples

Plasma samples were processed and analyzed as previously described (76). Briefly, total lipid extract was obtained from 100 μl of plasma, using modified Bligh and Dyer extraction (77). Plasma total lipid extracts were separated on an Dionex UltiMate 3000 UPLC system (Thermo Fisher Scientific, San Jose, CA, USA) using a Kinetex C₈ 150 × 2.1 mm, 2.6-μm column (Phenomenex, Sydney, NSW, Australia). After injection of the samples (10 μl), the column effluent was directly introduced into the heated electrospray ionization source of an Orbitrap Fusion mass spectrometer (Thermo Fisher Scientific, San Jose, CA, USA), and analysis was performed in positive ionization mode. The relative quantification of lipid species was obtained from the area of their corresponding individual chromatographic peaks.

Statistical analysis

Comparison between experimental groups was evaluated using InStat software (GraphPad Software Inc.), applying a one-way ANOVA, followed by a Bonferroni post hoc test for multiple comparisons or a repeated measures two-way ANOVA for Sholl analysis. For single comparisons, either Student's *t* test (for parametric data) or Mann-Whitney *U* test (for nonparametric data) was used. Data are presented as means ± SEM from at least three independent experiments.

SUPPLEMENTARY MATERIALS

[stke.scienmag.org/cgi/content/full/12/586/eaaw0936/DC1](http://stke.sciencemag.org/cgi/content/full/12/586/eaaw0936/DC1)

Fig. S1. Protein interactions and cellular trafficking of GluN2Bwt- and GluN2B(P553T)-containing NMDARs.

Fig. S2. Altered biophysical properties of heterotrimeric GluN1-GluN2A-GluN2B(P553T) NMDARs.

Fig. S3. GluN2B(P553T) mutation alters GluA1 abundance in hippocampal neurons.

Fig. S4. Alignment of eumetazoan iGluRs showing the residues conservation of Pro⁵⁵³ and Phe⁶⁵³.

Table S1. Untargeted analysis of plasma sphingolipid profile in the GRIN2B(P553T) patient before and after L-serine dietary supplementation.

References (78, 79)

REFERENCES AND NOTES

- A. Rett, On a unusual brain atrophy syndrome in hyperammonemia in childhood. *Wien. Med. Wochenschr.* **116**, 723–726 (1966).
- M. Chahrour, H. Y. Zoghbi, The story of Rett syndrome: From clinic to neurobiology. *Neuron* **56**, 422–437 (2007).
- B. Hagberg, J. Aicardi, K. Dias, O. Ramos, A progressive syndrome of autism, dementia, ataxia, and loss of purposeful hand use in girls: Rett's syndrome: Report of 35 cases. *Ann. Neurol.* **14**, 471–479 (1983).
- R. E. Amir, I. B. Van den Veyver, M. Wan, C. Q. Tran, U. Francke, H. Y. Zoghbi, Rett syndrome is caused by mutations in X-linked *MECP2*, encoding methyl-CpG-binding protein 2. *Nat. Genet.* **23**, 185–188 (1999).
- J. L. Neul, H. Y. Zoghbi, Rett syndrome: A prototypical neurodevelopmental disorder. *Neuroscientist* **10**, 118–128 (2004).
- F. F. Hamdan, J. Gauthier, Y. Araki, D.-T. Lin, Y. Yoshizawa, K. Higashi, A.-R. Park, D. Spiegelman, S. Dobrzeniecka, A. Piton, H. Tomitori, H. Daoud, C. Massicotte, E. Henrion, O. Diallo, M. Shekarabi, C. Marineau, M. Shevell, B. Maranda, G. Mitchell, A. Nadeau, G. D'Anjou, M. Vanasse, M. Srour, R. G. Lafrenière, P. Drapeau, J. C. Lacaille, E. Kim, J.-R. Lee, K. Igashri, R. L. Huganir, G. A. Rouleau, J. L. Michaud, Excess of de novo deleterious mutations in genes associated with glutamatergic systems in nonsyndromic intellectual disability. *Am. J. Hum. Genet.* **88**, 306–316 (2011).
- D. Soto, X. Altafaj, C. Sindreu, Á. Bayés, Glutamate receptor mutations in psychiatric and neurodevelopmental disorders. *Commun. Integr. Biol.* **7**, e27887 (2014).
- L. Volk, S.-L. Chiu, K. Sharma, R. L. Huganir, Glutamate synapses in human cognitive disorders. *Annu. Rev. Neurosci.* **38**, 127–149 (2015).
- H. Monyer, N. Burnashev, D. J. Laurie, B. Sakmann, P. H. Seuberg, Developmental and regional expression in the rat brain and functional properties of four NMDA receptors. *Neuron* **12**, 529–540 (1994).
- T. Kutsuwada, K. Sakimura, T. Manabe, C. Takayama, N. Katakura, E. Kushiya, R. Natsume, M. Watanabe, Y. Inoue, T. Yagi, S. Aizawa, M. Arakawa, T. Takahashi, Y. Nakamura, H. Mori, M. Mishina, Impairment of suckling response, trigeminal neuronal pattern formation, and hippocampal LTD in NMDA receptor epsilon 2 subunit mutant mice. *Neuron* **16**, 333–344 (1996).
- N. Burnashev, P. Szepetowski, NMDA receptor subunit mutations in neurodevelopmental disorders. *Curr. Opin. Pharmacol.* **20**, 73–82 (2015).
- C. Hu, W. Chen, S. J. Myers, H. Yuan, S. F. Traynelis, Human GRIN2B variants in neurodevelopmental disorders. *J. Pharmacol. Sci.* **132**, 115–121 (2016).
- K. Platzer, H. Yuan, H. Schütz, A. Winschel, W. Chen, C. Hu, H. Kusumoto, H. O. Heyne, K. L. Helbig, S. Tang, M. C. Willing, B. T. Tinkle, D. J. Adams, C. Depienne, B. Keren, C. Mignot, E. Frengen, P. Strømme, S. Biskup, D. Döcker, T. M. Strom, H. C. Mefford, C. T. Myers, A. M. Muir, A. LaCroix, L. Sadleir, I. E. Scheffer, E. Brilstra, M. M. van Haelst, J. J. van der Smagt, L. A. Bok, R. S. Möller, U. B. Jensen, J. J. Millichap, A. T. Berg, E. M. Goldberg, I. De Bie, S. Fox, P. Major, J. R. Jones, E. H. Zackai, R. Abou Jamra, A. Rolfs, R. J. Leventer, J. A. Lawson, T. Roscioli, F. E. Jansen, E. Ranza, C. M. Korff, A.-E. Lehesjoki, C. Courage, T. Linnankivi, D. R. Smith, C. Stanley, M. Mintz, D. McKnight, A. Decker, W.-H. Tan, M. A. Tarnopolsky, L. I. Brady, M. Wolff, L. Dondit, H. F. Pedro, S. E. Parisotto, K. L. Jones, A. D. Patel, D. N. Franz, R. Vanzo, E. Marco, J. D. Ranells, N. Di Donato, W. B. Dobyns, B. Laube, S. F. Traynelis, J. R. Lemke, GRIN2B encephalopathy: Novel findings on phenotype, variant clustering, functional consequences and treatment aspects. *J. Med. Genet.* **54**, 460–470 (2017).
- J. R. Lemke, R. Hendrickx, K. Geider, B. Laube, M. Schwake, R. J. Harvey, V. M. James, A. Pepler, I. Steiner, K. Hörtogel, J. Neidhardt, S. Ruf, M. Wolff, D. Bartholdi, R. Caraballo, K. Platzer, A. Suls, P. De Jonghe, S. Biskup, S. Weckhuysen, GRIN2B mutations in west syndrome and intellectual disability with focal epilepsy. *Ann. Neurol.* **75**, 147–154 (2014).
- S. Endege, G. Rosenberger, K. Geider, B. Popp, C. Tamer, I. Stefanova, M. Milh, F. Kortüm, A. Fritsch, F. K. Pientka, Y. Hellendoorn, V. M. Kalscheuer, J. Kohlhase, U. Moog, G. Rappold, A. Rauch, H.-H. Ropers, S. von Spiczak, H. Tönnes, N. Vileneuve, L. Villard, B. Zabel, M. Zenker, B. Laube, A. Reis, D. Wieczorek, L. Van Maldergem, K. Kutsche, Mutations in *GRIN2A* and *GRIN2B* encoding regulatory subunits of NMDA receptors cause variable neurodevelopmental phenotypes. *Nat. Genet.* **42**, 1021–1026 (2010).
- J. de Ligt, M. H. Willemsen, B. W. M. van Bon, T. Kleefstra, H. G. Yntema, T. Kroes, A. T. Vulto-van Silfhout, D. A. Koolen, P. de Vries, C. Gilissen, M. del Rosario, A. Hoischen, H. Scheffer, B. B. A. de Vries, H. G. Brunner, J. A. Veltman, L. E. L. M. Vissers, Diagnostic exome sequencing in persons with severe intellectual disability. *N. Engl. J. Med.* **367**, 1921–1929 (2012).
- B. J. O'Rourke, P. Deriziotis, C. Lee, L. Vives, J. J. Schwartz, S. Girirajan, E. Karakoc, A. P. MacKenzie, S. B. Ng, C. Baker, M. J. Rieder, D. A. Nickerson, R. Bernier, S. E. Fisher, J. Shendure, E. E. Eichler, Exome sequencing in sporadic autism spectrum disorders identifies severe de novo mutations. *Nat. Genet.* **43**, 585–589 (2011).
- J.-P. Mothet, A. T. Parent, H. Wolosker, R. O. Brady Jr., D. J. Linden, C. D. Ferris, M. A. Rogawski, S. H. Snyder, D-serine is an endogenous ligand for the glycine site of the N-methyl-D-aspartate receptor. *Proc. Natl. Acad. Sci. U.S.A.* **97**, 4926–4931 (2000).
- T. Papouin, L. Ladepêche, J. Ruel, S. Sacchi, M. Labasque, M. Hanini, L. Groc, L. Legionni, J.-P. Mothet, S.-H. R. Oliet, Synaptic and extrasynaptic NMDA receptors are gated by different endogenous coagonists. *Cell* **150**, 633–646 (2012).

20. M. Lucariello, E. Vidal, S. Vidal, M. Saez, L. Roa, D. Huertas, M. Pineda, E. Dalfó, J. Dopazo, P. Jurado, J. Armstrong, M. Esteller, Whole exome sequencing of Rett syndrome-like patients reveals the mutational diversity of the clinical phenotype. *Hum. Genet.* **135**, 1343–1354 (2016).
21. M. Alsaloum, R. Kazi, Q. Gan, J. Amin, L. P. Wollmuth, A molecular determinant of subtype-specific desensitization in ionotropic glutamate receptors. *J. Neurosci.* **36**, 2617–2622 (2016).
22. S. F. Traynelis, L. P. Wollmuth, C. J. McBain, F. S. Menniti, K. M. Vance, K. K. Ogden, K. B. Hansen, H. Yuan, S. J. Myers, R. Dingledine, Glutamate receptor ion channels: Structure, regulation, and function. *Pharmacol. Rev.* **62**, 405–496 (2010).
23. V. Vyklický, B. Krausová, J. Černý, M. Ladislav, T. Smejkalová, B. Kysilov, M. Korinek, S. Danacikova, M. Horák, H. Chodounská, E. Kudová, L. Vyklický, Surface expression, function, and pharmacology of disease-associated mutations in the membrane domain of the human GluN2B subunit. *Front. Mol. Neurosci.* **11**, 110 (2018).
24. E. Gratasos-Batlle, N. Yefimenko, H. Cascos-García, D. Soto, AMPAR interacting protein CPT1C enhances surface expression of GluA1-containing receptors. *Front. Cell. Neurosci.* **8**, 469 (2015).
25. K. R. Tovar, M. J. McGinley, G. L. Westbrook, Triheteromeric NMDA receptors at hippocampal synapses. *J. Neurosci.* **33**, 9150–9160 (2013).
26. D. Stroebel, S. Carvalho, T. Grand, S. Zhu, P. Paoletti, Controlling NMDA receptor subunit composition using ectopic retention signals. *J. Neurosci.* **34**, 16630–16636 (2014).
27. M. P. Regaldo, A. Villarroel, J. Lerma, Intersubunit cooperativity in the NMDA receptor. *Neuron* **32**, 1085–1096 (2001).
28. W. Li, X. Xu, L. Pozzo-Miller, Excitatory synapses are stronger in the hippocampus of Rett syndrome mice due to altered synaptic trafficking of AMPA-type glutamate receptors. *Proc. Natl. Acad. Sci. U.S.A.* **113**, E1575–E1584 (2016).
29. M. Benveniste, J. Clements, L. Vyklický Jr., M. L. Mayer, A kinetic analysis of the modulation of N-methyl-D-aspartic acid receptors by glycine in mouse cultured hippocampal neurones. *J. Physiol.* **428**, 333–357 (1990).
30. D. Liao, R. H. Scannevin, R. Huganir, Activation of silent synapses by rapid activity-dependent synaptic recruitment of AMPA receptors. *J. Neurosci.* **21**, 6008–6017 (2001).
31. W.-Y. Lu, H.-Y. Man, W. Ju, W. S. Trimble, J. F. MacDonald, Y. T. Wang, Activation of synaptic NMDA receptors induces membrane insertion of new AMPA receptors and LTP in cultured hippocampal neurons. *Neuron* **29**, 243–254 (2001).
32. D. A. Fortin, M. A. Davare, T. Srivastava, J. D. Brady, S. Nygaard, V. A. Derkach, T. R. Soderling, Long-term potentiation-dependent spine enlargement requires synaptic Ca^{2+} -permeable AMPA receptors recruited by CaM-kinase I. *J. Neurosci.* **30**, 11565–11575 (2010).
33. H. Wolosker, D. T. Balu, J. T. Coyle, The rise and fall of the D-serine-mediated gliotransmission hypothesis. *Trends Neurosci.* **39**, 712–721 (2016).
34. H. Wolosker, S. Blackshaw, S. H. Snyder, Serine racemase: A glial enzyme synthesizing D-serine to regulate glutamate-N-methyl-D-aspartate neurotransmission. *Proc. Natl. Acad. Sci. U.S.A.* **96**, 13409–13414 (1999).
35. P. Paoletti, C. Bellone, Q. Zhou, NMDA receptor subunit diversity: Impact on receptor properties, synaptic plasticity and disease. *Nat. Rev. Neurosci.* **14**, 383–400 (2013).
36. C. A. Chapleau, G. D. Calfa, M. C. Lane, A. J. Albertson, J. L. Larimore, S. Kudo, D. L. Armstrong, A. K. Percy, L. Pozzo-Miller, Dendritic spine pathologies in hippocampal pyramidal neurons from Rett syndrome brain and after expression of Rett-associated MECP2 mutations. *Neurobiol. Dis.* **35**, 219–233 (2009).
37. B. J. O’Roak, L. Vives, S. Girirajan, E. Karakoc, N. Krumm, B. P. Coe, R. Levy, A. Ko, C. Lee, J. D. Smith, E. H. Turner, I. B. Stanaway, B. Vernot, M. Malig, C. Baker, B. Reilly, J. M. Akey, E. Borenstein, M. J. Rieder, D. A. Nickerson, R. Bernier, J. Shendure, E. E. Eichler, Sporadic autism exomes reveal a highly interconnected protein network of de novo mutations. *Nature* **485**, 246–250 (2012).
38. J. R. Lemke, R. Hendrickx, K. Geider, B. Laube, M. Schwake, R. J. Harvey, V. M. James, A. Pepler, I. Steiner, K. Hörtrogel, J. Neidhardt, S. Ruf, M. Wolff, D. Bartholdi, R. Caraballo, K. Platzer, A. Suls, P. De Jonghe, S. Biskup, S. Weckhuysen, *GRIN2B* mutations in west syndrome and intellectual disability with focal epilepsy. *Ann. Neurol.* **75**, 147–154 (2014).
39. L. G. Harsing Jr., P. Matyus, Mechanisms of glycine release, which build up synaptic and extrasynaptic glycine levels: The role of synaptic and non-synaptic glycine transporters. *Brain Res. Bull.* **93**, 110–119 (2013).
40. P. E. Chen, M. T. Geballe, E. Katz, K. Erreger, M. R. Livesey, K. K. O’Toole, P. Le, C. J. Lee, J. P. Snyder, S. F. Traynelis, D. J. A. Wyllie, Modulation of glycine potency in rat recombinant NMDA receptors containing chimeric NR2A/2D subunits expressed in *Xenopus laevis* oocytes. *J. Physiol.* **586**, 227–245 (2008).
41. S. M. David, P. B. Burger, A. Prakash, M. T. Geballe, R. Yadav, P. Le, K. Vellano, J. P. Snyder, S. F. Traynelis, Structural determinants of D-cycloserine efficacy at the NR1/NR2C NMDA receptors. *J. Neurosci.* **30**, 2741–2754 (2010).
42. J. Jaeken, M. Dethieux, J. P. Fryns, J. F. Collet, P. Alliet, E. Van Schaftingen, Phosphoserine phosphatase deficiency in a patient with Williams syndrome. *J. Med. Genet.* **34**, 594–596 (1997).
43. J. H. Yang, A. Wada, K. Yoshida, Y. Miyoshi, T. Sayano, K. Esaki, M. O. Kinoshita, S. Tomonaga, N. Azuma, M. Watanabe, K. Hamase, K. Zaitsu, T. Machida, A. Messing, S. Itohara, Y. Hirabayashi, S. Furuya, Brain-specific *Phgdh* deletion reveals a pivotal role for L-serine biosynthesis in controlling the level of D-serine, an N-methyl-D-aspartate receptor co-agonist, in adult brain. *J. Biol. Chem.* **285**, 41380–41390 (2010).
44. R. Levin, A. E. Dor-Abarbanel, S. Edelman, A. R. Durrant, K. Hashimoto, D. C. Javitt, U. Heresco-Levy, Behavioral and cognitive effects of the N-methyl-D-aspartate receptor co-agonist D-serine in healthy humans: Initial findings. *J. Psychiatr. Res.* **61**, 188–195 (2015).
45. F. R. Turpin, B. Potier, J. R. Dulong, P.-M. Sinet, J. Alliot, S. H. R. Oliet, P. Dutar, J. Epelbaum, J.-P. Mothet, J.-M. Billard, Reduced serine racemase expression contributes to age-related deficits in hippocampal cognitive function. *Neurobiol. Aging* **32**, 1495–1504 (2011).
46. J.-M. Billard, D-Serine in the aging hippocampus. *J. Pharm. Biomed. Anal.* **116**, 18–24 (2015).
47. S. N. van der Crabben, N. M. Verhoeven-Duijf, E. H. Brilstra, L. Van Maldergem, T. Coskun, E. Rubio-Gozalbo, R. Berger, T. J. de Koning, An update on serine deficiency disorders. *J. Inher. Metab. Dis.* **36**, 613–619 (2013).
48. S. S. Sparrow, D. V. Cicchetti, Diagnostic uses of the Vineland Adaptive Behavior Scales. *J. Pediatr. Psychol.* **10**, 215–225 (1985).
49. H. Li, R. Durbin, Fast and accurate short read alignment with Burrows-Wheeler transform. *Bioinformatics* **25**, 1754–1760 (2009).
50. A. Bayés, L. N. van de Lagemaat, M. O. Collins, M. D. R. Croning, I. R. Whittle, J. S. Choudhary, S. G. N. Grant, Characterization of the proteome, diseases and evolution of the human postsynaptic density. *Nat. Publ. Group* **14**, 19–21 (2011).
51. A. Bayés, M. O. Collins, C. M. Galtrey, C. Simonnet, M. Roy, M. D. R. Croning, G. Gou, L. N. van de Lagemaat, D. Milward, I. R. Whittle, C. Smith, J. S. Choudhary, S. G. N. Grant, Human post-mortem synapse proteome integrity screening for proteomic studies of postsynaptic complexes. *Mol. Brain* **7**, 88 (2014).
52. P. Kumar, S. Henikoff, P. C. Ng, Predicting the effects of coding non-synonymous variants on protein function using the SIFT algorithm. *Nat. Protoc.* **4**, 1073–1081 (2009).
53. I. A. Adzhubei, S. Schmidt, L. Peshkin, V. E. Ramensky, A. Gerasimova, P. Bork, A. S. Kondrashov, S. R. Sunyaev, A method and server for predicting damaging missense mutations. *Nat. Publ. Group* **7**, 248–249 (2010).
54. Y. Choi, A. P. Chan, PROVEAN web server: A tool to predict the functional effect of amino acid substitutions and indels. *Bioinformatics* **31**, 2745–2747 (2015).
55. J. M. Schwarz, D. N. Cooper, M. Schuelke, D. Seelow, MutationTaster2: Mutation prediction for the deep-sequencing age. *Nat. Methods* **11**, 361–362 (2014).
56. P. C. Ng, S. Henikoff, Predicting the effects of amino acid substitutions on protein function. *Annu. Rev. Genomics Hum. Genet.* **7**, 61–80 (2006).
57. Y. Choi, G. E. Sims, S. Murphy, J. R. Miller, A. P. Chan, Predicting the functional effect of amino acid substitutions and indels. *PLOS ONE* **7**, e46688 (2012).
58. M. J. Landrum, J. M. Lee, G. R. Riley, W. Jang, W. S. Rubinstein, D. M. Church, D. R. Maglott, ClinVar: Public archive of relationships among sequence variation and human phenotype. *Nucleic Acids Res.* **42**, D980–D985 (2014).
59. P. D. Stenson, M. Mort, E. V. Ball, K. Shaw, A. D. Phillips, D. N. Cooper, The Human Gene Mutation Database: Building a comprehensive mutation repository for clinical and molecular genetics, diagnostic testing and personalized genomic medicine. *Hum. Genet.* **133**, 1–9 (2014).
60. International HapMap 3 Consortium, D. M. Altshuler, F. Yu, L. Peltonen, P. E. Bonnen, R. A. Gibbs, P. I. W. de Bakker, P. Deloukas, S. B. Gabriel, R. Gwilliam, S. Hunt, M. Inouye, X. Jia, A. Palotie, M. Parkin, P. Whittaker, K. Chang, A. Hawes, L. R. Lewis, Y. Ren, D. Wheeler, D. M. Muzny, C. Barnes, K. Darvishi, M. Hurles, J. M. Korn, K. Kristiansson, C. Lee, S. A. McCarrol, J. Nemesh, E. Dermitzakis, S. B. Montgomery, S. Pollack, N. Soranzo, C. Gonzaga-Jauregui, A. Keinan, V. Anttila, W. Brodeur, M. J. Daly, S. Leslie, G. McVean, L. Moutsianas, H. Nguyen, S. F. Schaffner, Q. Zhang, M. J. R. Ghori, R. McGinnis, W. McLaren, A. L. Price, F. Takeuchi, S. R. Grossman, I. Shlyakhter, E. B. Hostettler, P. C. Sabeti, C. A. Adebamowo, M. W. Foster, D. R. Gordon, J. Licinio, M. C. Manca, P. A. Marshall, I. Matsuda, D. Ngare, V. O. Wang, D. Reddy, C. N. Rotimi, C. D. Royal, R. R. Sharp, C. Zeng, L. D. Brooks, J. E. McEwen, Integrating common and rare genetic variation in diverse human populations. *Nature* **467**, 52–58 (2010).
61. E. Karakas, H. Furukawa, Crystal structure of a heterotetrameric NMDA receptor ion channel. *Science* **344**, 992–997 (2014).
62. B. Webb, A. Sali, Comparative protein structure modeling using MODELLER. *Curr. Protoc. Bioinformatics* **47**, 5.6.1–5.6.32 (2014).
63. Q. Wang, A. A. Canutescu, R. L. Dunbrack Jr., SCWRL and MolIDE: Computer programs for side-chain conformation prediction and homology modeling. *Nat. Protoc.* **3**, 1832–1847 (2008).
64. A. Cordoní, G. Caltabiano, L. Pardo, Membrane protein simulations using AMBER force field and Berger lipid parameters. *J. Chem. Theory Comput.* **8**, 948–958 (2012).
65. S. Pronk, S. Päll, R. Schulz, P. Larsson, P. Bjelkmar, R. Apostolov, M. R. Shirts, J. C. Smith, P. M. Kasson, D. van der Spoel, B. Hess, E. Lindahl, GROMACS 4.5: A high-throughput and highly parallel open source molecular simulation toolkit. *Bioinformatics* **29**, 845–854 (2013).

66. A. Riesgo, N. Farrar, P. J. Windsor, G. Giribet, S. P. Leys, The analysis of eight transcriptomes from all poriferan classes reveals surprising genetic complexity in sponges. *Mol. Biol. Evol.* **31**, 1102–1120 (2014).
67. R. C. Edgar, MUSCLE: Multiple sequence alignment with high accuracy and high throughput. *Nucleic Acids Res.* **32**, 1792–1797 (2004).
68. K. Tamura, G. Stecher, D. Peterson, A. Filipski, S. Kumar, MEGA6: Molecular evolutionary genetics analysis version 6.0. *Mol. Biol. Evol.* **30**, 2725–2729 (2013).
69. F. Ronquist, M. Teslenko, P. van der Mark, D. L. Ayres, A. Darling, S. Höhna, B. Larget, L. Liu, M. A. Suchard, J. P. Huelsenbeck, MrBayes 3.2: Efficient Bayesian phylogenetic inference and model choice across a large model space. *Syst. Biol.* **61**, 539–542 (2012).
70. S. Vicini, J. F. Wang, J. H. Li, W. J. Zhu, Y. H. Wang, J. H. Luo, B. B. Wolfe, D. R. Grayson, Functional and pharmacological differences between recombinant *N*-methyl-D-aspartate receptors. *J. Neurophysiol.* **79**, 555–566 (1998).
71. C. Grau, K. Arató, J. M. Fernández-Fernández, A. Valderrama, C. Sindreu, C. Fillat, I. Ferrer, S. de la Luna, X. Altafaj, DYRK1A-mediated phosphorylation of GluN2A at Ser(1048) regulates the surface expression and channel activity of GluN1/GluN2A receptors. *Front. Cell. Neurosci.* **8**, 331 (2014).
72. J. Schindelin, C. T. Rueden, M. C. Hiner, K. W. Eliceiri, The ImageJ ecosystem: An open platform for biomedical image analysis. *Mol. Reprod. Dev.* **82**, 518–529 (2015).
73. F. J. Sigworth, The variance of sodium current fluctuations at the node of Ranvier. *J. Physiol.* **307**, 97–129 (1980).
74. W. F. Visser, N. M. Verhoeven-Duif, R. Ophoff, S. Bakker, L. W. Klomp, R. Berger, T. J. de Koning, A sensitive and simple ultra-high-performance-liquid chromatography-tandem mass spectrometry based method for the quantification of D-amino acids in body fluids. *J. Chromatogr. A* **1218**, 7130–7136 (2011).
75. A. Ormazabal, Á. García-Cazorla, Y. Fernández, E. Fernández-Álvarez, J. Campistol, R. Artuch, HPLC with electrochemical and fluorescence detection procedures for the diagnosis of inborn errors of biogenic amines and pterins. *J. Neurosci. Methods* **142**, 153–158 (2005).
76. A. Seyer, S. Boudah, S. Broudin, C. Junot, B. Colsch, Annotation of the human cerebrospinal fluid lipidome using high resolution mass spectrometry and a dedicated data processing workflow. *Metabolomics* **12**, 91 (2016).
77. E. G. Bligh, W. J. Dyer, A rapid method of total lipid extraction and purification. *Can. J. Biochem. Physiol.* **37**, 911–917 (1959).
78. A. M. Waterhouse, J. B. Procter, D. M. A. Martin, M. Clamp, G. J. Barton, Jalview version 2—A multiple sequence alignment editor and analysis workbench. *Bioinformatics* **25**, 1189–1191 (2009).
79. D. Ramos-Vicente, J. Ji, E. Gratacós-Batlle, G. Gou, R. Reig-Viader, J. Luis, D. Burguera, E. Navas-Perez, J. García-Fernández, P. Fuentes-Prior, H. Escrivá, N. Roher, D. Soto, Á. Bayés, Metazoan evolution of glutamate receptors reveals unreported phylogenetic groups and divergent lineage-specific events. *eLife* **7**, e35774 (2018).

Acknowledgments: We acknowledge the help from N. Verhoeven and J. Gerrits (Universitair Medisch Centrum Utrecht, The Netherlands), as well as R. Artuch and A. Ormazábal (Hospital Sant Joan de Déu, Barcelona, Spain), for conducting the analytical measurements of amino acids in biofluids. We thank S. Jurado (Instituto de Neurociencias, Alicante, Spain) for guidance in cLTP experiments and the “Medicinal Computational Laboratory” from Universitat Autònoma de Barcelona for providing computing facilities. We also acknowledge P. Paoletti (ENS, Paris, France) for providing the plasmids allowing the studies with triheteromeric NMDARs. **Funding:** This work was supported by the grants PI16/00851 [ISCIII, cofunded by European Regional Development Fund (ERDF), a way to build Europe], La Marató (project no. 20140210), PCIN-2014-105 (MINECO), and Miguel Servet Program (CP116/00021, ISCIII) to X.A.; BFU2017-83317-P (MICINN) to D.S.; PI15/01082 (ISCIII) to Á.G.-C.; SAF2016-77830-R to M.O.; BFU2012-34398 and BFU2015-69717-P (MINECO), Career Integration Grant (ref. 304111), Marie Curie Intra-European Fellowship (ref. 221540), and Ramón y Cajal Fellowship (RYC-2011-08391p) to Á.B.; SAF2012-40102 (MINECO/FEDER), FP7 Marie Curie CIG grant (#631035), and Ramón y Cajal (RYC-2011-08026) to C.S.; PI17/00296 and RETIC RD16/0008/0014 to X.G.; and MetaboHUB project (ANR-11-INBS-0010) to B.C. C.A. received an FPI contract (MINECO). X.A., C.S., and Á.B. also benefit from the financial support of AGAUR (SGR14-297). A.S.-G. benefits from a Fundación Tatiana Pérez de Guzmán el Bueno PhD fellowship. We thank CERCA Programme/Generalitat de Catalunya for institutional support. **Author contributions:** X.A. designed the study, in collaboration with Á.G.-C., D.S., M.O., X.G., and C.S. D.S., X.G., R.G.-D., and E.G.-B. conducted the electrophysiological recordings. M.O. developed the structural model and performed the bioinformatic analysis. Á.B. and D.R.-V. performed the phylogenetic analysis. C.S., C.A., C.G., and M.G.-S. performed the cLTP analysis. C.G., A.S.-G., and S.L. performed the morphological analysis. E.C.-V. and B.C. performed the lipidomic studies. A.L.-S. performed the behavioral assessments. V.F.-D. and F.C. performed the pharmacological studies. J.A. generated and validated the genetic data. Á.G.-C. coordinated the clinical part of the study. X.A. wrote the manuscript with the help of Á.G.-C., D.S., M.O., and all authors proofread the manuscript. **Competing interests:** The authors declare that they have no competing interests. **Data and materials availability:** All data needed to evaluate the conclusions in the paper are present in the paper or the Supplementary Materials

Submitted 16 November 2018

Accepted 24 May 2019

Published 18 June 2019

10.1126/scisignal.aaw0936

Citation: D. Soto, M. Olivella, C. Grau, J. Armstrong, C. Alcon, X. Gasull, A. Santos-Gómez, S. Locubiche, M. G. de Salazar, R. García-Díaz, E. Gratacós-Batlle, D. Ramos-Vicente, E. Chu-Van, B. Colsch, V. Fernández-Dueñas, F. Ciruela, Á. Bayés, C. Sindreu, A. López-Sala, Á. García-Cazorla, X. Altafaj, L-Serine dietary supplementation is associated with clinical improvement of loss-of-function *GRIN2B*-related pediatric encephalopathy. *Sci. Signal.* **12**, eaaw0936 (2019).

ALZHEIMER'S DISEASE

Reduced non-rapid eye movement sleep is associated with tau pathology in early Alzheimer's disease

Brendan P. Lucey^{1,2*}, Austin McCullough³, Eric C. Landsness¹, Cristina D. Toedebusch¹, Jennifer S. McLeland¹, Aiad M. Zaza³, Anne M. Fagan^{1,2,4}, Lena McCue⁵, Chengjie Xiong⁵, John C. Morris^{1,2,4}, Tammie L. S. Benzinger^{3,4}, David M. Holtzman^{1,2,4*}

Copyright © 2019
The Authors, some
rights reserved;
exclusive licensee
American Association
for the Advancement
of Science. No claim
to original U.S.
Government Works

In Alzheimer's disease (AD), deposition of insoluble amyloid- β (A β) is followed by intracellular aggregation of tau in the neocortex and subsequent neuronal cell loss, synaptic loss, brain atrophy, and cognitive impairment. By the time even the earliest clinical symptoms are detectable, A β accumulation is close to reaching its peak and neocortical tau pathology is frequently already present. The period in which AD pathology is accumulating in the absence of cognitive symptoms represents a clinically relevant time window for therapeutic intervention. Sleep is increasingly recognized as a potential marker for AD pathology and future risk of cognitive impairment. Previous studies in animal models and humans have associated decreased non-rapid eye movement (NREM) sleep slow wave activity (SWA) with A β deposition. In this study, we analyzed cognitive performance, brain imaging, and cerebrospinal fluid (CSF) AD biomarkers in participants enrolled in longitudinal studies of aging. In addition, we monitored their sleep using a single-channel electroencephalography (EEG) device worn on the forehead. After adjusting for multiple covariates such as age and sex, we found that NREM SWA showed an inverse relationship with AD pathology, particularly tauopathy, and that this association was most evident at the lowest frequencies of NREM SWA. Given that our study participants were predominantly cognitively normal, this suggested that changes in NREM SWA, especially at 1 to 2 Hz, might be able to discriminate tau pathology and cognitive impairment either before or at the earliest stages of symptomatic AD.

INTRODUCTION

Aggregation of amyloid- β (A β) into oligomers and fibrils that are present in extracellular A β plaques in the brain is a key early step in Alzheimer's disease (AD) pathogenesis and begins to occur ~15 to 20 years before the onset of cognitive decline (1). The buildup of insoluble A β is followed by the intracellular aggregation of tau and its spread from the medial temporal lobe to different neocortical regions (1, 2). Localized tau aggregation in the medial temporal lobe during normal aging is probably independent of A β ; however, in AD, its spread to the neocortex appears to be downstream from A β buildup and correlates strongly with neuronal cell loss, synaptic loss, brain atrophy, and cognitive impairment. These findings are strongly supported by genetic, pathological, and biomarker data in both sporadic and inherited AD (1, 2). By the time even the earliest clinical symptoms of AD are detectable, A β accumulation is close to reaching its peak, and there is almost always some neocortical tau pathology (3). A β 42, the isoform of A β most prone to aggregate in insoluble plaques, decreases in cerebrospinal fluid (CSF) with brain amyloid deposition and correlates with amyloid positron emission tomography (PET) (4). The CSF tau/A β 42 ratio is related to the dual effect of amyloid and tau pathology and predicts conversion to early symptomatic AD (5–7). There is also neuronal and synaptic loss in several brain regions relevant to memory and thinking (3). The

period in which AD pathology is accumulating in the absence of cognitive symptoms has been termed "preclinical" AD (8, 9).

A bidirectional relationship between sleep and AD has been proposed on the basis of studies in animal models and humans (10–12). Numerous studies have shown that sleep-wake activity is disturbed in individuals with dementia due to AD (13, 14). Sleep disturbance has been measured via self-report, such as with questionnaires and sleep logs, as well as actigraphy and polysomnography. Increasing evidence also supports sleep disturbance as a marker for AD pathology and future risk of cognitive impairment (15–22). For instance, self-reported sleep disturbances, such as poor sleep quality and short sleep duration, have been associated with increased risk of cognitive impairment (15) and increased A β deposition on [¹¹C]Pittsburgh compound B (PiB) PET scans (16). Furthermore, excessive daytime sleepiness reported by a cohort of older adults was associated with increased longitudinal A β accumulation on PiB-PET scans (17). Sleep logs and actigraphy monitoring have found that reduced sleep efficiency and increased nap frequency in cognitively normal individuals were associated with A β deposition (18). Studies with polysomnography have associated increased risk of cognitive impairment in older adults with sleep-disordered breathing (19–21) and periodic limb movements during sleep (22).

In addition to sleep disturbance as a putative marker of AD pathology, evidence also supports the hypothesis that disturbed sleep increases AD risk, at least in part, via an A β mechanism (11). We have found that A β concentrations in CSF fluctuate with sleep-wake activity in both mice (23) and humans (24). This A β cycling pattern has been replicated in multiple studies (25) and assays (26). A β concentrations are directly regulated by neuronal activity (27–31) and evidence in mice suggests that decreased interstitial fluid (ISF) during sleep results, at least in part, from altered neuronal/metabolic activity decreasing A β production/release. In humans, we have recently

¹Department of Neurology, Washington University School of Medicine, St. Louis, MO 63110, USA. ²Hope Center for Neurological Disorders, Washington University School of Medicine, St. Louis, MO 63110, USA. ³Department of Radiology, Washington University School of Medicine, St. Louis, MO 63110, USA. ⁴Knight Alzheimer's Disease Research Center, Washington University School of Medicine, St. Louis, MO 63110, USA. ⁵Division of Biostatistics, Washington University School of Medicine, St. Louis, MO 63110, USA.

*Corresponding author. Email: luceyb@wustl.edu (B.P.L.); holtzman@wustl.edu (D.M.H.)

shown that targeted slow wave sleep disruption (32) and sleep deprivation (33) will increase overnight CSF A β concentrations by 10 to 30% most likely due to increased A β production/release. There is also evidence that A β clearance is increased during sleep due to increased ISF bulk flow (for example, “glymphatic” clearance) (34).

Studies in animal models using electroencephalography (EEG) to monitor different sleep stages have found changes in sleep parameters and EEG power linked with both A β and tau pathology. For instance, A β deposition in APPswe/PS1 δ E9 mice led to disruption of the sleep-wake cycle (35), whereas increasing tauopathy in P301S tau transgenic mice was associated with decreased time in rapid eye movement (REM) and non-REM (NREM) sleep, increased wakefulness, and decreased NREM slow wave activity (SWA) (36). In humans, atrophy and A β accumulation in the medial prefrontal cortex (mPFC) were correlated with both decreased NREM SWA and impaired overnight hippocampus-dependent memory consolidation in cognitively normal older adults (37, 38). Although that cross-sectional study provides associative evidence between A β deposition, NREM sleep disruption, and memory impairment, tau pathology was not assessed. Longitudinal studies with AD biomarkers and cognitive evaluations are needed to establish both the sequential links between these events and causation (39), especially in relation to both A β and tau.

In this study, we monitored sleep-wake activity in 119 participants enrolled in longitudinal studies of aging at the Knight Alzheimer’s Disease Research Center at Washington University. Sleep-wake activity was monitored over six nights with a single-channel EEG worn on the forehead (Sleep Profiler, Advanced Brain Monitoring), actigraphy (Actiwatch 2, Philips Respironics), and sleep logs. In addition, each participant was assessed for sleep-disordered breathing and periodic leg movements with a home sleep test (Alice PDx, Philips Respironics). Participants who underwent cognitive testing, apolipoprotein E (ApoE) genotyping, and assessment of AD biomarkers in CSF [A β 42, tau, phosphorylated tau (p-tau)] or PET scans with [18 F]AV-45 (florbetapir) amyloid and [18 F]AV-1451 (flortaucipir) tau tracers were included in the analyses. Because tau pathology, but not A β pathology, is best associated with cognitive decline in AD, we hypothesized that decreased NREM SWA would be associated with increased tau pathology.

RESULTS

One hundred nineteen participants aged >60 years old enrolled in longitudinal studies of aging at the Knight Alzheimer’s Disease Research Center at Washington University in St. Louis, MO, were recruited for the study. Cognitive performance was evaluated by the Clinical Dementia Rating (CDR) (40, 41). Participants also underwent AV-45 amyloid and AV-1451 tau PET imaging and/or lumbar puncture to measure CSF A β 42, tau, and p-tau concentrations. Sleep monitoring was performed for up to six nights with sleep logs, actigraphy, and a single-channel EEG. Average sleep parameters for participants with PET imaging and CSF biomarkers were not substantially different between amyloid negative versus amyloid positive, tau negative versus tau positive, and CDR 0 versus CDR 0.5 groups regardless of modality used to measure sleep-wake activity (tables S1 and S2). In participants with PET imaging, REM latency was lower in amyloid-positive participants ($t_{36} = 2.98$, $P = 0.005$) but longer in CDR 0.5 individuals ($t_{36} = -2.49$, $P = 0.018$). Amyloid-positive participants had lower wake after sleep onset (WASO)

Table 1. Participant characteristics.

| | PET imaging Mean (SD)/n (%) (N = 38) | CSF Mean (SD)/n (%) (N = 104) |
|--|--|-------------------------------------|
| Age (years) | 73.8 (5.3) | 74.57 (5.20) |
| Sex | | |
| Men | 18 (47.4) | 59 (56.7) |
| Women | 20 (52.6) | 45 (43.3) |
| Race | | |
| African-American | 3 (7.9) | 11 (10.6) |
| Caucasian | 35 (92.1) | 92 (88.5) |
| Asian | 0 (0.0) | 0 (0.0) |
| More than one | 0 (0.0) | 1 (1.0) |
| CDR | | |
| 0 | 29 (76.3) | 83 (79.8) |
| 0.5 | 9 (23.7) | 21 (20.2) |
| ApoE4 | | |
| Negative | 25 (65.8) | 58 (55.8) |
| Positive | 13 (34.2) | 45 (43.3) |
| Sleep medications | | |
| Yes | 4 (10.5) | 12 (11.5) |
| No | 34 (89.5) | 92 (88.5) |
| AHI (respiratory events/hour)* | | |
| Negative (AHI < 5) | 20 (52.6) | 38 (36.5) |
| Mild (AHI 5–15) | 13 (34.2) | 43 (41.4) |
| Moderate (AHI 15–30) | 5 (13.2) | 18 (17.3) |
| Severe (AHI > 30) | 0 (0) | 5 (4.8) |
| PLMI (leg movements/hour) | | |
| Negative (PLMI < 15) | 21 (55.3) | 49 (47.1) |
| Low (PLMI 15–45) | 7 (18.4) | 33 (31.7) |
| High (PLMI > 45) | 10 (26.3) | 22 (21.2) |
| AV-45 PET SUVR | 1.44 (0.61) | — |
| AV-1451 PET SUVR | 1.40 (0.49) | — |
| A β 42 (pg/ml) | — | 1012.59 (367.94) |
| t-tau (pg/ml) | — | 245.46 (119.69) |
| p-tau (pg/ml) | — | 23.66 (13.46) |
| AD pathology | | |
| Amyloid negative/tau negative | 20 (52.6) | 31 (29.8) |
| Amyloid positive/tau negative | 9 (23.7) | 35 (33.7) |
| Amyloid positive/tau positive | 8 (21.1) | 27 (25.9) |
| Amyloid negative/tau positive | 1 (2.6) | 11 (10.6) |
| Time interval from scan/lumbar puncture to sleep study (years) | | |
| AV-45 PET | 0.29 (0.48) | 1.00 (2.60) |
| AV-1451 PET | 0.29 (0.40) | |

*For the participants who underwent PET imaging (N = 38), 4 of 38 participants used continuous positive airway pressure therapy during sleep monitoring. For participants with CSF (N = 104), 12 of 104 participants used continuous positive airway pressure therapy and 1 participant used lateral position therapy device during sleep monitoring.

measured by actigraphy ($t_{35} = 2.07, P = 0.046$), whereas sleep-onset latency measured by actigraphy was prolonged in CDR 0.5 individuals ($t_{35} = -2.33, P = 0.026$). For participants with CSF, CDR 0.5 individuals were found to have longer REM latency measured by EEG ($t_{104} = -2.91, P = 0.0044$) and longer self-reported total sleep time (TST) ($t_{104} = -2.27, P = 0.025$). When measured by actigraphy, sleep efficiency was decreased ($t_{106} = 3.40, P = 0.0009$), sleep-onset latency was prolonged ($t_{106} = -3.86, P = 0.0002$), and WASO was greater ($t_{106} = -2.68, P = 0.0086$) in CDR 0.5 participants compared to CDR 0.

Thirty-eight participants with AV-45 amyloid and AV-1451 tau PET imaging and 104 participants with CSF A β 42, tau, and p-tau underwent monitoring with the single-channel EEG device. Twenty-seven participants had both PET imaging and lumbar punctures. Characteristics for all participants are provided in Table 1. Of the participants with PET imaging, 52.6% (20 of 38) of participants were amyloid and tau negative, with 9 participants amyloid positive but tau negative and 8 participants positive for both amyloid and tau (Table 1). One participant was found to be tau positive but amyloid negative. Amyloid-negative/positive status was set at a standardized uptake value ratio (SUVR) of 1.19 (42, 43), and tau-negative/positive status was set at an SUVR of 1.22 (44). Average amyloid and tau burden on PET are shown in Figs. 1 and 2. For participants with CSF, previously published cutoffs for amyloid positive (CSF A β 42 < 1098 pg/ml) and tau positive (CSF tau > 242 pg/ml) were used to define AD pathology (45). Of the participants with CSF, 29.8% were negative for amyloid and tau, 33.7% were amyloid positive but tau negative, 25.9% were positive for both amyloid and tau, and 10.6% were amyloid negative but tau positive (Table 1).

Decreased NREM SWA with increased tauopathy

Multiple factors may affect sleep and/or AD pathology including age, sex, and sleep disorders. To assess the relationship between NREM SWA and tau pathology, we performed general linear mixed models of NREM SWA with a mean AV-1451 tau PET composite, age, sex, race, ApoE4 status, CDR, apnea-hypopnea index (AHI), periodic limb movement index (PLMI), and sleep medications. The composite of the mean AV-1451 tau SUVR was determined from the average SUVR of the entorhinal cortex, amygdala, lateral occipital, and lateral temporal regions.

As AV-1451 tau SUVR increased, all-night 1- to 4.5-Hz SWA was decreased (Table 2). Because previous work found an inverse relation-

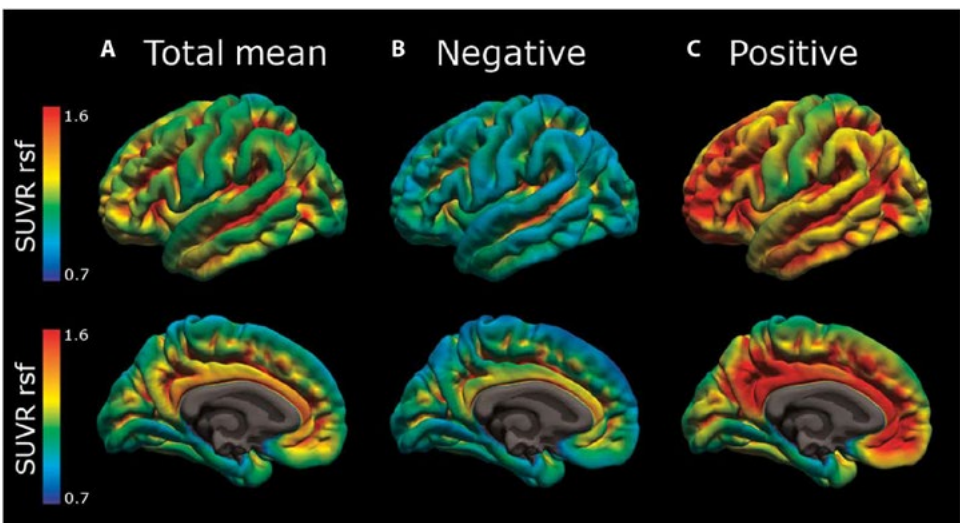


Fig. 1. Mean amyloid pathology for the 38 participants with PET imaging. Mean AV-45 amyloid pathology in (A) all, (B) amyloid-negative, and (C) amyloid-positive subjects as measured in SUVR units after partial volume correction using a regional spread function (rsf).

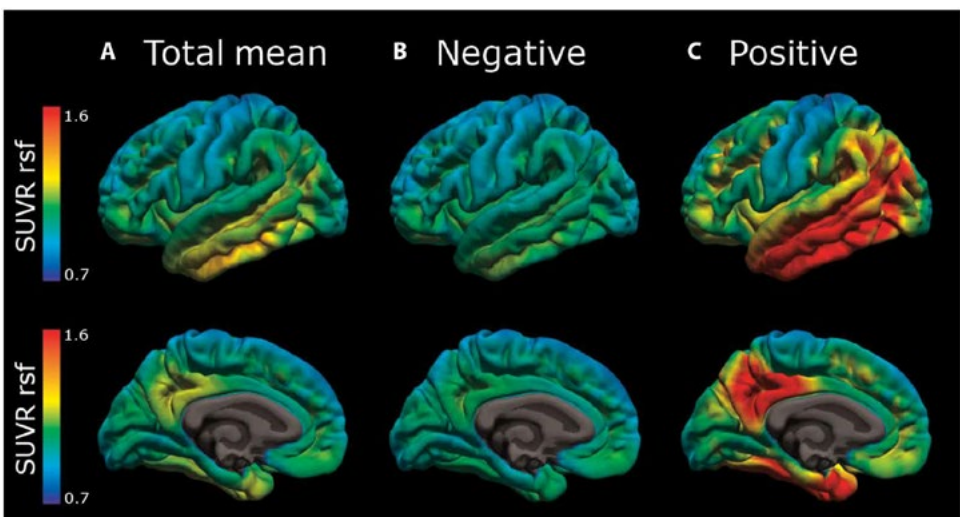


Fig. 2. Mean tau pathology for the 38 participants with PET imaging. Mean AV-1451 tau pathology in (A) all, (B) tau-negative, and (C) tau-positive subjects as measured in SUVR units after partial volume correction using a regional spread function.

ship between the slowest frequencies and amyloid deposition in the mPFC (38), we tested different frequency ranges (1 to 2 Hz, 2 to 3 Hz, and 3 to 4 Hz) in this model and found that this inverse relationship between NREM SWA and tau was maximal in the 1- to 2-Hz range (Table 2). In our model, time represents longitudinal sleep monitoring over multiple nights. Time was not significant in the model ($P > 0.05$), supporting previous reports that the EEG power measures are stable with small within-subject night-to-night variability (46, 47). Age and sex were also inversely associated with NREM SWA. These findings are not surprising given the well-described decline in NREM SWA with increased age and male sex (48, 49). CDR showed negative association with 1- to 2-Hz NREM SWA, indicating that 1- to 2-Hz NREM SWA decreased with worsening tau pathology and cognitive impairment.

To investigate how regional differences in AV-1451 tau PET were associated with NREM SWA, we performed general linear mixed

Table 2. Relationship of NREM SWA to AV-1451 tau PET composite after adjusting for age, sex, race, CDR, ApoE4 status, AHI, PLMI, sleep medications, and time. Linear mixed models were used to calculate the estimates and *P* values for the 38 participants with PET imaging. Time, longitudinal sleep monitoring.

| Dependent variable | Covariate | Estimate | SE | F statistic (df) | P |
|--------------------|----------------------------|----------|--------|------------------|-------|
| 1–4.5 Hz SWA | Mean AV-1451 tau composite | -8.889 | 2.625 | 11.46 (1,27) | 0.002 |
| | Age | -0.670 | 0.243 | 7.59 (1,28) | 0.010 |
| | Sex | -7.850 | 2.636 | 8.87 (1,28) | 0.006 |
| | CDR | -6.882 | 3.312 | 4.32 (1,29) | 0.047 |
| | Race | -9.299 | 4.950 | 3.53 (1,27) | 0.071 |
| | ApoE4 status | +4.002 | 2.891 | 1.92 (1,27) | 0.178 |
| | Sleep medications | +3.225 | 4.468 | 0.52 (1,27) | 0.476 |
| | AHI | +0.141 | 0.166 | 0.73 (1,28) | 0.401 |
| | PLMI | +0.121 | 0.0537 | 5.09 (1,28) | 0.032 |
| | Time | +0.0001 | 0.142 | 0.00 (1,145) | 0.999 |
| 1–2 Hz SWA | Mean AV-1451 tau composite | -21.477 | 6.123 | 12.30 (1,28) | 0.002 |
| | Age | -1.539 | 0.567 | 7.36 (1,28) | 0.011 |
| | Sex | -18.542 | 6.148 | 9.10 (1,28) | 0.005 |
| | CDR | -18.339 | 7.750 | 5.60 (1,29) | 0.025 |
| | Race | -21.620 | 11.537 | 3.51 (1,27) | 0.072 |
| | ApoE4 status | +9.044 | 6.732 | 1.80 (1,27) | 0.190 |
| | Sleep medications | +8.298 | 10.410 | 0.64 (1,27) | 0.432 |
| | AHI | 0.346 | 0.387 | 0.80 (1,28) | 0.379 |
| | PLMI | 0.273 | 0.125 | 4.76 (1,28) | 0.038 |
| | Time | 0.013 | 0.355 | 0.00 (1,146) | 0.970 |
| 2–3 Hz SWA | Mean AV-1451 tau composite | -5.919 | 1.998 | 8.78 (1,28) | 0.006 |
| | Age | -0.509 | 0.186 | 7.51 (1,28) | 0.011 |
| | Sex | -5.577 | 2.009 | 7.71 (1,28) | 0.010 |
| | CDR | -3.654 | 2.500 | 2.14 (1,28) | 0.155 |
| | Race | -6.496 | 3.773 | 2.96 (1,28) | 0.096 |
| | ApoE4 status | +2.925 | 2.210 | 1.75 (1,28) | 0.197 |
| | Sleep medications | +1.731 | 3.410 | 0.26 (1,28) | 0.616 |
| | AHI | +0.085 | 0.126 | 0.46 (1,28) | 0.504 |
| | PLMI | +0.092 | 0.041 | 5.02 (1,28) | 0.033 |
| | Time | -0.013 | 0.095 | 0.02 (1,29) | 0.891 |
| 3–4 Hz SWA | Mean AV-1451 tau composite | -2.186 | 0.766 | 8.16 (1,27) | 0.008 |
| | Age | -0.181 | 0.071 | 6.44 (1,28) | 0.017 |
| | Sex | -2.028 | 0.772 | 6.90 (1,28) | 0.014 |
| | CDR | -1.150 | 0.957 | 1.44 (1,27) | 0.240 |
| | Race | -2.406 | 1.447 | 2.76 (1,27) | 0.108 |
| | ApoE4 status | +1.004 | 0.849 | 1.40 (1,28) | 0.247 |
| | Sleep medications | +0.420 | 1.308 | 0.10 (1,27) | 0.750 |
| | AHI | +0.027 | 0.048 | 0.32 (1,28) | 0.577 |
| | PLMI | +0.035 | 0.016 | 4.84 (1,28) | 0.036 |
| | Time | -0.004 | 0.038 | 0.01 (1,28) | 0.914 |

modeling for NREM SWA in frequency ranges of 1 to 4.5 Hz, 1 to 2 Hz, 2 to 3 Hz, and 3 to 4 Hz with each region of interest (ROI).

Whereas decreased NREM SWA at all slow wave frequencies was associated with increased tau pathology measured by the AV-1451 tau PET composite, regional analyses, uncorrected for multiple comparisons, found that this relationship was most evident in the entorhinal, parahippocampal, inferior parietal, insula, isthmus cingulate, lingual, supramarginal, and orbitofrontal regions (table S3 and fig. S1). After correcting for multiple comparisons, multiple regions on AV-1451 tau PET remained significant for 1- to 4.5-Hz NREM SWA including the entorhinal, parahippocampal, orbital frontal, precuneus, inferior parietal, and inferior temporal regions (all $P < 0.05$; see Fig. 3 and table S3). This relationship was driven by 1- to 2-Hz NREM SWA, with only the lingual and medial orbital frontal regions on AV-1451 tau PET significantly associated with 2- to 3-Hz and 3- to 4-Hz NREM SWA (all $P < 0.05$). The significance map for 1- to 2-Hz NREM SWA (Fig. 3) shows a similar spatial pattern of tauopathy seen for other changes in AD, such as cortical thickness (44, 50–52).

Decreased 1- to 2-Hz NREM SWA with increased A β deposition

Using the same model as for AV-1451 tau PET, we assessed the relationship between NREM SWA and AV-45 amyloid PET. The mean cortical AV-45 amyloid composite was calculated as the average SUVR for the frontal, temporal, and parietal lobes. All-night 1- to 4.5-Hz SWA was not associated with AV-45 amyloid PET (Table 3). Then, we tested NREM SWA in frequency ranges of 1 to 2 Hz, 2 to 3 Hz, and 3 to 4 Hz. There was an inverse relationship between 1- to 2-Hz NREM SWA and the mean cortical AV-45 amyloid composite ($P = 0.043$; Table 3).

Uncorrected for multiple comparisons, decreased NREM SWA at 1 to 4.5 Hz and 1 to 2 Hz was associated with increased A β deposition in frontal, temporal, and inferior parietal regions, as well as the supramarginal and isthmus cingulate regions (table S4 and fig. S2). At 2 to 3 Hz and 3 to 4 Hz, however, this inverse association with A β deposition was seen in fewer regions including the inferior parietal, isthmus cingulate, transtemporal, supramarginal, middle frontal, and pars opercularis regions (table S4 and fig. S2). After

correcting for multiple comparisons, there were no regions on AV-45 amyloid PET associated with NREM SWA (table S4).

Decreased NREM SWA linked with increased CSF tau/A β 42 ratio but not CSF A β 42

To further assess the relationship between NREM SWA and AD pathology, we analyzed 104 participants with CSF in the same model used in participants with PET imaging except CSF A β 42 and tau/A β 42 measurements were used as covariates in place of AV-45 amyloid PET and AV-1451 tau PET, respectively. NREM SWA did not correlate with A β 42 after adjusting for all covariates, whereas CDR, race, ApoE4 status, and sleep medications showed correlation with A β 42 (Table 4).

Previous work found that tau/A β 42 ratio is sensitive to early stages of AD pathology and predicts cognitive decline from normal to impaired over several years (5–7). Furthermore, poor sleep has been associated with higher tau/A β 42 ratio (53). Tau/A β 42 ratio also controls for the relationship between A β 42 and tau. In the same model used to investigate the relationship between NREM SWA and tau PET, there was a significant inverse association between NREM SWA and tau/A β 42 ($P < 0.05$; Table 5), indicating that NREM SWA decreased as the tau/A β 42 ratio increased (meaning greater AD pathology). CSF tau is a marker of neuronal injury, and CSF p-tau is a marker for neurofibrillary tangles (54); therefore, we also tested the same model with p-tau/A β 42 ratio and found a similar inverse relationship with NREM SWA as tau/A β 42 (table S5). Similar to our findings for tau PET, the relationships between NREM SWA and both tau/A β 42 and p-tau/A β 42 ratios were maximal at the lowest 1- to 2-Hz frequencies. CDR, race, ApoE4 status, and sleep medications were also significantly associated with NREM SWA in the model (all $P < 0.05$; Table 5).

Specific sleep parameters associated with AD pathology

Previous studies have shown a relationship between various sleep parameters and AD pathology (16–18, 53). To investigate the relationship between other sleep parameters in our model, we compared the relationship between sleep parameters measured by the single-channel EEG device, actigraphy, and sleep logs to the mean AV-45 amyloid and AV-1451 tau composites using the same linear mixed model as above (table S6). Sleep parameters tested in the models included TST, sleep efficiency, sleep latency, REM onset latency, WASO, time in each sleep stage, number of arousals, and time spent napping per day (table S6). No sleep parameters measured by sleep log or actigraphy were associated with AV-45 amyloid PET. For EEG-derived sleep parameters, REM latency ($F_{1,30} = 12.5$, $P = 0.001$) and sleep latency ($F_{1,29} = 4.4$, $P = 0.045$) had significant negative relationships with A β , suggesting that as A β deposition increased, the time to fall asleep and enter REM sleep decreased.

TST measured by single-channel EEG device ($F_{1,28} = 5.99$, $P = 0.021$) and sleep log ($F_{1,29} = 4.80$, $P = 0.037$) was positively associated with increased tauopathy in tau PET. That is, participants slept

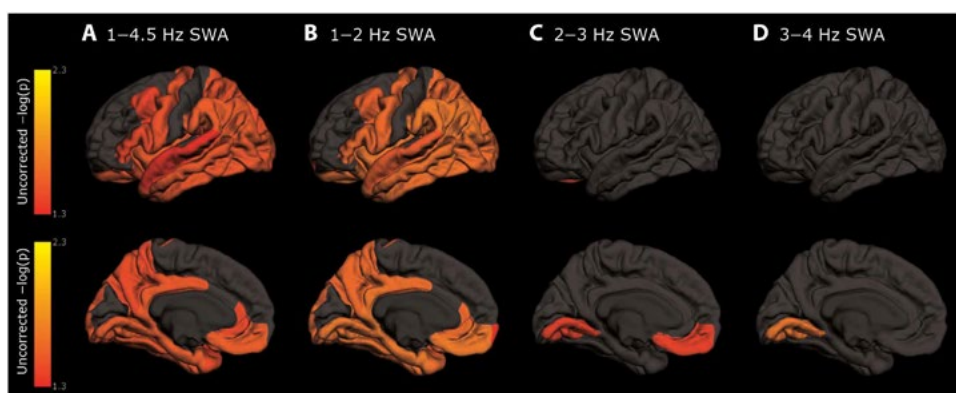


Fig. 3. Regional differences in the relationship between NREM SWA and tau PET. Regional differences in NREM SWA at 1 to 4.5 Hz (A), 1 to 2 Hz (B), 2 to 3 Hz (C), and 3 to 4 Hz (D) on AV-1451 tau PET after correction for multiple comparisons for the 38 participants with PET imaging. Linear mixed models were performed with NREM SWA as dependent variable and covariates age, sex, race, CDR, ApoE4 status, AHI, PLMI, sleep medications, and time. Each AV-1451 tau PET region was included in the model individually and was corrected for multiple comparisons. The P value in the model from each region was mapped on a brain image and transformed to a logarithmic scale ($P < 0.05 = >1.30$).

Table 3. Relationship of NREM SWA to AV-45 amyloid PET composite after adjusting for age, sex, race, CDR, ApoE4 status, AHI, PLMI, sleep medications, and time. Linear mixed models were used to calculate the estimates and *P* values for the 38 participants with PET imaging.

| Dependent variable | Covariate | Estimate | SE | F statistic (df) | P |
|--------------------|---------------------------------------|----------|--------|------------------|-------|
| 1–4.5 Hz SWA | Mean cortical AV-45 amyloid composite | -4.926 | 2.422 | 4.14 (1,28) | 0.052 |
| | Age | -0.680 | 0.270 | 6.36 (1,28) | 0.018 |
| | Sex | -8.590 | 2.948 | 8.49 (1,28) | 0.007 |
| | CDR | -3.489 | 3.463 | 1.02 (1,29) | 0.322 |
| | Race | -10.003 | 5.567 | 3.23 (1,27) | 0.083 |
| | ApoE4 status | +2.946 | 3.327 | 0.78 (1,27) | 0.384 |
| | Sleep medications | +3.124 | 4.963 | 0.40 (1,27) | 0.534 |
| | AHI | +0.123 | 0.183 | 0.45 (1,28) | 0.507 |
| | PLMI | +0.084 | 0.062 | 1.83 (1,28) | 0.187 |
| | Time | -0.003 | 0.142 | 0.00 (1,145) | 0.982 |
| 1–2 Hz SWA | Mean cortical AV-45 amyloid composite | -12.017 | 5.676 | 4.48 (1,28) | 0.043 |
| | Age | -1.563 | 0.632 | 6.12 (1,28) | 0.020 |
| | Sex | -20.401 | 6.914 | 8.71 (1,28) | 0.006 |
| | CDR | -10.138 | 8.139 | 1.55 (1,29) | 0.223 |
| | Race | -23.326 | 13.041 | 3.20 (1,27) | 0.085 |
| | ApoE4 status | +6.427 | 7.786 | 0.68 (1,27) | 0.416 |
| | Sleep medications | -8.086 | 11.625 | 0.48 (1,27) | 0.493 |
| | AHI | +0.299 | 0.431 | 0.48 (1,28) | 0.493 |
| | PLMI | +0.184 | 0.146 | 1.59 (1,28) | 0.218 |
| | Time | +0.003 | 0.355 | 0.00 (1,146) | 0.994 |
| 2–3 Hz SWA | Mean cortical AV-45 amyloid composite | -3.239 | 1.814 | 3.19 (1,28) | 0.085 |
| | Age | -0.514 | 0.202 | 6.48 (1,28) | 0.017 |
| | Sex | -6.066 | 2.205 | 7.57 (1,28) | 0.010 |
| | CDR | -1.472 | 2.568 | 0.33 (1,28) | 0.571 |
| | Race | -6.936 | 4.167 | 2.77 (1,28) | 0.107 |
| | ApoE4 status | +2.196 | 2.498 | 0.77 (1,28) | 0.387 |
| | Sleep medications | +1.613 | 3.716 | 0.19 (1,28) | 0.668 |
| | AHI | 0.073 | 0.137 | 0.29 (1,28) | 0.598 |
| | PLMI | +0.067 | 0.046 | 2.09 (1,28) | 0.159 |
| | Time | -0.014 | 0.095 | 0.02 (1,29) | 0.886 |
| 3–4 Hz SWA | Mean cortical AV-45 amyloid composite | -1.350 | 0.682 | 3.91 (1,28) | 0.058 |
| | Age | -0.183 | 0.076 | 5.80 (1,28) | 0.023 |
| | Sex | -2.229 | 0.830 | 7.21 (1,28) | 0.012 |
| | CDR | -0.339 | 0.963 | 0.12 (1,27) | 0.727 |
| | Race | -2.645 | 1.565 | 2.86 (1,27) | 0.102 |
| | ApoE4 status | +0.682 | 0.939 | 0.53 (1,28) | 0.474 |
| | Sleep medications | +0.425 | 1.396 | 0.09 (1,27) | 0.763 |
| | AHI | +0.024 | 0.051 | 0.21 (1,28) | 0.647 |
| | PLMI | +0.024 | 0.017 | 1.94 (1,28) | 0.175 |
| | Time | -0.003 | 0.038 | 0.01 (1,27) | 0.928 |

Table 4. Relationship of NREM SWA to A β 42 after adjusting for age, sex, race, CDR, ApoE4 status, AHI, PLMI, sleep medications, and time. Linear mixed models were used to calculate the estimates and *P* values for the 104 participants with CSF.

| Dependent variable | Covariate | Estimate | SE | F statistic (df) | P |
|--------------------|-------------------|----------|--------|------------------|-------|
| 1–4.5 Hz SWA | A β 42 | +0.004 | 0.003 | 1.44 (1,10) | 0.257 |
| | Age | +0.021 | 0.188 | 0.01 (1,12) | 0.911 |
| | Sex | +0.457 | 2.687 | 0.03 (1,12) | 0.868 |
| | CDR | +8.270 | 3.304 | 6.27 (1,15) | 0.024 |
| | Race | -10.031 | 3.910 | 6.58 (1,10) | 0.029 |
| | ApoE4 status | -6.597 | 2.897 | 5.18 (1,11) | 0.044 |
| | Sleep medications | -17.910 | 6.102 | 8.62 (1,12) | 0.013 |
| | AHI | -0.007 | 0.151 | 0.00 (1,11) | 0.966 |
| | PLMI | +0.055 | 0.041 | 1.83 (1,13) | 0.199 |
| | Time | -0.174 | 0.167 | 1.08 (1,76) | 0.302 |
| 1–2 Hz SWA | A β 42 | +0.008 | 0.007 | 1.48 (1,11) | 0.248 |
| | Age | +0.077 | 0.447 | 0.03 (1,12) | 0.866 |
| | Sex | +0.900 | 6.394 | 0.02 (1,12) | 0.890 |
| | CDR | +18.082 | 7.873 | 5.28 (1,16) | 0.036 |
| | Race | -21.715 | 9.301 | 5.45 (1,11) | 0.040 |
| | ApoE4 status | -15.565 | 6.894 | 5.10 (1,12) | 0.044 |
| | Sleep medications | -44.695 | 14.524 | 9.47 (1,13) | 0.009 |
| | AHI | -0.056 | 0.360 | 0.02 (1,12) | 0.879 |
| | PLMI | +0.086 | 0.097 | 0.78 (1,14) | 0.393 |
| | Time | -0.489 | 0.401 | 1.49 (1,77) | 0.226 |
| 2–3 Hz SWA | A β 42 | +0.003 | 0.002 | 2.44 (1,9) | 0.153 |
| | Age | +0.003 | 0.128 | 0.00 (1,11) | 0.980 |
| | Sex | +0.299 | 1.846 | 0.03 (1,11) | 0.874 |
| | CDR | +7.227 | 2.203 | 10.76 (1,14) | 0.005 |
| | Race | -8.654 | 2.739 | 9.98 (1,8) | 0.013 |
| | ApoE4 status | -5.372 | 2.009 | 7.15 (1,10) | 0.024 |
| | Sleep medications | -13.941 | 4.198 | 11.03 (1,11) | 0.007 |
| | AHI | +0.016 | 0.105 | 0.02 (1,10) | 0.884 |
| | PLMI | +0.059 | 0.028 | 4.52 (1,12) | 0.054 |
| | Time | -0.085 | 0.125 | 0.47 (1,16) | 0.504 |
| 3–4 Hz SWA | A β 42 | +0.002 | 0.001 | 4.09 (1,12) | 0.066 |
| | Age | -0.023 | 0.072 | 0.10 (1,13) | 0.759 |
| | Sex | -0.216 | 1.027 | 0.04 (1,13) | 0.837 |
| | CDR | +2.623 | 1.074 | 5.97 (1,12) | 0.032 |
| | Race | -3.301 | 1.538 | 4.61 (1,12) | 0.053 |
| | ApoE4 status | -1.964 | 1.121 | 3.07 (1,13) | 0.104 |
| | Sleep medications | -6.387 | 2.267 | 7.94 (1,12) | 0.016 |
| | AHI | +0.018 | 0.058 | 0.10 (1,12) | 0.763 |
| | PLMI | +0.024 | 0.015 | 2.72 (1,13) | 0.124 |
| | Time | -0.012 | 0.052 | 0.06 (1,15) | 0.815 |

longer with increased tauopathy. Self-reported time napping on sleep logs was increased with greater tau pathology ($F_{1,27} = 9.28$, $P = 0.005$) (table S6). This suggests that participants with greater tau pathology

experienced daytime sleepiness despite increased TST. All other sleep parameters measured by EEG, actigraphy, and sleep log did not show correlation with tauopathy. Using the same model, no

Table 5. Relationship of NREM SWA to tau/A β 42 ratio after adjusting for age, sex, race, CDR, ApoE4 status, AHI, PLMI, sleep medications, and time. Linear mixed models were used to calculate the estimates and *P* values for the 104 participants with CSF.

| Dependent variable | Covariate | Estimate | SE | F statistic (df) | P |
|--------------------|-------------------|----------|--------|------------------|--------|
| 1–4.5 Hz SWA | Tau/A β 42 | -10.788 | 4.673 | 5.33 (1,12) | 0.040 |
| | Age | +0.034 | 0.170 | 0.04 (1,12) | 0.846 |
| | Sex | +0.838 | 2.350 | 0.13 (1,12) | 0.728 |
| | CDR | +7.567 | 2.880 | 6.90 (1,14) | 0.020 |
| | Race | -13.860 | 3.818 | 13.18 (1,9) | 0.006 |
| | ApoE4 status | -6.961 | 2.645 | 6.92 (1,11) | 0.024 |
| | Sleep medications | -19.697 | 5.565 | 12.53 (1,12) | 0.004 |
| | AHI | +0.056 | 0.141 | 0.16 (1,11) | 0.699 |
| | PLMI | +0.060 | 0.037 | 2.59 (1,13) | 0.132 |
| | Time | -0.154 | 0.169 | 0.83 (1,70) | 0.365 |
| 1–2 Hz SWA | Tau/A β 42 | -25.757 | 11.078 | 5.41 (1,13) | 0.038 |
| | Age | +0.106 | 0.403 | 0.07 (1,12) | 0.797 |
| | Sex | +1.571 | 5.571 | 0.08 (1,12) | 0.783 |
| | CDR | +16.425 | 6.807 | 5.82 (1,14) | 0.030 |
| | Race | -31.133 | 9.074 | 11.77 (1,10) | 0.007 |
| | ApoE4 status | -16.216 | 6.278 | 6.67 (1,12) | 0.025 |
| | Sleep medications | -49.386 | 13.196 | 14.01 (1,13) | 0.003 |
| | AHI | +0.103 | 0.333 | 0.10 (1,12) | 0.762 |
| | PLMI | +0.100 | 0.0875 | 1.31 (1,13) | 0.272 |
| | Time | -0.435 | 0.406 | 1.15 (1,74) | 0.288 |
| 2–3 Hz SWA | Tau/A β 42 | -11.594 | 3.251 | 12.72 (1,11) | 0.004 |
| | Age | +0.008 | 0.122 | 0.00 (1,12) | 0.952 |
| | Sex | +0.343 | 1.680 | 0.04 (1,12) | 0.842 |
| | CDR | +6.431 | 1.765 | 13.27 (1,8) | 0.006 |
| | Race | -12.567 | 2.739 | 21.06 (1,9) | 0.001 |
| | ApoE4 status | -5.995 | 1.889 | 10.07 (1,11) | 0.009 |
| | Sleep medications | -19.944 | 3.810 | 27.40 (1,10) | 0.0004 |
| | AHI | +0.069 | 0.097 | 0.50 (1,10) | 0.496 |
| | PLMI | +0.058 | 0.025 | 5.28 (1,11) | 0.042 |
| | Time | -0.082 | 0.129 | 0.41 (1,17) | 0.533 |
| 3–4 Hz SWA | Tau/A β 42 | -5.549 | 1.687 | 10.82 (1,10) | 0.008 |
| | Age | -0.019 | 0.064 | 0.09 (1,11) | 0.773 |
| | Sex | -0.001 | 0.878 | 0.00 (1,11) | 0.999 |
| | CDR | +2.223 | 0.911 | 5.95 (1,10) | 0.036 |
| | Race | -5.076 | 1.403 | 13.08 (1,8) | 0.006 |
| | ApoE4 status | -2.104 | 0.978 | 4.63 (1,10) | 0.057 |
| | Sleep medications | -6.784 | 1.965 | 11.92 (1,9) | 0.007 |
| | AHI | +0.040 | 0.050 | 0.64 (1,10) | 0.444 |
| | PLMI | +0.029 | 0.013 | 4.78 (1,10) | 0.053 |
| | Time | -0.019 | 0.053 | 0.13 (1,15) | 0.719 |

sleep parameters measured by EEG, actigraphy, or sleep log were associated with CSF tau/A β 42 (table S7).

DISCUSSION

Our study showed that NREM SWA has an inverse relationship with AD pathology measured by PET imaging and CSF biomarkers. That is, NREM SWA decreased with increased evidence of A β deposition and tau accumulation. For PET, this relationship was stronger with tau than with A β pathology. We also showed that increased CSF tau/A β 42 ratio, another marker of AD pathology, was inversely associated with NREM SWA. We observed these associations after adjustment for multiple potential confounders, particularly age, sex, and CDR, supporting a strong relationship independent of these factors. Although AV-45 amyloid PET showed a similar inverse relationship with NREM SWA as AV-1451 tau PET, the estimated magnitude of this association was greater for tau and the findings with CSF tau/A β 42 suggest that tau is critical for this relationship. Because the study participants were predominantly cognitively normal with the remaining showing only very mild impairment, this suggests that decreased NREM SWA, especially at the lowest 1- to 2-Hz frequencies, might be associated with tau pathology either before or at the earliest stages of cognitive decline.

Regional analyses of the PET images found that decreases in NREM SWA were most pronounced with A β deposition in areas of the frontal, temporal, and parietal lobes. There was no association in our models between NREM SWA and CSF A β 42. Previous findings associated decreased NREM SWA, particularly at the lowest 0.6- to 1-Hz frequencies, with A β deposition in the mPFC on PiB-PET imaging (38). Because we recorded a single-channel EEG from the forehead, we were unable to localize the NREM SWA more specifically than to the frontal lobes. This location of electrode placement likely contributes to the robust relationship between NREM SWA and tau pathology in the frontal regions. We were also unable to test frequencies in the 0.6- to 1-Hz range due to hardware limitation of the single-channel EEG device (55, 56). Another recent study reported associations between baseline excessive daytime sleepiness and longitudinal A β deposition in the anterior cingulate, posterior cingulate-precuneus, and parietal regions (17). After correcting for multiple comparisons, our study found no association between 1- to 2-Hz SWA and A β deposition in all brain regions analyzed.

For AV-1451 tau PET, regions known to be involved with AD progression showed associations with decreased NREM SWA including the orbitofrontal, entorhinal, parahippocampal, lingual, and inferior parietal regions. These relationships were most evident in the 1- to 2-Hz range, and the association remained valid after correcting for multiple comparisons. This spatial pattern is similar to other imaging changes in AD, such as cortical thickness (50–52). Decreased cortical thickness, however, does not explain our findings because the PET ROIs were volume-corrected.

We were also able to compare the relationship between PET imaging with AV-45 amyloid and AV-1451 tau tracers, as well as CSF A β 42 and tau/A β 42, to sleep parameters measured with different methods such as sleep logs. Although NREM SWA was associated with AD pathology, traditional sleep parameters measured by single-channel EEG-based sleep scoring, actigraphy, or sleep logs generally did not show association in our study. SWA is a measure of sleep homeostasis and may be altered even when other sleep parameters are unchanged (57). Increased TST measured by the single-channel

EEG and sleep log were associated with increasing tau pathology on PET, as was self-reported increased time napping. These results, coupled with the NREM SWA findings, suggest that the quality of sleep decreases with increasing tau despite increased sleep time. Furthermore, self-reported napping time per day may be an important question to screen individuals for tauopathy.

A strength of our study is the multiple modalities of both sleep monitoring and biomarkers for AD pathology available from all of our participants. In addition to PET imaging, CSF biomarkers, and different sleep measures, we were able to adjust for multiple variables that affect sleep and AD pathology. Model covariates, such as sex, race, ApoE4, and sleep medications, need further study in other larger cohorts and longitudinal studies. A weakness of this study, however, is that we cannot establish whether or not sleep disturbances preceded or followed the development of AD pathology. Furthermore, this study included only 38 participants in the imaging analyses, and therefore, a limitation of these analyses is overfitting a model with 10 covariates. Another limitation of our study is that stages of AD pathology (for example, amyloid negative/tau negative) differed between participants with PET imaging and CSF. These limitations are offset by the complementary findings between NREM SWA and AD pathology with both PET imaging and CSF biomarkers. Previous work that reported these associations between sleep parameters and AD pathology generally included larger numbers of participants than our study. However, the fact that we could see robust differences in NREM SWA in relation to tau pathology measured on tau PET and CSF tau/A β 42 suggests strong relationships between the variables analyzed.

With the rising incidence of AD in an aging population, our findings have potential application in both clinical trials and patient screening for AD to noninvasively monitor for progression of AD pathology. For instance, periodically measuring NREM SWA, in conjunction with other biomarkers, may have utility monitoring AD risk or response to an AD treatment. To apply our findings in these settings, further longitudinal studies are needed to confirm the timing of when NREM SWA decreases in relation to increased A β deposition and tauopathy.

MATERIALS AND METHODS

Study design

This is an ongoing longitudinal observational study to assess the association between sleep parameters and the AD biomarkers in which sleep-wake activity was observed over six nights. All sleep data collected by 3 April 2018 were included in the analysis. One hundred nineteen participants enrolled in longitudinal studies at the Knight Alzheimer's Disease Research Center at Washington University in St. Louis, MO, were recruited thus far to participate in this study. All participants were >60 years old and assessed clinically with a standard protocol that included obtaining a CDR, which ranged from 0 (no impairment) to 3 (maximal impairment) (40, 41). Participants who completed all assessments were included in the analysis. Of the 38 participants who completed PET imaging, 29 participants (76.3%) had a score of 0 and 9 participants (23.7%) had a score of 0.5. These percentages were similar to 104 participants who underwent lumbar puncture for CSF collection with 79.8% CDR 0 and 20.2% CDR 0.5. ApoE genotype was obtained from the Knight Alzheimer's Disease Research Center Genetics Core. Participants also reported if they were taking any of the following

medications that could affect sleep: benzodiazepine receptor agonists (zolpidem, zaleplon, eszopiclone), benzodiazepines (triazolam, temazepam, alprazolam), ramelteon, gabapentin, dopamine agonists (ropinirole, pramipexole, rotigotine), doxepin, antihistamines, anti-depressants, and narcotics. Participants were listed as on a sleep medication if they were taking at least one medication from this list. Participant demographic information is shown in Table 1. The study protocol was approved by the Washington University Institutional Review Board. All participants provided written informed consent and were compensated for their participation in the study.

Sleep monitoring

Sleep was assessed longitudinally in all participants using three separate measures over six nights at home: (i) sleep logs, (ii) actigraphy (Actiwatch 2, Philips Respironics), and (iii) a single-channel EEG device worn on the forehead (Sleep Profiler, Advanced Brain Monitoring). Sleep logs and actigraphy were scored as previously reported (18). Single-channel EEG sleep studies were visually scored by registered polysomnographic technologists using criteria adapted from the standard American Academy of Sleep Medicine (AASM) criteria (56). Sleep parameters for time in each sleep stage, sleep latency, sleep efficiency, WASO, and TST were calculated. Nights were excluded if >10% of the recording was artifactual or if the bed and rise times did not match the sleep log and/or actigraphy. All participants needed at least two nights from the single-channel EEG device that met these criteria to be included in this analysis.

Because of the increased prevalence of sleep apnea and periodic leg movements during sleep with age, all participants were monitored for one night with a home sleep test (Alice PDx, Philips Respironics). Bed and rise times were confirmed with sleep logs and actigraphy. A minimum of 4 hours artifact-free recording was obtained for all participants. Respiratory events and periodic leg movements were scored by registered polysomnographic technologists using AASM criteria; hypopneas were scored using 4% oxygen desaturation (58). AHI and PLMI were calculated per hour of monitoring time for each participant.

Spectral power analysis

SWA during NREM sleep was calculated from each single-channel EEG study using Matlab (MathWorks, Natick, MA), as previously described (56, 59, 60). To briefly summarize, the EEG signal was down-sampled to 128 Hz for analysis to eliminate processing error. The single-channel EEG device filtered the signal during acquisition with a 0.1– to 0.6-band-stop filter. We then applied a band-pass (two-way least-squares finite impulse response) filter between 0.5 and 40 Hz. Spectral analysis was performed in consecutive 6-s epochs (Welch method, Hamming window, no overlap). Artifacts were excluded in a semiautomatic method. Power in the 20- to 30-Hz and 1- to 4.5-Hz bands for each electrode across all epochs of a recording was displayed. The operator (B.P.L.) then selected a threshold between the 95th and 99.5% threshold of power to remove artifactual epochs. This resulted in fewer than 4% of all epochs being rejected as artifactual.

Magnetic resonance imaging

T1-weighted images were acquired using a magnetization-prepared rapid gradient-echo sequence on a Siemens Biograph mMR or Tim Trio 3T scanner. Scans had a resolution of either 1 × 1 × 1 mm or 1 × 1 × 1.25 mm. Parcellations of the T1-weighted image into cortical

and subcortical regions were performed with FreeSurfer v5.3-HCP (61) for use in the processing of PET data.

PET imaging

Thirty-eight participants underwent PET imaging with both amyloid and tau tracers. Amyloid PET imaging was performed using [¹⁸F]AV-45 (florbetapir). Data from the 50 to 70 post-injection window were analyzed with an in-house pipeline using FreeSurfer-derived ROIs (PET Unified Pipeline, <https://github.com/ysu001/PUP>) (43, 61). Tau PET imaging was completed using [¹⁸F]AV-1451 (flortaucipir). Data from the 80- to 100-min post-injection window were analyzed. Unprocessed tau PET images were reviewed by a nuclear medicine-trained physician to evaluate for off-target tracer binding; before analysis, one potential participant with sleep monitoring and a tau PET scan was excluded because of high bone marrow uptake in the frontal cortex. Regional signal estimates for both tracers were transformed into SUVRs by using cerebellar cortex as the reference region. Data were partial volume-corrected using a regional spread function technique (62, 63). ROI PET data were presented as the average across hemispheres for statistical analysis. For global analyses, summary measures of SUVR 1.19 were used for amyloid negative/positive on AV-45 amyloid PET (42, 43), and summary measures of SUVR 1.22 were used for tau negative/positive on AV-1451 tau PET (44).

CSF biomarkers

CSF was collected under a standardized protocol (45). After fasting overnight, participants underwent a lumbar puncture at 8 a.m. CSF (20 to 30 ml) was collected by gravity drip into a 50-ml conical tube using a 22-gauge atraumatic Sprotte spinal needle, gently inverted to disrupt potential gradient effects, and centrifuged at low speed to pellet any cellular debris. Samples were aliquoted (500 µl) in polypropylene tubes and stored at -80°C until analysis. CSF Aβ42, total tau, and p-tau 181 were measured as previously described using an automated electrochemiluminescence immunoassay (Elecys on the cobas e 601 analyzer, Roche) (45, 64).

Statistical analysis

All data were entered into a secure, web-based application designed to support data capture for research studies [Research Electronic Data Capture (REDCap)] (65). Statistical significance for all analyses was set at $P < 0.05$. No methods were used to predetermine sample sizes. All serial sleep monitoring nights were analyzed with general linear mixed models using an unstructured covariance structure to account for the dependencies among the longitudinal measurements (66). For analyses of the participants who completed PET imaging, AV-45 amyloid and AV-1451 tau PET SUVR, mean-centered age (mean age 74.8 years), sex, race, CDR, ApoE4 status (negative/positive), mean-centered AHI (mean AHI 9.8 respiratory events per hour of monitoring time), mean-centered PLMI (mean PLMI 23.2 leg movements per hour of monitoring time), and sleep medication (yes/no) were treated as fixed effects. Analyses of participants with CSF were the same as those with imaging biomarkers, and there were no differences in mean-centered age (mean age 74.5 years), mean-centered AHI (mean AHI 9.8 respiratory events per hour of monitoring time), and mean-centered PLMI (mean PLMI 23 leg movements per hour of monitoring time). The time covariate was longitudinal sleep monitoring over multiple nights and was treated as a random effect with random intercepts and slopes used to accommodate

individual variation. The normality assumption was verified through residual plots. Statistical analyses for mixed models were performed using Statistical Analysis Software (SAS). Regional analysis of AV-45 amyloid and AV-1451 tau PET was performed using R 3.3.2 (67) with the same model except for individual ROI rather than whole-brain composite indices. Bonferroni correction was used when comparing between multiple brain regions. Differences in sleep parameters between amyloid-negative/positive and tau-negative/positive groups were determined by unpaired two-tailed *t* test.

SUPPLEMENTARY MATERIALS

www.scientifictranslationalmedicine.org/cgi/content/full/11/474/eau6550/DC1

Fig. S1. Relationship between NREM SWA and tau PET varies by region when uncorrected for multiple comparisons.

Fig. S2. Relationship between NREM SWA and amyloid PET varies by region when uncorrected for multiple comparisons.

Table S1. Group differences in average sleep parameters between amyloid negative/positive, tau negative/positive, and CDR 0/0.5 for participants with PET imaging.

Table S2. Group differences in average sleep parameters between amyloid negative/positive, tau negative/positive, and CDR 0/0.5 for participants with CSF.

Table S3. Relationship of NREM SWA power to AV-1451 tau PET regions after adjusting for age, sex, race, CDR, ApoE4 status, AHI, PLMI, sleep medications, and time.

Table S4. Relationship of NREM SWA to AV-45 amyloid PET regions after adjusting for age, sex, race, CDR, ApoE4 status, AHI, PLMI, sleep medications, and time.

Table S5. Relationship of NREM SWA to p-tau/A β 42 ratio after adjusting for age, sex, race, CDR, ApoE4 status, AHI, PLMI, sleep medications, and time.

Table S6. Relationship of sleep parameters to AV-45 amyloid and AV-1451 tau PET after adjusting for age, sex, race, CDR, ApoE4 status, AHI, PLMI, sleep medications, and time.

Table S7. Relationship of sleep parameters to tau/A β 42 ratio after adjusting for age, sex, race, CDR, ApoE4 status, AHI, PLMI, sleep medications, and time.

REFERENCES AND NOTES

- R. J. Bateman, C. Xiong, T. L. Benzinger, A. M. Fagan, A. Goate, N. C. Fox, D. S. Marcus, N. J. Cairns, X. Xie, T. M. Blazey, D. M. Holtzman, A. Santacruz, V. Buckles, A. Oliver, K. Moulder, P. S. Aisen, B. Ghetti, W. E. Klunk, E. McDade, R. N. Martins, C. L. Masters, R. Mayeux, J. M. Ringman, M. N. Rossor, P. R. Schofield, R. A. Sperling, S. Salloway, J. C. Morris, Dominantly Inherited Alzheimer Network, Clinical and biomarker changes in dominantly inherited Alzheimer's disease. *N. Engl. J. Med.* **367**, 795–804 (2012).
- C. R. Jack, D. S. Knopman, W. J. Jagust, L. M. Shaw, P. S. Aisen, M. W. Weiner, R. C. Petersen, J. Q. Trojanowski, Hypothetical model of dynamic biomarkers of the Alzheimer's pathological cascade. *Lancet Neurol.* **9**, 119–128 (2010).
- J. C. Morris, J. L. Price, Pathologic correlates of nondemented aging, mild cognitive impairment, and early-stage Alzheimer's disease. *J. Molec. Neurosci.* **17**, 101–118 (2001).
- A. M. Fagan, M. A. Mintun, R. H. Mach, S.-Y. Lee, C. S. Dence, A. R. Shah, G. N. LaRossa, M. L. Spinner, W. E. Klunk, C. A. Mathis, S. T. DeKosky, J. C. Morris, D. M. Holtzman, Inverse relation between *in vivo* amyloid imaging load and cerebrospinal fluid A β 42 in humans. *Ann. Neurol.* **59**, 512–519 (2006).
- A. M. Fagan, C. M. Roe, C. Xiong, M. A. Mintun, J. C. Morris, D. M. Holtzman, Cerebrospinal fluid tau/ β -amyloid(42) ratio as a prediction of cognitive decline in nondemented older adults. *Arch. Neurol.* **64**, 343–349 (2007).
- G. Li, I. Sokal, J. F. Quinn, J. B. Leverenz, M. Brodey, G. Schellenberg, J. Kaye, M. Raskind, J. Zhang, E. R. Peskind, T. J. Montine, CSF tau/A β 42 ratio for increased risk of mild cognitive impairment: A follow-up study. *Neurology* **69**, 631–639 (2007).
- O. Hansson, H. Zetterberg, P. Buchhave, E. Londos, K. Blennow, L. Minthon, Association between CSF biomarkers and incipient Alzheimer's disease in patients with mild cognitive impairment: A follow-up study. *Lancet Neurol.* **5**, 228–234 (2006).
- J. L. Price, J. C. Morris, Tangles and plaques in nondemented aging and "preclinical" Alzheimer's disease. *Ann. Neurol.* **45**, 358–368 (1999).
- R. A. Sperling, P. S. Aisen, L. A. Beckett, D. A. Bennett, S. Craft, A. M. Fagan, T. Iwatsubo, C. R. Jack Jr., J. Kaye, T. J. Montine, D. C. Park, E. M. Reiman, C. C. Rowe, E. Siemers, Y. Stern, K. Yaffe, M. C. Carrillo, B. Thies, M. Morrison-Bogorad, M. V. Wagster, C. H. Phelps, Toward defining the preclinical stages of Alzheimer's disease: Recommendations from the National Institute on Aging-Alzheimer's Association workgroups on diagnostic guidelines for Alzheimer's disease. *Alzheimers Dement.* **7**, 280–292 (2011).
- Y.-E. Ju, B. P. Lucey, D. M. Holtzman, Sleep and Alzheimer disease pathology—A bidirectional relationship. *Nat. Rev. Neurol.* **10**, 115–119 (2014).
- B. P. Lucey, R. J. Bateman, Amyloid- β diurnal pattern: Possible role of sleep in Alzheimer's disease pathogenesis. *Neurobiol. Aging* **35**, S29–S34 (2014).
- E. S. Musiek, D. M. Holtzman, Mechanisms linking circadian clocks, sleep, and neurodegeneration. *Science* **354**, 1004–1008 (2016).
- D. A. Weldemichael, G. T. Grossberg, Circadian rhythm disturbances in patients with Alzheimer's disease. *Int. J. Alzheimers Dis.* **2010**, 716453 (2010).
- S. M. McCurry, R. G. Logsdon, L. Teri, L. E. Gibbons, W. A. Kukull, J. D. Bowen, W. C. McCormick, E. B. Larson, Characteristics of sleep disturbance in community-dwelling Alzheimer's disease patients. *J. Geriatr. Psychiatry Neurol.* **12**, 53–59 (2016).
- S. P. Tworoger, S. Lee, E. S. Schernhammer, F. Grodstein, The association of self-reported sleep duration, difficulty sleeping, and snoring with cognitive function in older women. *Alzheimer Dis. Assoc. Disord.* **20**, 41–48 (2006).
- A. P. Spira, A. A. Gamaldo, Y. An, M. N. Wu, E. M. Simonsick, M. Bilgel, Y. Zhou, D. F. Wong, L. Ferrucci, S. M. Resnick, Self-reported sleep and β -amyloid deposition in community-dwelling older adults. *JAMA Neurol.* **70**, 1537–1543 (2013).
- D. Z. Carvalho, E. K. St Louis, D. S. Knopman, B. F. Boeve, V. J. Lowe, R. O. Roberts, M. Mielke, S. A. Przybelski, M. M. Machulda, R. C. Petersen, C. R. Jack, P. Vemuri, Association of excessive daytime sleepiness with longitudinal β -amyloid accumulation in elderly persons without dementia. *JAMA Neurol.* **75**, 672–680 (2018).
- Y.-E. Ju, J. S. McLeland, C. D. Toedebusch, C. Xiong, A. M. Fagan, S. Duntley, J. C. Morris, D. M. Holtzman, Sleep quality and preclinical Alzheimer disease. *JAMA Neurol.* **70**, 587–593 (2013).
- K. Yaffe, A. M. Laffan, S. L. Harrison, S. Redline, A. P. Spira, K. E. Ensrud, S. Ancoli-Israel, K. L. Stone, Sleep-disordered breathing, hypoxia, and risk of mild cognitive impairment and dementia in older women. *JAMA* **306**, 613–619 (2011).
- S. Ancoli-Israel, B. W. Palmer, J. R. Cooke, J. Corey-Bloom, L. Fiorentino, L. Natarajan, L. Liu, L. Ayalon, F. He, J. S. Loredo, Cognitive effects of treating obstructive sleep apnea in Alzheimer's disease: A randomized controlled study. *J. Am. Geriatr. Soc.* **56**, 2076–2081 (2008).
- J. R. Cooke, L. Ayalon, B. W. Palmer, J. S. Loredo, J. Corey-Bloom, L. Natarajan, L. Liu, S. Ancoli-Israel, Sustained use of CPAP slows deterioration of cognition, sleep, and mood in patients with Alzheimer's disease and obstructive sleep apnea: A preliminary study. *J. Clin. Sleep Med.* **5**, 305–309 (2009).
- Y. Leng, T. Blackwell, K. L. Stone, T. D. Hoang, S. Redline, K. Yaffe, Periodic limb movements in sleep are associated with greater cognitive decline in older men without dementia. *Sleep* **39**, 1807–1810 (2016).
- J.-E. Kang, M. M. Lim, R. J. Bateman, J. J. Lee, L. P. Smyth, J. R. Cirrito, N. Fujiki, S. Nishino, D. M. Holtzman, Amyloid- β dynamics are regulated by orexin and the sleep-wake cycle. *Science* **326**, 1005–1007 (2009).
- Y. Huang, R. Potter, W. Sigurdson, A. Santacruz, S. Shih, Y.-E. Ju, T. Kasten, J. C. Morris, M. Mintun, S. Duntley, R. J. Bateman, Effects of age and amyloid deposition on A β dynamics in the human central nervous system. *Arch. Neurol.* **69**, 51–58 (2012).
- B. P. Lucey, C. Gonzales, U. Das, J. Li, E. R. Siemers, J. R. Slemmon, R. J. Bateman, Y. Huang, G. B. Fox, J. A. Claassen, D. Slats, M. M. Verbeek, G. Tong, H. Soares, M. J. Savage, M. Kennedy, M. Forman, M. Sjögren, R. Margolin, X. Chen, M. R. Farlow, R. A. Dean, J. F. Waring, An integrated multi-study analysis of intra-subject variability in cerebrospinal fluid amyloid- β concentrations collected by lumbar puncture and indwelling lumbar catheter. *Alzheimers Res. Ther.* **7**, 53 (2015).
- B. P. Lucey, K. G. Mawuenyega, B. W. Patterson, D. L. Elbert, V. Ovod, T. Kasten, J. C. Morris, R. J. Bateman, Associations between β -amyloid kinetics and the β -amyloid diurnal pattern in the central nervous system. *JAMA Neurol.* **74**, 207–215 (2017).
- A. W. Bero, P. Yan, J. H. Roh, J. R. Cirrito, F. R. Stewart, M. E. Raichle, J.-M. Lee, D. M. Holtzman, Neuronal activity regulates the regional vulnerability to amyloid- β deposition. *Nat. Neurosci.* **14**, 750–756 (2011).
- J. R. Cirrito, J.-E. Kang, J. Lee, F. R. Stewart, D. K. Verges, L. M. Silverio, G. Bu, S. Mennerick, D. M. Holtzman, Endocytosis is required for synaptic activity-dependent release of amyloid- β in vivo. *Neuron* **58**, 42–51 (2008).
- J. R. Cirrito, K. A. Yamada, M. B. Finn, R. S. Sloviter, K. R. Bales, P. C. May, D. D. Schoepp, S. M. Paul, S. Mennerick, D. M. Holtzman, Synaptic activity regulates interstitial fluid amyloid- β levels in vivo. *Neuron* **48**, 913–922 (2005).
- D. K. Verges, J. L. Restivo, W. D. Goebel, D. M. Holtzman, J. R. Cirrito, Opposing synaptic regulation of amyloid- β metabolism by NMDA receptors *in vivo*. *J. Neurosci.* **31**, 11328–11337 (2011).
- F. Kamenetz, T. Tomita, H. Hsieh, G. Seabrook, D. Borcak, T. Iwatsubo, S. Sisodia, R. Malinow, APP processing and synaptic function. *Neuron* **37**, 925–937 (2003).
- Y.-E. S. Ju, S. J. Ooms, C. Sutphen, S. L. Macauley, M. A. Zangrilli, G. Jerome, A. M. Fagan, E. Mignot, J. M. Zempel, J. A. Claassen, D. M. Holtzman, Slow wave sleep disruption increases cerebrospinal fluid amyloid- β levels. *Brain* **140**, 2104–2111 (2017).
- B. P. Lucey, T. J. Hicks, J. S. McLeland, C. D. Toedebusch, J. Boyd, D. L. Elbert, B. W. Patterson, J. Baty, J. C. Morris, V. Ovod, K. G. Mawuenyega, R. J. Bateman, Effect of sleep on overnight cerebrospinal fluid amyloid- β kinetics. *Ann. Neurol.* **83**, 197–204 (2018).
- L. Xie, H. Kang, Q. Xu, M. J. Chen, Y. Liao, M. Thiagarajan, J. O'Donnell, D. J. Christensen, C. Nicholson, J. J. Illiff, T. Takano, R. Deane, M. Nedergaard, Sleep drives metabolite clearance from the adult brain. *Science* **342**, 373–377 (2013).

35. J. H. Roh, Y. Huang, A. W. Bero, T. Kasten, F. R. Stewart, R. J. Bateman, D. M. Holtzman, Disruption of the sleep-wake cycle and diurnal fluctuation of amyloid- β in mice with Alzheimer's disease pathology. *Sci. Transl. Med.* **4**, 150ra122 (2012).
36. J. K. Holth, T. E. Mahan, G. O. Robinson, A. Rocha, D. M. Holtzman, Altered sleep and EEG power in the P301S tau transgenic mouse model. *Ann. Clin. Transl. Neurol.* **4**, 180–190 (2017).
37. B. A. Mander, V. Rao, B. Lu, J. M. Saletin, J. R. Lindquist, S. Ancoli-Israel, W. Jagust, M. P. Walker, Prefrontal atrophy, disrupted NREM slow waves and impaired hippocampal-dependent memory in aging. *Nat. Neurosci.* **16**, 357–364 (2013).
38. B. A. Mander, S. M. Marks, J. W. Vogel, V. Rao, B. Lu, J. M. Saletin, S. Ancoli-Israel, W. J. Jagust, M. P. Walker, β -Amyloid disrupts human NREM slow waves and related hippocampus-dependent memory consolidation. *Nat. Neurosci.* **18**, 1051–1057 (2015).
39. B. P. Lucey, D. M. Holtzman, How amyloid, sleep, and memory connect. *Nat. Neurosci.* **18**, 933–934 (2015).
40. J. C. Morris, The clinical dementia rating (CDR): Current version and scoring rules. *Neurology* **43**, 2412–2414 (1993).
41. L. Berg, J. P. Miller, M. Storandt, J. Duchek, J. C. Morris, E. H. Rubin, W. J. Burke, L. A. Coben, Mild senile dementia of the Alzheimer type: 2. Longitudinal assessment. *Ann. Neurol.* **23**, 477–484 (1988).
42. T. L. Benzinger, M. Raichle, D. Koudelis, T. Butler, R. Hornbeck, C. Pulizos, *Knight ADRC Research Imaging (KARI) Methods and Definitions DR14 v1.1* (Washington University in St Louis, 2018).
43. Y. Su, G. M. D'Angelo, A. G. Vlassenko, G. Zhou, A. Z. Snyder, D. S. Marcus, T. M. Blazey, J. J. Christensen, S. Vora, J. C. Morris, M. A. Mintun, T. L. Benzinger, Quantitative analysis of PIB-PET with FreeSurfer ROIs. *PLOS ONE* **8**, e73377 (2013).
44. S. Mishra, B. A. Gordon, Y. Su, J. Christensen, K. Friedrichsen, K. Jackson, R. Hornbeck, D. A. Balota, N. J. Cairns, J. C. Morris, B. M. Ances, T. L. Benzinger, AV-1451 PET imaging of tau pathology in preclinical Alzheimer disease: Defining a summary measure. *Neuroimage* **161**, 171–178 (2017).
45. S. E. Schindler, J. D. Gray, B. A. Gordon, C. Xiong, R. Batrla-Utermann, M. Quan, S. Wahl, T. L. S. Benzinger, D. M. Holtzman, J. C. Morris, A. M. Fagan, Cerebrospinal fluid biomarkers measured by Elecsys assays compared to amyloid imaging. *Alzheimers Dement.* **1**–10 (2018).
46. X. Tan, I. Campbell, I. Feinberg, Internight reliability and benchmark values for computer analyses of non-rapid eye movement (NREM) and REM EEG in normal young adult and elderly subjects. *Clin. Neurophysiol.* **112**, 1540–1552 (2001).
47. H. Zheng, M. Sowers, D. J. Buysse, F. Consens, H. M. Kravitz, K. A. Matthews, J. F. Owens, E. B. Gold, M. Hall, Sources of variability in epidemiological studies of sleep using repeated nights of in-home polysomnography: SWAN sleep study. *J. Clin. Sleep Med.* **8**, 87–96 (2012).
48. N. Fukuda, H. Honma, M. Kohsaka, R. Kobayashi, S. Sakakibara, S. Kohsaka, T. Koyama, Gender difference of slow wave sleep in middle aged and elderly subjects. *Psychiatry Clin. Neurosci.* **53**, 151–153 (1999).
49. E. Van Cauter, R. Leproult, L. Plat, Age-related changes in slow wave sleep and REM sleep and relationship with growth hormone and cortisol levels in healthy men. *JAMA* **284**, 861–868 (2000).
50. K. A. Johnson, A. Schultz, R. A. Betensky, J. A. Becker, J. Sepulcre, D. Rentz, E. Mormino, J. Chhatwal, R. Amariglio, K. Papp, G. Marshall, M. Albers, S. Mauro, L. Pepin, J. Alverio, K. Judge, M. Philiostant, T. Shoup, D. Yokell, B. Dickerson, T. Gomez-Isla, B. Hyman, N. Vasdev, R. Sperling, Tau positron emission tomographic imaging in aging and early Alzheimer disease. *Ann. Neurol.* **79**, 110–119 (2016).
51. C. Xia, S. J. Makarets, C. Caso, S. McGinnis, S. N. Gomperts, J. Sepulcre, T. Gomez-Isla, B. T. Hyman, A. Schultz, N. Vasdev, K. A. Johnson, B. C. Dickerson, Association of in vivo [¹⁸F]AV-1451 tau PET imaging results with cortical atrophy and symptoms in typical and atypical Alzheimer disease. *JAMA Neurol.* **74**, 427–436 (2017).
52. M. R. Brier, B. Gordon, K. Friedrichsen, J. McCarthy, A. Stern, J. Christensen, C. Owen, P. Aldea, Y. Su, J. Hassenstab, N. J. Cairns, D. M. Holtzman, A. M. Fagan, J. C. Morris, T. L. Benzinger, B. M. Ances, Tau and A β imaging, CSF measures, and cognition in Alzheimer's disease. *Sci. Transl. Med.* **8**, 338ra366 (2016).
53. K. E. Sprecher, R. L. Kosciuk, C. M. Carlsson, H. Zetterberg, K. Blennow, O. C. Okonkwo, M. A. Sager, S. Asthana, S. C. Johnson, R. M. Benca, B. B. Bendlin, Poor sleep is associated with CSF biomarkers of amyloid pathology in cognitively normal adults. *Neurology* **89**, 445–453 (2017).
54. K. Buerger, M. Ewers, T. Pirttilä, R. Zinkowski, I. Alafuzoff, S. J. Teipel, J. DeBernardis, D. Kerkman, C. McCulloch, H. Soininen, H. Hampel, CSF phosphorylated tau protein correlates with neocortical neurofibrillary pathology in Alzheimer's disease. *Brain* **129**, 3035–3041 (2006).
55. Sleep Profiler Scoring Manual, Sleep Profiler Scoring Manual: Signal Pattern Definition and Application of Sleep Staging Rules: Advanced Brain Monitoring, 2015, available at: <https://advancedbrainmonitoring.app.box.com/s/ovzbqj70s03zogk0y4m3> (accessed 3 November 2015).
56. B. P. Lucey, J. S. McLeland, C. D. Toedebusch, J. Boyd, J. C. Morris, E. C. Landsness, K. Yamada, D. M. Holtzman, Comparison of a single-channel EEG sleep study to polysomnography. *J. Sleep Res.* **25**, 625–635 (2016).
57. E. D. Chinoy, D. J. Frey, D. N. Kaslovsky, F. G. Meyer, K. P. Wright Jr., Age-related changes in slow wave activity rise time and NREM sleep EEG with and without zolpidem in healthy young and older adults. *Sleep Med.* **15**, 1037–1045 (2014).
58. C. Iber, *The AASM Manual for Scoring of Sleep and Associated Events: Rules, Terminology and Technical Specifications: Version 2.1* (American Academy of Sleep Medicine, 2014).
59. E. C. Landsness, D. Crupi, B. K. Hulse, M. J. Peterson, R. Huber, H. Ansari, M. Coen, C. Cirelli, R. M. Benca, M. F. Ghilardi, G. Tononi, Sleep-dependent improvement in visuomotor learning: A causal role for slow waves. *Sleep* **32**, 1273–1284 (2009).
60. E. C. Landsness, M. R. Goldstein, M. J. Peterson, G. Tononi, R. M. Benca, Antidepressant effects of selective slow wave sleep deprivation in major depression: A high-density EEG investigation. *J. Psychiatr. Res.* **45**, 1019–1026 (2011).
61. B. Fischl, FreeSurfer. *Neuroimage* **62**, 774–781 (2012).
62. Y. Su, T. M. Blazey, A. Z. Snyder, M. E. Raichle, R. C. Hornbeck, P. Aldea, J. C. Morris, T. L. Benzinger, Quantitative amyloid imaging using image-derived arterial input function. *PLOS ONE* **10**, e0122920 (2015).
63. O. G. Rousset, Y. Ma, A. C. Evans, Correction for partial volume effects in PET: Principle and validation. *J. Nucl. Med.* **39**, 904–911 (1998).
64. T. Bittner, H. Zetterberg, C. E. Teunissen, R. E. Ostlund Jr., M. Militello, U. Andreasson, I. Hubæk, D. Gibson, D. C. Chu, U. Eichenlaub, P. Heiss, U. Kobold, A. Leinenbach, K. Madin, E. Manuilova, C. Rabe, K. Blennow, Technical performance of a novel, fully automated electrochemiluminescence immunoassay for the quantitation of β -amyloid (1–42) in human cerebrospinal fluid. *Alzheimers Dement.* **12**, 517–526 (2016).
65. P. A. Harris, R. Taylor, R. Thielke, J. Payne, N. Gonzalez, J. G. Conde, Research electronic data capture (REDCap)—a metadata-driven methodology and workflow process for providing translational research informatics support. *J. Biomed. Inform.* **42**, 377–381 (2009).
66. D. Hedeker, in *Encyclopedia of Statistics in Behavioral Science*, B. S. Everitt, D. C. Howell, Eds. (John Wiley & Sons Ltd., 2005), pp. 729–738.
67. R Development Core Team, *R: A Language and Environment for Statistical Computing* (R Foundation for Statistical Computing, 2013).

Acknowledgments: We are indebted to the participants for their contributions to this study. We thank C. Cruchaga and I. Gordon for their contributions to this project.

Funding: This study was supported by the following grants from the NIH: P01 AG03991, P01 AG026276, P50 AG05681, P30 NS098577, K76 AG054863, UL1 TR000448, P30 CA091842, KL2 TR000450, and R01 EB009352. The Ellison Medical Foundation, the Willman Scholar Fund, the Foundation for Barnes-Jewish Hospital, and a Physician Scientist Training Award from the American Sleep Medicine Foundation also supported this study. Precursor for [¹⁸F]AV-1451 (flortaucipir) and technology transfer for production were provided by Avid Radiopharmaceuticals, a wholly owned subsidiary of Eli Lilly. Doses of [¹⁸F]AV45 (florbetapir) and support for acquisition of the scans were provided by Avid Radiopharmaceuticals. The funding sources had no role in the study design, data collection, management, analysis, interpretation of the data, or manuscript preparation.

Author contributions: B.P.L.: conception and design, acquisition of data, analysis and interpretation of data, and drafting of manuscript; A.M.: analysis and interpretation of data and revising of manuscript; E.C.L.: analysis and interpretation of data and revising of manuscript; C.D.T.: acquisition of data and revising of manuscript; J.S.M.: acquisition of data and revising of manuscript; A.M.Z.: analysis and interpretation of data and revising of manuscript; A.M.F.: acquisition of data, analysis and interpretation of data, and revising of manuscript; L.M.: analysis and interpretation of data and revising of manuscript; CX: analysis and interpretation of data and revising of manuscript; J.C.M.: acquisition of data, analysis and interpretation of data, and revising of manuscript; T.L.S.B.: acquisition of data, analysis and interpretation of data, and revising of manuscript; D.M.H.: conception and design, acquisition of data, analysis and interpretation of data, and drafting of manuscript. **Competing interests:** B.P.L., A.M., E.C.L., C.D.T., J.S.M., A.M.Z., L.M., and C.X. declare that they have no competing interests. D.M.H. co-founded and is on the scientific advisory board of C₂N Diagnostics. D.M.H. consults for Genentech, AbbVie, Proclara, and Denali. Washington University receives research grants to the laboratory of D.M.H. from C₂N Diagnostics, AbbVie, and Denali. Neither J.C.M. nor his family owns stock or has equity interest (outside of mutual funds or other externally directed accounts) in any pharmaceutical or biotechnology company. J.C.M. is currently participating in clinical trials of antidementia drugs from Eli Lilly and Company and Biogen. He receives research support from Eli Lilly/Avid Radiopharmaceuticals and is funded by NIH grants P50AG005681, P01AG003991, P01AG026276, and UF01AG032438. T.L.S.B. is currently participating in clinical trials of antidementia drugs from Eli Lilly and Company, Biogen, Roche, and Janssen. She receives research support from Eli Lilly/Avid Radiopharmaceuticals (including support for AV-45 and AV-1451 in this work) and is

funded by NIH grants P50AG005681, P01AG003991, P01AG026276, UF01AG032438, R01AG05326, RF1AG053550, R01AG054567-01A1, and R01AG052550-01A1. A.M.F. has received research funding from Biogen, Fujirebio, and Roche Diagnostics. She is a member of the scientific advisory boards for Roche, Genentech, and AbbVie and also consults for Araclon/Grifols and DiamirR. **Data and materials availability:** All data associated with this study are present in the paper or in the Supplementary Materials. These data are available by request from the Knight Alzheimer's Disease Research Center at Washington University in St. Louis. [¹⁸F]AV-1451 (flortaucipir) was produced under a material transfer agreement between Washington University and Avid Radiopharmaceuticals.

Submitted 6 July 2018
Resubmitted 24 October 2018
Accepted 12 December 2018
Published 9 January 2019
10.1126/scitranslmed.aau6550

Citation: B. P. Lucey, A. McCullough, E. C. Landsness, C. D. Toedebusch, J. S. McLeland, A. M. Zaza, A. M. Fagan, L. McCue, C. Xiong, J. C. Morris, T. L. S. Benzinger, D. M. Holtzman, Reduced non-rapid eye movement sleep is associated with tau pathology in early Alzheimer's disease. *Sci. Transl. Med.* **11**, eaau6550 (2019).



Science Webinars help you keep pace with emerging scientific fields!

Stay informed about scientific breakthroughs and discoveries.

Gain insights into current research from top scientists.

Take the opportunity to ask questions during live broadcasts.



Get alerts about upcoming free webinars.

Sign up at: webinar.sciencemag.org/stayinformed

NEURODEGENERATIVE DISEASE

A farnesyltransferase inhibitor activates lysosomes and reduces tau pathology in mice with tauopathy

Israel Hernandez^{1*}, Gabriel Luna^{1*}, Jennifer N. Rauch¹, Surya A. Reis², Michel Giroux¹, Celeste M. Karch³, Daniel Bocitor¹, Youssef E. Sibih¹, Nadia J. Storm⁴, Antonio Diaz⁴, Susmita Kaushik⁴, Cezary Zekanowski⁵, Alexander A. Kang¹, Cassidy R. Hinman¹, Vesna Cerovac¹, Elmer Guzman¹, Honjun Zhou¹, Stephen J. Haggarty², Alison M. Goate⁶, Steven K. Fisher^{1,7}, Ana M. Cuervo⁴, Kenneth S. Kosik^{1,7†}

Tau inclusions are a shared feature of many neurodegenerative diseases, among them frontotemporal dementia caused by tau mutations. Treatment approaches for these conditions include targeting posttranslational modifications of tau proteins, maintaining a steady-state amount of tau, and preventing its tendency to aggregate. We discovered a new regulatory pathway for tau degradation that operates through the farnesylated protein, Rhes, a GTPase in the Ras family. Here, we show that treatment with the farnesyltransferase inhibitor lonafarnib reduced Rhes and decreased brain atrophy, tau inclusions, tau sumoylation, and tau ubiquitination in the rTg4510 mouse model of tauopathy. In addition, lonafarnib treatment attenuated behavioral abnormalities in rTg4510 mice and reduced microgliosis in mouse brain. Direct reduction of Rhes in the rTg4510 mouse by siRNA reproduced the results observed with lonafarnib treatment. The mechanism of lonafarnib action mediated by Rhes to reduce tau pathology was shown to operate through activation of lysosomes. We finally showed in mouse brain and in human induced pluripotent stem cell-derived neurons a normal developmental increase in Rhes that was initially suppressed by tau mutations. The known safety of lonafarnib revealed in human clinical trials for cancer suggests that this drug could be repurposed for treating tauopathies.

INTRODUCTION

The tauopathies constitute a broad range of neurodegenerative diseases, all of which share the hallmark feature of tau inclusions. Although tau-related diseases including Alzheimer's disease and chronic traumatic encephalopathy are serious public health problems (1), no disease-modifying treatment currently exists for these conditions. Generally, approaches to treatment have directly targeted the tau protein and include tau antibodies (2), antisense oligonucleotides (3), caspase cleavage products (4), and anti-aggregation agents (5). However, few pharmacologic interventions directed toward tau pathways have reached clinical trials. Interventions in upstream pathways such as inhibitors of tau phosphorylation (6) or acetylation (7) have shown some efficacy in animal models, but none of these approaches has had success in human clinical trials to date. Rapidly growing interest in autophagy as a downstream pathway that mediates tau clearance (8–10) as well as the implication of autophagy and lysosomes in other neurodegenerative conditions (11–13) suggest therapeutic opportunities. In Huntington's disease (HD), a pathway linked to autophagy is mediated by the *RASD2* gene, which encodes the Rhes protein, a small guanosine triphosphatase (GTPase) member of the

Ras superfamily (14). *RASD2* became of interest in HD because it was thought to be expressed mainly in the striatum (15). However, in humans, Rhes expression is clearly evident in the cerebral cortex (16). Rhes activates autophagy independently of mammalian target of rapamycin (mTOR) via interaction with beclin 1 (17). Furthermore, Rhes has been shown to modulate the aggregation state of mutant Huntingtin (mHtt), the protein mutated in HD, by promoting its sumoylation and reducing cell survival (18). This toxicity involves binding of Rhes to mHtt and requires the Rhes CXXX farnesylated membrane attachment site (18). We inferred that the induction of autophagy is a pharmacological class effect of farnesyltransferase inhibition (19) and could be relevant for tauopathies. Therefore, we studied farnesyltransferase as a therapeutic target for the treatment of tauopathies. We used the farnesyltransferase inhibitor lonafarnib, a drug for which there is extensive clinical experience (20–22), and tested it in the rTg4510 mouse model of tauopathy.

RESULTS

Farnesylation inhibition attenuates tau pathology in the rTg4510 mouse model of tauopathy

Lonafarnib is a potent farnesyltransferase inhibitor with a K_i (inhibition constant) in the nanomolar range (23), which crosses the blood-brain barrier and has only a few minor side effects in humans (21). We sought to determine the effects of lonafarnib administration in the rTg4510 mouse, a widely used model of frontotemporal dementia (24). These mice develop tau tangles in the cerebral cortex by 4 months of age and in the hippocampus by 5.5 months of age along with the loss of about 60% of their hippocampal CA1 neurons (24). Spatial memory deficits become apparent by 2.5 to 4 months of age, and electrophysiological properties of cortical neurons are affected before the accumulation of tau pathology (25, 26). To precisely determine

¹Neuroscience Research Institute, University of California, Santa Barbara, Santa Barbara, CA 93106, USA. ²Department of Neurology, Massachusetts General Hospital, Chemical Neurobiology Lab, and Center for Genomic Medicine, Harvard Medical School, Boston, MA 02114, USA. ³Department of Psychiatry, Washington University School of Medicine in St. Louis, St. Louis, MO 63110, USA. ⁴Department of Developmental and Molecular Biology and Institute for Aging Studies, Albert Einstein College of Medicine, New York, NY 10461, USA. ⁵Laboratory of Neurogenetics, Mossakowski Medical Research Centre, Polish Academy of Sciences, 5 Pawinskiego St., 02-106 Warsaw, Poland. ⁶Department of Neuroscience, Icahn School of Medicine at Mount Sinai, New York, NY 10029, USA. ⁷Department of Molecular, Cellular, and Developmental Biology, University of California, Santa Barbara, Santa Barbara, CA 93106, USA.

*These authors contributed equally to this work.

†Corresponding author. Email: kenneth.kosik@lifesci.ucsb.edu

Copyright © 2019
The Authors, some
rights reserved;
exclusive licensee
American Association
for the Advancement
of Science. No claim
to original U.S.
Government Works

the effects of lonafarnib, we first replicated the time course for the onset of tau pathology in rTg4510 mice (Fig. 1, A to K, and fig. S1). Similar to the reported data, immunoreactivity for the conformational tau antibody MC1, corresponding to neurofibrillary tangles throughout the hippocampus, amygdala, entorhinal cortex, and cerebral cortex (Fig. 1A, green), was first detected at ~16 weeks of age (fig. S1D). Immunoreactivity progressed by 20 weeks of age to a mean of 93.0 ± 13.6 MC1-positive cells/mm² in the cerebral cortex and 67.6 ± 13.1 MC1-positive cells/mm² in the hippocampus (Fig. 1, D and E). Wild-type (WT) mice showed no detectable MC1-positive neurons (Fig. 1C).

Lonafarnib treatment was initiated at 10 weeks of age. Lonafarnib was resuspended in 20% 2-hydroxypropyl-β-cyclodextrin as vehicle, and rTg4510 mice were gavaged on an intermittent schedule, with 5 days on and 5 days off at 80 mg/kg per day (27). Mice were evaluated at 20 weeks of age (Fig. 2, A to H) and showed that drug treatment reduced MC1 immunoreactivity. The MC1 immunoreactivity in the lonafarnib-treated mouse cortex (88.8 ± 8.1 MC1-positive cells/mm²) and hippocampus (27.4 ± 5.2 MC1-positive cells/mm²) was significantly reduced compared to either vehicle-treated mice (183.3 ± 10.4 MC1-positive cells/mm² in the cortex and 82.2 ± 6.8 MC1-positive cells/mm² in the hippocampus; cortex: $P = 0.006$, hippocampus: $P = 0.001$; Fig. 2H) or untreated age-matched transgenic mice (cortex: $P = 0.049$, hippocampus: $P = 9.6 \times 10^{-6}$). Comparable results were obtained by immunostaining mouse brain sections with the phospho-tau antibody PHF-1 (cortex: $P = 3.2 \times 10^{-4}$, hippocampus: $P = 3.59 \times 10^{-5}$; fig. S2, A to F). Farnesyltransferase activity was inhibited in the brains of lonafarnib-treated mice, as determined by the appearance of an unfarnesylated heat shock protein HDJ-2 band in cortical lysates, but was not observed in untreated rTg4510 mice (fig. S2G). The presence of the unfarnesylated band in mice treated with vehicle alone remains unexplained. In contrast to chronic administration, lonafarnib was ineffective as an acute intervention. rTg4510 mice gavaged daily with lonafarnib for 2 weeks (80 mg/kg per day), beginning at 20 weeks of age when tau pathology was widespread, failed to alter the location and extent of the MC1-immunostained pathology when compared to age-matched vehicle-treated transgenic mice (fig. S3).

Chronic lonafarnib treatment also prevented the reduction in brain size among aged transgenic mice. The brain coronal section area of littermate controls and transgenic mice did not differ at 5 weeks of age but diminished by 20 weeks as the mice aged (Fig. 1B). Lonafarnib-treated rTg4510 mice at 20 weeks of age had larger coronal brain areas than either vehicle-treated or untreated age-matched transgenic mice [$P = 1.3 \times 10^{-3}$, analysis of variance (ANOVA); Fig. 2A].

Microglia counts, assessed by Iba1 immunostaining at 5 and 20 weeks of age (Fig. 1, F and G, and fig. S1), decreased with age (Fig. 1H) in the control mouse cortex ($P = 0.049$) and hippocampus ($P = 0.014$) but remained elevated in 20-week-old rTg4510 mice. At 5 weeks of age, no statistical difference was observed in microglial counts between control and transgenic mice. However, by 20 weeks, this difference was significant in both the cortex and hippocampus (cortex: $P = 0.019$, hippocampus: $P = 0.005$; Fig. 1H). Lonafarnib-treated 20-week-old rTg4510 mice (Fig. 2, I to L) had a significant reduction in hippocampal microgliosis compared to age-matched vehicle-treated transgenic mice ($P = 0.022$; Fig. 2M) but had no effect on cortical microgliosis ($P = 0.67$, ANOVA).

Cortical astrogliosis was observed in transgenic mice as increased glial fibrillary acidic protein (GFAP) immunoreactivity (Fig. 1A,

red), which became apparent from ~12 weeks of age and preceded the appearance of MC1-positive neurons (fig. S1). As transgenic mice aged, anti-GFAP immunoreactivity increased in the cortex but not in the hippocampus (Fig. 1, I to K). Lonafarnib treatment decreased cortical astrocyte immunostaining when compared to vehicle-treated mice ($P = 0.041$; Fig. 2, N to R) but displayed no effect on the hippocampus ($P = 0.236$, ANOVA).

Attenuation of behavioral abnormalities in rTg4510 mice by farnesyltransferase inhibition

As rTg4510 transgenic mice age, they display progressive behavioral impairments. Marble burial and nest shredding behaviors (28, 29) are affected early, and by 30 weeks of age, transgenic animals have progressed to hyperexcitability and obsessive circling. Using the same lonafarnib treatment protocol (27, 30), beginning at 10 weeks of age, we sought to reduce or prevent the behavioral deficits induced by tau pathology. Nest building was assessed at 20 weeks. WT littermates produced well-rounded nests (Fig. 3A); however, untreated rTg4510 mice displayed poor nest shredding and, in some instances, left bedding material completely undisturbed (Fig. 3B). Lonafarnib treatment rescued nest building (Fig. 3C). At 5 weeks of age, littermate controls and transgenic mice produced nests with similar scores (control mice, 3.58 ± 0.13 ; transgenic mice, 3.23 ± 0.12 ; $P = 1.00$). Whereas control mice nesting scores did not significantly change with time ($P = 1.00$), transgenic mice nesting scores declined ($P = 1.9 \times 10^{-11}$; Fig. 3D). Twenty-week-old transgenic mice treated with lonafarnib had significantly higher nesting scores than vehicle-treated age-matched transgenic mice ($P < 3.3 \times 10^{-12}$) and did not differ from those of age-matched control mice ($P = 1.00$; Fig. 3D). On the other hand, the marble burial deficit was observable at 5 weeks in transgenic mice, and it remained unaltered by age (Fig. 3, E to G). In contrast to nest building, the marble burial deficit (Fig. 3, E and F) was not improved by the drug in the transgenic mice (Fig. 3H) when compared to vehicle-treated mice ($P = 1.00$) or untreated mice ($P = 0.231$). The very early emergence of the marble burial deficit before lonafarnib administration, in contrast to shredding behavior, which emerged later, may account for this difference. Lonafarnib does not appear to reverse existing pathology or behavioral deficits. rTg4510 mice exhibited circling behavior at 20 weeks of age. Lonafarnib appeared to prevent circling that lasted longer than 5 min at a time (movie S1). Circling was absent in control mice (observed in zero of six mice) and was frequently observed at 20 weeks of age in transgenic mice (five of six; $P = 3.42 \times 10^{-3}$). rTg4510 mice treated with vehicle continued to exhibit circling behavior (four of six; $P = 0.014$), whereas those treated according to the chronic intermittent lonafarnib regimen rarely developed this behavior (one of six; $P = 0.296$) and engaged in more normal exploratory behaviors in the testing cage (movie S1).

Farnesyltransferase inhibition with lonafarnib enhances lysosomal protein degradation

To determine the mechanism of action of lonafarnib, we focused on its previously suggested role in autophagy (31). Using NIH3T3 mouse fibroblasts expressing the tandem reporter mCherry–green fluorescent protein (GFP)–LC3B (32) to monitor macroautophagy (Fig. 4 and fig. S4), lonafarnib treatment resulted in a dose-dependent increase in macroautophagy flux, as revealed by an overall increase in autophagic vacuoles mostly due to an increase in autolysosome abundance. At lower concentrations, the number of autophagosomes

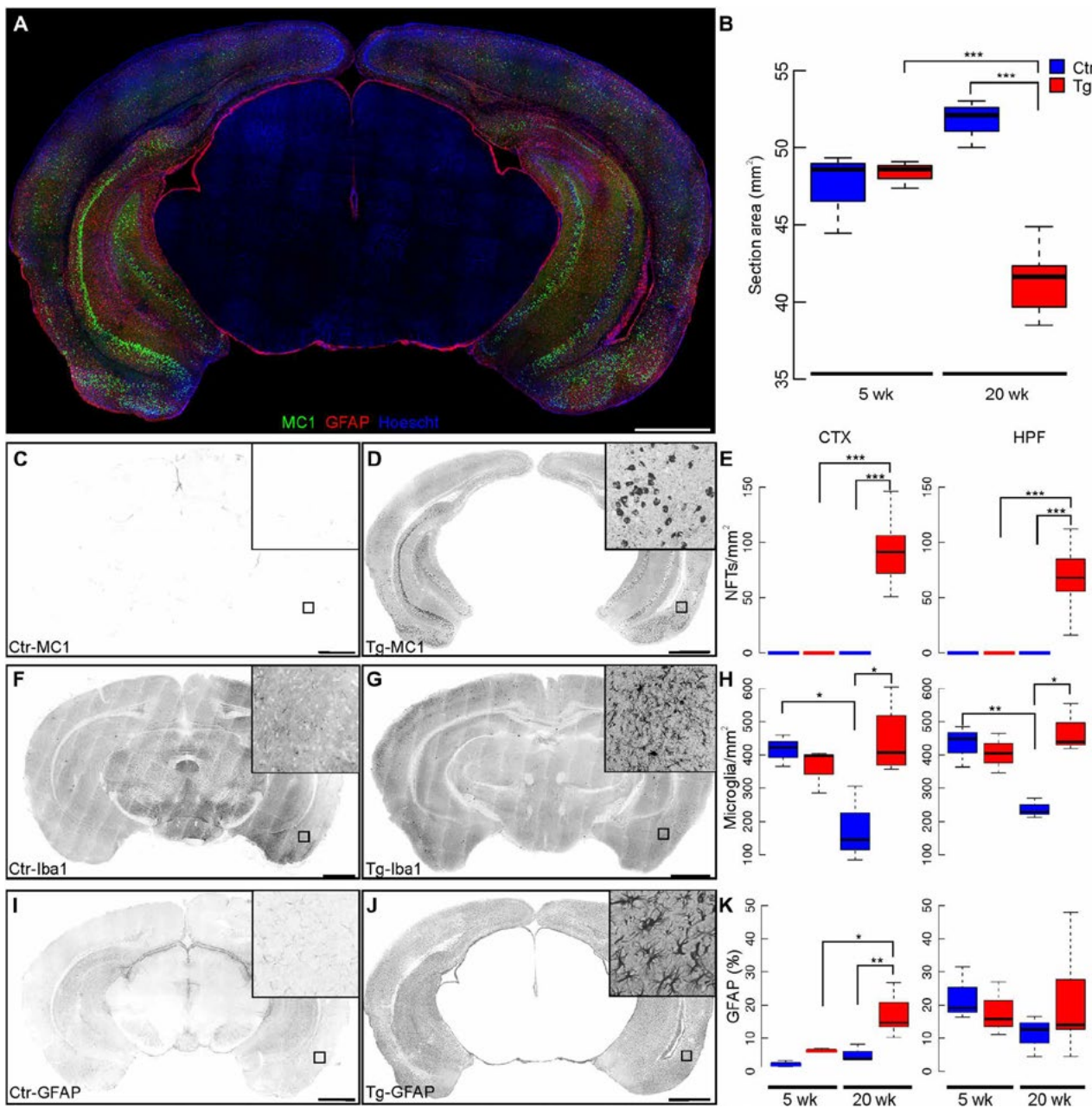


Fig. 1. Baseline time course of tau pathology in the rTg4510 mouse model of tauopathy. (A) Representative mosaic of a coronal section from rTg4510 mouse brain immunostained with MC1 antibody (green) or GFAP (red) and counterstained with Hoechst (cell nuclei, blue). (B) The coronal section area of the micrographs was computed. At 5 weeks of age, rTg4510 transgenic (Tg) mice did not differ in brain size from their nontransgenic littermates ($P = 0.942$). However at 20 weeks, the coronal section area was significantly reduced in transgenic mice compared to both age-matched controls and younger transgenic animals ($P = 6.94 \times 10^{-4}$). (C) Twenty-week-old control littermates (Ctr) show no immunostaining of brain tissue with MC1, (D) whereas 20-week-old transgenic mice show a high density of neurons strongly labeled with MC1 in both cerebral cortex (CTX) and hippocampal formation (HPF). (E) Quantification of neurofibrillary tangles (NFTs/ mm^2) in the cortex and hippocampus. Representative micrographs showing microglia (Iba1-positive cells) in 20-week-old control (F) and transgenic (G) mice. (H) Quantification of microglia per square millimeter density reveals that there is no microglia age-related decline in rTg4510 transgenic mice. At 20 weeks of age in the control mouse cerebral cortex, there were 178.5 ± 66.2 microglia/ mm^2 versus 444.2 ± 55.9 microglia/ mm^2 in the rTg4510 mice ($P = 1.9 \times 10^{-3}$). In the control mouse hippocampus, there were 236.7 ± 17.7 microglia/ mm^2 versus 471.0 ± 42.0 microglia/ mm^2 in the rTg4510 mice ($P = 5.11 \times 10^{-3}$). Astrocytes labeled with GFAP antibody in (I) nontransgenic control and (J) transgenic mice at 20 weeks of age showed cortical astrogliosis accompanying MC1 immunoreactivity in the rTg4510 mice. Activated hypertrophied astrocytes are shown in the inset. (K) Percentage area in the coronal sections stained for GFAP was calculated. The cortical GFAP signal ($P = 9.14 \times 10^{-4}$, ANOVA) quantified in rTg4510 mice at 20 weeks of age increased compared to age-matched control mice ($P = 9.2 \times 10^{-3}$). The cortical GFAP signal also increased in 20-week-old transgenic mice compared to 5-week-old transgenic mice ($P = 0.020$). The hippocampal GFAP signal in transgenic and control mice at 5 and 20 weeks of age did not differ ($P = 0.676$, ANOVA). Statistics shown for Tukey's HSD (honestly significant difference) post hoc tests. Group sizes: $n = 3$ (female:male ratio; control 5 wk, 2:1; Tg 5 wk, 1:2; Ctr 20 wk, 1:2; Tg 20 wk, 2:1). Scale bars, 1 mm. * $P < 0.05$, ** $P < 0.01$, *** $P < 0.001$.

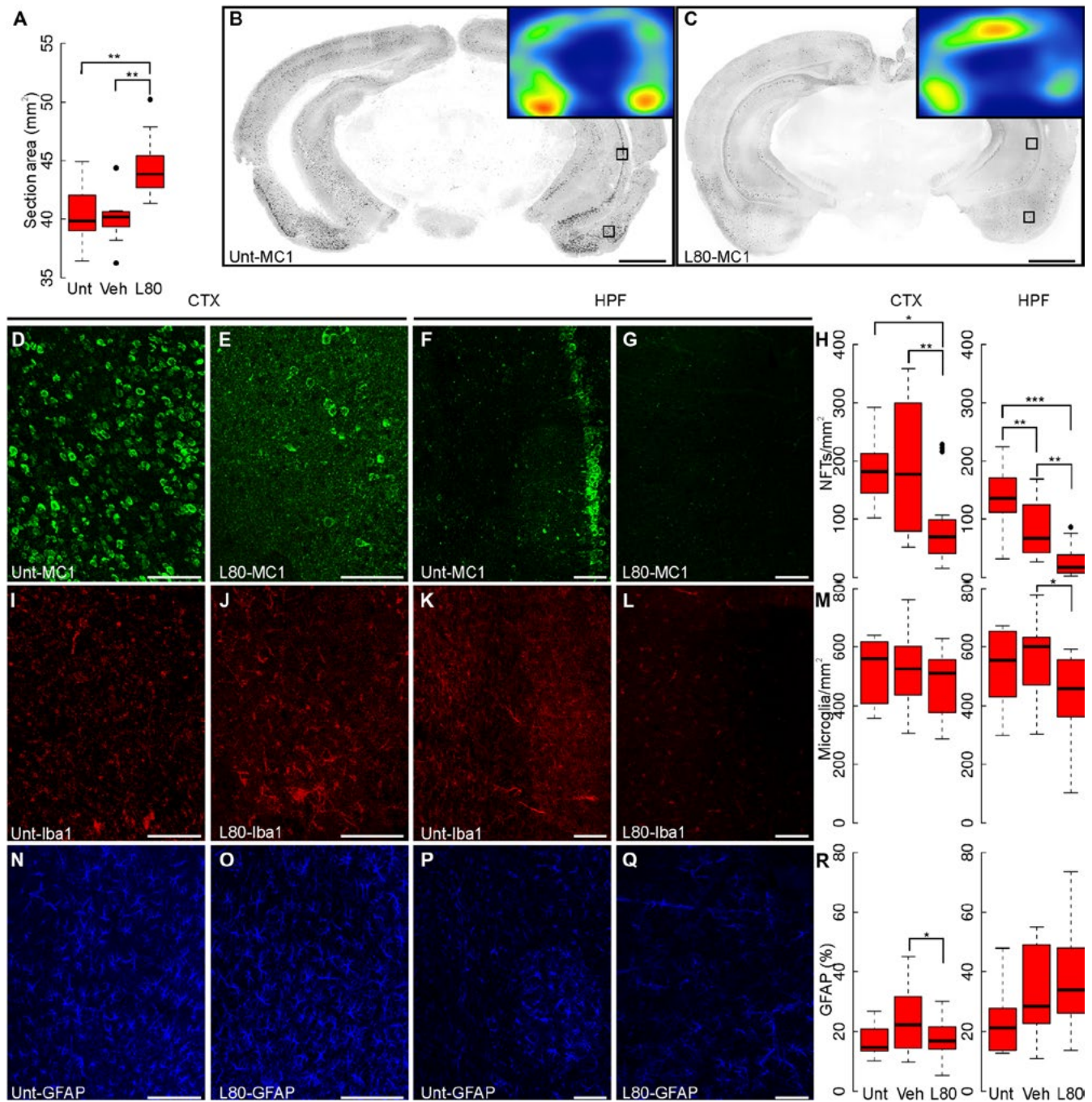


Fig. 2. Lonafarnib treatment prevents neurofibrillary tangle formation and microgliosis. (A) Brain coronal section area in 20-week-old rTg4510 transgenic mice that received chronic oral administration of lonafarnib (L80) versus untreated transgenic mice (Unt) or transgenic mice treated with vehicle alone (Veh). (B and C) Reduction of the extent of MC1 immunoreactivity in lonafarnib (L80)-treated transgenic mice compared to untreated mice. Scale bars, 1 mm. (D to G) Detail of insets of (B) and (C) showing representative MC1 immunoreactivity for the cortex (CTX) and hippocampus (HPF) of either untreated or lonafarnib-treated (L80) 20-week-old transgenic mice. (H) Large-scale coronal section mosaics quantified for MC1 immunoreactivity per square millimeter indicate a reduction of tau pathology after lonafarnib treatment (L80) when compared to untreated mice or animals treated with vehicle alone. (I to L) Density of microglia in the cortex and hippocampus of transgenic mice treated with lonafarnib (L80) or untreated is shown by Iba1 immunolabeling. Hippocampal microglial reactivity declined upon lonafarnib treatment. (M) Microglia quantification of coronal section mosaics in both the cortex and hippocampus of transgenic mice treated with lonafarnib. No statistically significant differences were observed in the cortex ($P = 0.667$, ANOVA) of lonafarnib-treated transgenic animals (489.16 ± 10.32 Iba1-positive cells/ mm^2) when compared to vehicle-treated (520.35 ± 10.71 Iba1-positive cells/ mm^2) or untreated animals (515.45 ± 11.03 Iba1-positive cells/ mm^2). (N to Q) Astrocytes immunostained for GFAP in the cortex or hippocampus of untreated and lonafarnib-treated rTg4510 mice and (R) quantification of GFAP signal in full coronal slices. Neither lonafarnib (L80) nor vehicle alone altered astrocytes in 20-week-old transgenic mice in the hippocampus ($P = 0.236$, ANOVA), but a significant reduction was observed in the cortex when comparing lonafarnib-treated to vehicle-treated mice ($P = 0.042$). Statistics shown for Tukey's HSD post hoc tests. Group sizes: $n = 6$ (female:male ratio; Unt, 1:5; Veh, 3:3; L80, 3:3). Scale bars, 100 μm . * $P < 0.05$, ** $P < 0.01$, and *** $P < 0.001$.

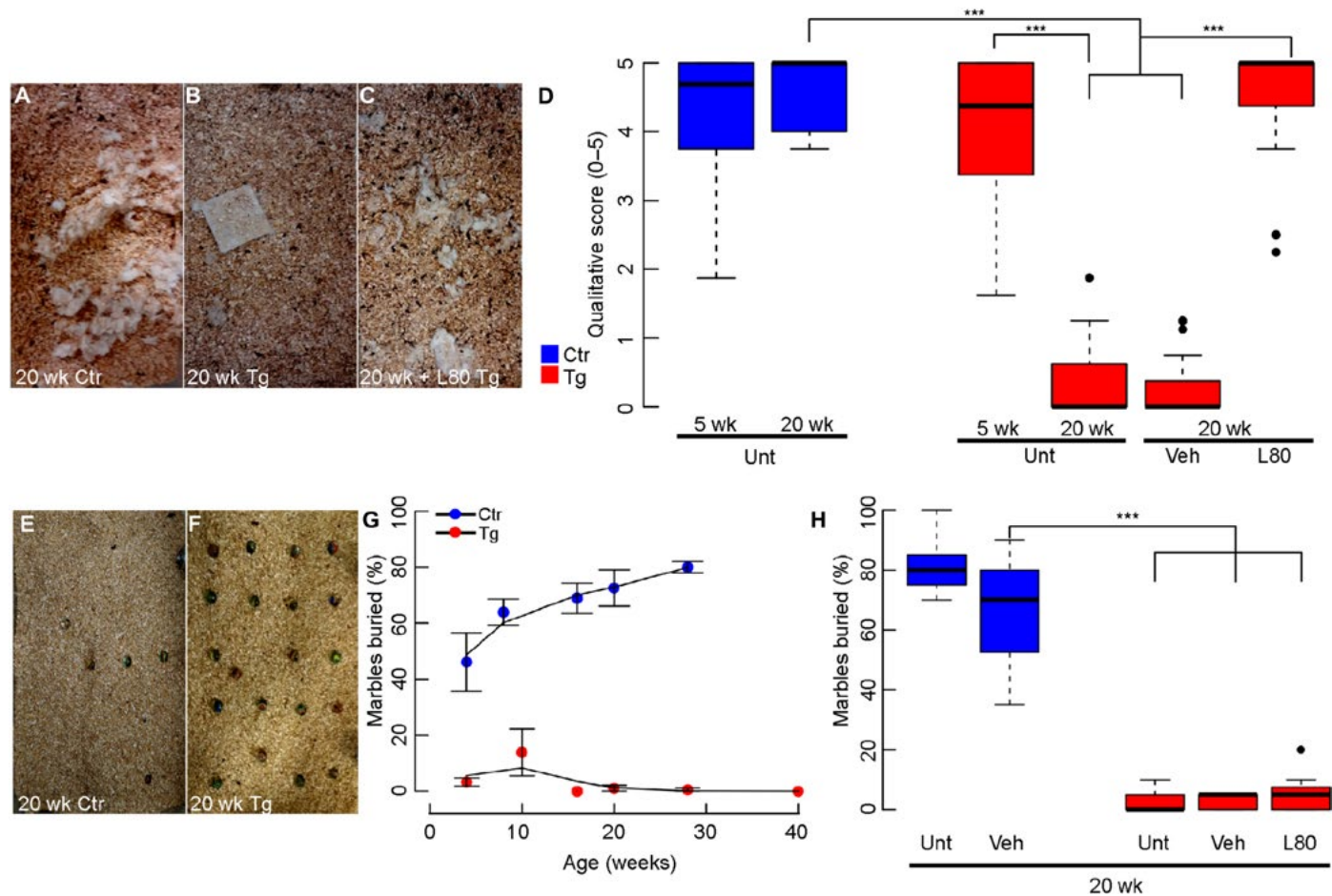


Fig. 3. Chronic lonafarnib treatment ameliorates a nest building deficit in rTg4510 mice. (A) At 20 weeks of age, littermate control mice display normal nest shredding behavior, but (B) transgenic animals failed to demonstrate nest shredding, as shown in the representative photographs. (C) Lonafarnib-treated 20-week-old rTg4510 animals shredded their nest. (D) Twenty-week-old transgenic mice had nest quality scores averaging 0.3 ± 0.1 in untreated mice or 0.2 ± 0.1 in mice treated with vehicle (Veh) alone, whereas the age-matched WT mouse nest shredding score averaged 3.7 ± 0.1 (both, $P < 5.3 \times 10^{-9}$). Chronic and intermittent oral administration of lonafarnib (L80) (80 mg/kg per day) rescued nest building, with nest scores averaging 3.5 ± 0.2 for treated mice. Qualitative scores were blindly assigned by observers using a scale from zero for untouched nesting material to five for a fully shredded nest ($n = 6$). (E) Twenty-week-old littermate control mice buried $80 \pm 2.0\%$ of the 20 marbles in 30 min, but (F) 20-week-old transgenic mice completely lacked digging behavior. (G) Control mice increased the percentage of marbles buried with age. They buried 40% of the marbles at 5 weeks of age and peaked at 30 weeks of age with an average of 80% of the marbles buried. Transgenic mice failed to bury marbles as early as 5 weeks of age {two-way ANOVA: genotype, $P < 2 \times 10^{-16}$; age, $P = 0.140$ [not significant (n.s.)]; interaction, $P = 1.93 \times 10^{-5}$ }. (H) Marble burial deficits were rescued by neither lonafarnib (L80) nor vehicle treatment. Data are presented as box plots of percentage marbles buried per treatment group. Statistics shown for post hoc Wilcoxon tests. $n = 9$ (female:male ratio; Ctr Unt, 8:4; Tg Unt, 4:8; Tg Veh, 5:4; Tg L80, 4:5). *** $P < 0.001$.

remained unchanged, suggesting their accelerated clearance by lysosomes (Fig. 4, A to C, and fig. S4, A and B). Similar results were reproduced in neuroblastoma N2a cells (fig. S4C). Macroautophagy up-regulation by lonafarnib was confirmed using immunoblotting to quantify flux of LC3 and the autophagy receptor p62 in both cell types (fig. S5). Lonafarnib-treated rTg4510 mice also displayed changes in these two autophagy-related proteins compatible with increased macroautophagy in brain lysates (fig. S5, C to E). The accumulation of p62 and a trend toward higher LC3-II protein observed in brain lysates from rTg4510 mice at 20 weeks of age were markedly reduced in the lonafarnib-treated rTg4510 mice to the point that these animals no longer differed significantly from control mice ($P = 0.1579$; fig. S5, C to E). The stimulatory effect of lonafarnib was preferentially on basal macroautophagy, as inferred by the fact that addition of lonafarnib to NIH3T3 mouse fibroblasts in which macroautophagy was induced

either by paraquat or thapsigargin did not further increase macroautophagy flux (fig. S4D). To determine whether lonafarnib also stimulated other forms of autophagy and to confirm that the observed increase in macroautophagy was not a consequence of a blockage in another degradation pathway, we used a photoswitchable reporter for chaperone-mediated autophagy (CMA) (KFERQ-PS-Dendra) (Fig. 4D and fig. S4, E and F) (8, 33) and a KFERQ-split-Venus double reporter for endosomal autophagy (Fig. 4E) (8, 34). Lonafarnib stimulated both forms of selective autophagy with maximal effect in the lower concentration range. In the case of CMA, the stimulatory effect of lonafarnib was more pronounced on basal CMA, but a significant increase was still observed after inducing CMA with paraquat or thapsigargin ($P = 0.041$ for paraquat and $P = 0.003$ for thapsigargin; fig. S4, E and F). Inhibition of lysosomal proteolysis with NH₄Cl and leupeptin in NIH3T3 cells expressing the KFERQ-split-Venus

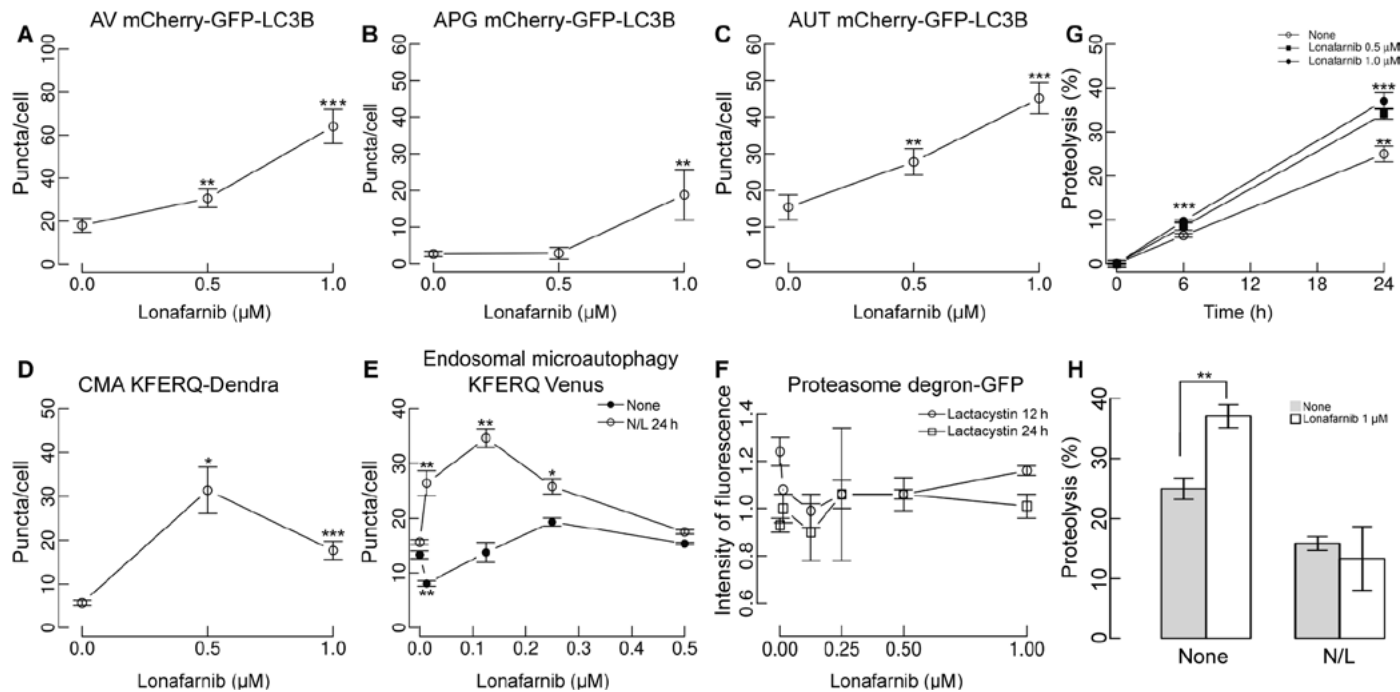


Fig. 4. Inhibition of farnesyltransferase activates autophagy. (A to C) NIH3T3 cells expressing the tandem reporter mCherry-GFP-LC3B were exposed to the indicated concentrations of lonafarnib for 48 hours. The quantified number of autophagic vacuoles (AV), autophagosomes (APG), and autolysosomes (AUT) is shown. (D) NIH3T3 cells expressing the KFERQ-Dendra reporter were photoswitched and treated with lonafarnib as indicated above. CMA was quantified by the number of fluorescent puncta positive for the photoconverted Dendra per cell. (E) NIH3T3 cells expressing N- and C-terminal KFERQ-split-Venus and treated with lonafarnib for 48 hours either were treated with 20 mM NH₄Cl and 100 μM leupeptin (N/L) or were left untreated for the last 24 hours to quantify the effect of lonafarnib on targeting (None) and degradation (N/L) by endosomal microautophagy. Quantifications in (A) to (G) were done in at least 2500 cells per condition in three different experiments using high-content microscopy. (F) Results for NIH3T3 cells expressing degron-GFP and treated with lonafarnib for 48 hours and supplemented with 100 μM lactacystin for the last 12 or 24 hours. Proteasome-dependent degradation was calculated as the increase in the intensity of fluorescence upon lactacystin addition and after discounting the increase observed in cells treated under the same conditions but expressing a nonubiquitatable degron-GFP mutant. Values are expressed relative to the proteasome degradation in cells not treated with lonafarnib that were given an arbitrary value of one. (G) Total rates of intracellular protein degradation measured in NIH3T3 cells labeled with [³H]leucine for 48 hours. The rate of proteolysis was calculated as the percentage of the initial acid-precipitable radioactivity (proteins) transformed into acid-soluble radioactivity (amino acids and small peptides) at the indicated times. (H) The contribution of lysosomes to total protein degradation was analyzed by supplementing cells with NH₄Cl and leupeptin. Data are presented as means ± SEM ($n = 6$ wells in three independent experiments). * $P < 0.05$, ** $P < 0.01$, and *** $P < 0.001$.

reporter demonstrated that lonafarnib not only promoted more efficient delivery of substrate to late endosome/multivesicular bodies via endosomal microautophagy but also stimulated efficient internalization and degradation in this compartment (Fig. 4E). Lonafarnib had no measurable effect on proteasome-dependent degradation monitored in the same cell type using a degron-GFP reporter (Fig. 4F) (35).

The overall effect in all types of autophagy suggested a direct effect of lonafarnib in endosomal/lysosomal compartments shared by all of these autophagic pathways without influencing the proteasome. To assess this possibility, we evaluated proteolysis of long-half-life proteins after labeling newly synthesized proteins with [³H]leucine for a 48-hour pulse. Lonafarnib increased proteolysis in a dose-dependent manner (Fig. 4G), an effect that was abolished in the presence of NH₄Cl and leupeptin (Fig. 4H). These data support the idea that lonafarnib treatment resulted in an overall improvement in lysosomal function and the pathways that mediate delivery of cargo to this compartment.

Rhes inhibition can reduce tau-related pathology

We sought the relevant targets of farnesyltransferase inhibition that could account for the ameliorative effects of lonafarnib on tau pa-

thology in rTg4510 mice. Ras family members are among the prominent substrates of farnesyltransferase, and this modification is required for their correct localization at the inner surface of the plasma membrane and for their biological activity. Of particular interest was the Ras family member, Rhes, because it is prenylated by farnesyltransferase (14), activates autophagy, and can modulate the aggregation state of mHtt by promoting its sumoylation (18). To demonstrate that the effect of lonafarnib on tau pathology in rTg4510 mice could, in part, be accounted for by the inhibition of Rhes farnesylation, we modulated Rhes directly. Adeno-associated viral vectors (AAVs) carrying Rhes for overexpression or Rhes small interfering RNA (siRNA) for silencing were injected into the right entorhinal cortex of 10-week-old rTg4510 mice. When analyzed at 20 weeks of age (Fig. 5, A to F), silencing of Rhes using a microRNA backbone (Rhes-miR) markedly reduced the number of MC1-positive neurons (cortex: $P = 3.99 \times 10^{-4}$; hippocampus: $P = 3.61 \times 10^{-3}$; Fig. 5H), reduced microgliosis (cortex: $P = 1.50 \times 10^{-4}$; hippocampus: $P = 3.3 \times 10^{-4}$; Fig. 5I), and increased the coronal section area ($P = 0.002$; Fig. 5G). Therefore, Rhes inhibition recapitulated the effects of lonafarnib treatment. Rhes overexpression did not appear to worsen tau pathology (Fig. 5).

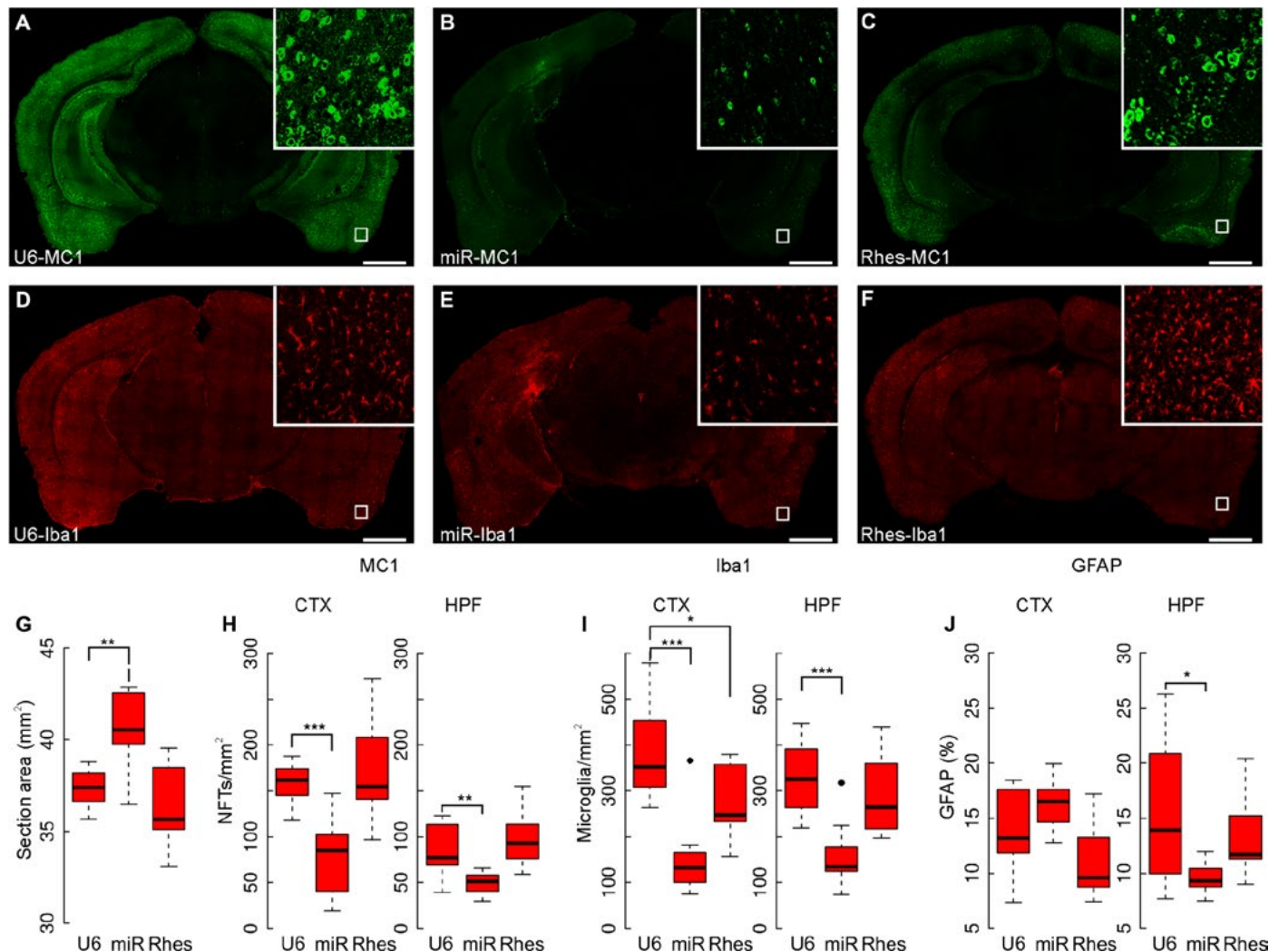


Fig. 5. Rhes suppression mimics the protective effect of lonafarnib in rTg4510 mice. Ten-week-old transgenic rTg4510 mice were intracranially infected with AAV 2/5 containing either U6, Rhes-miR, or Rhes-WT constructs and were sacrificed at 20 weeks of age. (A to C) Full mosaic immunohistochemistry for MC1 immunoreactivity after Rhes suppression by Rhes-miR showed fewer neurofibrillary tangles than did transduction with U6 or Rhes-WT. (D to F) Full mosaic immunohistochemistry for Iba1 was also reduced in mice treated with Rhes-miR. The quantification of micrographs indicates (G) significantly increased coronal section area for Rhes-miR ($40.53 \pm 0.70 \text{ mm}^2$; $P = 0.002$) but not Rhes-WT ($36.41 \pm 0.79 \text{ mm}^2$; $P = 0.307$) in injected transgenic mice compared to U6 ($37.33 \pm 0.36 \text{ mm}^2$). (H) There were a reduced number of MC1-positive cells per square millimeter both in the cerebral cortex (CTX) and hippocampus (HPF). The cortical density of MC1-positive cells per square millimeter in animals injected with U6 was 157.81 ± 12.56 compared to Rhes-miR (78.76 ± 8.88 MC1-positive cells/ mm^2 ; $P = 3.90 \times 10^{-4}$) or Rhes overexpression (172.15 ± 13.12 MC1-positive cells/ mm^2 ; $P = 0.487$). In the hippocampus, injected mice had 86.09 ± 9.28 MC1-positive cells/ mm^2 compared to Rhes-miR (49.15 ± 7.01 MC1-positive cells/ mm^2 ; $P = 3.61 \times 10^{-3}$) or Rhes overexpression (92.86 ± 9.64 MC1-positive cells/ mm^2 ; $P = 0.635$). (I) Rhes-miR reduced the number of microglia per square millimeter in the cortex and hippocampus in Rhes-miR-injected rTg4510 mice. Rhes-miR-injected transgenic mice showed a significant reduction in the cortex (compared to U6 control; $P = 1.50 \times 10^{-4}$) and hippocampus (compared to U6 control; $P = 3.02 \times 10^{-4}$), whereas Rhes-WT showed a reduction in the cortex ($P = 0.027$) with no effect observed in the hippocampus ($P = 0.531$). (J) No significant change was observed in astrocytic immunoreactivity in the cerebral cortex for either Rhes-miR ($P = 0.182$) or Rhes-WT overexpression ($P = 0.094$) compared to U6 controls. In the hippocampus, Rhes-miR significantly reduced GFAP immunostaining compared to U6 controls ($P = 0.029$) but not when compared to Rhes-WT overexpression ($P = 0.343$). $n = 3$ (female:male ratio; U6, 0:3; Rhes-miR, 0:3; Rhes, 3:0). Scale bars, 1 mm. * $P < 0.05$, ** $P < 0.01$, and *** $P < 0.001$.

Farnesyltransferase inhibition and Rhes suppression reduce global sumoylation and ubiquitination

We examined the effects of lonafarnib treatment or Rhes suppression upon sumoylation and ubiquitination in rTg4510 mice. These protein modifications are prominent features of tau pathology, and tau can undergo both modifications (34, 36, 37). Lonafarnib administration significantly altered the number of cells with detectable sumoylation ($P = 0.002$; fig. S6, A to D and I) and ubiquitination ($P = 0.048$; fig. S6,

E to H and L). Using the number of double- and single-labeled cells, we computed Bayesian probabilities for cells labeled by MC1, given that they were labeled with anti-sumo (fig. S6J) or anti-ubiquitin (fig. S6M). rTg4510 mice showed many sumo- and ubiquitin-positive cells without MC1 immunoreactivity (fig. S6, J and M). However, when using MC1 immunoreactivity as a prior, most MC1-positive cells were also labeled with sumo or ubiquitin (fig. S6, K and N). Treatment with lonafarnib significantly altered these probabilities of MC1-positive

labeling given sumoylation ($P = 2.71 \times 10^{-5}$; fig. S6J) or ubiquitination ($P = 0.016$; fig. S6M). The effects of lonafarnib on ubiquitin immunostaining were successfully replicated in total protein lysates from the cortex of treated rTg4510 mice (fig. S6, Q and R). However, because of the high variability of sumo measurements, densitometric analyses did not achieve statistical significance (fig. S6P). Rhes silencing similarly affected sumoylation but not ubiquitination (fig. S6, A, B, and I; $P = 0.047$ and fig. S6, E, F, and L; $P = 0.4033$). Treatment with Rhes-miR did not significantly reduce the double labeling of MC1-positive cells that were positive for sumo ($P = 0.063$; fig. S6J) but reduced those that were positive for ubiquitin ($P = 0.007$; fig. S6M).

Linking lonafarnib treatment to Rhes-mediated effects on tau pathology

To link Rhes-induced tau pathology to Rhes farnesylation, we cultured mouse hippocampal neurons for 3 weeks, at which time we transduced an AAV (serotype 2/5) expressing Rhes, a GTPase-inactive Rhes mutant (Rhes S33N), or a microRNA to silence Rhes (Rhes-miR). As expected, Rhes overexpression markedly increased PHF-1 immunoreactivity (Fig. 6, A and B). Because the Rhes GTPase mutant increased PHF-1 tau and the Rhes-WT (Fig. 6A), we focused on Rhes as a substrate for prenylation by farnesyltransferase (38). The farnesyltransferase inhibitor lonafarnib, when added to the culture medium, prevented PHF-1 tau accumulation in the presence of Rhes overexpression in a dose-dependent manner. A four-parameter log-logistic modeling (R package, drc) was statistically significant for each parameter estimated and provided the parameters for calculating an IC_{50} (median inhibitory concentration) of 61.00 nM (Fig. 6, C and D).

We asked whether lonafarnib prevented PHF-1 tau accumulation, at least in part, by promoting degradation of Rhes through autophagic pathways. By overexpressing mCherry-Rhes in HeLa cells, we validated that lonafarnib was effective in reducing both total Rhes and the membrane-like Rhes fraction (fig. S7). However, inhibition of lysosomal proteolysis (with NH_4Cl /leupeptin) or macroautophagy (with 3MA) did not support lysosomal degradation of Rhes in the presence of increasing lonafarnib concentrations (fig. S8).

To determine whether the profile of proteostasis stimulation observed for lonafarnib paralleled its effects in hippocampal primary mouse neurons, 3-week-old cultures were transduced to overexpress Rhes in the presence of 250 nM lonafarnib and then were treated with either NH_4Cl /leupeptin, a lysosome inhibitor, or MG-132, a proteasome inhibitor. As predicted, the proteasome inhibitor MG-132 had no effect on the reduction of Rhes-mediated PHF-1 accumulation in the presence of lonafarnib (Fig. 6E). In contrast, lysosomal inhibition with NH_4Cl and leupeptin was effective in blocking lonafarnib action, as observed by the steady accumulation of PHF-1 immunoreactivity (Fig. 6, E to G). p62 served as a positive control because it is known to undergo lysosomal degradation (Fig. 6H).

Selective effects of lonafarnib on phospho-tau accumulation

Lonafarnib administration in rTg4510 mice specifically reduced pathological tau as detected by Western blot with antibodies against PHF-1, MC1, AT8, and AT100 in mouse cortical protein lysates, without a significant effect on total tau, as detected with TAU5 antibody (lonafarnib-treated versus untreated, $P = 0.600$; lonafarnib-treated versus vehicle, $P = 0.999$; Fig. 6, I to N). In addition, sarkosyl-insoluble high-molecular weight tau observed in vehicle-treated aged rTg4510 mice was not present in aged mice treated with lonafarnib (Fig. 6O). Lonafarnib treatment also reduced phospho-tau in human

induced pluripotent stem cell (hiPSC)-derived neurons, which was readily detectable in these cells using an enzyme-linked immunosorbent assay (ELISA) specific for human phospho-tau Thr¹⁸¹. hiPSC-derived neurons expressing either MAPT-WT or MAPT-R406W were cultured for 4 weeks and then treated with either dimethyl sulfoxide (DMSO) or 10 μ M lonafarnib for an additional 9 days. Intracellular phospho-tau was significantly reduced by lonafarnib treatment (fig. S9A, $P = 0.02$, and fig. S9B, $P = 0.03$). Phospho-tau was also elevated in hiPSC-derived neurons carrying the pathogenic MAPT-P301L mutation ($P = 1 \times 10^{-4}$; fig. S9C), despite the caveat that these cells were insufficiently mature to express 4R tau abundantly. hiPSC-derived neuron protein lysates treated with λ -phosphatase and then blotted with E3T antibody, which is specific for tau 4R isoforms, demonstrated expression of the alternatively spliced tau exon (fig. S9D).

Rhes expression during development homeostatically regulates tau

hiPSC-derived neurons were obtained from patients with frontotemporal dementia harboring the MAPT mutations P301L (39), G55R (40), V337M (41), R406W (42), or C9ORF72 expansion (43). hiPSC-derived neurons from patients and from clinically healthy age-matched controls were analyzed by RNA sequencing (RNAseq) (Fig. 7A). Three genes were differentially expressed with the same sign in their log fold change (log FC) for every MAPT mutation hiPSC cell line, but were not differentially expressed in the C9ORF72 (chromosome 9 open reading frame 72) line or in any control lines (Fig. 7B; fig. S10, D and E; and data file S1). One of the three genes was RASD2, which encodes Rhes (Fig. 7B). The other two genes were the serine-threonine kinase, NEK9 (fig. S10D), and the zinc finger protein, ZFP41 (fig. S10E). The neuronal markers MAPT, which encodes tau (Fig. 7C), and TUBB3, which encodes pan-neuronal β -tubulin (Fig. 7D), were not differentially expressed among neurons from patients carrying tau mutations. The DE genes were validated by digital reverse transcription polymerase chain reaction (RT-PCR) quantification for their expression in total RNA samples taken from each of the hiPSC-derived neuronal lines at 5 weeks using GAPDH (glyceraldehyde-3-phosphate dehydrogenase) as internal control (Fig. 7, E to G, and fig. S10, F and G). Further statistical validation was obtained by bootstrapping ANOVA tests ($k = 1000$) of their expression counts per million (CPM) [bootstrapped P values: RASD2, $P = 8 \times 10^{-3}$; ZFP41, $P = 0.047$; NEK9, $P = 0.348$ (n.s.)] (44). Differential expression of RASD2 in tau mutant hiPSC-derived neurons was confirmed in a set of isogenic control cell lines. Real-time RT-PCR in three independent sets of hiPSC-derived neurons with different MAPT mutations and their isogenic control counterparts showed the expected differential expression of RASD2 (MAPT-P301L/P301S, Fig. 7H; MAPT-V337M, Fig. 7I; and MAPT-R406W, Fig. 7J). In agreement with the RNAseq data, MAPT expression did not change significantly in any of the isogenic control cell lines ($P = 0.514$, ANOVA, Fig. 7K; $P = 0.4019$, Welch t -test, Fig. 7L; $P = 0.4334$, Welch t -test, Fig. 7M).

RASD2 expression was decreased in the hiPSC-derived neurons from frontotemporal patients carrying tau mutations relative to the neurons from healthy person controls. As these neurons differentiated, RASD2 expression increased in the control line; however, in MAPT-P301L and MAPT-V337M lines, RASD2 remained low throughout differentiation (Fig. 8A). Over this same time period, MAPT expression increased and showed no statistical difference between cells with and without tau mutations (Fig. 8B). Thus, under control conditions, RASD2 expression rose coincident with increased tau, but this

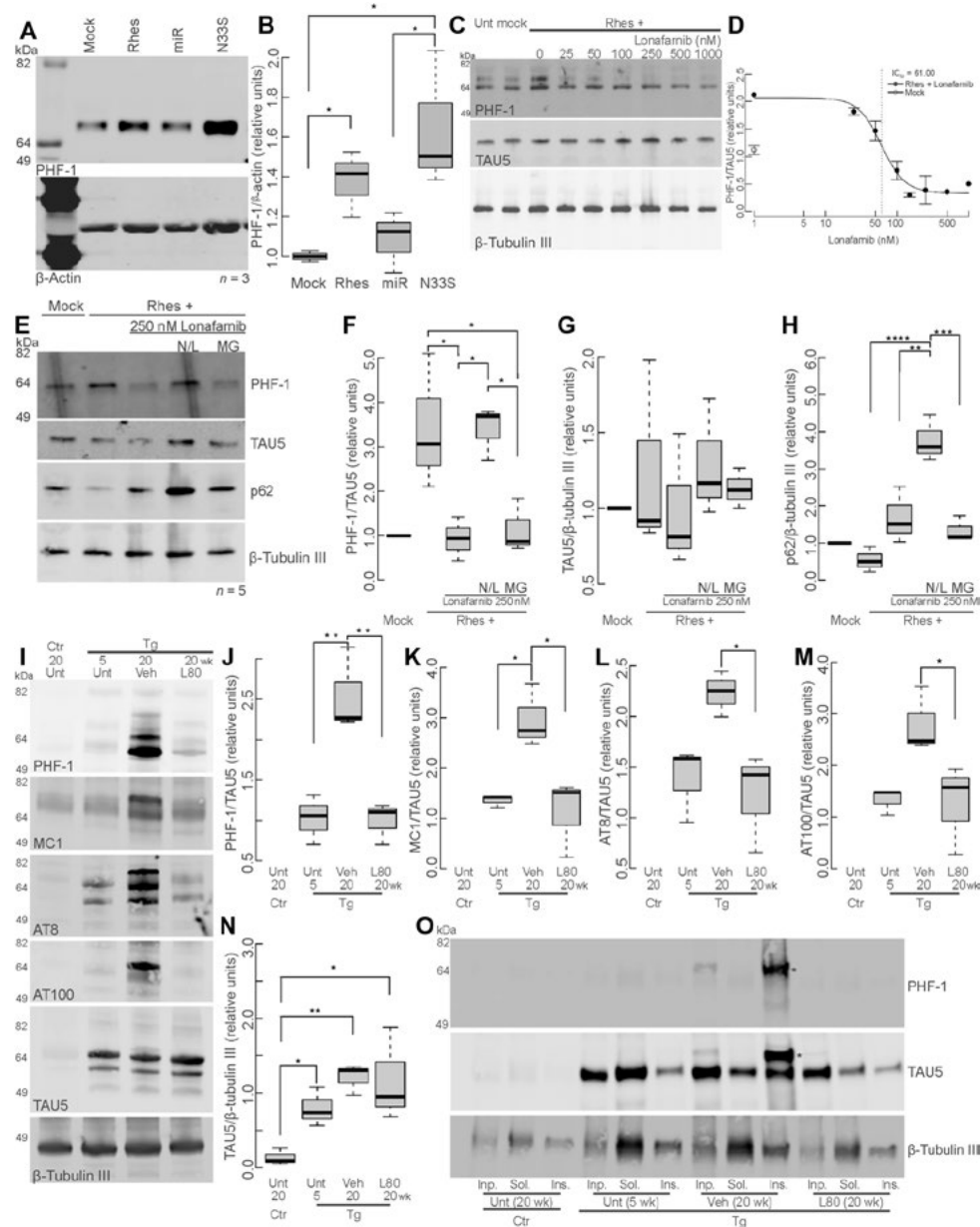


Fig. 6. Farnesyltransferase inhibition prevents Rhes-mediated tau accumulation and activates autophagy. (A) Overexpression of either Rhes-WT or the GTPase-inactive mutant Rhes-S33N but not Rhes silenced by microRNA (Rhes-miR) in hippocampal primary mouse neurons increased PHF-1 phospho-tau. Representative blot (A) and densitometry quantification (B) of independent replicates. (C) Farnesyltransferase inhibition with Lonafarnib rescued the Rhes-induced increase in phosphorylated tau in a dose-dependent manner. Representative blot (C) and densitometry quantification (D) of independent replicates. β-Actin was used for a loading and normalization control. A four-parameter log-logistic model fit (R package, drc) is shown [(B) $P = 0.006$; (C) $P = 0.010$; (D) $P < 1 \times 10^{-4}$, $IC_{50} = 61.00$ nM, $P < 1 \times 10^{-4}$]. (E to H) Primary mouse neuronal cultures (Mock) were transduced with AAV 2/5 to overexpress Rhes and then were either left untreated (Rhes-positive), treated with 250 nM Lonafarnib alone (Lon), or additionally treated either with a cocktail containing 20 mM NH₄Cl and 100 μM leupeptin (N/L) to block lysosomal-mediated proteolysis or with 5 μM MG-132 (N-carbobenzyloxy-L-leucyl-L-leucyl-L-leucinal) (MG) to block proteasome activity. Cell lysates were obtained at 12 hours, or cell media and inhibitors were replenished at 12 hours and lysates were collected at 24 hours, as indicated. (E) Proteins in the cell lysates were separated by SDS-polyacrylamide gel electrophoresis (SDS-PAGE) and then Western-blotted for PHF-1 S496/phospho-tau, total tau (TAU5), and p62. (F) PHF-1 antibody was normalized to TAU5; (G) TAU5 or (H) p62 was normalized to β-tubulin III and plotted as means ± SEM. Lonafarnib prevented a Rhes-mediated PHF-1 increase, an effect reversed by lysosomal proteolysis inhibition (N/L) but not by proteasome inhibition (MG). (I) Western blot of cortical lysates from untreated rTg4510 mice at 20 weeks of age (Ctr), untreated (Unt) transgenic mice at 5 weeks of age, and either vehicle (Veh) or Lonafarnib-treated transgenic mice at 20 weeks of age. Western blots (I) were treated with antibodies to pathological tau, total tau (TAU5), and β-tubulin III as the loading control; (J to N) their respective densitometric quantifications are presented. Phosphorylated and conformational tau were normalized to TAU5, and TAU5 was normalized to β-tubulin III ($n = 3$). (O) Sarkosyl-insoluble tau fractions were isolated from mouse cortical lysates; a 64-kDa apparent high-molecular weight tau band is indicated by the asterisk in cortical lysates from aged rTg4510 mice, but no comparable band was detectable in control, young, or age-matched Lonafarnib-treated rTg4510 mice. (A and B and I to N) $n = 3$. (I to N) Female:male ratio; Unt Ctr 20 wk, 0:3; Unt Tg 5 wk, 1:2; Veh Tg 20 wk, 1:2; L80 Tg 20 wk, 2:1. (C and D and E to H) $n = 5$ independent experiments. Statistical analysis: one-way ANOVA and Tukey's HSD post hoc tests. * $P < 0.05$, ** $P < 0.01$, *** $P < 0.001$, and **** $P < 1 \times 10^{-4}$.

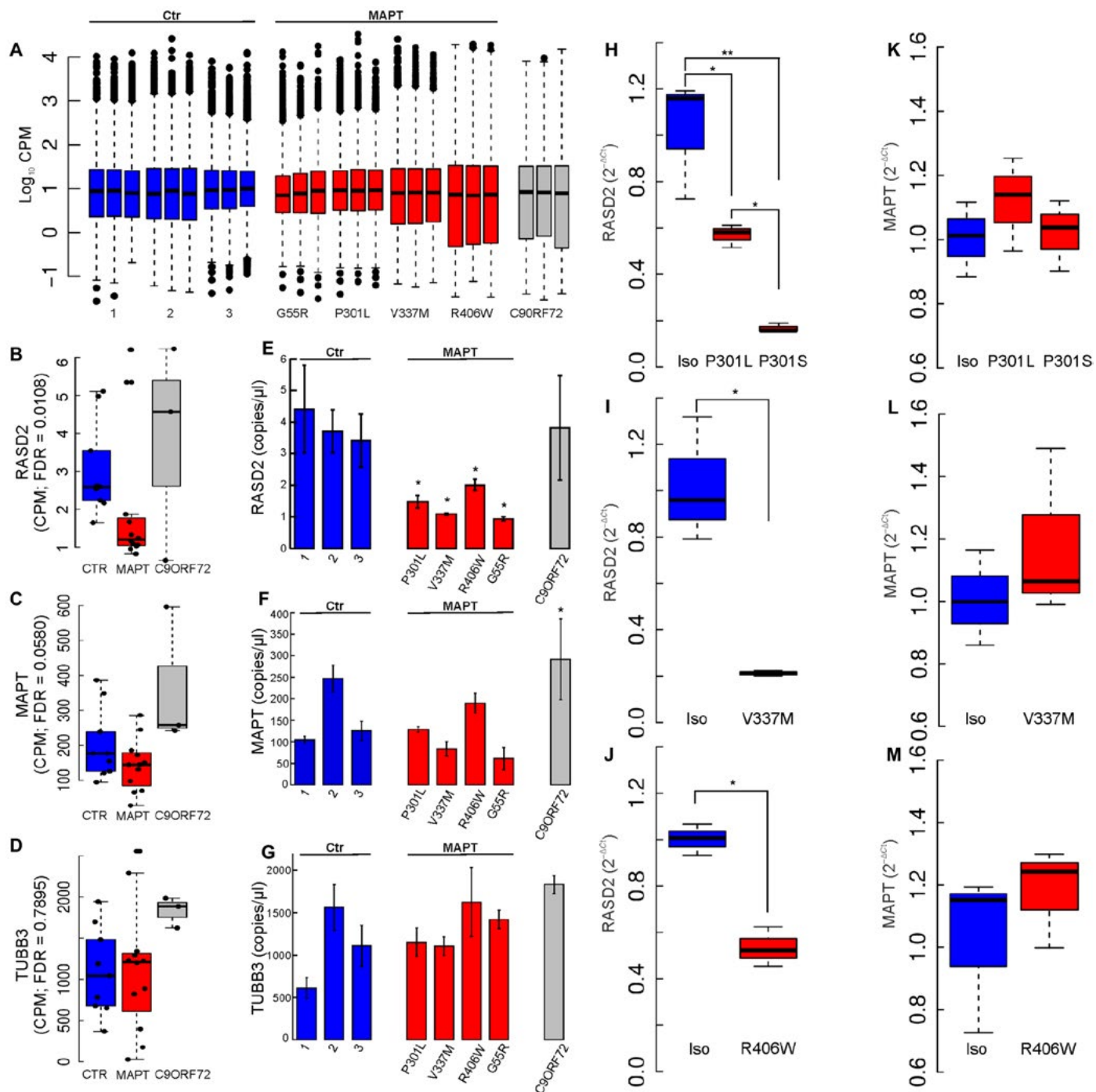


Fig. 7. RASD2 expression is reduced in transcriptome profiles of hiPSC-derived neurons from patients with frontotemporal dementia carrying MAPT mutations. (A) RNAseq of hiPSC-derived neurons from patients with frontotemporal dementia carrying *MAPT* mutations (G55R, P301L, V337M, and R406W) or a C9ORF72 expansion versus three age-matched healthy controls cultured for 5 weeks. Box plots of normalized CPMs per library are shown. (B) RASD2 expression was deregulated across each patient line carrying *MAPT* mutations. FDR, false discovery rate. (C) *MAPT* expression did not change across iPSC-derived neurons with different *MAPT* mutations. (D) TUBB3 was highly expressed and remained unaltered across samples. Digital PCR data (E to G) presented as mean copies/μl ± SEM validated the findings of each of these genes for each cell line studied. RASD2 suppression in the presence of tau mutations in neurons differentiated from hiPSCs compared to their respective isogenic control lines was verified by TaqMan RT-PCR using (H) F0510 cells harboring P301L and P301S mutations ($P = 1.45 \times 10^{-3}$, ANOVA), (I) hiPSC-derived neurons harboring the *MAPT*-V337M mutation ($P = 0.035$, *t* test), and (J) hiPSC-derived neurons harboring the *MAPT*-R406W mutation ($P = 2.14 \times 10^{-3}$, *t* test). (K to M) *MAPT* expression remained unchanged in hiPSC-derived neurons carrying different *MAPT* mutations and in the corrected isogenic lines. * $P < 0.05$ and ** $P < 0.01$.

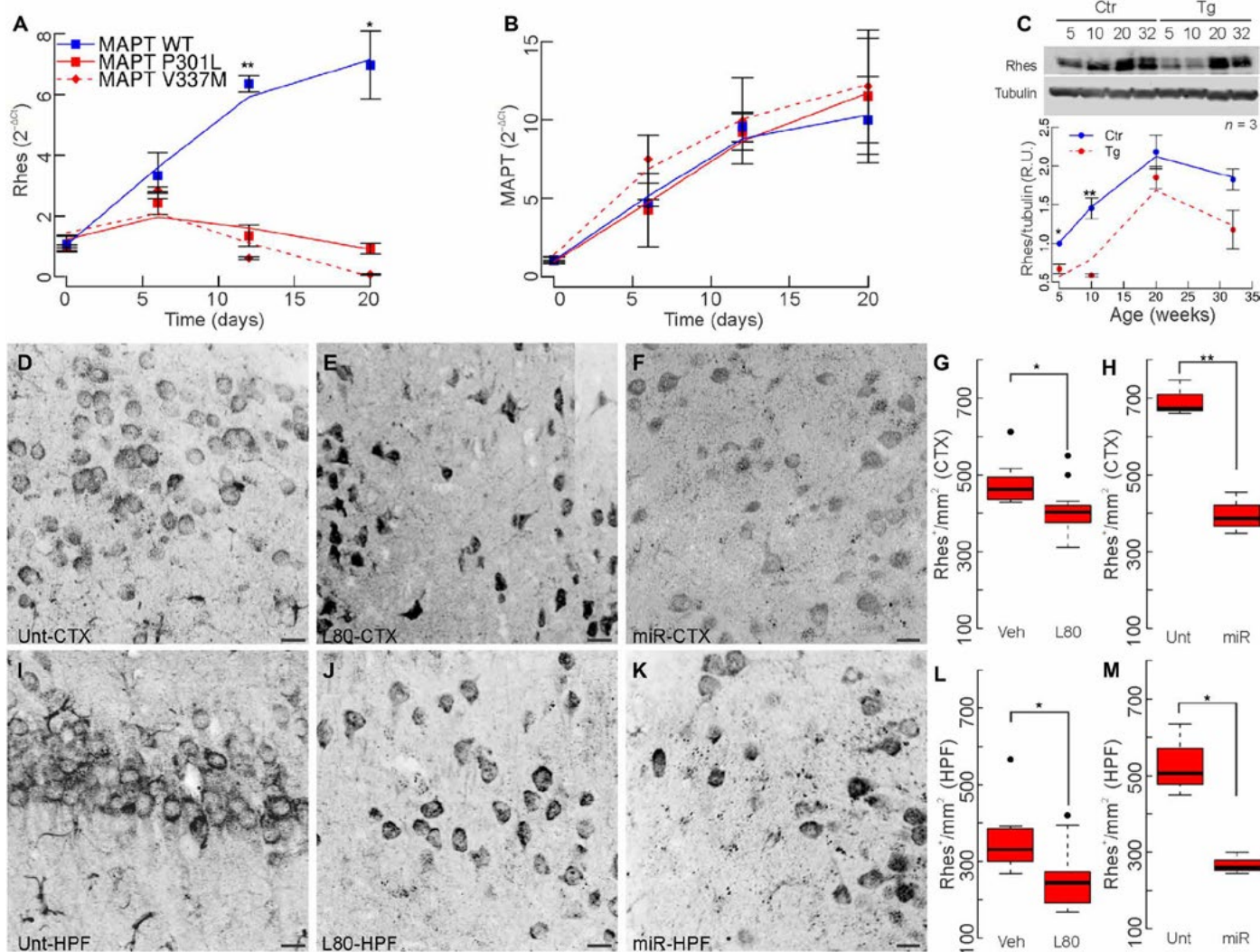


Fig. 8. Rhes expression increases as neurons age, which can be prevented by tau mutations. (A) Rhes expression is reduced in *MAPT*-P301L and *MAPT*-V337M hiPSC-derived neurons during hiPSC differentiation into neurons as early as the neurorosette stage; Rhes expression increases during differentiation into neurons of hiPSCs carrying *MAPT*-WT. (B) *MAPT* expression increases continuously during neuronal differentiation regardless of *MAPT* genotype. (C) Rhes quantification in the brains of rTg4510 transgenic mice and littermate controls. Rhes increases as both transgenic and control mice age, but these increases are significantly lower than for younger transgenic mice [two-way ANOVA: age, $P = 3.24 \times 10^{-3}$; genotype, $P = 8.01 \times 10^{-3}$; interaction, $P = 0.88$ (n.s.)]. (D to M) Rhes reduction in 20-week-old transgenic mice by both Lonafarnib and Rhes-miR treatments. Untreated rTg4510 mice had a mean of 693.3 ± 27.0 Rhes-positive cells/mm² in the cortex (CTX) and 530.0 ± 54.9 cells/mm² in the hippocampus (HPF). Chronic administration of Lonafarnib reduced Rhes to 409.1 ± 18.5 cells/mm² ($P = 5.62 \times 10^{-3}$) in the cortex and to 252.6 ± 23.7 cells/mm² ($P = 9.29 \times 10^{-3}$) in the hippocampus. Rhes-miR treatment reduced Rhes to 396.27 ± 31.52 cells/mm² ($P = 0.002$) in the cortex and to 268.1 ± 16.1 cells/mm² ($P = 0.033$) in the hippocampus. Statistics shown for Wilcoxon tests. (A to C) $n = 3$ (female:male ratio; Ctrs 5 wk 1:2, 10 wk 0:3, 20 wk 2:1, 32 wk 2:1; Tg 5 wk 3:0, 10 wk 0:3, 20 wk 2:1, 32 wk 1:2). (D to M) $n = 3$ (female:male ratio; Unt, 0:3; L80, 3:3; Veh, 3:3; Rhes-miR, 1:2). Scale bars, 100 μ m. * $P < 0.05$ and ** $P < 0.01$.

physiological increase was suppressed in the presence of tau mutations. Because iPSC-derived neurons remained relatively immature, tracking *RASD2* at more advanced ages was not possible. Therefore, the *RASD2* transcript was measured in rTg4510 transgenic mouse (24) brains and those of their littermate controls at 5, 10, 20, and 32 weeks. Consistent with cultured cell line results, as mice aged, Rhes increased (Fig. 8C). Rhes expression was lower in younger transgenic mice (5 and 10 weeks of age) that expressed mutant tau than their littermate controls that expressed only WT mouse tau. However, by 20 and 32 weeks of age, the difference between transgenic mice and littermate controls was no longer significant. These

observations suggested that a compensatory Rhes reduction could protect younger animals by maintaining lower Rhes expression. Lonafarnib-mediated lowering of Rhes expression, as observed in the animal experiments, replicated the early homeostatic response to tau mutations in the rTg4510 mouse cortex (Fig. 8, D to H) and hippocampus (Fig. 8, I to M).

DISCUSSION

Attempts to treat the genetic tauopathies have been impeded by the absence of an understanding of the molecular pathways that connect

genotype to phenotype. The effects of the farnesyltransferase inhibitor lonafarnib on tau pathology allowed this drug to serve as a probe for the discovery of disease-relevant pathways. Although farnesyltransferase inhibitors, such as lonafarnib, affect many farnesylated substrates, the major effects of the drug appear to be mediated through membrane-associated Rhes. Therefore, the data point to this regulated pathway as a druggable target for tauopathies and possibly other neurodegenerative diseases where pathological inclusions are mediated by lysosomal dysfunction. Lonafarnib had its principal effect on enhancing protein degradation in the lysosome (Fig. 4). When Rhes was overexpressed in mouse primary neurons to increase PHF-1 and the neurons were then treated with lonafarnib, the effects of the drug on PHF-1 were prevented by the lysosomal inhibitors NH₄Cl and leupeptin (Fig. 6, E to H). Furthermore, inhibition of Rhes in the rTg4510 mouse phenocopied the effects of lonafarnib (Fig. 5). Positing the lysosome as the drug target in the mouse is consistent with observations that the P301L tau mutation interferes with the degradation of tau through all autophagic pathways (8).

Contributing to the mechanism of Rhes action is its role as a sumo ligase (18). Tau is both sumoylated (36) and ubiquitinated (37, 45). However, in contrast to mHtt, which was reported to bind to Rhes (18), we did not observe an interaction between Rhes and tau in coimmunoprecipitates of rTg4510 cortical lysates (fig. S11). Both Rhes-miR and lonafarnib were able to suppress sumoylation and ubiquitination in rTg4510 mice (fig. S6). We observed some sumo- and ubiquitin-positive cells in the absence of MC1 immunoreactivity, suggesting the presence of substrates other than tau for these proteins (fig. S6, K and N). Both lonafarnib and Rhes-miR decreased the probabilities of double labeling, thereby suggesting a link between the Rhes pathway and activation of sumoylation and ubiquitination (fig. S6). However, we could not observe changes in tau sumoylation or tau ubiquitination in the brain cortex of lonafarnib-treated mice (fig. S11), which could imply that sumo or ubiquitin targets, other than tau, are sensitive to this treatment and their identification warrants further investigation.

Many questions remain regarding the pathway, from membrane disassociation of Rhes to lysosomal activation (fig. S12). Farnesylation of Rhes may serve as a switch between its effect on mTOR to inhibit autophagy and on beclin-Bcl2 to activate autophagy. The regulation of autophagy by Rhes under neurodegenerative disease conditions was reported to be independent of mTOR (17); hence, strategies that activate mTOR may not be opportune therapeutic options. On the other hand, strategies that activate autophagy have shown beneficial effects (10, 46). One limitation of our study is the broad effect of farnesyltransferase inhibition on many farnesylated proteins in cells besides Rhes. Whereas these broad effects of farnesyltransferase inhibition do not appear to be toxic, how they contribute to our findings will require further study.

From stem cells (47) to aged cells (48), proteostasis is a highly regulated process over the lifespan. Rhes is developmentally regulated, being low in neuronal precursor cells and young animals and gradually increasing with maturation (Fig. 8). The persistently reduced Rhes in iPSC-derived neurons harboring tau mutations (Fig. 7) suggested a homeostatic response to the mutation (17, 49) by which the cell can sense tau mutations before inclusions are evident and respond by activating the lysosome through endogenous reduction of Rhes. An increase in lysosomal proteolysis in response to mutant tau expression has been reported (8). Immature iPSC-derived neurons and young rTg4510 mice appeared to compensate for the deleterious

effects of the tau mutation by reducing Rhes (Figs. 7 and 8). Under control conditions, the *RASD2* transcript expression increased coincident with increases in tau, whereas this rise in Rhes failed to occur in the presence of tau mutations (Fig. 8, A and B). Tracking Rhes in iPSC-derived neurons was limited by the fact that these cells do not fully mature. However, as tau pathology in rTg4510 mice advanced, cells escaped from the autoregulatory controls that lower Rhes to protect the cell, resulting in an increase in Rhes (Fig. 8C). This Rhes sensor system appeared to be sufficiently sensitive to detect the tau P301L mutation in the alternatively spliced tau exon 10, although its expression was low in iPSC-derived neurons (fig. S9D). A similarly complex picture regarding the role of Rhes in HD and Parkinson's disease has been proposed (17, 50). Rhes is down-regulated in these diseases (50–52), yet in HD, increasing Rhes expression augments cytotoxicity (39). Thus, the Rhes pathway serves as a highly sensitive sensor. By inhibiting Rhes farnesylation, Rhes is reduced probably because of its degradation when released from cell membranes.

The pharmacological approach described here will likely require early and chronic intervention. Once tau pathology emerged, lonafarnib was no longer effective. Nevertheless, the broad implication of proteostasis in many neurodegenerative diseases including Parkinson's disease, HD, Alzheimer's disease, and frontotemporal dementia (48, 53, 54) requires a concerted effort to explore relevant pathways for therapeutic effects. The safety profile of lonafarnib (21, 22) makes this drug a promising candidate for repurposing to treat tauopathies due to tau mutations.

MATERIALS AND METHODS

Study design

Using tau transgenic rTg4510 mice, we evaluated the effects of farnesyltransferase inhibition on one of its substrates, Rhes. The farnesyltransferase inhibitor lonafarnib and siRNA-mediated suppression were used to assess tau pathology and related behaviors in the mice. The study design included quantitative immunohistochemistry on mouse brain tissue for markers of tau pathology as well as behavioral testing such as marble burial, nesting, and circling. Mice were randomly assigned to experimental groups, and behavioral testing was documented by blinded investigators. Using primary cultures of hippocampal neurons from mice, we tested the effects of lonafarnib on phospho-tau. We determined the mechanism of lonafarnib action as an effector of tau protein degradation by probing autophagic/lysosomal and proteasome pathways in cell lines. Last, we used human neurons generated from iPSCs derived from patients with frontotemporal dementia harboring MAPT mutations to search for differential gene expression associated with the tau mutations.

Animal studies

This study was conducted in accordance with the National Institutes of Health *Guide for the Care and Use of Laboratory Animals* and the Association and Accreditation of Laboratory Animal Care International guidelines and under the authorization of the Institutional Animal Care and Use Committee and the University of California, Santa Barbara. Animals were placed on a standard rodent diet ad libitum and housed under a 12-hour/12-hour light-dark cycle.

Transgenic rTg4510 mice (24) were purchased from the Jackson Laboratory (Bar Harbor, ME) and maintained by breeding B6 *CamKII-tTA* heterozygotes (003010) with FVB.tetO-MAPT-P301L

heterozygotes (015815). Weanlings were PCR-genotyped with DNA obtained from an oral swab (Puritan, Guilford, ME) using KAPA mouse genotyping kits for DNA extraction and amplification (Kapa Biosystems, Wilmington, MA), as suggested by the Jackson Laboratory (PCR primers used: forward, oIMR8746; tTA reverse, oIMR8747; tTA control forward, oIMR8744; tTA control reverse, oIMR874; MAPT forward, 14159; MAPT reverse, 14160; MAPT control forward, oIMR7338; MAPT control reverse, oIMR7339). Identified double transgenics were used in the experiments and reported here as transgenics; littermates identified as negative for both tTA and *MAPT-P301L* were used as nontransgenic controls, where indicated. Doxycycline was not used to turn off the expression of *MAPT-P301L* transgene in this study.

Lonafarnib was synthesized by Cayman Chemical Company (Ann Arbor, MI), certified 99.9% or higher purity by high-performance liquid chromatography, and stored lyophilized at -20°C . Lonafarnib (100 \times) was dissolved in DMSO heated to 95°C until the solution was clear and 12 mg/ml was resuspended in 20% (2-hydroxypropyl)- β -cyclodextrin (Sigma-Aldrich) as a vehicle. Resuspended solution was stored at 4°C for less than a week. Ten-week-old rTg4510 mice were orally administered lonafarnib (80 mg/kg per day) or vehicle alone by gavage feeding in an alternate schedule of five consecutive days followed by five resting days for 10 weeks. Cortical protein lysates were blotted with HDJ-2 (KA2A5.6, Invitrogen, MA5-12748) to determine the farnesylation state of HDJ-2 after lonafarnib treatment in mice.

Overexpression and silencing of Rhes were achieved by stereotactic injections of ice-cold lactated ringer dialyzed AAVs (AAV 2/5) carrying either Rhes-IRES-GFP (Rhes), an engineered Rhes-targeted synthetic microRNA (Rhes-miR), or U6 alone to the entorhinal cortex on bregma coordinates -0.30 (anteroposterior), -2.00 (lateral), and -4.80 (dorsalventral). Stereotactic injections of 1×10^9 viral particles were performed on rTg4510 mice at 10 weeks of age. Packaged viral vectors were provided by B. Davidson (University of Pennsylvania) and kept at -80°C until dialysis.

Sample preparation and immunocytochemistry

Animals were transcardially perfused using 4% paraformaldehyde in 0.1 M sodium cacodylate (Electron Microscopy Sciences, Hatfield, PA) for 15 min at room temperature. Brains were then dissected and immersion-fixed for 48 hours at 4°C . Immunocytochemistry was carried as described elsewhere (55). Briefly, samples were rinsed 5 \times 5 min in phosphate-buffered saline (PBS; pH 7.4) and then coronally sectioned at 100 μm using a vibratome (Leica, Lumberton, NJ). Sections were immersed in normal donkey serum 1:20 in PBS containing 0.5% bovine serum albumin, 0.1% Triton X-100, and 0.1% sodium azide (PBTA) at 4°C on a rotator for continuous overnight agitation followed by immersion in MC1 (provided by P. Davies, Feinstein Institute for Medical Research, Manhasset, NY; mouse monoclonal, 1:200), anti-Iba1 (Wako Laboratory Chemicals, Richmond, VA; rabbit polyclonal, 1:200), anti-GFAP (Abcam, San Francisco, CA; chicken polyclonal, 1:500), anti-RASD2 (GeneTex, Irvine, CA; GTX85428, rabbit polyclonal), anti-ubiquitin (Abcam, ab7780; rabbit polyclonal), and anti-sumo 1 (Abcam, ab11672; rabbit monoclonal) diluted in PBTA. The following day, sections were rinsed 5 \times 5 min in PBTA and 1 \times 1 hour in PBTA and then placed in secondary antibodies (donkey anti-mouse 568, anti-rabbit 488, and anti-chicken 647 (Jackson ImmunoResearch Laboratories, West Grove, PA; 1:200)). Last, secondary antibodies were rinsed and mounted using VECTASHIELD (Vector Laboratories Inc., Burlingame, CA) on a glass slide and sealed

under an 18 \times 18 #0 micro-coverslip (Thomas Scientific, Swedesboro, NJ) using nail polish.

Large-scale mosaic acquisition, registration, and image analysis

Specimens were screened and imaged using an Olympus Fluoview 1000 laser scanning confocal microscope (Center Valley, PA) equipped with an argon 488-nm photodiode laser and HeNe 543/633-nm photodiode lasers as well as precision motorized stage (Applied Scientific Instrumentation Inc., Eugene, OR). Three coronal sections per mouse that spanned the hippocampal formation from anterior to posterior were selected. Mosaics were captured using an UPlanSApo 20 \times air lens, 0.75 numerical aperture at 1- μm intervals along the z axis and a pixel array of 800 \times 800 in the x-y axes. Image stacks were collected sequentially using the Olympus Fluoview software version 4.2 with 5% overlap between individual tiles. Alignment and registration of individual tiles were performed in a semiautomated fashion by Imago 1.5 (Mayachitra Inc., Santa Barbara, CA).

Whole-brain mosaics were manually segmented into either hippocampal or cortical regions using Fiji version 2.0.0. Images were set as 8-bit, and thresholds were manually adjusted. Total number of MC1-positive neurons and Iba1-positive microglia were quantified using Fiji's Analyze Particles function (56). Segmentation of anti-GFAP staining was performed using Weka (57), a third-party library included in Fiji. The numbers of Rhes-positive, sumo-positive, and ubiquitin-positive cells were quantified in Fiji by discretely counting cells positively immunostained over threshold adjustments indicated above on confocal z-stacks of micrographs collected at 1024 \times 1024 pixel arrays.

Behavioral characterization

Nest shredding behavior was qualitatively measured according to published guidelines (29) with modifications. Briefly, unscented nestlets were provided during husbandry and kept in the cage for 24 hours. Nest shredding behavior overnight was estimated on a 0 to 5 scale, with 0 indicating unshredded bedding material and 5 denoting a completely shredded nest that displayed a rounded appearance. Twenty-five blinded independent observers reviewed images of overnight nests, and the average quality scores were calculated. After this time, a picture of the remaining nestlet or the nest was taken, and the pictures were scored on a 0 to 5 scale: 0 for an unshredded nest, 1 and 2 for nests slightly to moderately shredded, 3 and 4 for nests that were shredded but the appearance of the nest was flat, and 5 for nests that were fully shredded and the appearance of the nest was round and full. Scores of each nest were assigned blindly by 25 independent observers, and these scores were averaged to produce net-scores (Fig. 3D). Kruskal-Wallis tests followed by Wilcoxon post hoc tests were used to determine statistical significance in the difference of means.

Marble burial was evaluated as previously reported (28) with minor modifications as follows: 20 marbles of 15 mm in diameter were spaced by 4 cm in five rows of four marbles each on the surface of a gently packed 5-cm-deep wood chip bedding in a double-size rat cage. A mouse was left alone in the cage for 30 min and then returned to its housing cage. An observer blinded to the treatment counted the number of marbles buried. Any marble buried more than two-thirds of its size was counted. Each mouse was assessed three times on consecutive days, at the same time in the afternoon, and data were reported as average \pm SEM of the percentage of buried marbles per animal. A two-way ANOVA test was used to evaluate the effect of

aging and genotype in marble burying. Kruskal-Wallis tests followed by Wilcoxon post hoc test were used to determine statistical significance of marble burying in transgenic mice treated or left untreated with lonafarnib.

rTg4510 transgenic mice displayed left-patterned accelerated gate (circling) behavior, which was often spontaneous but could also be stimulated by the presence of an observer. To quantify, mice were observed during marble burial experiments and categorically assigned to either circling or not circling categories. Circling never fully stopped during the observation period, which was longer than 5 min. The ratio of circling mice to the total number of mice was determined ($n = 6$). Statistical significance was evaluated with a two-sample test for equality of proportions without continuity correction (R, prop. test) to rTg4510 control mice.

Evaluation of intracellular proteolysis and autophagy in lonafarnib-treated cells

Mouse fibroblasts (NIH3T3) or neuroblastoma N2a cells were obtained from the American Type Culture Collection. Cells were maintained in Dulbecco's modified Eagle's medium (DMEM) (Sigma-Aldrich, St. Louis, MO) in the presence of 10% newborn calf serum (NCS), penicillin (50 μ g/ml), and streptomycin (50 μ g/ml) at 37°C with 5% CO₂ and treated with varying concentrations of lonafarnib (0.25 to 1 μ M).

Macroautophagy activity in intact cells was measured upon transduction with lentivirus carrying the mCherry-GFP-LC3 tandem construct (32). Cells were plated on coverslips or glass-bottom 96-well plates, and fluorescence was read in both channels. Puncta positive for both fluorophores correspond to autophagosomes, whereas those only positive for the red fluorophore correspond to autolysosomes. Autophagic flux was determined as the conversion of autophagosomes (yellow) to autolysosomes (puncta; red). In a second set of experiments, macroautophagy activity was determined by immunoblot for LC3 (2775, Cell Signaling Technology, 1:1000) and p62 of cells exposed to inhibitors of lysosomal degradation (100 μ M leupeptin/20 mM NH₄Cl). Autophagic flux was calculated as the increase in these two proteins in inhibitor-treated cells relative to untreated. Markers of macroautophagy were also evaluated by immunoblot for these two proteins in brain lysates from WT and rTg4510 transgenic mice treated or not with lonafarnib.

CMA activity was quantified in intact cells using the photoswitchable KFERQ-PS-Dendra2 reporter transduced into cells using lentiviral delivery (33). Cells were photoswitched with a 405-nm light-emitting diode (Norlux) for 4 min with an intensity of 3.5 mA (current constant). CMA activity was quantified as the number of Dendra photoconverted positive puncta per cell. Endosomal microautophagy (34) activity was measured in intact cells using a recently developed N-terminal KFERQ-split-Venus and C-terminal KFERQ-split-Venus (8). As the half proteins are targeted to the multivesicular bodies in late endosomes, the confined space inside these vesicles favors the interaction of the two parts, and once Venus is joined, punctate fluorescence results. The amount of reporter undergoing degradation in this compartment can be estimated by comparing the number of puncta in cells treated or not with NH₄Cl and leupeptin to inhibit luminal degradation.

To determine possible changes in proteasome-dependent degradation, cells were transduced with lentivirus carrying the degron-GFP (35) that will undergo rapid degradation inside cells unless lactacystin is added to inhibit proteasome activity. Rates of degradation are calculated as the increase in total cellular fluorescence upon

addition of lactacystin, and discounting changes in cells transduced with lentivirus carrying a mutant-degron-GFP, unable to undergo selective proteasome degradation.

For all reporters, cells plated in glass-bottom 96-well plates were treated for the indicated times, and after fixation, images were acquired using a high-content microscope (Operetta, PerkinElmer). Images of nine different fields per well were captured, resulting in an average of 2500 to 3000 cells. Nuclei and puncta were identified using the manufacturer's software. The number of particles/puncta per cell was quantified using the "particle identifier" function in the cytosolic region after thresholding in nonsaturated images (58). In all cases, focal plane thickness was set at 0.17 μ m and sections with maximal nucleus diameter were selected for quantification. Values are presented as the number of puncta per cell section that, in our acquisition conditions, represents 10 to 20% of the total puncta per cell in flat cells such as NIH3T3 and 2 to 5% of the total puncta per cell in round cells such as N2a.

To measure degradation of long-lived proteins, confluent cells were labeled with [³H]leucine (2 μ Ci/ml) for 48 hours at 37°C and then extensively washed and maintained in complete (10% NCS) or serum-deprived medium containing an excess of unlabeled leucine (2.8 mM) to prevent reutilization of radiolabeled leucine (59). Aliquots of the medium taken at different times were precipitated with trichloroacetic acid, and proteolysis was measured as the percentage of the initial acid-insoluble radioactivity (protein) transformed into acid-soluble radioactivity (amino acids and small peptides) at the end of the incubation. Total radioactivity incorporated into cellular proteins was determined as the amount of acid-precipitable radioactivity in labeled cells immediately after washing.

All numerical results are reported as means \pm SEM. Statistical significance of the difference between experimental groups was analyzed by two-tailed unpaired Student's *t* test. Differences were considered statistically significant for *P* < 0.05.

Evaluation of proteolysis contribution to lonafarnib-enhanced tau degradation

Hippocampal primary mouse neuronal cocultures were prepared from E19 mouse hippocampi, dissected and dissociated with 2.5% trypsin, and plated in poly-L-lysine-coated cell culture six-well plates at a density of 250,000 neurons per well. Hippocampal neurons were matured for 3 weeks in neurobasal medium supplemented with N2, B-27, and L-glutamine with 1% penicillin and streptomycin cocktail. Neurons were fed by replacing half of the culture medium with prewarmed and freshly supplemented medium twice per week. Cells were then transduced with 1×10^9 AAV 2/5 particles per well to either overexpress or silence Rhes and simultaneously treated with lonafarnib at varying concentrations ranging from 0 to 1 μ M. Cell lysates were obtained 24 hours after treatment with radioimmunoprecipitation assay buffer after adding proteasome inhibitor cocktail (cComplete, Roche, Branford, CT) and phosphatase inhibitor cocktail (Sigma-Aldrich), as per the manufacturer's instructions. Proteins were separated with SDS-PAGE and wet-transferred to nitrocellulose. Membranes were then blotted with PHF-1 and β -actin (1:1000, each) and imaged using a LI-COR fluorescent scanner.

To dissect the contribution of diverse proteolysis pathways, hippocampal primary mouse neurons treated as described above with AAV 2/5 to overexpress Rhes in the presence of 250 nM lonafarnib were further treated in the presence of either a cocktail of 20 mM NH₄Cl and 100 μ M leupeptin to prevent lysosomal-mediated proteolysis or 5 μ M

MG-132 to block proteasome-mediated proteolysis or were left untreated. Cell lysates were collected as described above 12 hours after treatments, or treatments were replenished at 12 hours, and lysates were collected 24 hours after treatments began. Membranes were blotted with PHF-1, p62 (ab56416, Abcam) at 1:1000, or β -tubulin III (Sigma-Aldrich) at 1:5000.

Statistical analysis

Specific statistical analyses performed for different experimental procedures varied depending on the specific experimental technique. Therefore, the statistical methodologies are specified within the Materials and Methods subsections. In more general terms, normality assumption was tested with the Shapiro-Wilk test, where normality assumption was rejected if $P < 0.05$. When comparing averages in two groups, two-sided Student's t test or Welch t test was performed when normality assumption was not rejected, and Mann-Whitney U test was performed otherwise. For comparing averages on multiple groups, one-way ANOVA followed by Tukey's HSD post hoc tests were evaluated if the normality assumption was not rejected, and Kruskal-Wallis tests followed by Wilcoxon tests were used otherwise. To assess the effect on a dependent variable when two independent variables such as age and phenotype were measured, two-way ANOVA tests were performed. Differences in the mean were considered to be significant when $P < 0.05$, and degree of significance was reported with * $P < 0.05$, ** $P < 0.01$, *** $P < 0.001$, and **** $P < 1 \times 10^{-4}$, respectively.

For experiments involving mice, sample size (n) and female:male ratios used at each experiment are indicated in the figure legends. Power analysis was performed to verify that a power greater than 0.80 was obtained while minimizing unnecessary animal usage in replication. For experiments using cell lines or hiPSC-derived neuron cultures, the number of independent biological replicates is reported (N).

SUPPLEMENTARY MATERIALS

www.sciencetranslationalmedicine.org/cgi/content/full/11/485/eaat3005/DC1

Materials and Methods

Fig. S1. Tau pathology progression in rTg4510 transgenic mice.

Fig. S2. PHF-1 immunoreactivity is reduced by lonafarnib treatment.

Fig. S3. Acute treatment of lonafarnib does not alter tau pathology in aged rTg4510 transgenic mice.

Fig. S4. Effect of lonafarnib in macroautophagy and CMA.

Fig. S5. Farnesyltransferase activity inhibition activates autophagy.

Fig. S6. Sumo and ubiquitin are reduced by lonafarnib and Rhes-miR treatments.

Fig. S7. Lonafarnib's effect on Rhes localization.

Fig. S8. Degradation of Rhes is insensitive to lysosomal proteolysis blocking.

Fig. S9. Lonafarnib treatment is effective in reducing phospho-tau in iPSC-derived neurons.

Fig. S10. Transcriptomic analysis of hiPSC-derived neurons harboring tau mutations.

Fig. S11. Ubiquitinated and sumoylated tau are not altered by lonafarnib treatment.

Fig. S12. Model for a Rhes pathway mechanism.

Movie S1. Lonafarnib attenuates behavioral circling in rTg4510 (mp4).

Data file S1: Differentially expressed genes in hiPSC-derived neurons with MAPT variants (Excel file).

Data file S2: Quantification data for rTg4510-treated mice (excel file).

References (61–65)

REFERENCES AND NOTES

- C. U. Onyike, J. Diehl-Schmid, The epidemiology of frontotemporal dementia. *Int. Rev. Psychiatry* **25**, 130–137 (2013).
- J. Götz, A. Ittner, L. M. Ittner, Tau-targeted treatment strategies in Alzheimer's disease. *Br. J. Pharmacol.* **165**, 1246–1259 (2012).
- S. L. DeVos, R. L. Miller, K. M. Schoch, B. B. Holmes, C. S. Kebodeaux, A. J. Wegener, G. Chen, T. Shen, H. Tran, B. Nichols, T. A. Zanardi, H. B. Kordasiewicz, E. E. Swayze, C. F. Bennett, M. I. Diamond, T. M. Miller, Tau reduction prevents neuronal loss and reverses pathological tau deposition and seeding in mice with tauopathy. *Sci. Transl. Med.* **9**, eaag0481 (2017).
- E. Mead, D. Kestoras, Y. Gibson, L. Hamilton, R. Goodson, S. Jones, S. Eversden, P. Davies, M. O'Neill, M. Hutton, P. Szekeres, J. Wolak, Halting of Caspase activity protects tau from MC1-conformational change and aggregation. *J. Alzheimers Dis.* **54**, 1521–1538 (2016).
- K. Hochgräfe, A. Sydow, D. Matenia, D. Cadinu, S. Könen, O. Petrova, M. Pickhardt, P. Goll, F. Morellini, E. Mandelkow, E.-M. Mandelkow, Preventive methylene blue treatment preserves cognition in mice expressing full-length pro-aggregant human tau. *Acta Neuropathol. Commun.* **3**, 25 (2015).
- X. Zhang, I. Hernandez, D. Rei, W. Mair, J. K. Laha, M. E. Cornwell, G. D. Cuny, L.-H. Tsai, J. A. J. Steen, K. S. Kosik, Diaminothiazoles modify tau phosphorylation and improve the tauopathy in mouse models. *J. Biol. Chem.* **288**, 22042–22056 (2013).
- S.-W. Min, X. Chen, T. E. Tracy, Y. Li, Y. Zhou, C. Wang, K. Shirakawa, S. S. Minami, E. Defensor, S. A. Mok, P. D. Sohn, B. Schilling, X. Cong, L. Ellerby, B. W. Gibson, J. Johnson, N. Krogan, M. Shamloo, J. Gestwicki, E. Masliah, E. Verdin, L. Gan, Critical role of acetylation in tau-mediated neurodegeneration and cognitive deficits. *Nat. Med.* **21**, 1154–1162 (2015).
- B. Caballero, Y. Wang, A. Diaz, I. Tasset, Y. R. Juste, B. Stiller, E.-M. Mandelkow, E. Mandelkow, A. M. Cuervo, Interplay of pathogenic forms of human tau with different autophagic pathways. *Aging Cell* **17**, e12692 (2018).
- J. L. Guo, A. Buist, A. Soares, K. Callaerts, S. Calafate, F. Stevenaert, J. P. Daniels, B. E. Zoll, A. Crowe, K. R. Brunden, D. Moehrs, V. M. Y. Lee, The dynamics and turnover of tau aggregates in cultured cells: Insights into therapies for tauopathies. *J. Biol. Chem.* **291**, 13175–13193 (2016).
- A. Lopez, S. E. Lee, K. Wojta, E. M. Ramos, E. Klein, J. Chen, A. L. Boxer, M. L. Gorno-Tempini, D. H. Geschwind, L. Schlotawa, N. V. Ogrzyko, E. H. Bigio, E. Rogalski, S. Weintraub, M. M. Mesulam, Tauopathy Genetics Consortium, A. Fleming, G. Coppola, B. L. Miller, D. C. Rubinsztein, A152T tau allele causes neurodegeneration that can be ameliorated in a zebrafish model by autophagy induction. *Brain* **140**, 1128–1146 (2017).
- R. A. Nixon, The role of autophagy in neurodegenerative disease. *Nat. Med.* **19**, 983–997 (2013).
- M. C. Chang, K. Srinivasan, B. A. Friedman, E. Suto, Z. Modrusan, W. P. Lee, J. S. Kaminker, D. V. Hansen, M. Sheng, Progranulin deficiency causes impairment of autophagy and TDP-43 accumulation. *J. Exp. Med.* **214**, 2611–2628 (2017).
- M. P. Nelson, M. Boutin, T. E. Tse, H. Lu, E. D. Haley, X. Ouyang, J. Zhang, C. Auray-Blais, J. J. Shacta, The lysosomal enzyme alpha-galactosidase A is deficient in Parkinson's disease brain in association with the pathologic accumulation of alpha-synuclein. *Neurobiol. Dis.* **110**, 68–81 (2018).
- J. Colicelli, Human RAS superfamily proteins and related GTPases. *Sci. STKE* **2004**, RE13 (2004).
- D. Spano, I. Branchi, A. Rosica, M. T. Pirro, A. Riccio, P. Mithbaokar, A. Affuso, C. Arra, P. Campolongo, D. Terracciano, V. Macchia, J. Bernal, E. Alleva, R. Di Lauro, Rhes is involved in striatal function. *Mol. Cell. Biol.* **24**, 5788–5796 (2004).
- D. Vitucci, A. Di Giorgio, F. Napolitano, B. Pelosi, G. Blasi, F. Errico, M. T. Attrotto, B. Gelao, L. Fazio, P. Taurisano, A. Di Maio, V. Marsili, M. Pasqualetti, A. Bertolino, A. Usiello, Rasd2 modulates prefronto-striatal phenotypes in humans and "schizophrenia-like behaviors" in mice. *Neuropsychopharmacology* **41**, 916–927 (2016).
- R. G. Mealer, A. J. Murray, N. Shahani, S. Subramanian, S. H. Snyder, Rhes, a striatal-selective protein implicated in Huntington disease, binds beclin-1 and activates autophagy. *J. Biol. Chem.* **289**, 3547–3554 (2014).
- S. Subramanian, K. M. Sixt, R. Barrow, S. H. Snyder, Rhes, a striatal specific protein, mediates mutant-huntingtin cytotoxicity. *Science* **324**, 1327–1330 (2009).
- J. Pan, E. Song, C. Cheng, M.-H. Lee, S.-C. J. Yeung, Farnesyltransferase inhibitors-induced autophagy: Alternative mechanisms? *Autophagy* **5**, 129–131 (2009).
- L. B. Gordon, J. Massaro, R. B. D'Agostino Sr., S. E. Campbell, J. Brazier, W. T. Brown, M. E. Kleinman, M. W. Kieran, Progeria Clinical Trials Collaborative, Impact of farnesylation inhibitors on survival in Hutchinson-Gilford progeria syndrome. *Circulation* **130**, 27–34 (2014).
- M. W. Kieran, R. J. Packer, A. Onar, S. M. Blaney, P. Phillips, I. F. Pollack, J. R. Geyer, S. Gururangan, A. Banerjee, S. Goldman, C. D. Turner, J. B. Belasco, A. Broniscer, Y. Zhu, E. Frank, P. Kirschmeier, P. Statkevich, A. Yver, J. M. Boyett, L. E. Kun, Phase I and pharmacokinetic study of the oral farnesyltransferase inhibitor lonafarnib administered twice daily to pediatric patients with advanced central nervous system tumors using a modified continuous reassessment method: A Pediatric Brain Tumor Consortium study. *J. Clin. Oncol.* **25**, 3137–3143 (2007).
- S. Yust-Katz, D. Liu, Y. Yuan, V. Liu, S. Kang, M. Groves, V. Puduvalli, V. Levin, C. Conrad, H. Colman, S. Hsu, W. K. A. Yung, M. R. Gilbert, Phase 1/1b study of lonafarnib and temozolamide in patients with recurrent or temozolamide refractory glioblastoma. *Cancer* **119**, 2747–2753 (2013).
- A. Desjardins, D. A. Reardon, K. B. Peters, S. Threatt, A. D. Coan, J. E. Herndon II, A. H. Friedman, H. S. Friedman, J. J. Vredenburgh, A phase I trial of the farnesyl transferase

- inhibitor, SCH 66336, with temozolomide for patients with malignant glioma. *J. Neurooncol.* **105**, 601–606 (2011).
24. K. Santacruz, J. Lewis, T. Spires, J. Paulson, L. Kotilinek, M. Ingelsson, A. Guimaraes, M. DeTure, M. Ramsden, E. McGowan, C. Forster, M. Yue, J. Orne, C. Janus, A. Mariash, M. Kuskowski, B. Hyman, M. Hutton, K. H. Ashe, Tau suppression in a neurodegenerative mouse model improves memory function. *Science* **309**, 476–481 (2005).
 25. N. Menkes-Caspi, H. G. Yamin, V. Kellner, T. L. Spires-Jones, D. Cohen, E. A. Stern, Pathological tau disrupts ongoing network activity. *Neuron* **85**, 959–966 (2015).
 26. J. L. Crimins, A. B. Rocher, J. I. Luebke, Electrophysiological changes precede morphological changes to frontal cortical pyramidal neurons in the rTg4510 mouse model of progressive tauopathy. *Acta Neuropathol.* **124**, 777–795 (2012).
 27. G. Liu, S. A. Taylor, C. H. Marrinan, Y. Hsieh, W. R. Bishop, P. Kirschmeier, B. J. Long, Continuous and intermittent dosing of lonafarnib potentiates the therapeutic efficacy of docetaxel on preclinical human prostate cancer models. *Int. J. Cancer* **125**, 2711–2720 (2009).
 28. R. M. J. Deacon, Digging and marble burying in mice: Simple methods for in vivo identification of biological impacts. *Nat. Protoc.* **1**, 122–124 (2006).
 29. R. M. J. Deacon, Assessing nest building in mice. *Nat. Protoc.* **1**, 1117–1119 (2006).
 30. D. Gabriel, D. D. Shafry, L. B. Gordon, K. Djabali, Intermittent treatment with farnesyltransferase inhibitor and sulforaphane improves cellular homeostasis in Hutchinson-Gilford progeria fibroblasts. *Oncotarget* **8**, 64809–64826 (2017).
 31. J. W. Wojtkowiak, K. M. Sane, M. Kleinman, B. F. Sloane, J. J. Reiners Jr., R. R. Mattingly, Aborted autophagy and nonapoptotic death induced by farnesyl transferase inhibitor and lovastatin. *J. Pharmacol. Exp. Ther.* **337**, 65–74 (2011).
 32. S. Kimura, T. Noda, T. Yoshimori, Dissection of the autophagosome maturation process by a novel reporter protein, tandem fluorescent-tagged LC3. *Autophagy* **3**, 452–460 (2007).
 33. H. Koga, M. Martinez-Vicente, F. Macian, V. V. Verkhusha, A. M. Cuervo, A photoconvertible fluorescent reporter to track chaperone-mediated autophagy. *Nat. Commun.* **2**, 386 (2011).
 34. R. Sahu, S. Kaushik, C. C. Clement, E. S. Cannizzo, B. Scharf, A. Follenzi, I. Potolicchio, E. Nieves, A. M. Cuervo, L. Santambrogio, Microautophagy of cytosolic proteins by late endosomes. *Dev. Cell* **20**, 131–139 (2011).
 35. R. Greussing, H. Unterluggauer, R. Koziel, A. B. Maier, P. Jansen-Dürr, Monitoring of ubiquitin-proteasome activity in living cells using a Degron (dgn)-destabilized green fluorescent protein (GFP)-based reporter protein. *J. Vis. Exp.* e3327 (2012).
 36. H.-B. Luo, Y.-Y. Xia, X.-J. Shu, Z.-C. Liu, Y. Feng, X.-H. Liu, G. Yu, G. Yin, Y.-S. Xiong, K. Zeng, J. Jiang, K. Ye, X.-C. Wang, J.-Z. Wang, SUMOylation at K340 inhibits tau degradation through deregulating its phosphorylation and ubiquitination. *Proc. Natl. Acad. Sci. U.S.A.* **111**, 16586–16591 (2014).
 37. L. Petruccielli, D. Dickson, K. Kehoe, J. Taylor, H. Snyder, A. Grover, M. De Lucia, E. McGowan, J. Lewis, G. Prihar, J. Kim, W. H. Dillmann, S. E. Browne, A. Hall, R. Voellmy, Y. Tsuboi, T. M. Dawson, B. Wolozin, J. Hardy, M. Hutton, CHIP and Hsp70 regulate tau ubiquitination, degradation and aggregation. *Hum. Mol. Genet.* **13**, 703–714 (2004).
 38. P. Vargiu, R. D. Abajo, J. A. Garcia-Ranea, A. Valencia, P. Santisteban, P. Crespo, J. Bernal, The small GTP-binding protein, Rhes, regulates signal transduction from G protein-coupled receptors. *Oncogene* **23**, 559–568 (2004).
 39. M. G. Spillantini, M. Goedert, Tau pathology and neurodegeneration. *Lancet Neurol.* **12**, 609–622 (2013).
 40. A. Iyer, N. E. Lapointe, K. Zielke, M. Berdynski, E. Guzman, A. Barczak, M. Chodakowska-Zebrowska, M. Bartkowska, S. Feinstein, C. Zekanowski, A novel MAPT mutation, G55R, in a frontotemporal dementia patient leads to altered tau function. *PLOS ONE* **8**, e76409 (2013).
 41. M. Hutton, C. L. Lendon, P. Rizzu, M. Baker, S. Froelich, H. Houlden, S. Pickering-Brown, S. Chakraverty, A. Isaacs, A. Grover, J. Hackett, J. Adamson, S. Lincoln, D. Dickson, P. Davies, R. C. Petersen, M. Stevens, E. de Graaff, E. Wauters, J. van Baren, M. Hillebrand, M. Joosse, J. M. Kwon, P. Nowotny, L. K. Che, J. Norton, J. C. Morris, L. A. Reed, J. Trojanowski, H. Basun, L. Lannfelt, M. Neystat, S. Fahn, F. Dark, T. Tannenberg, P. R. Dodd, N. Hayward, J. B. J. Kwok, P. R. Schofield, A. Andreadis, J. Snowden, D. Craufurd, D. Neary, F. Owen, B. A. Oostra, J. Hardy, A. Goate, J. van Swieten, D. Mann, T. Lynch, P. Heutink, Association of missense and 5'-splice-site mutations in tau with the inherited dementia FTDP-17. *Nature* **393**, 702–705 (1998).
 42. M. Hasegawa, M. J. Smith, M. Goedert, Tau proteins with FTDP-17 mutations have a reduced ability to promote microtubule assembly. *FEBS Lett.* **437**, 207–210 (1998).
 43. M. DeJesus-Hernandez, I. R. Mackenzie, B. F. Boeve, A. L. Boxer, M. Baker, N. J. Rutherford, A. M. Nicholson, N. A. Finch, H. Flynn, J. Adamson, N. Kouri, A. Wojtas, P. Sengdy, G.-Y. R. Hsiung, A. Karydas, W. W. Seeley, K. A. Josephs, G. Coppola, D. H. Geschwind, Z. K. Wszolek, H. Feldman, D. S. Knopman, R. C. Petersen, B. L. Miller, D. W. Dickson, K. B. Boylan, N. R. Graff-Radford, R. Rademakers, Expanded GGGGCC hexanucleotide repeat in noncoding region of C9ORF72 causes chromosome 9p-linked FTD and ALS. *Neuron* **72**, 245–256 (2011).
 44. B. Zhou, W. H. Wong, A bootstrap-based non-parametric ANOVA method with applications to factorial microarray data. *Stat. Sin.* **21**, 495 (2011).
 45. D. C. Garretto, I. Hernandez, P. Neveu, T. Papagiannakopoulos, K. S. Kosik, The cochaperone BAG2 sweeps paired helical filament- insoluble tau from the microtubule. *J. Neurosci.* **29**, 2151–2161 (2009).
 46. V. Schaeffer, I. Lavenir, S. Ozcelik, M. Tolnay, D. T. Winkler, M. Goedert, Stimulation of autophagy reduces neurodegeneration in a mouse model of human tauopathy. *Brain* **135**, 2169–2177 (2012).
 47. J. Jang, Y. Wang, H.-S. Kim, M. A. Lalli, K. S. Kosik, Nrf2, a regulator of the proteasome, controls self-renewal and pluripotency in human embryonic stem cells. *Stem Cells* **32**, 2616–2625 (2014).
 48. R. I. Morimoto, A. M. Cuervo, Proteostasis and the aging proteome in health and disease. *J. Gerontol. A Biol. Sci. Med. Sci.* **69** (suppl. 1), S33–S38 (2014).
 49. J. H. Lee, L. Tededor, Y. H. Chen, A. M. Monteys, M. J. Sowada, L. M. Thompson, B. L. Davidson, Reinstating aberrant mTORC1 activity in Huntington's disease mice improves disease phenotypes. *Neuron* **85**, 303–315 (2015).
 50. F. Napolitano, E. Booth Warren, S. Migliarini, D. Punzo, F. Errico, Q. Li, M.-L. Thiolat, A. L. Vesco, P. Calabresi, E. Bezard, M. Morelli, C. Konradi, M. Pasqualetti, A. Usiello, Decreased Rhes mRNA levels in the brain of patients with Parkinson's disease and MPTP-treated macaques. *PLOS ONE* **12**, e0181677 (2017).
 51. P. A. Desplats, K. E. Kass, T. Gilman, G. D. Stanwood, E. L. Woodward, S. R. Head, J. G. Sutcliffe, E. A. Thomas, Selective deficits in the expression of striatal-enriched mRNAs in Huntington's disease. *J. Neurochem.* **96**, 743–757 (2006).
 52. T. Seredenina, O. Gokce, R. Luthi-Carter, Decreased striatal RGS2 expression is neuroprotective in Huntington's disease (HD) and exemplifies a compensatory aspect of HD-induced gene regulation. *PLOS ONE* **6**, e22231 (2011).
 53. V. Prahlad, R. I. Morimoto, Integrating the stress response: Lessons for neurodegenerative diseases from *C. elegans*. *Trends Cell Biol.* **19**, 52–61 (2009).
 54. C. Voisine, J. S. Pedersen, R. I. Morimoto, Chaperone networks: Tipping the balance in protein folding diseases. *Neurobiol. Dis.* **40**, 12–20 (2010).
 55. G. Luna, S. Kjellstrom, M. R. Verardo, G. P. Lewis, J. Byun, P. A. Sieving, S. K. Fisher, The effects of transient retinal detachment on cavity size and glial and neural remodeling in a mouse model of X-linked retinoschisis. *Invest. Ophthalmol. Vis. Sci.* **50**, 3977–3984 (2009).
 56. J. Schindelin, I. Arganda-Carreras, E. Frise, V. Kaynig, M. Longair, T. Pietzsch, S. Reisch, C. Rueden, S. Saalfeld, B. Schmid, J.-Y. Tinevez, D. J. White, V. Hartenstein, K. Eliceiri, P. Tomancak, A. Cardona, Fiji: An open-source platform for biological-image analysis. *Nat. Methods* **9**, 676–682 (2012).
 57. I. Arganda-Carreras, V. Kaynig, C. Rueden, K. W. Eliceiri, J. Schindelin, A. Cardona, H. S. Seung, Trainable Weka segmentation: A machine learning tool for microscopy pixel classification. *Bioinformatics* **33**, 2424–2426 (2017).
 58. S. Kaushik, A. M. Cuervo, Chapter 19 methods to monitor chaperone-mediated autophagy. *Methods Enzymol.* **452**, 297–324 (2009).
 59. J. S. Auteri, A. Okada, V. Bochaki, J. F. Dice, Regulation of intracellular protein degradation in IMR-90 human diploid fibroblasts. *J. Cell. Physiol.* **115**, 167–174 (1983).
 60. D. Kim, G. Pertea, C. Trapnell, H. Pimentel, R. Kelley, S. L. Salzberg, TopHat2: Accurate alignment of transcriptomes in the presence of insertions, deletions and gene fusions. *Genome Biol.* **14**, R36 (2013).
 61. H. Li, B. Handsaker, A. Wysoker, T. Fennell, J. Ruan, N. Homer, G. Marth, G. Abecasis, R. Durbin, 1000 Genome Project Data Processing Subgroup, The Sequence Alignment/Map format and SAMtools. *Bioinformatics* **25**, 2078–2079 (2009).
 62. K. D. Pruitt, J. Harrow, R. A. Harte, C. Wallin, M. Diekhans, D. R. Maglott, S. Searle, C. M. Farrell, J. E. Loveland, B. J. Ruef, E. Hart, M.-M. Suner, M. J. Landrum, B. Aken, S. Ayling, R. Baertsch, J. Fernandez-Banet, J. L. Cherry, V. Curwen, M. DiCuccio, M. Kelis, J. Lee, M. F. Lin, M. Schuster, A. Shkeda, C. Amid, G. Brown, O. Dukhanina, A. Frankish, J. Hart, B. L. Maidak, J. Mudge, M. R. Murphy, T. Murphy, J. Rajan, B. Rajput, L. D. Riddick, C. Snow, C. Steward, D. Webb, J. A. Weber, L. Wilming, W. Wu, E. Birney, D. Haussler, T. Hubbard, J. Ostell, R. Durbin, D. Lipman, The consensus coding sequence (CCDS) project: Identifying a common protein-coding gene set for the human and mouse genomes. *Genome Res.* **19**, 1316–1323 (2009).
 63. M. D. Robinson, D. J. McCarthy, G. K. Smyth, edgeR: A Bioconductor package for differential expression analysis of digital gene expression data. *Bioinformatics* **26**, 139–140 (2009).
 64. D. J. McCarthy, Y. Chen, G. K. Smyth, Differential expression analysis of multifactor RNA-Seq experiments with respect to biological variation. *Nucleic Acids Res.* **40**, 4288–4297 (2012).
 65. M. E. Ritchie, B. Phipson, D. Wu, Y. Hu, C. W. Law, W. Shi, G. K. Smyth, limma powers differential expression analyses for RNA-sequencing and microarray studies. *Nucleic Acids Res.* **43**, e47 (2015).

Acknowledgments: We thank B. Davidson for designing and packaging AAVs used in this study; P. Davies for providing MC1, PHF-1, and ET3 antibodies; and Y. Huang for reprogramming CTR2 and CTR3 iPSC lines. We thank the NINDS Cell Repository for the fibroblast lines from the MAPT P301L and V337M mutation carriers, as well as H.-S. Kim and C. Park for reprogramming the MAPT-G55R iPSC line. We also thank P. Lansbury and M. Duggan for providing lonafarnib plasma and brain concentrations after oral administration to mice. **Funding:** This work was

funded by the Tau Consortium (K.S.K., A.M.C., A.M.G., and C.M.K.); NIH grants 1U54NS100717 (K.S.K. and A.M.C.), R01AG056058 (K.S.K.), R01AG054008 (A.M.G.), and AG046374 (C.M.K.); NSF grant ISS-0808772 and Information Technology Research (ITR) grant 0331697 (S.K.F.); Cohen Veterans Bioscience (K.S.K.); and the Leo and Ann Albert Charitable Trust (K.S.K.). N.J.S. was supported by a postdoctoral EMBO fellowship. **Author contributions:** I.H. and G.L. designed and performed experiments and wrote the manuscript. I.H. performed the statistical analyses. J.N.R., S.A.R., and S.J.H. performed experiments on Rhes biochemistry. M.G. performed mouse experiments and maintained colonies. D.B. and Y.E.S. performed immunohistochemistry and microscopy experiments. A.A.K. performed computational quantifications of brain micrographs and mosaics. C.R.H. and V.C. performed neuronal differentiation from hiPSCs. E.G. performed IonTorrent sequencing for RNAseq experiments. H.Z. performed RNA sequence mapping and quality control. C.M.K. and A.M.G. contributed isogenic neuron complementary DNA for Rhes quantitation and iPSC line generation. C.Z. identified patients with frontotemporal dementia carrying the MAPT-G55R mutation, collected skin fibroblasts, and prepared primary fibroblast cultures. N.J.S., A.D., S.K., and A.M.C. designed and performed experiments of lonafarnib's effects in proteolysis and lysosomes. S.K.F. performed image analysis and critiqued the manuscript. K.S.K. conceived the experiments and wrote the manuscript. **Competing interests:** K.S.K. consults for ADRx. A.M.C. is cofounder of Selphagy. A.M.G. has served on the scientific advisory board of Denali Therapeutics (2015–2018) and has consulted for Cognition Therapeutics, AbbVie, Eisai, Biogen, GSK, and Pfizer. S.J.H. has consulted for Rodin Therapeutics, Frequency Therapeutics, Psy Therapeutics, and AstraZeneca and has

received speaker fees from Amgen and Merck. K.S.K. and I.H. are coinventors on patent no. US2018/013712 entitled "Treatment of neurodegenerative conditions by disruption of Rhes."

Data and materials availability: All data associated with this paper are in the main text or Supplementary Materials. hiPSCs used in this study were obtained under material transfer agreements executed at UCSB (Kosik-Huang, 014344-0002, and 014344-0003). All digital image datasets used for spatial analyses have been deposited to BisQue (Bio-Image Semantic Query User Environment) (60) and are publically available for further use with permission: https://bisque.ece.ucsb.edu/client_service/view?resource=https://bisque.ece.ucsb.edu/data_service/00-iZXFv5ELXaikLm12viaSRJ.

Submitted 14 February 2018

Resubmitted 15 August 2018

Accepted 30 November 2018

Published 27 March 2019

10.1126/scitranslmed.aat3005

Citation: I. Hernandez, G. Luna, J. N. Rauch, S. A. Reis, M. Giroux, C. M. Karch, D. Boctor, Y. E. Sibih, N. J. Storm, A. Diaz, S. Kaushik, C. Zekanowski, A. A. Kang, C. R. Hinman, V. Cerovac, E. Guzman, H. Zhou, S. J. Haggarty, A. M. Goate, S. K. Fisher, A. M. Cuervo, K. S. Kosik, A farnesyltransferase inhibitor activates lysosomes and reduces tau pathology in mice with tauopathy. *Sci. Transl. Med.* **11**, eaat3005 (2019).



北京大學
PEKING UNIVERSITY

Exploration of Brain Extracellular Space in China



Professor Hongbin Han is the director of a key laboratory at Peking University (PKU) who is working on brain Extracellular Space (ECS), an incompletely understood and explored area which

provides an immediate living environment for neural circuit and accounts for approximately 15%-20% of the total volume in a living brain. Twenty-five years ago, as an interventional radiologist, Han engaged himself in the early diagnosis and treatment of cerebral ischemia. While studying the permeability of blood-brain barrier (BBB) by using dynamic contrast enhanced MRI, he, by accident, acquired a parameter of the space outside the cellular and vascular compartments. It was the first time that the ECS parameter of the human brain was detected and demonstrated by MRI. Since then, for 15 years, he and his team have been working on developing new ECS measuring methods which can visualize the dynamic drainage process of labeled brain Interstitial Fluid (ISF) and obtain ECS parameters in the deep brain. There are two methods, RTI-TMA+ and IOI, which can help acquire the biophysical parameters of brain ECS one or two-dimensionally, while the ECS in the deep brain cannot be detected and analyzed. Tracer-based MRI, the only one based on anisotropic modeling, can acquire and calculate the molecular diffusion



parameters on a large scale and visualize the drainage route of the labeled ISF in the whole brain.

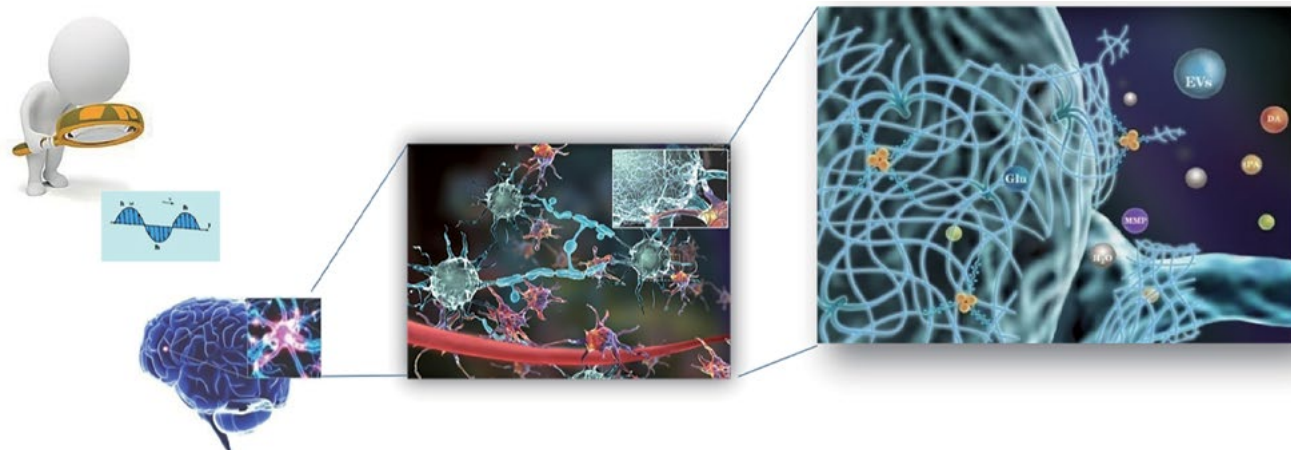
By using their self-developed measuring system, Prof. Han and his team have made a series of discoveries about ECS and ISF. They have found that the brain ISF drains in a compartmentalized ECS system and the biophysical characteristics in separated ECS divisions are different: the traced ISF from the caudate nucleus drains to the ipsilateral cortex along myelin fiber tracts, while in the opposite direction, its movement to the adjacent thalamus is completely impeded by a barrier structure which has been identified as the converged, compact myelin fascicle. After verifying the nature of the barrier structure between different drainage divisions, Prof. Han proposed the hypothesis of "compartmentalized homeostasis" and thus demonstrated that the brain is protected not only by BBB which avoids exogenous damage through the vascular system, but also by an internal ISF drainage barrier to avoid harmful interference from other ECS divisions.

With the new findings and the proposed

hypothesis, an innovative therapeutic method for encephalopathy with local drug delivery via the brain ECS has been established. By using this new administration method, the drug is delivered directly to the space around neurons or target regions, overwhelming the impedance from BBB, thus removing the obstacles of low efficiency in traditional drug administration and re-adopting Citicoline, a neuroprotective drug declared ineffective by *Nature Reviews Neurology* in 2012. As the tracer-based MRI method can accurately calculate and predict the drug transportation and distribution routes in ECS, the location of drug administration and the concentration dose can be precisely designed according to the characteristics of the lesions. The results have shown that the treatment effect, with only 1/800 of the standard dosage, is 6 times better than the traditional method. Furthermore, the efficiency in administering the herbal medicine "Acteoside" via ECS at PKU School of Pharmaceutical Sciences, has also been enhanced. The research was approved as a US patented invention in 2015. Recently, a non-invasive brain ECS imaging technique has been established using MRI, which can scan ECS structure in the human brain.

Today, these new measuring techniques and technologies have been applied in many frontier fields, such as neuroscience, new drug development, development and aging, aerospace medicine, clinical encephalopathy treatment and artificial neural network modeling. Neurologists used to focus only on brain cells and neural circuit, and few achievements have been made in treating AD and stroke patients via the two-compartment model. With the two-compartment model upgraded to the three-compartment model, more breakthroughs in neuroscience are expected to be made in the future.

Please feel free to contact Professor Hongbin Han, hanhongbin@bjmu.edu.cn



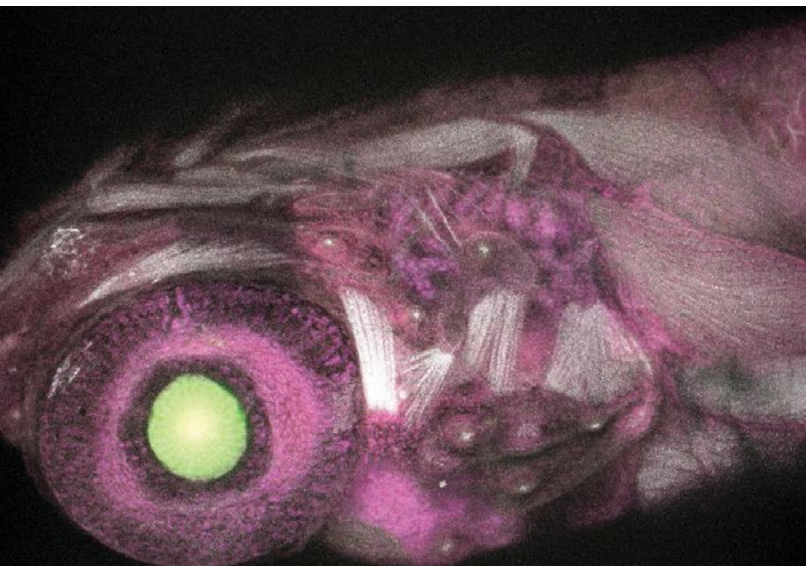


NIS-Elements **AI**

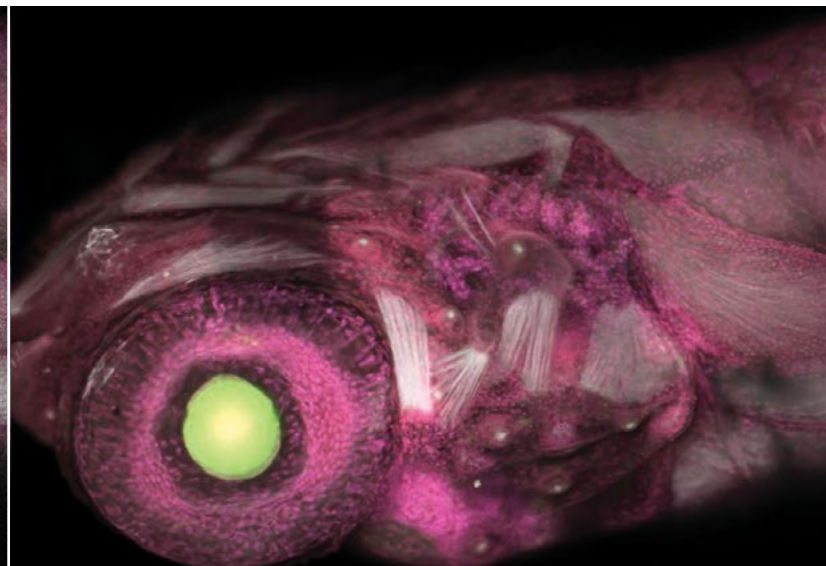
Push Your Imaging Past the Limits

NIS-Elements AI

Predictive Imaging with Deep Learning



Original



With Denoise.AI

Nikon's new Artificial Intelligence (AI) feature for its NIS-Elements imaging software leverages deep learning to remove shot noise from resonant confocal images in real-time, resulting in breathtakingly clear images using minimal excitation power.

**See Nikon at Neuroscience 2019
Booth #1201**

To see how Nikon is using AI to transform your imaging,
visit www.microscope.healthcare.nikon.com/nis-elements-ai

